

APPLICATIONS AND OPTIMIZATION OF TITANIUM CATALYSIS

By

Tanner James McDaniel

A DISSERTATION

Submitted to  
Michigan State University  
in partial fulfillment of the requirements  
for the degree of

Chemistry – Doctor of Philosophy

2017

# ABSTRACT

## APPLICATIONS AND OPTIMIZATION OF TITANIUM CATALYSIS

By

Tanner James McDaniel

Nitrogen containing compounds, such as amines, imines, enamines and a variety of heterocycles are incredibly valuable. These compounds are prevalent in many pharmaceuticals, organic dyes, solar cells, and natural products. Therefore, new synthetic routes into these nitrogen containing compounds is highly desirable. Our group has been exploring a titanium-catalyzed multicomponent coupling reaction to synthesize a wide variety of nitrogen containing compounds (**Chapter 1**). Using these titanium-based catalysts, our group has developed a variety of substituted quinolines, which have been shown to be novel proteasome inhibitors (**Chapter 2**). Our group has also developed a new tool to help evaluate ligand donation, which has allowed us to expand and develop a better understanding of the titanium-based catalysts (**Chapters 3 & 4**).

To My Family and Friends

## ACKNOWLEDGMENTS

First, I would like to thank Professor Aaron Odom (i.e. academic dad). I knew in undergrad that I wanted to join your research group for my graduate research. Thank you for letting be a part of your group, as well as, all the support and guidance you have given me. I am eternally grateful for all that you have taught me over the years.

I would also like to thank all my committee members: 1) Professor Xuefei Huang for being my second reader, and for giving me advice through my second-year seminar and candidacy exam. 2) Professor Jetze Tepe for being an incredible collaborator over the years, on the quinoline project, and being a great teacher in heterocycles. 3) Professor William Wulff for letting me contribute to his natural product database, and being a great organic synthesis teacher. Each one of my committee members have provided me with support, advice, and inspiration throughout my graduate studies.

I would like to give a special thanks to Professor Mitch Smith. He provided me with motivation, advice, and guidance throughout graduate school. Even though he wasn't on my committee, he was always excited to discuss chemistry with me.

In addition, I would like to thank Dr. Richard Staples for always being there to give guidance and advice. I would also like to thank Dr. Daniel Holmes for all his help with our NMR studies and giving Brennan and I our own NMR.

During my graduate studies I was fortunate to go through the program with some amazing people. These people provided support, motivation and made each day enjoyable at Michigan State University. Thank you, Elizabeth, Olivia, Pengchao, Yu-ling, Behnaz, Kristin, Tim, Kristen,



Corey, Travis, Taylor, Cody, Dani, Matt, Josh, Mersedeh, Dan, Evan, Caitlin, Suzi, Ross, Guangtu, and Amrendra.

Special thanks to my academic brother (Brennan) and academic sister (Kelly) for being amazing friends throughout graduate school and providing me with advice along the way.

My family and friends have always supported me through my adventures. Thank you all for the love and support you gave me through the years. Thank you, Mom, Dad, Darla, Alice, Tatum, Susan, Cindy, Alex, Ian, Josh, Cody and Chelsea.

Lastly, I would like to thank my wife Michelle. Throughout graduate school you provided me with encouragement, motivation and support. Whenever I was stressed, coming home to you and Atom (dog) always made me feel better. Thank you for being an understanding, caring, and patient person.

# TABLE OF CONTENTS

<b>LIST OF TABLES .....</b>	<b>viii</b>
<b>LIST OF FIGURES .....</b>	<b>x</b>
<b>LIST OF SCHEMES .....</b>	<b>xix</b>
<b>KEY TO ABBREVIATIONS .....</b>	<b>xxii</b>
<b>Chapter 1. Introduction to Group-4 Transition Metal C-N Bond Formation .....</b>	<b>1</b>
1.1 Background and Motivation .....	1
1.2 Hydroamination Introduction.....	2
1.3 The Mechanisms for Transition Metal Catalyzed Hydroamination .....	6
1.4 The Hydroamination of Alkynes in the Odom Group .....	12
1.5 Iminoamination in the Odom Group.....	17
1.6 The Synthesis of Nitrogen-based Heterocycles in the Odom Group.....	22
REFERENCES .....	23
<b>Chapter 2. Substituted Quinolines as Non-Covalent Proteasome Inhibitors.....</b>	<b>27</b>
2.1 Introduction to the Proteasome .....	27
2.2 Proteasome Inhibitors .....	31
2.3 Classical Examples of Quinoline Synthesis.....	40
2.4 The Odom Group's Quinoline Synthesis.....	42
2.5 Results and Discussion .....	45
2.6 Conclusion .....	59
2.7 Experimental .....	60
REFERENCES .....	128
<b>Chapter 3: Quantifying Ancillary Ligand Effects in Titanium(IV) Catalyzed Hydroamination<sup>1</sup>.....</b>	<b>134</b>
3.1 Introduction.....	134
3.2 Background.....	135
3.3 Ligand Donor Parameter (LDP).....	138
3.4 Titanium-Catalyzed Hydroamination of Alkynes.....	140
3.5 Percent Buried Volume (% V <sub>bur</sub> ) .....	142
3.6 Synthesis, Kinetics and Model Progression.....	145
3.7 Results and Discussion .....	172
3.8 Conclusion .....	178
3.9 Experimental .....	179
REFERENCES .....	258

<b>Chapter 4. Quantifying Unsymmetrical Ancillary Ligand Effects in Titanium(IV)</b>	
<b>Catalyzed Hydroamination .....</b>	<b>263</b>
4.1 Background and Motivation .....	263
4.2 Introduction into Unsymmetrical Ligand Environments .....	263
4.3 Model Considerations and Ligand Development .....	268
4.4 Results and Discussion .....	278
4.5 Future Ligand Development .....	283
4.6 Conclusion .....	286
4.7 Experimental .....	287
REFERENCES .....	331

## LIST OF TABLES

<b>Table 1.1.</b> Thermodynamic data for various hydroamination reactions. <sup>7, 10</sup> .....	3
<b>Table 1.2.</b> Thermodynamic data for the hydroamination of ethylene and ammonia at various temperatures. <sup>10</sup> .....	4
<b>Table 1.3.</b> Alkyne hydroamination using catalysts $\text{Ti}(\text{dpma})(\text{NMe}_2)_2$ ( <b>1</b> ), $\text{Ti}(\text{dpm})(\text{NMe}_2)_2$ ( <b>2</b> ). <sup>41-42</sup> .....	15
<b>Table 1.4.</b> Hydroamination of enynes using $\text{Ti}(\text{dpm})(\text{NMe}_2)_2$ ( <b>2</b> ) or $\text{Ti}(\text{dap})_2(\text{NMe}_2)_2$ ( <b>3</b> ). <sup>43</sup> .....	16
<b>Table 2.1.</b> Structure and IC <sub>50</sub> of substituted quinolines ( <b>1-7</b> ) for inhibition of CT-L activity of the 20S proteasome. ....	46
<b>Table 2.2.</b> Structure and IC <sub>50</sub> of substituted quinolines ( <b>4, 7-12</b> ), by varying substituents in the R1 and R2 positions, for inhibition of CT-L activity of the 20S proteasome. ....	51
<b>Table 2.3.</b> Structure and IC <sub>50</sub> of substituted quinolines ( <b>7, 9, 13-18</b> ), by varying substituents in the R3–R5 positions, for inhibition of CT-L activity of the 20S proteasome. ....	53
<b>Table 2.4.</b> Structure and IC <sub>50</sub> of substituted quinolines, by varying substituents in the R4 positions, for inhibition of CT-L activity of the 20S proteasome. ....	55
<b>Table 2.5.</b> Structure and IC <sub>50</sub> of substituted quinolines, by varying substituents in the R1, R2, R4 positions, for inhibition of CT-L activity of the 20S proteasome. ....	57
<b>Table 2.6.</b> Statistical analysis for the inhibition of chymotryptic-like activity of purified human 20S proteasome (Quinoline <b>1</b> to <b>5</b> ). ....	85
<b>Table 2.7.</b> Statistical analysis for the inhibition of chymotryptic-like activity of purified human 20S proteasome (Quinoline <b>6</b> to <b>10</b> ). ....	86
<b>Table 2.8.</b> Statistical analysis for the inhibition of chymotryptic-like activity of purified human 20S proteasome (Quinoline <b>11</b> to <b>15</b> ). ....	87
<b>Table 2.9.</b> Statistical analysis for the inhibition of chymotryptic-like activity of purified human 20S proteasome (Quinoline <b>16</b> to <b>20</b> ). ....	88
<b>Table 2.10.</b> Statistical analysis for the inhibition of chymotryptic-like activity of purified human 20S proteasome (Quinoline <b>21</b> to <b>25</b> ). ....	89
<b>Table 2.11.</b> Statistical analysis for the inhibition of chymotryptic-like activity of purified human 20S proteasome (Quinoline <b>26</b> to <b>30</b> ). ....	90

<b>Table 2.12.</b> Statistical analysis for the inhibition of chymotryptic-like activity of purified human 20S proteasome (Quinoline <b>31</b> to <b>35</b> ). .....	91
<b>Table 2.13.</b> Statistical analysis for the inhibition of chymotryptic-like activity of purified human 20S proteasome (Quinoline <b>36</b> to <b>38</b> ). .....	92
<b>Table 3.1.</b> Rates, LDP, and % V <sub>bur</sub> Used for Modeling.....	183
<b>Table 4.1.</b> Rates, LDP and % V <sub>bur</sub> for titanium catalysts with symmetrical <sup>10</sup> and unsymmetrical ligands. <sup>13</sup> .....	279
<b>Table 4.2.</b> Predicted rate, using previous model, versus experimental rate. ....	280

## LIST OF FIGURES

<b>Figure 1.1.</b> [2+2]-cycloaddition of amine and alkene. <sup>10</sup> .....	3
<b>Figure 1.2.</b> [2+2]-cycloaddition between a metal-imido and olefin. ....	10
<b>Figure 1.3.</b> Effects of precatalyst on regioselectivity using an aryl amine. <sup>41, 46</sup> .....	21
<b>Figure 2.1.</b> The composition of the 26S proteasome. <sup>6</sup> .....	28
<b>Figure 2.2.</b> FDA approved proteasome inhibitors bortezomib, carfilzomib, and ixazomib. ....	36
<b>Figure 2.3.</b> Groll's noncovalent sulfonamide substituted quinoline inhibitor. <sup>54</sup> .....	38
<b>Figure 2.4.</b> Quinoline allosteric proteasome inhibitors. ....	39
<b>Figure 2.5.</b> The quinoline scaffold and the numbering system. ....	40
<b>Figure 2.6.</b> Evaluation of quinoline <b>7</b> 's CT-L, Casp-L, and T-L activities in purified human 20S proteasome. The fluorogenic substrates Suc-LLVY-AMC, Z-LLE-AMC and Boc-LRR-AMC were used, respectively. <sup>57</sup> .....	47
<b>Figure 2.7.</b> Lineweaver-Burke plot using quinoline <b>7</b> and substrate Suc-LLVY-AMC. <sup>57</sup> .....	48
<b>Figure 2.8.</b> Evaluation of quinoline <b>7</b> using HeLa NF-κB-luc cells. <sup>57</sup> .....	49
<b>Figure 2.9.</b> Evaluation of quinoline <b>25</b> 's CT-L, Casp-L, and T-L activities in purified human 20S proteasome. The fluorogenic substrates Suc-LLVY-AMC, Z-LLE-AMC and Boc-LRR-AMC were used, respectively. ....	58
<b>Figure 2.10.</b> The inhibition of chymotryptic-like activity of purified human 20S proteasome (Quinolines <b>1</b> to <b>8</b> ). ....	80
<b>Figure 2.11.</b> The inhibition of chymotryptic-like activity of purified human 20S proteasome (Quinolines <b>9</b> to <b>16</b> ). ....	81
<b>Figure 2.12.</b> The inhibition of chymotryptic-like activity of purified human 20S proteasome (Quinolines <b>7</b> to <b>24</b> ). ....	82
<b>Figure 2.13.</b> The inhibition of chymotryptic-like activity of purified human 20S proteasome (Quinolines <b>25</b> to <b>32</b> ). ....	83
<b>Figure 2.14.</b> The inhibition of chymotryptic-like activity of purified human 20S proteasome (Quinolines <b>33</b> to <b>38</b> ). ....	84

<b>Figure 2.15.</b> $^1\text{H}$ NMR spectra for compound 2-ethyl-3-cyclohexenyl-5,7-dimethylquinoline ( <b>8</b> ).	93
<b>Figure 2.16.</b> $^{13}\text{C}$ NMR spectra for compound 2-ethyl-3-cyclohexenyl-5,7-dimethylquinoline ( <b>8</b> ).	94
<b>Figure 2.17.</b> $^1\text{H}$ NMR spectra for compound 6-bromo-3-cyclohexenyl-2-methylquinoline ( <b>16</b> ).	95
<b>Figure 2.18.</b> $^{13}\text{C}$ NMR spectra for compound 6-bromo-3-cyclohexenyl-2-methylquinoline ( <b>16</b> ).	96
<b>Figure 2.19.</b> $^1\text{H}$ NMR spectra for compound 6-chloro-3-cyclohexenyl-2-methylquinoline ( <b>17</b> ).	97
<b>Figure 2.20.</b> $^{13}\text{C}$ NMR spectra for compound 6-chloro-3-cyclohexenyl-2-methylquinoline ( <b>17</b> ).	98
<b>Figure 2.21.</b> $^1\text{H}$ NMR spectra for compound 6-butyl-3-cyclohexenyl-2-methylquinoline ( <b>20</b> ).	99
<b>Figure 2.22.</b> $^{13}\text{C}$ NMR spectra for compound 6-butyl-3-cyclohexenyl-2-methylquinoline ( <b>20</b> ).	100
<b>Figure 2.23.</b> $^1\text{H}$ NMR spectra for compound 3-cyclohexenyl-6-(N,N-dimethylamino)quinoline ( <b>21</b> ).	101
<b>Figure 2.24.</b> $^{13}\text{C}$ NMR spectra for compound 3-cyclohexenyl-6-(N,N-dimethylamino)quinoline ( <b>21</b> ).	102
<b>Figure 2.25.</b> $^1\text{H}$ NMR spectra for compound 3-cyclohexenyl-2-ethyl-6(N,N-dimethylamino)quinoline ( <b>23</b> ).	103
<b>Figure 2.26.</b> $^{13}\text{C}$ NMR spectra for compound 3-cyclohexenyl-2-ethyl-6(N,N-dimethylamino)quinoline ( <b>23</b> ).	104
<b>Figure 2.27.</b> $^1\text{H}$ NMR spectra for compound 3-cyclohexenyl-5,6,7-trimethoxy-2-methylquinoline ( <b>27</b> ).	105
<b>Figure 2.28.</b> $^{13}\text{C}$ NMR spectra for compound 3-cyclohexenyl-5,6,7-trimethoxy-2-methylquinoline ( <b>27</b> ).	106
<b>Figure 2.29.</b> $^1\text{H}$ NMR spectra for compound 3-cyclohexenyl-6-isopropyl-2-methylquinoline ( <b>28</b> ).	107
<b>Figure 2.30.</b> $^{13}\text{C}$ NMR spectra for compound 3-cyclohexenyl-6-isopropyl-2-methylquinoline ( <b>28</b> ).	108
<b>Figure 2.31.</b> $^1\text{H}$ NMR spectra for compound 3-cyclohexyl-6-(N,N-dimethylamino)quinoline ( <b>29</b> ).	109

<b>Figure 2.32.</b> $^{13}\text{C}$ NMR spectra for compound 3-cyclohexyl-6-(N,N-dimethylamino)quinoline (29).	110
<b>Figure 2.33.</b> $^1\text{H}$ NMR for compound 3-cyclohexyl-2-methyl-6-(N,N-dimethylamino)quinoline (30).	111
<b>Figure 2.34.</b> $^{13}\text{C}$ NMR for compound 3-cyclohexyl-2-methyl-6-(N,N-dimethylamino)quinoline (30).	112
<b>Figure 2.35.</b> $^1\text{H}$ NMR spectra for compound 3- <i>tert</i> -butyl-6-(N,N-dimethylamino)quinoline (32).	113
<b>Figure 2.36.</b> $^{13}\text{C}$ NMR spectra for compound 3- <i>tert</i> -butyl-6-(N,N-dimethylamino)quinoline (32).	114
<b>Figure 2.37.</b> $^1\text{H}$ NMR spectra for compound 2-butyl-6-(N,N-dimethylamino)quinoline (33).	115
<b>Figure 2.38.</b> $^{13}\text{C}$ NMR spectra for compound 2-butyl-6-(N,N-dimethylamino)quinoline (33).	116
<b>Figure 2.39.</b> $^1\text{H}$ NMR spectra for compound 2,3-diethyl-N,N-dimethylquinoline (34).	117
<b>Figure 2.40.</b> $^{13}\text{C}$ NMR spectra for compound 2,3-diethyl-N,N-dimethylquinoline (34).	118
<b>Figure 2.41.</b> $^1\text{H}$ NMR spectra for compound 2,3-diphenyl-6-(N,N-dimethylamino)quinoline (35).	119
<b>Figure 2.42.</b> $^{13}\text{C}$ NMR spectra for compound 2,3-diphenyl-6-(N,N-dimethylamino)quinoline (35).	120
<b>Figure 2.43.</b> $^1\text{H}$ NMR spectra for compound 6-butyl-2-methyl-3-phenylquinoline (36).	121
<b>Figure 2.44.</b> $^{13}\text{C}$ NMR spectra for compound 6-butyl-2-methyl-3-phenylquinoline (36).	122
<b>Figure 2.45.</b> $^1\text{H}$ NMR spectra for compound 6-isopropyl-2-methyl-3-phenylquinoline (37).	123
<b>Figure 2.46.</b> $^{13}\text{C}$ NMR spectra for compound 6-isopropyl-2-methyl-3-phenylquinoline (37).	124
<b>Figure 2.47.</b> $^1\text{H}$ NMR spectra for compound 6-bromo-2-methyl-3-phenylquinoline (38).	125
<b>Figure 2.48.</b> $^{13}\text{C}$ NMR spectra for compound 6-bromo-2-methyl-3-phenylquinoline (38).	126
<b>Figure 2.49.</b> Crystal structure of 6-bromo-3-cyclohexenyl-2-methylquinoline (38).	127
<b>Figure 3.1.</b> Tolman Electronic Parameter ( $\chi$ ). <sup>12</sup>	135
<b>Figure 3.2.</b> Tolman Cone Angle ( $\theta$ ). <sup>12</sup>	136
<b>Figure 3.3.</b> The Ligand Donor Parameter (LDP) system. <sup>1</sup>	138



<b>Figure 3.4.</b> Collection of LDP values for a variety of ligands. ....	139
<b>Figure 3.5.</b> The proposed mechanism for titanium-catalyzed alkyne hydroamination.....	140
<b>Figure 3.6.</b> Kinetic conditions for this study. <sup>1</sup> .....	141
<b>Figure 3.7.</b> Percent Buried Volume (% $V_{bur}$ ) is defined as the percent of the total volume of a sphere occupied by a ligand. For % $V_{bur}$ calculations 3.5 Å was selected as the value for the sphere radius (R) and metal-ligand length (d) is determined from the X-ray crystallography. <sup>26</sup>	142
<b>Figure 3.8.</b> Representation of how % $V_{bur}$ is measured. (a) <b>Top:</b> The catalyst Ti(dpm)(NMe <sub>2</sub> ) <sub>2</sub> was modeled from the unsubstituted chromium-pyrrole complex. This chromium complex is used to measure both electronics and sterics. (b) <b>Bottom:</b> A space-filling model representing the chromium-pyrrole complex, used to determine % $V_{bur}$ . The ligand of interest, pyrrole (shown in red), overlaps with the blue 3.5 Å sphere. The color mixing from this overlap (shown as purple) is the % $V_{bur}$ . <sup>1</sup> .....	144
<b>Figure 3.9.</b> Observed rate constants for various titanium dipyrrolemethane catalysts. <sup>27-28</sup> .....	146
<b>Figure 3.10.</b> Rates, LDP, and % $V_{bur}$ used for modeling catalysts 1a-1c. ....	151
<b>Figure 3.11.</b> Plot of experimental rate constant versus model predicted rate constant for catalysts 1a-1c. ....	151
<b>Figure 3.12.</b> Rates, LDP, and % $V_{bur}$ used for modeling catalysts 1d-2b.....	154
<b>Figure 3.13.</b> Plot of experimental rate constant versus model predicted rate constant for catalysts 1d-2b.....	155
<b>Figure 3.14.</b> Rate, LDP, and % $V_{bur}$ used for modeling catalyst 3. ....	157
<b>Figure 3.15.</b> Plot of experimental rate constant versus model predicted rate constant for catalyst 3.....	158
<b>Figure 3.16.</b> Rates, LDP, and % $V_{bur}$ used for modeling catalysts 4a-4b.....	162
<b>Figure 3.17.</b> Plot of experimental rate constant versus model predicted rate constant with catalysts 4a-4b. ....	163
<b>Figure 3.18.</b> Rate, LDP, and % $V_{bur}$ used for modeling catalyst 5. ....	165
<b>Figure 3.19.</b> Plot of experimental rate constant versus model predicted rate constant with catalyst 5. ....	165
<b>Figure 3.20.</b> Proposed products being produced by Ti(dpm <sup>3-[C<sub>6</sub>H<sub>3</sub>(CF<sub>3</sub>)<sub>2</sub>])(NMe<sub>2</sub>)<sub>2</sub> (5). ....</sup>	166
<b>Figure 3.21.</b> ORTEP structure of Ti(dithioBINAP)(NMe <sub>2</sub> ) <sub>2</sub> (6).....	168
<b>Figure 3.22.</b> Molecular weight calibration of Ti(dithioBINAP)(NMe <sub>2</sub> ) <sub>2</sub> (6) at 50 °C.....	169

<b>Figure 3.23.</b> Rate, LDP, and % Vbur used for modeling catalyst <b>6</b> .....	170
<b>Figure 3.24.</b> Plot of experimental rate constant versus model predicted rate constant with catalyst <b>6</b> . ....	170
<b>Figure 3.25.</b> Molecular weight calibration of Ti(dithioBINAP)(NMe <sub>2</sub> ) <sub>2</sub> ( <b>6</b> ) with excess aniline at 50 °C. ....	171
<b>Figure 3.26.</b> All titanium catalysts used in this study. ....	172
<b>Figure 3.27.</b> Completed plot for predicted versus experimental rate constant. ....	173
<b>Figure 3.28.</b> Natural and Scale Parameters .....	174
<b>Figure 3.29.</b> Mode of coordination. ....	175
<b>Figure 3.30.</b> A close-up of the model plot in <b>Figure 3.27</b> with the points for the hypothetical active species in the Ti(NMe <sub>2</sub> ) <sub>4</sub> catalysis added. <sup>1</sup> .....	177
<b>Figure 3.31.</b> Model plot with error bars. ....	181
<b>Figure 3.32.</b> DOSY spectrum of Ti(dithioBINAP)(NMe <sub>2</sub> ) <sub>2</sub> ( <b>6</b> ) at 25 °C.....	186
<b>Figure 3.33.</b> Molecular weight calibration of Ti(dithioBINAP)(NMe <sub>2</sub> ) <sub>2</sub> ( <b>6</b> ) at 25 °C.....	187
<b>Figure 3.34.</b> Molecular weight calibration of Ti(dithioBINAP)(NMe <sub>2</sub> ) <sub>2</sub> ( <b>6</b> ).....	188
<b>Figure 3.35.</b> Molecular weight calibration of Ti(dithioBINAP)(NMe <sub>2</sub> ) <sub>2</sub> ( <b>6</b> ) at 50 °C.....	188
<b>Figure 3.36.</b> Molecular weight calibration of Ti(dithioBINAP)(NMe <sub>2</sub> ) <sub>2</sub> ( <b>6</b> ) with addition of aniline (4 equiv.) at 50 °C. ....	190
<b>Figure 3.37.</b> Crystal structure of Ti(dpm <sup>2,2'-DiMe</sup> )(NMe <sub>2</sub> ) <sub>2</sub> ( <b>1b</b> ). ....	196
<b>Figure 3.38.</b> Crystal structure of Ti(dpm <sup>2-tolyl</sup> )(NMe <sub>2</sub> ) <sub>2</sub> ( <b>1e</b> ).....	199
<b>Figure 3.39.</b> Crystal structure of Ti(dpm <sup>2-phenyl</sup> )(NMe <sub>2</sub> ) <sub>2</sub> ( <b>1d</b> ). ....	202
<b>Figure 3.40.</b> Crystal structure of Ti( <i>bis</i> -phenoxide <sup>2tBu-4Me</sup> )(NMe <sub>2</sub> ) <sub>2</sub> ( <b>3</b> ). ....	207
<b>Figure 3.41.</b> Crystal structure of Ti(biphenol <sup>2-tBu-4,5-diMe</sup> ) (NMe <sub>2</sub> ) <sub>2</sub> ( <b>4a</b> ). ....	209
<b>Figure 3.42.</b> Crystal structure of Ti(dithioBINAP)(NMe <sub>2</sub> ) <sub>2</sub> ( <b>6</b> ).....	212
<b>Figure 3.43.</b> Crystal structure of NCr(N <sup>i</sup> Pr) <sub>2</sub> (6-BrS Nap). ....	214
<b>Figure 3.44.</b> Plot of [1-phenylpropyne] vs time with Ti(NMe <sub>2</sub> ) <sub>2</sub> ( <i>bis</i> -phenoxide <sup>2tBu-4Me</sup> ) ( <b>3</b> ).....	216
<b>Figure 3.45.</b> Plot of [1-phenylpropyne] vs time with Ti(NMe <sub>2</sub> ) <sub>2</sub> (biphenol <sup>2tBu-4,5-diMe</sup> ) ( <b>4a</b> ). ....	217

<b>Figure 3.46.</b> Plot of [1-phenylpropyne] vs time with $\text{Ti}(\text{dim}^{3\text{Me}})(\text{NMe}_2)_2$ ( <b>2a</b> ). .....	218
<b>Figure 3.47.</b> Plot of [1-phenylpropyne] vs time with $\text{Ti}(\text{dim}^{3\text{Me-5F}})(\text{NMe}_2)_2(\text{HNMe}_2)$ ( <b>2b</b> ). .....	219
<b>Figure 3.48.</b> Plot of [1-phenylpropyne] vs time with $\text{Ti}(\text{dpm}^{2-[\text{C}_6\text{H}_3(\text{CF}_3)_2]})(\text{NMe}_2)_2$ ( <b>1c</b> ). .....	220
<b>Figure 3.49.</b> Plot of [1-phenylpropyne] vs time with $\text{Ti}(\text{dpm}^{2-[\text{C}_6\text{H}_3(\text{CF}_3)_2]})(\text{NMe}_2)_2$ ( <b>1d</b> ). .....	221
<b>Figure 3.50.</b> Plot of [1-phenylpropyne] vs time with $\text{Ti}(\text{dpm}^{2-\text{tolyl}})(\text{NMe}_2)_2$ ( <b>1e</b> ). .....	222
<b>Figure 3.51.</b> Plot of [1-phenylpropyne] vs time with $\text{Ti}(\text{dpm})(\text{NMe}_2)_2$ ( <b>1a</b> ). .....	223
<b>Figure 3.52.</b> Plot of [1-phenylpropyne] vs time with $\text{Ti}(\text{dpm}^{2,2'-\text{DiMe}})(\text{NMe}_2)_2$ ( <b>1b</b> ). .....	224
<b>Figure 3.53.</b> Plot of [1-phenylpropyne] vs time with $\text{Ti}(\text{NMe}_2)_4$ . .....	225
<b>Figure 3.54.</b> Plot of [1-phenylpropyne] vs time with $\text{Ti}(\text{NMe}_2)_2(\text{biphenol}^{2\text{tBu-4-OMe}})$ ( <b>4b</b> ). .....	226
<b>Figure 3.55.</b> Plot of [1-phenylpropyne] vs time with $\text{Ti}(\text{dpm}^{3-[\text{C}_6\text{H}_3(\text{CF}_3)_2]})(\text{NMe}_2)_2$ ( <b>5</b> ). .....	227
<b>Figure 3.56.</b> Plot of [1-phenylpropyne] vs time with $\text{Ti}(\text{dithioBINAP})(\text{NMe}_2)_2$ ( <b>6</b> ). .....	228
<b>Figure 3.57.</b> $^1\text{H}$ NMR Spectrum of $\text{Ti}(\text{NMe}_2)_2(\text{dpm}^{2,2'-\text{DiMe}})$ ( <b>1b</b> ) in toluene- $\text{d}_8$ . .....	229
<b>Figure 3.58.</b> $^{13}\text{C}$ NMR Spectrum of $\text{Ti}(\text{NMe}_2)_2(\text{dpm}^{2,2'-\text{DiMe}})$ ( <b>1b</b> ) in toluene- $\text{d}_8$ . .....	230
<b>Figure 3.59.</b> $^1\text{H}$ NMR Spectrum of $\text{H}_2\text{dpm}^{2-\text{phenyl}}$ in $\text{C}_6\text{D}_6$ . .....	231
<b>Figure 3.60.</b> $^{13}\text{C}$ NMR Spectrum of $\text{H}_2\text{dpm}^{2-\text{phenyl}}$ in $\text{C}_6\text{D}_6$ . .....	232
<b>Figure 3.61.</b> $^1\text{H}$ NMR Spectrum of $\text{Ti}(\text{NMe}_2)_2(\text{dpm}^{2-\text{phenyl}})$ ( <b>1d</b> ) in $\text{C}_6\text{D}_6$ . .....	233
<b>Figure 3.62.</b> $^{13}\text{C}$ NMR Spectrum of $\text{Ti}(\text{NMe}_2)_2(\text{dpm}^{2-\text{phenyl}})$ ( <b>1d</b> ) in $\text{C}_6\text{D}_6$ . .....	234
<b>Figure 3.63.</b> $^1\text{H}$ NMR Spectrum of $\text{H}_2\text{dpm}^{2-\text{tolyl}}$ in $\text{C}_6\text{D}_6$ . .....	235
<b>Figure 3.64.</b> $^{13}\text{C}$ NMR Spectrum of $\text{H}_2\text{dpm}^{2-\text{tolyl}}$ in $\text{C}_6\text{D}_6$ . .....	236
<b>Figure 3.65.</b> $^1\text{H}$ NMR Spectrum of $\text{Ti}(\text{NMe}_2)_2(\text{dpm}^{2-\text{tolyl}})$ ( <b>1e</b> ) in toluene- $\text{d}_8$ . .....	237
<b>Figure 3.66.</b> $^{13}\text{C}$ NMR Spectrum of $\text{Ti}(\text{NMe}_2)_2(\text{dpm}^{2-\text{tolyl}})$ ( <b>1e</b> ) in toluene- $\text{d}_8$ . .....	238
<b>Figure 3.67.</b> $^1\text{H}$ NMR Spectrum of $\text{Ti}(\text{dim}^{3\text{Me}})(\text{NMe}_2)_2$ ( <b>2a</b> ) in $\text{C}_6\text{D}_6$ . .....	239
<b>Figure 3.68.</b> $^{13}\text{C}$ NMR Spectrum of $\text{Ti}(\text{dim}^{3\text{Me}})(\text{NMe}_2)_2$ ( <b>2a</b> ) in $\text{C}_6\text{D}_6$ . .....	240
<b>Figure 3.69.</b> $^1\text{H}$ NMR Spectrum of $\text{H}_2\text{dim}^{3\text{Me5F}}$ in $\text{C}_6\text{D}_6$ . .....	241
<b>Figure 3.70.</b> $^{13}\text{C}$ NMR Spectrum of $\text{H}_2\text{dim}^{3\text{Me5F}}$ in $\text{C}_6\text{D}_6$ . .....	242

<b>Figure 3.71.</b> $^{19}\text{F}$ NMR Spectrum of $\text{H}_2\text{dim}^{3\text{Me}_5\text{F}}$ in $\text{C}_6\text{D}_6$ .	243
<b>Figure 3.72.</b> $^1\text{H}$ NMR Spectrum of $\text{Ti}(\text{dim}^{3\text{Me}_5\text{F}})(\text{NMe}_2)_2(\text{HNMe}_2)$ ( <b>2b</b> ) in toluene- $\text{d}_8$ .	244
<b>Figure 3.73.</b> $^{13}\text{C}$ NMR Spectrum of $\text{Ti}(\text{dim}^{3\text{Me}_5\text{F}})(\text{NMe}_2)_2(\text{HNMe}_2)$ ( <b>2b</b> ) in toluene- $\text{d}_8$ .	245
<b>Figure 3.74.</b> $^{19}\text{F}$ NMR Spectrum of $\text{Ti}(\text{dim}^{3\text{Me}_5\text{F}})(\text{NMe}_2)_2(\text{HNMe}_2)$ ( <b>2b</b> ) in toluene- $\text{d}_8$ .	246
<b>Figure 3.75.</b> $^1\text{H}$ NMR Spectrum of $\text{Ti}(\text{NMe}_2)_2(\text{bis-phenoxide}^{2\text{tBu-4Me}})$ ( <b>3</b> ) in toluene- $\text{d}_8$ .	247
<b>Figure 3.76.</b> $^{13}\text{C}$ NMR Spectrum of $\text{Ti}(\text{NMe}_2)_2(\text{bis-phenoxide}^{2\text{tBu-4Me}})$ ( <b>3</b> ) in toluene- $\text{d}_8$ .	248
<b>Figure 3.77.</b> $^1\text{H}$ NMR Spectrum of $\text{Ti}(\text{NMe}_2)_2(\text{biphenol}^{2\text{tBu-4,5-diMe}})$ ( <b>4a</b> ) in $\text{C}_6\text{D}_6$ .	249
<b>Figure 3.78.</b> $^{13}\text{C}$ NMR Spectrum of $\text{Ti}(\text{NMe}_2)_2(\text{biphenol}^{2\text{tBu-4,5-diMe}})$ ( <b>4a</b> ) in $\text{C}_6\text{D}_6$ .	250
<b>Figure 3.79.</b> $^1\text{H}$ NMR Spectrum of $\text{Ti}(\text{NMe}_2)_2(\text{biphenol}^{2\text{tBu-4-OMe}})$ ( <b>4b</b> ) in $\text{C}_6\text{D}_6$ .	251
<b>Figure 3.80.</b> $^{13}\text{C}$ NMR Spectrum of $\text{Ti}(\text{NMe}_2)_2(\text{biphenol}^{2\text{tBu-4-OMe}})$ ( <b>4b</b> ) in $\text{C}_6\text{D}_6$ .	252
<b>Figure 3.81.</b> $^1\text{H}$ NMR Spectrum of $\text{Ti}(\text{dithioBINAP})(\text{NMe}_2)_2$ ( <b>6</b> ) in $\text{C}_6\text{D}_6$ .	253
<b>Figure 3.82.</b> $^{13}\text{C}$ NMR Spectrum of $\text{Ti}(\text{dithioBINAP})(\text{NMe}_2)_2$ ( <b>6</b> ) in $\text{C}_6\text{D}_6$ .	254
<b>Figure 3.83.</b> $^1\text{H}$ NMR Spectrum of $\text{NCr}(\text{N}^i\text{Pr}_2)_2(6\text{Br-SNap})$ in $\text{CDCl}_3$ .	255
<b>Figure 3.84.</b> $^{13}\text{C}$ NMR Spectrum of $\text{NCr}(\text{N}^i\text{Pr}_2)_2(6\text{Br-SNap})$ in $\text{CDCl}_3$ .	256
<b>Figure 3.85.</b> $^{14}\text{N}$ NMR Spectrum of $\text{NCr}(\text{N}^i\text{Pr}_2)_2(6\text{Br-SNap})$ in $\text{CDCl}_3$ .	257
<b>Figure 4.1.</b> Schrock's olefin metathesis catalyst. <sup>2</sup>	263
<b>Figure 4.2.</b> Comparison of the original <sup>10</sup> and new model.	269
<b>Figure 4.3.</b> Crystal Structure of $\text{Ti}(\text{dpm}^{2\text{-Me}})(\text{NMe}_2)_2$ ( <b>7a</b> ).	271
<b>Figure 4.4.</b> Crystal Structure of $\text{Ti}(\text{dpm}^{\text{TriMe}})(\text{NMe}_2)_2$ ( <b>7b</b> ).	274
<b>Figure 4.5.</b> Strategy for unsymmetrical ligands.	275
<b>Figure 4.6.</b> Proposed rate determining step of titanium-catalyzed hydroamination of alkynes.	281
<b>Figure 4.7.</b> Possible geometries for titanium species.	282
<b>Figure 4.8.</b> $^1\text{H}$ -NMR (top) and 1D-NOESY (bottom) spectra of $\text{H}_2\text{dpm}^{2,2'\text{-DiMe-3-DiCHO}}$	289
<b>Figure 4.9.</b> $^1\text{H}$ -NMR (top) and 1D-NOESY (bottom) spectra of $\text{H}_2\text{dpm}^{2,2'\text{-DiMe-3-DiCHO}}$	290
<b>Figure 4.10.</b> Crystal Structure of $\text{Ti}(\text{PyrOAr}^{2,4\text{-diterbutyl}})(\text{NMe}_2)_2$ ( <b>8</b> ).	296

<b>Figure 4.11.</b> Plot of [1-phenylpropyne] vs time with $\text{Ti}(\text{PyrOAr}^{2,4\text{-diterbutyl}})(\text{NMe}_2)_2$ ( <b>8</b> ).....	304
<b>Figure 4.12.</b> Plot of [1-phenylpropyne] vs time with $\text{Ti}(\text{dpm}^{2\text{Me}})(\text{NMe}_2)_2$ ( <b>7a</b> ).....	305
<b>Figure 4.13.</b> Plot of [1-phenylpropyne] vs time with $\text{Ti}(\text{dpm}^{2,2',3\text{-TriMe}})(\text{NMe}_2)_2$ ( <b>7b</b> ). ....	306
<b>Figure 4.14.</b> $^1\text{H}$ NMR Spectrum of 2,4-di- <i>tert</i> -butyl-6-(hydroxymethyl)phenol in $\text{C}_6\text{D}_6$ . ....	307
<b>Figure 4.15.</b> $^{13}\text{C}$ NMR Spectrum of 2,4-di- <i>tert</i> -butyl-6-(hydroxymethyl)phenol in $\text{C}_6\text{D}_6$ . ....	308
<b>Figure 4.16.</b> $^1\text{H}$ NMR Spectrum of $\text{HPyrHOAr}^{2,4\text{-diterbutyl}}$ in $\text{C}_6\text{D}_6$ . ....	309
<b>Figure 4.17.</b> $^{13}\text{C}$ NMR Spectrum of $\text{HPyrHOAr}^{2,4\text{-diterbutyl}}$ in $\text{C}_6\text{D}_6$ . ....	310
<b>Figure 4.18.</b> $^1\text{H}$ NMR Spectrum of $\text{Ti}(\text{PyrOAr}^{2,4\text{-diterbutyl}})(\text{NMe}_2)_2$ ( <b>8</b> ) in $\text{C}_6\text{D}_6$ .....	311
<b>Figure 4.19.</b> $^{13}\text{C}$ NMR Spectrum of $\text{Ti}(\text{PyrOAr}^{2,4\text{-diterbutyl}})(\text{NMe}_2)_2$ ( <b>8</b> ) in $\text{C}_6\text{D}_6$ .....	312
<b>Figure 4.20.</b> $^1\text{H}$ NMR Spectrum of $\text{H}_2\text{dpm}^{2,2'\text{-DiMe-3-CHO}}$ in $\text{DMSO-d}_6$ .....	313
<b>Figure 4.21.</b> $^{13}\text{C}$ NMR Spectrum of $\text{H}_2\text{dpm}^{2,2'\text{-DiMe-3-CHO}}$ in $\text{DMSO-d}_6$ .....	314
<b>Figure 4.22.</b> $^1\text{H}$ NMR Spectrum of $\text{H}_2\text{dpm}^{2,2',3\text{-TriMe}}$ in $\text{C}_6\text{D}_6$ . ....	315
<b>Figure 4.23.</b> $^{13}\text{C}$ NMR Spectrum of $\text{H}_2\text{dpm}^{2,2',3\text{-TriMe}}$ in $\text{C}_6\text{D}_6$ .....	316
<b>Figure 4.24.</b> $^1\text{H}$ NMR Spectrum of $\text{H}_2\text{dpm}^{2,2'\text{-DiMe-3,3'-DiCHO}}$ in $\text{DMSO-d}_6$ . ....	317
<b>Figure 4.25.</b> $^{13}\text{C}$ NMR Spectrum of $\text{H}_2\text{dpm}^{2,2'\text{-DiMe-3,3'-DiCHO}}$ in $\text{DMSO-d}_6$ . ....	318
<b>Figure 4.26.</b> $^1\text{H}$ NMR Spectrum of $\text{HPyr}^{2\text{-tolyl}}\text{HOAr}^{2,4\text{-diterbutyl}}$ in $\text{C}_6\text{D}_6$ . ....	319
<b>Figure 4.27.</b> $^{13}\text{C}$ NMR Spectrum of $\text{HPyr}^{2\text{-tolyl}}\text{HOAr}^{2,4\text{-diterbutyl}}$ in $\text{C}_6\text{D}_6$ .....	320
<b>Figure 4.28.</b> $^1\text{H}$ NMR Spectrum of $\text{H}_2\text{dpm}^{2\text{Me}}$ in $\text{C}_6\text{D}_6$ .....	321
<b>Figure 4.29.</b> $^{13}\text{C}$ NMR Spectrum of $\text{H}_2\text{dpm}^{2\text{Me}}$ in $\text{C}_6\text{D}_6$ .....	322
<b>Figure 4.30.</b> $^1\text{H}$ NMR Spectrum of $\text{H}_2\text{dpm}^{2,2',3\text{-TriMe}}$ in $\text{C}_6\text{D}_6$ .....	323
<b>Figure 4.31.</b> $^{13}\text{C}$ NMR Spectrum of $\text{H}_2\text{dpm}^{2,2',3\text{-TriMe}}$ in $\text{C}_6\text{D}_6$ .....	324
<b>Figure 4.32.</b> $^1\text{H}$ NMR Spectrum of $\text{Hind}^{3\text{Me}}\text{HOAr}^{2,4\text{-diterbutyl}}$ in $\text{C}_6\text{D}_6$ . ....	325
<b>Figure 4.33.</b> $^{13}\text{C}$ NMR Spectrum of $\text{Hind}^{3\text{Me}}\text{HOAr}^{2,4\text{-diterbutyl}}$ in $\text{C}_6\text{D}_6$ .....	326
<b>Figure 4.34.</b> $^1\text{H}$ NMR Spectrum of $\text{Ti}(\text{dpm}^{2\text{Me}})(\text{NMe}_2)_2$ ( <b>7a</b> ) in $\text{C}_6\text{D}_6$ . ....	327
<b>Figure 4.35.</b> $^{13}\text{C}$ NMR Spectrum of $\text{Ti}(\text{dpm}^{2\text{Me}})(\text{NMe}_2)_2$ ( <b>7a</b> ) in $\text{C}_6\text{D}_6$ . ....	328

<b>Figure 4.36.</b> $^1\text{H}$ NMR Spectrum of Tidpm <sup>2,2',3-TriMe</sup> (NMe <sub>2</sub> ) <sub>2</sub> ( <b>7b</b> ) in C <sub>6</sub> D <sub>6</sub> . .....	329
<b>Figure 4.37.</b> $^{13}\text{C}$ NMR Spectrum of Tidpm <sup>2,2',3-TriMe</sup> (NMe <sub>2</sub> ) <sub>2</sub> ( <b>7b</b> ) in C <sub>6</sub> D <sub>6</sub> . .....	330

## LIST OF SCHEMES

<b>Scheme 1.1.</b> Hydroamination of alkenes and alkynes.....	2
<b>Scheme 1.2.</b> Some possible amination routes via amine or alkene activation. <sup>6</sup> .....	5
<b>Scheme 1.3.</b> Hydroamination via attack of amine on $\pi$ -complexes. <sup>23</sup> .....	7
<b>Scheme 1.4.</b> The Marks hydroamination mechanism. <sup>25</sup> .....	8
<b>Scheme 1.5.</b> The first monomeric imidozirconocene complex. <sup>29</sup> .....	9
<b>Scheme 1.6.</b> The first titanium hydroamination catalyst. <sup>31</sup> .....	9
<b>Scheme 1.7.</b> The Bergman hydroamination mechanism. <sup>32-33</sup> .....	10
<b>Scheme 1.8.</b> The Sadow hydroamination mechanism. <sup>35</sup> .....	11
<b>Scheme 1.9.</b> Simplified mechanisms for olefin metathesis and hydroamination. <sup>39</sup> .....	12
<b>Scheme 1.10.</b> $\text{Ti}(\text{NMe}_2)_4$ alkyne hydroamination. <sup>40</sup> .....	13
<b>Scheme 1.11.</b> Synthesis of titanium hydroamination pre-catalysts. <sup>39</sup> .....	14
<b>Scheme 1.12.</b> Proposed mechanism for the titanium-catalyzed Iminoamination of alkynes. <sup>39, 44</sup> .....	17
<b>Scheme 1.13.</b> Effects of precatalyst on regioselectivity using an alkyl amine and alkyne. <sup>41</sup> .....	19
<b>Scheme 1.14.</b> Effects of precatalyst on regioselectivity using an alkyl amine and enyne. <sup>41</sup> .....	19
<b>Scheme 1.15.</b> Effects of precatalyst on regioselectivity using an aryl amine. <sup>39</sup> .....	20
<b>Scheme 1.16.</b> Nitrogen-based heterocycle synthesis using iminoamination of alkynes. ....	22
<b>Scheme 2.1.</b> The catalytic mechanism of the $\beta$ -subunits in the proteasome. <sup>10</sup> .....	29
<b>Scheme 2.2.</b> Aldehyde mechanism. <sup>10, 24</sup> .....	31
<b>Scheme 2.3.</b> Vinyl sulfones mechanism. <sup>10, 24</sup> .....	32
<b>Scheme 2.4.</b> Vinylamides mechanism. <sup>10, 24</sup> .....	32
<b>Scheme 2.5.</b> $\alpha'$ , $\beta'$ -epoxyketones mechanism. <sup>10, 24</sup> .....	33
<b>Scheme 2.6.</b> $\alpha$ -ketoaldehydes mechanism. <sup>10, 24</sup> .....	33

<b>Scheme 2.7.</b> $\beta$ -lactones mechanism. <sup>10, 24</sup> .....	34
<b>Scheme 2.8.</b> <i>Oxatiazol-2-ones</i> mechanism. <sup>10</sup> .....	34
<b>Scheme 2.9.</b> Boronates mechanism. <sup>10, 24</sup> .....	35
<b>Scheme 2.10.</b> Classical examples of quinoline synthesis. <sup>62</sup> .....	41
<b>Scheme 2.11.</b> Odom group's quinoline synthesis. <sup>64</sup> .....	42
<b>Scheme 2.12.</b> The proposed mechanism for quinoline synthesis. ....	43
<b>Scheme 2.13.</b> Synthesis of racemic Angustureine. <sup>67</sup> .....	44
<b>Scheme 3.1.</b> Synthesis of H <sub>2</sub> dpm and Ti(dpm)(NMe <sub>2</sub> ) <sub>2</sub> ( <b>1a</b> ). ....	147
<b>Scheme 3.2.</b> Synthesis of H <sub>2</sub> dpm <sup>2-[C<sub>6</sub>H<sub>3</sub>(CF<sub>3</sub>)<sub>2</sub>]</sup> and H <sub>2</sub> dpm <sup>2-Mes</sup> and titanium precatalysts. <sup>27</sup> .....	148
<b>Scheme 3.3.</b> Synthesis of H <sub>2</sub> dpm <sup>2,2'-DiMe</sup> and titanium precatalysts. ....	149
<b>Scheme 3.4.</b> Synthesis of H <sub>2</sub> dpm <sup>2-tolyl</sup> , H <sub>2</sub> dpm <sup>2-phenyl</sup> and titanium precatalysts. ....	152
<b>Scheme 3.5.</b> Synthesis of diindolylmethane catalysts. <b>(a) Top:</b> Synthesis of H <sub>2</sub> dim <sup>3Me</sup> and titanium precatalyst. <b>(b) Bottom:</b> Synthesis of H <sub>2</sub> dim <sup>3Me5F</sup> and titanium precatalyst. ....	153
<b>Scheme 3.6.</b> Synthesis of Ti( <i>bis</i> -phenoxide <sup>2tBu-4Me</sup> )(NMe <sub>2</sub> ) <sub>2</sub> ( <b>3</b> ). ....	156
<b>Scheme 3.7.</b> Attempted syntheses of titanium methylene bisphenoxide-based precatalysts. ....	159
<b>Scheme 3.8.</b> Synthesis of Ti(biphenol <sup>2tBu-4,5-DiMe</sup> )(NMe <sub>2</sub> ) <sub>2</sub> ( <b>4a</b> ). ....	160
<b>Scheme 3.9.</b> Synthesis of H <sub>2</sub> biphenol <sup>2tBu-4OMe</sup> and Ti(biphenol <sup>2tBu-4OMe</sup> )(NMe <sub>2</sub> ) <sub>2</sub> ( <b>4b</b> ). ....	161
<b>Scheme 3.10.</b> Attempted syntheses of titanium biphenol-based precatalysts. ....	161
<b>Scheme 3.11.</b> Synthesis of Ti(dpm <sup>3-[C<sub>6</sub>H<sub>3</sub>(CF<sub>3</sub>)<sub>2</sub>]</sup> )(NMe <sub>2</sub> ) <sub>2</sub> ( <b>5</b> ). ....	164
<b>Scheme 3.12.</b> Synthesis of Ti(dithioBINAP)(NMe <sub>2</sub> ) <sub>2</sub> ( <b>6</b> ). ....	168
<b>Scheme 4.1.</b> Synthesis of a MonoAlkoxide Pyrrolide (MAP) complex. <sup>2</sup> .....	264
<b>Scheme 4.2.</b> A simplified version of Eisenstein and Copéret's mechanistic model. <sup>6, 8</sup> .....	265
<b>Scheme 4.3.</b> A small representation of the molybdenum catalysts screened for the synthesis of quebrachamine. <sup>8-9</sup> .....	266
<b>Scheme 4.4.</b> Application of chiral molybdenum catalyst for the synthesis of ..... (+)-quebrachamine. <sup>8-9</sup> .....	267 267



<b>Scheme 4.5.</b> Synthesis of $\text{H}_2 \text{dpm}^{2\text{-Me}}$ and $\text{Ti}(\text{dpm}^{2\text{-Me}})(\text{NMe}_2)_2$ ( <b>7a</b> ). .....	270
<b>Scheme 4.6.</b> Possible isomers for $\text{H}_2\text{dpm}^{2,2'\text{-DiMe-CHO}}$ and $\text{H}_2\text{dpm}^{2,2'\text{-DiMe-DiCHO}}$ . .....	272
<b>Scheme 4.7.</b> Synthesis of $\text{H}_2\text{dpm}^{2,2'\text{-DiMe-3-CHO}}$ and $\text{H}_2\text{dpm}^{2,2'\text{-DiMe-3,3'-CHO}}$ . .....	273
<b>Scheme 4.8.</b> Synthesis of $\text{H}_2 \text{dpm}^{2,2',3\text{-TriMe}}$ and $\text{Ti}(\text{dpm}^{2,2',3\text{-TriMe}})(\text{NMe}_2)_2$ ( <b>7b</b> ). .....	273
<b>Scheme 4.9.</b> The attempted synthesis of $\text{Ti}(\text{pypm})(\text{NMe}_2)_2$ .....	274
<b>Scheme 4.10.</b> Synthesis of the phenol precursor, 2,4-di- <i>tert</i> -butyl-6-(hydroxymethyl)phenol. ....	275
<b>Scheme 4.11.</b> Synthesis of a variety of $\text{HPyrHOAr}^{2,4\text{-ditertbutyl}}$ , $\text{HInd}^{3\text{Me}}\text{HOAr}^{2,4\text{-ditertbutyl}}$ , $\text{HPyr}^{2\text{-tolyl}}\text{HOAr}^{2,4\text{-ditertbutyl}}$ . .....	276
<b>Scheme 4.12.</b> Synthesis of $\text{Ti}(\text{PyrOAr}^{2,4\text{-ditertbutyl}})(\text{NMe}_2)_2$ ( <b>8</b> ). .....	277
<b>Scheme 4.13.</b> Larock's indole synthesis. <sup>15</sup> .....	283
<b>Scheme 4.14.</b> Synthesis of 3-Ethyl-2-(1-hydroxycyclohexyl)indole. <sup>15</sup> .....	283
<b>Scheme 4.15.</b> Proposed synthesis of unsymmetrical indolyl-based ligands. ....	284
<b>Scheme 4.16.</b> Proposed synthesis of a phenol precursor and unsymmetrical phenol-based ligands. ....	285

## KEY TO ABBREVIATIONS

% V <sub>bur</sub>	Percent Buried Volume
3CC	Three-Component Coupling
5AHQ	5-amino-8-hydroxyquinoline
Boc	tert-Butoxycarbonyl
Bu <sup>t</sup> bpy	4,4'-tert-butyl-2,2'-bipyridine
Casp-L	Caspase-Like
CHO	Aldehyde
Conv.	Conversion
Cp	Cyclopentadiene
CT-L	Chymotrypsin-Like
Dim	Diindolylmethane
DiMe	Dimethyl
DiCHO	Dialdehyde
DMF	Dimethylformamide
DME	Dimethoxyethane
DMSO	Dimethyl sulfoxide
DOSY	Diffusion Ordered Spectroscopy
Et <sub>2</sub> O	Diethyl ether
Equiv.	Equivalent
GC/FID	Gas Chromatography Flame Ionization Detector
GC/MS	Gas Chromatography Mass Spectrometry

h	hour(s)
H <sub>2</sub> dpm	5,5-dimethyldipyrrolylmethane
H <sub>2</sub> dpma	N,N-(dipyrrolyl- $\alpha$ -methyl)-N-methylamine
H <sub>2</sub> pypm	2-[1-methyl-1-(2-pyrrolidiny)ethyl]-1H-pyrrole
HBpin	Pinacolborane
Hdap	$\alpha$ -(dimethyl-aminomethyl)pyrrole
HRMS	High Resolution Mass Spectrometry
IC <sub>50</sub>	Half Maximal Inhibitory Concentration
IgG	Immunoglobulin G
IgA	Immunoglobulin A
Ind	Indole
LDP	Ligand Donor Parameter
min	Minute(s)
MSU	Michigan State University
MW	Molecular weight
NOESY	Nuclear Overhauser Effect Spectroscopy
NMR	Nuclear magnetic resonance
OAc	Acetate
Py	Pyrrole
Pyr	Pyridine
RT	Room temperature
s	second(s)
SDS	Sodium dodecyl sulfate

TFA	Trifluoroacetic acid
THF	Tetrahydrofuran
T-L	Trypsin-Like
TMS	Trimethylsilyl
TriMe	Trimethyl

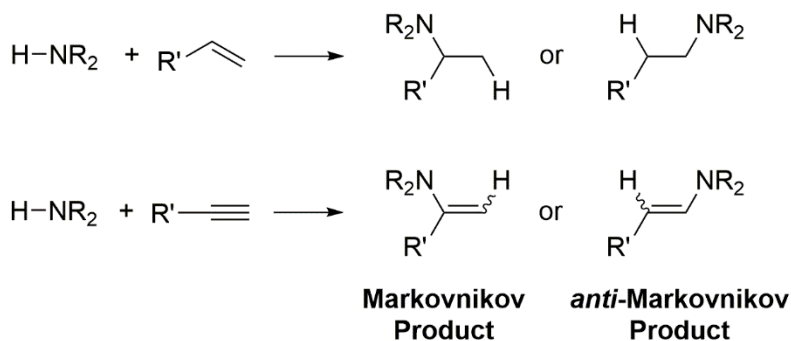
## Chapter 1. Introduction to Group-4 Transition Metal C-N Bond Formation

### 1.1 Background and Motivation

Nitrogen containing compounds, such as amines, imines, enamines and other nitrogen-containing compounds are incredibly valuable and commercially important specialty chemicals, bulk chemicals, and pharmaceuticals.<sup>1</sup> Therefore, synthetic routes incorporating nitrogen into organic compounds is highly desired. Ammonia ( $\text{NH}_3$ ) has always been the ideal starting material to synthesize aliphatic amines and many industrial processes were developed around ammonia. Some general production methods for aliphatic amines, involve the condensation of ammonia with alcohols, or with carbonyl compounds.<sup>2</sup> Even though these methods are still used today, these routes suffer from several disadvantages. The main disadvantage of using this approach is that these compounds, alcohols and carbonyl compounds, are already refined products! For instance, most alcohols are produced from olefins through either hydration<sup>3</sup> or through a sequential hydroformylation–hydrogenation process.<sup>4-5</sup> Furthermore, both of these methods are multiple step processes and suffer from poor atom-economy. From this perspective, if aliphatic amines could be synthesized directly from the olefins, in a single step, this would be more advantageous and more atom-economical.




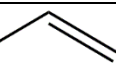
## 1.2 Hydroamination Introduction

The hydroamination of alkenes and alkynes is the formal addition of an N–H bond across a carbon-carbon multiple bond.<sup>6</sup> (**Scheme 1.1**) This seemingly simple transformation is a 100% atom-economical route to generate amines and imines from alkenes and alkynes.<sup>7</sup>



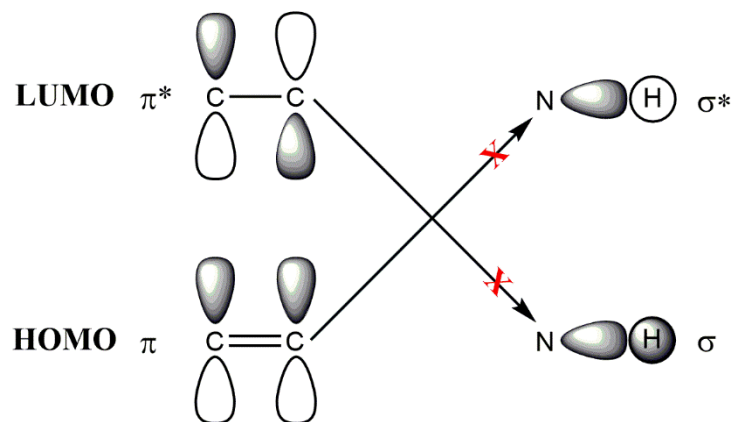
**Scheme 1.1.** Hydroamination of alkenes and alkynes.

From a thermodynamic perspective, the addition of simple amines or ammonia to alkenes is attainable. At room temperature, the reaction is slightly exothermic but close to thermoneutral. (**Table 1.1**) Currently, there is no experimental enthalpy ( $\Delta H^\circ$ ) data available for the addition of simple amines or ammonia to alkynes. As a result, we cannot compare the thermodynamics for the addition of amine to alkene or alkyne. However, the addition of ammonia to acetylene was estimated (using AM1-semiempirical calculations) to be  $\sim 63 \text{ kJ}\cdot\text{mol}^{-1}$  ( $\sim 15 \text{ kcal/mol}$ ) more exothermic than ethylene.<sup>6, 8-9</sup> Thus, thermodynamically, the addition of amine to alkynes is more favorable.

Reaction	$\Delta_R G^\circ$ (kJ·mol <sup>-1</sup> )	$\Delta_R H^\circ$ (kJ·mol <sup>-1</sup> )	$\Delta_R S^\circ$ (J mol <sup>-1</sup> K <sup>-1</sup> )
 + NH <sub>3</sub> $\rightleftharpoons$ EtNH <sub>2</sub>	-14.7	-52.7	-127.3
 + EtNH <sub>2</sub> $\rightleftharpoons$ Et <sub>2</sub> NH	-33.4	-78.7	-152.2
 + Et <sub>2</sub> NH $\rightleftharpoons$ Et <sub>3</sub> N	-30.0	-79.5	-166.3
<i>n</i> -butyl  + NH <sub>3</sub> $\rightleftharpoons$ ( <i>n</i> -hexyl)NH <sub>2</sub>	-4.9	-45.4	-136.4

**Table 1.1.** Thermodynamic data for various hydroamination reactions.<sup>7, 10</sup>

To make matters worse, the direct addition of simple amines or ammonia to alkenes or alkynes has a high activation barrier. This arises from an electrostatic repulsion interaction between the electron rich  $\pi$ -bond, from the alkene or alkyne, and the lone pair on the approaching amine.<sup>9</sup> Furthermore, the [2+2]-cycloaddition reaction between the amine (N–H) and the alkene (C=C) is a symmetry-forbidden process and unfavorable because of the high energy difference between the  $\alpha$ (N–H) and  $\pi^*(C=C)$  or  $\alpha^*(N-H)$  and  $\pi(C=C)$  orbitals.<sup>10</sup> (**Figure 1.1**)



**Figure 1.1.** [2+2]-cycloaddition of amine and alkene.<sup>10</sup>

Due to the negative entropy of the reaction, conducting the reaction at elevated temperatures, to overcome this barrier, is hindering as the equilibrium starts to shift towards the reactants as the temperature increases. (**Table 1.2**)

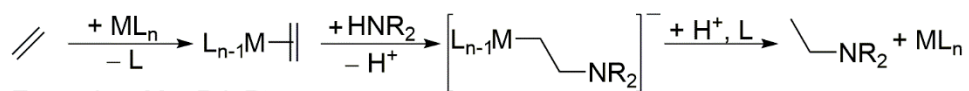
Reaction	$\Delta G^\circ$ (kJ•mol <sup>-1</sup> )	Temperature K (° C)
$\text{CH}_2=\text{CH}_2 + \text{NH}_3 \rightleftharpoons \text{EtNH}_2$	-14.7	298.15
	-11.5	323.15
	-5.2	373.15
	7.6	473.15

**Table 1.2.** Thermodynamic data for the hydroamination of ethylene and ammonia at various temperatures.<sup>10</sup>

With these limitations, utilizing a catalyst would provide an alternative, lower energy pathway and make this reaction achievable at lower temperatures. To address these limitations numerous catalysts have been developed to overcome this high-energy barrier. To achieve this transformation two general strategies have been used: 1) alkene (or alkyne) activation and 2) amine (N–H) activation.<sup>6</sup> (**Scheme 1.2**)

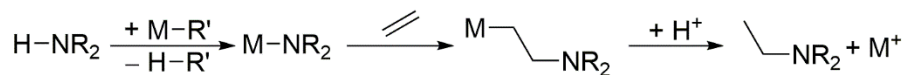


### Alkene Activation

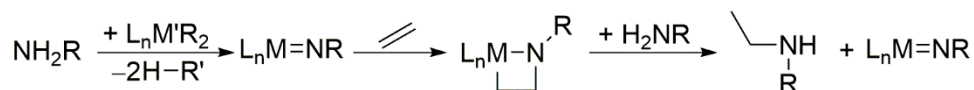


Examples: M = Pd, Pt

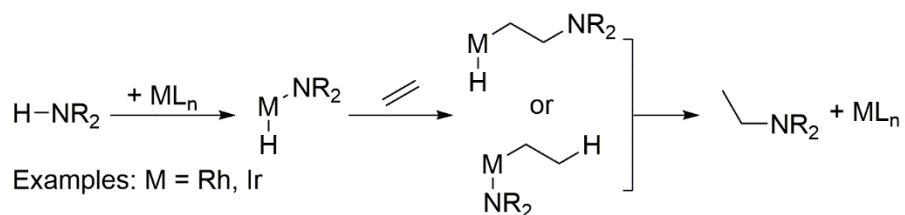
### Amine Activation



Examples: M = Li, Na



Examples: M = Zr, U



Examples: M = Rh, Ir

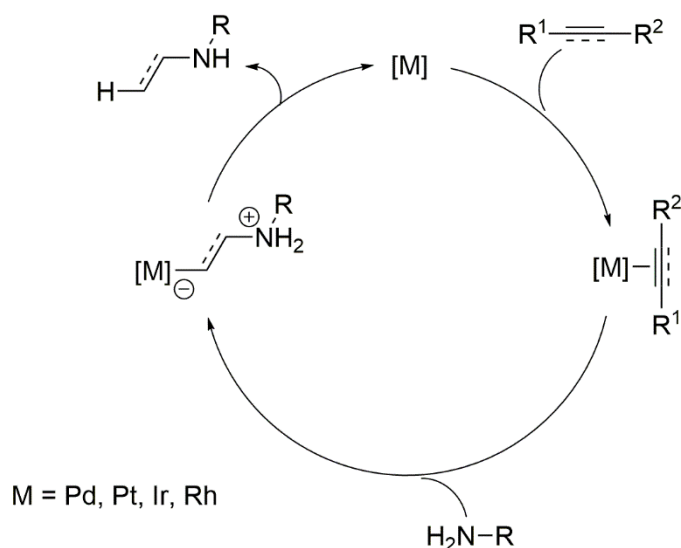
**Scheme 1.2.** Some possible amination routes via amine or alkene activation.<sup>6</sup>

### 1.3 The Mechanisms for Transition Metal Catalyzed Hydroamination

This section will briefly discuss the different mechanisms for transition metal catalyzed hydroamination of alkynes (or alkenes). With the exception of the first mechanism, the last three mechanisms have all been proposed in group-4 C–N bond formation processes (specifically zirconium). Furthermore, additional information is provided for the [2+2]-cycloaddition mechanism because this process is closely related to our group's research.

#### *Hydroamination via attack of amine on $\pi$ -complexes*

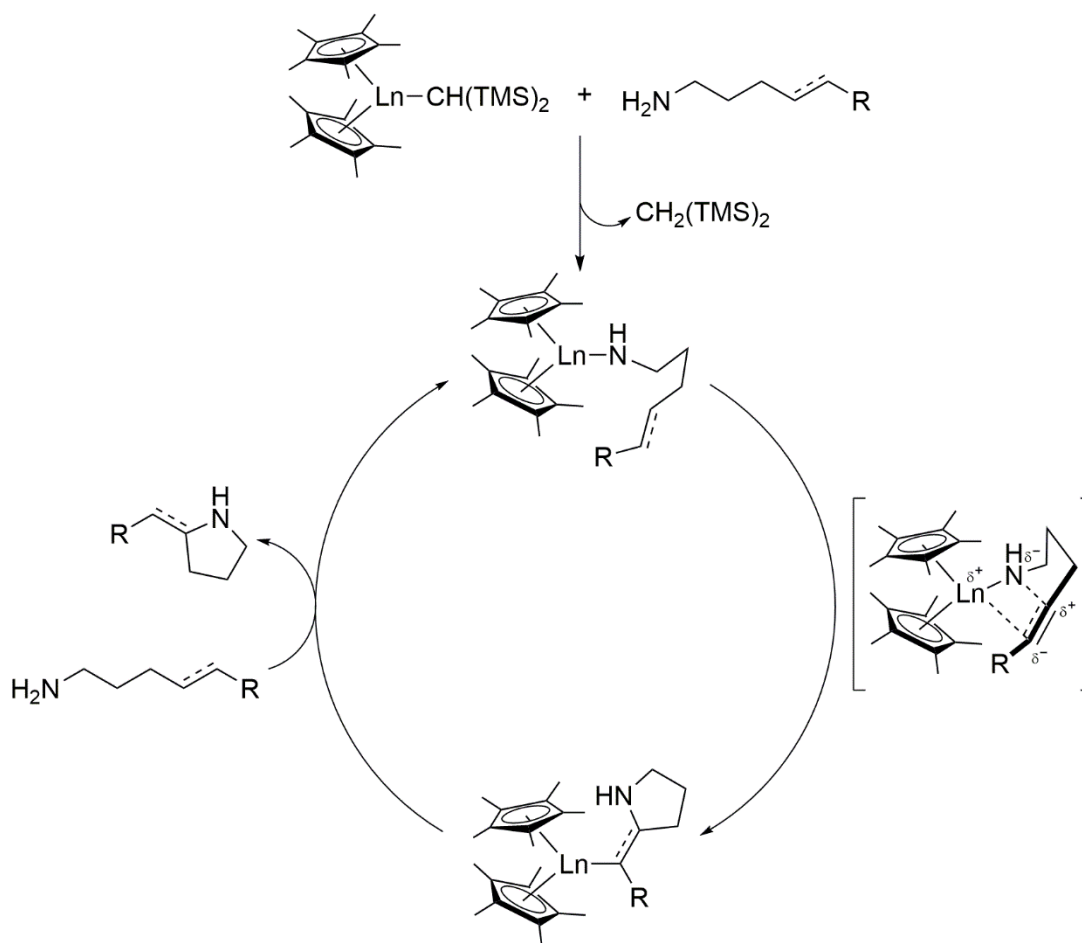
Due to electrostatic repulsion, amines do not readily undergo direct nucleophilic addition of a carbon-carbon multiple bond. However, if the  $\pi$ -system on the alkyne, or alkene, is activated by a neighboring group or is electron-deficient, the direct addition can occur.<sup>11-14</sup> The  $\pi$ -system can also be affected *via* coordination by a late-transition metal. As shown in **Scheme 1.3**, the transition metal is coordinated to the alkyne or alkene through the  $\pi$ -system. This coordination, to an electrophilic transition metal, results in an umpolung that renders the olefin susceptible to nucleophilic attack by the amine.<sup>6, 15-16</sup> This attack produces a metal-vinyl (or metal-alkyl) intermediate, which undergoes protonolysis at the metal-carbon bond to regenerate the catalyst and the enamine or amine product. This general mechanism has been proposed to occur by palladium(II)<sup>17</sup>, platinum(II)<sup>18-19</sup>, cationic rhodium<sup>20-21</sup>, and iridium complexes.<sup>21-22</sup>



**Scheme 1.3.** Hydroamination via attack of amine on  $\pi$ -complexes.<sup>23</sup>

*Hydroamination by insertions of alkynes or alkenes into metal amides*

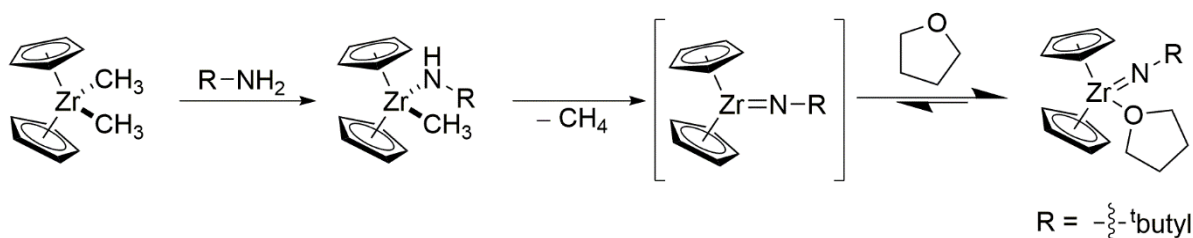
Another mechanism by which hydroamination can occur is through the insertion of the alkyne (or alkene) into a metal amide bond. While there are iridium(I) complexes that are proposed to operate by this mechanism<sup>24</sup>, the best known example come from lanthanide complexes. Marks and co-workers, have extensively studied the lanthanide-catalyzed hydroamination of alkynes, alkenes and dienes.<sup>25</sup> Their work has provided a general pathway for this mechanism, using aminoalkenes. As shown in **Scheme 1.4**, the precatalyst undergoes protonolysis to generate the active catalyst (a metal amido complex). The alkyne (or alkene) can then coordinate to the metal center, which undergoes a migratory insertion generating an amino-vinyl or alkyl intermediate. Protonolysis of this metal-carbon bond, by another equivalent of the amine substrate, regenerates the catalyst and releases the cyclized amine product. This mechanism has also been proposed for group(IV) cationic<sup>26</sup>, calcium<sup>27</sup>, and zinc<sup>28</sup> complexes.



**Scheme 1.4.** The Marks hydroamination mechanism.<sup>25</sup>

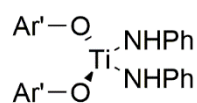
#### *Hydroamination by [2+2]-cycloaddition*

In the late 1980's Bergman and co-workers started exploring the reactivity of metal-oxo ( $M=O$ ) and metal-imido ( $M=NR$ ) complexes. At this time, there was an absence in literature of monomeric group 4 metal-oxo and metal-imido complexes. In 1988, Bergman and co-workers reported the first monomeric imidozirconocene ( $Cp_2Zr=NR$ ) complexes and reactivity of this species.<sup>29</sup>



**Scheme 1.5.** The first monomeric imidozirconocene complex.<sup>29</sup>

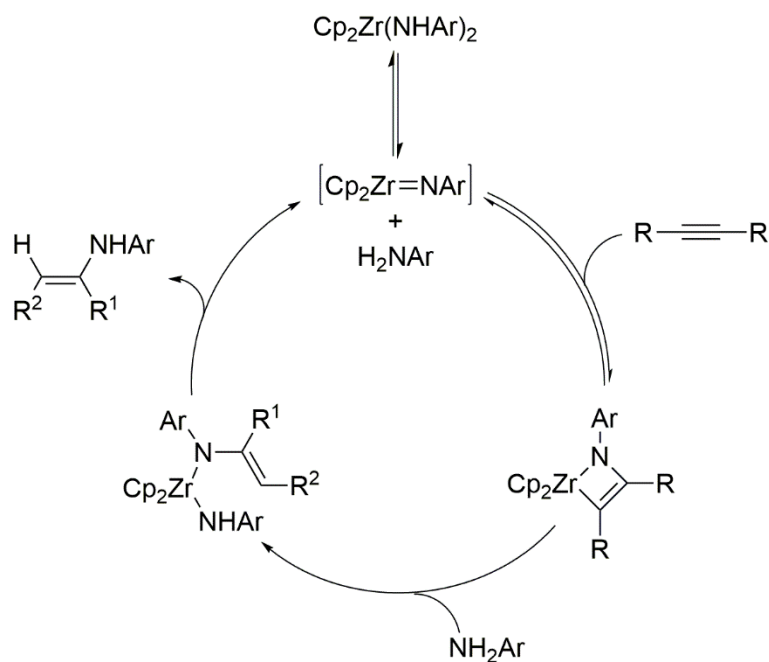
In these reactivity studies, they discovered if they had an alkyne present while they generated the zirconium-imido species it could be trapped as an azazirconacyclobutene via [2+2]-cycloaddition. This, along with reports by Wolczanski and co-workers<sup>30</sup>, was the first glimpse into the rich chemistry these group-4 metal-imido complexes had to offer. Encouraged by the initial studies of Bergman and Wolczanski, Rothwell and co-workers began exploring the chemistry of titanium-imido complexes. In 1990, they report that “the bis(phenylamido) complex will catalyze the reaction of aniline with 3-hexyne to produce the *N*-phenylimine of 3-hexanone.”<sup>31</sup>



**Ar' = 2,6-diphenylphenol**

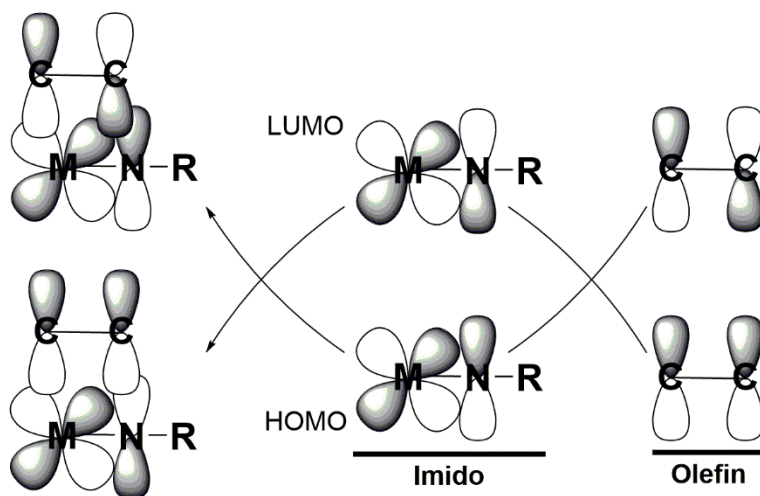
**Scheme 1.6.** The first titanium hydroamination catalyst.<sup>31</sup>

Successive work by Bergman and co-workers provided a detailed look into the mechanism of zirconium intermolecular hydroamination of alkynes.<sup>32-33</sup> As shown in **Scheme 1.7**, the bis-amido zirconocene precatalyst undergoes  $\alpha$ -elimination to form the catalytically active species, a zirconium-imido. This zirconium-imido undergoes a reversible [2+2]-cycloaddition to form an azazirconacyclobutene. This azazirconacyclobutene undergoes protonolysis, using another equivalent of amine, to form an enamido amido complex. After a second proton transfer from the amido group the catalyst is regenerated and the enamine product is released. This mechanism is proposed for other neutral group(IV)<sup>34</sup> and even uranium<sup>8</sup> complexes.



**Scheme 1.7.** The Bergman hydroamination mechanism.<sup>32-33</sup>

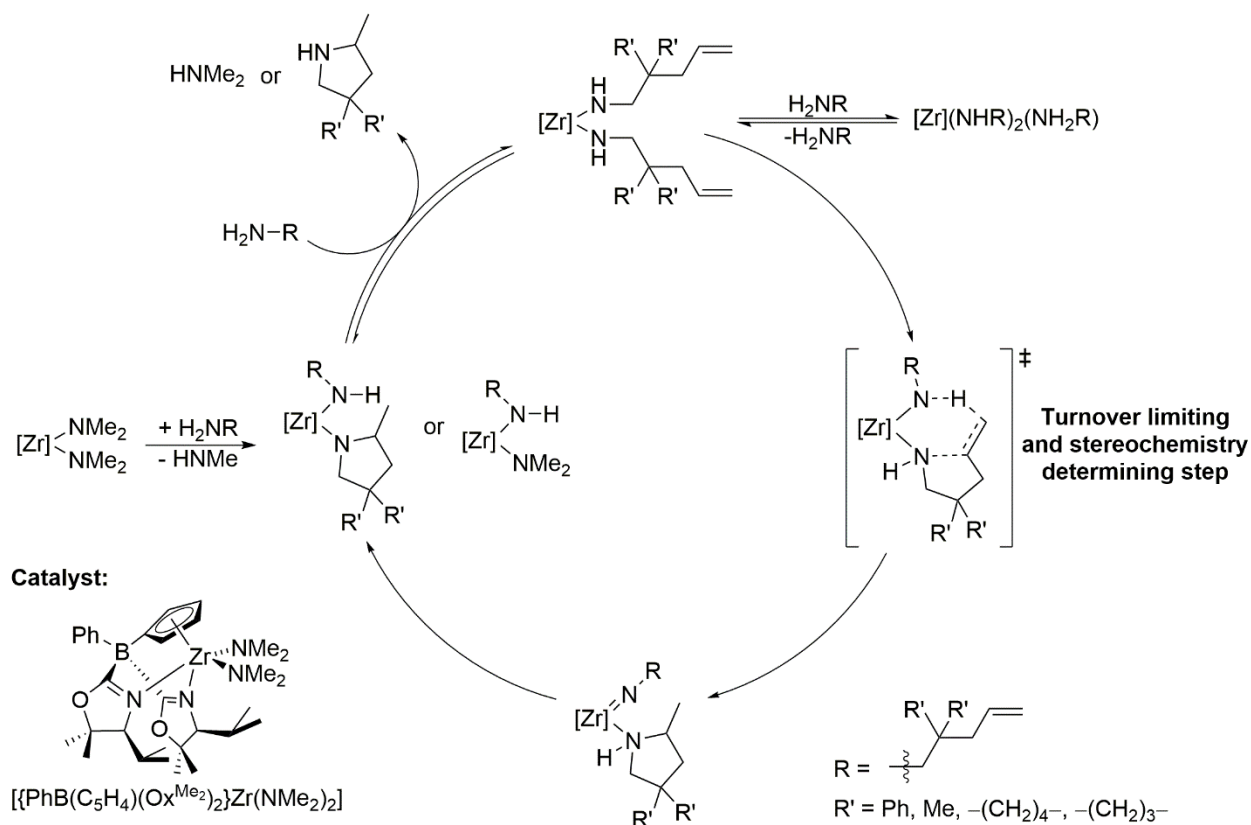
As we saw in **Figure 1.1**, the [2+2]-cycloaddition between the amine (N-H) and the alkene (C=C) was symmetry-forbidden and unfavorable. However, when a transition metal imido (M=N) undergoes a [2+2]-cycloaddition, the resulting process is symmetry-allowed. (**Figure 1.2**) Thus, this favorable process provides a low energy pathway.



**Figure 1.2.** [2+2]-cycloaddition between a metal-imido and olefin.

### Hydroamination through a zirconium-catalyzed concerted C–N and C–H bond formation

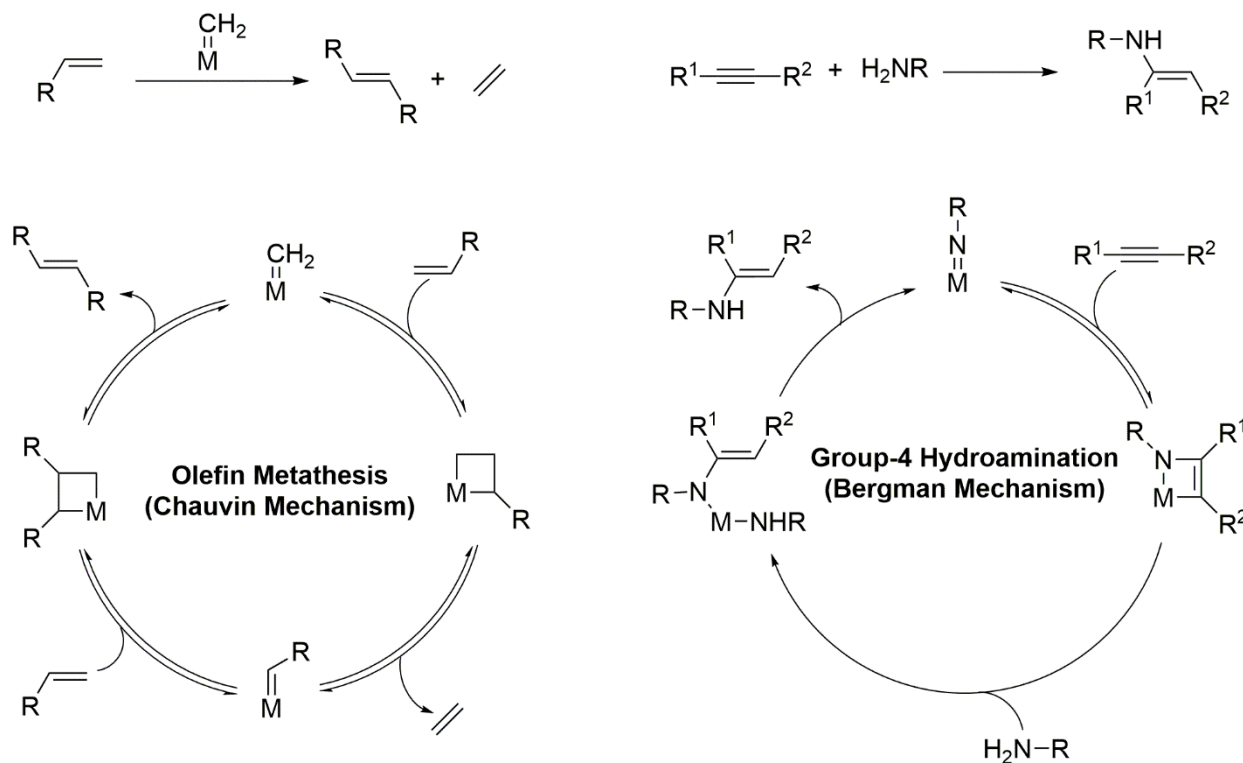
In 2011, Sadow and co-workers proposed a new mechanism for intramolecular alkene hydroamination.<sup>35</sup> In this mechanism (**Scheme 1.8**), after the sequential protolytic replacement of dimethylamide, a zirconium bis-amidoalkene complex is formed (top of the catalytic cycle). Next, is an intermolecular cyclization to produce a zirconium-imido amine complex. A key discovery that Sadow's group made was that the cleavage of the N–H bond and the C–N and C–H bond formation is concerted, during the cyclization step. After the cyclization, the amine transfers a proton producing a zirconium bis-amide complex. In the presence of another equivalent of the amine substrate, the cyclized amine product is released, and the catalyst is regenerated. Since this study, Sadow's group has further investigated this mechanism using aminodialkenes and aminodialkynes.<sup>36</sup>



**Scheme 1.8.** The Sadow hydroamination mechanism.<sup>35</sup>

## 1.4 The Hydroamination of Alkynes in the Odom Group

Many early studies of group-4 hydroamination utilized catalysts with cyclopentadienyl derivatives as their ancillaries. Even though these derivatives are a common ancillary ligand for metal-ligand multiple bond catalysis, they may not be the best. Our research group was inspired to find new ancillary ligand motifs and study the effects on carbon-nitrogen (C-N) and carbon-carbon (C-C) bond forming reactions. At the time, one reaction that has been extensively studied for ancillary ligand effects involving metal-ligand multiple bonds is in Schrock's olefin metathesis.<sup>37</sup> Schrock's olefin metathesis proceeds through the Chauvin mechanism<sup>38</sup> and involves [2+2] and retro-[2+2] cycloaddition processes. When comparing the Chauvin mechanism (olefin metathesis) to the Bergman mechanism (alkyne hydroamination) the two have many similarities (**Scheme 1.9**).

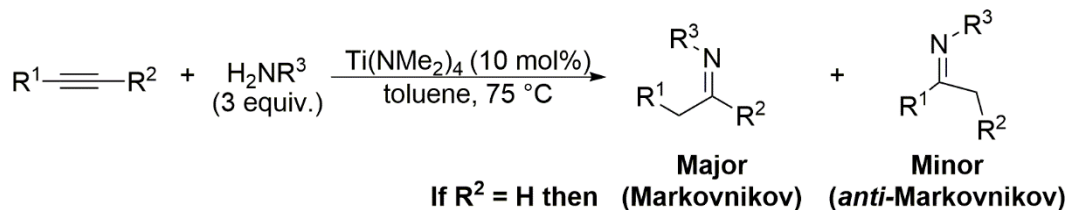


**Scheme 1.9.** Simplified mechanisms for olefin metathesis and hydroamination.<sup>39</sup>

One of the discoveries that Schrock's group had made during their olefin metathesis studies was that they observed an increase in reactivity by increasing the Lewis acidity of the metal center



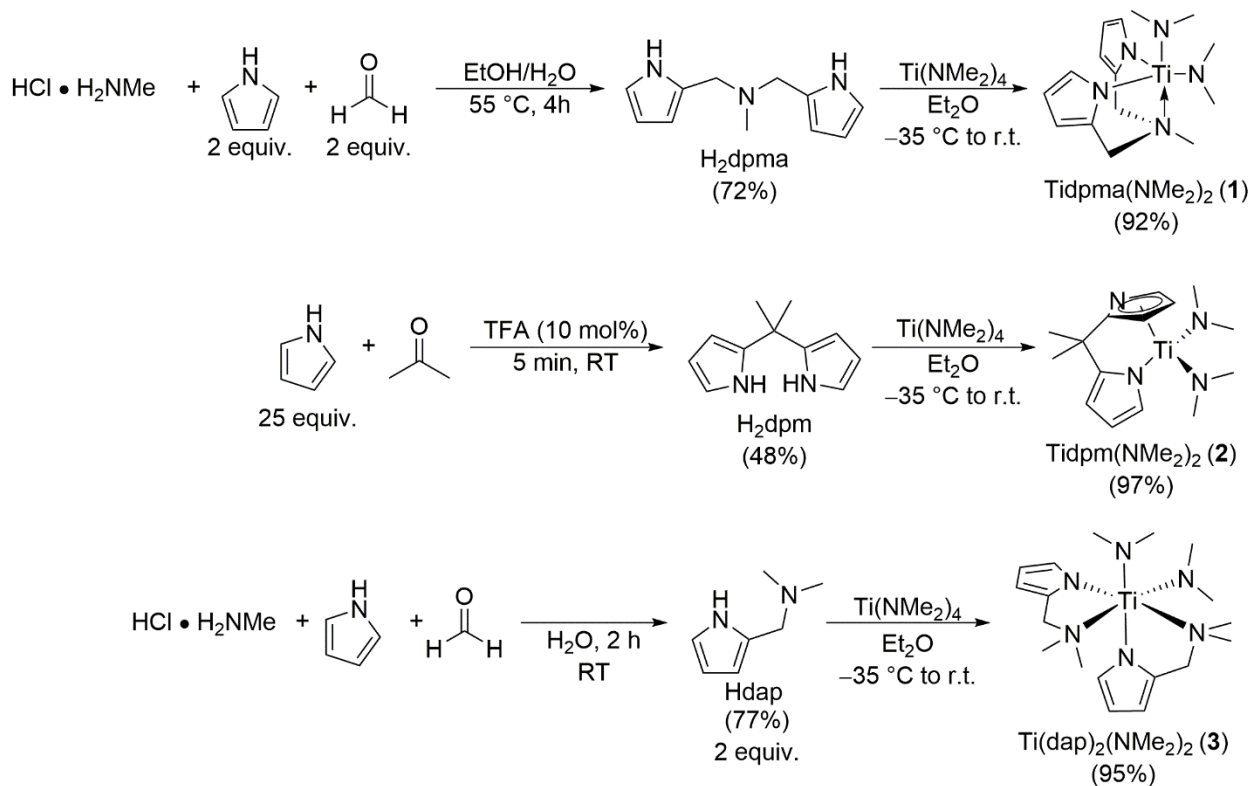
in their d<sup>0</sup>-molybdenum catalysts.<sup>37</sup> Our group was intrigued by this observation and wondered if it was applicable to other d<sup>0</sup> metal-ligand multiple bond catalysis, like titanium-catalyzed alkyne hydroamination. Our group was the first to report that the commercially available Ti(NMe<sub>2</sub>)<sub>4</sub> was an effective pre-catalyst for intermolecular hydroamination of alkynes. Ti(NMe<sub>2</sub>)<sub>4</sub> was very effective when using aryl amines but failed when alkyl amines were employed.<sup>40</sup>



**Scheme 1.10.** Ti(NMe<sub>2</sub>)<sub>4</sub> alkyne hydroamination.<sup>40</sup>

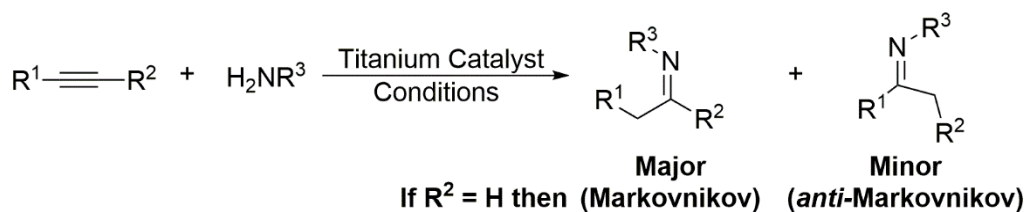
Consequently, our group started to investigate other ancillary ligands to overcome this limitation. Unlike Ti(NMe<sub>2</sub>)<sub>4</sub>, where all ligands are protolytically labile, we needed ancillaries that cannot be displaced from the metal center. Hence, a multidentate chelating ligand would provide stability of the catalytic species and would be difficult to displace. In the case of Ti(NMe<sub>2</sub>)<sub>4</sub> all these ligands are strong  $\pi$ -donors, which should quench the desirable Lewis acidity. Lastly, to make the chemistry widely accessible, the ligands should be cheap and readily available. To meet this criterion our group pursued pyrrolyl-based ancillary ligands. Pyrrole, unlike dimethyl amide, is not strongly  $\pi$ -donating because  $\pi$ -donation to the metal directly competes with the aromatic stabilization energy of pyrrole (~21 kcal/mol<sup>-1</sup>).<sup>39</sup> As a result, metal-centers utilizing pyrrole ancillary ligands are more Lewis acidic and electron deficient. Furthermore, pyrrole can easily be modified by using well-known condensation reactions, allowing multidentate ligands to be easily made. The Odom group's first pyrrole-based ancillary ligand, H<sub>2</sub>dpma, could be synthesized in a single step *via* a double Mannich condensation of pyrrole, formaldehyde and methylamine hydrochloride. Other pyrrole-based ancillary ligands, such as, H<sub>2</sub>dpm and Hdap were also made.

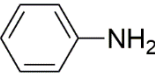
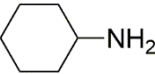
Shown in **Scheme 1.11**, is the synthesis of each of these ancillary ligands and their respective titanium pre-catalysts.



**Scheme 1.11.** Synthesis of titanium hydroamination pre-catalysts.<sup>39</sup>

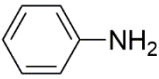
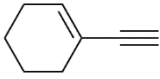
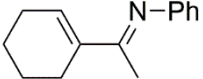
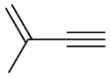
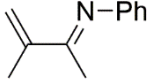
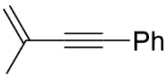
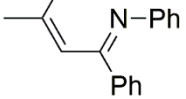
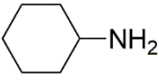
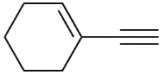
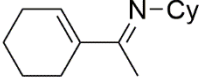
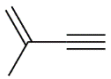
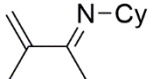
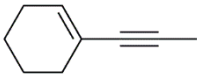
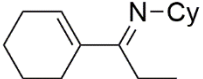
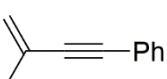
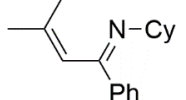
Each of these pyrrolyl-based catalysts are very efficient alkyne hydroamination catalysts, although, each exhibit their own unique reactivity and selectivity for the transformation. When comparing  $\text{Tidpma(NMe}_2)_2$  (**1**) to  $\text{Tidpm(NMe}_2)_2$  (**2**), we observed drastic differences in regioselectivity. For example, when using aniline and 1-hexyne as substrates,  $\text{Tidpma(NMe}_2)_2$  (**1**) is more selective for the Markonikov product (>50:1), whereas  $\text{Tidpm(NMe}_2)_2$  (**2**) gave a selectivity of 6:1. Another example is when aniline and 1-phenylpropyne were used as substrates. When using  $\text{Tidpma(NMe}_2)_2$  (**1**), we observed high selectivity for the liner product (50:1), whereas  $\text{Tidpm(NMe}_2)_2$  (**2**) exhibits high selectivity for the branched product (1:19). (**Table 1.4**)



Amine	Alkyne	Catalyst	Conditions	% Yield	Selectivity
	<i>n</i> -Butyl—C≡C—H	<b>1</b> (10 mol %)	75 °C, 6 h	90	>50:1
		<b>2</b> (5 mol %)	25 °C, 5 min	71	6:1
	Et—C≡C—Et	<b>1</b> (10 mol %)	75 °C, 72 h	63	N/A
		<b>2</b> (5 mol %)	50 °C, 24 h	94	N/A
	Ph—C≡C—H	<b>1</b> (10 mol %)	75 °C, 8 h	38	2:1
		<b>2</b> (5 mol %)	25 °C, 5 min	41	3.6:1
	Ph—C≡C—Ph	<b>1</b> (10 mol %)	130 °C, 74 h	99	N/A
		<b>2</b> (5 mol %)	75 °C, 24 h	84	N/A
	<i>n</i> -Butyl—C≡C—H	<b>1</b> (10 mol %)	75 °C, 72 h	73	2:1
		<b>Data not available</b>			
	Et—C≡C—Et	<b>1</b> (10 mol %)	130 °C, 24 h	57	N/A
		<b>2</b> (10 mol %)	75 °C, 24 h	73	N/A
	Ph—C≡C—H	<b>1</b> (10 mol %)	75 °C, 20 h	50	1:6
		<b>2</b> (5 mol %)	25 °C, 10 h	54	1.6:1
	Ph—C≡C—Ph	<b>1</b> (10 mol %)	130 °C, 24 h	70	N/A
		<b>2</b> (10 mol %)	75 °C, 48 h	72	N/A
	Ph—C≡C—Me	<b>1</b> (10 mol %)	130 °C, 29 h	99	1:4
		<b>2</b> (10 mol %)	75 °C, 24 h	93	11:1

**Table 1.3.** Alkyne hydroamination using catalysts Tidpma(NMe<sub>2</sub>)<sub>2</sub> (**1**), Tidpm(NMe<sub>2</sub>)<sub>2</sub> (**2**).<sup>41-42</sup>

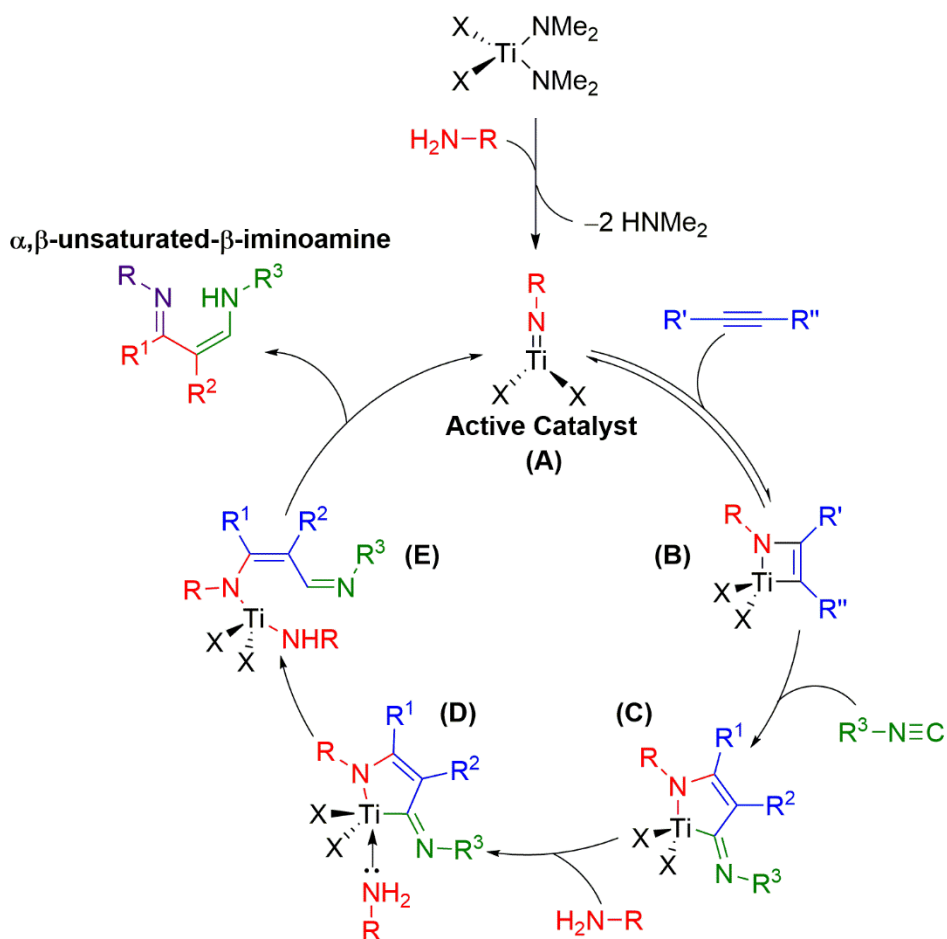
Generally, Tidpm(NMe<sub>2</sub>)<sub>2</sub> (**2**) is the more active catalyst and requires shorter reaction times. This catalyst was also found to be efficient for the hydroamination of enynes, which contain an internal alkyne. However, being a very active catalyst can have some draw-backs. When it came to the hydroamination of enynes that contained a terminal alkyne, it was a relatively poor catalyst. For these highly reactive and sensitive (to polymerization) enynes, Ti(dap)<sub>2</sub>(NMe<sub>2</sub>)<sub>2</sub> (**3**) was often the preferred catalyst. (**Table 1.4**)

Amine	Enyne	Catalyst (10 mol %) and Conditions	% Yield	Product
		<b>3</b> , 50 °C, 16 h	88	
		<b>3</b> , 50 °C, 44 h	64	
		<b>3</b> , 130 °C, 19 h	70	
		<b>3</b> , 50 °C, 24 h	78	
		<b>3</b> , 50 °C, 19 h	73	
		<b>2</b> , 100 °C, 5 h	73	
		<b>2</b> , 100 °C, 70 h	73	

**Table 1.4.** Hydroamination of enynes using  $\text{Ti}(\text{dpm})(\text{NMe}_2)_2$  (**2**) or  $\text{Ti}(\text{dap})_2(\text{NMe}_2)_2$  (**3**).<sup>43</sup>

## 1.5 Iminoamination in the Odom Group

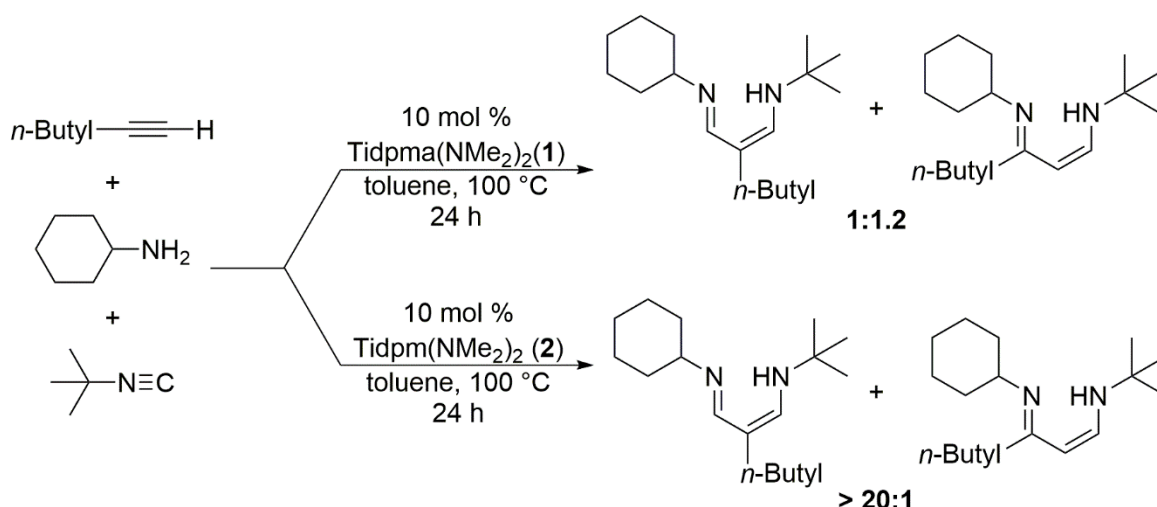
According to the Bergman hydroamination mechanism, (**Section 1.3**), after the [2+2]-cycloaddition, a reactive titanium-carbon bond is generated. This intermediate is trapped during the slow step<sup>34</sup> in the catalysis by a proton from another equivalent of amine. With this in mind, our group wondered if this intermediate could be trapped with something other than a simple proton. Our group decided to try to trap this intermediate with an isonitrile derivative. Our group discovered that *tert*-butylisonitrile could indeed trap this intermediate to form a C-C bond! The proposed mechanism for this reaction is a slight modification of the Bergman hydroamination mechanism. (**Scheme 1.12**)<sup>32-33</sup>



**Scheme 1.12.** Proposed mechanism for the titanium-catalyzed Iminoamination of alkynes.<sup>39, 44</sup>

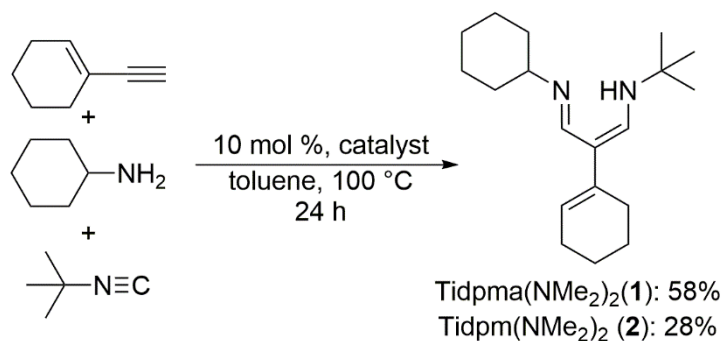
The titanium-precatalyst undergoes protonolysis to form a titanium-imido, the active catalyst. **(A)** Once again, the active catalyst undergoes [2+2]-cycloaddition with the alkyne to form the azatitanacyclobutene. **(B)** Once here, instead of undergoing protonolysis by an amine, the metallacycle undergoes an isonitrile insertion to form a new 5-membered metallacycle. **(C)** After coordination of another equivalent of amine **(D)**, the metallocycle undergoes protonolysis of the titanium-carbon bond. **(E)** After another proton transfer, the product is released, and the catalyst is regenerated. **(E to A)** The final product is essentially a iminyl and an amino group added across the carbon-carbon triple bond, i.e. iminoamination of alkyne. The products formed are  $\alpha,\beta$ -unsaturated- $\beta$ -iminoamines, which are tautomers of unsymmetrical 1,3-diimines.<sup>45</sup> This atom-economical multicomponent coupling, thermodynamically, is calculated to be exothermic ( $\Delta H \approx 65$  kcal/mol). Entropically, one would presume this process is unfavorable, but iminoamination is calculated to have a large driving force ( $\Delta G \approx -41$  kcal/mol).<sup>44</sup>

Generally, our group uses the precatalysts  $\text{Tidpma}(\text{NMe}_2)_2$  (**1**) and  $\text{Tidpm}(\text{NMe}_2)_2$  (**2**) for the iminoamination of alkynes and yields (on average) are around 70% for most substrates. This reaction does require longer reaction times (12-48 h) compared to hydroamination. Utilizing these catalysts, we can control the regioselectivity for the addition to the alkyne. As shown in **Scheme 1.13**, when using cyclohexylamine, 1-hexyne, and *tert*-butylisonitrile in the presence of 10 mol%  $\text{Tidpma}(\text{NMe}_2)_2$  (**1**) two regiomeric 3CC products are observed in a 1:1.2 ratio. When the precatalyst  $\text{Tidpm}(\text{NMe}_2)_2$  (**2**) is used, the opposite regioselectivity is observed in a >20:1 ratio.



**Scheme 1.13.** Effects of precatalyst on regioselectivity using an alkyl amine and alkyne.<sup>41</sup>

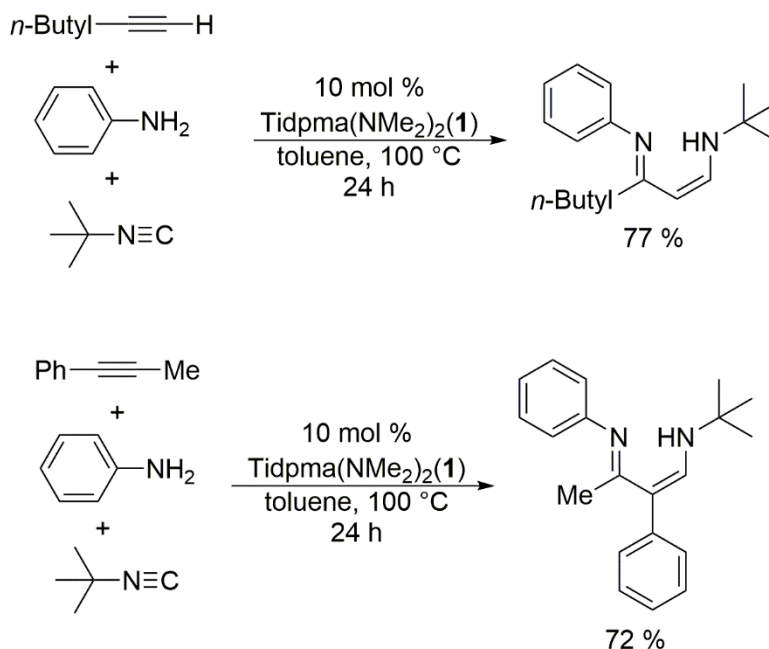
Moving from a terminal alkyl alkyne to a terminal enyne,  $\text{Tidpm}(\text{NMe}_2)_2$  (**2**) is the preferred catalyst. Using the catalyst  $\text{Tidpma}(\text{NMe}_2)_2$  (**1**) results in inferior yields of the 3CC product. Interestingly, as shown in **Scheme 1.14**, both these catalysts produce a single regioisomer with only a trace of the other isomer detected.



**Scheme 1.14.** Effects of precatalyst on regioselectivity using an alkyl amine and enyne.<sup>41</sup>

The regioselectivity can be further influenced by switching the amine from cyclohexylamine to aniline. When a terminal alkyl alkyne is used, in the presence of  $\text{Tidpma}(\text{NMe}_2)_2$  (**1**), a single regioisomer is observed. (**Scheme 1.15**) However, as we previously saw in **Scheme 1.14**, this is the opposite regioselectivity observed when  $\text{Tidpm}(\text{NMe}_2)_2$  (**2**) was used with cyclohexylamine. By simply changing the amine substrate (and catalyst), we can

selectively gain access to the two possible regioisomers. *This strategy has become useful in our group's heterocyclic syntheses (Section 1.6).* However, when an internal aryl alkyne (or terminal aryl alkyne<sup>45</sup>) is used, a single isomer is observed.

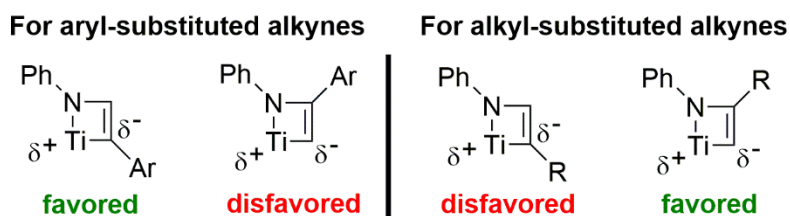


**Scheme 1.15.** Effects of precatalyst on regioselectivity using an aryl amine.<sup>39</sup>

If we recall, in **Table 1.3**, when phenylacetylene and aniline were used in the hydroamination reaction,  $\text{Tidpma(NMe}_2)_2$  (**1**) exhibited slightly higher selectivity (2:1) for the Markovnikov product. This is the opposite trend that is observed when phenylacetylene is used in the 3CC reaction. Thus, the major products in iminoamination and hydroamination may not come from the azatitanacyclobutene intermediate. “*The regioselectivity for the 3CC reaction is set by the [2+2]-cycloaddition, in combination with the relative trapping rates of the isonitrile. Which is presumably a reflection of Curtin-Hammett kinetics (i.e. two different trapping agents with different relative trapping rates for the metallacycles)*”.<sup>44</sup> It is proposed that the regioselectivity of the alkyne addition is electronically controlled. When an arene (or vinyl) substituent is found on the alkyne, the partial anionic charge (on the carbon adjacent to the metal) can be stabilized through



the  $\pi$ -system. In the case of a terminal alkyl alkyne, having the alkyl substituent on the carbon adjacent to the nitrogen is preferred. (**Figure 1.3**)

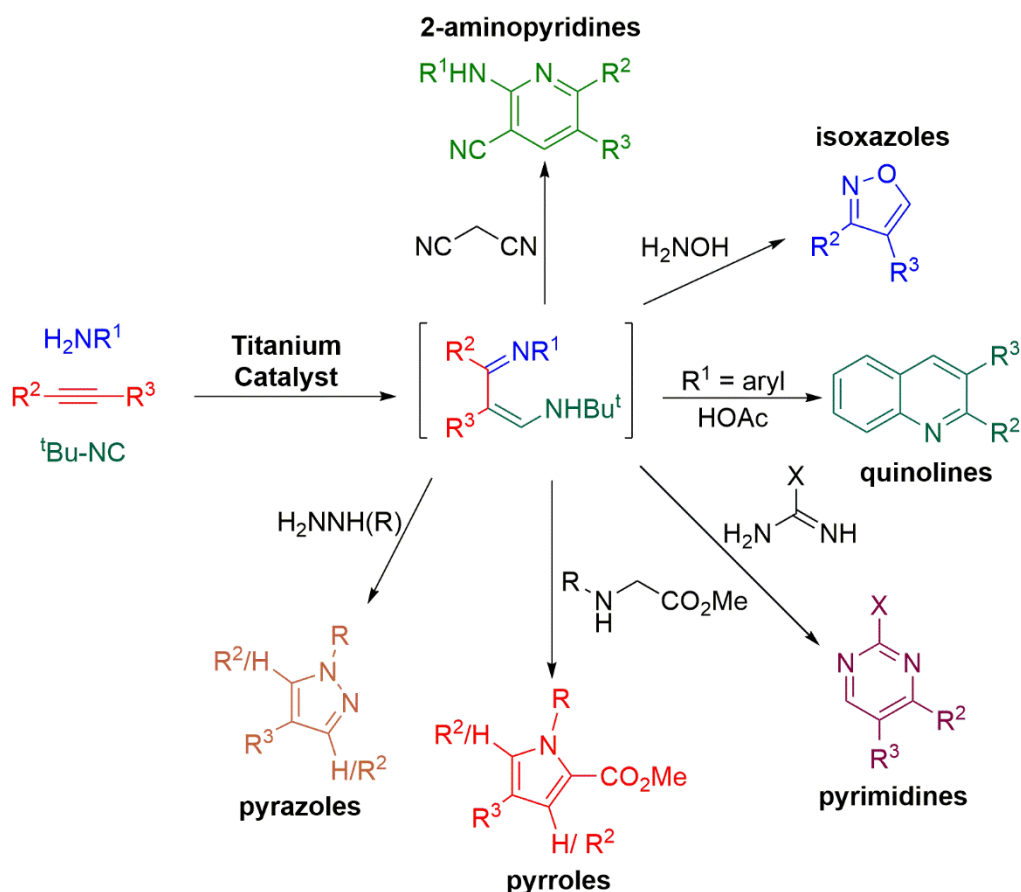


**Figure 1.3.** Effects of precatalyst on regioselectivity using an aryl amine.<sup>41, 46</sup>

Like hydroamination, iminoamination is an 100% atom-economical reaction and provides an invaluable route into the formation of new C–C and C–N bonds. In the last decade, our group has expanded this chemistry for the synthesis of a multitude of nitrogen-based products.

## 1.6 The Synthesis of Nitrogen-based Heterocycles in the Odom Group

Nitrogen-based heterocycles are common motifs found in pharmaceuticals, agrochemicals and even solar cell dyes.<sup>44, 47</sup> Since the discovery of our group's three-component coupling (3CC) reaction, we have utilized these products to synthesize a variety of nitrogen-based heterocycles. Starting from an amine, alkyne, and isonitrile, the 3CC product is formed. Once the 3CC is formed, another reagent is added to construct the desired heterocycle. All the heterocycles, shown in **Scheme 1.16**, can be made in a one-pot, two-step sequence. With a large variety of commercially available amines and alkynes, we have access to a multitude of possible heterocyclic products. This allows us to rapidly screen these heterocycles for various applications.



**Scheme 1.16.** Nitrogen-based heterocycle synthesis using iminoamination of alkynes.

## **REFERENCES**

## REFERENCES

1. Müller, T. E.; Hultsch, K. C.; Yus, M.; Foubelo, F.; Tada, M., *Chem. Rev.* **2008**, *108*, 3795-3892.
2. Roose, P.; Eller, K.; Henkes, E.; Rossbacher, R.; Höke, H., Amines, Aliphatic. In *Ullmann's Encyclopedia of Industrial Chemistry*, Wiley-VCH Verlag GmbH & Co. KGaA: 2000.
3. Sherman, P. D.; Kavasmaneck, P. R., *Kirk-Othmer Encyclopedia of Chemistry and Technology*. Wiley: New York, 1980; Vol. 2, 338.
4. Brunet, J.-J.; Neibecker, D., Catalytic Hydroamination of Unsaturated Carbon-Carbon Bonds. In *Catalytic Heterofunctionalization*, Wiley-VCH Verlag GmbH: 2001; pp 91-141.
5. Falbe, J.; Bahrmann, H., *New Syntheses with Carbon Monoxide*. Springer-Verlag GmbH: 1980.
6. Müller, T. E.; Beller, M., *Chem. Rev.* **1998**, *98*, 675-704.
7. Taube, R., Reaction with Nitrogen Compounds: Hydroamination. In *Applied Homogeneous Catalysis with Organometallic Compounds*, Wiley-VCH Verlag GmbH: 2008; pp 513-524.
8. Straub, T.; Haskel, A.; Neyroud, T. G.; Kapon, M.; Botoshansky, M.; Eisen, M. S., *Organometallics* **2001**, *20*, 5017-5035.
9. Pohlki, F.; Doye, S., *Chem. Soc. Rev.* **2003**, *32*, 104-114.
10. Steinborn, D.; Taube, R., *Z. Chem.* **1986**, *26*, 349.
11. Suminov, S. I.; Kost, A. N., *Russ. Chem. Rev.* **1969**, *38*, 884.
12. Chekulaeva, I. A.; Kondrat'eva, L. V., *Russ. Chem. Rev.* **1965**, *34*, 669.
13. Burgada, R.; Mohri, A., *Phosphorus and Sulfur and the Related Elements* **1982**, *13*, 85-95.
14. Gibson, M. S., *The Chemistry of the Amino Group*. John Wiley & Sons: New York, 1968.
15. Hegedus, L. S., *Angew. Chem. Int. Ed. Engl.* **1988**, *27*, 1113-1126.
16. Eisenstein, O.; Hoffmann, R., *J. Am. Chem. Soc.* **1981**, *103*, 4308-4320.
17. Åkermark, B.; Bäckvall, J. E.; Hegedus, L. S.; Zetterberg, K.; Siirala-Hansén, K.; Sjöberg, K., *Journal of Organometallic Chemistry* **1974**, *72*, 127-138.

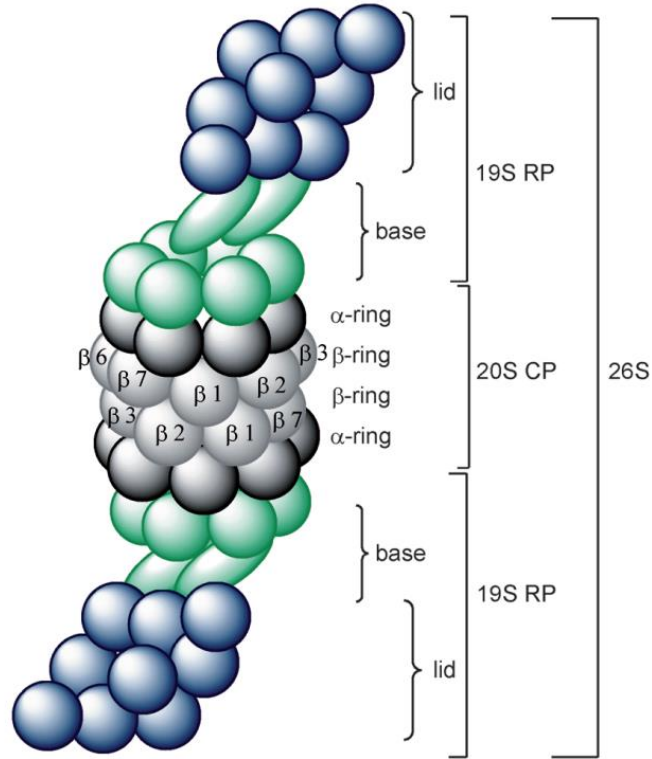
18. Bender, C. F.; Widenhoefer, R. A., *J. Am. Chem. Soc.* **2005**, *127*, 1070-1071.
19. Qian, H.; Widenhoefer, R. A., *Org. Lett.* **2005**, *7*, 2635-2638.
20. Burling, S.; Field, L. D.; Messerle, B. A., *Organometallics* **2000**, *19*, 87-90.
21. Burling, S.; Field, L. D.; Messerle, B. A.; Turner, P., *Organometallics* **2004**, *23*, 1714-1721.
22. Field, L. D.; Messerle, B. A.; Wren, S. L., *Organometallics* **2003**, *22*, 4393-4395.
23. Hartwig, J. F., *Organotransition Metal Chemistry: From Bonding to Catalysis*. University Science Books: Mill Valley, California, 2010, pg. 713.
24. Casalnuovo, A. L.; Calabrese, J. C.; Milstein, D., *J. Am. Chem. Soc.* **1988**, *110*, 6738-6744.
25. Hong, S.; Marks, T. J., *Acc. Chem. Res.* **2004**, *37*, 673-86.
26. Gribkov, D. V.; Hultsch, K. C., *Angew. Chem. Int. Ed.* **2004**, *43*, 5542-5546.
27. Crimmin, M. R.; Casely, I. J.; Hill, M. S., *J. Am. Chem. Soc.* **2005**, *127*, 2042-2043.
28. Zulys, A.; Dochnahl, M.; Hollmann, D.; Löhnwitz, K.; Herrmann, J.-S.; Roesky, P. W.; Blechert, S., *Angew. Chem. Int. Ed.* **2005**, *44*, 7794-7798.
29. Walsh, P. J.; Hollander, F. J.; Bergman, R. G., *J. Am. Chem. Soc.* **1988**, *110*, 8729-8731.
30. Cummins, C. C.; Baxter, S. M.; Wolczanski, P. T., *J. Am. Chem. Soc.* **1988**, *110*, 8731-8733.
31. Hill, J. E.; Proffitt, R. D.; Fanwick, P. E.; Rothwell, I. P., *Angew. Chem. Int. Ed. Engl.* **1990**, *29*, 664-665.
32. Walsh, P. J.; Baranger, A. M.; Bergman, R. G., *J. Am. Chem. Soc.* **1992**, *114*, 1708-1719.
33. Baranger, A. M.; Walsh, P. J.; Bergman, R. G., *J. Am. Chem. Soc.* **1993**, *115*, 2753-2763.
34. Pohlki, F.; Doye, S., *Angew. Chem. Int. Ed.* **2001**, *40*, 2305-2308.
35. Manna, K.; Xu, S.; Sadow, A. D., *Angew. Chem. Int. Ed. Engl.* **2011**, *50*, 1865-8.
36. Manna, K.; Eedugurala, N.; Sadow, A. D., *J. Am. Chem. Soc.* **2015**, *137*, 425-35.
37. Schrock, R. R., *Chem. Rev.* **2002**, *102*, 145-180.
38. Jean-Louis Hérisson, P.; Chauvin, Y., *Die Makromolekulare Chemie* **1971**, *141*, 161-176.

- 39. Odom, A. L., *Dalton Trans* **2005**, 225-33.
- 40. Shi, Y. H.; Ciszewski, J. T.; Odom, A. L., *Organometallics* **2001**, 20, 3967-3969.
- 41. Marjumder, S., *Ph. D. Dissertation, Michigan State University* **2009**.
- 42. Cao, C.; Ciszewski, J. T.; Odom, A. L., *Organometallics* **2001**, 20, 5011-5013.
- 43. Cao, C.; Li, Y.; Shi, Y.; Odom, A. L., *Chem Commun (Camb)* **2004**, 2002-3.
- 44. Odom, A. L.; McDaniel, T. J., *Acc. Chem. Res.* **2015**, 150821102447001.
- 45. Cao, C.; Shi, Y.; Odom, A. L., *J. Am. Chem. Soc.* **2003**, 125, 2880-1.
- 46. Dissanayake, A. A., *Ph. D. Dissertation, Michigan State University* **2013**.
- 47. Chenier, P. J., *Survey of Industrial Chemistry*. John Wiley & Sons: New York, 1986.

## Chapter 2. Substituted Quinolines as Non-Covalent Proteasome Inhibitors

### 2.1 Introduction to the Proteasome

Proteins undergo constant proteolysis for the regulation of intracellular processes to maintain biological homeostasis.<sup>1-2</sup> During this process, misfolded and nonessential proteins are tagged with ubiquitin. These ubiquitylated proteins are marked for proteolytic degradation by the 26S proteasome. The 26S proteasome is a massive (2.5 MDa), multi-subunit complex that degrades proteins into smaller peptides. The 26S consists of a hollow barrel shaped 20S proteolytic core and this core is capped with two 19S regulatory particles.<sup>3</sup> (**Figure 2.1**) The 20S core is a threonine protease and is made up of four stacked rings, two  $\alpha$ -rings and two  $\beta$ -rings. These  $\beta$ -rings each contain three distinct catalytic subunits ( $\beta$ 1,  $\beta$ 2 and  $\beta$ 5) that exhibit caspase-like (Casp-L), trypsin-like (T-L) and chymotrypsin-like (CT-L) activity, respectively.<sup>4</sup> Each subunit cleaves peptide bonds through the same mechanism, however, they differ in substrate preferences. For instance, Casp-L prefers acidic residues, whereas, T-L prefers basic residues and CT-L prefers large hydrophobic residues. The 19S, on the other hand, is responsible for the recognition of ubiquitylated proteins. Once recognized these proteins undergo unfolding and translocation into the 20S core.<sup>5</sup>

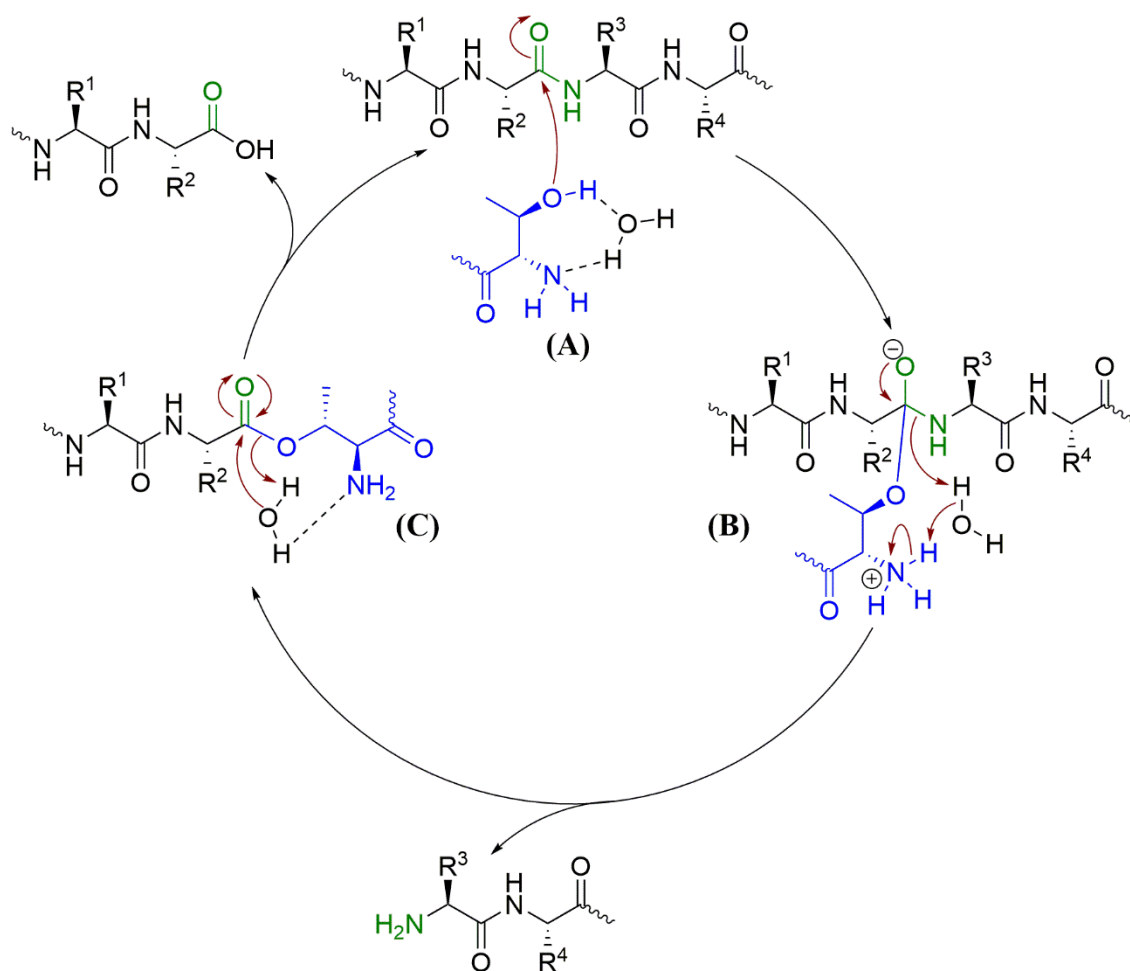


**Figure 2.1.** The composition of the 26S proteasome.<sup>6</sup>

While each subunit helps with proteolytic degradation, one is a larger contributor than the others. The role of each active site ( $\beta 1$ ,  $\beta 2$  and  $\beta 5$ ) in cell growth and proteolytic degradation was addressed through site-directed mutations in the yeast *S. cerevisiae*. Through mutation of the catalytic threonine, in the  $\beta 5$  active sites, significantly stunted growth, increased production of abnormal proteins (thus, causing more misfolded proteins to be produced) and increased accumulation of proteasome substrates.<sup>7-8</sup> When similar mutations were done to the  $\beta 1$  sites, no accumulation of substrates was observed. Deactivation of the  $\beta 2$  sites only slightly reduced growth rates and only some model substrates showed reduced degradation rate.<sup>8-9</sup> Even deactivating both the  $\beta 1$  and  $\beta 2$  sites showed fewer defects than when just the  $\beta 5$  site itself was deactivated. Therefore, the  $\beta 5$  sites (chymotrypsin-like) seem to be the more important sites for the breakdown of proteins.<sup>7-9</sup>



Even though the contribution of each site is different, for the breakdown of proteins, each site ( $\beta 1$ ,  $\beta 2$  and  $\beta 5$ ) operates through the same mechanism. Each site contains a hydroxyl group on an N-terminal threonine which serves as a catalytic nucleophile. This N-terminal threonine is what is responsible for cleaving peptide bonds. The catalytic mechanism is shown below in **Scheme 2.1**. First, the N-terminal threonine's hydroxy group attacks the amide carbonyl (**A**). This produces a tetrahedral intermediate, which collapses down releasing the primary amine segment of the peptide (**B**). Next, the newly formed ester undergoes hydrolysis which releases the carboxylic acid segment of the peptide (**C**). Thus, turning over the catalytic cycle by regenerating the catalytic threonine.



**Scheme 2.1.** The catalytic mechanism of the  $\beta$ -subunits in the proteasome.<sup>10</sup>

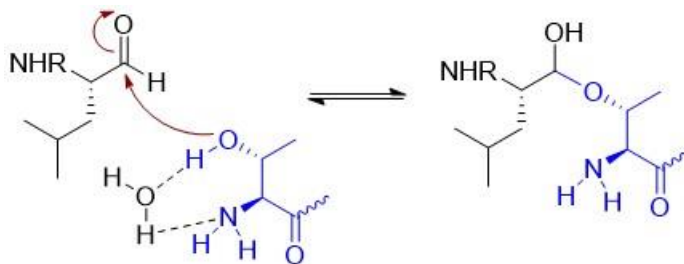
This process is a vital part of the ubiquitin-proteasome pathway. The ubiquitin-proteasome pathway is a crucial quality-control pathway for recently synthesized proteins in eukaryotic cells.<sup>10-12</sup> This pathway also participates in the regulation of many cellular functions, through targeted destruction of regulatory proteins. For instance, the progression of the cell-cycle is nearly impossible without timely degradation of cyclins and cyclin-dependent kinase inhibitors through the ubiquitin-proteasome pathway.<sup>10, 13</sup> This discovery suggests the inhibition of the proteasome should block this process and thus, prevent malignant cells from proliferating. Originally proteasome inhibitors were developed initially as anti-inflammatory agents, when cultured cancer cells were treated with proteasome inhibitors, it caused rapid apoptosis. Better yet, this apoptosis was selective for transformed cells, thus lessening the concern that proteasome inhibitors could be too toxic if they inhibited the protein quality-control capacity, through ubiquitin-proteasome pathway, in normal cells.<sup>10, 14</sup> Generally, cancer cells have higher levels of proteasome activity when compared to non-transformed cells. This is presumably due to the cancer cell's increased metabolism and high levels of growth factors. Consequently, cancer cells should be more sensitive to proteasome inhibitors.<sup>6, 15</sup> In light of these discoveries, modulation of the proteasome function has manifested itself as an important tactic to treat various diseases<sup>16-17</sup> and a few proteasome inhibitors have been clinically approved.<sup>18-20</sup>

## 2.2 Proteasome Inhibitors

Proteasome inhibitors are very diverse, and can be divided into different groups depending on whether they form a covalent bond with the threonine in the active site or not (i.e. covalent or noncovalent inhibitors). In addition, allosteric proteasome inhibitors (i.e. an inhibitor that does not interact with the active site) have also been studied.<sup>10</sup> Each of these three kinds of inhibitors will be discussed in this section.

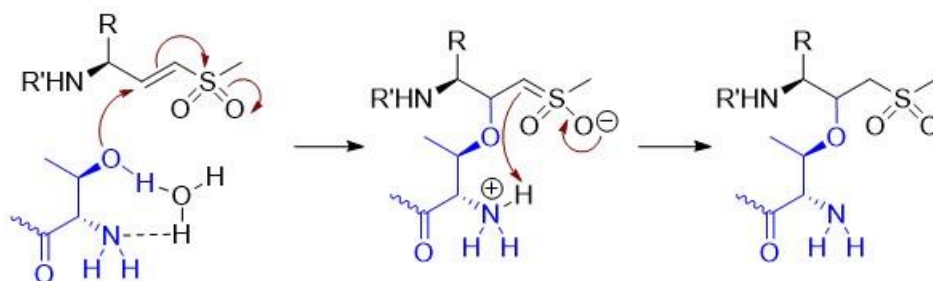
Covalent inhibitors generally feature a peptide moiety and an electrophilic warhead (i.e. trap) that can interact with the threonine in the active site. Depending on the nature of the electrophilic warhead, there are eight major classes of covalent proteasome inhibitors each are briefly described below: aldehydes, vinyl sulfones, vinylamides,  $\alpha',\beta'$ -epoxyketones,  $\alpha$ -ketoaldehydes,  $\beta$ -lactones, oxatiazol-2-ones and boronates.

1) *Aldehydes* (or more specifically peptide aldehydes) were the first proteasome inhibitors developed.<sup>21</sup> The aldehyde's electrophilic carbonyl carbon reacts with the threonine in the active site forming a hemiacetal, that is reversible.<sup>22</sup> (**Scheme 2.2**) However, using this kind of electrophilic warhead has some drawbacks. Utilizing this reaction mechanism, serine or cysteine proteases can also target the aldehyde, and they can be inactivated through oxidation. These two drawbacks could limit the therapeutic potential of this kind of inhibitor.<sup>10, 23-24</sup>



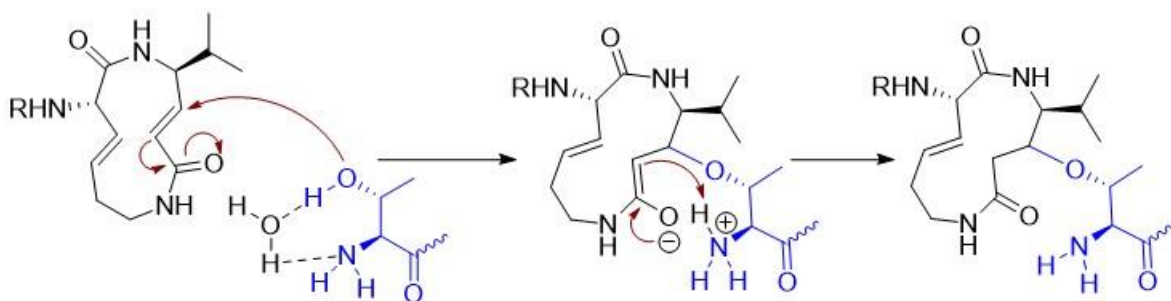
**Scheme 2.2.** Aldehyde mechanism.<sup>10, 24</sup>

2) *Vinyl sulfones* react via a Michael-type 1,4-addition with the threonine in the active site. This results in the formation of an ether bond that is irreversible.<sup>25-26</sup> Again, this is a nonspecific reaction mechanism and therefore the thiol group on cysteine proteases also react with these vinyl sulfones.<sup>24-25</sup>



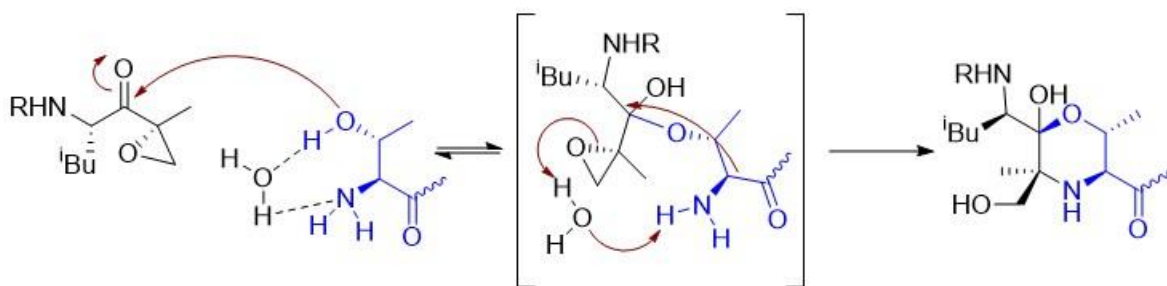
**Scheme 2.3.** Vinyl sulfones mechanism.<sup>10, 24</sup>

3) *Vinylamides* (*syrbactins*) also react via a Michael-type 1,4-addition. This 12-membered lactam reacts with the threonine forming an ether bond that is again, irreversible. Similarly, to the vinyl sulfones, vinyl amides can also suffer from a nonspecific mechanism and could inhibit cysteine proteases as well.<sup>24, 27</sup>



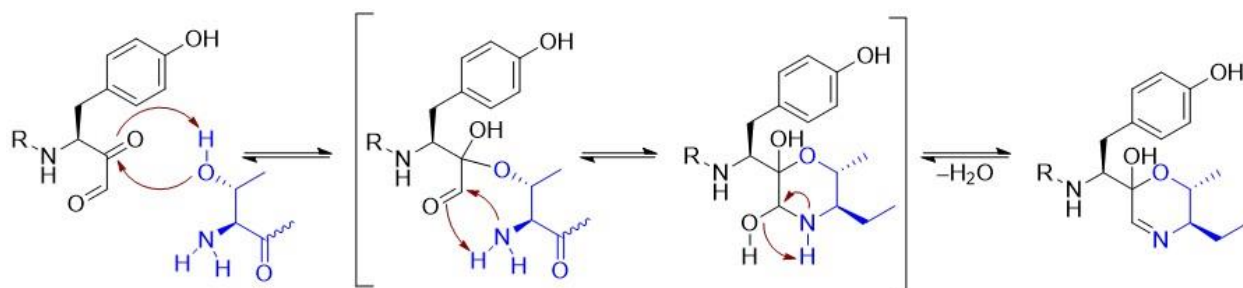
**Scheme 2.4.** Vinylamides mechanism.<sup>10, 24</sup>

4)  $\alpha'$ ,  $\beta'$ -epoxyketones react with the threonine through a two-step mechanism. First, the formation of the a hemiketal, that is reversible. Followed by a nucleophilic attack on the epoxide forming a morpholine ring, that is irreversible.<sup>28</sup>



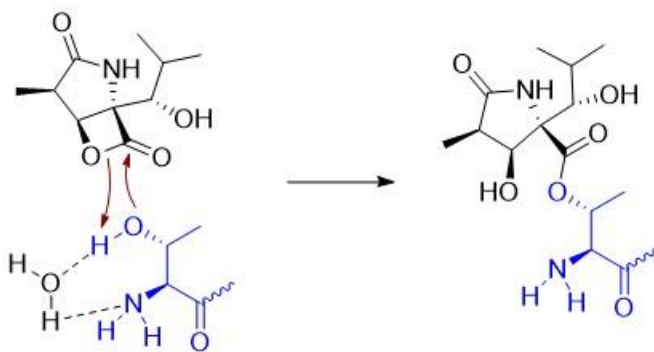
**Scheme 2.5.**  $\alpha'$ ,  $\beta'$ -epoxyketones mechanism.<sup>10, 24</sup>

5)  $\alpha$ -ketoaldehydes proceed through a similar mechanism as saw in the  $\alpha'$ ,  $\beta'$ -epoxyketones. First, a reversible hemiketal is the formed. Then, a nucleophilic attack on the aldehyde forms a hemiaminal intermediate that undergoes condensation to give a reversible oxazine ring. Due to this unique mode of action, both  $\alpha'$ ,  $\beta'$ -epoxyketones and  $\alpha$ -ketoaldehydes are the most specific functional head groups for 20S proteasome inhibition.<sup>24</sup>



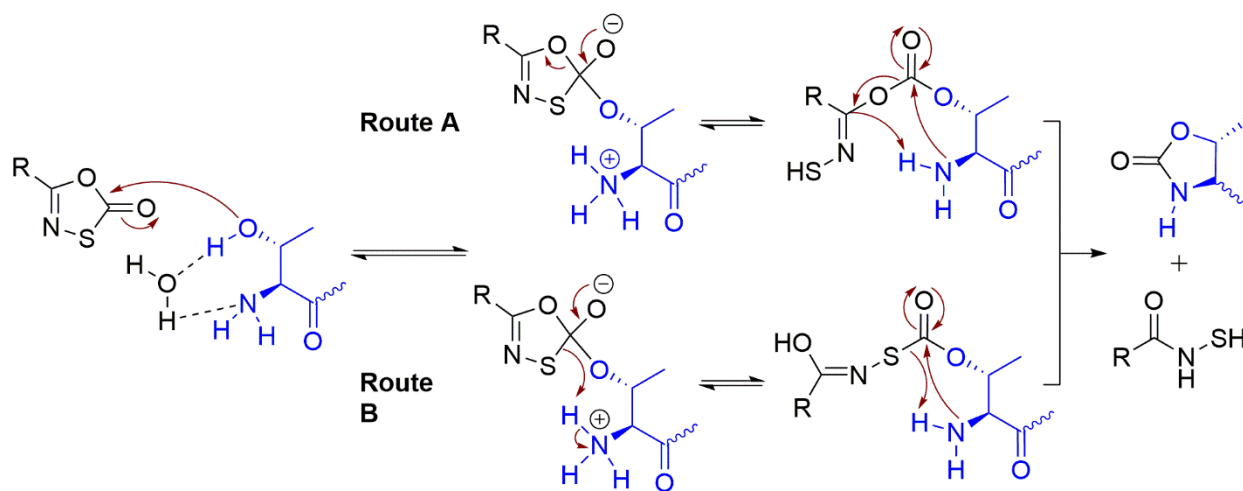
**Scheme 2.6.**  $\alpha$ -ketoaldehydes mechanism.<sup>10, 24</sup>

6)  $\beta$ -lactones react via nucleophilic attack of the threonine causing the lactone to ring open, forming the  $\alpha$ -hydroxy ester.



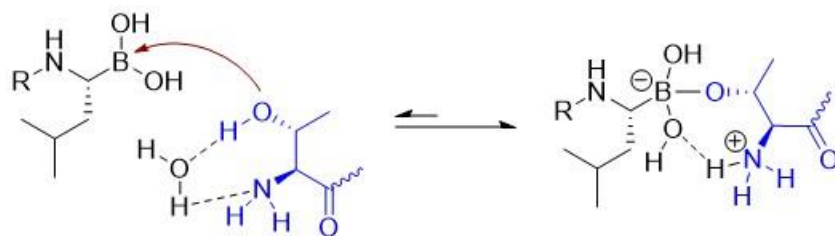
**Scheme 2.7.**  $\beta$ -lactones mechanism.<sup>10, 24</sup>

7) *Oxatiazol-2-ones* react through nucleophilic attack of the threonine. This results in ring opening of the heterocycle to form the carbonate or thiocarbonate. These carbonates undergo another attack by the threonine causing it to cyclize to the oxazolidine-2-one. While these kinds of inhibitors are very specific and irreversible, they are limited to mycobacterial proteasomes at this time.<sup>10</sup>



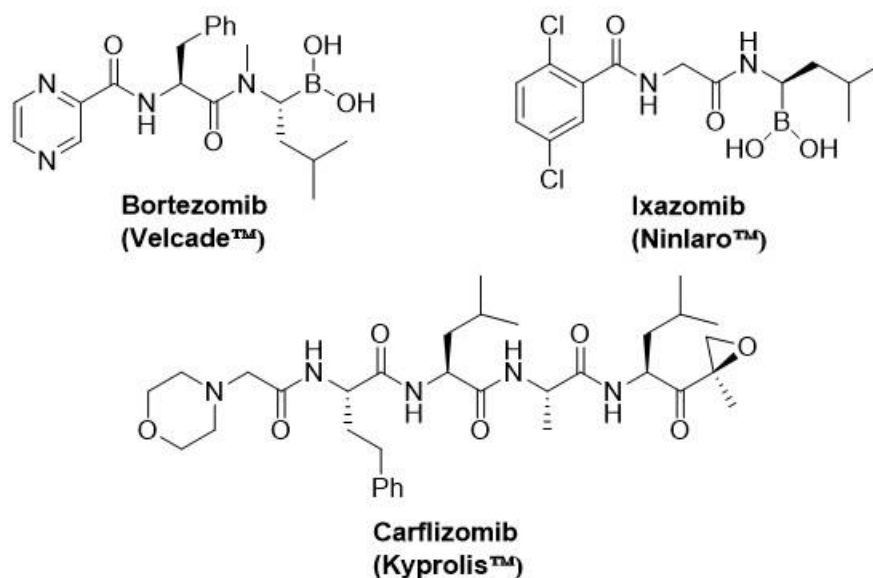
**Scheme 2.8.** *Oxatiazol-2-ones* mechanism.<sup>10</sup>

8) *Boronates* react *via* nucleophilic attack of the threonine creating a reversible borate anion. However, this tetrahedral borate is stabilized through hydrogen bonding thus enhancing its affinity, making the reverse reaction difficult.



**Scheme 2.9.** Boronates mechanism.<sup>10, 24</sup>

As shown, there are many different modes by which these covalent inhibitors can inhibit the proteasome. Currently, the U.S. Food and Drug Administration (FDA) has approved three proteasome inhibitors for various types of cancers; bortezomib, carfilzomib, and ixazomib. **(Figure 2.2)** Bortezomib was the first proteasome inhibitor,<sup>11</sup> which was approved by the FDA in 2003, for the treatment of multiple myeloma.<sup>29</sup> Bortezomib's success thus validated the proteasome as an anti-cancer target.<sup>30</sup> A few years later, in 2008, bortezomib was also approved for the treatment of mantle cell lymphoma.<sup>31</sup> In 2012, carfilzomib became the second FDA approved proteasome inhibitor as a treatment for multiple myeloma. More recently, in 2015, Ixazomib became the first FDA approved proteasome inhibitor that was orally-available for the treatment of multiple myeloma.<sup>32</sup>



**Figure 2.2.** FDA approved proteasome inhibitors bortezomib, carfilzomib, and ixazomib.

Multiple myeloma is a cancer that is formed by malignant plasma cells found in the bone marrow. The American Cancer Society estimates, in 2017, over 30,000 new cases will be diagnosed and over 12,500 deaths will occur from multiple myeloma.<sup>33</sup> From 1995-2000, the five-year survival rate for multiple myeloma patients was just under 34%. Since the discovery and FDA approval of proteasome inhibitors in 2003, the five-year survival rate had increased over 15%; for 2007-2013, the five-year survival rate was 49.6%.<sup>34</sup> These proteasome inhibitors, especially bortezomib, have had a profound impact as a treatment for multiple myeloma. But, why does inhibiting the proteasome work so well against multiple myeloma? As mentioned in section 2.1, a main function of the ubiquitin-proteasome pathway is quality control of newly synthesized proteins. As it turns out, multiple myeloma cells are the most active protein secretors of all cell types.<sup>10</sup> Multiple myeloma cells secrete and synthesize high amounts of immunoglobulins (IgG or IgA), which are very complex proteins to synthesize.<sup>35-36</sup> IgG is a multiple chain protein and if one of the protein chains fails to fold or assemble properly, then it is degraded by the proteasomes through the endoplasmic reticulum-degradation pathway. This high



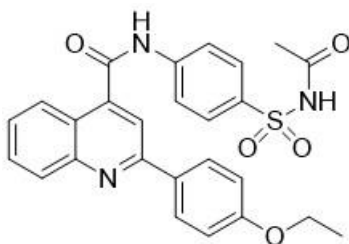
rate of immunoglobulin synthesis in multiple myeloma cells places a high burden on the proteasomes. Thus, multiple myeloma cells are under permanent endoplasmic reticulum stress which can easily trigger, *via* proteasome inhibition, the unfolded protein response.<sup>10, 37</sup> Furthermore, this high production of IgG by multiple myeloma cells heightens their sensitivity to proteasome inhibition (i.e. more sensitive than normal cells). Consequently, partial proteasome inhibition is sufficient to kill multiple myeloma cells.<sup>38</sup>

Bortezomib, carfilzomib, and ixazomib have substantiated the proteasome as an important anti-cancer target but can have some unwanted effects. Every one of these FDA approved proteasome inhibitors are peptide-based suicide inhibitors and are all competitive inhibitors that bind inside of active site(s) of the proteasome. A major drawback to inhibitors, like bortezomib, that operate by this mechanism is patients become resistant to the drug. This resistance is due to mutations inside the active sites of the 20S proteasome. Mutations that occur in the  $\beta 5$  subunit, decrease the affinity of this subunit to bortezomib. This results in a decrease in inhibition of the chymotrypsin-like activity, which then displays bortezomib resistance.<sup>39</sup> In addition, these inhibitors completely block global protein proteolysis, this induces apoptosis, as well as, triggers a transcriptional feedback loop which results in the production of new proteasome subunits.<sup>40</sup> Furthermore, peptidase cleavage triggers a rapid clearance of these inhibitors.<sup>18, 41</sup> The initial burst in inhibition, from these drugs, is highly effective in inducing apoptosis. However, the adverse effects limit these peptide-based suicide inhibitors to blood cancers.

Nonpeptidic and noncovalent proteasome inhibitors may reduce some of these drawbacks and could even expand into a broader clinical profile.<sup>41-42</sup> While these kinds of inhibitors are less common than their covalent counter-parts, they have gained traction as viable alternatives to suicide peptide-based inhibitors.<sup>43</sup> Some examples of noncovalent nonpeptidic proteasome

modulators are oxadiazoles<sup>44</sup>, hydroxyureas<sup>45</sup>, sulfone or piperazine agents<sup>46</sup> and tamoxifen derivatives.<sup>47</sup> The Jetze Tepe group, here at MSU, has even explored phakellins<sup>48</sup> and imidazolines<sup>49-50</sup> as noncovalent nonpeptidic proteasome inhibitors.

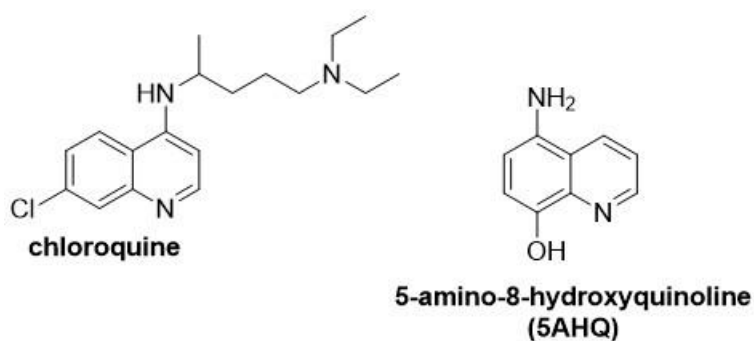
Substituted quinolines represent a new class of proteasome inhibitors and could be very interesting. In 2010, Lawrence and co-workers discovered a novel class of nonpeptidic, noncovalent proteasome inhibitors; hydrophthoquinone derivatives.<sup>51-52</sup> Interestingly, these derivatives are also selective, over non-transformed cells, for cancer cells. This could help to expand the range of anticancer activity.<sup>53</sup> In 2015, Groll and co-workers discovered a noncovalent sulfonamide substituted quinoline inhibitor. (**Figure 2.3**) Interestingly, this quinoline derivative only inhibited the  $\beta 1/\beta 2$  subunits and did not inhibit  $\beta 5$  chymotryptic activity, meaning they identified a new possible binding motif.<sup>54</sup>



**Figure 2.3.** Groll's noncovalent sulfonamide substituted quinoline inhibitor.<sup>54</sup>

Further reports by Gaczynska and co-workers demonstrated that chloroquine and 5-amino-8-hydroxyquinoline (or 5AHQ) were allosteric proteasome inhibitors (i.e. an inhibitor binding at a site different from the active site). Through NMR studies they found that chloroquine and 5AHQ (**Figure 2.4**) modulate the activity of the proteasome by binding between the  $\alpha$  and  $\beta$  subunits (i.e.  $\alpha/\beta$  interface) of the thermoplasma proteasome.<sup>55</sup> A report by Schimmer and co-workers found 5AHQ to be a non-competitive inhibitor of the human proteasome.<sup>56-57</sup> Another important finding by Schimmer's group was that they found 5AHQ to be effective against bortezomib-resistant cell

lines. Demonstrating another advantage for the use of mechanistically distinct proteasome inhibitors.<sup>49, 58-59</sup>



**Figure 2.4.** Quinoline allosteric proteasome inhibitors.

With these reports in mind, we surmise that maybe some of these nonpeptidic, noncovalent quinolines may occupy a common allosteric binding site.<sup>55, 57</sup>

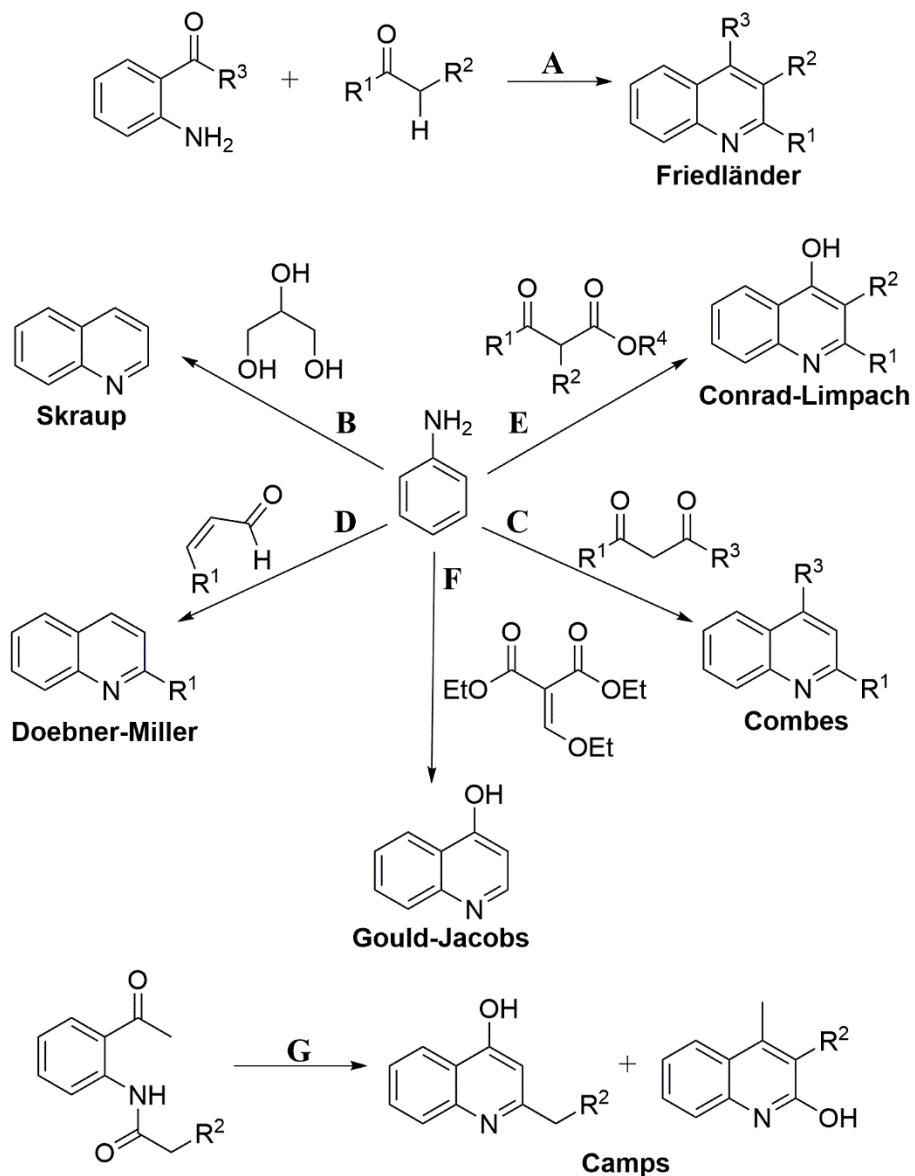
### 2.3 Classical Examples of Quinoline Synthesis

In 1834, quinoline was discovered by Friedlieb Rouge that he obtained through the distillation of coal tar. However, the structure (**Figure 2.5**) wasn't elucidated until 1871, when Dewar observed similarities between pyridine and quinoline.<sup>60-62</sup>



**Figure 2.5.** The quinoline scaffold and the numbering system.

Over 180 years later, the main source of commercial quinoline is still coal tar, *albeit* numerous reactions have been developed for its synthesis.<sup>63</sup> The structural motif of quinoline can be readily prepared through many classical synthetic routes from commercially available materials. Shown in **Scheme 2.10**, is the Friedländer synthesis (**A**), made *via ortho*-aminoacetophenones. The Skraup (**B**), Combes (**C**), Doebner-Miller (**D**), Conrad-Limpach (**E**), and Gould-Jacobs (**F**) syntheses made from aniline derivatives. There is also the Camps (**G**) quinoline synthesis made *via ortho*-acylaminoacetophenone.

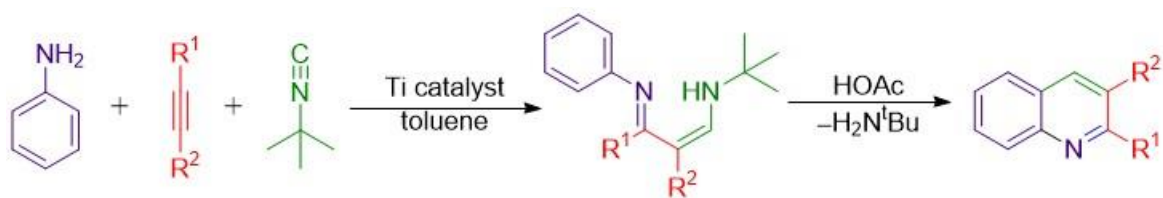


**Scheme 2.10.** Classical examples of quinoline synthesis.<sup>62</sup>

These classical synthetic routes for quinolines are versatile and efficient, but most of these routes use a great excess of reagents and can produce a significant amount of waste. The discovery of alternative green methods would be advantageous.

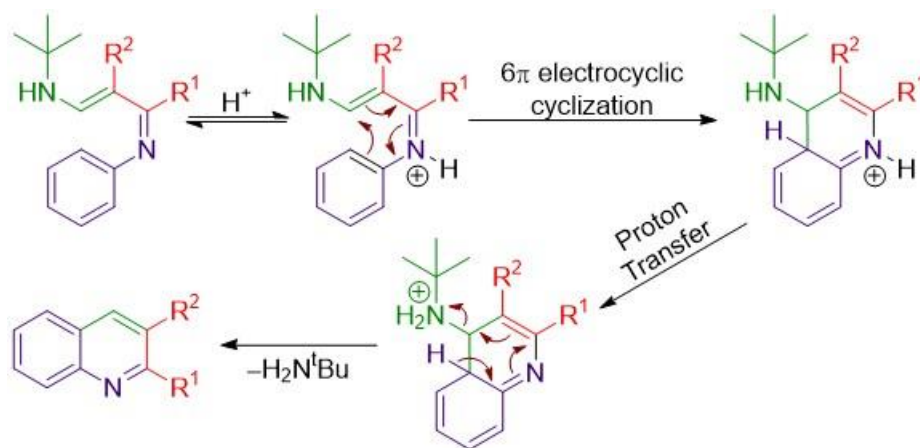
## 2.4 The Odom Group's Quinoline Synthesis

In 2009, our group published a study on the synthesis of substituted quinolines through a titanium-catalyzed multicomponent coupling reaction.<sup>64</sup> In this reaction, we can couple an amine (aniline derivative), alkyne, and an isonitrile to make these  $\alpha$ ,  $\beta$ -unsaturated- $\beta$ -iminoamines, which are tautomers of 1,3-diimines. By simply adding acetic acid to this multicomponent product, we can cyclize the product in on itself to produce a substituted quinoline. (**Scheme 2.11**) Using this route takes advantage of the numerous commercially available aniline and alkyne derivatives.



**Scheme 2.11.** Odom group's quinoline synthesis.<sup>64</sup>

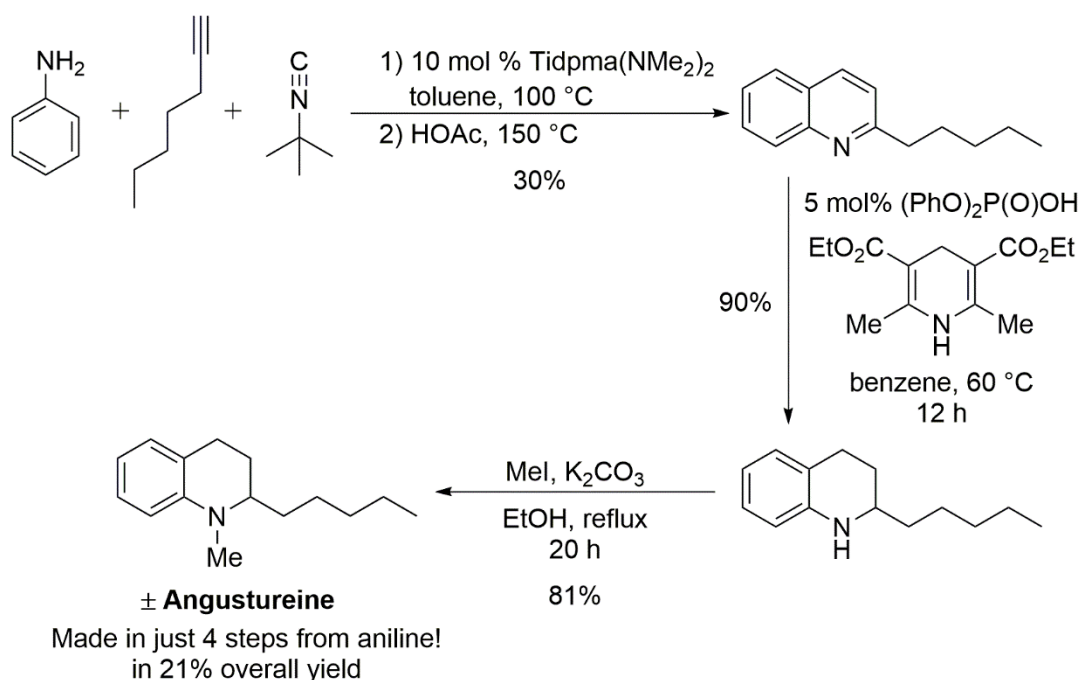
The proposed catalytic cycle for the synthesis of the three-component coupling product (discussed in **Chapter 1, Section 1.5**) is based on a modified mechanism for titanium-catalyzed hydroamination.<sup>65-66</sup> This quinoline synthesis is complementary of the Combes quinoline synthesis. As we saw in **Section 2.4**, the Combes quinoline synthesis utilizes the condensation of aniline derivatives with 1,3-dicarbonyls to form different quinoline derivatives. The proposed cyclization of the three-component coupling product is shown below in **Scheme 2.12**. First, the three-component coupling product is protonated, which leads to a  $6\pi$ -electrocyclic cyclization. After a proton transfer, the ring undergoes aromatization with concomitant loss of *tert*-butyl amine to produce the substituted quinoline.



**Scheme 2.12.** The proposed mechanism for quinoline synthesis.

Based on this methodology, the quinoline product will always be unsubstituted in the 4-position. As we saw in **Chapter 1 (Section 1.5)**, the regioselectivity of this reaction is set by the [2+2]-cycloaddition and the relative trapping rates of isonitrile. The regioselectivity can be electronically controlled when an aryl (or vinylic) alkyne is used. This occurs through a stabilization of the partial anionic charge that is adjacent to the metal center, in the azatitanacyclobutene intermediate. As a result, substitution in the 3-position is favored for aryl- or vinyl- substituted alkynes. (*For more details on the regioselectivity of the titanium-catalyzed three component coupling, refer to Chapter 1, Section 1.5*)

This methodology has even been expanded with amine-substituted heterocycles, to make a variety of new heterocycles, such as: thienopyridines, benzothienopyridines, pyrrolopyridazines, indolopyridazines.<sup>64</sup> Our group, in collaboration with the Wulff group, was even able to utilize this quinoline synthesis for the natural product Angustureine. As shown in **Scheme 2.13**, this natural product was readily made using commercially available materials.



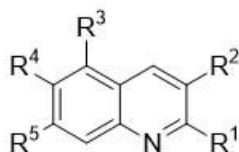
**Scheme 2.13.** Synthesis of racemic Angustureine.<sup>67</sup>

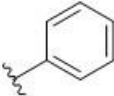
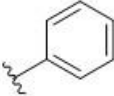
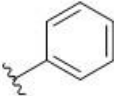
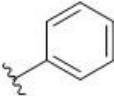
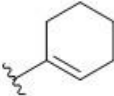
As we saw previously in **Chapter 1** and in this section, our titanium-catalyzed multicomponent coupling provides a unique approach for the synthesis of many nitrogen-based heterocycles. Nitrogen-based heterocycles are a very common motif in pharmaceuticals. 59% of the U.S. FDA approved small-molecule drugs contain a nitrogen heterocycle. Of all those nitrogen heterocycles, pyridine is the second most common heterocycle found in approved drugs.<sup>68</sup> With this in mind, our group wondered what biological applications could our heterocyclic syntheses have.



## 2.5 Results and Discussion

In collaboration with the Tepe group, a library of diverse compounds was screened *in vitro* using purified human 20S proteasome and the fluorogenic peptide substrate, Suc-LLVY-AMC, as the substrate for CT-L activity.<sup>57</sup> The rate of hydrolysis was monitored by observing the increase in fluorescence at 37 °C, over 30 minutes. The linear portion, of the curves obtained were then used to calculate the half maximal inhibitory concentration (i.e. IC<sub>50</sub> values). The IC<sub>50</sub> indicates how much of a substance (in our case different quinoline derivatives) is needed to inhibit the CT-L activity of the human proteasome by half. Of the initial quinolines tested (see **Table 2.1**), only a few were found to have low micromolar efficacies for the 20S human proteasome inhibition. Quinoline **7** demonstrated modest inhibition of CT-L activity with an IC<sub>50</sub> of 14.4 μM.

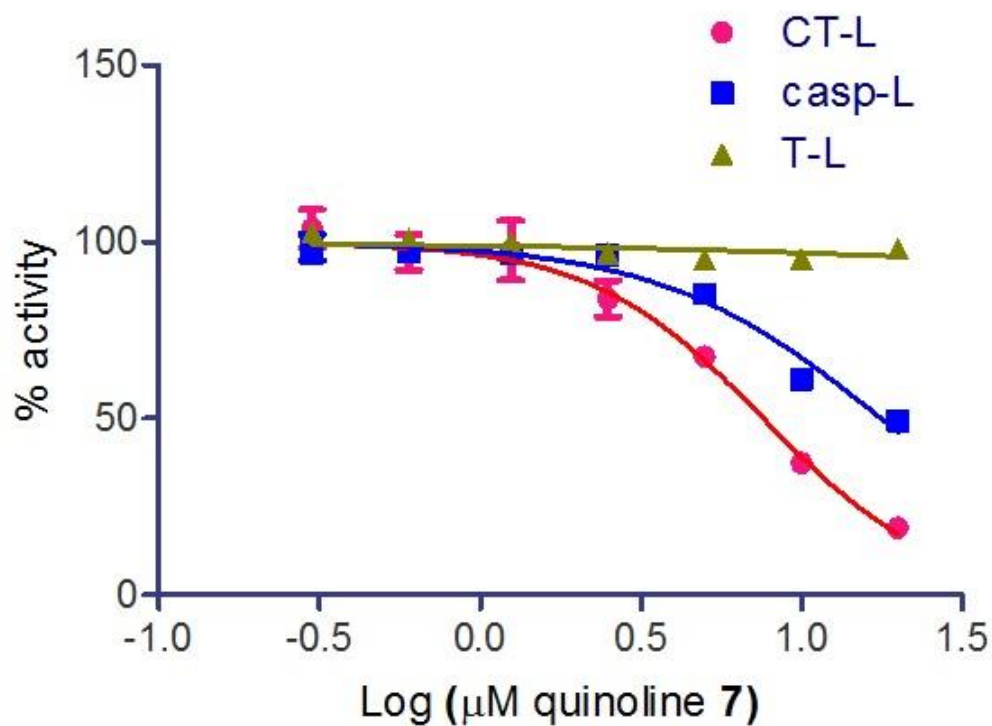


	R <sup>1</sup>	R <sup>2</sup>	R <sup>3</sup>	R <sup>4</sup>	R <sup>5</sup>	IC <sub>50</sub> (μM)
<b>Bortezomib</b>	–	–	–	–	–	0.0062 (±0.0003)
<b>1</b>	CH <sub>3</sub>	H	H	H	H	>25
<b>2</b>	H	CH <sub>3</sub>	H	H	H	>25
<b>3</b>	H		H	H	H	>25
<b>4</b>	H		CH <sub>3</sub>	H	CH <sub>3</sub>	23.6 (±1.9)
<b>5</b>	CH <sub>3</sub>		H	CH <sub>3</sub>	H	19.2 (±0.3)
<b>6</b>	CH <sub>3</sub>		CH <sub>3</sub>	H	CH <sub>3</sub>	15.3 (±2.4)
<b>7</b>	CH <sub>3</sub>		CH <sub>3</sub>	H	CH <sub>3</sub>	14.4 (±0.5)

**Table 2.1.** Structure and IC<sub>50</sub> of substituted quinolines (**1-7**) for inhibition of CT-L activity of the 20S proteasome. All IC<sub>50</sub> values are averages of two independent experiments (each performed in triplicate).<sup>57</sup>

Quinoline **7** was then further evaluated for its inhibition towards the proteasome's caspase (β1)-like activity and tryptic (β2)-like activity. This was conducted *in vitro* using by using purified human 20S proteasome with their respected fluorogenic peptide substrates, Z-LLE-AMC and Boc-LRR-AMC.<sup>69</sup> As shown in **Figure 2.6**, quinoline **7** inhibits caspase-like activity with an IC<sub>50</sub> of

17.7  $\mu\text{M}$ . This is similar to the activity quinoline **7** exhibited for inhibition of chymotrypsin-like activity ( $\text{IC}_{50} = 14.4 \mu\text{M}$ ). However, quinoline **7** did not seem to inhibit trypsin-like activity ( $\text{IC}_{50} = >25$ ) in the human 20S proteasome.



**Figure 2.6.** Evaluation of quinoline **7**'s CT-L, Casp-L, and T-L activities in purified human 20S proteasome. The fluorogenic substrates Suc-LLVY-AMC, Z-LLE-AMC and Boc-LRR-AMC were used, respectively.<sup>57</sup>

Next, we decided to investigate the mechanism by which quinoline **7** inhibits the human 20S proteasome. Through Michaelis-Menton kinetics, the  $K_M$  and  $V_{\max}$  was determined. The Michaelis-Menton equation is shown below in Equation 1.

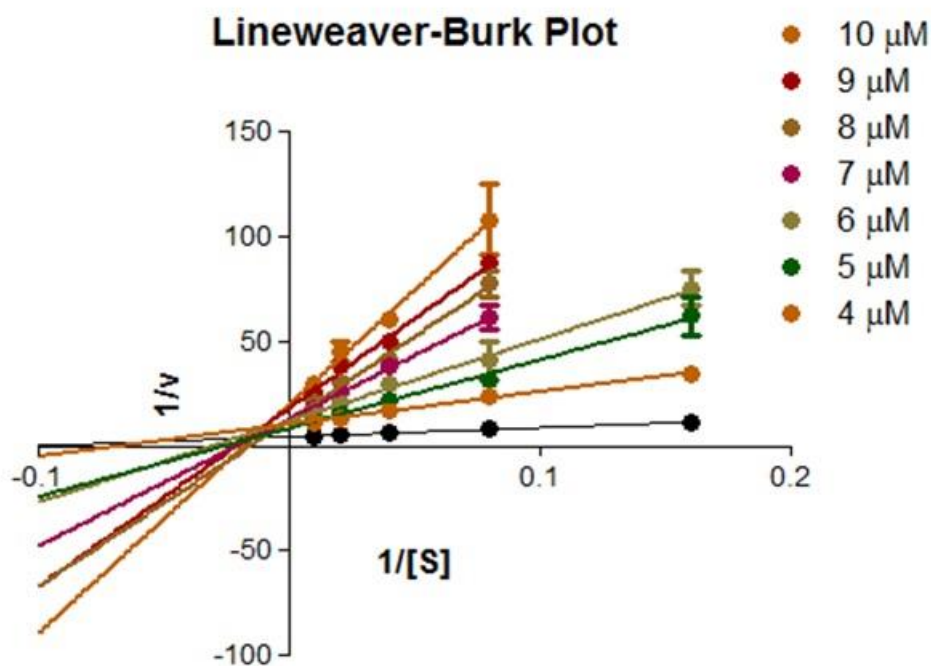
$$V_0 = \frac{V_{\max} [S]}{K_m + [S]} \quad \text{Equation 1}$$

$K_M$ , i.e., Michaelis constant, is defined as the concentration of substrate at half the maximum velocity.  $V_{\max}$  is defined as the maximum rate or velocity which the enzyme catalyzes a reaction

and  $V_0$  is the initial rate or velocity. This was further investigated using a Lineweaver-Burk double reciprocal plot of the kinetic data. The Lineweaver-Burk equation is shown below in Equation 2.

$$\frac{1}{V_0} = \frac{K_m}{V_{max} [S]} + \frac{1}{V_{max}} \quad \text{Equation 2}$$

The analysis of kinetic data of CT-L activity of human 20S proteasome revealed that, when the concentration of the substrate (Suc-LLVY-AMC) was increased incrementally while taking five measurements at different concentrations of quinoline **7** or vehicle, the  $K_M$  increases as the concentration of substrate increases and the  $V_{max}$  of the CT-L activity decreases. (**Figure 2.7**)<sup>57</sup>

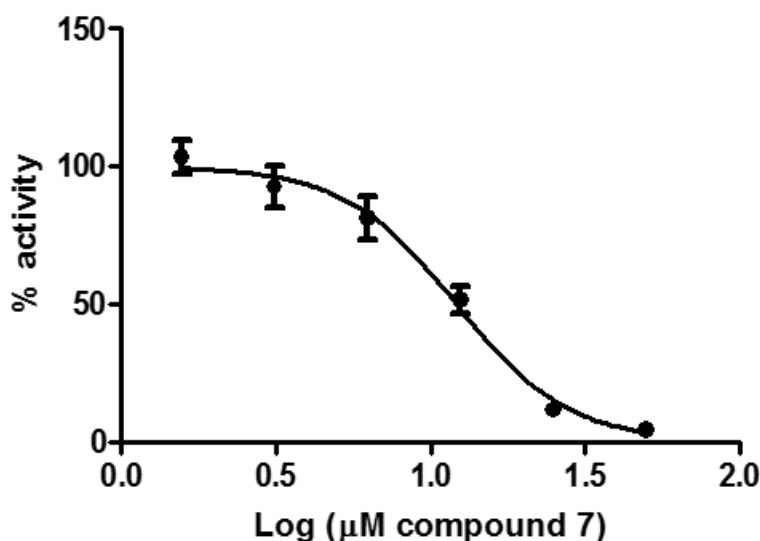


**Figure 2.7.** Lineweaver-Burke plot using quinoline **7** and substrate Suc-LLVY-AMC.<sup>57</sup>

This trend is consistent with a mixed-type inhibition and is also consistent with allosteric-type modulation of proteasomal activity.<sup>70</sup> Meaning quinoline **7** is binding at a site different from the active site, and this event results in inhibition of the proteasome activity.

Thus, quinoline **7** was evaluated further to determine if inhibition of the proteasome activity would translate to cell culture. Consequently, quinoline **7** was examined for its inhibition

of NF- $\kappa$ B regulation. (**Figure 2.8**) Proteasome inhibition affects many critical signaling pathways. Proteasome inhibitors' anti-cancer activity has been, in some extent, linked to their ability to inhibit the anti-apoptotic, pro-inflammatory NF- $\kappa$ B signaling pathway.<sup>71-72</sup> NF- $\kappa$ B is a nuclear transcription factor that is sequestered in the cytoplasm by I $\kappa$ B, an inhibitory protein. If the NF- $\kappa$ B becomes activated by cytokines, like TNF- $\alpha$ , I $\kappa$ B undergoes rapid ubiquitinylation and proteasomal degradation. This releases NF- $\kappa$ B for nuclear gene transcription and translocation.<sup>73</sup> If the proteasome is inhibited, it prevents the proteolytic degradation of I $\kappa$ B. This causes an accumulation of cytosolic ubiquitinylated I $\kappa$ B, once the NF- $\kappa$ B pathway is activated.<sup>74</sup>



**Figure 2.8.** Evaluation of quinoline 7 using HeLa NF- $\kappa$ B-luc cells.<sup>57</sup>

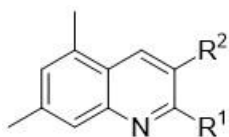
Quinoline 7's *in vitro* proteasome inhibition translated well to cell culture and was able to prevent NF- $\kappa$ B gene transcription ( $IC_{50} = 12.1 \mu$ M) in a dose-response manner. *It should be stated that these last three experiments, i.e., evaluation of quinoline 7's different activities, the kinetic analysis and the cell cultures, were conducted by our collaborator Dr. Theresa Lansdell.*

With the cellular validation of quinoline 7's *in vitro* proteasome activity in hand, we can now begin to explore other quinoline derivatives. By using the three component coupling reaction

(Section 2.4) to explore different quinoline derivatives, we can develop a Structure-Activity Relationship (SAR), i.e., the relationship between the chemical structure of a molecule and its biological activity. Through developing an SAR, we can gain insight into how to improve the potency for our quinoline proteasome inhibitors. At this point, we began to synthesize different quinolines that were successively evaluated for their ability to inhibit CT-L activity of the human 20S proteasome.

To evaluate the structural requirements for activity, we began changing substituents in the different positions. Since our initial results suggested that we need substitution in the  $R^1$ ,  $R^2$ ,  $R^3$  and  $R^5$  for activity, we decided to only modify one position and keep the remaining three positions identical. We first examined changes to the  $R^1$  position and observed how the changes made affect the activity. (Table 2.2) Moving from a methyl substituent to ethyl resulted in a moderate decrease in activity. (7 to 8) When the 2-methyl group was removed, we observed virtually no change, and the  $IC_{50}$  values are within error of each other. (7 to 9) We then began to modify the  $R^2$  position, we observed more drastic changes to the activity. Replacing cyclohexene with an isopropylene group resulted in an inactive compound. (8 to 10) This suggests the cyclohexene moiety is important for activity. Hydrogenation of the cyclohexene to cyclohexane revealed almost a 2-fold increase in potency! (7 to 11) Thus, giving us our first single digit micromolar inhibitor. Recalling quinoline 4 and 6 in our initial screening, we observed an arguable decrease in activity changing the substituent in the  $R^2$  position from cyclohexene to phenyl. (7 to 6) However, when the phenyl group was maintained, in the  $R^2$  position, and the methyl in the  $R^1$  position was removed a significant decrease in activity was observed. (6 to 4) Further modification, changing both substituents in the  $R^1$  and  $R^2$  to phenyl, resulted in an inactive compound. (12) These results

suggest the need for small hydrophobic moieties in the R<sup>1</sup> position and slightly large hydrophobic moieties in the R<sup>2</sup> position.

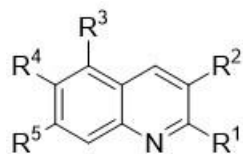


	R <sup>1</sup>	R <sup>2</sup>	IC <sub>50</sub> (μM)
<b>4</b>	H		23.6 (±1.9)
<b>6</b>	CH <sub>3</sub>		15.3 (±2.4)
<b>7</b>	CH <sub>3</sub>		14.4 (±0.5)
<b>8</b>	CH <sub>2</sub> CH <sub>3</sub>		19.9 (±0.7)
<b>9</b>	H		13.8 (±1.3)
<b>10</b>	CH <sub>2</sub> CH <sub>3</sub>		>25
<b>11</b>	CH <sub>3</sub>		8.2 (±1.2)
<b>12</b>			>25

**Table 2.2.** Structure and IC<sub>50</sub> of substituted quinolines (**4**, **7-12**), by varying substituents in the R<sup>1</sup> and R<sup>2</sup> positions, for inhibition of CT-L activity of the 20S proteasome. *All IC<sub>50</sub> values are averages of two independent experiments (each performed in triplicate).* <sup>57</sup>

From here we decided to explore substituents in the R<sup>3</sup>–R<sup>5</sup> positions to see how they affect the activity. (**Table 2.3**) Removal of the methyl groups in the R<sup>3</sup> and R<sup>5</sup> positions resulted in a complete loss of activity. (**7 to 13**) This result suggests the need for hydrophobic groups in these positions. As we saw previously, quinoline **9** had almost identical activity as quinoline **7**. However, even replacement of the methyl groups in the R<sup>3</sup> and R<sup>5</sup> positions to lipophilic chloride or bromides couldn't restore the activity. (**9 to 14 and 15**) When the R<sup>4</sup> position was explored with different halogens, we observe that by increasing the lipophilic bulk restores the activity. (**18→16**) These results suggest a hydrophobic binding interaction on the benzo-portion of our quinoline scaffold.

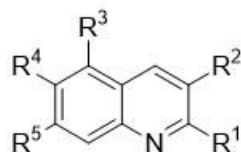




	<b>R<sup>1</sup></b>	<b>R<sup>2</sup></b>	<b>R<sup>3</sup></b>	<b>R<sup>4</sup></b>	<b>R<sup>5</sup></b>	<b>IC<sub>50</sub> (μM)</b>
<b>7</b>	CH <sub>3</sub>		CH <sub>3</sub>	H	CH <sub>3</sub>	14.4 (±0.5)
<b>9</b>	H		CH <sub>3</sub>	H	CH <sub>3</sub>	13.8 (±1.3)
<b>13</b>	CH <sub>3</sub>		H	H	H	>25.0
<b>14</b>	H		Cl	H	Cl	>25.0
<b>15</b>	H		Br	H	Br	>25.0
<b>16</b>	CH <sub>3</sub>		H	Br	H	9.9 (± 0.6)
<b>17</b>	CH <sub>3</sub>		H	Cl	H	>25
<b>18</b>	CH <sub>3</sub>		H	F	H	>25

**Table 2.3.** Structure and IC<sub>50</sub> of substituted quinolines (**7**, **9**, **13-18**), by varying substituents in the R<sup>3</sup>–R<sup>5</sup> positions, for inhibition of CT-L activity of the 20S proteasome. *All IC<sub>50</sub> values are averages of two independent experiments (each performed in triplicate).*<sup>57</sup>

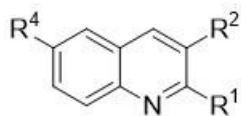
To further evaluated this trend, we examined different substituents in the R<sup>4</sup> position. (Table 2.4) Incorporating a methyl or butyl group we again observe similar activity. (19 and 20) Thus, validating that the binding pocket seems to accept large hydrophobic moieties in the R<sup>3</sup>–R<sup>5</sup> positions of the quinoline scaffold. Similarly, incorporating a dimethylamino moiety in the R<sup>4</sup> position (22) seems to fill the hydrophobic pockets that are occupied by the two methyl groups, in the R<sup>3</sup> and R<sup>5</sup> positions, in quinoline 7.<sup>57</sup> We again observed only minor changes when changing the R<sup>1</sup> position of this derivative. (22 to 21 and 23) Moving from dimethylamino to morpholine moiety in the R<sup>4</sup> position a decrease in activity is observed. (22 to 24) However, when a piperidine group was installed we see the restoration of activity. (24 to 25) Interestingly, when the dimethylamino group is replaced with a smaller methoxy moiety a complete loss in activity is observed. (22 to 26) Incorporating, neighboring methoxy groups (in the R<sup>3</sup> and R<sup>5</sup> position) only partially restores the activity. (26 to 27) Considering the complete lack of activity in 26, it seems the restoration of activity could be due to the positioning of the methyl groups on the dimethylamino moiety inside the hydrophobic pocket, instead of a possible hydrogen bond accepting role. This was further validated by quinoline 30, which incorporates an isopropyl group in the R<sup>4</sup> position, and most of the activity is retained. These results suggest that the methyl groups on the dimethylamino moiety could occupy similar pockets, given the close vicinity to the R<sup>3</sup> and R<sup>5</sup> positions.



	R <sup>1</sup>	R <sup>2</sup>	R <sup>3</sup>	R <sup>4</sup>	R <sup>5</sup>	IC <sub>50</sub> (μM)
<b>19</b>	CH <sub>3</sub>		H	CH <sub>3</sub>	H	8.5 (± 0.1)
<b>20</b>	CH <sub>3</sub>		H	(CH <sub>2</sub> ) <sub>3</sub> CH <sub>3</sub>	H	7.6 (± 1.3)
<b>21</b>	H		H	N(CH <sub>3</sub> ) <sub>2</sub>	H	6.3 (±0.3)
<b>22</b>	CH <sub>3</sub>		H	N(CH <sub>3</sub> ) <sub>2</sub>	H	6.1 (±0.2)
<b>23</b>	CH <sub>2</sub> CH <sub>3</sub>		H	N(CH <sub>3</sub> ) <sub>2</sub>	H	5.6 (± 0.4)
<b>24</b>	CH <sub>3</sub>		H		H	9.1 (±0.5)
<b>25</b>	CH <sub>3</sub>		H		H	5.4 (±0.1)
<b>26</b>	CH <sub>3</sub>		H	OCH <sub>3</sub>	H	>25.0
<b>27</b>	CH <sub>3</sub>		OCH <sub>3</sub>	OCH <sub>3</sub>	OCH <sub>3</sub>	15.6 (±0.7)
<b>28</b>	CH <sub>3</sub>		H	CH(CH <sub>3</sub> ) <sub>2</sub>	H	7.8 (±0.1)

**Table 2.4.** Structure and IC<sub>50</sub> of substituted quinolines, by varying substituents in the R<sup>4</sup> positions, for inhibition of CT-L activity of the 20S proteasome. *All IC<sub>50</sub> values are averages of two independent experiments (each performed in triplicate).*<sup>57</sup>

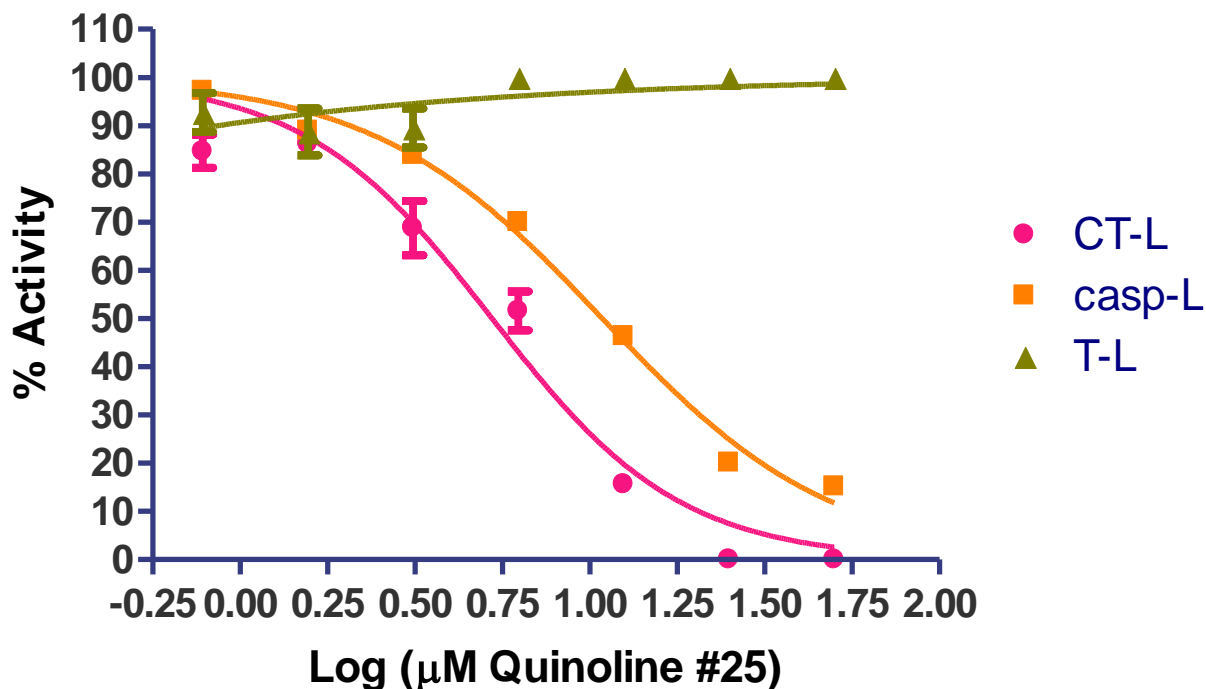
Recalling a previous observation, when we moved to a fully saturated cyclohexyl moiety we observed almost a 2-fold increase in activity. (**7** to **11**) Intrigued by this, we decided to try this with these more potent dimethylamino derivatives. (**Table 2.5**) However, we did not observe the same drastic change in activity that was observed previously. (**21** to **29** and **22** to **30**) Moving back to a phenyl moiety in the R<sup>2</sup> position, we again observed a drop-in activity that is consistent with our previous findings. (**22** to **31**, **20** to **36**, and **28** to **37**) Further exploration of different substituents in the R<sup>1</sup> and R<sup>2</sup> positions, when utilizing the dimethylamino group in the R<sup>4</sup> position, did not yield any more active compounds. When a bulky *tert*-butyl group was incorporated into the R<sup>2</sup> position, we observed a complete loss in activity. (**29** to **32**) Utilizing a butyl group in the R<sup>1</sup> position, or having phenyl groups in the R<sup>1</sup> and R<sup>2</sup> position, was also inactive and was only slightly restored when ethyl groups were incorporated into the R<sup>1</sup> and R<sup>2</sup> positions. (**33**, **35** to **34**)



	R <sup>1</sup>	R <sup>2</sup>	R <sup>3</sup>	R <sup>4</sup>	R <sup>5</sup>	IC <sub>50</sub> (μM)
<b>29</b>	H		H	N(CH <sub>3</sub> ) <sub>2</sub>	H	5.5 (±0.8)
<b>30</b>	CH <sub>3</sub>		H	N(CH <sub>3</sub> ) <sub>2</sub>	H	6.7 (± 0.2)
<b>31</b>	CH <sub>3</sub>		H	N(CH <sub>3</sub> ) <sub>2</sub>	H	10.0 (±0.6)
<b>32</b>	H	C(CH <sub>3</sub> ) <sub>3</sub>	H	N(CH <sub>3</sub> ) <sub>2</sub>	H	>25.0
<b>33</b>	(CH <sub>2</sub> ) <sub>3</sub> CH <sub>3</sub>	H	H	N(CH <sub>3</sub> ) <sub>2</sub>	H	>25.0
<b>34</b>	CH <sub>2</sub> CH <sub>3</sub>	CH <sub>2</sub> CH <sub>3</sub>	H	N(CH <sub>3</sub> ) <sub>2</sub>	H	18.7 (±1.0)
<b>35</b>			H	N(CH <sub>3</sub> ) <sub>2</sub>	H	>25
<b>36</b>	CH <sub>3</sub>		H	(CH <sub>2</sub> ) <sub>3</sub> CH <sub>3</sub>	H	21.6 (±1.1)
<b>37</b>	CH <sub>3</sub>		H	CH(CH <sub>3</sub> ) <sub>2</sub>	H	>25.0
<b>38</b>	CH <sub>3</sub>		H	Br	H	>25.0

**Table 2.5.** Structure and IC<sub>50</sub> of substituted quinolines, by varying substituents in the R<sub>1</sub>, R<sub>2</sub>, R<sub>4</sub> positions, for inhibition of CT-L activity of the 20S proteasome. *All IC<sub>50</sub> values are averages of two independent experiments (each performed in triplicate).*<sup>57</sup>

Having moved away from our original lead (**7**) we decided to re-evaluate our new lead compound (**25**) to see if we still observe the same selectivity for CT-L and Casp-L activities over T-L activity, *in vitro*. As shown in **Figure 2.9**, we do see the same trend and quinoline **25** inhibits Casp-L activity with an IC<sub>50</sub> of 10.9  $\mu$ M but does not inhibit T-L activity.



**Figure 2.9.** Evaluation of quinoline **25**'s CT-L, Casp-L, and T-L activities in purified human 20S proteasome. The fluorogenic substrates Suc-LLVY-AMC, Z-LLE-AMC and Boc-LRR-AMC were used, respectively.

## **2.6 Conclusion**

Currently, all FDA approved proteasome inhibitors are competitive and peptide-based. We are in dire need for new classes of small molecule proteasome inhibitors to overcome the inevitable resistance and limitations of the current drugs. Using our titanium-catalyzed multicomponent coupling reaction, we can synthesize noncovalent, nonpeptidic, low micromolar proteasome inhibitors.

## 2.7 Experimental

This experimental is taken from our publication: McDaniel, T. J.; Lansdell, T. A.; Dissanayake, A. A.; Azevedo, L. M.; Claes, J.; Odom, A. L.; Tepe, J. J., *Bioorg. Med. Chem.* **2016**, *24*, 2441.

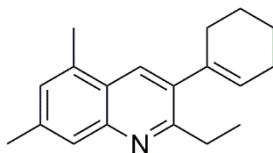
### General Considerations

All manipulations of air sensitive compounds were carried out in an MBraun drybox under a purified nitrogen atmosphere. Toluene was purified by sparging with dry N<sub>2</sub> and water was removed by running through activated alumina systems purchased from Solv-Tex. <sup>1</sup>H, <sup>13</sup>C and <sup>19</sup>F spectra were recorded on VXR-500 spectrometers. Melting points are uncorrected and measured on a Mel-Temp II apparatus (Laboratory Devices Inc, USA) with a mercury thermometer in an open capillary tube. Ti(NMe<sub>2</sub>)<sub>2</sub>dpma and Ti(NMe<sub>2</sub>)<sub>2</sub>dpm were made following the literature procedures.<sup>75-77</sup> Ti(NMe<sub>2</sub>)<sub>2</sub>dpm was used for all the quinolines synthesized, with the exceptions **32** and **33** in which Ti(NMe<sub>2</sub>)<sub>2</sub>dpma was used. *Tert*-butylisocyanide was made according to the literature procedure<sup>78</sup> and purified by distillation under dry nitrogen but it may also be purchased from Sigma Aldrich. Hexanes and ethyl acetate were purchased from Mallinckrodt chemicals and used as received. Alkynes were purchased either from Sigma Aldrich or from GFC chemicals and were dried/distilled from barium oxide under dry nitrogen before use. Amines were purchased from Sigma Aldrich, dried over KOH and distilled under nitrogen. Palladium(II) acetate, potassium *tert*-butoxide and 2-(dicyclohexylphosphino)biphenyl (97%) were also purchased from Sigma Aldrich and used as received. 2-methylquinoline (**1**), 3-methylquinoline (**2**), were purchased from TCI America. 3-phenylquinoline (**3**) was synthesized through via literature procedure.<sup>79</sup> 3-cyclohexenyl-2,5,7-trimethylquinoline (**7**), 2,5,7-trimethyl-3-phenylquinoline (**6**), 5,7-dimethyl-2,3-diphenylquinoline (**12**), 2-methyl-3-phenyl-6-(N,N-dimethylamino)quinoline



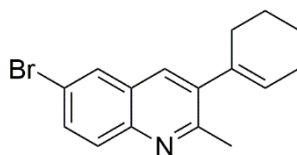
(**31**) were synthesized *via* literature procedure.<sup>64</sup> Quinolines (**9-15**), (**18**), (**19**), (**22**), (**24-26**) synthesized using *via* literature procedure.<sup>80</sup>

## Synthesis and Characterization Quinoline Compounds



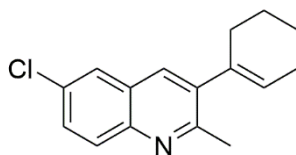
### 2-ethyl-3-cyclohexenyl-5,7-dimethylquinoline (**8**)

In a nitrogen filled glove box, a 10 mL pressure tube, equipped with a magnetic stir bar was loaded with  $\text{Ti}(\text{NMe}_2)_2\text{dpm}$  (0.10 mmol, 30.8 mg) and dissolved in dry toluene (2 mL). The solution was loaded with the 3,5-dimethylaniline (1.0 mmol, 121 mg), 1-(but-1-ynyl)cyclohex-1-ene (1.0 mmol, 134 mg) and *tert*-butylisocyanide (1.5 mmol, 171  $\mu\text{L}$ ). The pressure tube was sealed with a Teflon screw cap, taken out of the dry box and heated at 100 °C for 48 h in a silicone oil bath. Volatiles were removed *in vacuo*, and glacial acetic acid (2 mL) was added. The mixture was then heated at 150 °C for 24 h. The pressure tube was then allowed to cool to room temperature, diluted in dichloromethane and neutralized with saturated  $\text{NaHCO}_3$  solution. The organic layer was further extracted with additional dichloromethane, washed with brine, dried over  $\text{NaSO}_4$ , filtered and concentrated *in vacuo*. The crude product was dry loaded onto alumina and purification was accomplished by column chromatography on neutral alumina using hexanes:ethyl acetate (9:1, v/v) as the eluent to provide the product as a light-yellow oil 102 mg (38%).  $^1\text{H}$  NMR ( $\text{CDCl}_3$ , 500 MHz, 20 °C):  $\delta$  = 1.51-1.61 (7 H, m) 1.99-2.03 (2 H, m,  $\text{CH}_2$ ), 2.14-2.16 (2 H, m,  $\text{CH}_2$ ), 2.21 (3 H, s,  $\text{CH}_3$ ), 2.31 (3 H, s,  $\text{CH}_3$ ), 3.04-3.09 (2H, q,  $J$  = 8 Hz,  $\text{CH}_2$ ), 5.60-5.62 (1 H, m, CH), 6.86 (1 H, s, Ar-H), 7.85 (1 H, s, Ar-H), 8.05 (1 H, s, Ar-H).  $^{13}\text{C}$  NMR ( $\text{CDCl}_3$ , 125 MHz, 20 °C):  $\delta$  = 13.6, 18.0, 21.3, 22.0, 23.0, 25.3, 29.1, 30.8, 124.3, 126.7, 126.8, 128.4, 130.5, 133.3, 136.5, 137.9, 138.0, 148.2, 160.9. MS (EI):  $m/z$  265 ( $\text{M}^+$ ). HRMS  $[\text{M}]^+$ : Found:  $m/z$  265.1840.; Calcd for  $\text{C}_{19}\text{H}_{23}\text{N}$  265.1830.



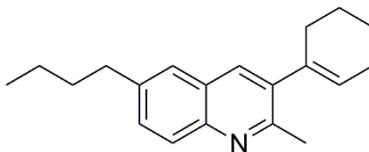
**6-bromo-3-cyclohexenyl-2-methylquinoline (16)**

In a nitrogen filled glove box, a 10 mL pressure tube, equipped with a magnetic stir bar was loaded with  $\text{Ti}(\text{NMe}_2)_2\text{dpm}$  (0.10 mmol, 30.8 mg) and dissolved in dry toluene (2 mL). The solution was loaded with 4-bromoaniline (1.0 mmol, 172 mg), 1-(prop-1-ynyl)cyclohex-1-ene (1.0 mmol, 120 mg) and *tert*-butylisocyanide (1.5 mmol, 171  $\mu\text{L}$ ). The pressure tube was sealed with a Teflon screw cap, taken out of the dry box and heated at 100 °C for 48 h in a silicone oil bath. Volatiles were removed *in vacuo*, and glacial acetic acid (2 mL) was added. The mixture was then heated at 150 °C for 24 h. The pressure tube was then allowed to cool to room temperature, diluted in dichloromethane and neutralized with saturated  $\text{NaHCO}_3$  solution. The organic layer was further extracted with additional dichloromethane, washed with brine, dried over  $\text{NaSO}_4$ , filtered and concentrated *in vacuo*. The crude product was dry loaded onto alumina and purification was accomplished by column chromatography on neutral alumina using hexanes:ethyl acetate (9:1, v/v) as the eluent to provide the product as a light brown oil 103 mg (34%)  $^1\text{H}$  NMR ( $\text{C}_6\text{D}_6$ , 500 MHz, 20 °C):  $\delta$  = 1.45-1.54 (4 H, m,  $\text{CH}_2$ ), 1.93-1.96 (4 H, m,  $\text{CH}_2$ ), 2.60 (3 H, s,  $\text{CH}_3$ ), 5.41-5.42 (1 H, m, CH), 7.13 (1 H, s, Ar-H), 7.38-7.40 (1 H, dd,  $J$  = 2 Hz, 9 Hz, Ar-H), 7.58-7.59 (1 H, d,  $J$  = 2 Hz, Ar-H), 7.88-7.90 (1 H, d,  $J$  = 9 Hz, Ar-H).  $^{13}\text{C}$  NMR ( $\text{C}_6\text{D}_6$ , 125 MHz, 20 °C):  $\delta$  = 21.9, 22.8, 23.6, 25.3, 29.7, 119.2, 127.2, 128.2, 129.2, 130.7, 131.8, 132.7, 137.1, 138.6, 145.7, 157.8. MS (EI):  $m/z$  301 ( $\text{M}^+$ ). HRMS  $[\text{M}]^+$ : Found:  $m/z$  301.0480.; Calcd for  $\text{C}_{16}\text{H}_{16}\text{BrN}$  301.0466.



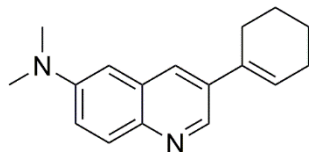
**6-chloro-2-methyl-3-cyclohexenylquinoline (17)**

In a nitrogen filled glove box, a 10 mL pressure tube, equipped with a magnetic stir bar was loaded with  $\text{Ti}(\text{NMe}_2)_2\text{dpm}$  (0.10 mmol, 30.8 mg) and dissolved in dry toluene (2 mL). The solution was loaded with 4-chloroaniline (1.0 mmol, 127 mg), 1-(prop-1-ynyl)cyclohex-1-ene (1.0 mmol, 120 mg) and *tert*-butylisocyanide (1.5 mmol, 171  $\mu\text{L}$ ). The pressure tube was sealed with a Teflon screw cap, taken out of the dry box and heated at 100 °C for 48 h in a silicone oil bath. Volatiles were removed *in vacuo*, and glacial acetic acid (2 mL) was added. The mixture was then heated at 150 °C for 24 h. The pressure tube was then allowed to cool to room temperature, diluted in dichloromethane and neutralized with saturated  $\text{NaHCO}_3$  solution. The organic layer was further extracted with additional dichloromethane, washed with brine, dried over  $\text{NaSO}_4$ , filtered and concentrated *in vacuo*. The crude product was dry loaded onto alumina and purification was accomplished by column chromatography on neutral alumina using hexanes:ethyl acetate (9:1, v/v) as the eluent to provide the product as a light yellow oil 54 mg (21%).  $^1\text{H}$  NMR ( $\text{CDCl}_3$ , 500 MHz, 20 °C):  $\delta$  = 1.72-1.75 (2 H, quin,  $J$  = 11 Hz,  $\text{CH}_2$ ), 1.79-1.82 (2 H, quin,  $J$  = 12 Hz,  $\text{CH}_2$ ), 2.21 (2 H, m,  $\text{CH}_2$ ), 2.25 (2 H, m,  $\text{CH}_2$ ), 2.67 (3 H, s,  $\text{CH}_3$ ), 6.32 (1 H, m CH), 7.54-7.57 (1 H, dd,  $J$  = 2 Hz, 9 Hz, Ar-H), 7.69 (1 H, s, Ar-H), 7.70-7.71 (1H, d,  $J$  = 3 Hz, Ar-H), 7.91-7.93 (1 H, d,  $J$  = 9 Hz, Ar-H).  $^{13}\text{C}$  NMR ( $\text{CDCl}_3$ , 125 MHz, 20 °C):  $\delta$  = 21.9, 22.9, 23.7, 25.4, 30.0, 125.8, 127.6, 127.9, 129.6, 129.8, 131.2, 133.5, 136.9, 139.1, 144.9, 158.2. MS (EI):  $m/z$  257 ( $\text{M}^+$ ). HRMS [ $\text{M}$ ] $^+$ : Found:  $m/z$  257.0963.; Calcd for  $\text{C}_{16}\text{H}_{16}\text{ClN}$  257.0971.



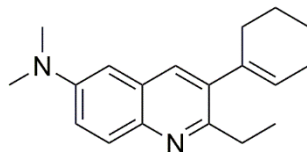
*6-butyl-3-cyclohexenyl-2-methylquinoline (20)*

In a nitrogen filled glove box, a 10 mL pressure tube, equipped with a magnetic stir bar was loaded with  $\text{Ti}(\text{NMe}_2)_2\text{dpm}$  (0.10 mmol, 30.8 mg) and dissolved in dry toluene (2 mL). The solution was loaded with 4-butylniline (1.0 mmol, 149 mg), 1-(prop-1-ynyl)cyclohex-1-ene (1.0 mmol, 120 mg) and *tert*-butylisocyanide (1.5 mmol, 171  $\mu\text{L}$ ). The pressure tube was sealed with a Teflon screw cap, taken out of the dry box and heated at 100 °C for 48 h in a silicone oil bath. Volatiles were removed *in vacuo*, and glacial acetic acid (2 mL) was added. The mixture was then heated at 150 °C for 24 h. The pressure tube was then allowed to cool to room temperature, diluted in dichloromethane and neutralized with saturated  $\text{NaHCO}_3$  solution. The organic layer was further extracted with additional dichloromethane, washed with brine, dried over  $\text{NaSO}_4$ , filtered and concentrated *in vacuo*. The crude product was dry loaded onto alumina and purification was accomplished by column chromatography on neutral alumina using hexanes:ethyl acetate (9:1, v/v) as the eluent to provide the product as a viscous yellow oil 87 mg (32%).  $^1\text{H}$  NMR ( $\text{CDCl}_3$ , 500 MHz, 20 °C):  $\delta$  = 0.94-0.96 (3 H, t,  $J$  = 7 Hz,  $\text{CH}_3$ ), 1.35-1.43 (2 H, sext,  $J$  = 15 Hz,  $\text{CH}_2$ ), 1.65-1.71 (2 H, quin,  $J$  = 15 Hz,  $\text{CH}_2$ ), 1.71-1.76 (2 H, quin,  $J$  = 11 Hz,  $\text{CH}_2$ ), 1.79-1.84 (2 H, quin,  $J$  = 10 Hz,  $\text{CH}_2$ ), 2.22 (2H, m,  $\text{CH}_2$ ), 2.27 (2 H, m,  $\text{CH}_2$ ), 2.68 (3 H, s,  $\text{CH}_3$ ), 2.76-2.79 (2 H, t,  $J$  = 8 Hz,  $\text{CH}_2$ ), 5.70 (1 H, s, CH), 7.48-7.50 (2 H, m, Ar-H), 7.73 (1 H, s, Ar-H) 7.91-7.93 (1 H, d,  $J$  = 9 Hz, Ar-H).  $^{13}\text{C}$  NMR ( $\text{CDCl}_3$ , 125 MHz, 20 °C):  $\delta$  = 14.0, 22.1, 22.3, 23.0, 23.6, 25.5, 30.2, 33.5, 35.6, 125.5, 126.9, 127.3, 127.9, 130.4, 134.0, 137.4, 138.1, 140.3, 145.4, 156.7. MS (EI):  $m/z$  279 ( $\text{M}^+$ ). HRMS  $[\text{M}+\text{H}]^+$ : Found:  $m/z$  280.2062; Calcd for  $\text{C}_{20}\text{H}_{26}\text{N}$  280.2065.



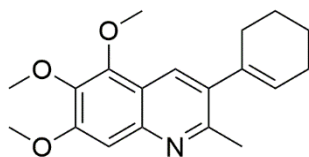
*3-cyclohexenyl-6-(N,N-dimethylamino)quinoline (21)*

In a nitrogen filled glove box, a 10 mL pressure tube, equipped with a magnetic stir bar was loaded with  $\text{Ti}(\text{NMe}_2)_2\text{dpm}$  (0.10 mmol, 30.8 mg) and dissolved in dry toluene (2 mL). The solution was loaded with 4-(dimethylamino)aniline (1.0 mmol, 136 mg), 1-ethynylcyclohex-1-ene (1.0 mmol, 106 mg) and *tert*-butylisonitrile (1.5 mmol, 171  $\mu\text{L}$ ). The pressure tube was sealed with a Teflon screw cap, taken out of the dry box and heated at 100 °C for 24 h in a silicone oil bath. Volatiles were removed *in vacuo*, and glacial acetic acid (2 mL) was added. The mixture was then heated at 150 °C for 24 h. The pressure tube was then allowed to cool to room temperature, diluted in dichloromethane and neutralized with saturated  $\text{NaHCO}_3$  solution. The organic layer was further extracted with additional dichloromethane, washed with brine, dried over  $\text{NaSO}_4$ , filtered and concentrated *in vacuo*. The crude product was dry loaded onto alumina and purification was accomplished by column chromatography on neutral alumina using hexanes:ethyl acetate (9:1, v/v) as the eluent to provide the product as a viscous yellow oil 97 mg (38%).  $^1\text{H}$  NMR ( $\text{CDCl}_3$ , 500 MHz, 20 °C):  $\delta$  = 1.41-1.46 (2 H, m,  $\text{CH}_2$ ), 1.52-1.57 (2 H, m,  $\text{CH}_2$ ), 1.95-1.97 (2 H, m,  $\text{CH}_2$ ), 2.23-2.4 (2 H, m,  $\text{CH}_2$ ), 2.51 (6 H, s,  $\text{N}(\text{CH}_3)_2$ ), 6.08-6.1 (1 H, m, CH), 6.64-6.65 (1 H, d,  $J$  = 3 Hz, Ar-H), 6.95-6.97 (1 H, dd,  $J$  = 3 Hz, 9 Hz, Ar-H), 7.67-7.69 (1 H, d,  $J$  = 2 Hz, Ar-H), 8.26-8.28 (1 H, d,  $J$  = 9 Hz, Ar-H), 9.03-9.04 (1 H, d,  $J$  = 2 Hz, Ar-H).  $^{13}\text{C}$  NMR ( $\text{CDCl}_3$ , 125 MHz, 20 °C):  $\delta$  = 22.0, 22.8, 25.8, 26.9, 39.9, 105.3, 118.5, 125.9, 128.2, 129.6, 130.1, 134.3, 135.0, 142.1, 144.9, 148.6. MS (EI):  $m/z$  252 ( $\text{M}^+$ ). HRMS  $[\text{M}]^+$ : Found:  $m/z$  252.1634.; Calcd for  $\text{C}_{17}\text{H}_{20}\text{N}_2$  252.1626.



*3-cyclohexenyl-2-ethyl-6(N,N-dimethylamino) quinoline (23)*

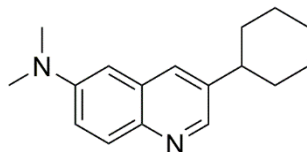
In a nitrogen filled glove box, a 10 mL pressure tube, equipped with a magnetic stir bar was loaded with  $\text{Ti}(\text{NMe}_2)_2\text{dpm}$  (0.10 mmol, 30.8 mg) and dissolved in dry toluene (2 mL). The solution was loaded with 4-(dimethylamino)aniline (1.0 mmol, 136 mg), 1-(but-1-ynyl)cyclohex-1-ene (1.0 mmol, 134 mg) and *tert*-butylisocyanide (1.5 mmol, 171  $\mu\text{L}$ ). The pressure tube was sealed with a Teflon screw cap, taken out of the dry box and heated at 100 °C for 48 h in a silicone oil bath. Volatiles were removed *in vacuo*, and glacial acetic acid (2 mL) was added. The mixture was then heated at 150 °C for 24 h. The pressure tube was then allowed to cool to room temperature, diluted in dichloromethane and neutralized with saturated  $\text{NaHCO}_3$  solution. The organic layer was further extracted with additional dichloromethane, washed with brine, dried over  $\text{NaSO}_4$ , filtered and concentrated *in vacuo*. The crude product was dry loaded onto alumina and purification was accomplished by column chromatography on neutral alumina using hexanes:ethyl acetate (9:1, v/v) as the eluent to provide the product as a viscous light-yellow oil 109 mg (39%).  $^1\text{H}$  NMR ( $\text{CDCl}_3$ , 500 MHz, 20 °C):  $\delta$  = 1.52-1.60 (7 H, m), 1.98-2.01 (2 H, m,  $\text{CH}_2$ ), 2.12-2.17 (2 H, m,  $\text{CH}_2$ ), 2.52 (6 H, s,  $\text{N}(\text{CH}_3)_2$ ), 3.03-3.07 (2 H, quart,  $J$  = 7 Hz,  $\text{CH}_2$ ), 5.59 (1 H, m), 6.65 (1 H, d,  $J$  = 3 Hz, Ar-H), 6.98-7.00 (1 H, dd,  $J$  = 3 Hz, 9 Hz, Ar-H), 7.50 (1 H, s, Ar-H), 8.20-8.22 (1 H, d,  $J$  = 9 Hz, Ar-H).  $^{13}\text{C}$  NMR ( $\text{CDCl}_3$ , 125 MHz, 20 °C):  $\delta$  = 13.7, 22.1, 23.1, 25.4, 28.9, 30.7, 40.1, 105.1, 118.7, 126.3, 128.2, 128.4, 129.7, 132.7, 138.0, 141.9, 148.0, 157.2. MS (EI):  $m/z$  280 ( $\text{M}^+$ ). HRMS  $[\text{M}]^+$ : Found:  $m/z$  280.1928.; Calcd for  $\text{C}_{19}\text{H}_{24}\text{N}_2$  280.1939.



*3-cyclohexenyl-5,6,7-trimethoxy-2-methylquinoline (27)*

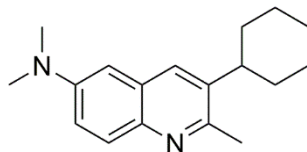
In a nitrogen filled glove box, a 10 mL pressure tube, equipped with a magnetic stir bar was loaded with  $\text{Ti}(\text{NMe}_2)_2\text{dpm}$  (0.10 mmol, 30.8 mg) and dissolved in dry toluene (2 mL). The solution was loaded with 3,4,5-trimethoxyaniline (1.0 mmol, 183 mg), 1-(prop-1-ynyl)cyclohex-1-ene (1.0 mmol, 120 mg) and *tert*-butylisocyanide (1.5 mmol, 171  $\mu\text{L}$ ). The pressure tube was sealed with a Teflon screw cap, taken out of the dry box and heated at 100 °C for 48 h in a silicone oil bath. Volatiles were removed *in vacuo*, and glacial acetic acid (2 mL) was added. The mixture was then heated at 150 °C for 24 h. The pressure tube was then allowed to cool to room temperature, diluted in dichloromethane and neutralized with saturated  $\text{NaHCO}_3$  solution. The organic layer was further extracted with additional dichloromethane, washed with brine, dried over  $\text{Na}_2\text{SO}_4$ , filtered and concentrated *in vacuo*. The crude product was dry loaded onto alumina and purification was accomplished by column chromatography on neutral alumina using hexanes:ethyl acetate (9:1, v/v) as the eluent to provide the product as a viscous light-yellow oil 131 mg (42%).  $^1\text{H}$  NMR ( $\text{CDCl}_3$ , 500 MHz, 20 °C):  $\delta$  = 1.71-1.76 (2 H, m,  $\text{CH}_2$ ), 1.79-1.84 (2 H, m,  $\text{CH}_2$ ), 2.23 (2 H, m,  $\text{CH}_2$ ), 2.27 (2 H, m,  $\text{CH}_2$ ), 2.65 (3 H, s,  $\text{CH}_3$ ), 3.97 (3 H, s,  $\text{OCH}_3$ ), 3.99 (3 H, s,  $\text{OCH}_3$ ), 4.06 (3 H, s,  $\text{OCH}_3$ ), 5.69 (1 H, s, Ar-H), 7.20 (1 H, s, Ar-H), 7.98 (1 H, s, Ar-H).  $^{13}\text{C}$  NMR ( $\text{CDCl}_3$ , 125 MHz, 20 °C):  $\delta$  = 22.0, 23.0, 23.4, 25.5, 30.3, 56.1, 61.2, 61.6, 103.2, 117.8, 127.4, 129.0, 136.0, 137.5, 140.3, 144.3, 146.8, 155.4, 156.8. MS (EI):  $m/z$  313 ( $\text{M}^+$ ). HRMS  $[\text{M}+\text{H}]^+$ : Found:  $m/z$  314.1763.; Calcd for  $\text{C}_{19}\text{H}_{24}\text{NO}_3$  314.1756. M.p.: 93-95 °C.





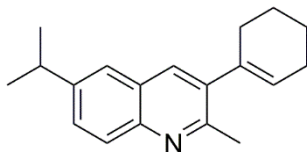
*3-cyclohexenyl-6-(N,N-dimethylamino)quinoline (28)*

3-cyclohexenyl-6-(N,N-dimethylamino)quinoline (**21**) (80 mg, 0.32 mmol) was dissolved in 6 mL of ethanol and hydrogenated at low pressure, using a hydrogen balloon, over 10% palladium on carbon (120 mg) at room temperature (25 °C) overnight. Purification was accomplished via filtration through neutral alumina followed by column chromatography on neutral alumina using hexanes:ethyl acetate (9:1, v/v), which afforded the desired compound as a viscous light-yellow oil 75 mg (93%). <sup>1</sup>H NMR (CDCl<sub>3</sub>, 500 MHz, 20 °C): δ = 1.07-1.11 (1 H, m, CH<sub>2</sub>), 1.18-1.22 (2 H, m, CH<sub>2</sub>), 1.27-1.33 (2 H, m, CH<sub>2</sub>), 1.58-1.60 (1 H, m, CH<sub>2</sub>), 1.64-1.68 (2 H, m, CH<sub>2</sub>), 1.74-1.77 (2 H, m, CH<sub>2</sub>), 2.33-2.38 (1 H, m, CH), 2.52 (6 H, s, N(CH<sub>3</sub>)<sub>2</sub>), 6.65-6.66 (1 H, d, *J* = 3 Hz, Ar-H), 6.97-6.99 (1 H, dd, *J* = 3 Hz, 9 Hz, Ar-H), 7.52 (1 H, d, *J* = 2 Hz, Ar-H), 8.26-8.28 (1 H, d, *J* = 9 Hz, Ar-H), 8.71-8.72 (1 H, d, *J* = 2 Hz, Ar-H). <sup>13</sup>C NMR (CDCl<sub>3</sub>, 125 MHz, 20 °C): δ = 26.0, 26.7, 34.0, 40.0, 42.0, 105.1, 118.4, 129.8, 128.9, 130.2, 140.2, 142.1, 147.4, 148.4. MS (EI): *m/z* 254 (M<sup>+</sup>). HRMS [M]<sup>+</sup>: Found: *m/z* 254.1774.; Calcd for C<sub>17</sub>H<sub>22</sub>N<sub>2</sub> 254.1783.



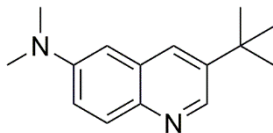
*3-cyclohexyl-2-methyl-6-(N,N-dimethylamino)quinoline (29)*

2-methyl-3-cyclohexenyl-6-(N,N-dimethylamino)quinoline (**22**) (100 mg, 0.38 mmol) was dissolved in 6 mL of ethanol and hydrogenated at low pressure, using a hydrogen balloon, over 10% palladium on carbon (150 mg) at room temperature (25 °C) overnight. Purification was accomplished via filtration through neutral alumina followed by column chromatography on neutral alumina using hexanes:ethyl acetate (9:1, v/v), which afforded the desired compound as a viscous yellow oil 98 mg (97%). <sup>1</sup>H NMR (CDCl<sub>3</sub>, 500 MHz, 20 °C): δ = 1.16-1.33 (4 H, m, CH<sub>2</sub>), 1.63-1.79 (4 H, m, CH<sub>2</sub>), 2.55 (6 H, s, CH<sub>3</sub>), 2.71 (3 H, s, CH<sub>3</sub>), 6.72-6.73 (1 H, d, *J* = 3 Hz, Ar-H), 6.99-7.01 (1 H, dd, *J* = 3 Hz, 9 Hz, Ar-H), 7.63 (1 H, s, Ar-H), 8.20-8.22 (1 H, d, *J* = 9 Hz, Ar-H). <sup>13</sup>C NMR (CDCl<sub>3</sub>, 125 MHz, 20 °C): δ = 25.6, 26.3, 27.0, 33.7, 39.9, 40.2, 105.3, 118.4, 129.0, 129.5, 129.6, 139.2, 141.3, 148.0, 153.4. MS (EI): *m/z* 268 (M<sup>+</sup>). HRMS [M]<sup>+</sup>: Found: *m/z* 268.1934.; Calcd for C<sub>18</sub>H<sub>24</sub>N<sub>2</sub> 268.1939.



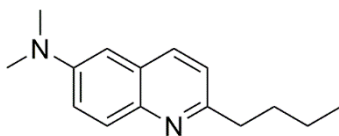
*3-cyclohexenyl-6-isopropyl-2-methylquinoline (30)*

In a nitrogen filled glove box, a 10 mL pressure tube, equipped with a magnetic stir bar was loaded with  $\text{Ti}(\text{NMe}_2)_2\text{dpm}$  (0.10 mmol, 30.8 mg) and dissolved in dry toluene (2 mL). The solution was loaded with 4-isopropylaniline (1.0 mmol, 135 mg), 1-(prop-1-ynyl)cyclohex-1-ene (1.0 mmol, 120 mg) and *tert*-butylisonitrile (1.5 mmol, 171  $\mu\text{L}$ ). The pressure tube was sealed with a Teflon screw cap, taken out of the dry box and heated at 100 °C for 48 h in a silicone oil bath. Volatiles were removed *in vacuo*, and glacial acetic acid (2 mL) was added. The mixture was then heated at 150 °C for 24 h. The pressure tube was then allowed to cool to room temperature, diluted in dichloromethane and neutralized with saturated  $\text{NaHCO}_3$  solution. The organic layer was further extracted with additional dichloromethane, washed with brine, dried over  $\text{NaSO}_4$ , filtered and concentrated *in vacuo*. The crude product was dry loaded onto alumina and purification was accomplished by column chromatography on neutral alumina using hexanes:ethyl acetate (9:1, v/v) as the eluent to provide the product as a viscous yellow oil 112 mg (43%).  $^1\text{H}$  NMR ( $\text{CDCl}_3$ , 500 MHz, 20 °C):  $\delta$  = 1.32-1.34 (6 H, d,  $J$  = 7 Hz,  $\text{CH}_3$ ), 1.71-1.75 (2 H, quin,  $J$  = 11 Hz,  $\text{CH}_2$ ), 1.78-1.83 (2 H, quin,  $J$  = 12 Hz,  $\text{CH}_2$ ), 2.21 (2 H, m,  $\text{CH}_2$ ), 2.26 (2 H, m,  $\text{CH}_2$ ), 2.68 (3 H, s,  $\text{CH}_3$ ), 3.02-3.11 (1 H, sept,  $J$  = 7 Hz, CH), 5.69 (1 H, s, CH), 7.53 (1 H, s, Ar-H), 7.53-7.55 (1H, app d,  $J$  = 9 Hz, Ar-H), 7.75 (1 H, s, Ar-H), 7.94-7.96 (1 H, d,  $J$  = 9 Hz, Ar-H).  $^{13}\text{C}$  NMR ( $\text{C}_6\text{D}_6$ , 125 MHz, 20 °C):  $\delta$  = 22.0, 23.0, 23.5, 23.7, 25.3, 30.0, 34.0, 123.3, 126.8, 127.1, 128.3, 129.0, 133.6, 137.7, 137.8, 145.7, 146.5, 156.3. MS (EI):  $m/z$  265 ( $\text{M}^+$ ). HRMS  $[\text{M}+\text{H}]^+$ : Found:  $m/z$  266.1907.; Calcd for  $\text{C}_{15}\text{H}_{20}\text{N}_2$  266.1909.



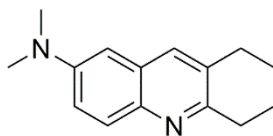
**3-tert-butyl-6-(N,N-dimethylamino)quinoline (31)**

In a nitrogen filled glove box, a 10 mL pressure tube, equipped with a magnetic stir bar was loaded with  $\text{Ti}(\text{NMe}_2)_2\text{dpma}$  (0.10 mmol, 32.3 mg) and dissolved in dry toluene (2 mL). The solution was loaded with 4-(dimethylamino)aniline (1.0 mmol, 136 mg), 3,3-dimethylbut-1-yne (1.0 mmol, 82 mg) and *tert*-butylisocyanide (1.5 mmol, 171  $\mu\text{L}$ ). The pressure tube was sealed with a Teflon screw cap, taken out of the dry box and heated at 100 °C for 24 h in a silicone oil bath. Volatiles were removed *in vacuo*, and glacial acetic acid (2 mL) was added. The mixture was then heated at 150 °C for 24 h. The pressure tube was then allowed to cool to room temperature, diluted in dichloromethane and neutralized with saturated  $\text{NaHCO}_3$  solution. The organic layer was further extracted with additional dichloromethane, washed with brine, dried over  $\text{NaSO}_4$ , filtered and concentrated *in vacuo*. The crude product was dry loaded onto alumina and purification was accomplished by column chromatography on neutral alumina using hexanes:ethyl acetate (9:1, v/v) as the eluent to provide the product as a viscous light brown oil 55 mg (24%).  $^1\text{H}$  NMR ( $\text{CDCl}_3$ , 500 MHz, 20 °C):  $\delta$  = 1.20 (9 H, s,  $\text{C}(\text{CH}_3)_3$ ), 2.53 (6H, s,  $\text{N}(\text{CH}_3)_2$ ), 6.67-6.68 (1 H, d,  $J$  = 3 Hz, Ar-H), 6.98-7.01 (1 H, dd,  $J$  = 3 Hz, 9 Hz, Ar-H), 7.72-7.73 (1 H, d,  $J$  = 3 Hz, Ar-H), 8.26-8.27 (1 H, d,  $J$  = 9 Hz, Ar-H), 8.96-8.98 (1 H, d,  $J$  = 2 Hz, Ar-H).  $^{13}\text{C}$  NMR ( $\text{CDCl}_3$ , 125 MHz, 20 °C):  $\delta$  = 30.6, 33.3, 40.0, 105.3, 118.4, 128.4, 129.5, 130.0, 141.5, 143.0, 146.0, 148.5. MS (EI):  $m/z$  228 ( $\text{M}^+$ ). HRMS  $[\text{M}]^+$ : Found:  $m/z$  228.1617.; Calcd for  $\text{C}_{15}\text{H}_{20}\text{N}_2$  228.1626.



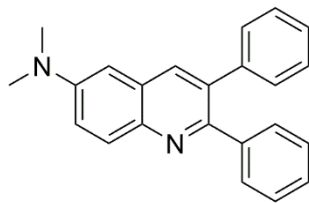
**2-butyl-6-(N,N-dimethylamino)quinoline (32)**

In a nitrogen filled glove box, a 10 mL pressure tube, equipped with a magnetic stir bar was loaded with  $\text{Ti}(\text{NMe}_2)_2\text{dpma}$  (0.10 mmol, 32.3 mg) and dissolved in dry toluene (2 mL). The solution was loaded with 4-(dimethylamino)aniline (1.0 mmol, 136 mg), 1-hexyne (1.0 mmol, 82 mg) and *tert*-butylisocyanide (1.5 mmol, 171  $\mu\text{L}$ ). The pressure tube was sealed with a Teflon screw cap, taken out of the dry box and heated at 100 °C for 24h in a silicone oil bath. Volatiles were removed *in vacuo*, and glacial acetic acid (2 mL) was added. The mixture was then heated at 150 °C for 24 h. The pressure tube was then allowed to cool to room temperature, diluted in dichloromethane and neutralized with saturated  $\text{NaHCO}_3$  solution. The organic layer was further extracted with additional dichloromethane, washed with brine, dried over  $\text{NaSO}_4$ , filtered and concentrated *in vacuo*. The crude product was dry loaded onto alumina and purification was accomplished by column chromatography on neutral alumina using hexanes:ethyl acetate (9:1, v/v) as the eluent to provide the product as a viscous brown oil 69 mg (30%).  $^1\text{H}$  NMR ( $\text{CDCl}_3$ , 500 MHz, 20 °C):  $\delta$  = 0.86-0.89 (3 H, t,  $J$  = 7 Hz,  $\text{CH}_3$ ), 1.32-1.39 (2 H, sext,  $J$  = 7 Hz,  $\text{CH}_2$ ), 1.82-1.88 (2H, quin,  $J$  = 7 Hz,  $\text{CH}_2$ ), 2.50 (6 H, s,  $\text{N}(\text{CH}_3)_2$ ), 2.92-2.95 (2 H, t,  $J$  = 7 Hz,  $\text{CH}_2$ ), 6.64-6.65 (1 H, d,  $J$  = 3 Hz, Ar-H), 6.92-6.93 (1 H, d,  $J$  = 8 Hz, Ar-H), 6.98-7.01 (1 H, dd,  $J$  = 3 Hz, 9 Hz, Ar-H), 7.61-7.63 (1 H, d,  $J$  = 8 Hz, Ar-H), 8.19-8.21 (1 H, d,  $J$  = 9 Hz, Ar-H).  $^{13}\text{C}$  NMR ( $\text{CDCl}_3$ , 125 MHz, 20 °C):  $\delta$  = 13.9, 22.6, 31.9, 39.5, 40.0, 105.4, 119.1, 121.4, 128.1, 130.1, 133.8, 142.9, 148.0, 158.4. MS (EI):  $m/z$  228 ( $\text{M}^+$ ). HRMS  $[\text{M}]^+$ : Found:  $m/z$  228.1616.; Calcd for  $\text{C}_{15}\text{H}_{20}\text{N}_2$  228.1626.



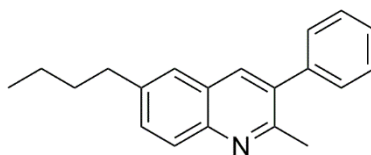
**2,3-diethyl-N,N-dimethylquinoline (33)**

In a nitrogen filled glove box, a 10 mL pressure tube, equipped with a magnetic stir bar was loaded with  $\text{Ti}(\text{NMe}_2)_2\text{dpm}$  (0.10 mmol, 30.8 mg) and dissolved in dry toluene (2 mL). The solution was loaded with 4-(dimethylamino)aniline (1.0 mmol, 136 mg), 3-hexyne (1.0 mmol, 82 mg) and *tert*-butylisocyanide (1.5 mmol, 171  $\mu\text{L}$ ). The pressure tube was sealed with a Teflon screw cap, taken out of the dry box and heated at 100 °C for 48 h in a silicone oil bath. Volatiles were removed *in vacuo*, and glacial acetic acid (2 mL) was added. The mixture was then heated at 150 °C for 24 h. The pressure tube was then allowed to cool to room temperature, diluted in dichloromethane and neutralized with saturated  $\text{NaHCO}_3$  solution. The organic layer was further extracted with additional dichloromethane, washed with brine, dried over  $\text{NaSO}_4$ , filtered and concentrated *in vacuo*. The crude product was dry loaded onto alumina and purification was accomplished by column chromatography on neutral alumina using hexanes:ethyl acetate (9:1, v/v) as the eluent to provide the product as a light brown solid 74 mg (33%).  $^1\text{H}$  NMR ( $\text{CDCl}_3$ , 500 MHz, 20 °C):  $\delta$  = 1.32-1.35 (3 H, t,  $J$  = 7 Hz,  $\text{CH}_3$ ), 1.35-1.38 (3 H, t,  $J$  = 7 Hz,  $\text{CH}_3$ ), 2.78-2.83 (2 H, q,  $J$  = 7 Hz,  $\text{CH}_2$ ), 2.95-2.99 (2 H, q,  $J$  = 7 Hz,  $\text{CH}_2$ ), 3.06 (6 H, s,  $\text{N}(\text{CH}_3)_2$ ), 6.79 (1 H, d,  $J$  = 2.8 Hz, Ar-H), 7.29-7.31 (1 H, dd,  $J$  = 3 Hz, 9 Hz, Ar-H), 7.71 (1 H, s, Ar-H), 7.89-7.91 (1 H, d,  $J$  = 9 Hz, Ar-H).  $^{13}\text{C}$  NMR ( $\text{CDCl}_3$ , 125 MHz, 20 °C):  $\delta$  = 13.9, 14.5, 25.1, 28.5, 41.9, 105.0, 118.6, 128.7, 128.9, 132.5, 135.2, 148.2, 158.8. MS (EI):  $m/z$  228 ( $\text{M}^+$ ). HRMS  $[\text{M}+\text{H}]^+$ : Found:  $m/z$  229.1712.; Calcd for  $\text{C}_{15}\text{H}_{20}\text{N}_2$  229.1705. M.p.: 64-66 °C.



**2,3-diphenyl-6-(N,N-dimethylamino)quinoline (35)**

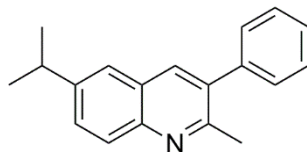
In a nitrogen filled glove box, a 10 mL pressure tube, equipped with a magnetic stir bar was loaded with  $\text{Ti}(\text{NMe}_2)_2\text{dpm}$  (0.20 mmol, 61.6 mg) and dissolved in dry toluene (2 mL). The solution was loaded with 4-(dimethylamino)aniline (1.0 mmol, 136 mg), diphenylacetylene (1.0 mmol, 178 mg) and *tert*-butylisocyanide (1.5 mmol, 171  $\mu\text{L}$ ). The pressure tube was sealed with a Teflon screw cap, taken out of the dry box and heated at 140 °C for 48 h in a silicone oil bath. Volatiles were removed *in vacuo*, and glacial acetic acid (2 mL) was added. The mixture was then heated at 150 °C for 24 h. The pressure tube was then allowed to cool to room temperature, diluted in dichloromethane and neutralized with saturated  $\text{NaHCO}_3$  solution. The organic layer was further extracted with additional dichloromethane, washed with brine, dried over  $\text{NaSO}_4$ , filtered and concentrated *in vacuo*. The crude product was dry loaded onto alumina and purification was accomplished by column chromatography on neutral alumina using hexanes:ethyl acetate (9:1, v/v) as the eluent to provide the product as a dark yellow solid 90 mg (28%).  $^1\text{H}$  NMR ( $\text{CDCl}_3$ , 500 MHz, 20 °C):  $\delta$  = 2.52 (1 H, s,  $\text{N}(\text{CH}_3)_2$ ), 6.63-6.64 (1 H, d,  $J$  = 3 Hz, Ar-H), 7.01-7.06 (5 H, m, Ar-H), 7.07-7.10 (2 H, m, Ar-H), 7.19-7.21 (2 H, m, Ar-H), 7.72-7.74 (3 H, m, Ar-H), 8.30-8.32 (1 H, d,  $J$  = 9 Hz, Ar-H).  $^{13}\text{C}$  NMR ( $\text{CDCl}_3$ , 125 MHz, 20 °C):  $\delta$  = 39.9, 104.6, 119.4, 126.7, 127.2, 127.53, 128.0, 128.9, 129.8, 130.4, 130.5, 134.7, 135.6, 141.2, 141.4, 142.3, 148.5, 153.9. MS (EI):  $m/z$  324 ( $\text{M}^+$ ). HRMS  $[\text{M}]^+$ : Found:  $m/z$  324.1642.; Calcd for  $\text{C}_{23}\text{H}_{20}\text{N}_2$  324.1626. M.p.: 159-161 °C.



**6-butyl-2-methyl-3-phenylquinoline (36)**

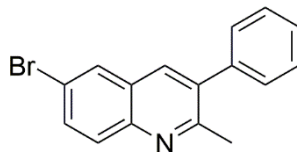
In a nitrogen filled glove box, a 10 mL pressure tube, equipped with a magnetic stir bar was loaded with  $\text{Ti}(\text{NMe}_2)_2\text{dpm}$  (0.10 mmol, 30.8 mg) and dissolved in dry toluene (2 mL). The solution was loaded with 4-butylaniline (1.0 mmol, 149 mg), 1-phenylpropyne (1.0 mmol, 116 mg) and *tert*-butylisocyanide (1.5 mmol, 171  $\mu\text{L}$ ). The pressure tube was sealed with a Teflon screw cap, taken out of the dry box and heated at 100 °C for 48 h in a silicone oil bath. Volatiles were removed *in vacuo*, and glacial acetic acid (2 mL) was added. The mixture was then heated at 150 °C for 24 h. The pressure tube was then allowed to cool to room temperature, diluted in dichloromethane and neutralized with saturated  $\text{NaHCO}_3$  solution. The organic layer was further extracted with additional dichloromethane, washed with brine, dried over  $\text{NaSO}_4$ , filtered and concentrated *in vacuo*. The crude product was dry loaded onto alumina and purification was accomplished by column chromatography on neutral alumina using hexanes:ethyl acetate (9:1, v/v) as the eluent to provide the product as a viscous yellow oil 101 mg (37%).  $^1\text{H}$  NMR ( $\text{CDCl}_3$ , 500 MHz, 20 °C):  $\delta$  = 0.95-0.98 (3H, t,  $J$  = 7 Hz,  $\text{CH}_3$ ), 1.37-1.45 (2 H, sext,  $J$  = 10 Hz,  $\text{CH}_2$ ), 1.68-1.74 (2 J, quin,  $J$  = 10 Hz,  $\text{CH}_2$ ), 2.67 (3 H, s,  $\text{CH}_3$ ), 2.79-2.82 (2 H, t,  $J$  = 5 Hz,  $\text{CH}_2$ ), 7.41-7.44 (3 H, m, Ar-H), 7.47-7.50 (2 H, m, Ar-H), 7.56-7.57 (2 H, m, Ar-H), 7.91 (1 H, s, Ar-H), 7.99-8.01 (1 H, d,  $J$  = 9 Hz, Ar-H).  $^{13}\text{C}$  NMR ( $\text{CDCl}_3$ , 125 MHz, 20 °C):  $\delta$  = 14.0, 22.4, 24.4, 33.5, 35.6, 125.7, 126.8, 127.5, 128.1, 128.4, 129.2, 131.0, 135.6, 135.7, 140.1, 140.8, 145.8, 156.3. MS (EI):  $m/z$  275 ( $\text{M}^+$ ). HRMS  $[\text{M}+\text{H}]^+$ : Found:  $m/z$  276.1750.; Calcd for  $\text{C}_{20}\text{H}_{22}\text{N}$  276.1752.





**6-isopropyl-2-methyl-3-phenylquinoline (37)**

In a nitrogen filled glove box, a 10 mL pressure tube, equipped with a magnetic stir bar was loaded with  $\text{Ti}(\text{NMe}_2)_2\text{dpm}$  (0.10 mmol, 30.8 mg) and dissolved in dry toluene (2 mL). The solution was loaded with 4-isopropylaniline (1.0 mmol, 135 mg), 1-phenylpropyne (1.0 mmol, 116 mg) and *tert*-butylisocyanide (1.5 mmol, 171  $\mu\text{L}$ ). The pressure tube was sealed with a Teflon screw cap, taken out of the dry box and heated at 100 °C for 48 h in a silicone oil bath. Volatiles were removed *in vacuo*, and glacial acetic acid (2 mL) was added. The mixture was then heated at 150 °C for 24 h. The pressure tube was then allowed to cool to room temperature, diluted in dichloromethane and neutralized with saturated  $\text{NaHCO}_3$  solution. The organic layer was further extracted with additional dichloromethane, washed with brine, dried over  $\text{NaSO}_4$ , filtered and concentrated *in vacuo*. The crude product was dry loaded onto alumina and purification was accomplished by column chromatography on neutral alumina using hexanes:ethyl acetate (9:1, v/v) as the eluent to provide the product as a viscous yellow oil 143 mg (55%).  $^1\text{H}$  NMR ( $\text{CDCl}_3$ , 500 MHz, 20 °C):  $\delta$  = 1.35-1.37 (2 H, d,  $J$  = 7 Hz,  $\text{CH}_3$ ), 2.67 (3 H, s,  $\text{CH}_3$ ), 3.06-3.15 (1 H, sept,  $J$  = 8 Hz, CH), 7.40-7.44 (3 H, m, Ar-H), 7.47-7.50 (2 H, m, Ar-H), 7.60 (1 H, s, Ar-H), 7.61-7.64 (1 H, dd,  $J$  = 9 Hz, Ar-H), 7.93 (1 H, s, Ar-H), 8.01-8.03 (1 H, d,  $J$  = 9 Hz, Ar-H).  $^{13}\text{C}$  NMR ( $\text{CDCl}_3$ , 125 MHz, 20 °C):  $\delta$  = 23.9, 24.5, 29.7, 34.1, 123.5, 126.8, 127.5, 128.2, 128.4, 129.2, 129.3, 135.6, 135.9, 140.1, 145.9, 146.7, 156.4. MS (EI):  $m/z$  261 ( $\text{M}^+$ ). HRMS  $[\text{M}+\text{H}]^+$ : Found:  $m/z$  262.1596.; Calcd for  $\text{C}_{19}\text{H}_{20}\text{N}$  262.1593.



**6-bromo-2-methyl-3-phenylquinoline (38)**

In a nitrogen filled glove box, a 10 mL pressure tube, equipped with a magnetic stir bar was loaded with  $\text{Ti}(\text{NMe}_2)_2\text{dpm}$  (0.10 mmol, 30.8 mg) and dissolved in dry toluene (2 mL). The solution was loaded with 4-bromoaniline (1.0 mmol, 172 mg), 1-phenylpropyne (1.0 mmol, 116 mg) and *tert*-butylisocyanide (1.5 mmol, 171  $\mu\text{L}$ ). The pressure tube was sealed with a Teflon screw cap, taken out of the dry box and heated at 100 °C for 48 h in a silicone oil bath. Volatiles were removed *in vacuo*, and glacial acetic acid (2 mL) was added. The mixture was then heated at 150 °C for 24 h. The pressure tube was then allowed to cool to room temperature, diluted in dichloromethane and neutralized with saturated  $\text{NaHCO}_3$  solution. The organic layer was further extracted with additional dichloromethane, washed with brine, dried over  $\text{NaSO}_4$ , filtered and concentrated *in vacuo*. The crude product was dry loaded onto alumina and purification was accomplished by column chromatography on neutral alumina using hexanes:ethyl acetate (9:1, v/v) as the eluent to provide the product as a light tan solid 337 mg (26%, on 5 mmol scale).  $^1\text{H}$  NMR ( $\text{CDCl}_3$ , 500 MHz, 20 °C):  $\delta$  = 2.66 (3 H, s,  $\text{CH}_3$ ), 7.39-7.41 (2H, m, Ar-H), 7.43-7.46 (1 H, m, Ar-H), 7.48-7.52 (2 H, m, Ar-H), 7.76-7.78 (1 H, dd,  $J$  = 2 Hz, 9 Hz, Ar-H), 7.87 (1 H, s, Ar-H), 7.93-7.95 (1 H, d,  $J$  = 9 Hz, Ar-H), 7.95-7.96 (1H, d,  $J$  = 2 Hz, Ar-H).  $^{13}\text{C}$  NMR ( $\text{CDCl}_3$ , 125 MHz, 20 °C):  $\delta$  = 24.7, 119.7, 127.8, 128.0, 128.5, 129.1, 129.4, 130.2, 132.7, 134.9, 136.6, 139.4, 145.6, 158.0. MS (EI):  $m/z$  297 ( $\text{M}^+$ ). HRMS  $[\text{M}+\text{H}]^+$ : Found:  $m/z$  298.0230.; Calcd for  $\text{C}_{16}\text{H}_{13}\text{BrN}$  298.0231. M.p.: 88-90 °C.

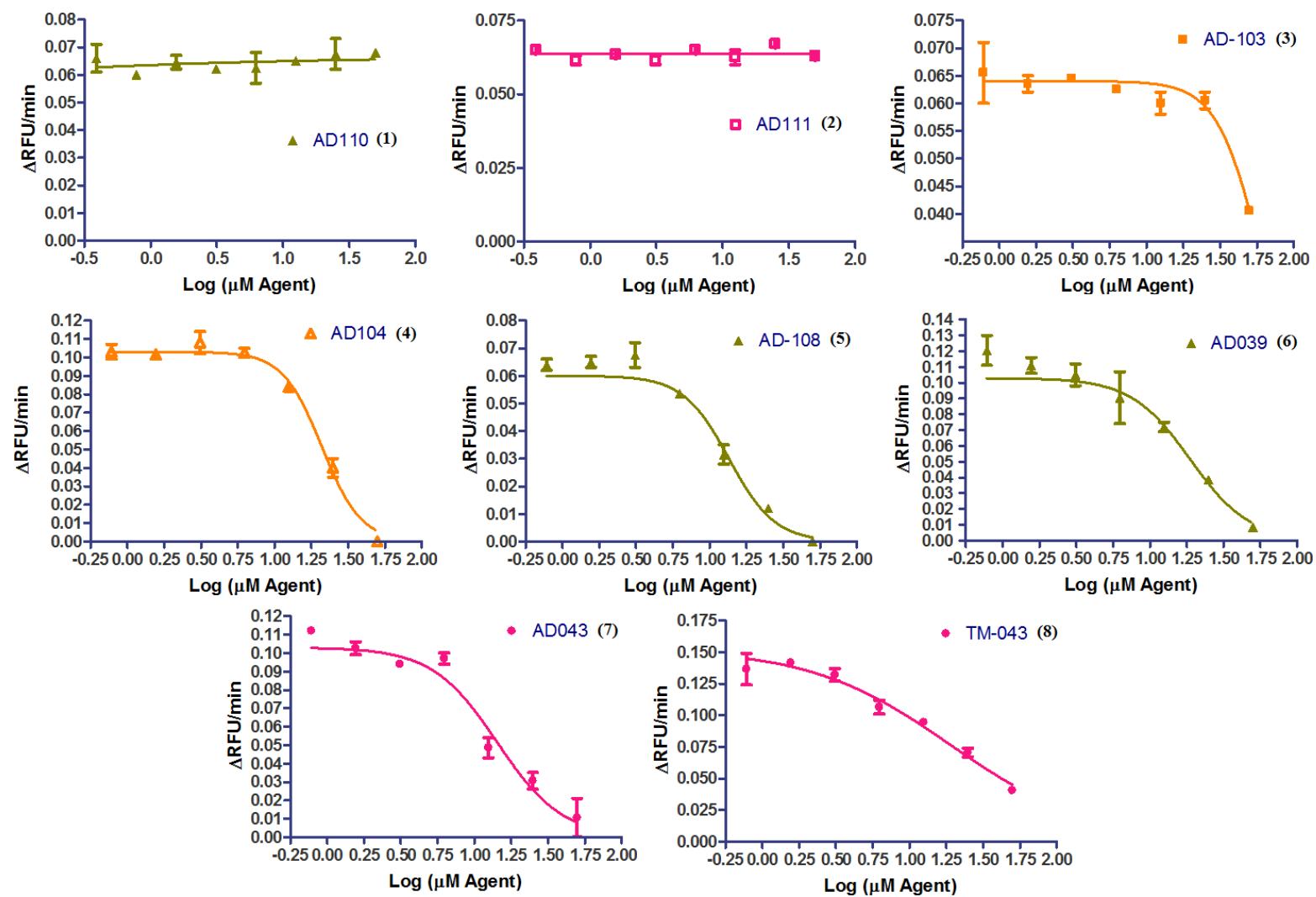
## 20S Proteasomal activity measurement

The fluorogenic substrates Suc-LLVY-AMC, Z-ARR-AMC, and Z-LLE-AMC were used to measure CT-L, T-L and casp-L proteasome activities, respectively. Assays were carried out in black, clear bottom 96 well plates in a 200  $\mu$ L reaction volume containing 1 nM of purified human 20S proteasome in 50 mM Tris-HCL pH 7.5 and 0.03% SDS containing 50  $\mu$ M fluorogenic substrate at 37 °C. The rate of cleavage of fluorogenic peptide substrates was determined by monitoring the fluorescence of released aminomethylcoumarin using a SpectraMax M5e multiwall plate reader at an excitation wavelength of 380 nm and emission wavelength of 460 nm. Fluorescence was measured every minute over a period of 30 minutes and the maximum increase in fluorescence per minute was used to calculate specific activities of each sample.

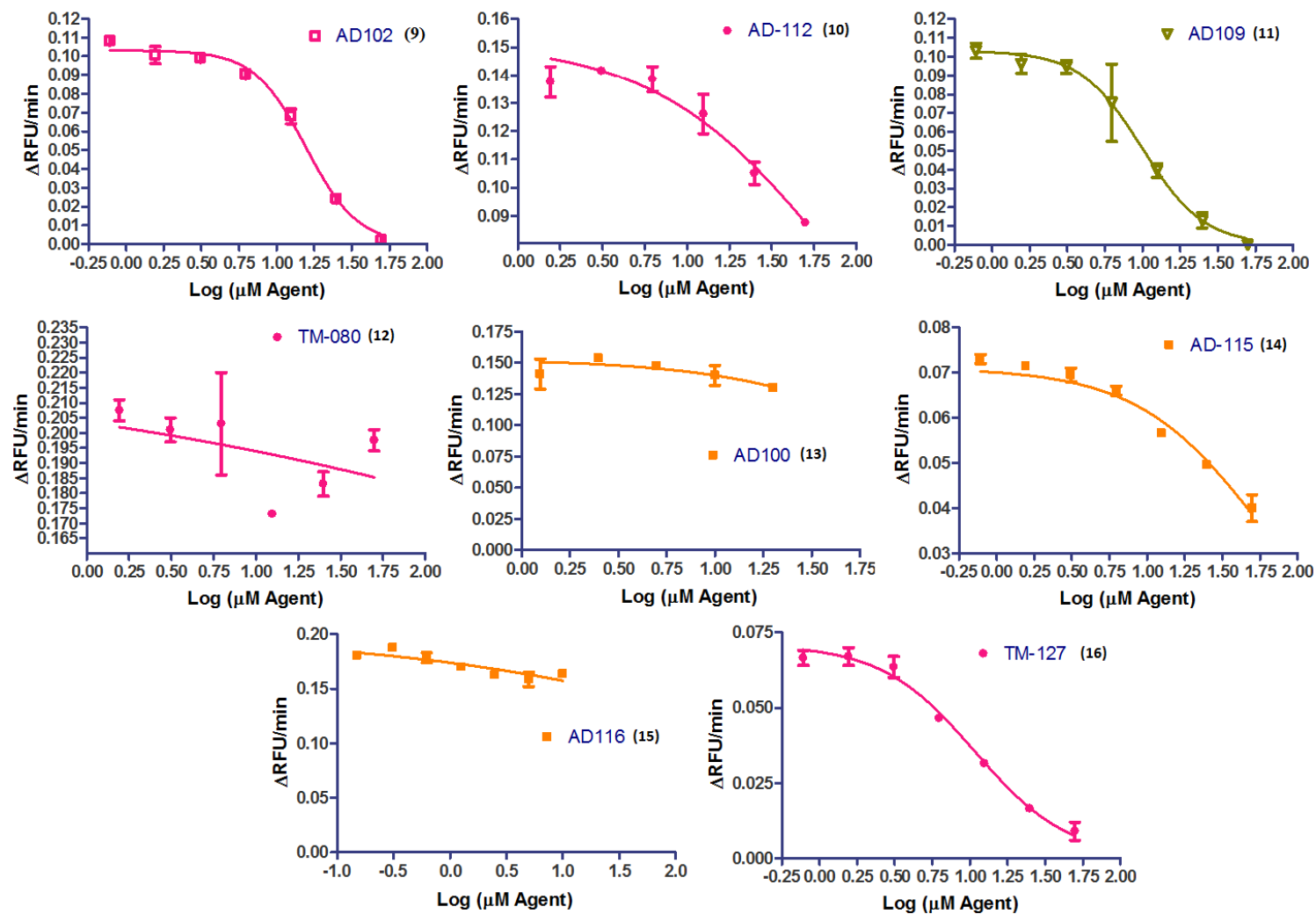
## Fluorescence Quenching Control

During the measurements of 20S proteasomal activity using Suc-LLVY-AMC as the fluorogenic substrate a fluorescence quenching control was ran simultaneously with these experiments. In one row on the clear bottom 96 well plate in a 200  $\mu$ L reaction volume containing 1 nM of purified human 20S proteasome in a 50 mM Tris-HCl pH 7.5 and 0.03% SDS and 50  $\mu$ M of the desired quinoline at 37 °C. This row was monitored using SpectraMax M5e multiwall plate reader at an excitation wavelength 380nm and emission wavelength at 460nm for any fluorescent interference stemming from the quinoline/enzyme interaction. No observable interference was observed except for **TM-124, quinoline #35**.

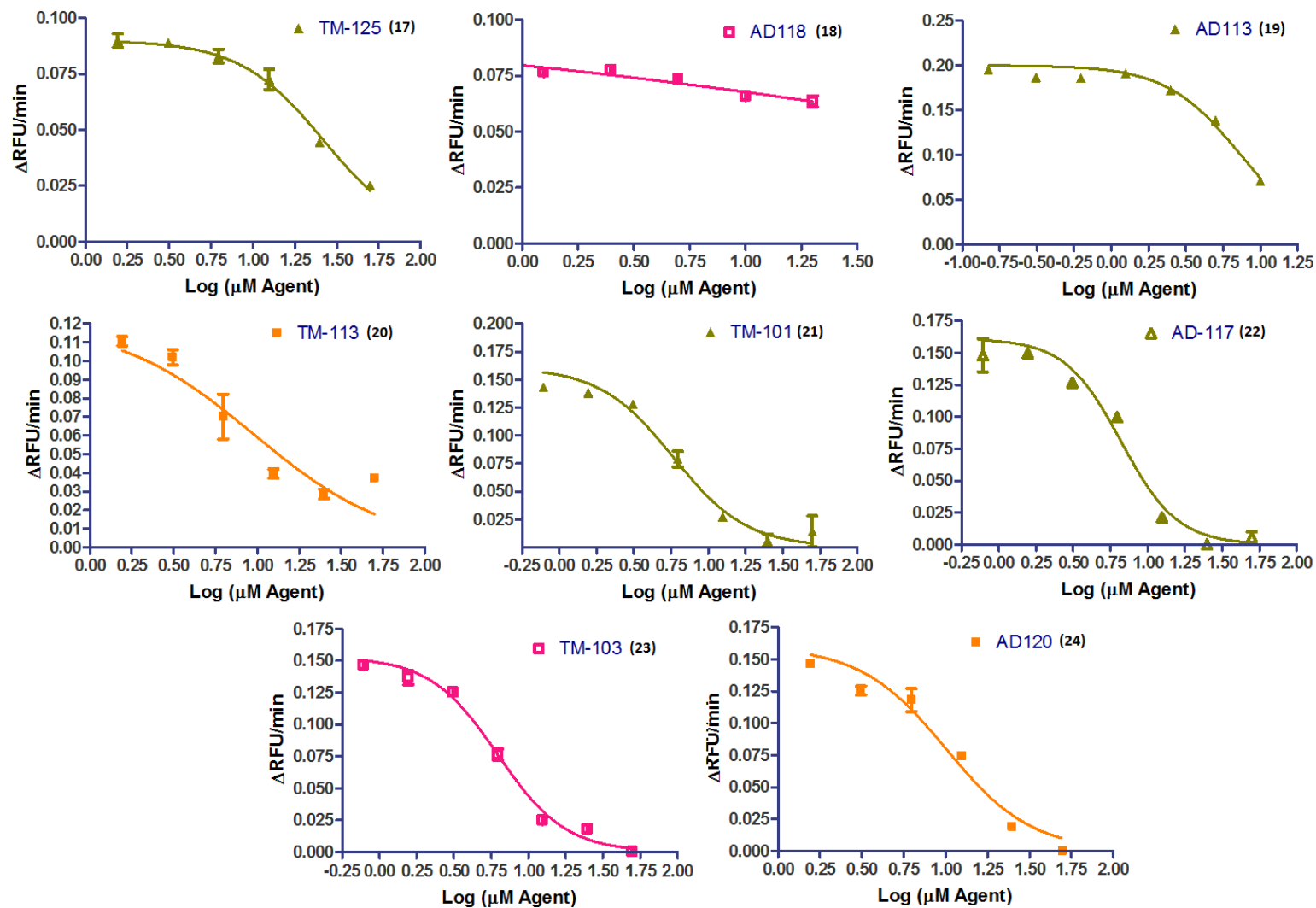
**TM-124** exhibited fluorescence quenching which lead to the perception that the quinoline inhibited the proteasome with a  $IC_{50} = \sim 2.3 \mu M$ , when in fact there wasn't proteasomal activity at all.



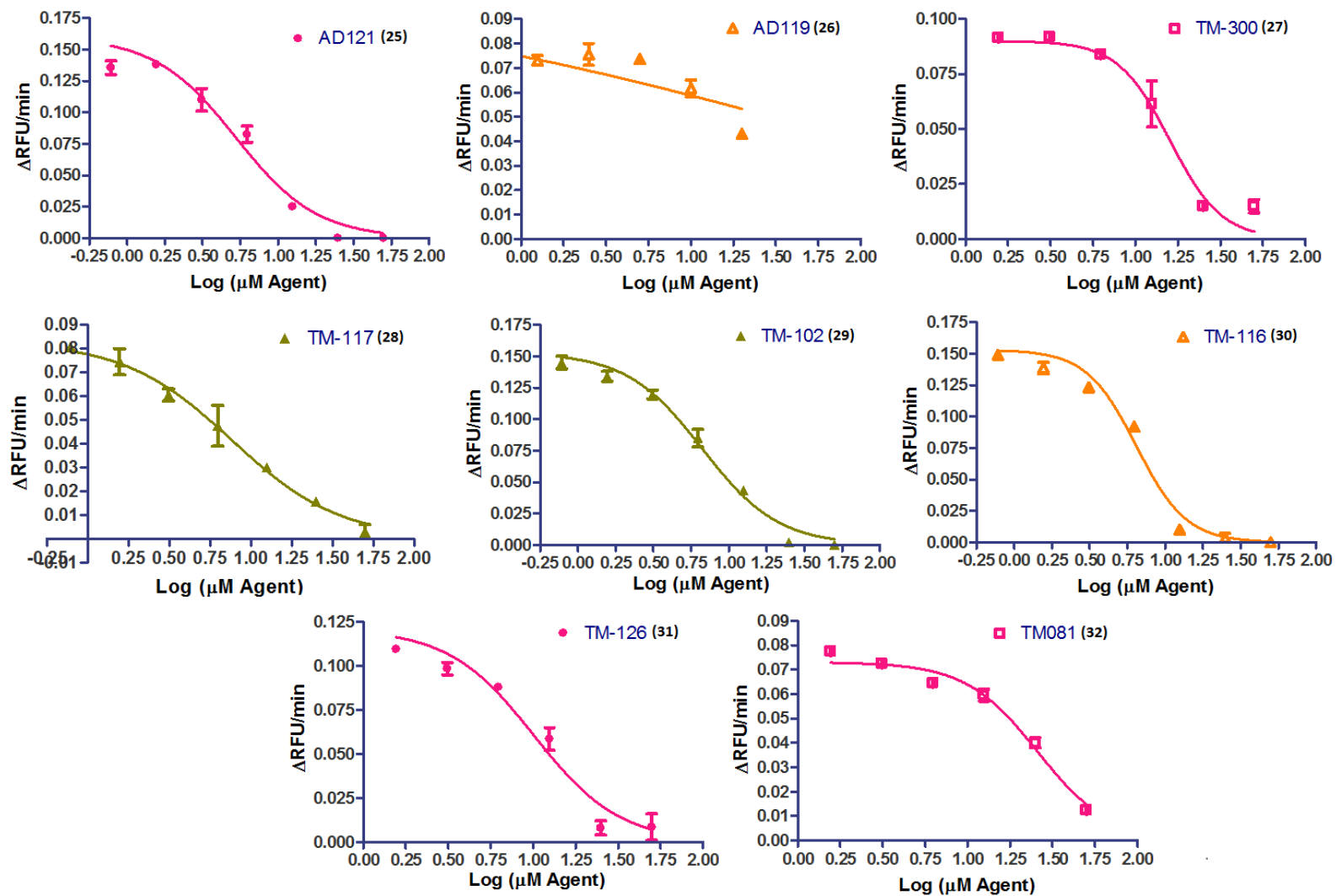
**Figure 2.10.** The inhibition of chymotryptic-like activity of purified human 20S proteasome (Quinolines 1 to 8).



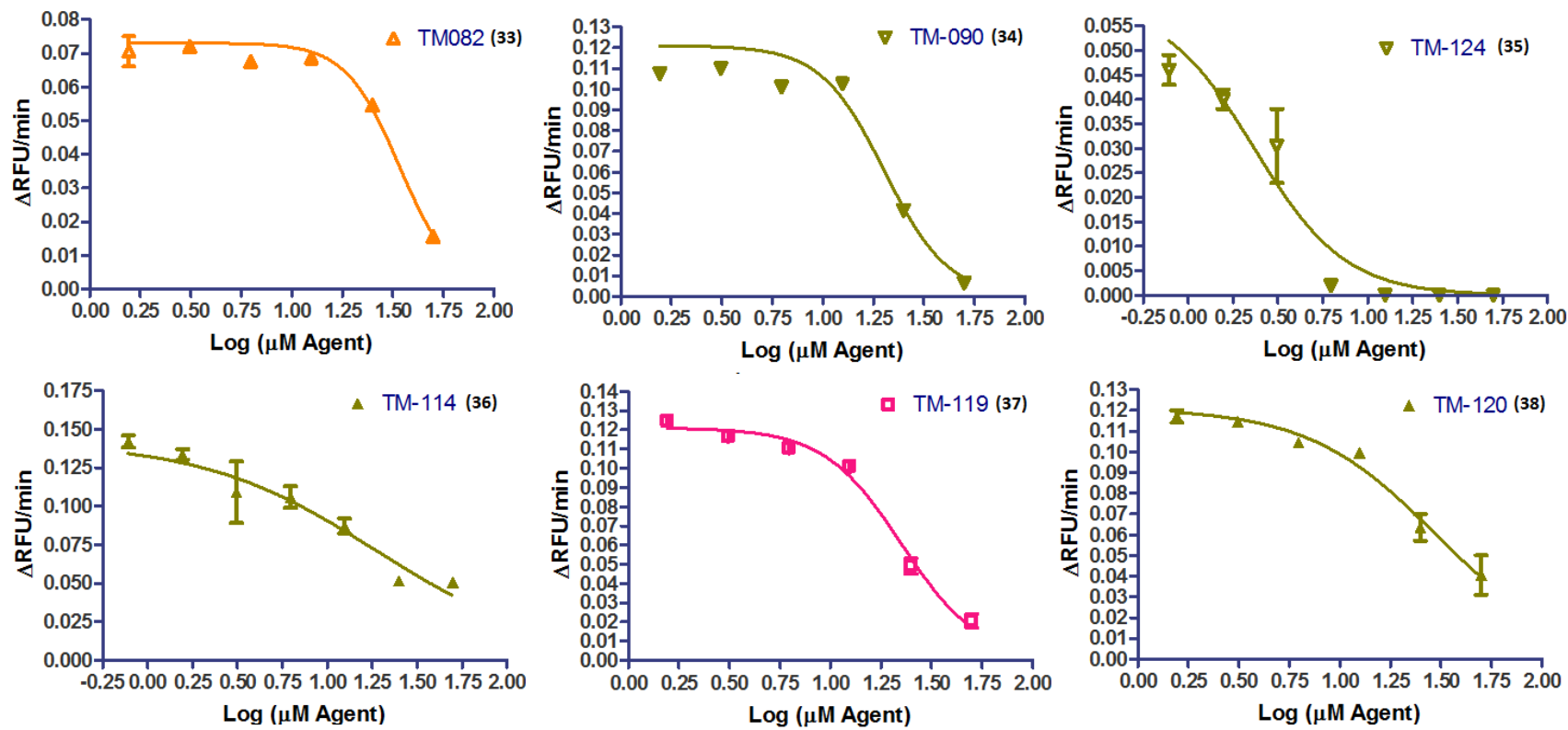
**Figure 2.11.** The inhibition of chymotryptic-like activity of purified human 20S proteasome (Quinolines **9** to **16**).



**Figure 2.12.** The inhibition of chymotryptic-like activity of purified human 20S proteasome (Quinolines 7 to 24).



**Figure 2.13.** The inhibition of chymotryptic-like activity of purified human 20S proteasome (Quinolines 25 to 32).



**Figure 2.14.** The inhibition of chymotryptic-like activity of purified human 20S proteasome (Quinolines 33 to 38).



	AD110 (1)	AD111 (2)	AD103 (3)	AD104 (4)	AD108 (5)
<b>Sigmoidal dose-response (variable slope)</b>					
<b>Best-fit values</b>					
<b>BOTTOM</b>	0	0	0	0	0
<b>TOP</b>	0.153	0.067	0.064	0.103	0.06
<b>LOGEC50</b>	2.196	-5.753	1.908	1.322	1.132
<b>HILLSLOPE</b>	-0.8588	0.2058	-1.501	-3.259	-2.791
<b>EC50</b>	156.9	1.77E-06	80.83	20.98	13.54
<b>Std. Error</b>					
<b>LOGEC50</b>	0.587	3.835	0.07863	0.01787	0.03306
<b>HILLSLOPE</b>	0.4622	0.1341	0.2812	0.3861	0.5405
<b>95% Confidence Intervals</b>					
<b>LOGEC50</b>	0.8420 to 3.549	-14.11 to 2.603	1.726 to 2.089	1.283 to 1.361	1.060 to 1.204
<b>HILLSLOPE</b>	-1.925 to 0.2070	-0.08633 to 0.4980	-2.149 to -0.8524	-4.101 to -2.418	-3.969 to -1.614
<b>EC50</b>	6.951 to 3542	7.767e-015 to 401.1	53.24 to 122.7	19.18 to 22.95	11.47 to 15.98
<b>Goodness of Fit</b>					
<b>Degrees of Freedom</b>	8	12	8	12	12
<b>R<sup>2</sup></b>	0.3591	0.1684	0.8968	0.9838	0.9631
<b>Absolute Sum of Squares</b>	0.0006809	5.94E-05	4.86E-05	0.0003347	0.0003402
<b>Sy.x</b>	0.009225	0.002225	0.002464	0.005281	0.005325
<b>Constraints</b>					
<b>BOTTOM</b>	BOTTOM = 0.0	BOTTOM = 0.0	BOTTOM = 0.0	BOTTOM = 0.0	BOTTOM = 0.0
<b>TOP</b>	TOP = 0.1530	TOP = 0.0670	TOP = 0.0640	TOP = 0.1030	TOP = 0.0600
<b>Data</b>					
<b>Number of X values</b>	5	8	7	7	7
<b>Number of Y replicates</b>	2	2	2	2	2
<b>Total number of values</b>	10	14	10	14	14
<b>Number of missing values</b>	0	2	4	0	0

**Table 2.6.** Statistical analysis for the inhibition of chymotryptic-like activity of purified human 20S proteasome (Quinoline **1** to **5**).

	AD039 (6)	AD043 (7)	TM-043 (8)	AD102 (9)	AD-112 (10)
<b>Sigmoidal dose-response (variable slope)</b>					
<b>Best-fit values</b>					
<b>BOTTOM</b>	0	0	0	0	0
<b>TOP</b>	0.103	0.103	0.153	0.103	0.152
<b>LOGEC50</b>	1.273	1.155	1.28	1.195	1.86
<b>HILLSLOPE</b>	-2.143	-1.973	-0.9075	-2.524	-0.8281
<b>EC50</b>	18.76	14.3	19.04	15.67	72.43
<b>Std. Error</b>					
<b>LOGEC50</b>	0.04102	0.0408	0.0394	0.0159	0.07215
<b>HILLSLOPE</b>	0.3928	0.3294	0.08148	0.205	0.1027
<b>95% Confidence Intervals</b>					
<b>LOGEC50</b>	1.182 to 1.365	1.067 to 1.244	1.194 to 1.366	1.160 to 1.230	1.699 to 2.021
<b>HILLSLOPE</b>	-3.018 to -1.268	-2.691 to -1.256	-1.085 to -0.7299	-2.971 to -2.078	-1.057 to -0.5993
<b>EC50</b>	15.20 to 23.15	11.66 to 17.55	15.63 to 23.20	14.47 to 16.97	50.02 to 104.9
<b>Goodness of Fit</b>					
<b>Degrees of Freedom</b>	10	12	12	12	10
<b>R<sup>2</sup></b>	0.9429	0.9462	0.9545	0.9901	0.9129
<b>Absolute Sum of Squares</b>	0.000967	0.001062	0.0007929	0.0002062	0.0004356
<b>Sy.x</b>	0.009834	0.009409	0.008129	0.004145	0.0066
<b>Constraints</b>					
<b>BOTTOM</b>	BOTTOM = 0.0	BOTTOM = 0.0	BOTTOM = 0.0	BOTTOM = 0.0	BOTTOM = 0.0
<b>TOP</b>	TOP = 0.1030	TOP = 0.1030	TOP = 0.1530	TOP = 0.1030	TOP = 0.1520
<b>Data</b>					
<b>Number of X values</b>	7	7	7	7	6
<b>Number of Y replicates</b>	2	2	2	2	2
<b>Total number of values</b>	12	14	14	14	12
<b>Number of missing values</b>	2	0	0	0	0

**Table 2.7.** Statistical analysis for the inhibition of chymotryptic-like activity of purified human 20S proteasome (Quinoline **6** to **10**).

	AD109 (11)	TM-080 (12)	AD100 (13)	AD-115 (14)	AD116 (15)
<b>Sigmoidal dose-response (variable slope)</b>					
<b>Best-fit values</b>					
<b>BOTTOM</b>	0	0	0	0	0
<b>TOP</b>	0.103	0.226	0.153	0.071	0.2
<b>LOGEC50</b>	0.9969	5.427	1.521	1.772	3.219
<b>HILLSLOPE</b>	-2.111	-0.1764	-2.711	-1.044	-0.2557
<b>EC50</b>	9.93	267080	33.19	59.18	1655
<b>Std. Error</b>					
<b>LOGEC50</b>	0.03965	3.202	0.265	0.04401	0.5925
<b>HILLSLOPE</b>	0.3594	0.1296	2.94	0.1044	0.05242
<b>95% Confidence Intervals</b>					
<b>LOGEC50</b>	0.9105 to 1.083	-1.708 to 12.56	0.9100 to 2.132	1.676 to 1.868	1.928 to 4.510
<b>HILLSLOPE</b>	-2.894 to -1.328	-0.4653 to 0.1124	-9.491 to 4.069	-1.271 to -0.8161	-0.3699 to -0.1414
<b>EC50</b>	8.138 to 12.12	0.0196 to 3.643e+12	8.128 to 135.6	47.46 to 73.81	84.66 to 32336
<b>Goodness of Fit</b>					
<b>Degrees of Freedom</b>	12	10	8	12	12
<b>R<sup>2</sup></b>	0.9524	0.1818	0.4787	0.9575	0.6998
<b>Absolute Sum of Squares</b>	0.001076	0.002017	0.002118	8.16E-05	0.0004621
<b>Sy.x</b>	0.009469	0.0142	0.01627	0.002607	0.006206
<b>Constraints</b>					
<b>BOTTOM</b>	BOTTOM = 0.0	BOTTOM = 0.0	BOTTOM = 0.0	BOTTOM = 0.0	BOTTOM = 0.0
<b>TOP</b>	TOP = 0.1030	TOP = 0.2260	TOP = 0.1530	TOP = 0.0710	TOP = 0.2000
<b>Data</b>					
<b>Number of X values</b>	7	6	5	7	7
<b>Number of Y replicates</b>	2	2	2	2	2
<b>Total number of values</b>	14	12	10	14	14
<b>Number of missing values</b>	0	0	0	0	0

**Table 2.8.** Statistical analysis for the inhibition of chymotryptic-like activity of purified human 20S proteasome (Quinoline **11** to **15**).

	TM-127 (16)	TM-125 (17)	AD118 (18)	AD113 (19)	TM-113 (20)
<b>Sigmoidal dose-response (variable slope)</b>					
<b>Best-fit values</b>					
<b>BOTTOM</b>	0	0	0	0	0
<b>TOP</b>	0.066	0.09	0.1	0.2	0.121
<b>LOGEC50</b>	0.9586	1.426	2.188	0.8687	0.9798
<b>HILLSLOPE</b>	-1.665	-1.713	-0.2707	-1.738	-1.06
<b>EC50</b>	9.092	26.66	154.3	7.39	9.545
<b>Std. Error</b>					
<b>LOGEC50</b>	0.02059	0.01892	0.2231	0.02202	0.06701
<b>HILLSLOPE</b>	0.1177	0.1285	0.03594	0.1633	0.1818
<b>95% Confidence Intervals</b>					
<b>LOGEC50</b>	0.9138 to 1.003	1.384 to 1.468	1.702 to 2.675	0.8207 to 0.9166	0.8305 to 1.129
<b>HILLSLOPE</b>	-1.921 to -1.408	-1.999 to -1.427	-0.3490 to -0.1924	-2.094 to -1.382	-1.465 to -0.6548
<b>EC50</b>	8.199 to 10.08	24.19 to 29.37	50.40 to 472.7	6.618 to 8.254	6.768 to 13.46
<b>Goodness of Fit</b>					
<b>Degrees of Freedom</b>	12	10	12	12	10
<b>R<sup>2</sup></b>	0.9883	0.9839	0.8395	0.9673	0.8687
<b>Absolute Sum of Squares</b>	9.38E-05	0.0001164	0.0001311	0.0007973	0.001683
<b>Sy.x</b>	0.002796	0.003412	0.003306	0.008151	0.01297
<b>Constraints</b>					
<b>BOTTOM</b>	BOTTOM = 0.0	BOTTOM = 0.0	BOTTOM = 0.0	BOTTOM = 0.0	BOTTOM = 0.0
<b>TOP</b>	TOP = 0.0660	TOP = 0.0900	TOP = 0.1000	TOP = 0.2000	TOP = 0.1210
<b>Data</b>					
<b>Number of X values</b>	7	6	7	7	6
<b>Number of Y replicates</b>	2	2	2	2	2
<b>Total number of values</b>	14	12	14	14	12
<b>Number of missing values</b>	0	0	0	0	0

**Table 2.9.** Statistical analysis for the inhibition of chymotryptic-like activity of purified human 20S proteasome (Quinoline **16** to **20**).

	TM-101 (21)	AD-117 (22)	TM-103 (23)	AD120 (24)	AD121 (25)
<b>Sigmoidal dose-response (variable slope)</b>					
<b>Best-fit values</b>					
<b>BOTTOM</b>	0	0	0	0	0
<b>TOP</b>	0.161	0.161	0.142	0.16	0.16
<b>LOGEC50</b>	0.7652	0.8222	0.6951	1.002	0.7207
<b>HILLSLOPE</b>	-1.756	-2.3	-1.5	-1.697	-1.612
<b>EC50</b>	5.824	6.641	4.956	10.05	5.256
<b>Std. Error</b>					
<b>LOGEC50</b>	0.03361	0.03003	0.03662	0.03567	0.03723
<b>HILLSLOPE</b>	0.212	0.325	0.186	0.214	0.1995
<b>95% Confidence Intervals</b>					
<b>LOGEC50</b>	0.6920 to 0.8385	0.7568 to 0.8877	0.6123 to 0.7780	0.9229 to 1.082	0.6396 to 0.8018
<b>HILLSLOPE</b>	-2.218 to -1.294	-3.009 to -1.592	-1.921 to -1.079	-2.173 to -1.220	-2.047 to -1.178
<b>EC50</b>	4.920 to 6.894	5.712 to 7.721	4.096 to 5.998	8.373 to 12.07	4.361 to 6.336
<b>Goodness of Fit</b>					
<b>Degrees of Freedom</b>	12	12	9	10	12
<b>R<sup>2</sup></b>	0.965	0.9701	0.9656	0.9614	0.9615
<b>Absolute Sum of Squares</b>	0.001572	0.00165	0.0008108	0.001403	0.001747
<b>Sy.x</b>	0.01145	0.01173	0.009491	0.01185	0.01207
<b>Constraints</b>					
<b>BOTTOM</b>	BOTTOM = 0.0	BOTTOM = 0.0	BOTTOM = 0.0	BOTTOM = 0.0	BOTTOM = 0.0
<b>TOP</b>	TOP = 0.1610	TOP = 0.1610	TOP = 0.1420	TOP = 0.1600	TOP = 0.1600
<b>Data</b>					
<b>Number of X values</b>	7	7	7	7	7
<b>Number of Y replicates</b>	2	2	2	2	2
<b>Total number of values</b>	14	14	11	12	14
<b>Number of missing values</b>	0	0	3	2	0

**Table 2.10.** Statistical analysis for the inhibition of chymotryptic-like activity of purified human 20S proteasome (Quinoline **21** to **25**).

	AD119 (26)	TM-300 (27)	TM-117 (28)	TM-102 (29)	TM-116 (30)
<b>Sigmoidal dose-response (variable slope)</b>					
<b>Best-fit values</b>					
<b>BOTTOM</b>	0	0	0	0	0
<b>TOP</b>	0.1	0.09	0.083	0.153	0.161
<b>LOGEC50</b>	1.478	1.203	0.8826	0.8245	0.8261
<b>HILLSLOPE</b>	-0.3197	-2.842	-1.309	-1.729	-2.45
<b>EC50</b>	30.04	15.94	7.631	6.675	6.7
<b>Std. Error</b>					
<b>LOGEC50</b>	0.2461	0.03177	0.03269	0.02508	0.03708
<b>HILLSLOPE</b>	0.07391	0.5078	0.1192	0.1535	0.4596
<b>95% Confidence Intervals</b>					
<b>LOGEC50</b>	0.9413 to 2.014	1.132 to 1.273	0.8114 to 0.9538	0.7698 to 0.8791	0.7435 to 0.9087
<b>HILLSLOPE</b>	-0.4807 to -0.1586	-3.973 to -1.711	-1.568 to -1.049	-2.064 to -1.395	-3.474 to -1.426
<b>EC50</b>	8.737 to 103.3	13.54 to 18.76	6.477 to 8.992	5.886 to 7.570	5.539 to 8.103
<b>Goodness of Fit</b>					
<b>Degrees of Freedom</b>	12	10	12	12	10
<b>R<sup>2</sup></b>	0.6228	0.9568	0.9727	0.9827	0.9487
<b>Absolute Sum of Squares</b>	0.000702	0.0005846	0.000292	0.0007782	0.002236
<b>Sy.x</b>	0.007649	0.007646	0.004933	0.008053	0.01495
<b>Constraints</b>					
<b>BOTTOM</b>	BOTTOM = 0.0	BOTTOM = 0.0	BOTTOM = 0.0	BOTTOM = 0.0	BOTTOM = 0.0
<b>TOP</b>	TOP = 0.1000	TOP = 0.0900	TOP = 0.0830	TOP = 0.1530	TOP = 0.1610
<b>Data</b>					
<b>Number of X values</b>	7	6	7	7	7
<b>Number of Y replicates</b>	2	2	2	2	2
<b>Total number of values</b>	14	12	14	14	12
<b>Number of missing values</b>	0	0	0	0	2

**Table 2.11.** Statistical analysis for the inhibition of chymotryptic-like activity of purified human 20S proteasome (Quinoline **26** to **30**).

	TM-126 (31)	TM081 (32)	TM082 (33)	TM-090 (34)	TM-124 (35)
<b>Sigmoidal dose-response (variable slope)</b>					
<b>Best-fit values</b>					
<b>BOTTOM</b>	0	0	0	0	0
<b>TOP</b>	0.121	0.073	0.073	0.121	0.06
<b>LOGEC50</b>	1.006	1.411	1.532	1.304	0.3684
<b>HILLSLOPE</b>	-1.727	-2.053	-3.277	-2.762	-1.709
<b>EC50</b>	10.13	25.75	34.03	20.16	2.336
<b>Std. Error</b>					
<b>LOGEC50</b>	0.03981	0.02302	0.01729	0.03416	0.05026
<b>HILLSLOPE</b>	0.2468	0.2151	0.356	0.5267	0.3146
<b>95% Confidence Intervals</b>					
<b>LOGEC50</b>	0.9169 to 1.094	1.359 to 1.462	1.493 to 1.570	1.228 to 1.381	0.2589 to 0.4779
<b>HILLSLOPE</b>	-2.277 to -1.177	-2.532 to -1.573	-4.070 to -2.484	-3.935 to -1.588	-2.394 to -1.023
<b>EC50</b>	8.258 to 12.42	22.88 to 28.98	31.14 to 37.19	16.92 to 24.02	1.815 to 3.006
<b>Goodness of Fit</b>					
<b>Degrees of Freedom</b>	10	10	10	10	12
<b>R<sup>2</sup></b>	0.95	0.9759	0.9739	0.9371	0.9139
<b>Absolute Sum of Squares</b>	0.001018	0.000143	0.0001249	0.001193	0.0004676
<b>Sy.x</b>	0.01009	0.003781	0.003534	0.01092	0.006242
<b>Constraints</b>					
<b>BOTTOM</b>	BOTTOM = 0.0	BOTTOM = 0.0	BOTTOM = 0.0	BOTTOM = 0.0	BOTTOM = 0.0
<b>TOP</b>	TOP = 0.1210	TOP = 0.0730	TOP = 0.0730	TOP = 0.1210	TOP = 0.0600
<b>Data</b>					
<b>Number of X values</b>	6	6	6	6	7
<b>Number of Y replicates</b>	2	2	2	2	2
<b>Total number of values</b>	12	12	12	12	14
<b>Number of missing values</b>	0	0	0	0	0

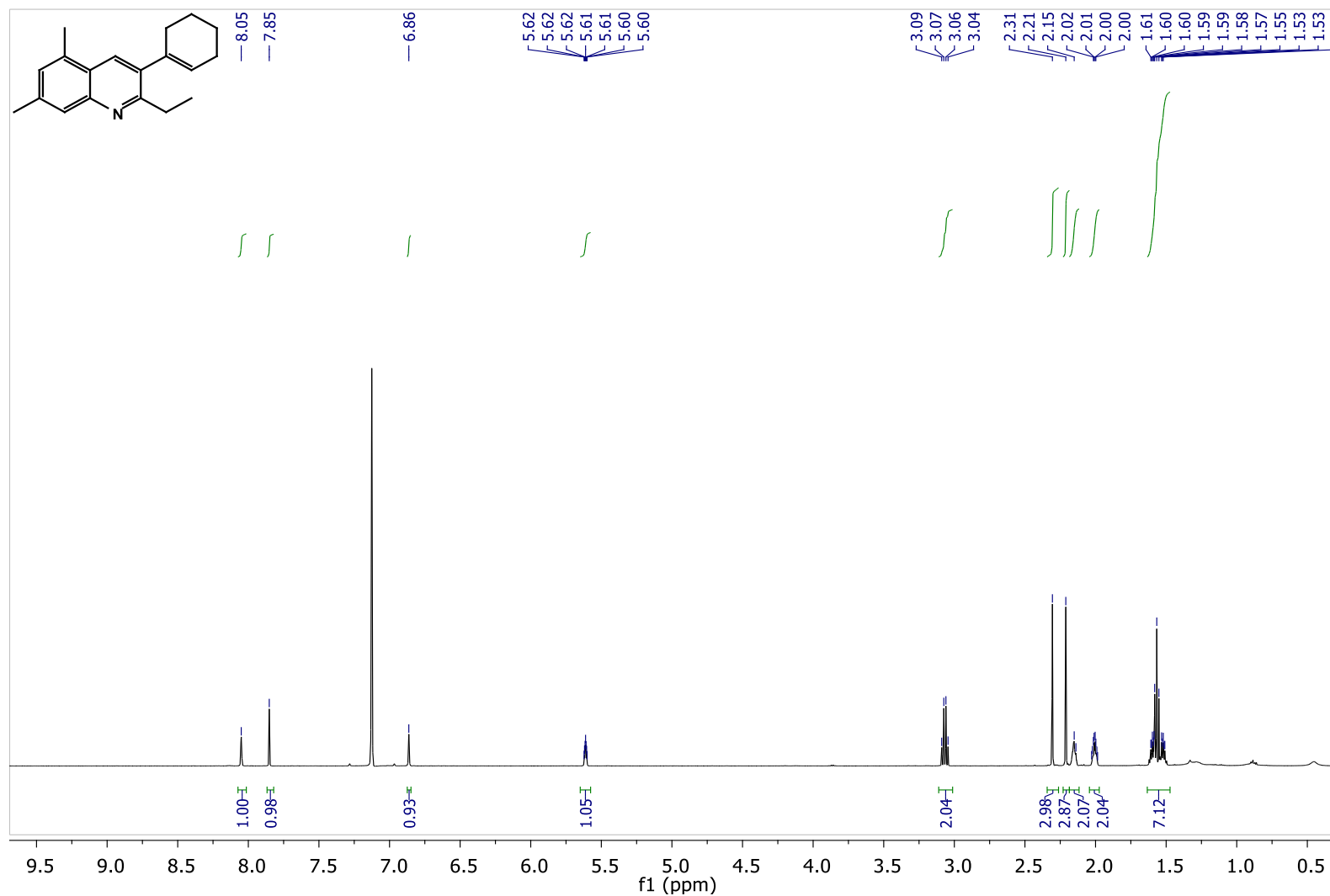
**Table 2.12.** Statistical analysis for the inhibition of chymotryptic-like activity of purified human 20S proteasome (Quinoline **31** to **35**).

	TM-114 (36)	TM-119 (37)	TM-120 (38)
<b>Sigmoidal dose-response (variable slope)</b>			
<b>Best-fit values</b>			
<b>BOTTOM</b>	0	0	0
<b>TOP</b>	0.142	0.121	0.121
<b>LOGEC50</b>	1.276	1.352	1.471
<b>HILLSLOPE</b>	-0.8933	-2.257	-1.378
<b>EC50</b>	18.87	22.5	29.59
<b>Std. Error</b>			
<b>LOGEC50</b>	0.06402	0.01827	0.03359
<b>HILLSLOPE</b>	0.1288	0.1983	0.1557
<b>95% Confidence Intervals</b>			
<b>LOGEC50</b>	1.136 to 1.415	1.311 to 1.393	1.396 to 1.546
<b>HILLSLOPE</b>	-1.174 to -0.6126	-2.699 to -1.815	-1.725 to -1.031
<b>EC50</b>	13.69 to 26.02	20.49 to 24.71	24.90 to 35.15
<b>Goodness of Fit</b>			
<b>Degrees of Freedom</b>	12	10	10
<b>R<sup>2</sup></b>	0.8951	0.9844	0.9532
<b>Absolute Sum of Squares</b>	0.001766	0.0002785	0.0004617
<b>Sy.x</b>	0.01213	0.005277	0.006795
<b>Constraints</b>			
<b>BOTTOM</b>	BOTTOM = 0.0	BOTTOM = 0.0	BOTTOM = 0.0
<b>TOP</b>	TOP = 0.1420	TOP = 0.1210	TOP = 0.1210
<b>Data</b>			
<b>Number of X values</b>	7	6	6
<b>Number of Y replicates</b>	2	2	2
<b>Total number of values</b>	14	12	12
<b>Number of missing values</b>	0	0	0

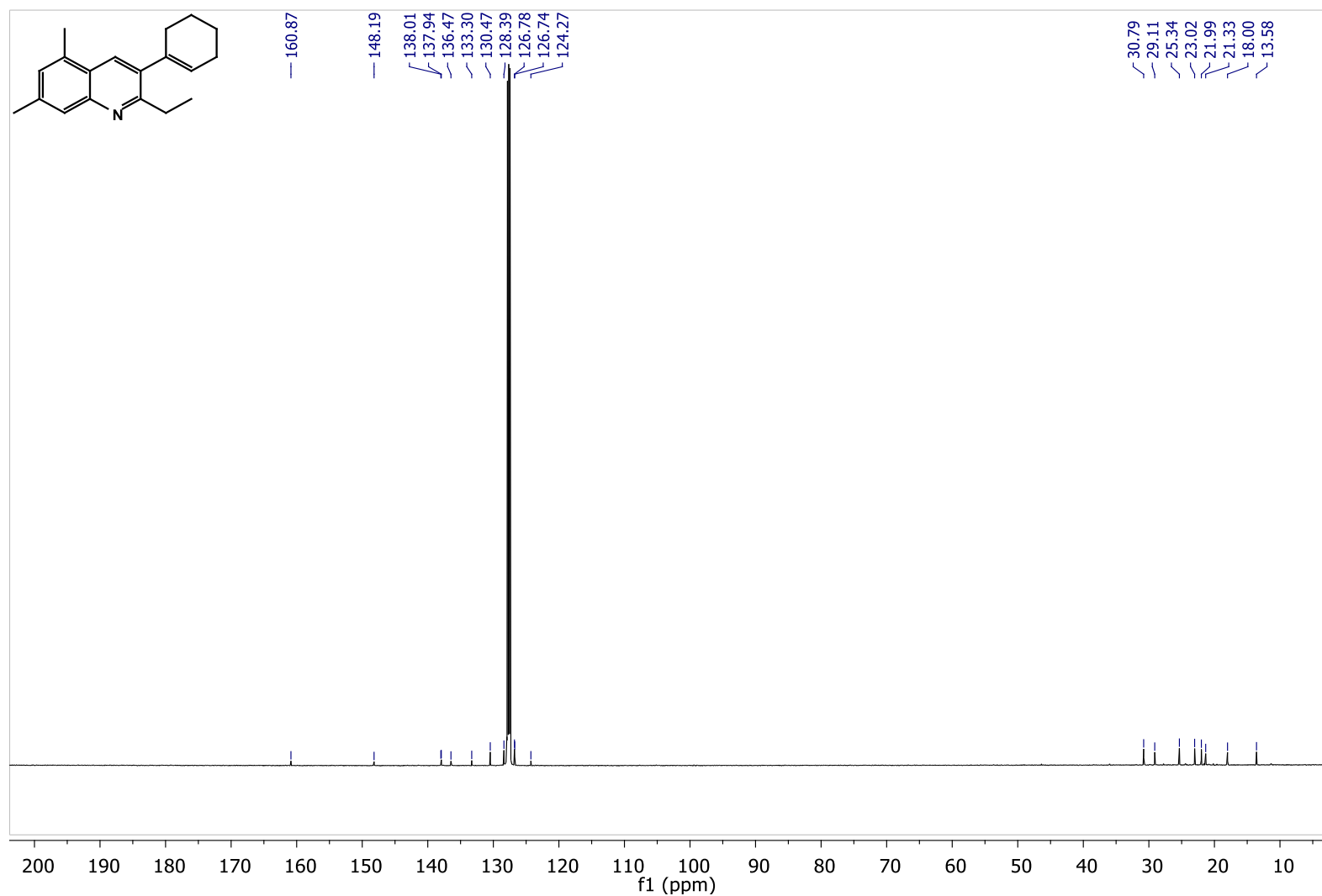
**Table 2.13.** Statistical analysis for the inhibition of chymotryptic-like activity of purified human 20S proteasome (Quinoline **36** to **38**).



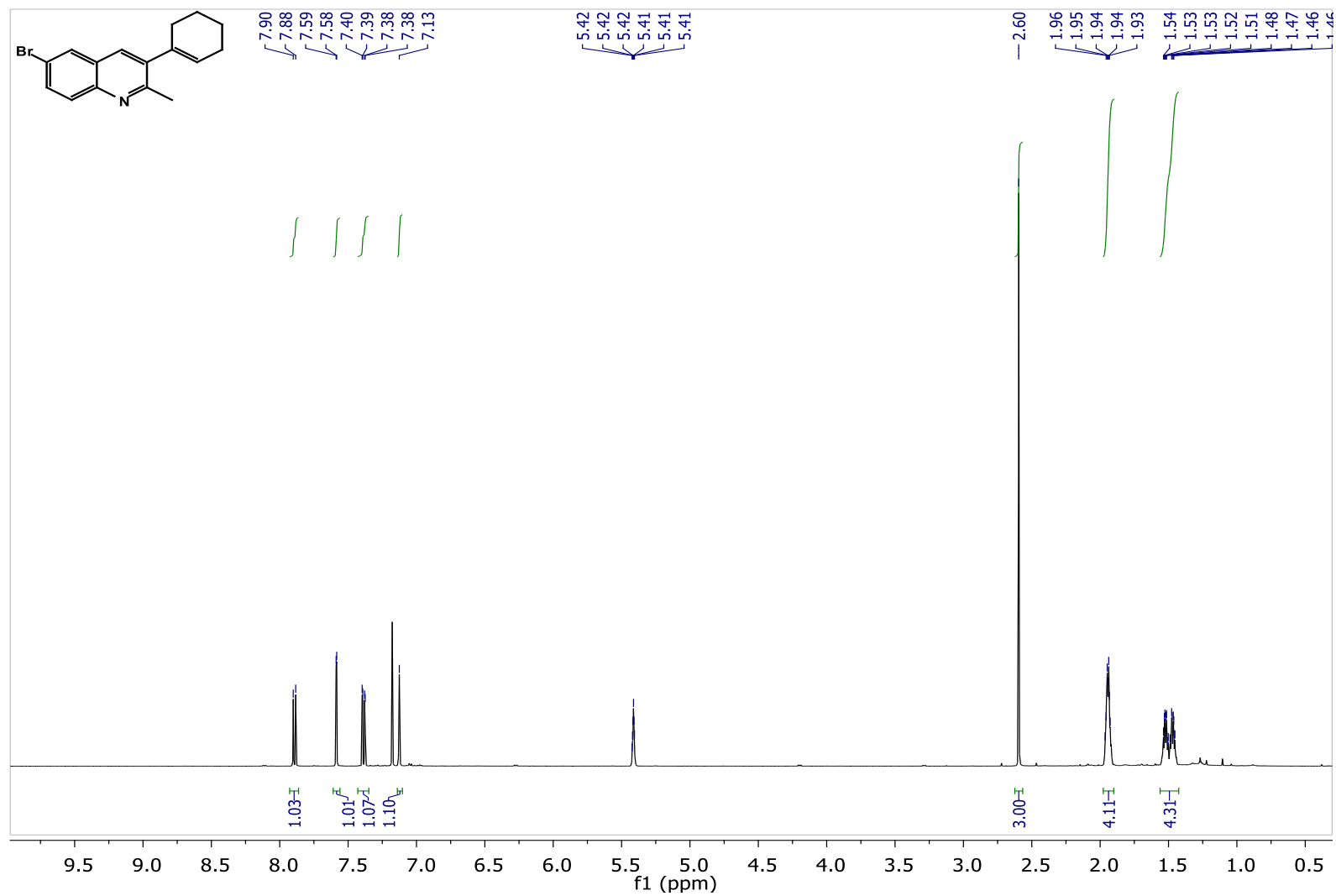
## NMR Spectra



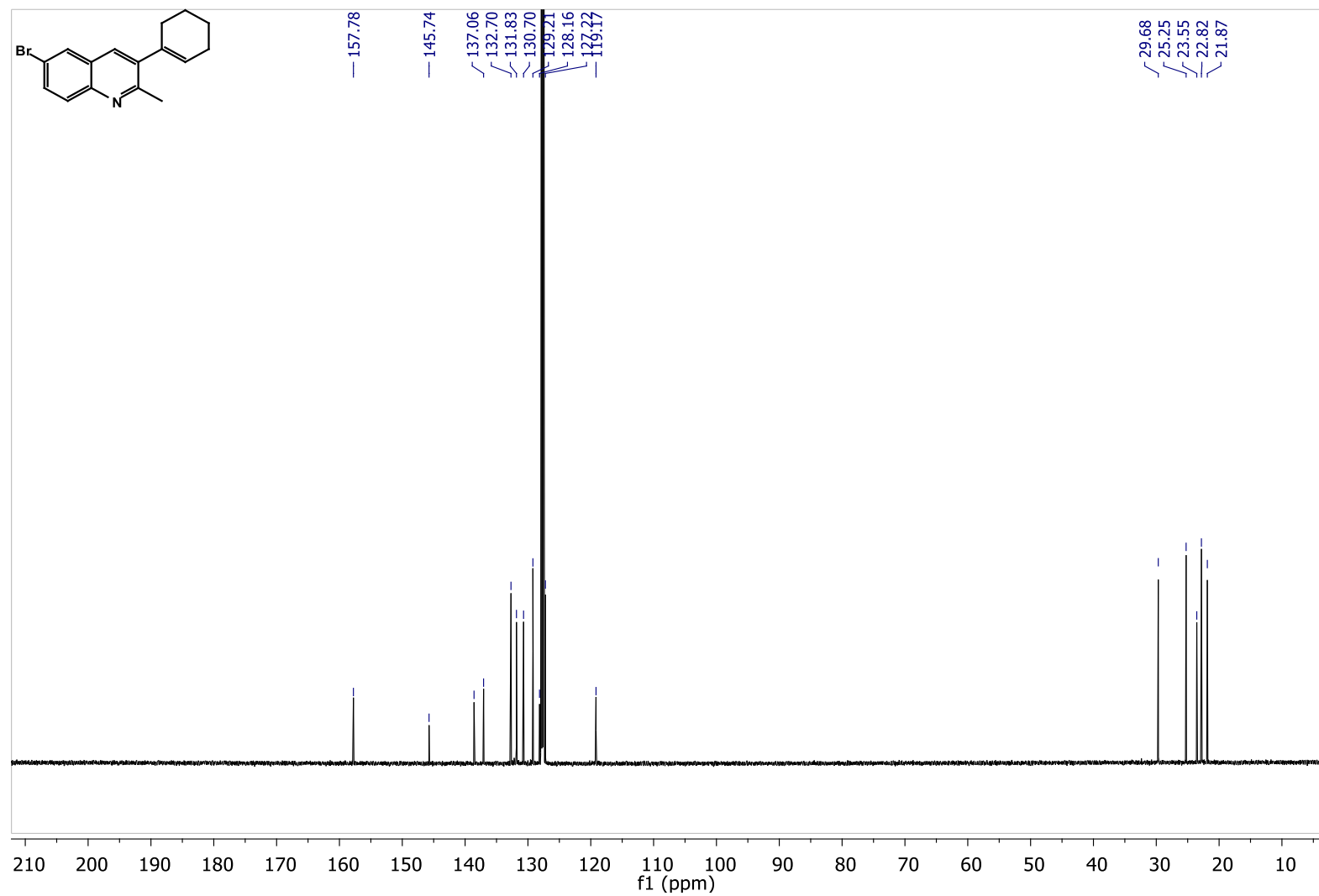
**Figure 2.15.** <sup>1</sup>H NMR spectra for compound 2-ethyl-3-cyclohexenyl-5,7-dimethylquinoline (8).



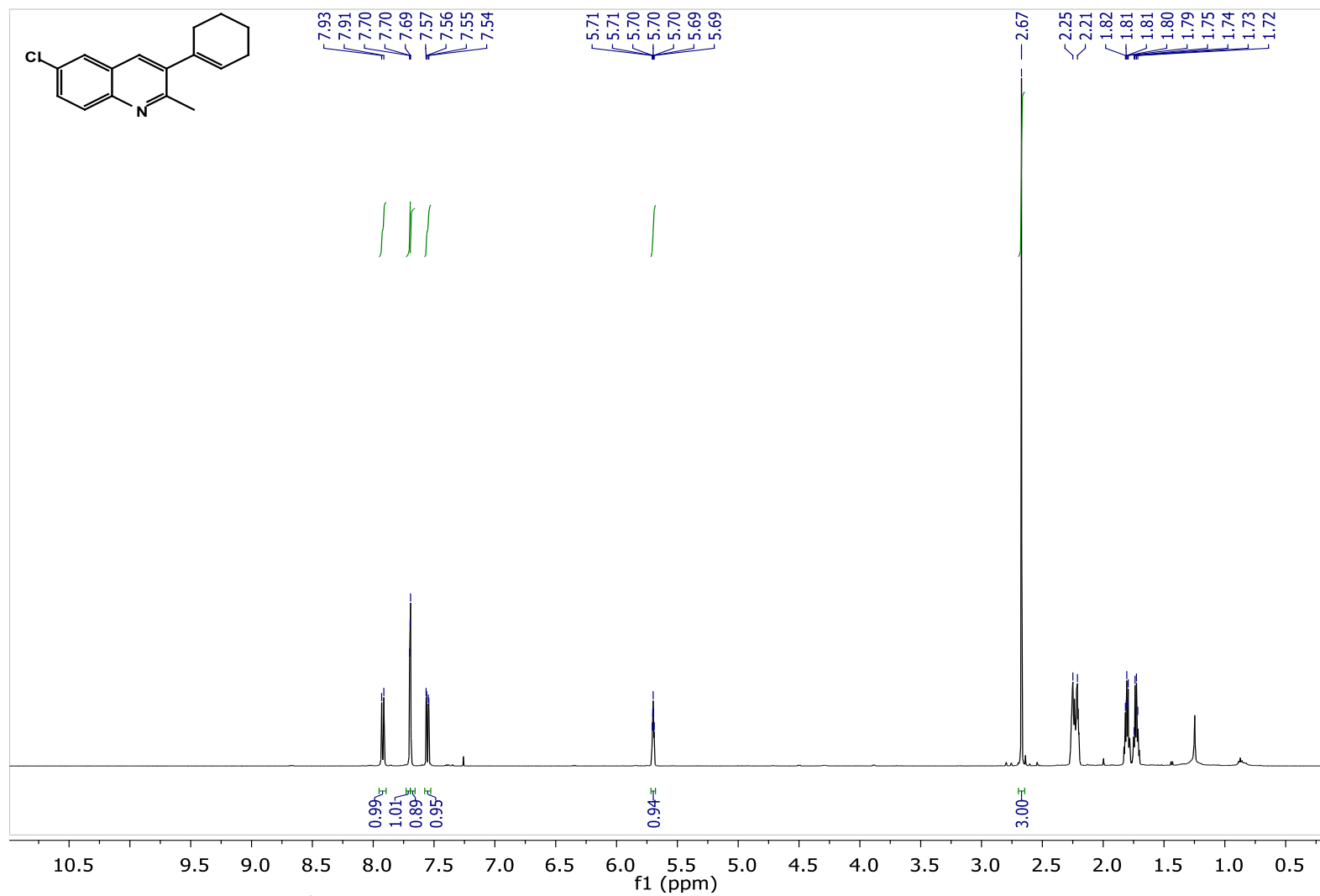
**Figure 2.16.**  $^{13}\text{C}$  NMR spectra for compound 2-ethyl-3-cyclohexenyl-5,7-dimethylquinoline (8).



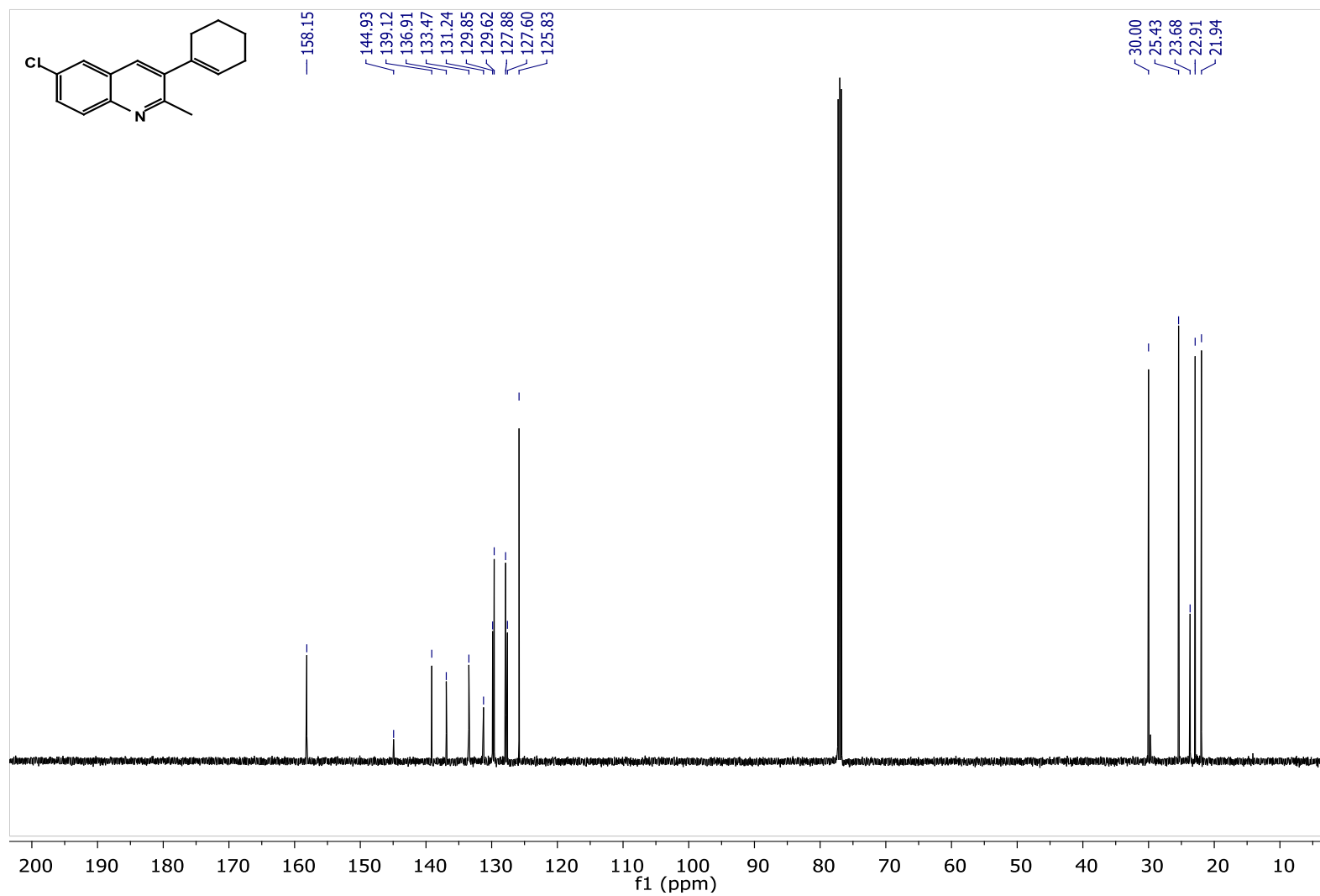
**Figure 2.17.** <sup>1</sup>H NMR spectra for compound 6-bromo-3-cyclohexenyl-2-methylquinoline (**16**).



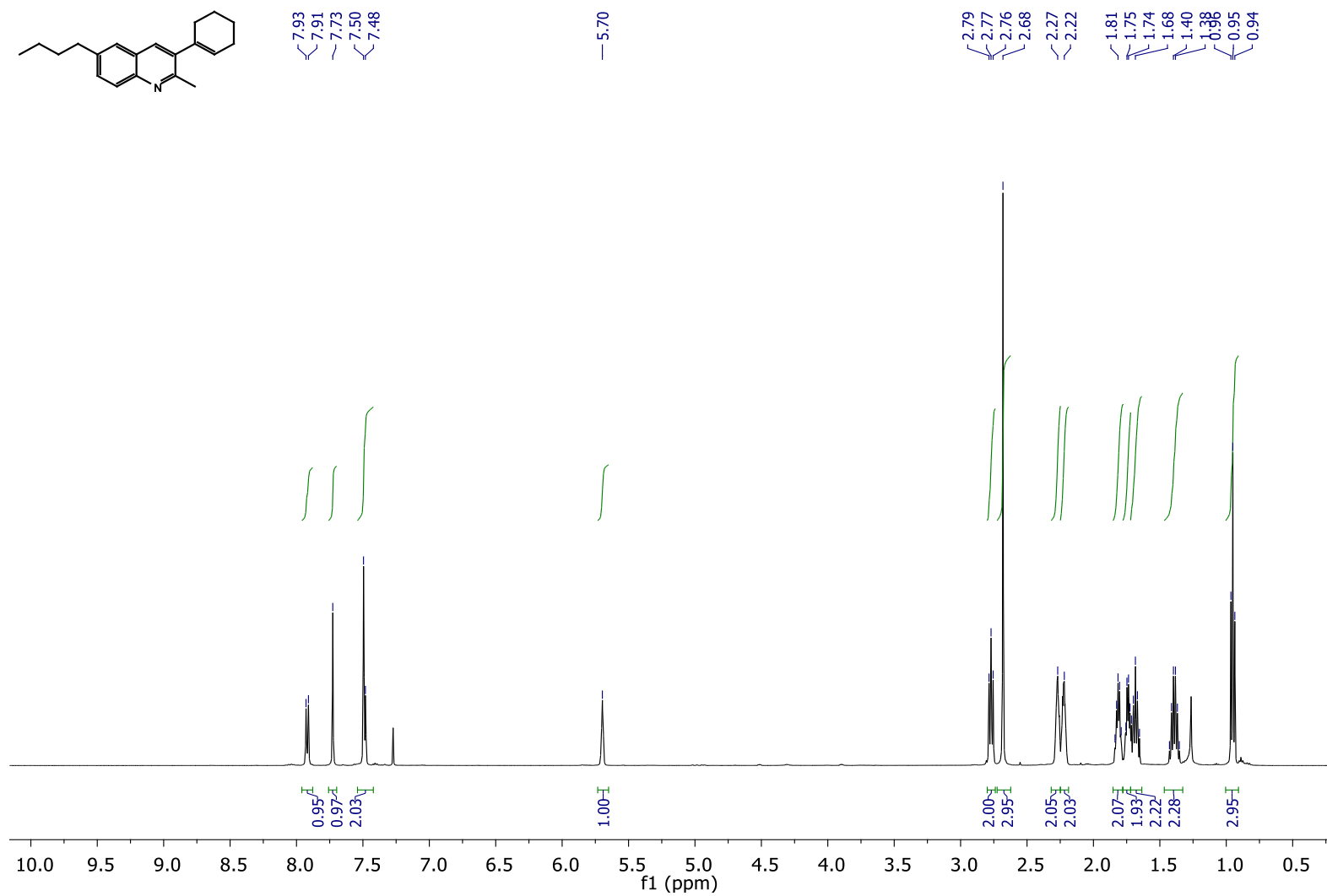
**Figure 2.18.** <sup>13</sup>C NMR spectra for compound 6-bromo-3-cyclohexenyl-2-methylquinoline (**16**).



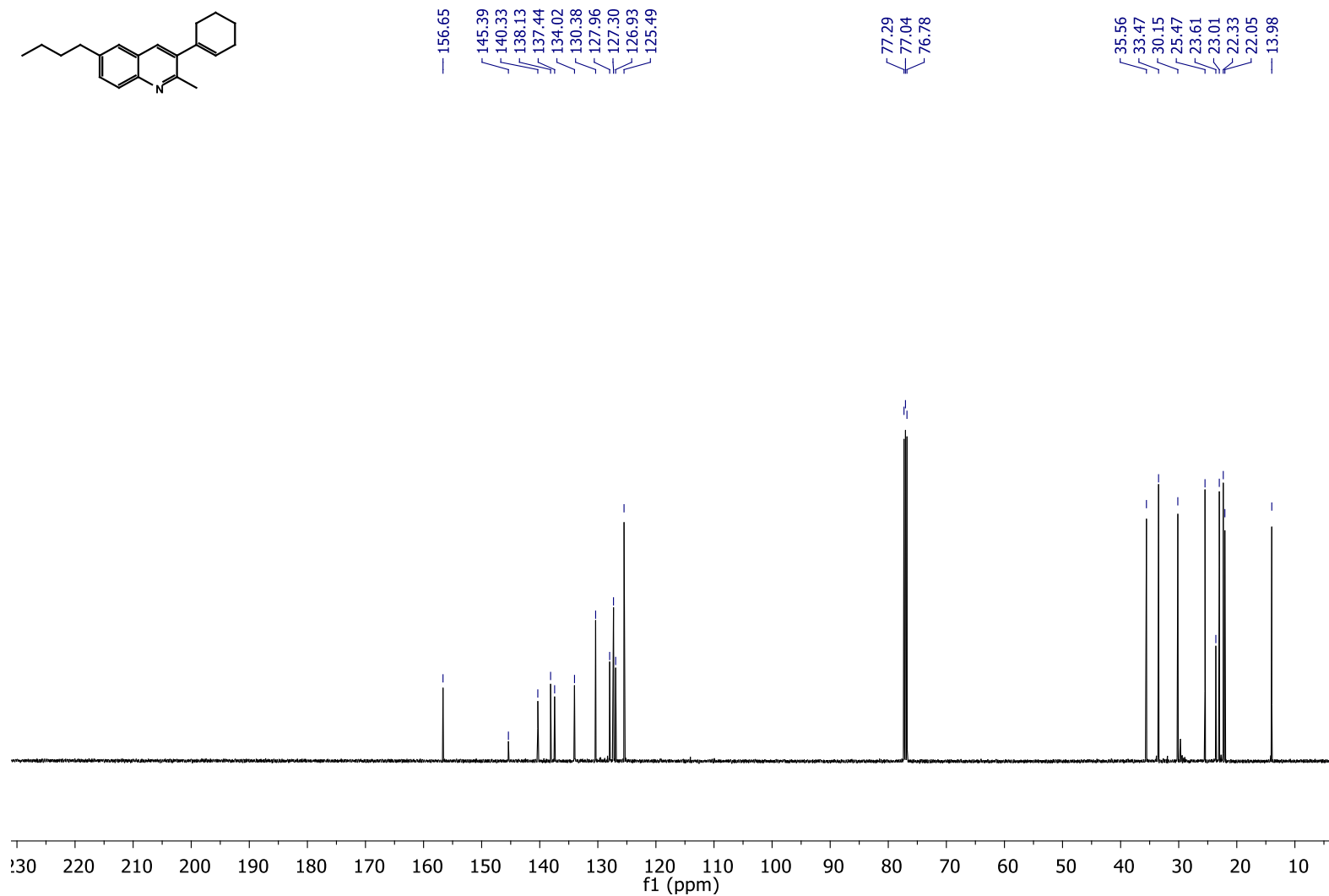
**Figure 2.19.** <sup>1</sup>H NMR spectra for compound 6-chloro-3-cyclohexenyl-2-methylquinoline (17).



**Figure 2.20.** <sup>13</sup>C NMR spectra for compound 6-chloro-3-cyclohexenyl-2-methylquinoline (**17**).

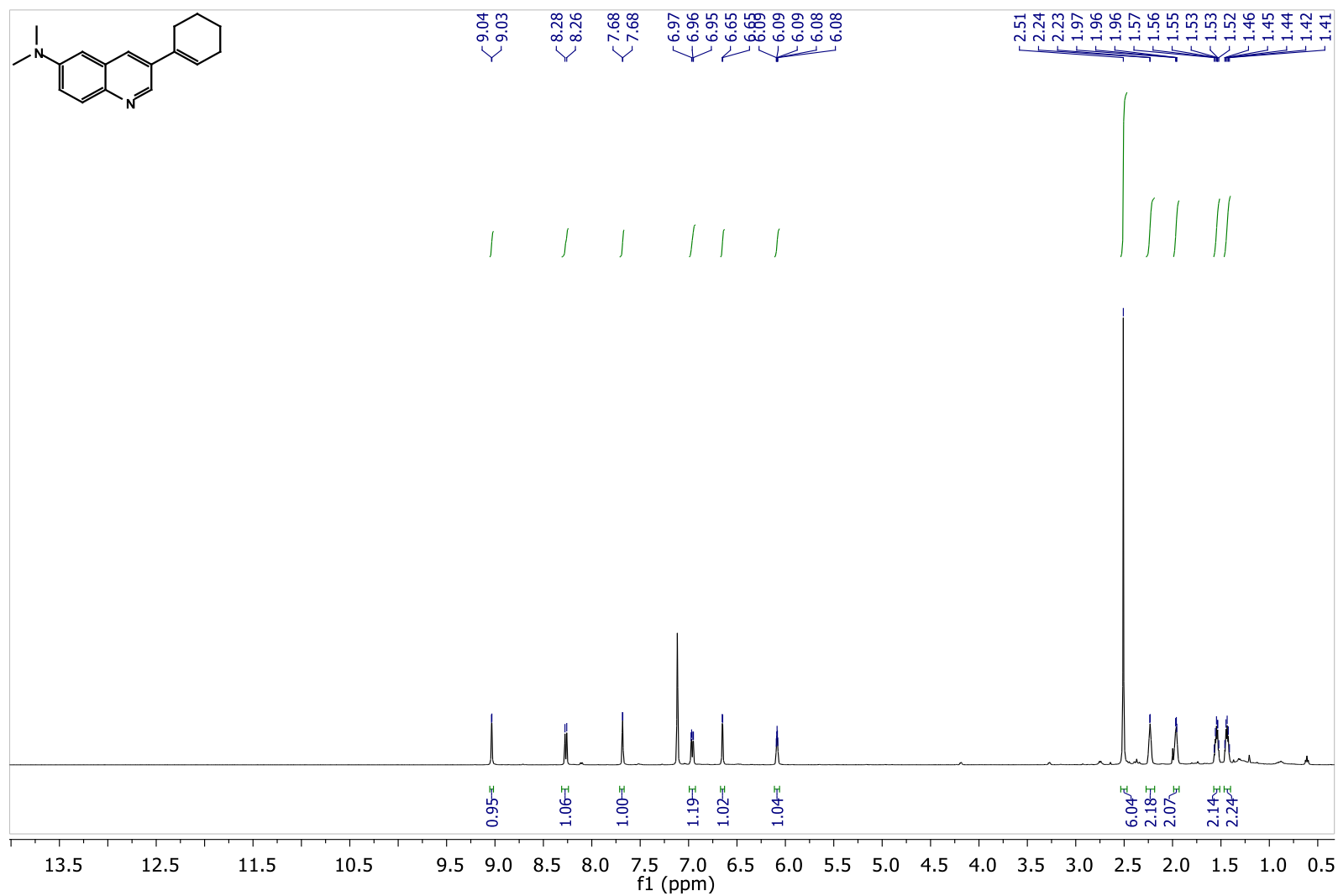


**Figure 2.21.** <sup>1</sup>H NMR spectra for compound 6-butyl-3-cyclohexenyl-2-methylquinoline (**20**).

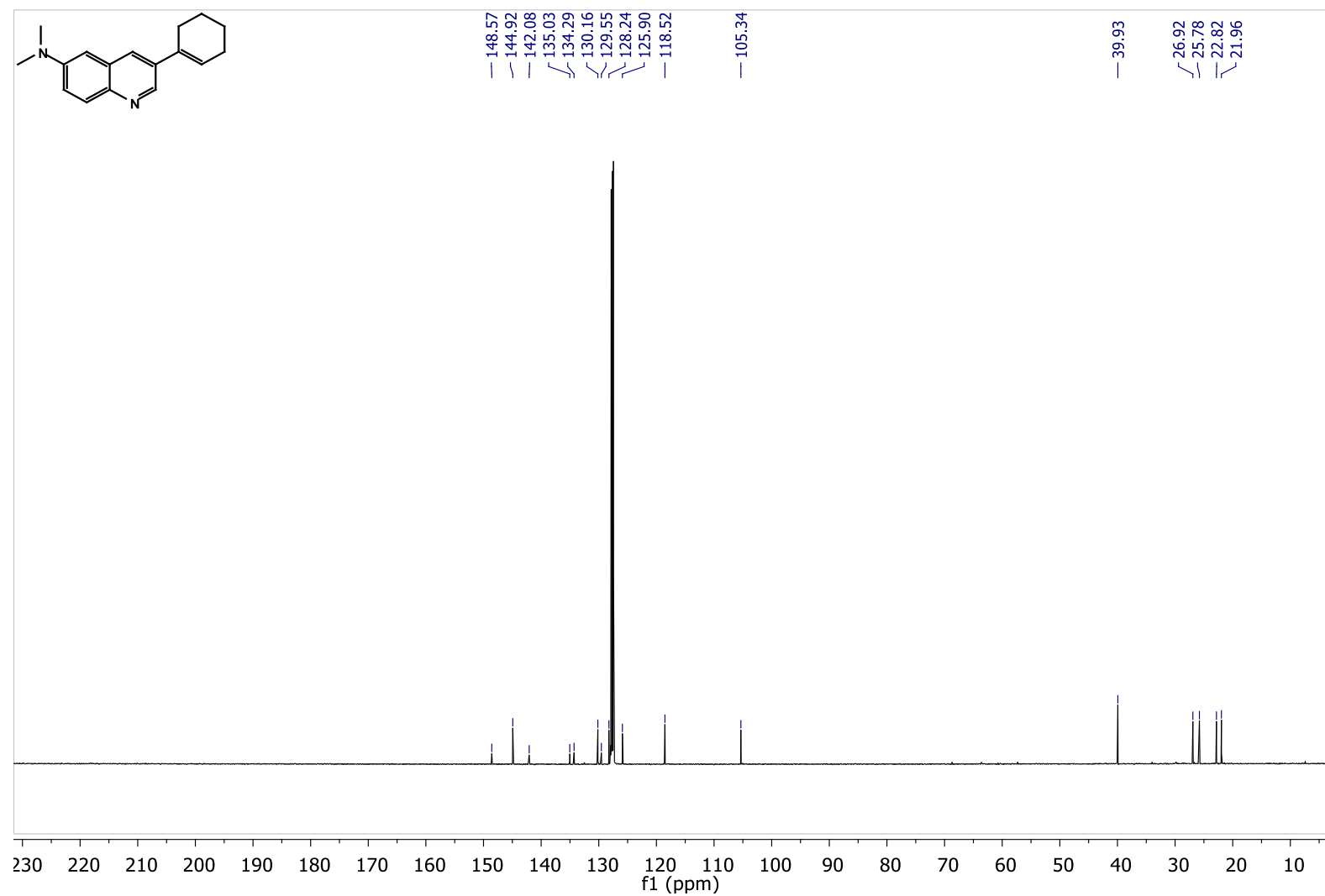


**Figure 2.22.** <sup>13</sup>C NMR spectra for compound 6-butyl-3-cyclohexenyl-2-methylquinoline (**20**).

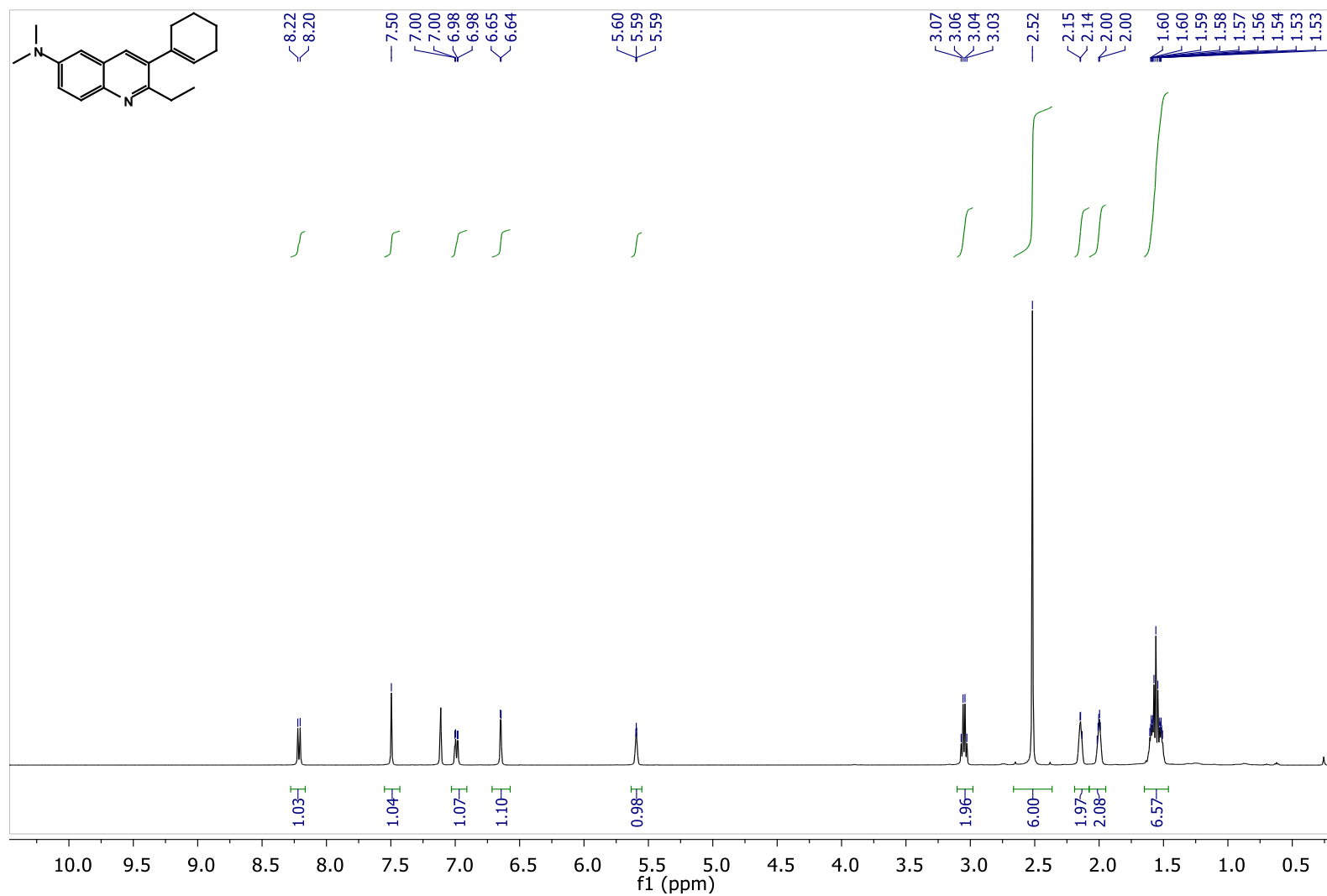




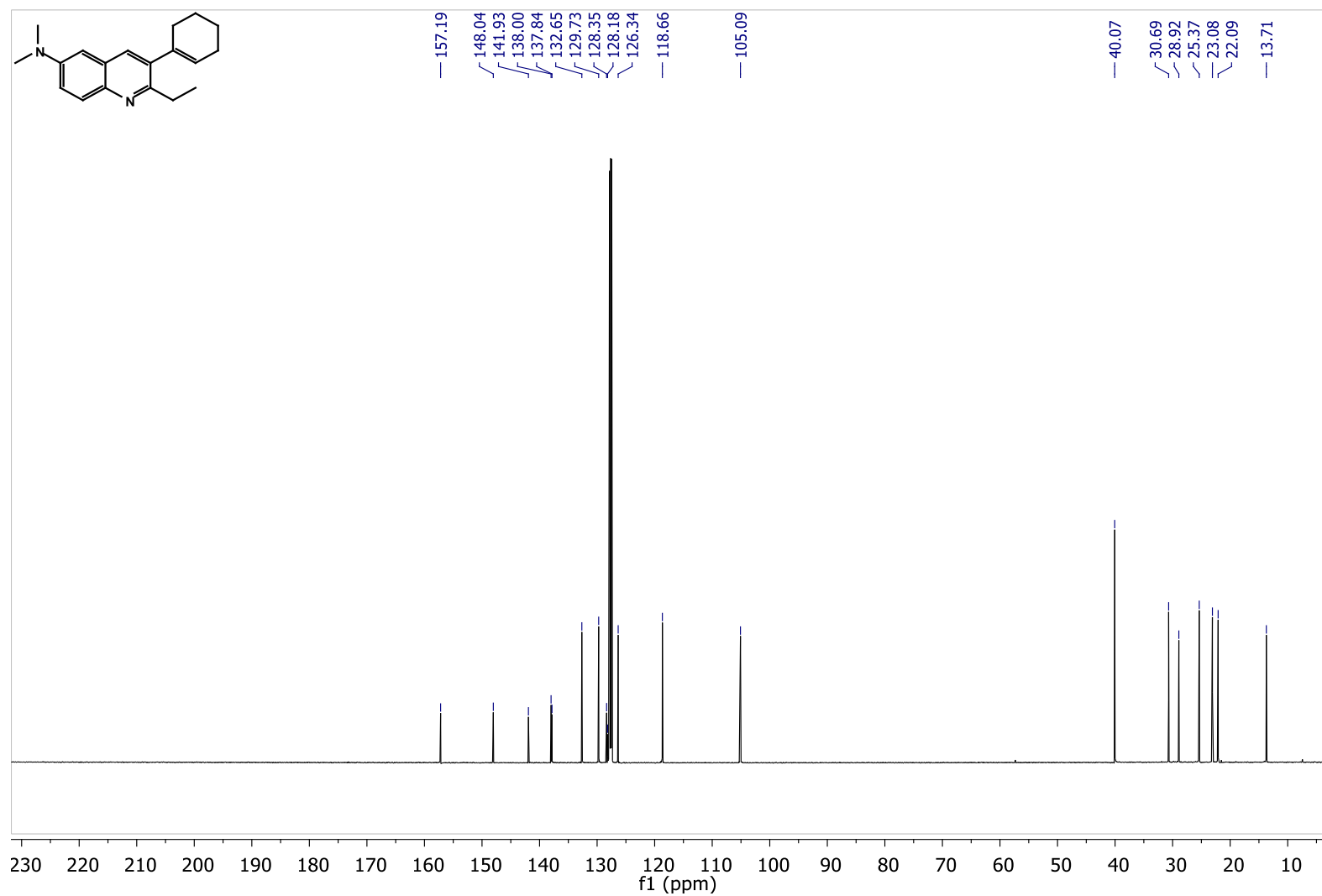
**Figure 2.23.** <sup>1</sup>H NMR spectra for compound 3-cyclohexenyl-6-(N,N-dimethylamino)quinoline (**21**)



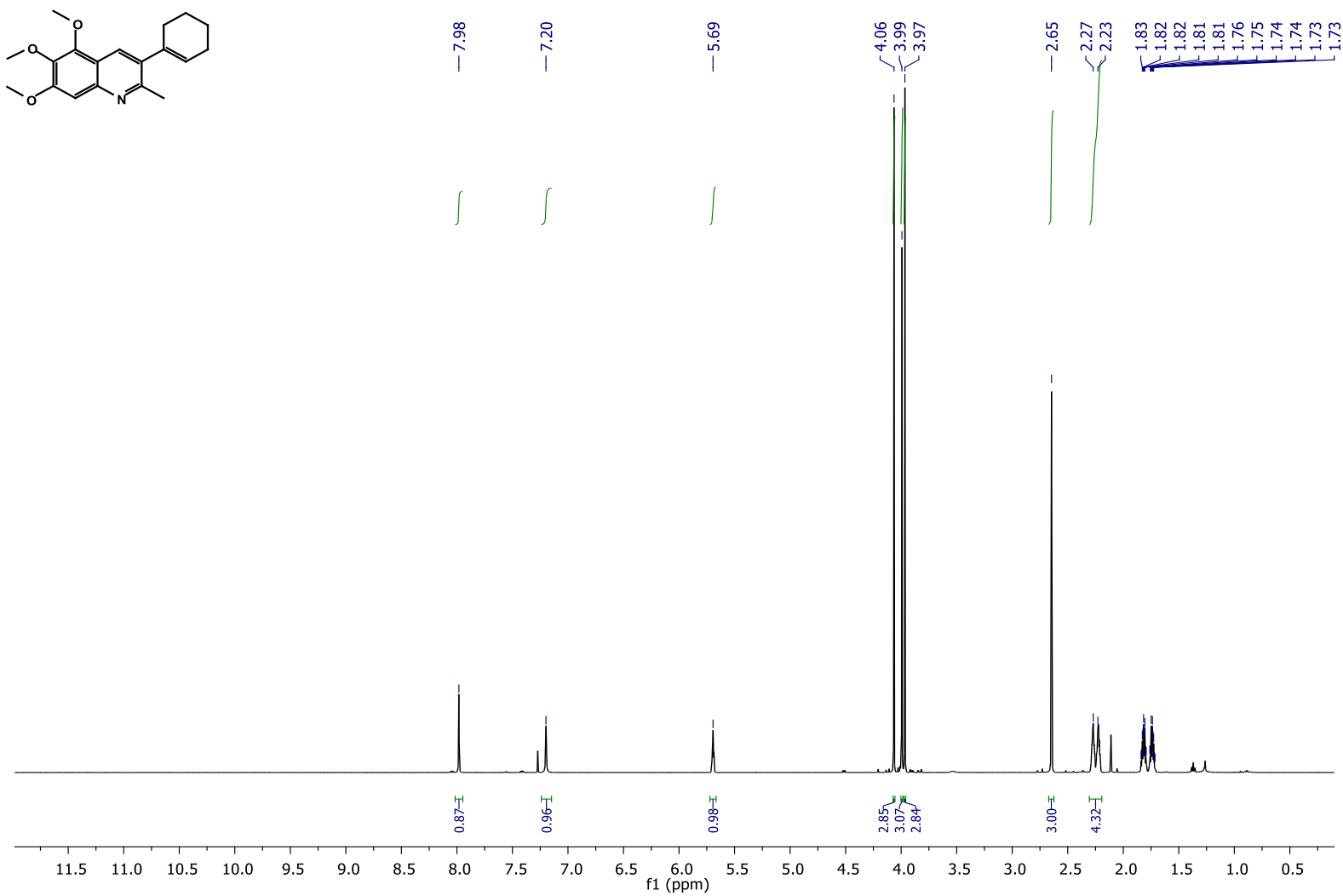
**Figure 2.24.** <sup>13</sup>C NMR spectra for compound 3-cyclohexenyl-6-(N,N-dimethylamino)quinoline (**21**)



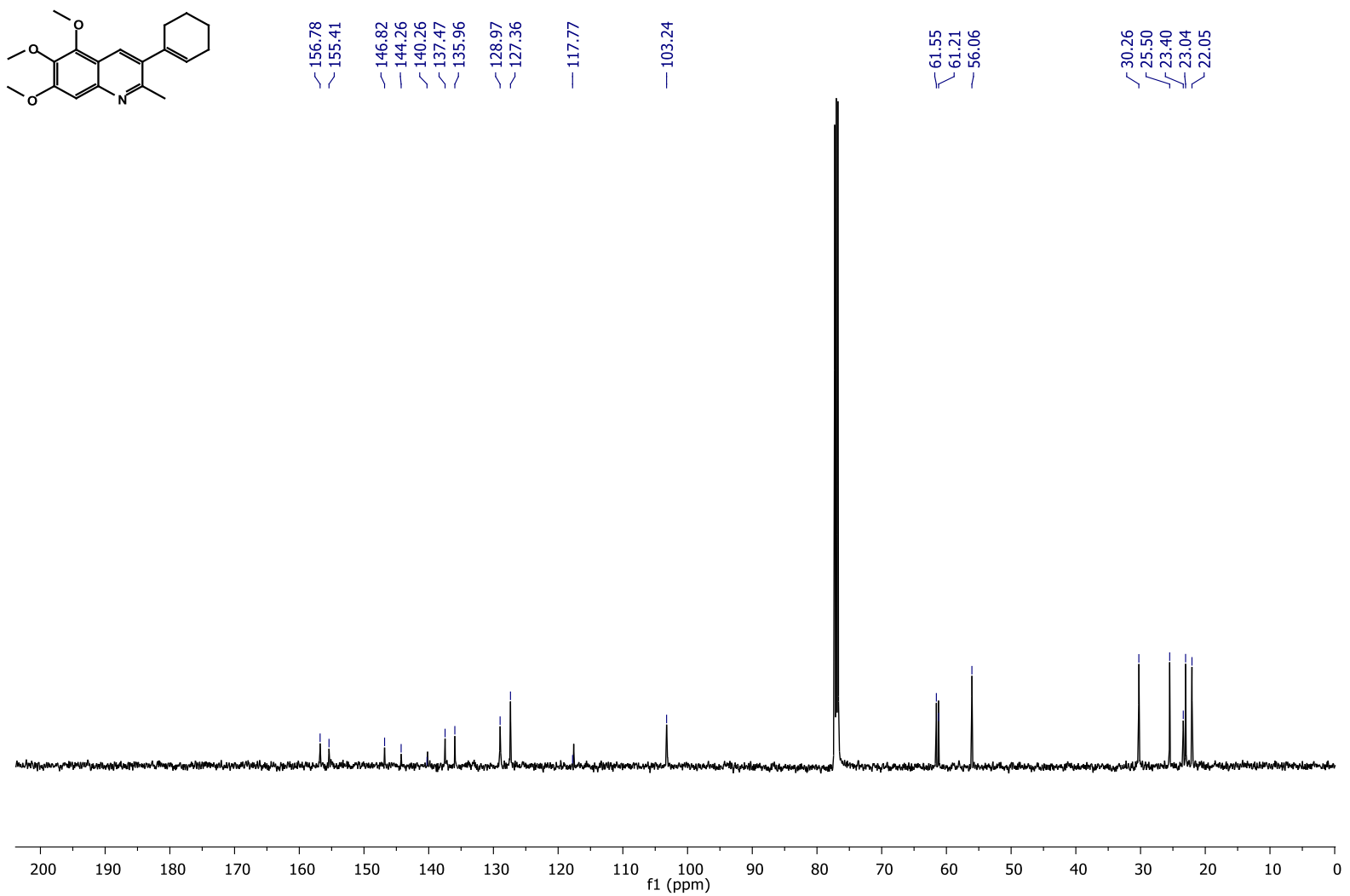
**Figure 2.25.**  $^1\text{H}$  NMR spectra for compound 3-cyclohexenyl-2-ethyl-6(N,N-dimethylamino)quinoline (**23**).



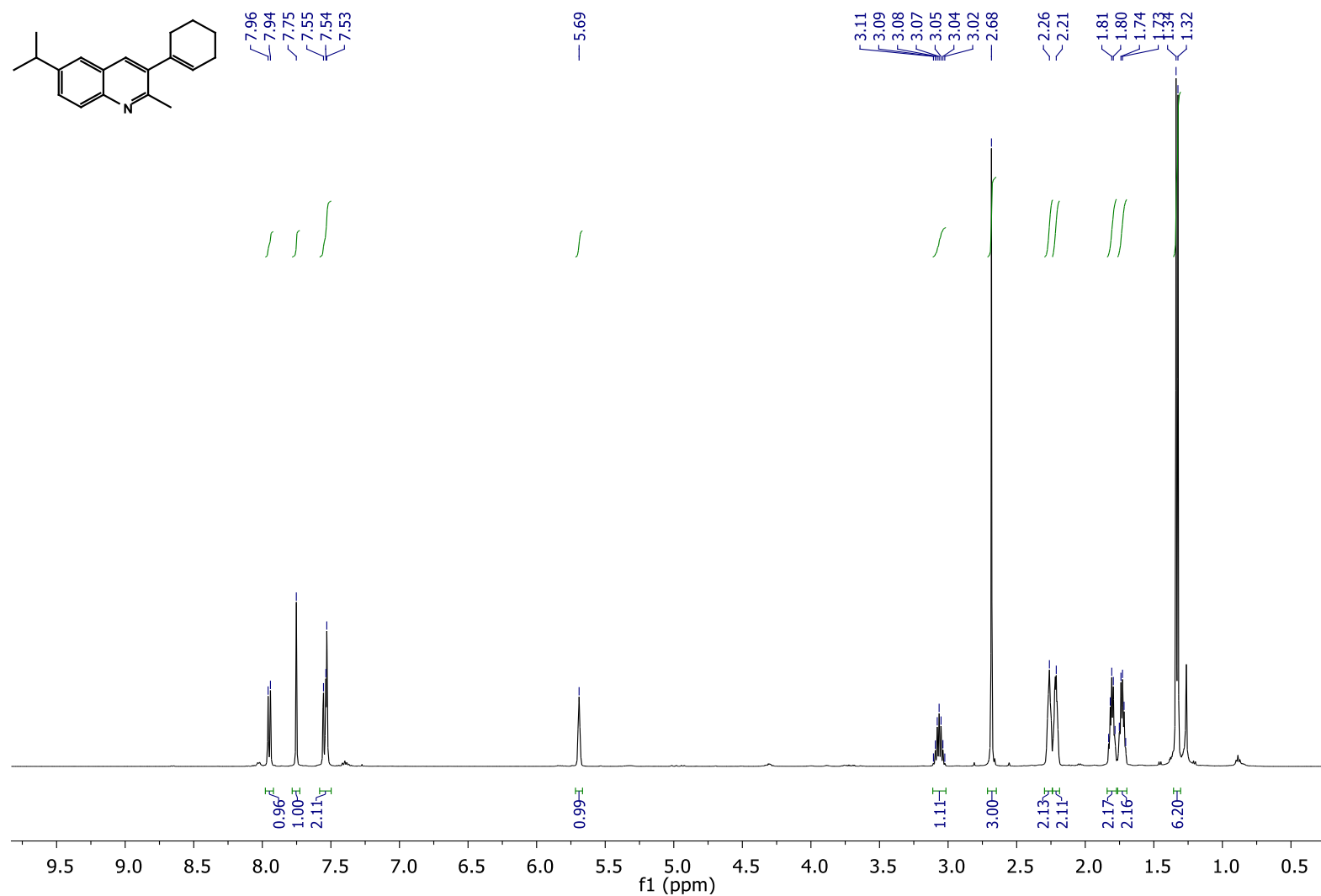
**Figure 2.26.**  $^{13}\text{C}$  NMR spectra for compound 3-cyclohexenyl-2-ethyl-6(N,N-dimethylamino)quinoline (**23**).



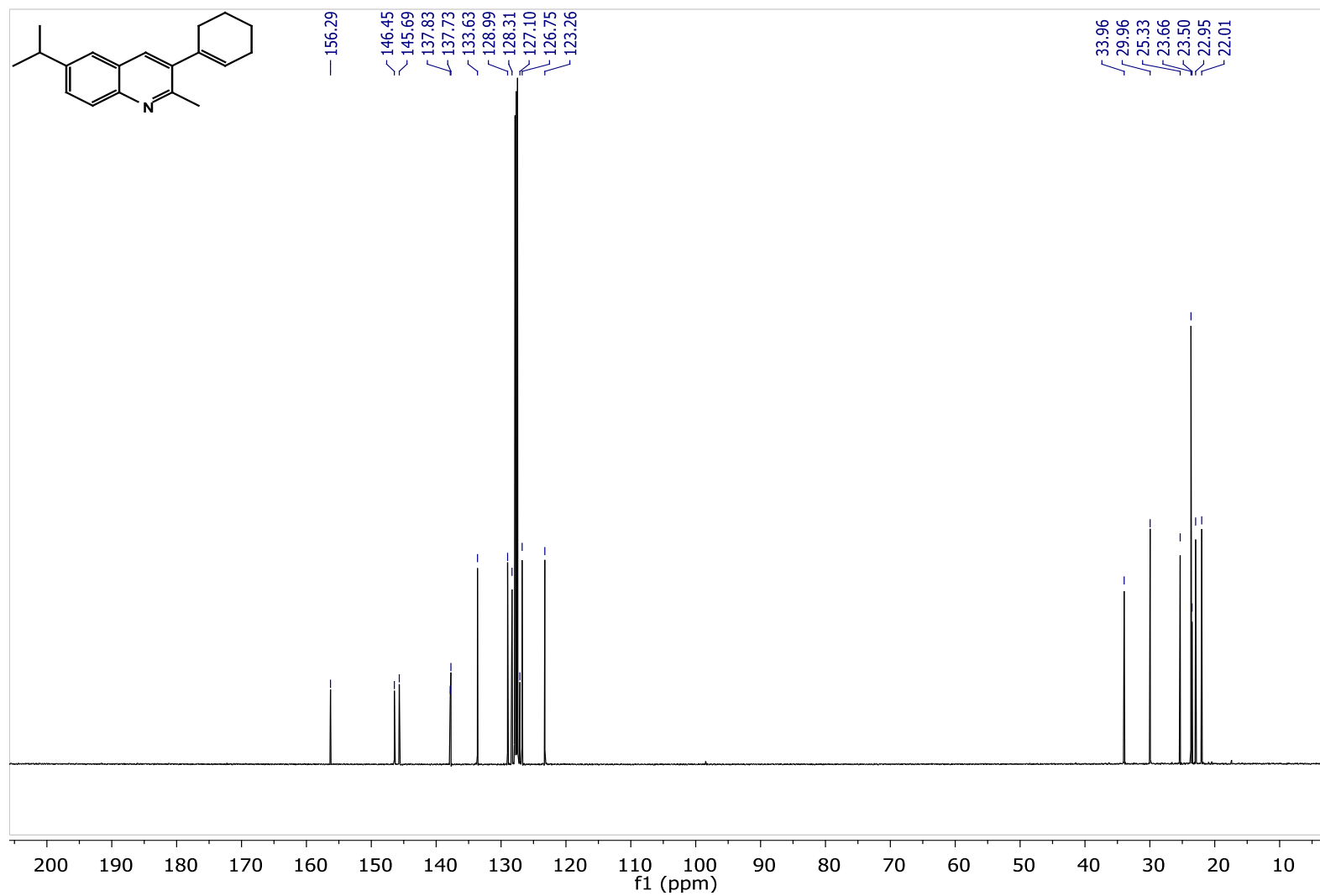
**Figure 2.27.** <sup>1</sup>H NMR spectra for compound 3-cyclohexenyl-5,6,7-trimethoxy-2-methylquinoline (27).



**Figure 2.28.** <sup>13</sup>C NMR spectra for compound 3-cyclohexenyl-5,6,7-trimethoxy-2-methylquinoline (**27**).

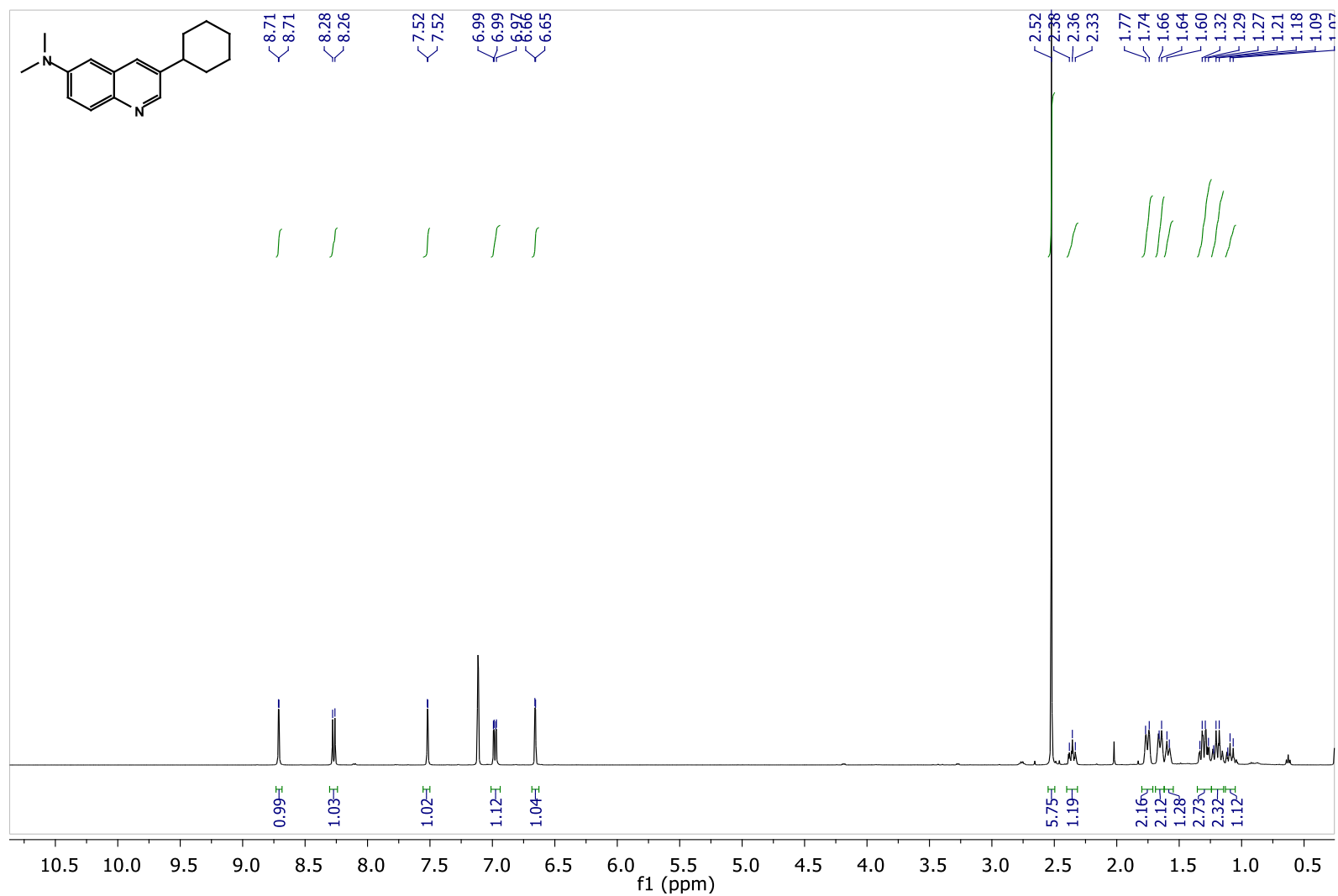


**Figure 2.29.** <sup>1</sup>H NMR spectra for compound 3-cyclohexenyl-6-isopropyl-2-methylquinoline (**28**).

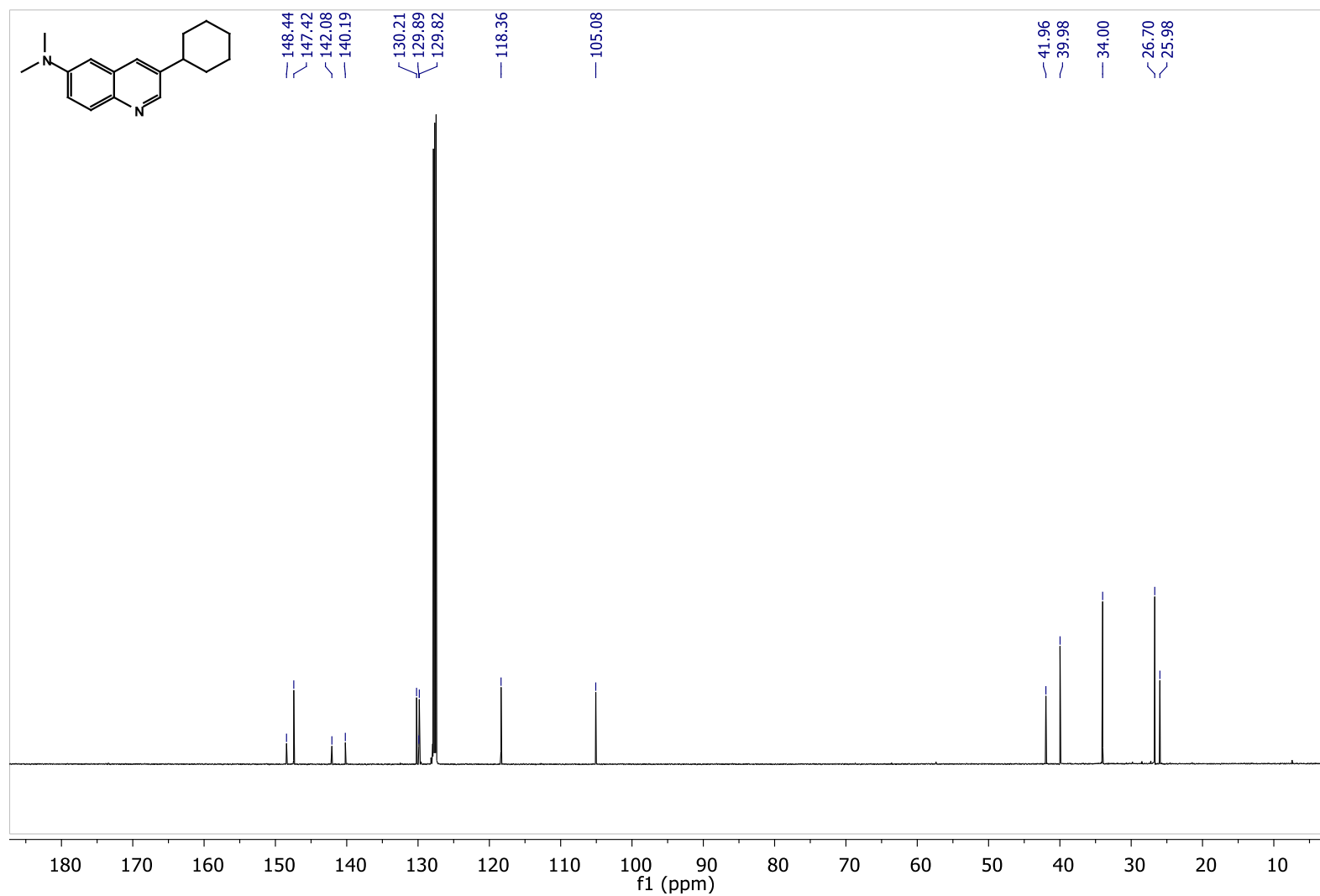


**Figure 2.30.**  $^{13}\text{C}$  NMR spectra for compound 3-cyclohexenyl-6-isopropyl-2-methylquinoline (**28**).

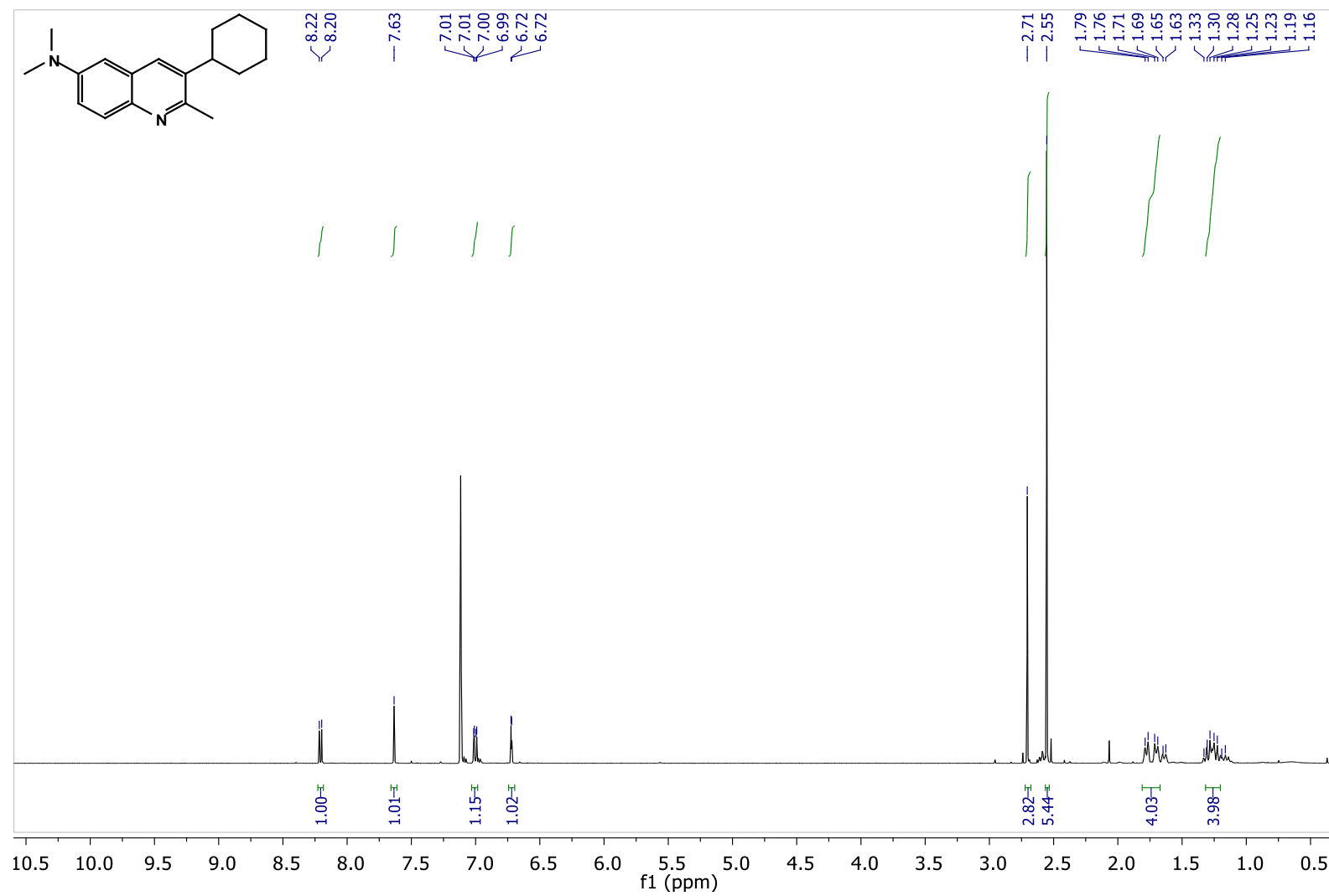




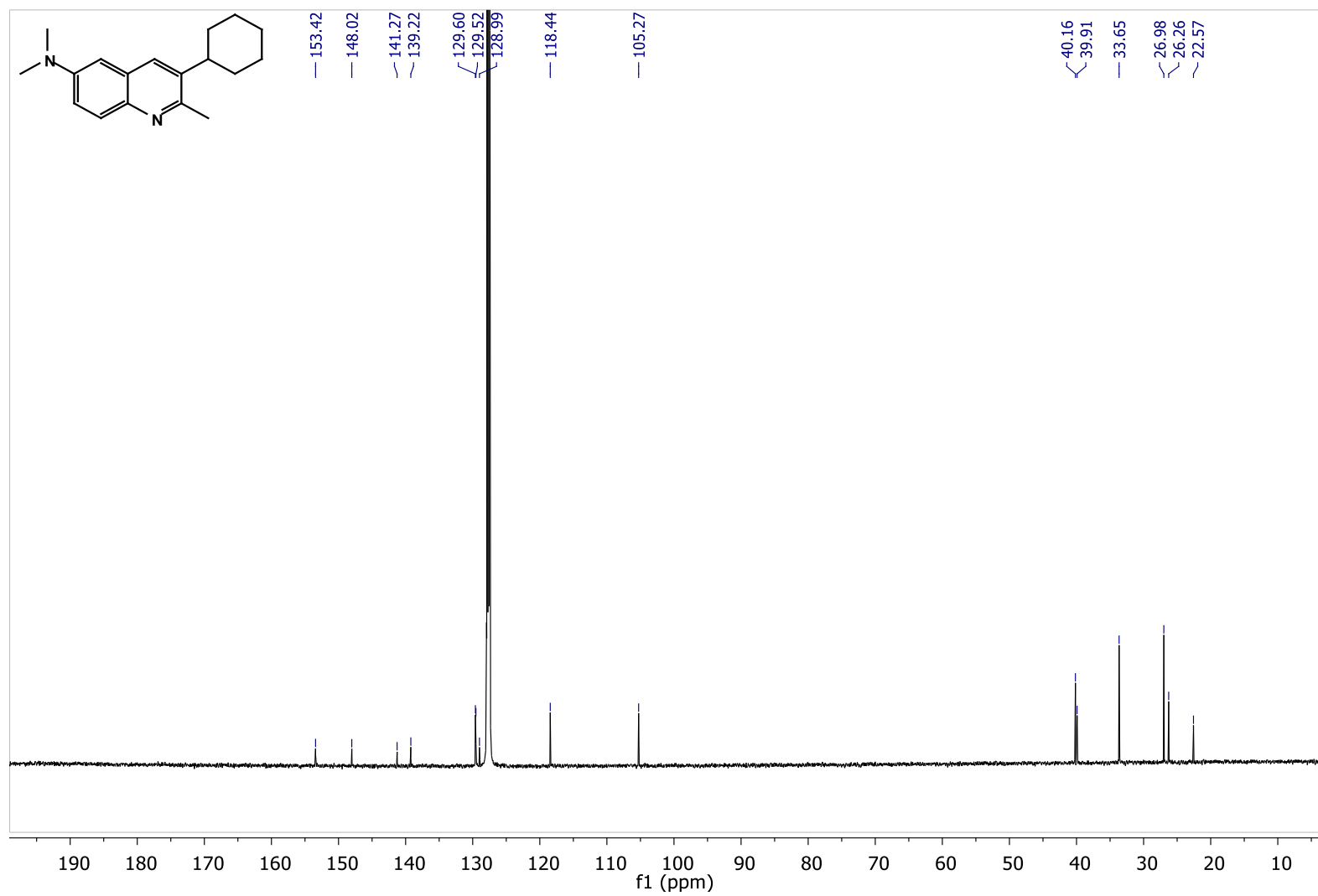
**Figure 2.31.**  $^1\text{H}$  NMR spectra for compound 3-cyclohexyl-6-(N,N-dimethylamino)quinoline (**29**).



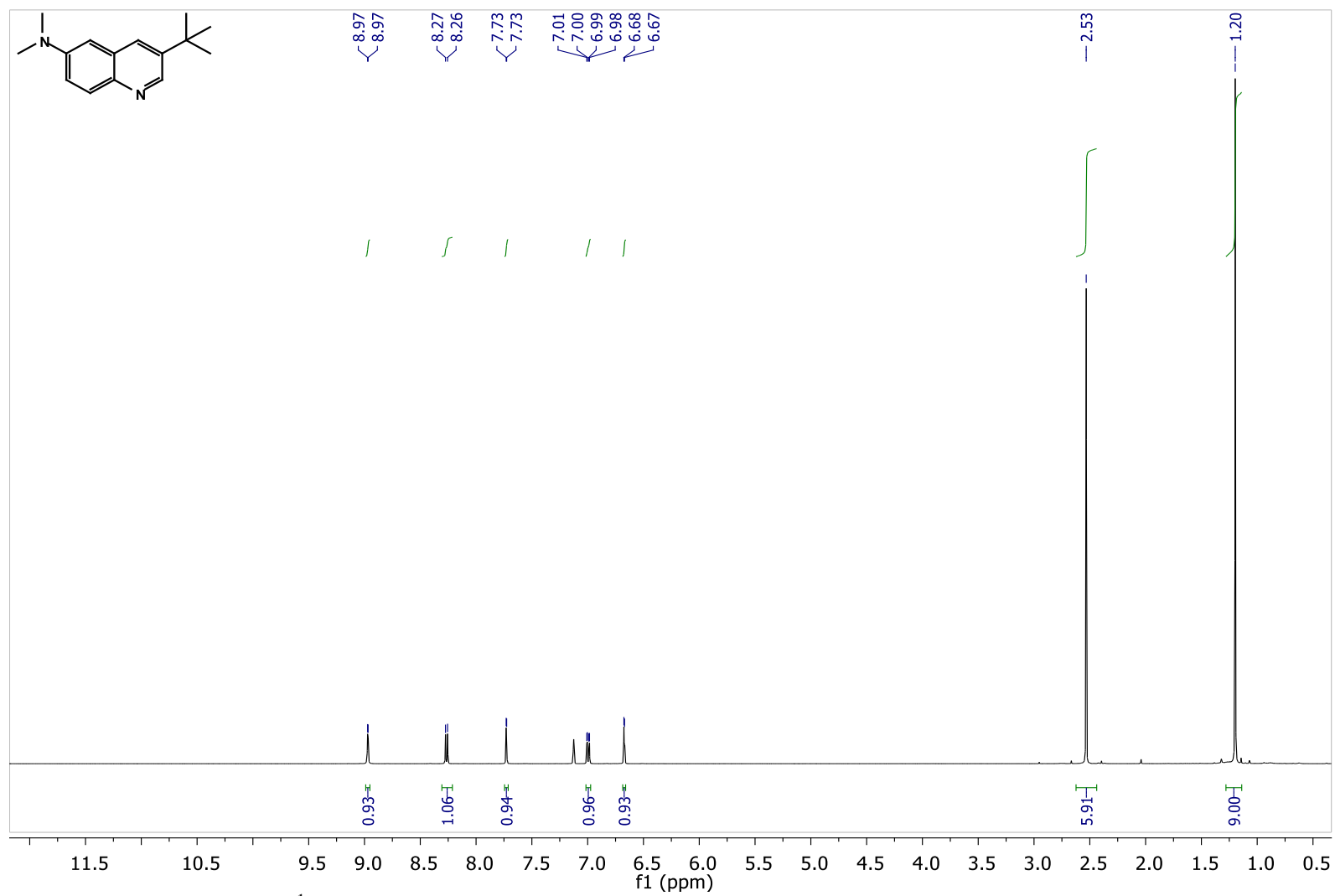
**Figure 2.32.** <sup>13</sup>C NMR spectra for compound 3-cyclohexyl-6-(N,N-dimethylamino)quinoline (**29**).



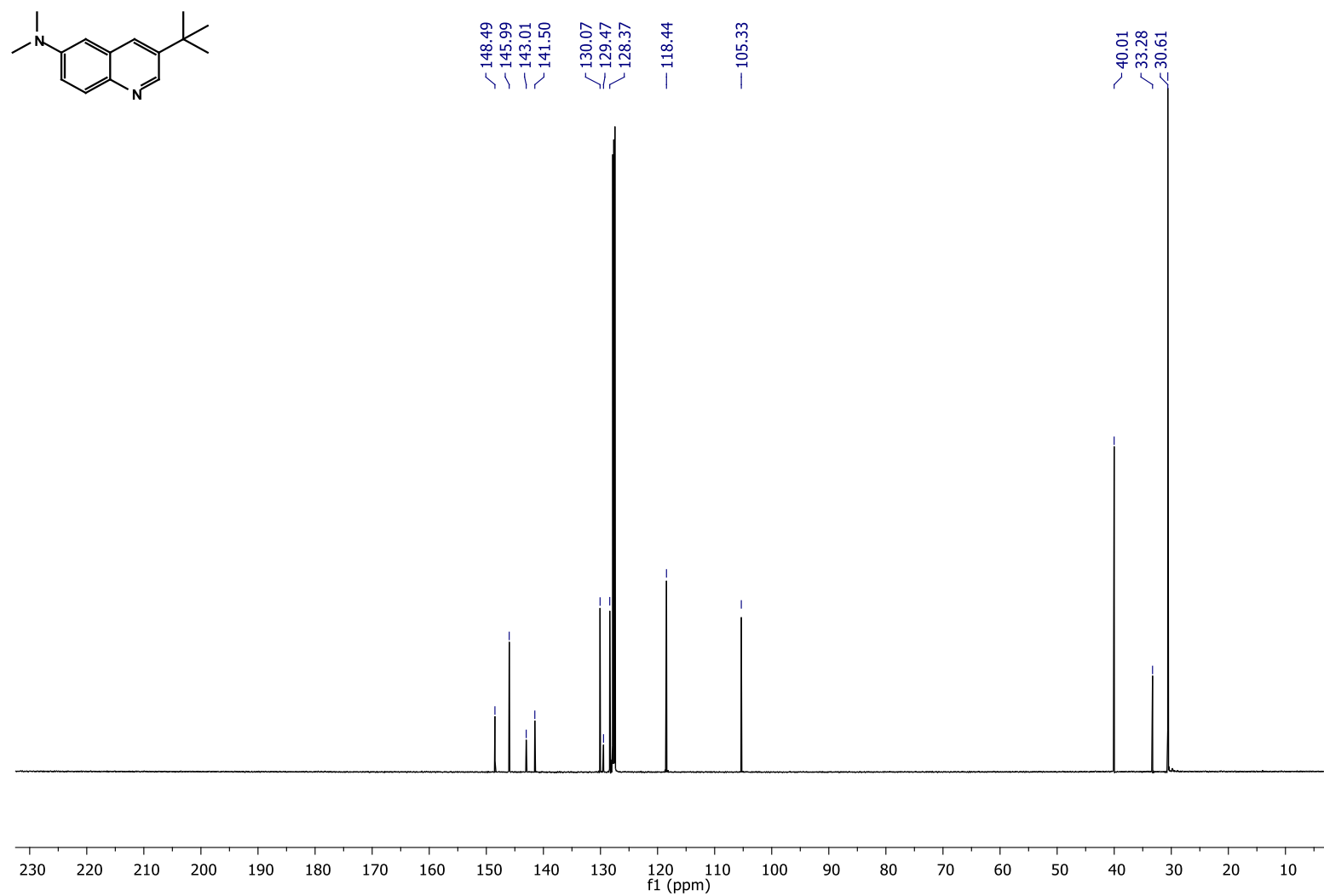
**Figure 2.33.** <sup>1</sup>H NMR for compound 3-cyclohexyl-2-methyl-6-(N,N-dimethylamino)quinoline (**30**).



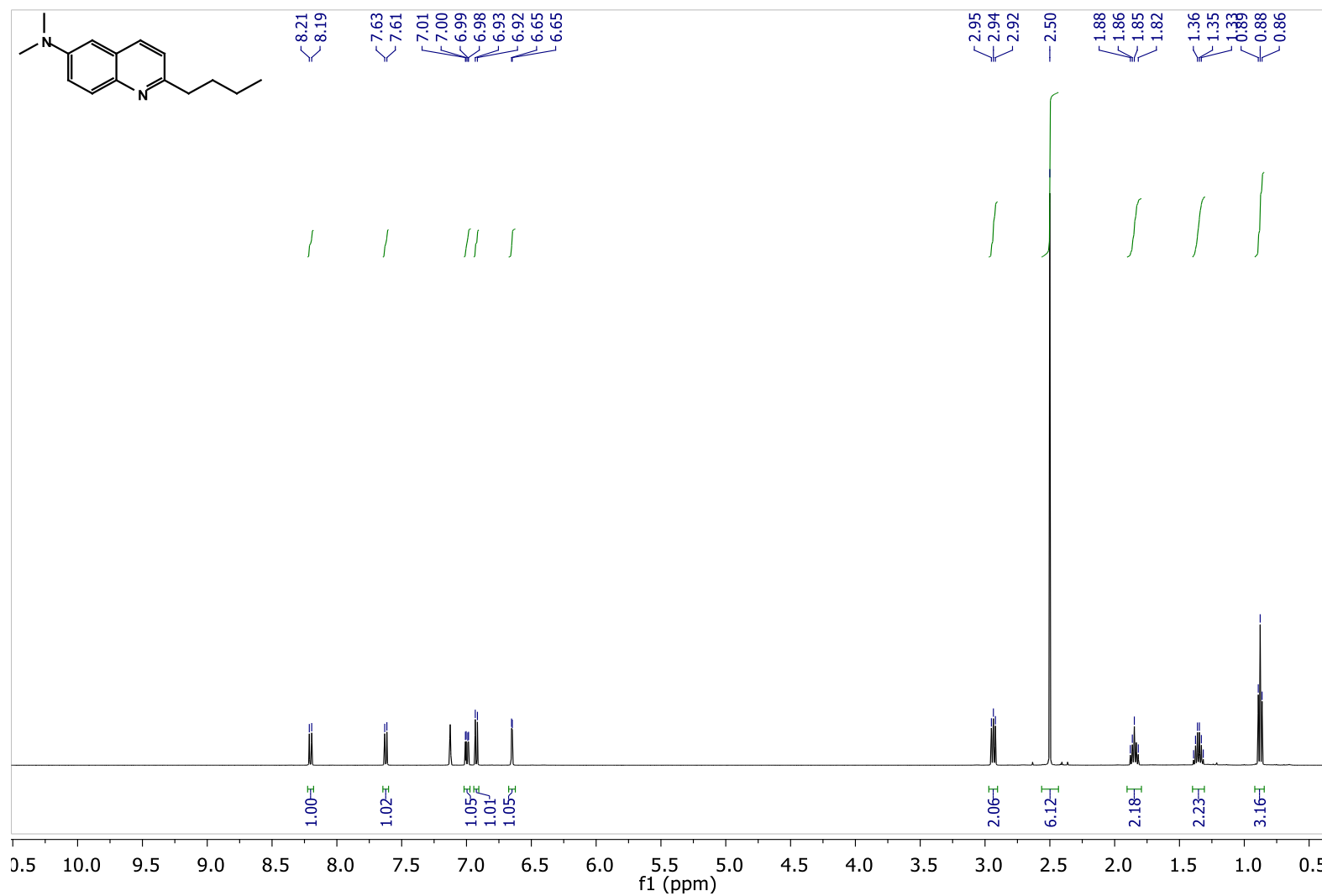
**Figure 2.34.**  $^{13}\text{C}$  NMR for compound 3-cyclohexyl-2-methyl-6-(N,N-dimethylamino)quinoline (**30**).



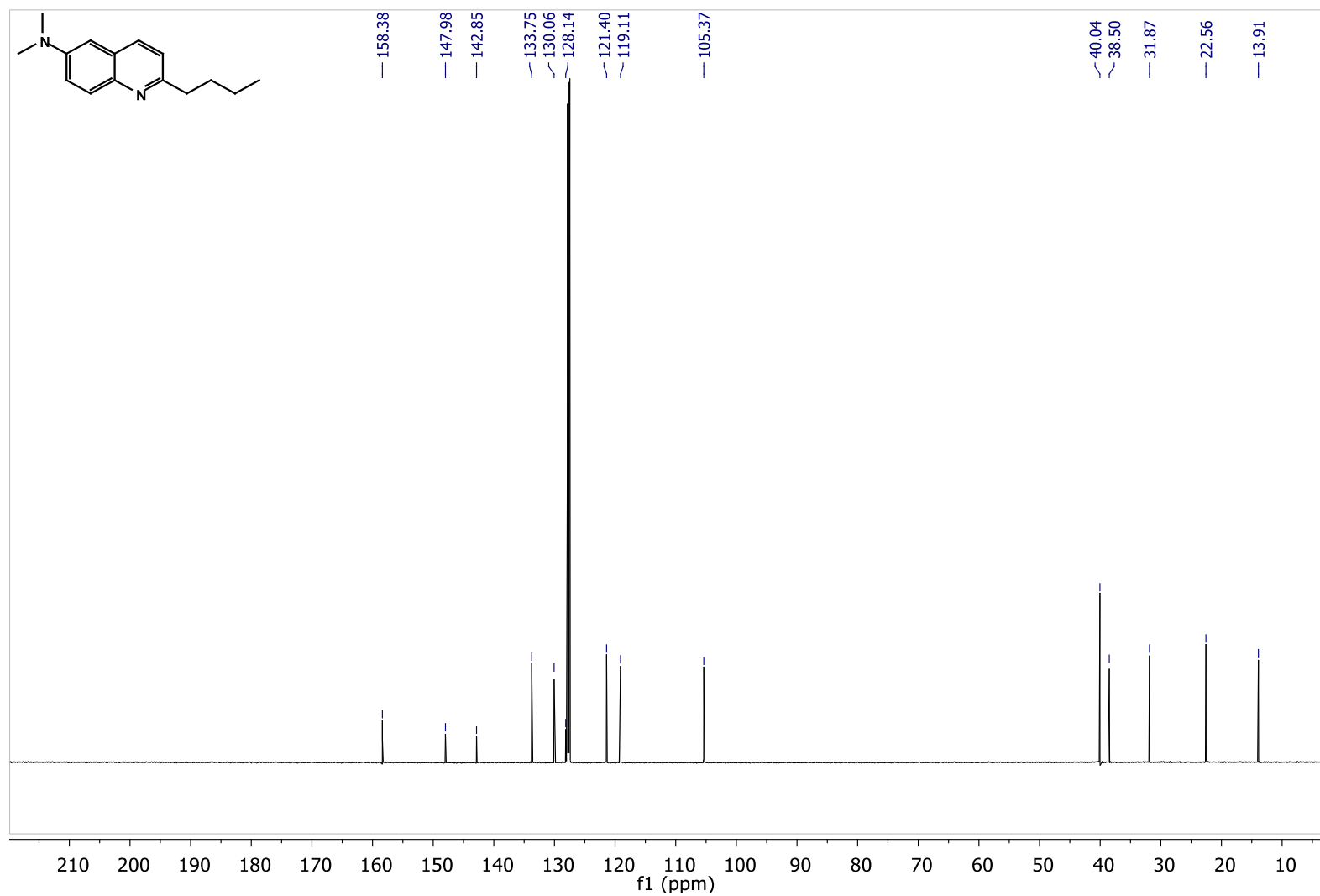
**Figure 2.35.** <sup>1</sup>H NMR spectra for compound 3-*tert*-butyl-6-(*N,N*-dimethylamino)quinoline (**32**).



**Figure 2.36.**  $^{13}\text{C}$  NMR spectra for compound 3-*tert*-butyl-6-(*N,N*-dimethylamino)quinoline (**32**).

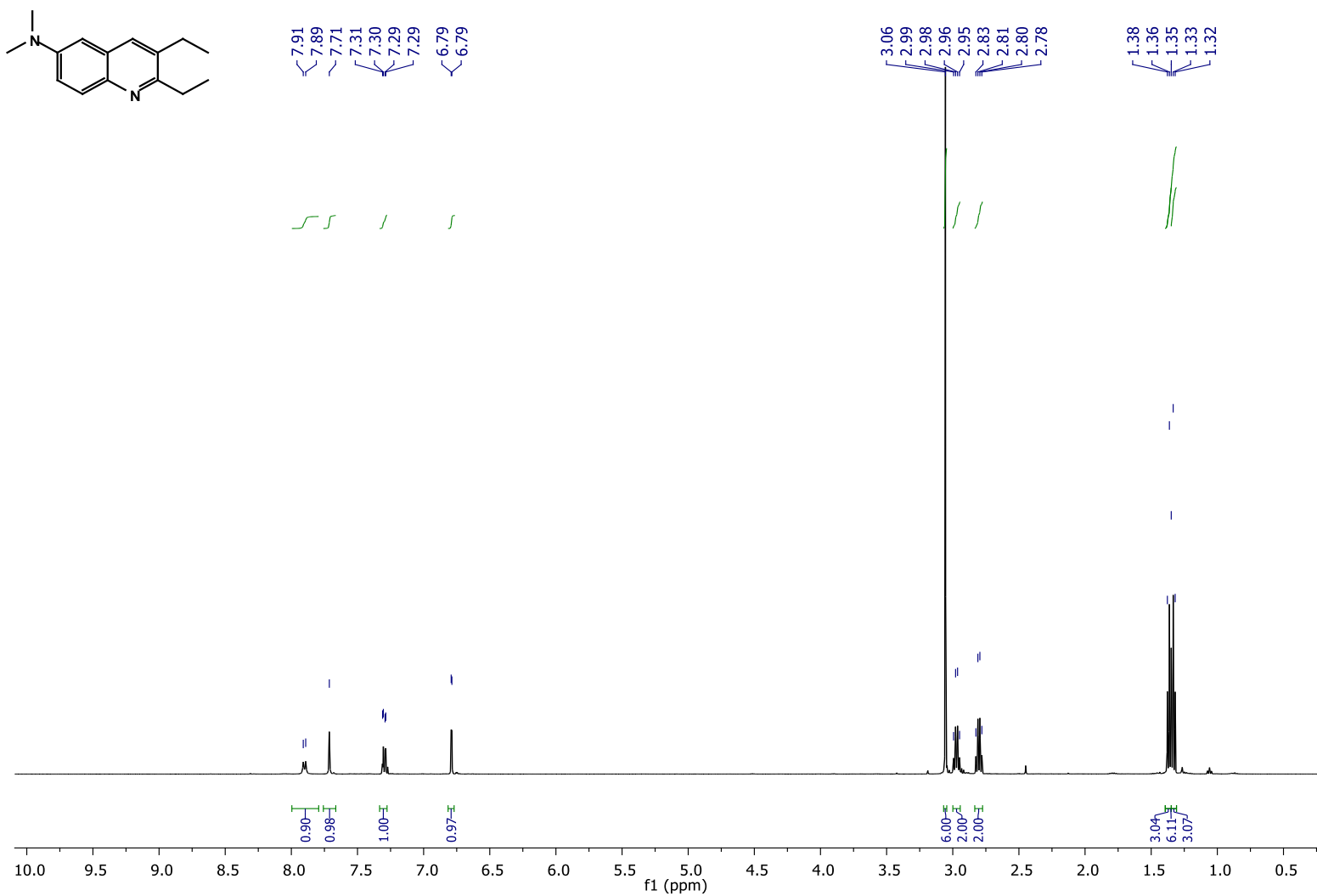


**Figure 2.37.** <sup>1</sup>H NMR spectra for compound 2-butyl-6-(N,N-dimethylamino)quinoline (**33**).

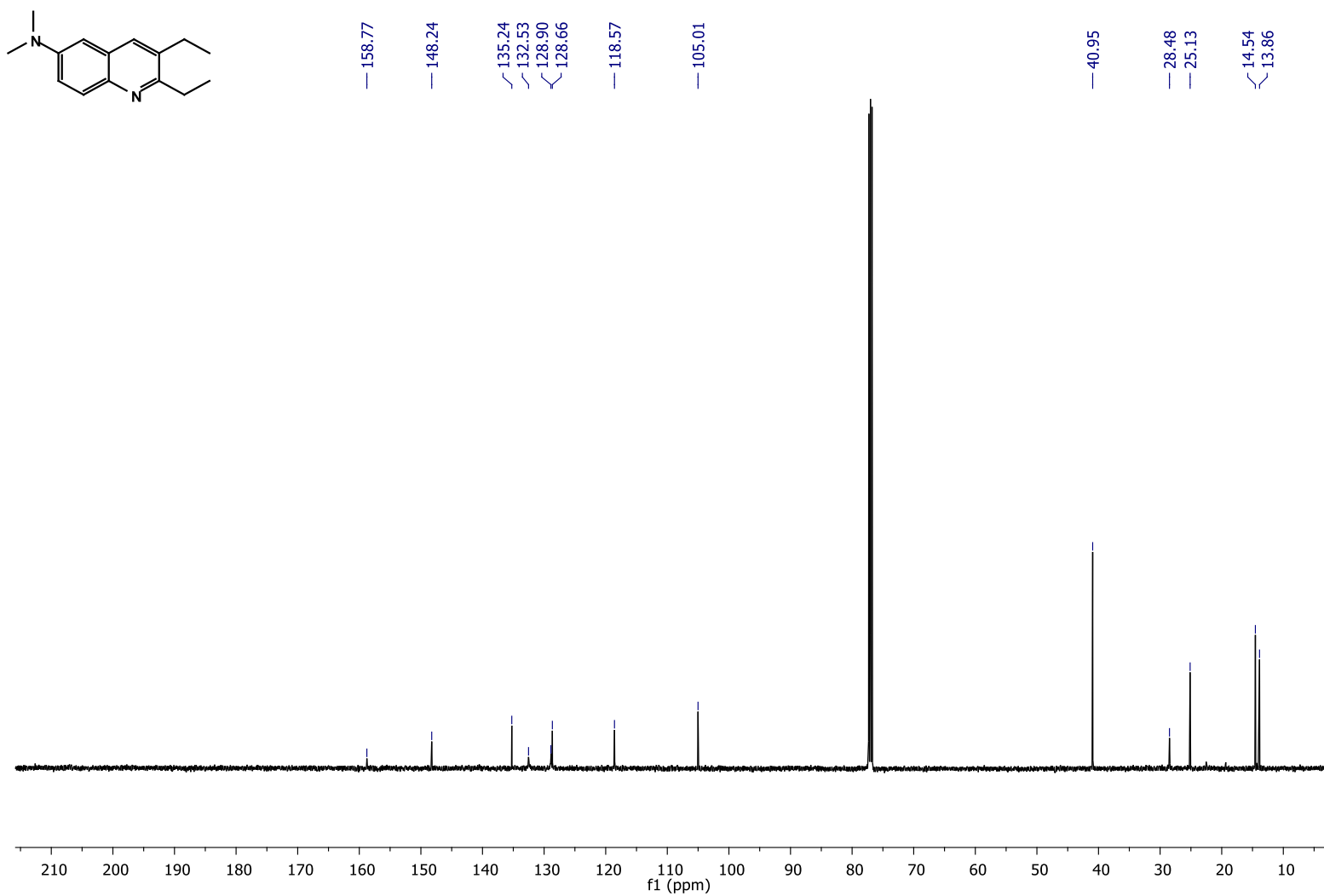


**Figure 2.38.** <sup>13</sup>C NMR spectra for compound 2-butyl-6-(N,N-dimethylamino)quinoline (**33**).

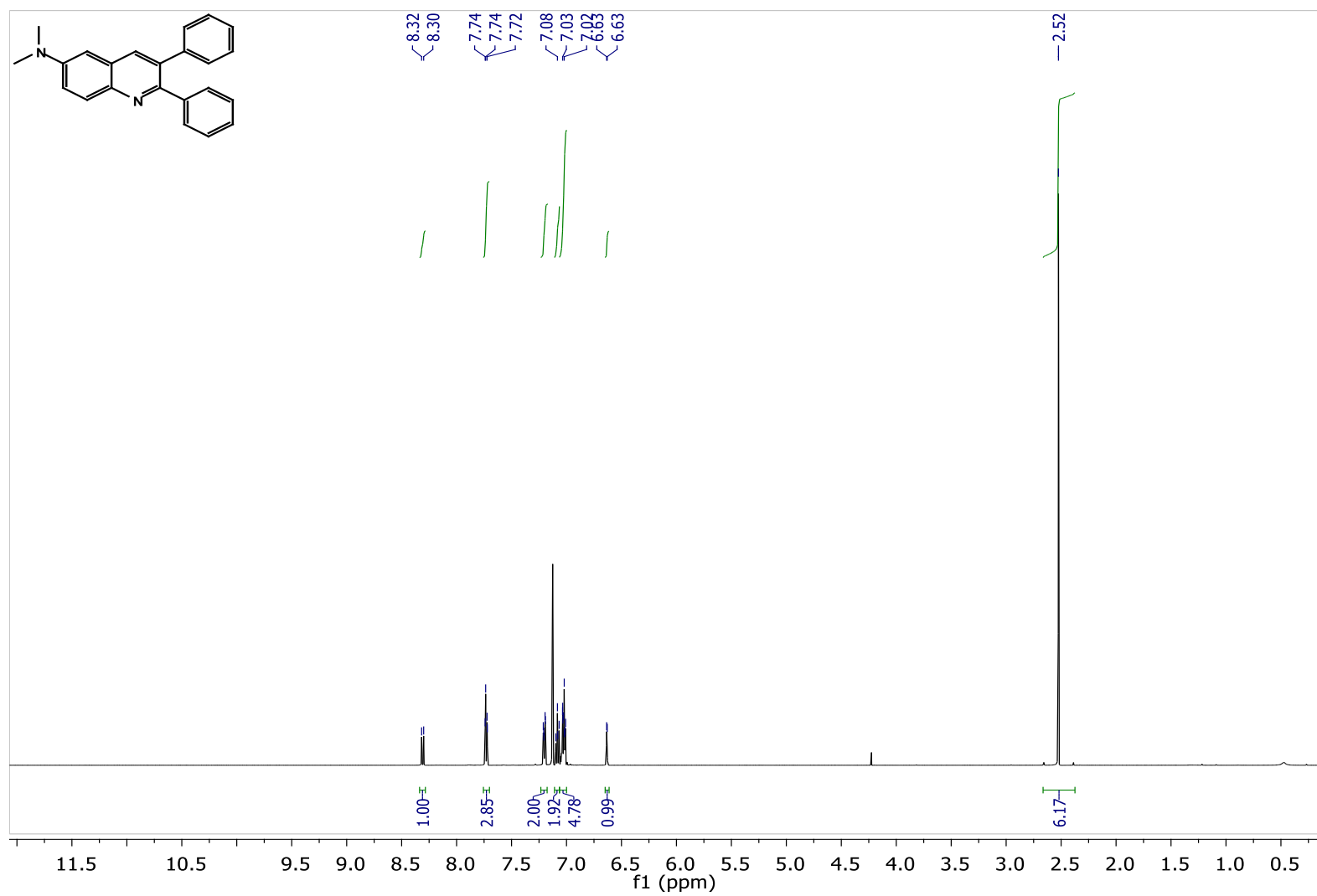




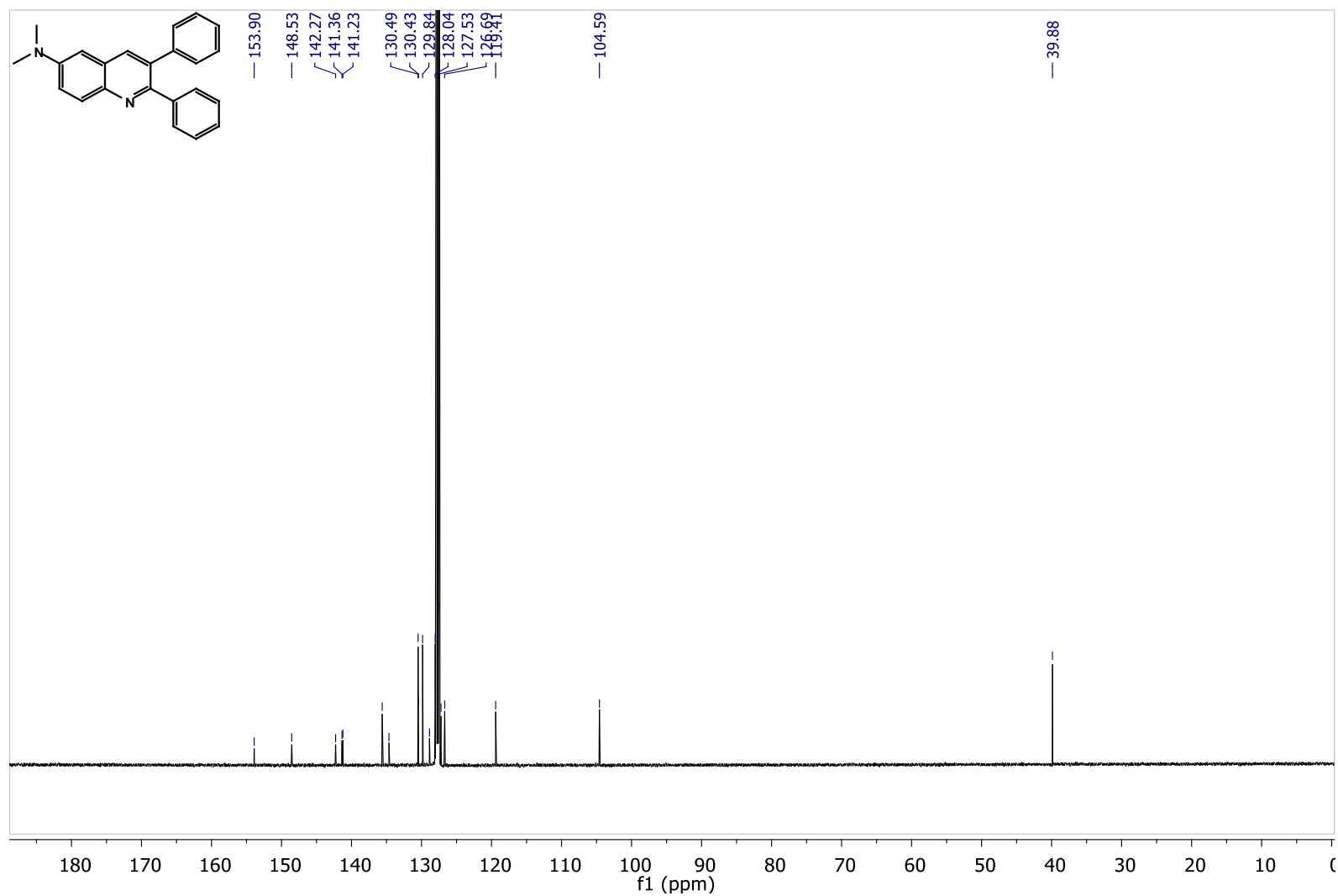
**Figure 2.39.** <sup>1</sup>H NMR spectra for compound 2,3-diethyl-N,N-dimethylquinoline (**34**).



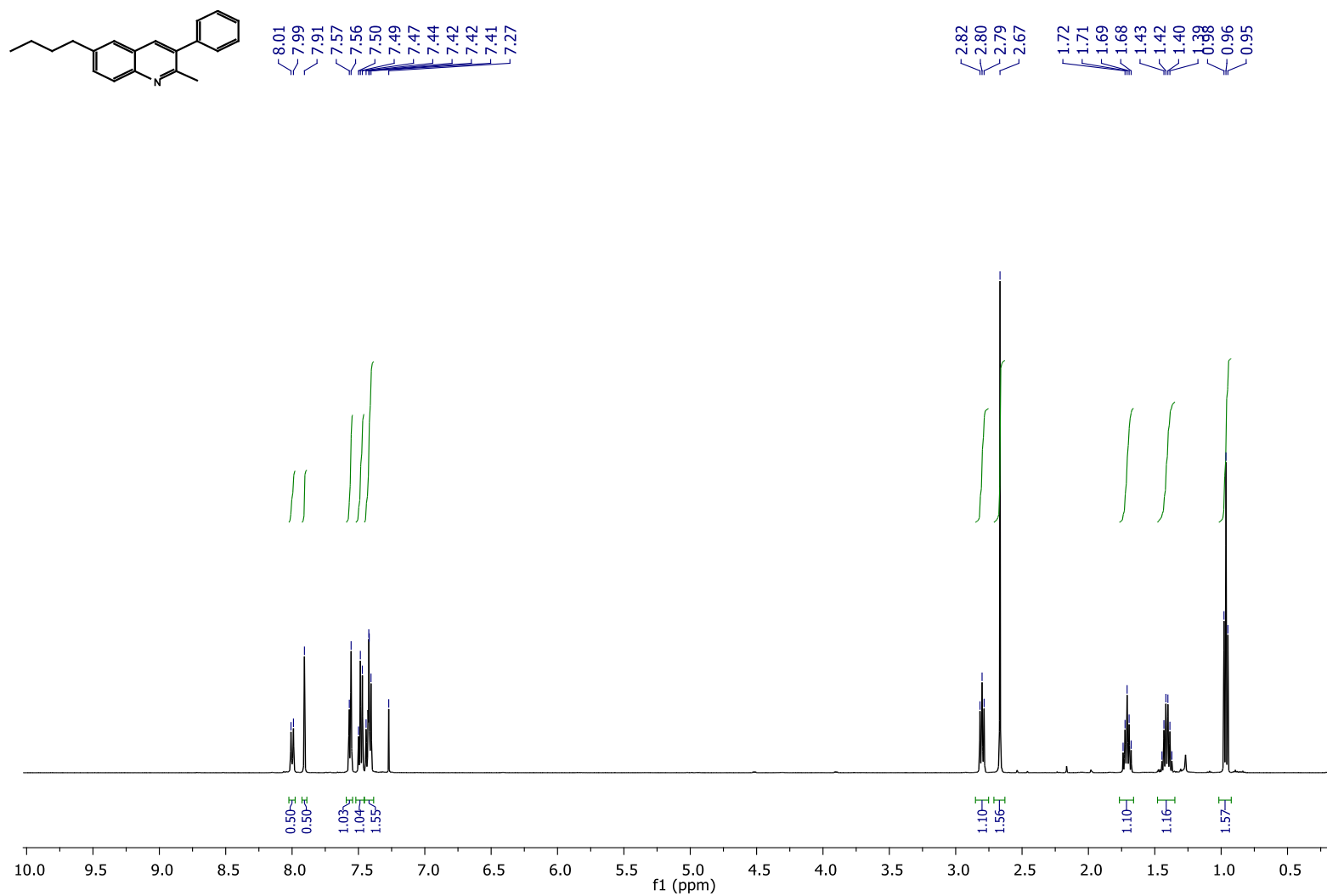
**Figure 2.40.** <sup>13</sup>C NMR spectra for compound 2,3-diethyl-N,N-dimethylquinoline (**34**).



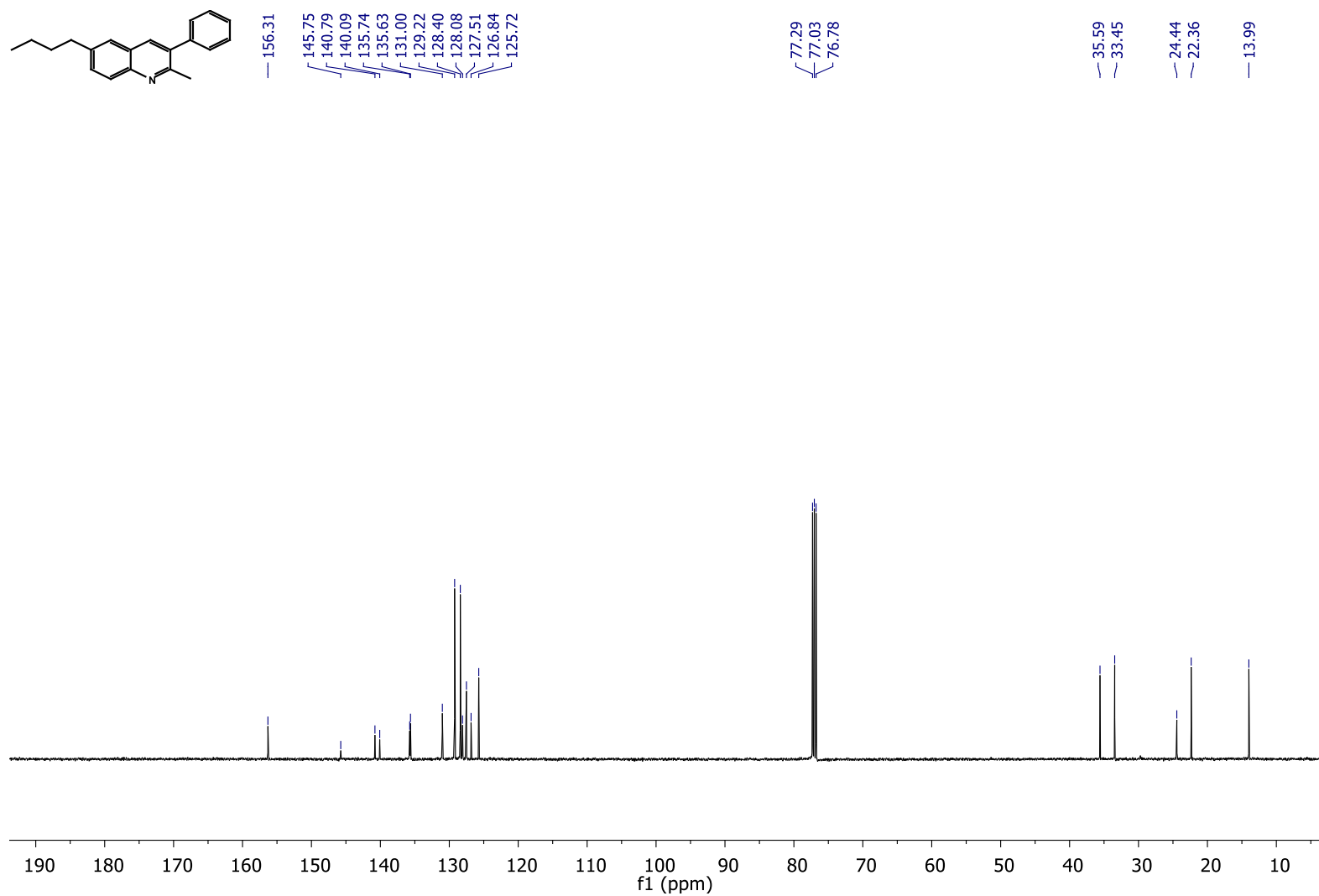
**Figure 2.41.** <sup>1</sup>H NMR spectra for compound 2,3-diphenyl-6-(N,N-dimethylamino)quinoline (**35**).



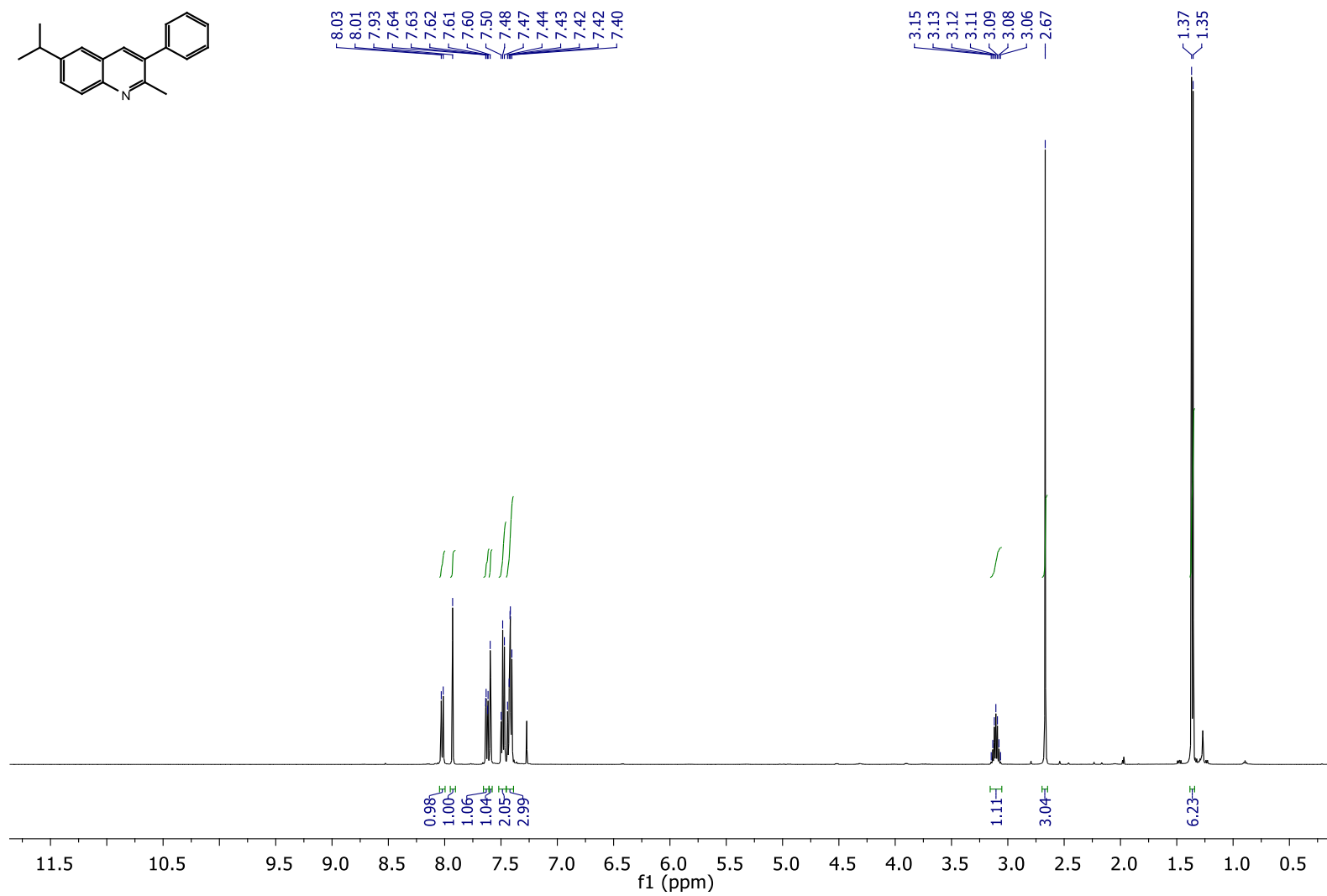
**Figure 2.42.** <sup>13</sup>C NMR spectra for compound 2,3-diphenyl-6-(N,N-dimethylamino)quinoline (**35**).



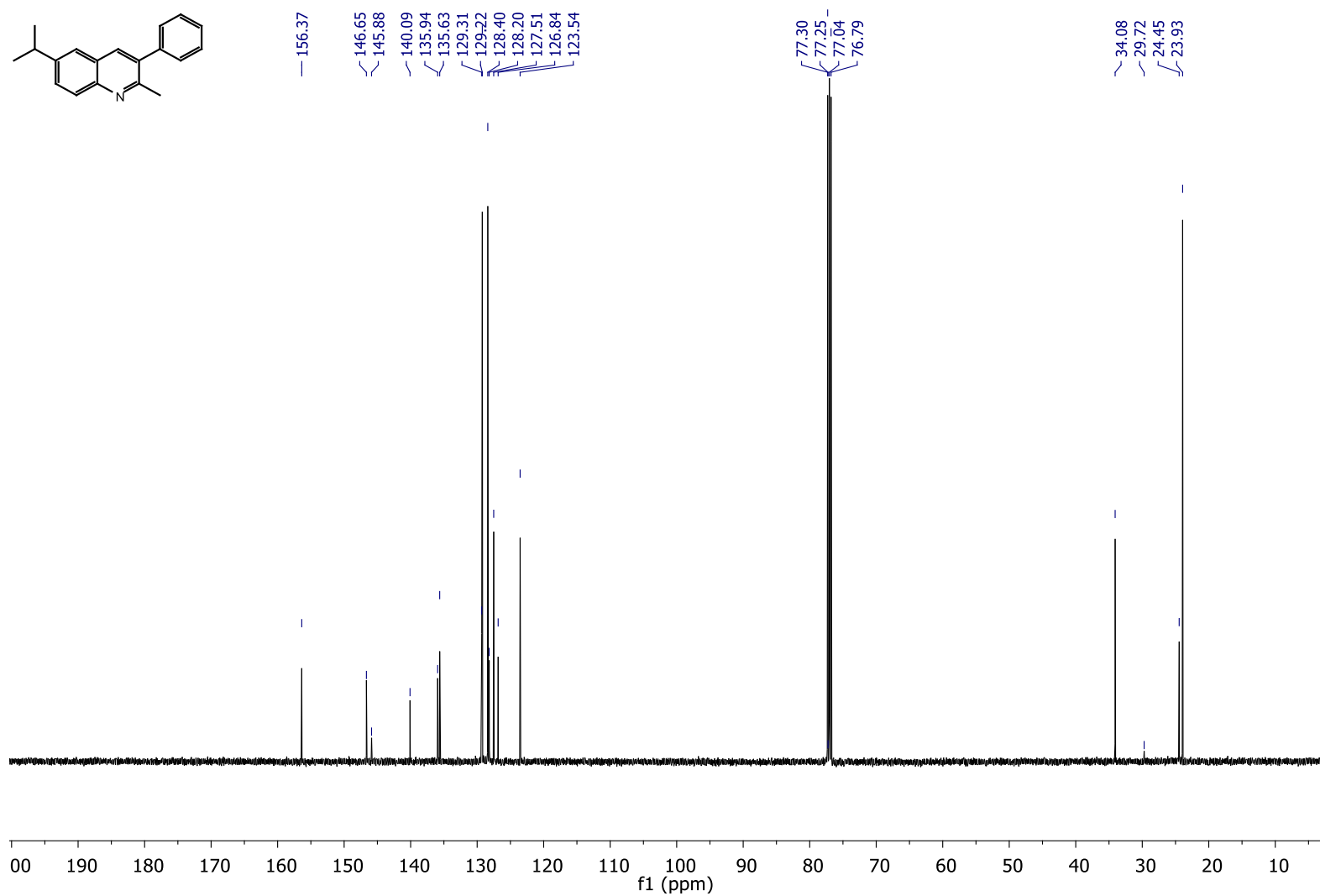
**Figure 2.43.** <sup>1</sup>H NMR spectra for compound 6-butyl-2-methyl-3-phenylquinoline (**36**).



**Figure 2.44.**  $^{13}\text{C}$  NMR spectra for compound 6-butyl-2-methyl-3-phenylquinoline (**36**).

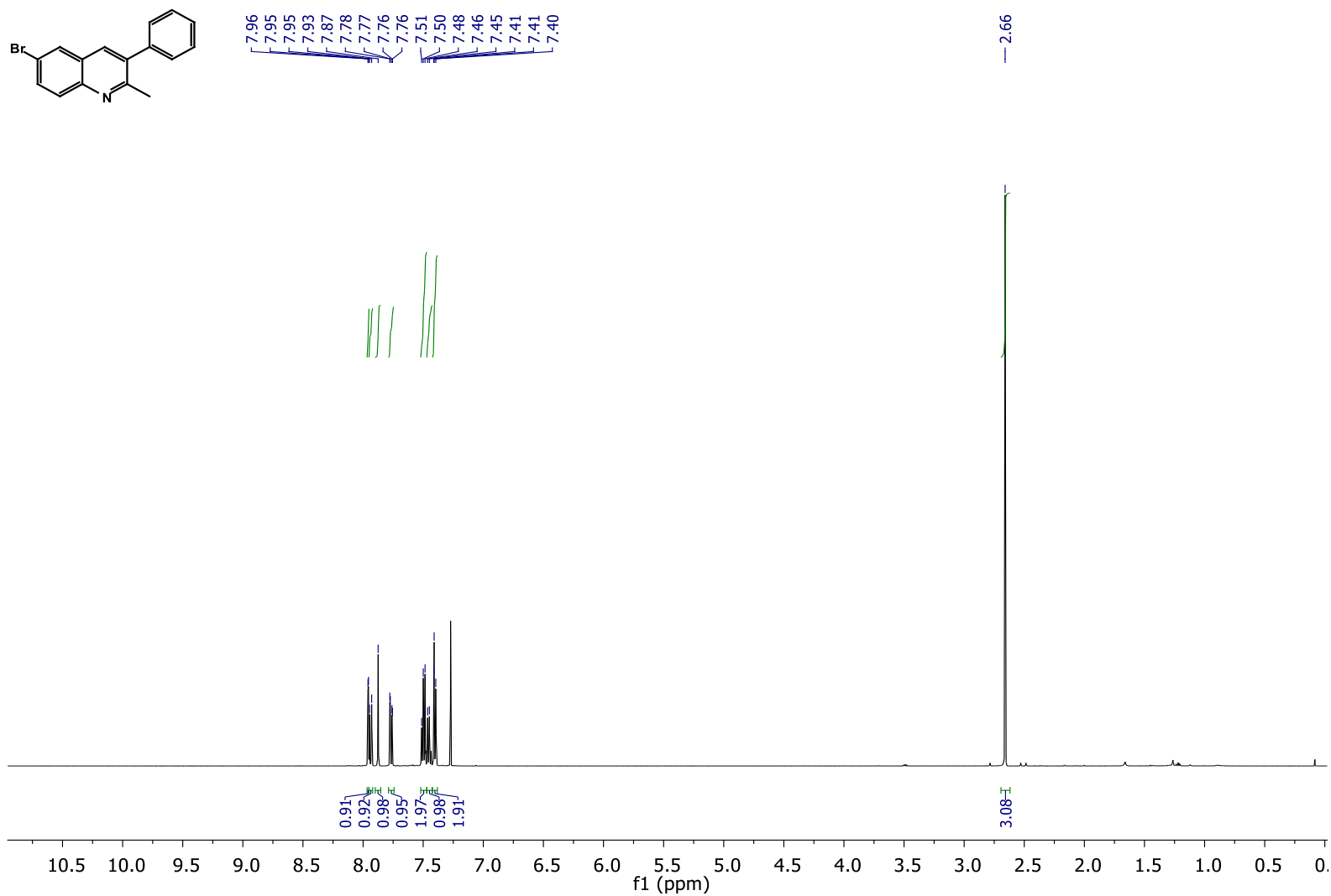


**Figure 2.45.** <sup>1</sup>H NMR spectra for compound 6-isopropyl-2-methyl-3-phenylquinoline (**37**).

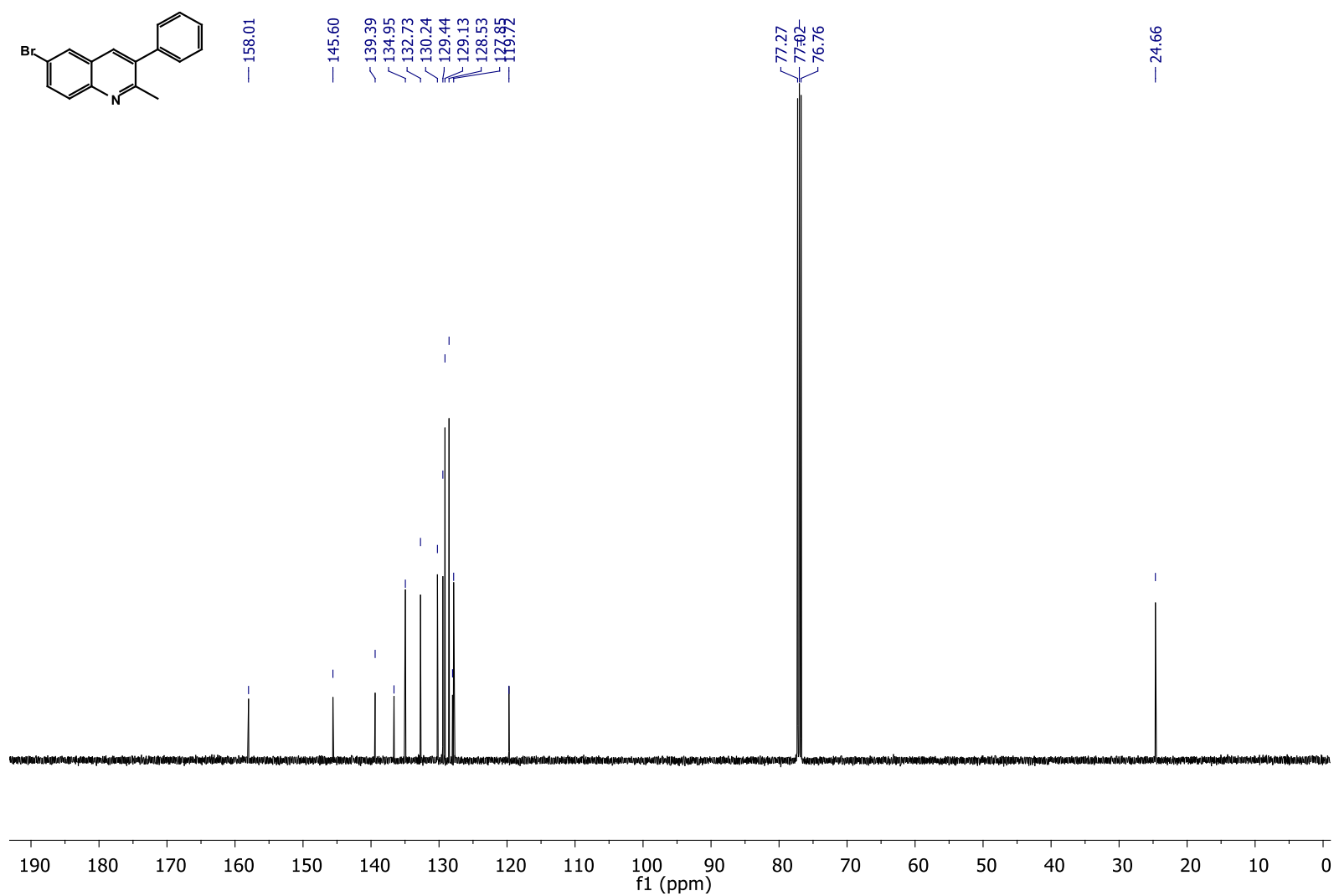


**Figure 2.46.** <sup>13</sup>C NMR spectra for compound 6-isopropyl-2-methyl-3-phenylquinoline (**37**).

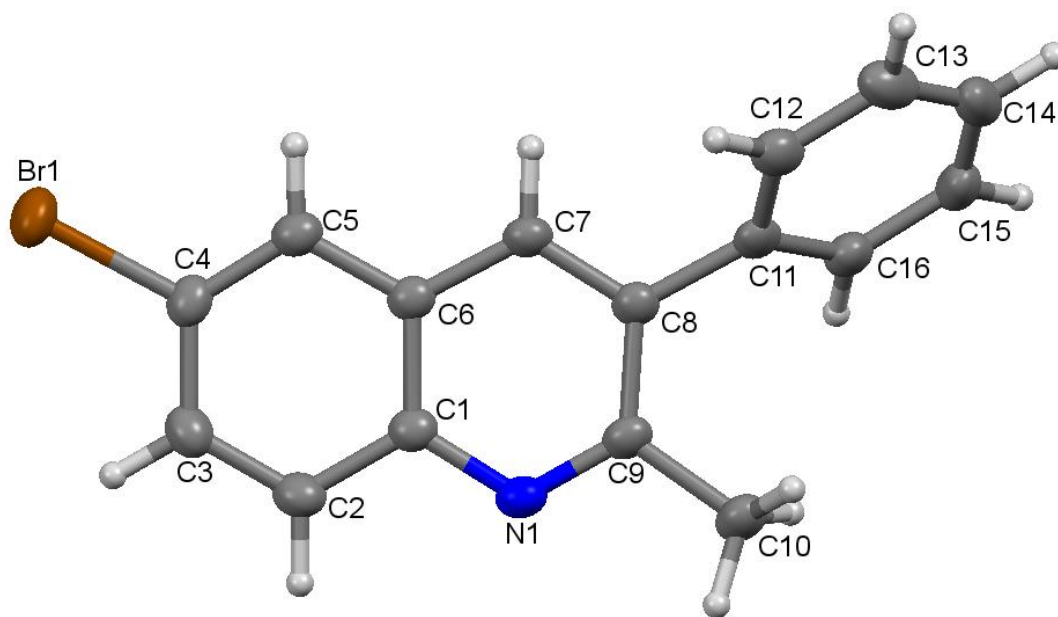




**Figure 2.47.** <sup>1</sup>H NMR spectra for compound-6-bromo-2-methyl-3-phenylquinoline (**38**).



**Figure 2.48.** <sup>13</sup>C NMR spectra for compound-6-bromo-2-methyl-3-phenylquinoline (**38**).



**Figure 2.49.** Crystal structure of 6-bromo-3-cyclohexenyl-2-methylquinoline (**38**).

## **REFERENCES**

## REFERENCES

1. Murata, S.; Yashiroda, H.; Tanaka, K., *Nat. Rev. Mol. Cell Biol.* **2009**, *10*, 104-115.
2. Groll, M.; Huber, R., *Biochim. Biophys. Acta* **2004**, *1695*, 33-44.
3. Ben-Nissan, G.; Sharon, M., *Biomolecules* **2014**, *4*, 862-84.
4. Groll, M.; Heinemeyer, W.; Jäger, S.; Ullrich, T.; Bochtler, M.; Wolf, D. H.; Huber, R., *Proc. Natl. Acad. Sci.* **1999**, *96*, 10976-10983.
5. Groll, M.; Ditzel, L.; Lowe, J.; Stock, D.; Bochtler, M.; Bartunik, H. D.; Huber, R., *Nature* **1997**, *386*, 463-471.
6. Rentsch, A.; Landsberg, D.; Brodmann, T.; Bülow, L.; Girbig, A.-K.; Kalesse, M., *Angew. Chem. Int. Ed.* **2013**, *52*, 5450-5488.
7. Chen, P.; Hochstrasser, M., *Cell* **1996**, *86*, 961-972.
8. Heinemeyer, W.; Fischer, M.; Krimmer, T.; Stachon, U.; Wolf, D. H., *J. Biol. Chem.* **1997**, *272*, 25200-25209.
9. Arendt, C. S.; Hochstrasser, M., *Proc. Natl. Acad. Sci. USA* **1997**, *94*, 7156-7161.
10. Kisselev, Alexei F.; van der Linden, W. A.; Overkleeft, Herman S., *Chem. Biol.* **2012**, *19*, 99-115.
11. Hershko, A.; Ciechanover, A., *Annu. Rev. Biochem* **1998**, *67*, 425-479.
12. Coux, O.; Tanaka, K.; Goldberg, A. L., *Annu. Rev. Biochem* **1996**, *65*, 801-847.
13. King, R. W.; Deshaies, R. J.; Peters, J.-M.; Kirschner, M. W., *Science* **1996**, *274*, 1652-1659.
14. Goldberg, A. L., Bortezomib's Scientific Origins and Its Tortuous Path to the Clinic. In *Bortezomib in the Treatment of Multiple Myeloma*, Ghobrial, I. M.; Richardson, P. G.; Anderson, K. C., Eds. Springer Basel: Basel, **2011**; pp 1-27.
15. Arlt, A.; Bauer, I.; Schafmayer, C.; Tepel, J.; Muerkoster, S. S.; Brosch, M.; Roder, C.; Kalthoff, H.; Hampe, J.; Moyer, M. P.; Folsch, U. R.; Schafer, H., *Oncogene* **2009**, *28*, 3983-96.
16. Stintzing, S.; Lenz, H.-J., *Clin. Cancer Res.* **2014**, *20*, 3064-3070.
17. Petroski, M. D., *BMC Biochem.* **2008**, *9*, S7.

18. Wang, Z.; Yang, J.; Kirk, C.; Fang, Y.; Alsina, M.; Badros, A.; Papadopoulos, K.; Wong, A.; Woo, T.; Bomba, D.; Li, J.; Infante, J. R., *Drug Metabolism and Disposition* **2013**, *41*, 230-237.
19. Zavrski, I.; Jakob, C.; Kaiser, M.; Fleissner, C.; Heider, U.; Sezer, O., Molecular and Clinical Aspects of Proteasome Inhibition in the Treatment of Cancer. In *Targeted Therapies in Cancer*, Dietel, M., Ed. Springer Berlin Heidelberg: Berlin, Heidelberg, **2007**; pp 165-176.
20. Chen, D.; Frezza, M.; Schmitt, S.; Kanwar, J.; Dou, Q. P., *Curr. Cancer Drug Targets* **2011**, *11*, 239-253.
21. Vinitsky, A.; Michaud, C.; Powers, J. C.; Orlowski, M., *Biochemistry* **1992**, *31*, 9421-9428.
22. Lowe, J.; Stock, D.; Jap, B.; Zwickl, P.; Baumeister, W.; Huber, R., *Science* **1995**, *268*, 533-539.
23. Lindsten, K.; Menendez-Benito, V.; Masucci, M. G.; Dantuma, N. P., *Nat Biotech* **2003**, *21*, 897-902.
24. Huber, E. M.; Groll, M., *Angew. Chem. Int. Ed. Engl.* **2012**, *51*, 8708-20.
25. Bogyo, M.; S., M. J.; Gaczynksa, M.; Tortorella, D.; Goldberg, A. L.; Ploegh, H., *Proc. Natl. Acad. Sci. USA* **1997**, *94*, 6629-634.
26. Borissenko, L.; Groll, M., *Chem. Rev.* **2007**, *107*, 687-717.
27. Groll, M.; Schellenberg, B.; Bachmann, A. S.; Archer, C. R.; Huber, R.; Powell, T. K.; Lindow, S.; Kaiser, M.; Dudler, R., *Nature* **2008**, *452*, 755-758.
28. Gräwert, M. A.; Gallastegui, N.; Stein, M.; Schmidt, B.; Kloetzel, P.-M.; Huber, R.; Groll, M., *Angew. Chem. Int. Ed.* **2011**, *50*, 542-544.
29. Curran, M.; McKeage, K., *Drugs* **2009**, *69*, 859-888.
30. Park, J.; Park, E.; Jung, C. K.; Kang, S. W.; Kim, B. G.; Jung, Y.; Kim, T. H.; Lim, J. Y.; Lee, S. E.; Min, C. K.; Won, K. A., *BMC Cancer* **2016**, *16*, 247.
31. Fisher, R. I.; Bernstein, S. H.; Kahl, B. S.; Djulbegovic, B.; Robertson, M. J.; Vos, S. d.; Epner, E.; Krishnan, A.; Leonard, J. P.; Lonial, S.; Stadtmauer, E. A.; O'Connor, O. A.; Shi, H.; Boral, A. L.; Goy, A., *J. Clin. Oncol.* **2006**, *24*, 4867-4874.
32. Gupta, N.; Labotka, R.; Liu, G.; Hui, A.-M.; Venkatakrishnan, K., *Invest. New Drugs* **2016**, *34*, 338-346.
33. Multiple myeloma. <https://www.cancer.org/cancer/multiple-myeloma.html>.

34. Cancer Stat Facts: Myeloma. <https://seer.cancer.gov/statfacts/html/mulmy.html>.
35. Bianchi, G.; Oliva, L.; Cascio, P.; Pengo, N.; Fontana, F.; Cerruti, F.; Orsi, A.; Pasqualetto, E.; Mezghrani, A.; Calbi, V.; Palladini, G.; Giuliani, N.; Anderson, K. C.; Sitia, R.; Cenci, S., *Blood* **2009**, *113*, 3040-3049.
36. Cenci, S.; van Anken, E.; Sitia, R., *Curr. Opin. Cell Biol.* **2011**, *23*, 216-222.
37. Obeng, E. A.; Carlson, L. M.; Gutman, D. M.; Harrington, W. J.; Lee, K. P.; Boise, L. H., *Blood* **2006**, *107*, 4907-4916.
38. Meister, S.; Schubert, U.; Neubert, K.; Herrmann, K.; Burger, R.; Gramatzki, M.; Hahn, S.; Schreiber, S.; Wilhelm, S.; Herrmann, M.; Jäck, H.-M.; Voll, R. E., *Cancer Res.* **2007**, *67*, 1783-1792.
39. Lü, S.; Wang, J., *Biomarker Research* **2013**, *1*, 13.
40. Radhakrishnan, S. K.; Lee, C. S.; Young, P.; Beskow, A.; Chan, J. Y.; Deshaies, R. J., *Mol. Cell* **2010**, *38*, 17-28.
41. Schwartz, R.; Davidson, T., *Oncology (Williston Park)* **2004**, *18*, 14.
42. Groll, M.; Huber, R.; Moroder, L., *J. Pept. Sci.* **2009**, *15*, 58-66.
43. Beck, P.; Dubiella, C.; Groll, M., *Biol. Chem.* **2012**, *393*, 1101-20.
44. Ozcan, S.; Kazi, A.; Marsilio, F.; Fang, B.; Guida, W. C.; Koomen, J.; Lawrence, H. R.; Sebt, S. M., *J. Med. Chem.* **2013**, *56*, 3783-3805.
45. Gallastegui, N.; Beck, P.; Arciniega, M.; Huber, R.; Hillebrand, S.; Groll, M., *Angew. Chem. Int. Ed.* **2012**, *51*, 247-249.
46. Basse, N.; Montes, M.; Maréchal, X.; Qin, L.; Bouvier-Durand, M.; Genin, E.; Vidal, J.; Villoutreix, B. O.; Reboud-Ravaux, M., *J. Med. Chem.* **2010**, *53*, 509-513.
47. Hasegawa, M.; Yasuda, Y.; Tanaka, M.; Nakata, K.; Umeda, E.; Wang, Y.; Watanabe, C.; Uetake, S.; Kunoh, T.; Shionyu, M.; Sasaki, R.; Shiina, I.; Mizukami, T., *Eur. J. Med. Chem.* **2014**, *71*, 290-305.
48. Beck, P.; Lansdell, T. A.; Hewlett, N. M.; Tepe, J. J.; Groll, M., *Angew. Chem. Int. Ed.* **2015**, *54*, 2830-2833.
49. Lansdell, T. A.; Hurchla, M. A.; Xiang, J.; Hovde, S.; Weilbaecher, K. N.; Henry, R. W.; Tepe, J. J., *ACS Chem. Biol.* **2013**, *8*, 578-587.

50. Azevedo, L. M.; Lansdell, T. A.; Ludwig, J. R.; Mosey, R. A.; Woloch, D. K.; Cogan, D. P.; Patten, G. P.; Kuszpit, M. R.; Fisk, J. S.; Tepe, J. J., *J. Med. Chem.* **2013**, *56*, 5974-5978.
51. Lawrence, H. R.; Kazi, A.; Luo, Y.; Kendig, R.; Ge, Y.; Jain, S.; Daniel, K.; Santiago, D.; Guida, W. C.; Sebti, S. M., *Bioorg. Med. Chem.* **2010**, *18*, 5576-92.
52. Ge, Y.; Kazi, A.; Marsilio, F.; Luo, Y.; Jain, S.; Brooks, W.; Daniel, K. G.; Guida, W. C.; Sebti, S. M.; Lawrence, H. R., *J. Med. Chem.* **2012**, *55*, 1978-1998.
53. Kazi, A.; Lawrence, H.; Guida, W. C.; McLaughlin, M. L.; Springett, G. M.; Berndt, N.; Yip, R. M.; Sebti, S. M., *Cell Cycle* **2009**, *8*, 1940-1951.
54. Beck, P.; Reboud-Ravaux, M.; Groll, M., *Angew. Chem. Int. Ed.* **2015**, *54*, 11275-11278.
55. Gaczynska, M.; Osmulski, P. A., *Antioxid Redox Signal* **2014**, *21*, 2286-301.
56. Li, X.; Wood, T. E.; Sprangers, R.; Jansen, G.; Franke, N. E.; Mao, X.; Wang, X.; Zhang, Y.; Verbrugge, S. E.; Adomat, H.; Li, Z. H.; Trudel, S.; Chen, C.; Religa, T. L.; Jamal, N.; Messner, H.; Cloos, J.; Rose, D. R.; Navon, A.; Guns, E.; Batey, R. A.; Kay, L. E.; Schimmer, A. D., *Journal of the National Cancer Institute* **2010**, *102*, 1069-1082.
57. McDaniel, T. J.; Lansdell, T. A.; Dissanayake, A. A.; Azevedo, L. M.; Claes, J.; Odom, A. L.; Tepe, J. J., *Bioorg. Med. Chem.* **2016**.
58. de Wilt, L. H.; Jansen, G.; Assaraf, Y. G.; van Meerloo, J.; Cloos, J.; Schimmer, A. D.; Chan, E. T.; Kirk, C. J.; Peters, G. J.; Kruyt, F. A., *Biochem. Pharmacol.* **2012**, *83*, 207-17.
59. Huber, Eva M.; Heinemeyer, W.; Groll, M., *Structure* **23**, 407-417.
60. Gurnos, J., *Quinolines: Part I. In The Chemistry of Heterocyclic Compounds*. John Willey & Sons, Inc.: Hoboken, NJ, 1977; Vol. 32.
61. Dobbin, L., *Journal of Chemical Education* **1934**, *11*, 596.
62. Batista, V. F.; Pinto, D. C. G. A.; Silva, A. M. S., *ACS Sustainable Chem. Eng.* **2016**, *4*, 4064-4078.
63. Collin, G.; Höke, H., Quinoline and Isoquinoline. In *Ullmann's Encyclopedia of Industrial Chemistry*, Wiley-VCH Verlag GmbH & Co. KGaA: 2000.
64. Majumder, S.; Gipson, K. R.; Odom, A. L., *Org. Lett.* **2009**, *11*, 4720-3.
65. Odom, A. L.; McDaniel, T. J., *Acc. Chem. Res.* **2015**, 150821102447001.
66. Odom, A. L., *Dalton Trans* **2005**, 225-33.



67. Marjumder, S., *Ph. D. Dissertation, Michigan State University* **2009**.
68. Vitaku, E.; Smith, D. T.; Njardarson, J. T., *J. Med. Chem.* **2014**, *57*, 10257-10274.
69. Gaczynksa, M.; Osmulski, P. A., *Methods Mol. Biol.* **2005**, *3*, 301.
70. Marangoni, A. G., *Enzyme Kinetics: A Modern Approach*. John Wiley & Sons: 2003.
71. Lee, S.-W.; Kim, J.-H.; Park, Y.-B.; Lee, S.-K., *Ann. Rheum. Dis.* **2009**, *68*, 1761-1767.
72. Nencioni, A.; Grunebach, F.; Patrone, F.; Ballestrero, A.; Brossart, P., *Leukemia* **2006**, *21*, 30-36.
73. Napetschnig, J.; Wu, H., *Annual Review of Biophysics* **2013**, *42*, 443-468.
74. Sors, A.; Jean-Louis, F.; Pellet, C.; Laroche, L.; Dubertret, L.; Courtois, G.; Bachelez, H.; Michel, L., *Blood* **2006**, *107*, 2354-63.
75. Harris, S. A.; Ciszewski, J. T.; Odom, A. L., *Inorganic chemistry* **2001**, *40*, 1987-8.
76. Shi, Y.; Hall, C.; Ciszewski, J. T.; Cao, C.; Odom, A. L., *Chem Commun (Camb)* **2003**, 586-7.
77. Novak, A.; Blake, A. J.; Wilson, C.; Love, J. B., *Chemical communications* **2002**, 2796-7.
78. Gokel, G. W.; Widera, R. P.; Weber, W. P., *Organic Syntheses* **1976**, *55*, 232.
79. Li, A.-H.; Beard, D. J.; Coate, H.; Honda, A.; Kadalbajoo, M.; Kleinberg, A.; Laufer, R.; Mulvihill, K. M.; Nigro, A.; Rastogi, P.; Sherman, D.; Siu, K. W.; Steinig, A. G.; Wang, T.; D., W.; A.P., C.; Mulvihill, M. J., *Synthesis* **2010**, 1678-1686.
80. Dissanayake, A. A., *Ph. D. Dissertation, Michigan State University* **2013**.

## Chapter 3: Quantifying Ancillary Ligand Effects in Titanium(IV) Catalyzed Hydroamination<sup>1</sup>

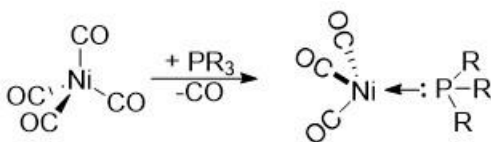
### 3.1 Introduction

Catalysis is indisputably one of the most important expressions in chemical innovation. Without catalysis our world would be immobile, dirty, hungry and unable to combat diseases.<sup>2</sup> A pivotal step towards designing and optimizing a catalyst, is understanding the affects that the ancillary ligands have on the metal center. For late transition metals, such as palladium, Tolman and others developed parameterization methods for phosphines ( $\text{PR}_3$ , where R = many different groups).<sup>3</sup> While phosphines are the most widely used ancillary ligands for that class of molecules, there is no standard ancillary ligand found for high valent chemistry where many different types of ligands are common. As a result, the problem of understanding the donor abilities of ligands for high valent metals is amplified due to the multitude of different ancillaries. Nevertheless, high valent metal centers like titanium(IV) are incredibly important to produce large scale commodity chemicals. For instance, polyolefins are made *via* Ziegler-Natta polymerization on massive scales, estimated at over 35 pounds of polymer per person on Earth per year.<sup>4-5</sup> High valent metals are even used to produce specialty chemicals, such as epoxides made through Sharpless epoxidation.<sup>6-7</sup> Despite how important high valent metal catalysis is there are limited tools for systematic catalyst optimization. In this chapter, we will discuss the detailed information that can be gained in high valent catalysis by using our experimentally defined parameterization system. This simple method can provide insight into the importance of ancillary ligand electronics and size for new catalyst designs, give clues into the nature of the catalyst at the rate determining steps, and alert the researcher to side reactions or competing catalyst degradation.

### 3.2 Background

For low valent transition metal chemistry, simple metrics for steric and donor properties have proven to be powerful tools for catalyst optimization.<sup>8</sup> Chadwick Tolman's review on electronic and steric effects of phosphines ligands, and their applications towards low valent catalysis bestowed the chemist with the necessary tools for rational catalyst optimization.<sup>3</sup> Tolman gave a single-parameter metric for sterics (i.e. the Tolman cone angle, or TCA) and by using the CO stretching frequencies in  $\text{Ni}(\text{CO})_3(\text{PR}_3)$  complexes gave a single-parameter metric for the donor properties.

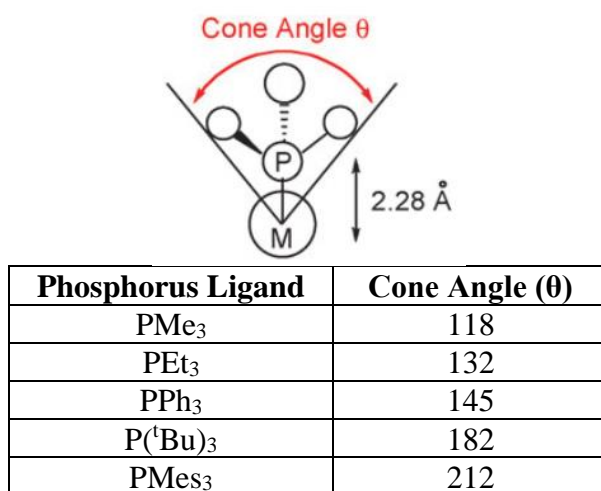
Using CO stretching frequencies to parametrize ligand effects on late transition metals predates Tolman's review. In 1959, Wilkinson and co-workers reported the CO stretching frequencies of transition metal carbonyls bearing phosphine/amine donors.<sup>9</sup> A few years later, Strohmeier and co-workers<sup>10</sup> demonstrated that phosphorus ligands could be ranked in an electronic series based off the CO stretching frequency for a variety of transition metal carbonyls. Tolman proposed using the CO stretching frequency of  $\text{Ni}(\text{CO})_3(\text{PR}_3)$  complexes as an experimental measure of electronics.<sup>11</sup> Doing so, quantifies the electronic effect (i.e. donor ability) of the phosphine ligand at the metal center, which he used as his electronic parameter ( $\chi$ ). Shown is **Figure 3.1**, is a small collection of CO stretching frequencies.



Phosphorus Ligand	CO $\nu$ , $\text{cm}^{-1}$
$\text{PF}_3$	2111
$\text{PCl}_3$	2097
$\text{P}(\text{OEt})_3$	2077
$\text{PPh}_3$	2069
$\text{PMe}_3$	2064

**Figure 3.1.** Tolman Electronic Parameter ( $\chi$ ).<sup>12</sup>

Later, Tolman introduced his iconic cone angle once it became clear that the ability of phosphorus ligands to compete for coordination positions on Ni(0) could not be explained in terms of their electronic character.<sup>3, 13</sup> Tolman's cone angle (assuming all three substituents on the phosphine are the same) is the apex angle of a cylindrical cone, that is centered at 2.28 Å from the center of the phosphorus atom, this he used as his steric parameter ( $\theta$ ). Shown is Figure 3.2, is a small collection of phosphines with their respected cone angles.



**Figure 3.2.** Tolman Cone Angle ( $\theta$ ).<sup>12</sup>

By using a single parameter for electronics ( $\chi$ ) and a single parameter for sterics ( $\theta$ ), these properties could be fit into Equation 1, where a, b and c are fitting coefficients and Z is the property being investigated.

$$Z = a + b(\chi) + c(\theta) \quad \text{Equation 1}$$

Using this mathematical model, he was able to show how the sterics and electronics of the phosphorus ligands correlate to a variety of applications, such as; ionization potentials of free phosphorus ligands, <sup>13</sup>C NMR chemical shifts of the carbonyls in Ni(CO)<sub>3</sub>L complexes, and enthalpies of reaction of phosphorus ligands with *trans*-[MePt(PMe<sub>2</sub>Ph)<sub>2</sub>(THF)]<sup>+</sup>.<sup>3, 14-15</sup> Ideally, this is the goal for high-valent metal based catalysis; i.e. being able to build a mathematical model to show the exact relationship between the sterics and electronics for the property being

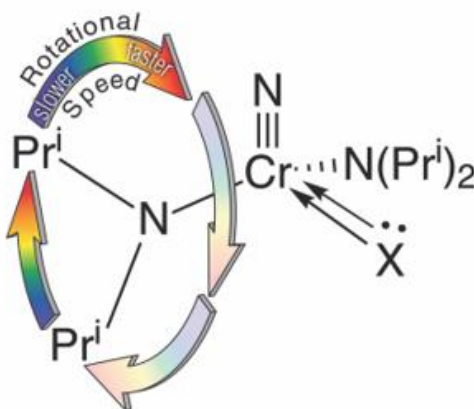
investigated. However, methods for determining donor abilities of ligands on high-valent transition metals are less well-known.

As stated previously, there are many common ancillaries for high valent metal systems. Titanium(IV), for example, has many common ancillaries, such as, cyclopentadienyl, chloride, bromide, carboxylate, phenoxide, pyrrolide, *tert*-butoxide, hexafluoro-*tert*-butoxide. But, if I were to ask you to list these ligands from least donating to most could you definitively do it? Usually, pKa values were used, however, interactions with hydrogen do not account for  $\pi$ -donor effects, that are expected to be quite significant for ligands like dimethylamide.<sup>16</sup> At the time, there was no parameterization system suited for this task.

### 3.3 Ligand Donor Parameter (LDP)

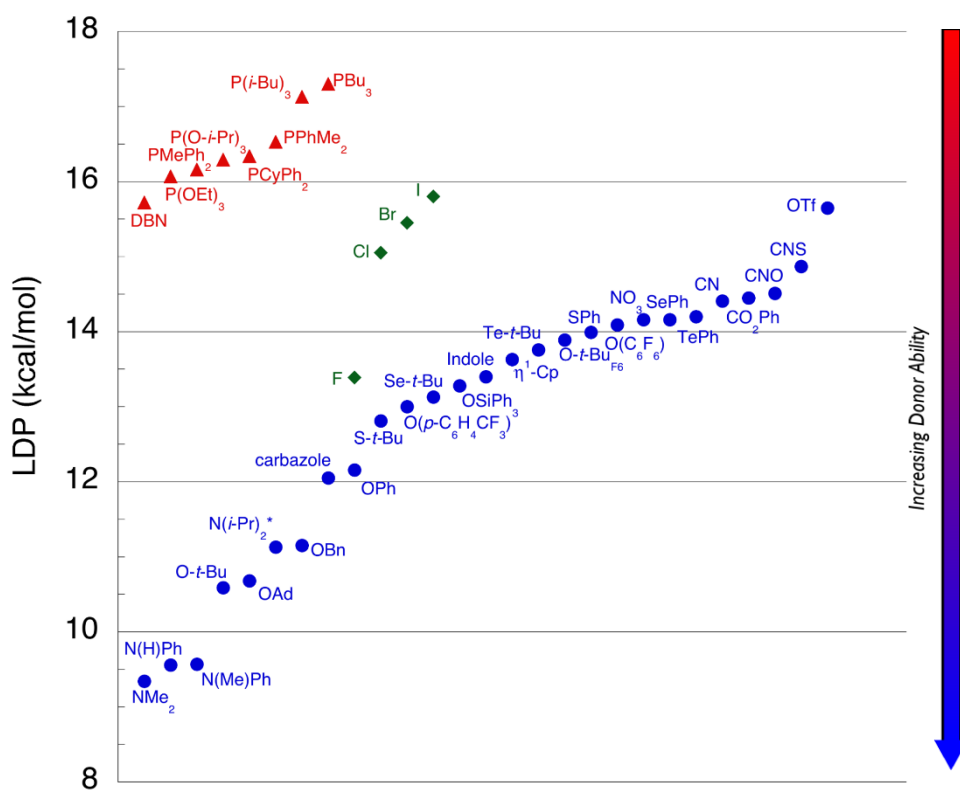
Which is why our group developed an experimentally defined donor parameter, which is similar to Tolman's electronic parameter  $\chi$ . Our donor parameter is applicable to high valent systems, and is based on synthetically versatile chromium(VI) nitride complexes. The values our system provides we call the Ligand Donor Parameter (LDP), which gives a measure of donor ability for ligands towards a high valent metal.<sup>8, 17</sup> In this system, one value is obtained that describes the combination of  $\sigma$ - and  $\pi$ -donor ability, just like Tolman's  $X$ . Previously in our group, we have been able to correlate this new parameter to many different effects that are sensitive to ligand variation, such as: angular overlap parameters, Hammett parameters for phenols,  $^{13}\text{C}$  NMR chemical shifts for tungsten alkylidene species, etc.<sup>8</sup>

The parameterization utilizes a competition between the diisopropylamide and the ligand, X, under interrogation in the compounds  $\text{NCr}(\text{NPr}^i)_2\text{X}$ . The ligand being interrogated has  $\sigma$ - and  $\pi$ -donation which is competing with the donation from the amide lone pair. As X becomes a strong donor the amido ligands rotate faster, as X becomes a weak donor the amido ligands rotate slower. In short, high LDP suggests the ligand is a weaker donor, and a low LDP suggests the ligand is a stronger donor. (**Figure 3.3**)



**Figure 3.3.** The Ligand Donor Parameter (LDP) system.<sup>1</sup>

Using NMR spectroscopy (typically spin saturation transfer) the rate constant for the amide rotation is measured. This can then be used to obtain a free energy barrier to rotation. To arrive at a temperature independent measurement, we assume that  $\Delta S^\ddagger = -9 \text{ cal/mol}\cdot\text{K}$ . This set value was determined using  $\text{NCr}(\text{NPr}^i_2)_2\text{I}$  over a wide temperature range. With these assumptions in place, the enthalpic barrier obtained is the LDP. **Figure 3.4**, shows some of ligands our group has explored of the last few years.<sup>8, 17-20</sup>

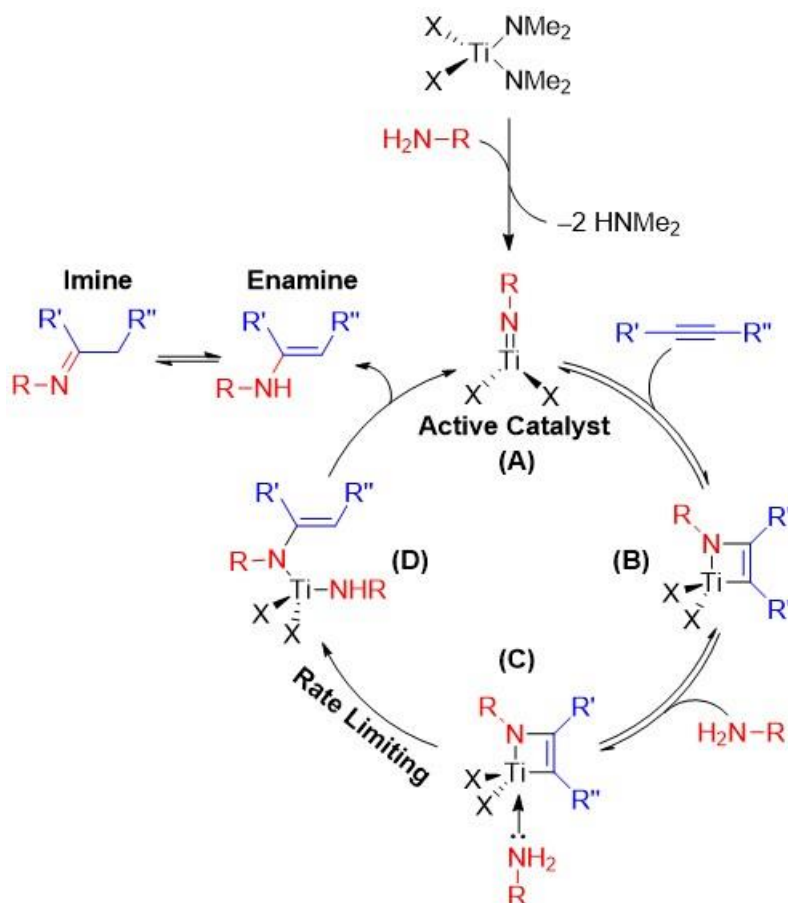


**Figure 3.4.** Collection of LDP values for a variety of ligands.

Using our experimentally defined donor parameter, we now have one piece to the puzzle needed to build a mathematical model. However, we still need a property to investigate and an experimental defined steric parameter.

### 3.4 Titanium-Catalyzed Hydroamination of Alkynes

Since this was our group's first attempt to model a reaction, we decided to examine a reaction that had been previously studied by our group and many others, that utilizes a variety of different ligands, titanium-catalyzed alkyne hydroamination.<sup>21</sup> Titanium-catalyzed alkyne hydroamination is an imide-based catalysis and is part of a growing group of methodologies for the efficient production of C–N and C–C bonds. The information we obtain here could be applicable to other titanium imido-based catalysis.<sup>22-23</sup> The mechanism for hydroamination, shown in **Figure 3.5**, was originally established by Bergman and co-workers.<sup>24-25</sup>



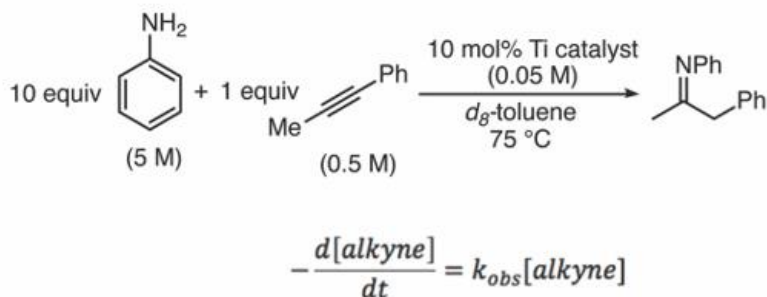
**Figure 3.5.** The proposed mechanism for titanium-catalyzed alkyne hydroamination.

Changes made to the ancillary ligands “X” can have dramatic effects. All of the precatalysts used in this study have two dimethylamide (NMe<sub>2</sub>) groups. These dimethylamides are



protolytically cleaved by a primary amine to generate the active catalyst, a titanium imido (Ti=NR, **A**). This titanium imido can undergo [2+2]-cycloaddition in the presence of an alkyne to form the 4-membered azatitanacyclobutene ring (**B**). After the coordination of another equivalent of amine, the Ti-C bond of the ring is protonated (**C** → **D**). Work done by Doye and co-workers has shown that, in titanium-catalyzed alkyne hydroamination, this protonolysis of the Ti-C bond is the rate determining step.<sup>25</sup> After another proton transfer, the organic product (enamine) is released, and the catalyst is regenerated (**D** → **A**).

Our goal for this study was to deduce how changing the sterics and electronics of the ancillary ligands affects the rate of the reaction. For our study, all of the reactions were run under pseudo-first order conditions with aniline and 1-phenylpropyne as substrates. Under these conditions the rate is then defined as being related to the consumption of alkyne. For all the catalyst used in this study, the major product generated is the imine shown in **Figure 3.6** and only a trace amount of the different regioisomer can be observed by GC/MS.

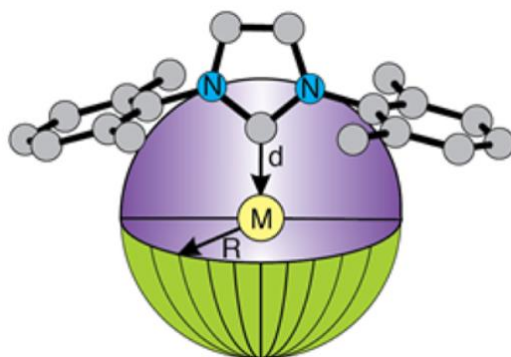


**Figure 3.6.** Kinetic conditions for this study.<sup>1</sup>

After determining the property we want to investigate, we are only missing an experimentally defined steric parameter before we can begin to build a model.

### 3.5 Percent Buried Volume (%V<sub>bur</sub>)

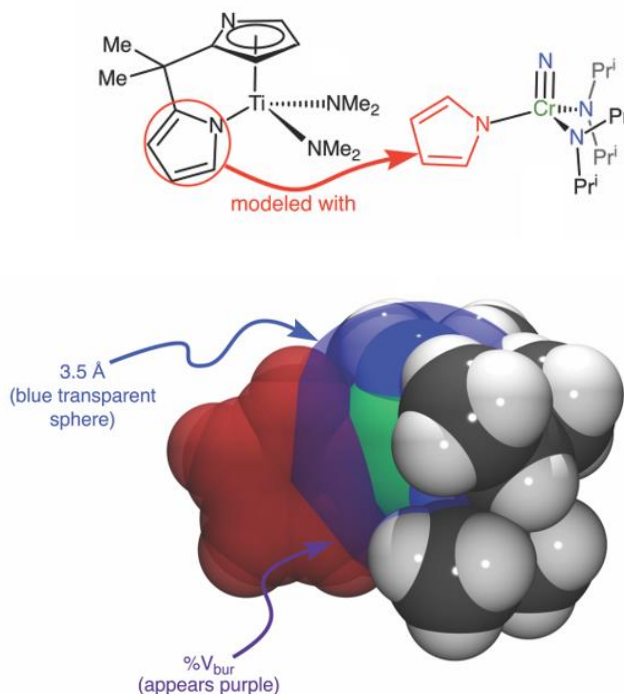
Inspired by Tolman's work with phosphines, we know he used a model that included a steric measure of the ligands. Instead of cone angle, which he used for phosphines, we decided to use a structurally based system developed by Cavallo and co-workers, Percent Buried Volume (%V<sub>bur</sub>).<sup>26</sup> Cavallo's system considers a 3.5 Å sphere around the metal center, this approximates the 1<sup>st</sup> coordination sphere of the metal. The ancillary ligand X under interrogation occupies a percentage of that sphere, this percentage is the %V<sub>bur</sub>. (See **Figure 3.7** and **3.8** for more details) This method has been shown to correlate well with Tolman's cone angle.<sup>12</sup> Since this method allows a wide variety of ligands to be compared, this makes %V<sub>bur</sub> a great option for high valent catalysis.



**Figure 3.7.** Percent Buried Volume (%V<sub>bur</sub>) is defined as the percent of the total volume of a sphere occupied by a ligand. For %V<sub>bur</sub> calculations 3.5 Å was selected as the value for the sphere radius (R) and metal-ligand length (d) is determined from the X-ray crystallography.<sup>26</sup>

For our study, the sterics (%V<sub>bur</sub>), and the electronics (LDP), were modeled off of chromium complexes. Doing this allows the values we obtain to potentially be applied to other high-valent metal catalyses. For instance, in our system the ligands we are interested in studying are symmetrical bidentate dianionic ligands, like the dipyrrolylmethane derivative shown in **Figure 3.8**. The chromium complexes using the heterocycle involved in the ligand are used to

determine the LDP and %  $V_{\text{bur}}$ . The linkers on the bidentate derivatives on titanium are ignored for this model. In short, the %  $V_{\text{bur}}$  and LDP is derived from half of the chelate. Take for example  $\text{Ti}(\text{dpm})(\text{NMe}_2)_2$ , which has a dipyrrolylmethane ligand, this ligand is modeled using the chromium complex bearing one pyrrole ligand. This relationship is highlighted at the top of **Figure 3.8**. The space filling model, shown at the bottom of **Figure 3.8**, represents the %  $V_{\text{bur}}$  on the chromium-pyrrole complex. The ligand under interrogation, pyrrole (shown in red), overlaps with the 3.5 Å sphere (shown as transparent blue); the percentage of this overlap (shown as purple) is the %  $V_{\text{bur}}$ .



**Figure 3.8.** Representation of how % $V_{bur}$  is measured. **(a) Top:** The catalyst  $Ti(dpm)(NMe_2)_2$  was modeled from the unsubstituted chromium-pyrrole complex. This chromium complex is used to measure both electronics and sterics. **(b) Bottom:** A space-filling model representing the chromium-pyrrole complex, used to determine % $V_{bur}$ . The ligand of interest, pyrrole (shown in red), overlaps with the blue 3.5 Å sphere. The color mixing from this overlap (shown as purple) is the % $V_{bur}$ .<sup>1</sup>

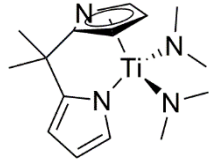
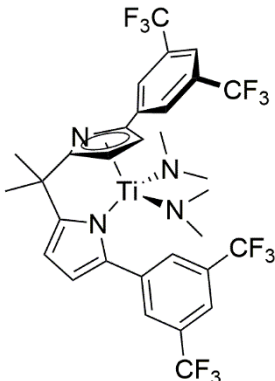
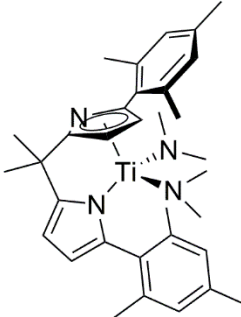
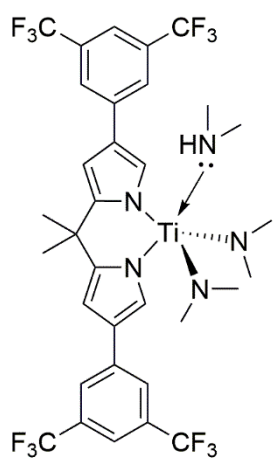
In order to build a mathematical model for understanding the reaction, we developed a series of related ligands base on pyrrole and indole with various steric and electronic properties. Once the LDP, % $V_{bur}$  and rate constants are in hand we can use Equation 2 to model the reaction.

$$k_{obs} \times 10^4 = a + b(LDP) + c(\%V_{bur}) \quad \text{Equation 2}$$

### 3.6 Synthesis, Kinetics and Model Progression

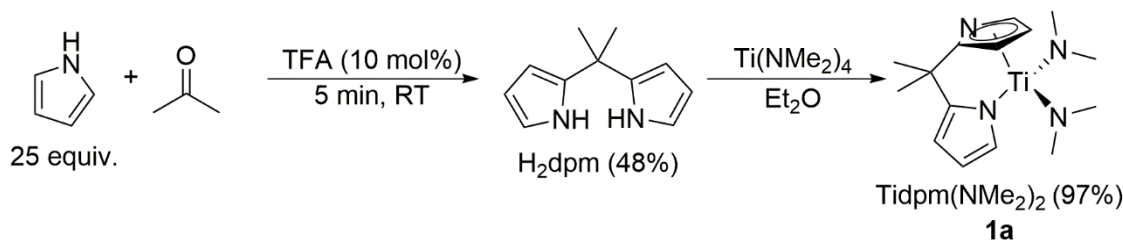
*It is my intent to present this section in such a way that details the progression of this project from beginning to end. This project was a deep collaboration between Brennan Billow and myself. Brennan was responsible for the “chromium side”, where he determined the LDP, % $V_{bur}$ , and later developed the model we now use. I was responsible for the “titanium side”, where I synthesized the different mono- and bi-dentate ligands and preformed the kinetic studies. In this section, I will describe the progression of this project, and the hurdles we encountered, from my perspective.*

Previously, our group has explored titanium 2,2'-diarylpyrrolylmethane and 3,3'-diarylpyrrolylmethane derivatives.<sup>27-28</sup> These studies provide the first glimpse into how changing the steric and electronic properties, of the ligands, effects the hydroamination reaction. **Figure 3.9** summarizes the findings.

Entry	Precatalyst	$K_{\text{obs}} (\times 10^{-7} \text{ s}^{-1})$
A	 $\text{Ti}(\text{dpm})(\text{NMe}_2)_2$ ( <b>1a</b> )	$1976 \pm 130$
B	 $\text{Ti}(\text{dpm}^{2-[\text{C}_6\text{H}_3(\text{CF}_3)_2]})(\text{NMe}_2)_2$ ( <b>1c</b> )	$780 \pm 30$
C	 $\text{Ti}(\text{dpm}^{2-\text{Mes}})(\text{NMe}_2)_2$	$403 \pm 30$
D	 $\text{Ti}(\text{dpm}^{3-[\text{C}_6\text{H}_3(\text{CF}_3)_2]})(\text{NMe}_2)_2$ ( <b>5</b> )	$6963 \pm 582$

**Figure 3.9.** Observed rate constants for various titanium dipyrrolemethane catalysts.<sup>27-28</sup>

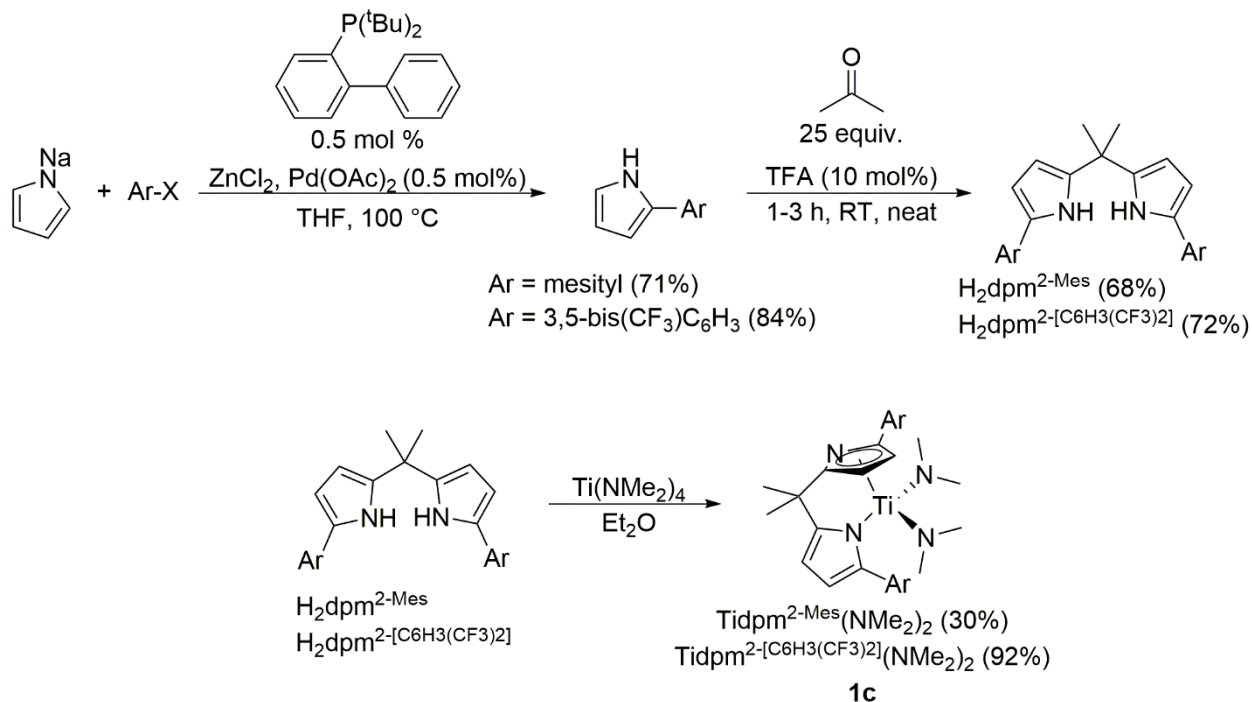
When comparing the rates from the 2,2'-diarylpyrrolylmethane and 3,3'-diarylpyrrolylmethane derivatives to the base structure,  $\text{Ti}(\text{dpm})(\text{NMe}_2)_2$  (**1a**), some trends arise: (1) increasing the size of the ligand, i.e. comparing **A** to **B** or **A** to **C**, decreases the rate. (2) introducing electron-withdrawing groups onto the dipyrrolylmethane moiety, i.e. comparing **B** to **C** or **A** to **D**, increases the rate. Based on our groups initial studies, we observe a crude relationship on how the sterics and electronics effects the rate of the reactions. That is, larger ancillary ligands tend to decrease the rate, whereas, electron-withdrawing ligands (i.e. electron deficient ligands) increase the rate. These findings provided a rational starting point for this project. *It is worth highlighting that to determine the electronics (LDP) and sterics ( $\%V_{bur}$ ) for each ligand, a viable synthetic route must be made for not only the chelating version on titanium, but, for half of their respected chelate for the chromium system as well.*



**Scheme 3.1.** Synthesis of  $\text{H}_2\text{dpm}$  and  $\text{Ti}(\text{dpm})(\text{NMe}_2)_2$  (**1a**).

The  $\text{H}_2\text{dpm}$  ligand is readily prepared *via* the TFA-catalyzed condensation of acetone in the presence of a large excess of pyrrole. The procedure, developed by Lindsey and co-workers<sup>29</sup>, is easily scalable to multiple gram quantities (>5 grams of product obtained). Using fractional distillation, the pure product can be isolated and starting material can be recovered. Thus, providing an efficient and inexpensive ligand synthesis. Addition of  $\text{H}_2\text{dpm}$  to  $\text{Ti}(\text{NMe}_2)_4$  produces our  $\text{Ti}(\text{dpm})(\text{NMe}_2)_2$  (**1a**) pre-catalyst in near quantitative yield. Through a similar synthesis the dipyrrolylmethane derivatives  $\text{H}_2\text{dpm}^{2-[\text{C}_6\text{H}_3(\text{CF}_3)_2]}$  and  $\text{H}_2\text{dpm}^{2-\text{Mes}}$  can be made. The synthesis of 2-arylpyrroles is accomplished by using the procedure established by Sadighi and co-workers.<sup>30</sup>

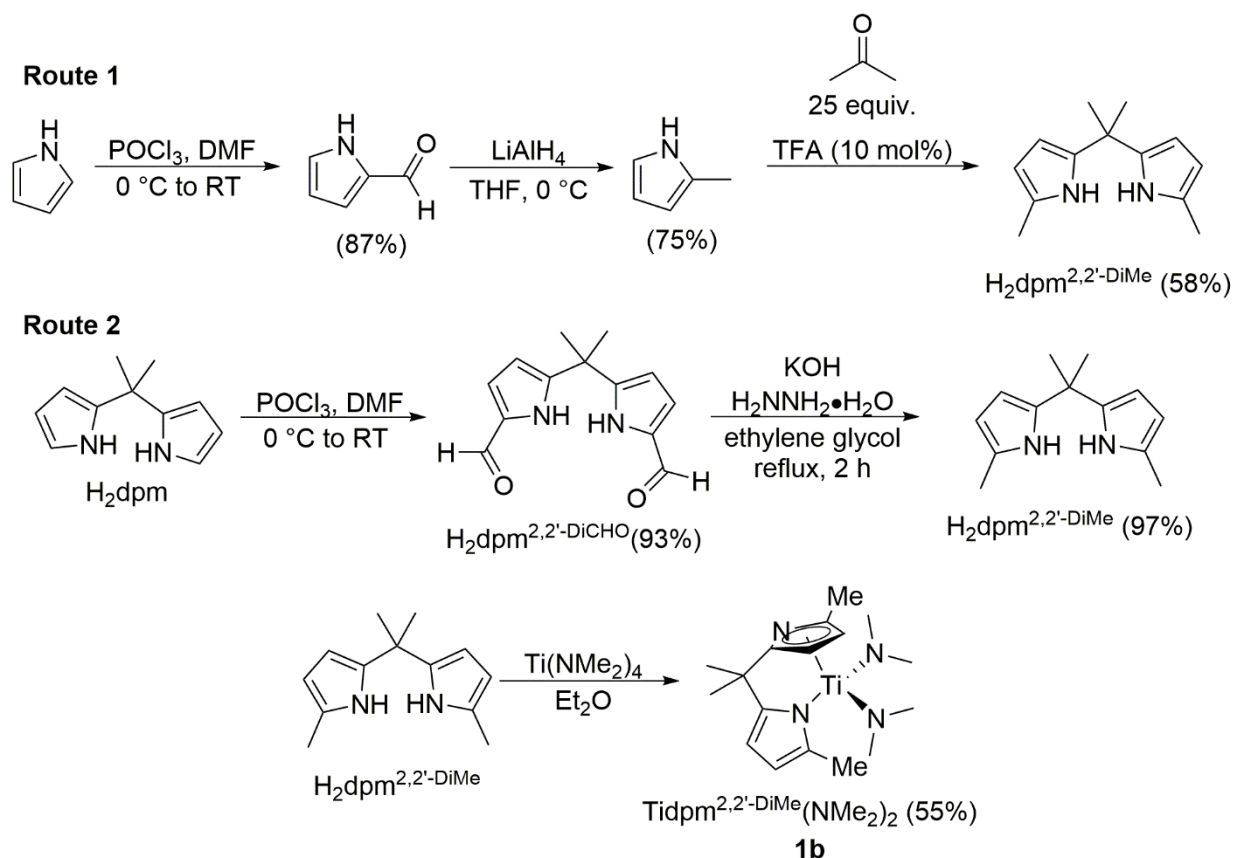
This procedure allows for the synthesis of 2-arylpyrroles, with a variety of electronic and steric profiles, on multigram scales and high yields. Shown below, in **Scheme 3.2**, is the synthesis of  $\text{H}_2\text{dpm}^{2\text{-}[\text{C}_6\text{H}_3(\text{CF}_3)_2]}$  and  $\text{H}_2\text{dpm}^{2\text{-Mes}}$  and their respected titanium pre-catalysts.<sup>27</sup>



**Scheme 3.2.** Synthesis of  $\text{H}_2\text{dpm}^{2\text{-}[\text{C}_6\text{H}_3(\text{CF}_3)_2]}$  and  $\text{H}_2\text{dpm}^{2\text{-Mes}}$  and titanium precatalysts.<sup>27</sup>

Starting from these known compounds, we can envision similar synthetic routes to modify the sterics and electronics of these ligands. As shown previously, incorporation of the aryl groups onto the 2-position of the dipyrrolylmethane moiety greatly decreases the rate from the base-structure,  $\text{Ti}(\text{dpm})(\text{NMe}_2)_2$  (**1a**). To gain a better insight into the steric and electronic demands of the dipyrrolylmethane moiety, moving from a bulky but electron-withdrawing substituent (i.e. aryl) to a small but electron-donating substituent (i.e. methyl), would provide a valuable data point.



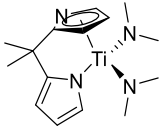
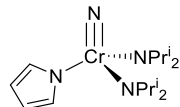
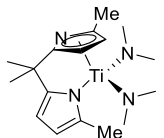
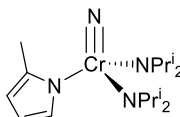
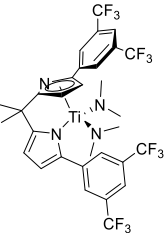
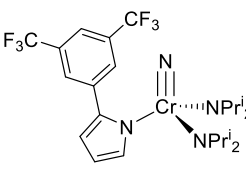


**Scheme 3.3.** Synthesis of  $\text{H}_2\text{dpm}^{2,2'\text{-DiMe}}$  and titanium precatalysts.

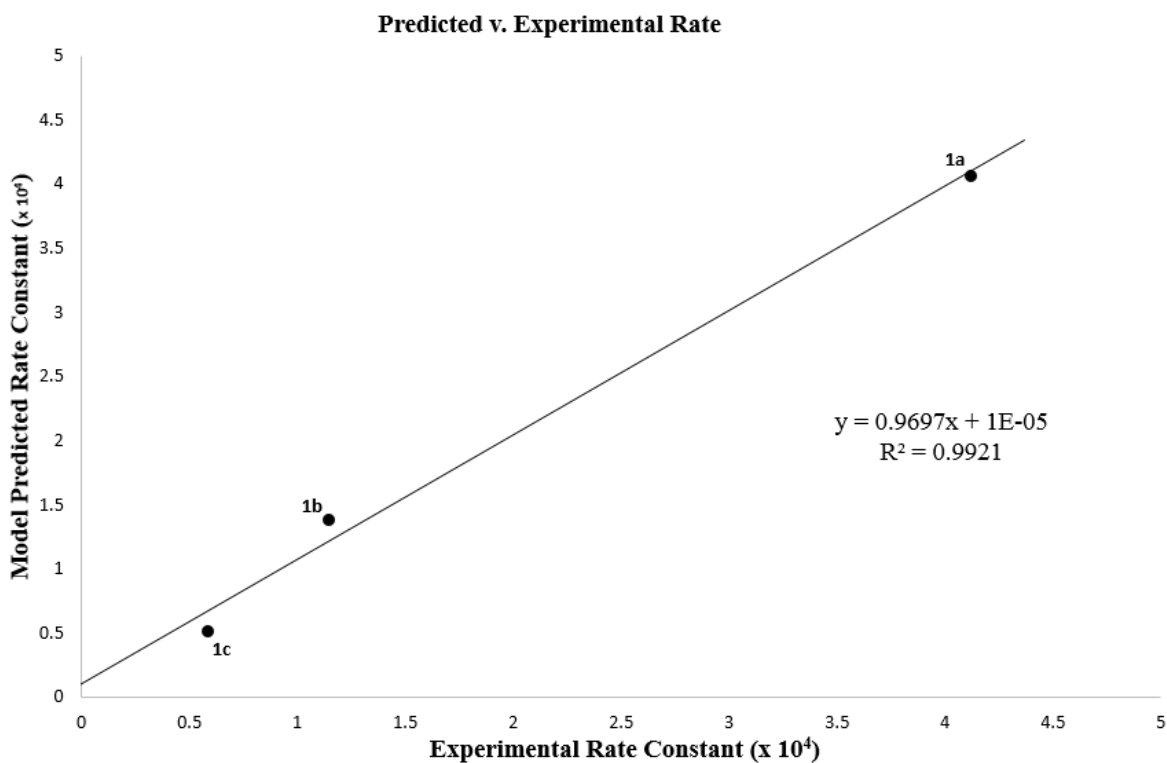
The synthesis of  $\text{H}_2\text{dpm}^{2\text{Me}}$  is shown above in **Scheme 3.3**. The synthesis of this ligand was originally achieved using Route 1. Starting from pyrrole, the pyrrole-2-carboxaldehyde can be synthesized, in high yield, *via* Vilsmeier-Haack formylation.<sup>31-32</sup> The aldehyde product is then reduced to give 2-methylpyrrole<sup>33</sup> that can then undergo the acid-catalyzed condensation with acetone to give the desired dipyrrolylmethane product. However, the scale-up of this condensation reaction resulted in lower yields. To seek a more advantageous route, we devised another synthesis starting from the readily-prepared  $\text{H}_2\text{dpm}$ . In a similar fashion,  $\text{H}_2\text{dpm}$  can undergo a double formylation to produce the  $\text{H}_2\text{dpm}^{2,2'\text{-DiCHO}}$  in high yields.  $\text{H}_2\text{dpm}^{2,2'\text{-DiCHO}}$  can undergo Wolff-Kishner reduction to yield the desired product,  $\text{H}_2\text{dpm}^{2\text{Me}}$ .<sup>34</sup> Unlike the initial route, this route was easily scalable with no depreciation in yield. Treating  $\text{Ti}(\text{NMe}_2)_4$  with  $\text{H}_2\text{dpm}^{2,2'\text{-DiMe}}$  yielded the

pre-catalyst  $\text{Ti}(\text{dpm}^{2,2'\text{-DiMe}})(\text{NMe}_2)_2$  which can be easily crystalized from a concentrated solution of pentane.

At this time, we decided to build a crude model with the data we had obtained to see what our initial results can tell us, as well as, potentially giving us insight to where to head next. We obtained the rate (using the conditions specified in **Section 3.3**, as well as, the LDP and %  $V_{\text{bur}}$  from the chromium complexes. However, the LDP and %  $V_{\text{bur}}$  for 2-mesitylpyrrole could not be determined due to its steric bulk. To understand how the electronics and sterics effect the rate of the reaction, we need to be able to accurately measure the LDP and %  $V_{\text{bur}}$ . Taking note of this, ligands we synthesize in the future will need to be less sterically bulky. From the data obtained, shown below in **Figure 3.10**, we can apply a least squares fit to build our initial model. Using this crude model, if we plot the calculated rate constant from the model versus our experimental rate constant, we obtain the plot shown in **Figure 3.11**. Even though this model was only built from a few data points we were excited to see that there indeed was a correlation. Motivated by these results, we began to synthesize new ligands to build a more robust model.

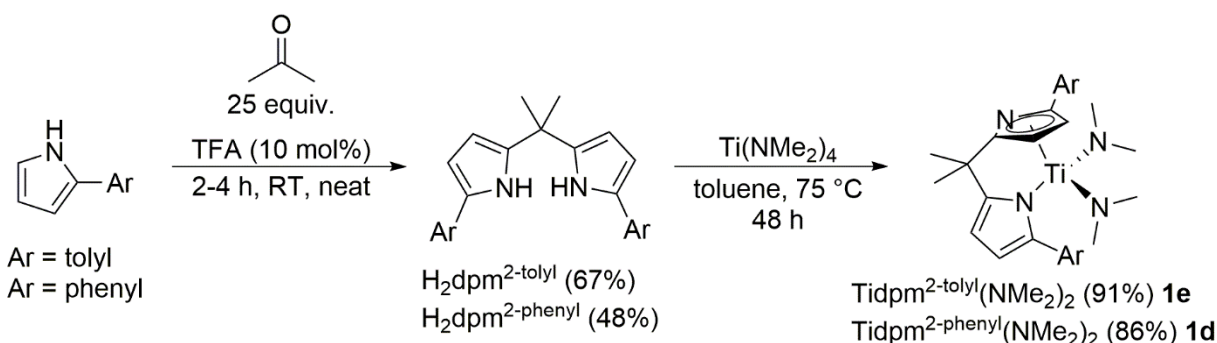
Ti Catalyst	Electronic Model LDP (kcal/mol)	Steric Model %V <sub>bur</sub>	k <sub>obs</sub> x 10 <sup>4</sup> (s <sup>-1</sup> )
 Ti(dpm)(NMe <sub>2</sub> ) <sub>2</sub> ( <b>1a</b> )	 13.64	20.4	4.16
 Ti(dpm-2,2'-DiMe)(NMe <sub>2</sub> ) <sub>2</sub> ( <b>1b</b> )	 13.46	23.7	1.35
 Ti(dpm-2-[C <sub>6</sub> H <sub>3</sub> (CF <sub>3</sub> ) <sub>2</sub> ])(NMe <sub>2</sub> ) <sub>2</sub> ( <b>1c</b> )	 14.32	27.9	0.581

**Figure 3.10.** Rates, LDP, and %V<sub>bur</sub> used for modeling catalysts **1a-1c**.



**Figure 3.11.** Plot of experimental rate constant versus model predicted rate constant for catalysts **1a-1c**.

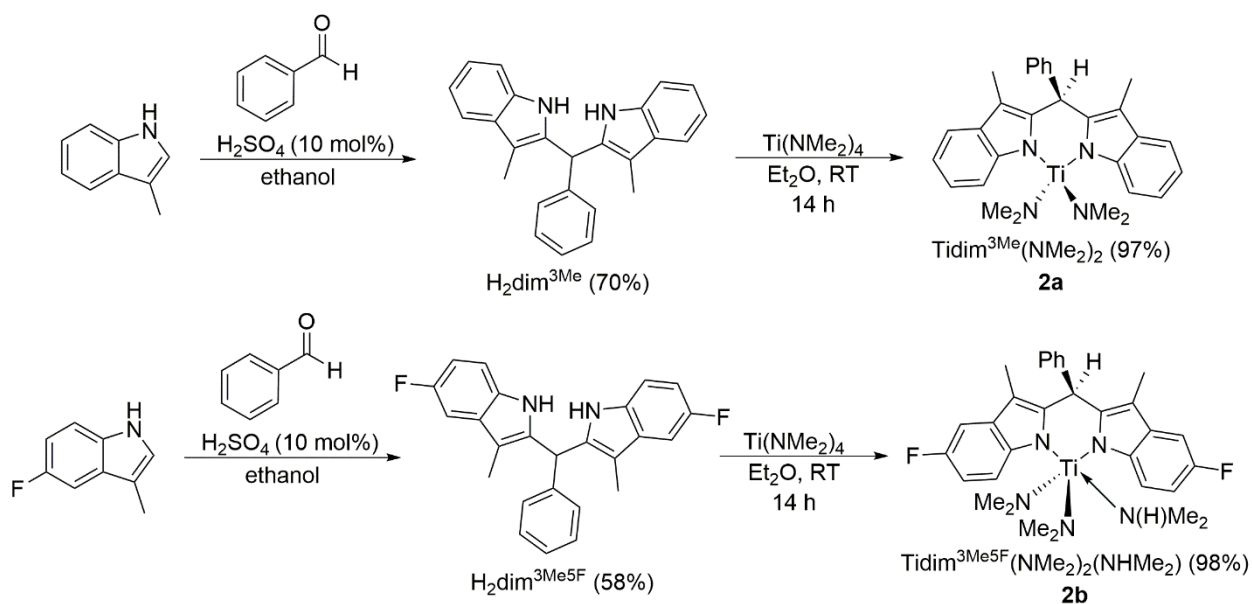
From our initial data, the three pre-catalysts seemed to differ more sterically than electronically. Moving forward we wanted to synthesize new ligands that were sterically similar but electronically different to gain a better understanding of how the electronics contribute to the rate. By utilizing Sadighi's 2-arylpyrrole procedure<sup>30</sup>, we can vary the electronics on the aryl groups without significantly impacting the sterics. Moving away from  $\text{H}_2\text{dpm}^{2-[\text{C}_6\text{H}_3(\text{CF}_3)_2]}$ , which has an electron deficient aryl groups to more electron rich aryl groups, we synthesized the *para*-tolyl and phenyl derivatives. The synthesis for  $\text{H}_2\text{dpm}^{2\text{-tolyl}}$ ,  $\text{H}_2\text{dpm}^{2\text{-phenyl}}$  and their respected titanium pre-catalysts is shown below in **Scheme 3.4**.



**Scheme 3.4.** Synthesis of  $\text{H}_2\text{dpm}^{2\text{-tolyl}}$ ,  $\text{H}_2\text{dpm}^{2\text{-phenyl}}$  and titanium precatalysts.

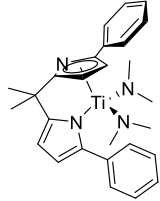
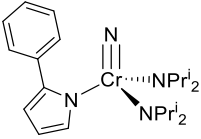
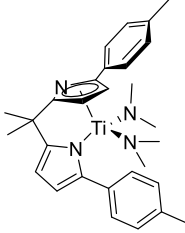
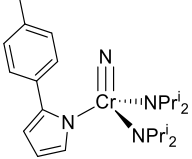
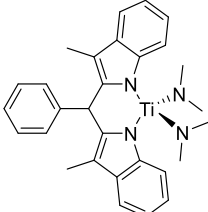
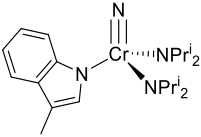
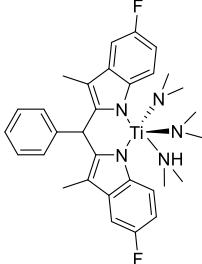
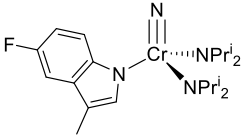
We wondered if the structurally similar diindolymethane derivatives would correlate well with our dipyrrolylmethanes. Mason and co-workers had previously explored these diindolymethane ligands for the ethylene polymerization.<sup>35-36</sup> One concern was that Mason's ligands were synthesized through the condensation of benzaldehyde with 3-methylindole. Meaning, the linker for this system are phenylmethane, whereas our linkers are dimethylmethane in the pyrrolyl ligands. Initially, we intended to keep the linkers the same for all our ligands to avoid any other influence that could affect the rate. However, the acid-catalyzed condensation of acetone with 3-methylindole produced low yields. (**Scheme 3.5**) Inevitably, we decided to continue using Mason's ligand and ligand synthesis. By using his procedure, we were also able to

prepare the analogous 5-fluoro derivative. The synthesis for  $\text{H}_2\text{dim}^{3\text{Me}}$ ,  $\text{H}_2\text{dim}^{3\text{Me5F}}$  and their respected titanium pre-catalysts is shown below in **Scheme 3.5**.

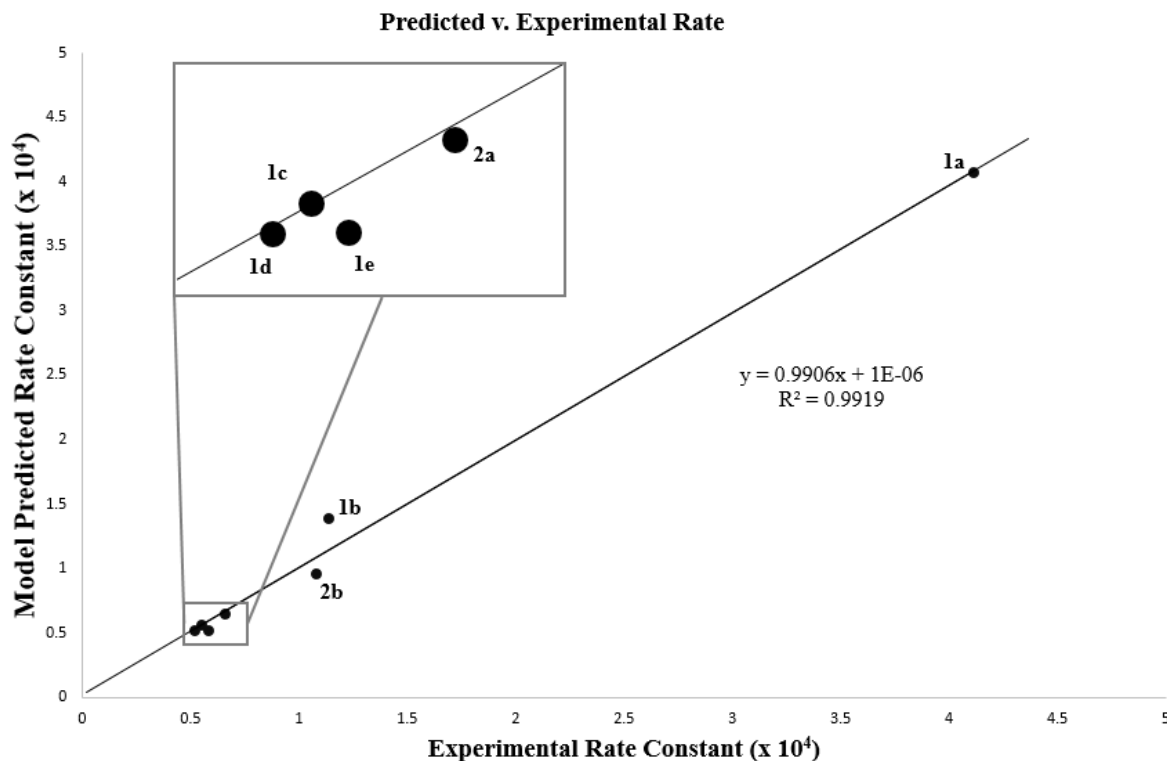


**Scheme 3.5.** Synthesis of diindolylmethane catalysts. **(a) Top:** Synthesis of  $\text{H}_2\text{dim}^{3\text{Me}}$  and titanium precatalyst. **(b) Bottom:** Synthesis of  $\text{H}_2\text{dim}^{3\text{Me5F}}$  and titanium precatalyst.

The rates, LDPs and %  $V_{\text{bur}}$  for these new ligands were collected. With this additional data, we updated our table and model to reflect the new data we had obtained. (**Figure 3.12**) The parameters we obtain from this model will be discussed in **Section 3.6**.

Ti Catalyst	Electronic Model LDP (kcal/mol)	Steric Model %V <sub>bur</sub>	k <sub>obs</sub> x 10 <sup>4</sup> (s <sup>-1</sup> )
 Ti(dpm <sup>2-phenyl</sup> )(NMe <sub>2</sub> ) <sub>2</sub> ( <b>1d</b> )	 14.03	27.1	0.522
 Ti(dpm <sup>2-tolyl</sup> )(NMe <sub>2</sub> ) <sub>2</sub> ( <b>1e</b> )	 13.91	26.7	0.552
 Ti(dim <sup>3Me</sup> )(NMe <sub>2</sub> ) <sub>2</sub> ( <b>2a</b> )	 12.49	22.6	0.662
 Ti(dim <sup>3Me5F</sup> )(NMe <sub>2</sub> ) <sub>2</sub> ( <b>2b</b> )	 12.66	22.6	1.08

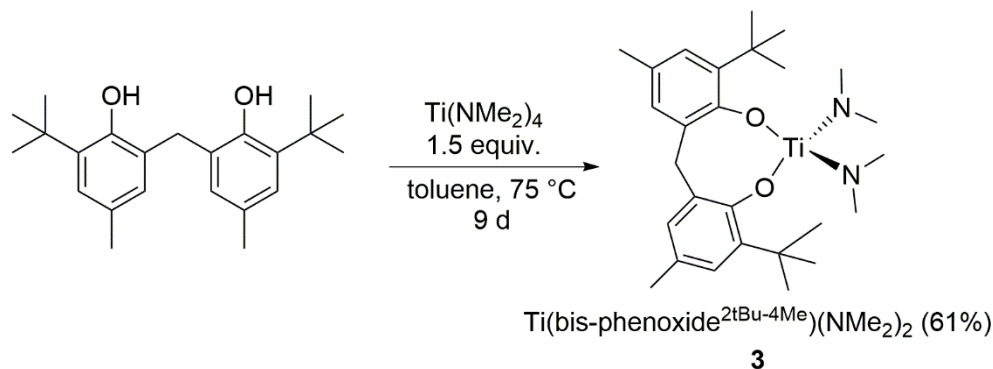
**Figure 3.12.** Rates, LDP, and %V<sub>bur</sub> used for modeling catalysts **1d-2b**.



**Figure 3.13.** Plot of experimental rate constant versus model predicted rate constant for catalysts **1d-2b**.

To our delight, the changes made to the linker seem to have no additional influence and the diindolylmethane and dipyrrolylmethane pre-catalysts correlated well with each other. These results indicate that we can indeed expand our model to other, structurally similar, heterocyclic ligands. This begs the question, can our model be expanded to more diverse ligand sets, other than heterocyclic ligands? As stated previously, there are many kinds of common ancillary ligands for titanium(IV). However, there are some general criteria we need to follow. For the titanium system, we want ligands that are dianionic, bidentate chelates. Also, the monodentate analogs of these ligands need to be compatible with the chromium system to obtain the LDP and %V<sub>bur</sub>. After deliberating, one potential candidate stood out from the rest, phenol-based ligands. Phenol-based ligands have been extensively studied for titanium-based catalyses<sup>37-39</sup>, including

hydroamination.<sup>21, 40-43</sup> Better yet, our group has also previously studied phenols using our LDP system<sup>8, 17</sup>, making them an excellent candidate. The first phenol-based ligand we decided to try was the commercially available 6,6'-Methylenebis(2-(tert-butyl)-4-methylphenol) ( $H_2bis$ -phenoxide<sup>2tBu-4Me</sup>), shown in **Scheme 3.6**. Previously, Beller and co-workers conducted a hydroamination study which included this ligand, but the precatalyst was never isolated.<sup>43</sup> Upon addition of the  $H_2bis$ -phenoxide<sup>2tBu-4Me</sup> to  $Ti(NMe_2)_4$ , in a 1:1 ratio, produced a mixture of  $Ti(bis$ -phenoxide<sup>2tBu-4Me</sup>)<sub>2</sub>,  $Ti(bis$ -phenoxide<sup>2tBu-4Me</sup>)( $NMe_2$ )<sub>2</sub> (**3**) and left over starting material. These products were unable to be separated at the time, but by increasing the equivalents of  $Ti(NMe_2)_4$  the preferred product  $Ti(bis$ -phenoxide<sup>2tBu-4Me</sup>)( $NMe_2$ )<sub>2</sub> (**3**) could be synthesized in high conversion. The remaining  $Ti(NMe_2)_4$  can be removed by washing with cold pentane.

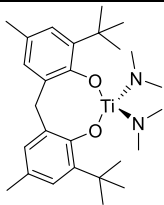
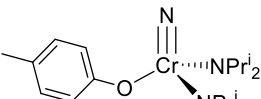
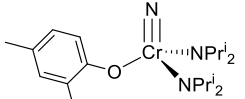


**Scheme 3.6.** Synthesis of  $Ti(bis$ -phenoxide<sup>2tBu-4Me</sup>)( $NMe_2$ )<sub>2</sub> (**3**).

Before further expanding this ligand set, we wanted to verify whether these phenol-based ligands would indeed correlate with our N-heterocyclic ligands. However, we encountered another complication with the chromium system. The monodentate analog (2-tert-butyl-4-methylphenol) on chromium was too bulky and interfered with the LDP measurement. However, unlike the 2-mesitylpyrrole, we could still obtain the % $V_{bur}$ . Because we were still able to measure the sterics of the ligand, we wondered if we could get an approximation of the LDP by using a smaller alkyl group, instead of *tert*-butyl. We hypothesized that using 2,4-dimethylphenol to measure the LDP,

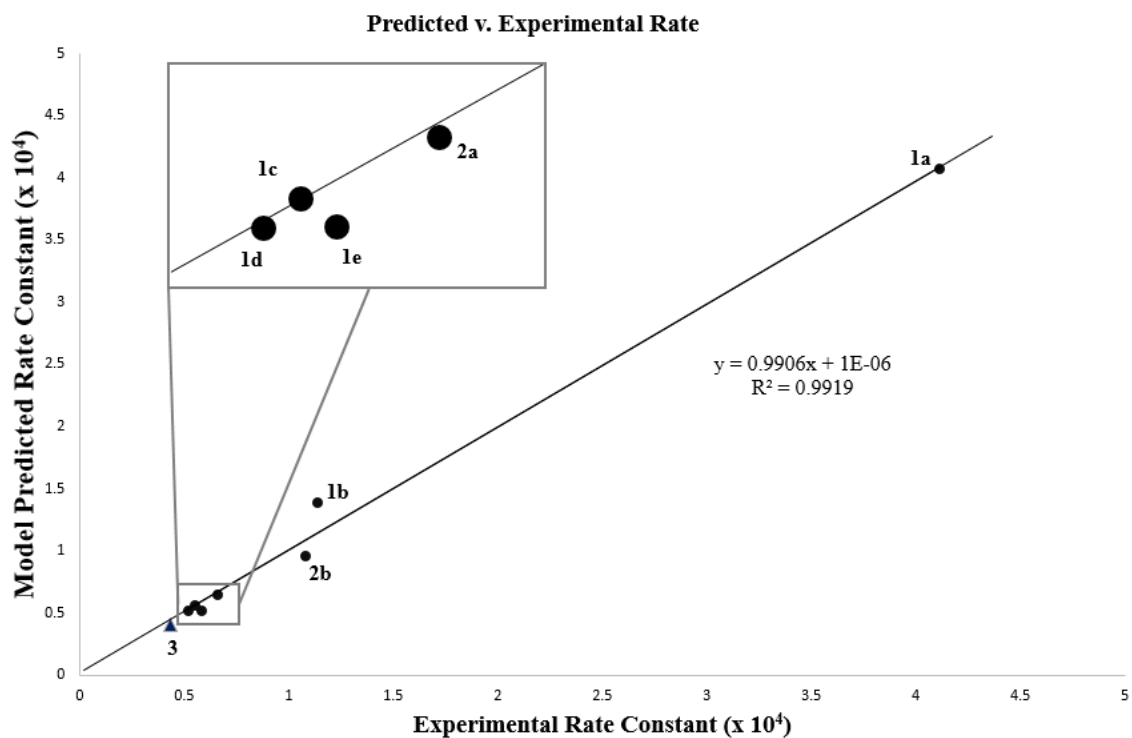


could give us a reasonable approximation for the donor ability of the bulkier analog. By using 2,4-dimethylphenol to obtain the LDP and 2-*tert*-butyl-4-methylphenol to obtain the %V<sub>bur</sub> we have all the necessary data. (**Figure 3.14**)

Ti Catalyst	Electronic Model LDP (kcal/mol)	Steric Model %V <sub>bur</sub> (if different)	k <sub>obs</sub> x 10 <sup>4</sup> (s <sup>-1</sup> )
 Ti(NMe <sub>2</sub> ) <sub>2</sub> (bis-phenoxide <sup>2tBu-4-Me</sup> ) ( <b>3</b> )	 11.98	 21.6	0.432

**Figure 3.14.** Rate, LDP, and %V<sub>bur</sub> used for modeling catalyst **3**.

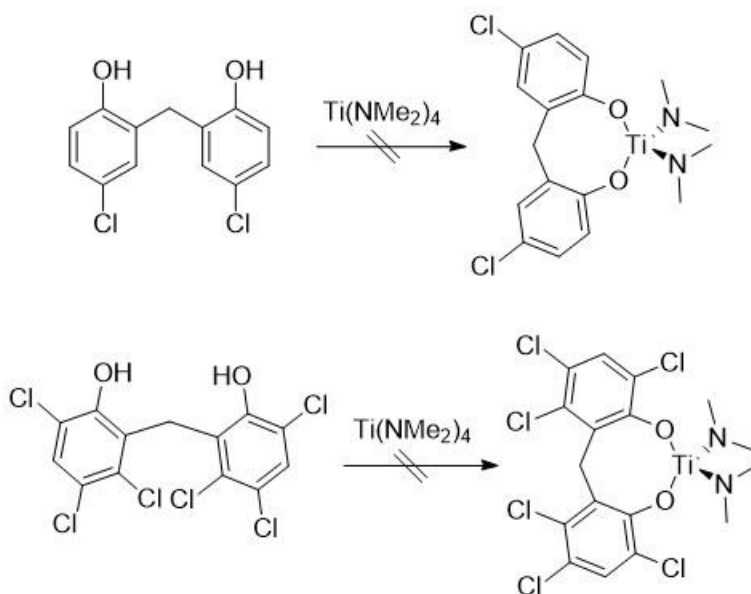
To our surprise, when we insert the data for the phenol-based ligand it correlates well with the pyrrole/indole-based model we had developed! (**Figure 3.15**) *From this point on, we used this same strategy to determine the LDP for other 2-*tert*-butylphenol derivatives.*



**Figure 3.15.** Plot of experimental rate constant versus model predicted rate constant for catalyst

**3.**

Using a similar approach that we used for the diindolylmethane derivatives, we began to synthesize more electronically and sterically different phenol-based ligands. This proved to be more difficult than expected, but these difficulties helped to identify possible flaws with this kind of ligand scaffold.

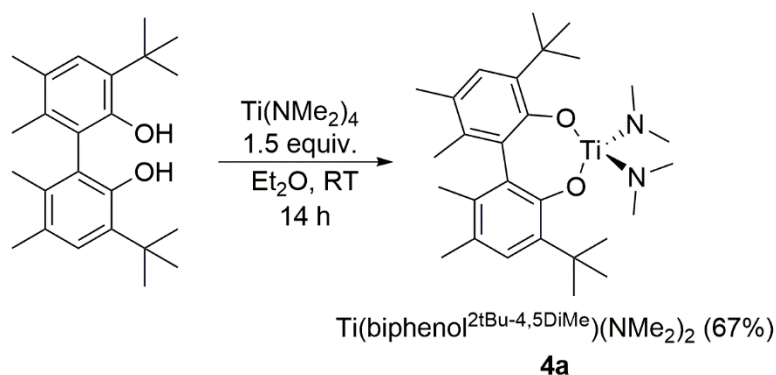


**Scheme 3.7.** Attempted syntheses of titanium methylene bisphenoxide-based precatalysts.

Looking back on these results we could identify some of the drawbacks with these methylene bisphenoxide ligands. First, insoluble dimers were produced without steric bulk in the *ortho* position. Second, making the phenol more electron deficient lead to hydrogen abstraction of the benzylic hydrogens and decomposition. Lastly, the synthesis of all these derivatives requires an excess of  $\text{Ti}(\text{NMe}_2)_4$  and can take days to go to completion. Taking all these drawbacks into consideration we began to search for a new phenol-based ligand motif. Since the steric bulk is essential to get monomeric products, the other complication seemed to arise from the linker itself.

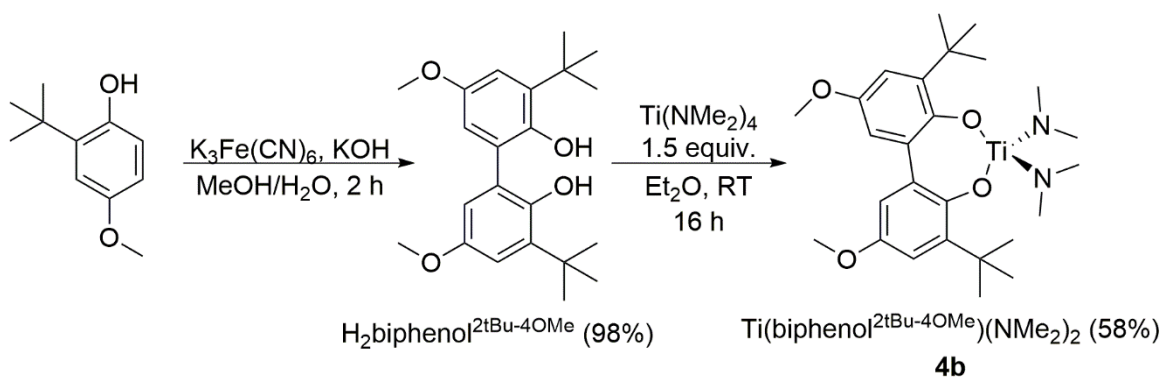
Beller and co-workers also explored biphenol derivatives in the same hydroamination study mentioned previously. One of the ligands they screened was the commercially available 3,3'-di-tert-butyl-5,5',6,6'-tetramethylbiphenyl-2,2'-diol ( $\text{H}_2\text{biphenol}^{2\text{tBu-4,5-DiMe}}$ ), but again, the precatalyst was never isolated.<sup>43</sup> Intrigued by this, we wondered if this could work for our model as well. One concern was that this biphenol doesn't have a linker, whereas all our current ligands do. However, as we previously saw with our diindolylmethane and dipyrrolylmethane derivatives changing the linker didn't seem to have any adverse effects. Keep in mind, that we also observed decomposition

when using some methylene bisphenoxide ligands; possibly due to the acidic benzylic hydrogens. But, by using a biphenol ligand motif we could alleviate this problem and potentially expand to other electronically different variants. From this perspective, it would be advantageous to determine if a linker is even necessary to correlate with our model. If the linker isn't necessary, it would open our model to even more diverse ligand sets. To this end, we decided to pursue this and synthesized  $\text{Ti}(\text{Biphenol}^{2\text{tBu-4,5-DiMe}})(\text{NMe}_2)_2$  (**4a**).



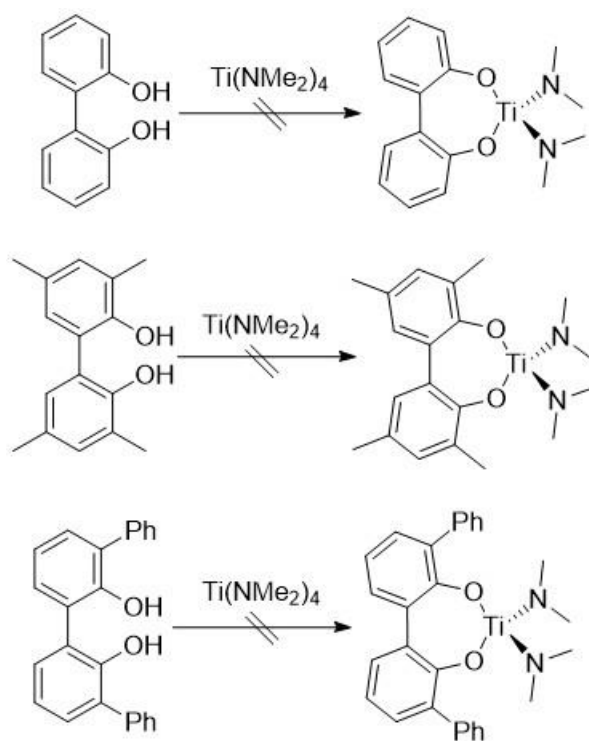
**Scheme 3.8.** Synthesis of  $\text{Ti}(\text{biphenol}^{2\text{tBu-4,5-DiMe}})(\text{NMe}_2)_2$  (**4a**).

To expand upon this new ligand, we also prepared another biphenol with similar steric but different electronic properties. Using a procedure by Ding and co-workers, we can obtain  $\text{H}_2\text{biphenol}^{2\text{tBu-4OMe}}$  through the iron-catalyzed oxidative homo-coupling of 2-*tert*-butylanisole.<sup>44</sup> Slow addition of  $\text{H}_2\text{biphenol}^{2\text{tBu-4OMe}}$  to  $\text{Ti}(\text{NMe}_2)_4$  produces the desired product  $\text{Ti}(\text{biphenol}^{4\text{tBu-4OMe}})(\text{NMe}_2)_2$  (**4b**) in moderate yield.



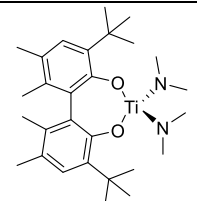
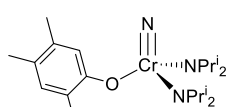
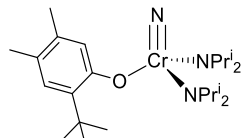
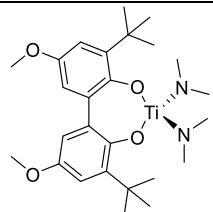
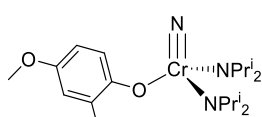
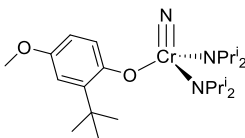
**Scheme 3.9.** Synthesis of  $\text{H}_2\text{biphenol}^{2\text{tBu}-4\text{OMe}}$  and  $\text{Ti}(\text{biphenol}^{2\text{tBu}-4\text{OMe}})(\text{NMe}_2)_2$  (**4b**).

It should be mentioned that at the same time we were exploring these biphenol derivatives, we also explored less bulky analogs as well. However, we again see the same trend as the bisphenoxide derivatives. Without the steric bulk, we observe high conversion to the unwanted  $\text{Ti}(\text{biphenol})_2$  or dimeric species. **Scheme 3.10** shows the attempted syntheses of other biphenol derivatives.

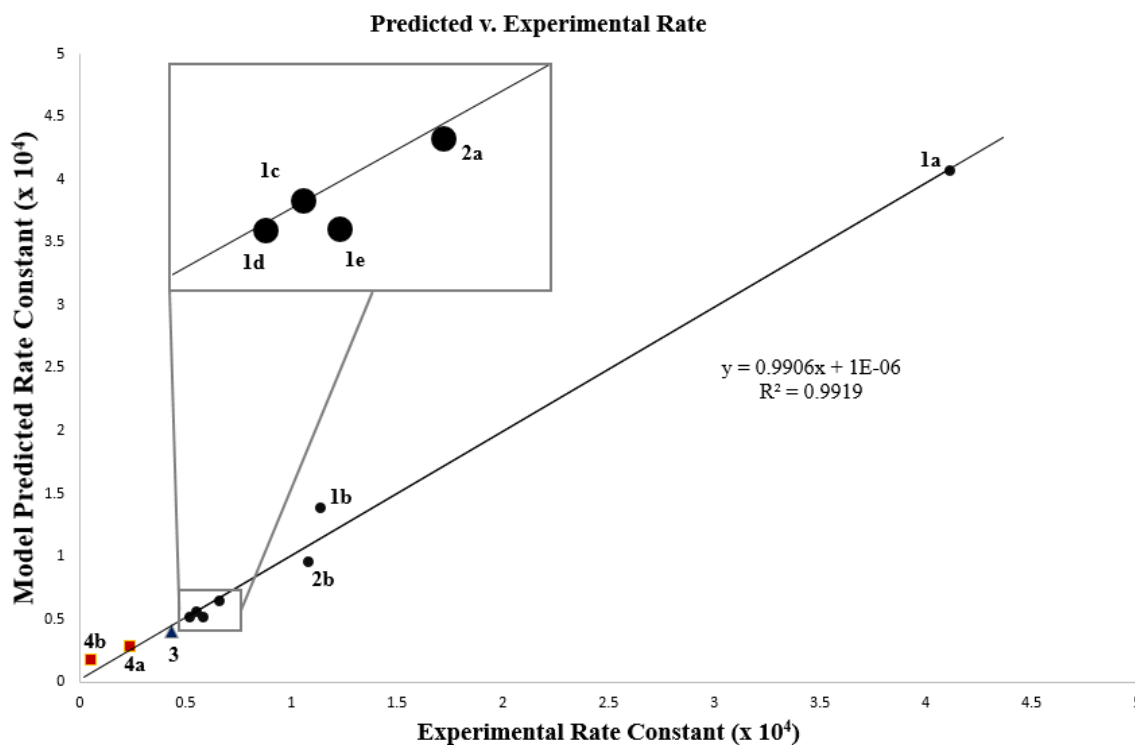


**Scheme 3.10.** Attempted syntheses of titanium biphenol-based precatalysts.

Shown below in **Figure 3.16**, is the data we collected from these new pre-catalysts along with the updated rate plot. Even without a linker, these new biphenol pre-catalysts still correlate well with our model.

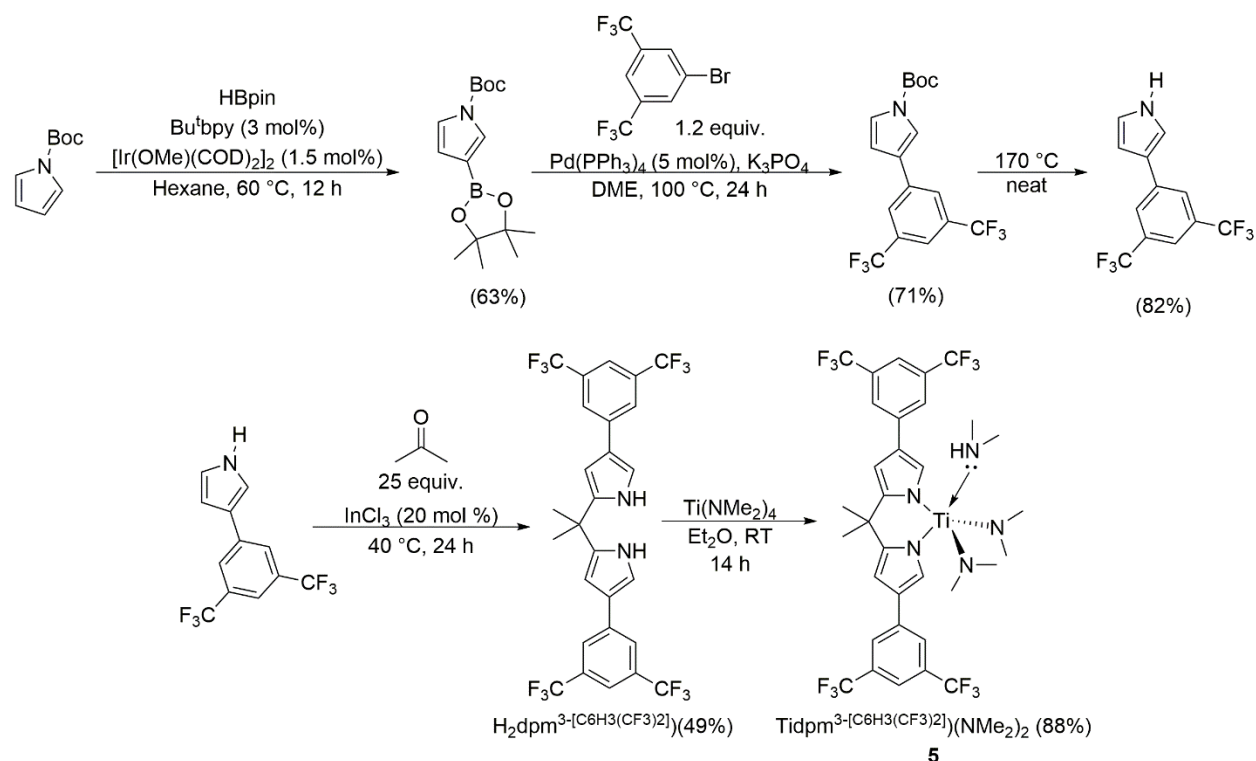
Ti Catalyst	Electronic Model LDP (kcal/mol)	Steric Model %V <sub>bur</sub> (if different)	k <sub>obs</sub> x 10 <sup>4</sup> (s <sup>-1</sup> )
 Ti(NMe <sub>2</sub> ) <sub>2</sub> (biphenol <sup>2-tBu-4,5-diMe</sup> ) ( <b>4a</b> )	 11.87	 21.5	0.244
 Ti(NMe <sub>2</sub> ) <sub>2</sub> (biphenol <sup>2-tBu-4-OMe</sup> )( <b>4b</b> )	 11.82	 21.5	.0546

**Figure 3.16.** Rates, LDP, and %V<sub>bur</sub> used for modeling catalysts **4a-4b**.



**Figure 3.17.** Plot of experimental rate constant versus model predicted rate constant with catalysts **4a-4b**.

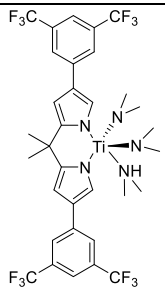
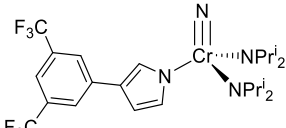
The original model we had developed, made just from indole and pyrrole ligands, still prevailed. Having established a robust model, we turned our attention to develop new and potentially faster catalysts. Previously, our group had developed a titanium(IV) hydroamination catalysts that was faster than  $\text{Ti}(\text{dpm})(\text{NMe}_2)_2$ . To expand our model even further we sought out to reinvestigate this catalyst. The known preparation of this catalyst utilizes Smith's borylation procedure<sup>45</sup> to obtain the protected pyrrole boronic ester. Suzuki cross-coupling with the respected aryl halide, followed by deprotection of the Boc group, *via* thermolysis (at 170 °C), provided the 3-aryl pyrrole. Lastly, the bidentate ligand is prepared *via* the  $\text{InCl}_3$ -catalyzed condensation of acetone in the presence of 3-aryl pyrrole.<sup>28</sup> The synthesis for this catalyst is shown in **Scheme 3.11**.



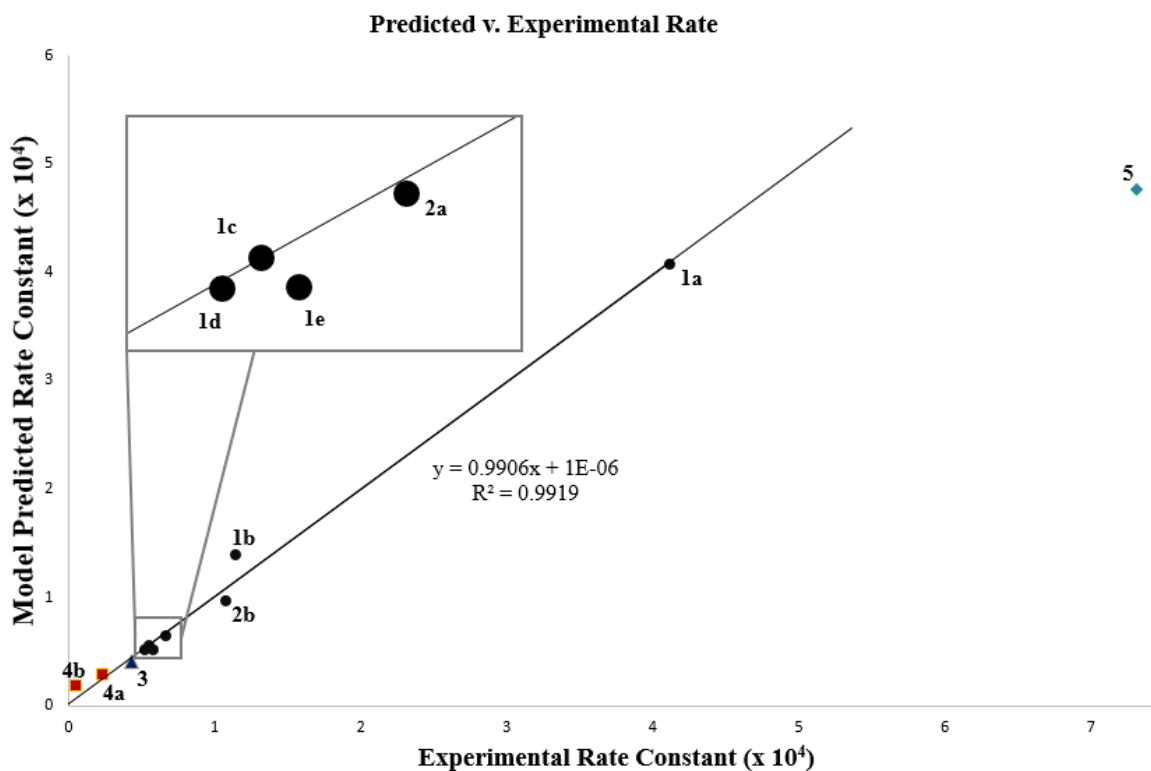
**Scheme 3.11.** Synthesis of  $\text{Ti(dpm}^{3\text{-[C}_6\text{H}_3\text{(CF}_3\text{)}_2\text{]})}(\text{NMe}_2)_2$  (**5**).

However, upon measuring the rate of this catalyst something unexpected occurred. When we plot the calculated rate versus the experimental rate we observe that the rate of this catalyst is faster than our model had predicted. Our model predicts that the rate of this catalyst will be  $4.7 \times 10^{-4} \text{ s}^{-1}$ , but the rate we obtained experimentally,  $7.3 \times 10^{-4} \text{ s}^{-1}$ , is significantly higher than that! Shown in the figures below is the LDP, %  $V_{\text{bur}}$  and rate data, as well as, the updated rate plot with this new precatalyst included.



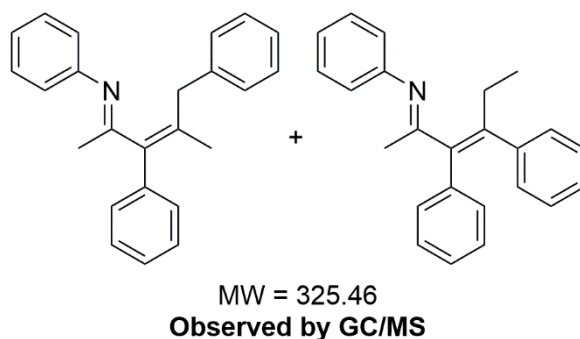
Ti Catalyst	Electronic Model LDP (kcal/mol)	Steric Model %V <sub>bur</sub> (if different)	k <sub>obs</sub> x 10 <sup>4</sup> (s <sup>-1</sup> )
 Ti(dpm) <sup>3</sup> -[C <sub>6</sub> H <sub>3</sub> (CF <sub>3</sub> ) <sub>2</sub> ](NMe <sub>2</sub> ) <sub>2</sub> ( <b>5</b> )	 14.06	20.3	7.32

**Figure 3.18.** Rate, LDP, and %V<sub>bur</sub> used for modeling catalyst **5**.



**Figure 3.19.** Plot of experimental rate constant versus model predicted rate constant with catalyst **5**.

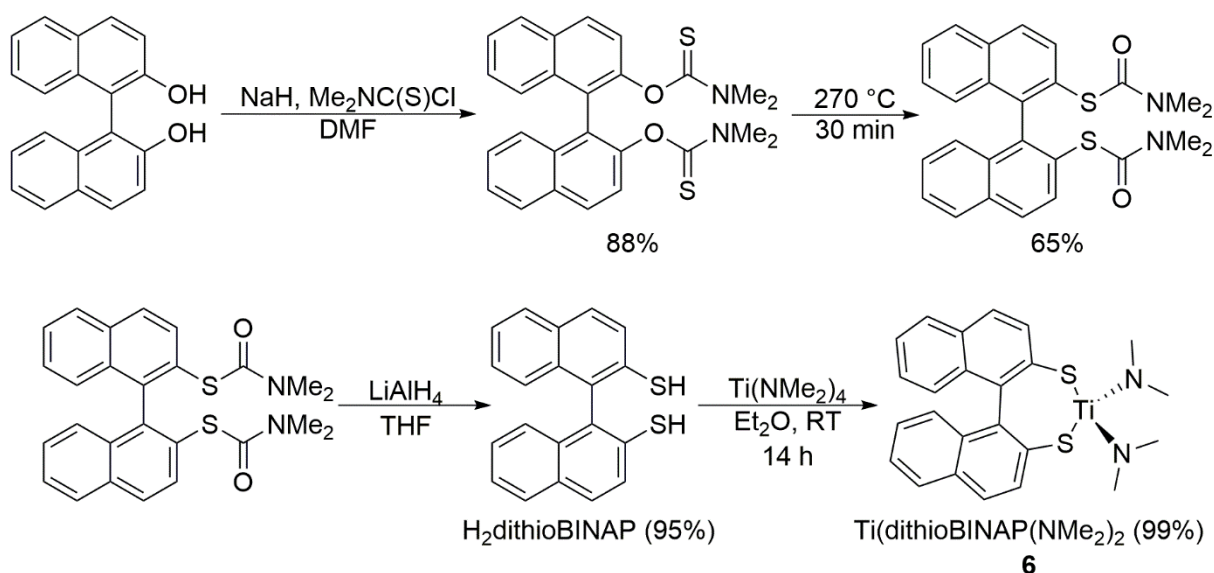
Interestingly, but equally frustratingly, we now needed to know why this catalyst deviates from our model. After examining the reaction mixture, from the kinetic experiments, we found our answer. That is, this catalyst produces additional products other than the expected imine. These by-products being produced incorporate more than one equivalent of alkyne. Since we are determining the rate by monitoring the disappearance of alkyne over time, we observe a faster rate than predicted. After multiple attempts, we could not successfully isolate the by-product being produced. Being in such a large excess of aniline (under the kinetic conditions) the  $^1\text{H}$  NMR is unintelligible, but we could gain information through GC/MS. Using GC/MS and GC/FID we observed the hydroamination product (MW = 209) is the major product being produced. Although there are multiple by-products being produced, two of the products are much more abundant and quite interesting. These two minor products have the same molecular weight (MW = 325) and what is interesting about that is; that molecular weight matches what we would expect from the coupling of amine with two equivalents of alkyne. **Figure 3.20** shows the two proposed products being produced. It is also possible that only one of these products is being produced and we are observing the E and Z isomer on the GC-MS.



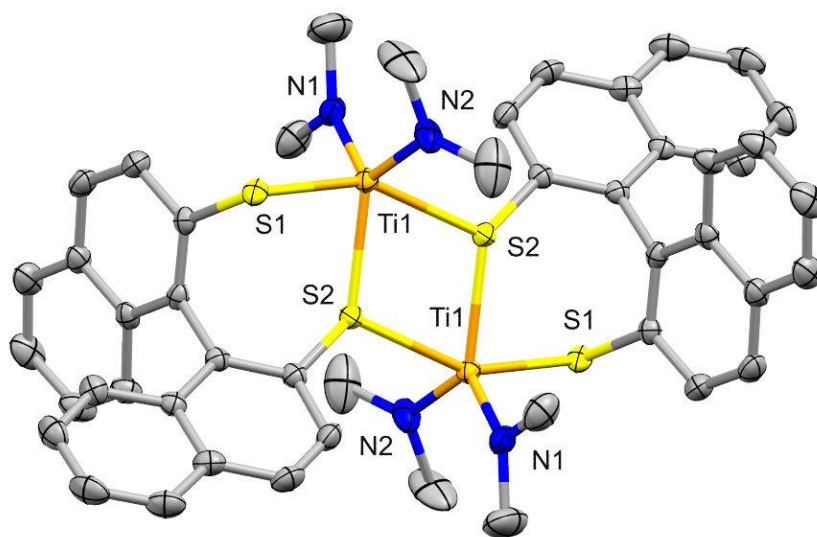
**Figure 3.20.** Proposed products being produced by  $\text{Ti}(\text{dpm}^{3-[\text{C}_6\text{H}_3(\text{CF}_3)_2]})(\text{NMe}_2)_2$  (**5**).

In many cases, unexpected products in a known reaction may be easily missed (as these were initially!), but the model led us to follow up the interesting new chemistry. Around the same time, we were investigating another catalyst that also exhibited some unique behavior.

Another ligand design we were interested in exploring, to hopefully develop a faster hydroamination catalyst, was a thiol-based ligand. For instance, the LDP of thiophenol (13.99 kcal/mol) and pyrrole (13.64 kcal/mol) are quite similar, but, thiophenol is even less donating. By moving to less a donating ligand, we may be able to produce a faster catalyst. The ligand we decided to pursue was 1,1'-binaphthalene-2,2'-dithiol ( $\text{H}_2\text{dithioBINAP}$ ). This ligand is prepared from 1,1'-bi-2-naphthol (BINOL) *via* Newman-Kwart thermal rearrangement.<sup>46-49</sup> After the deprotonation of BINOL with sodium hydride, thiocarbamoyl chloride is added to produce 1,1'-binaphthalene-2,2'-diyl O,O-*bis*(N,N-dimethylthiocarbamate). This product undergoes Newman-Kwart rearrangement (at 270 °C) to give the 1,1'-binaphthalene-2,2'-diyl S,S-*bis*(N,N-dimethylthiocarbamate), that upon treating with lithium aluminum hydride gives the desired ligand,  $\text{H}_2\text{dithioBINAP}$ .<sup>46-48, 50</sup> Addition of  $\text{H}_2\text{dithioBINAP}$  to  $\text{Ti}(\text{NMe}_2)_4$  produces the precatalyst  $\text{Ti}(\text{dithioBINAP})(\text{NMe}_2)_2$  (**6**) in high yield. (**Scheme 3.12**)



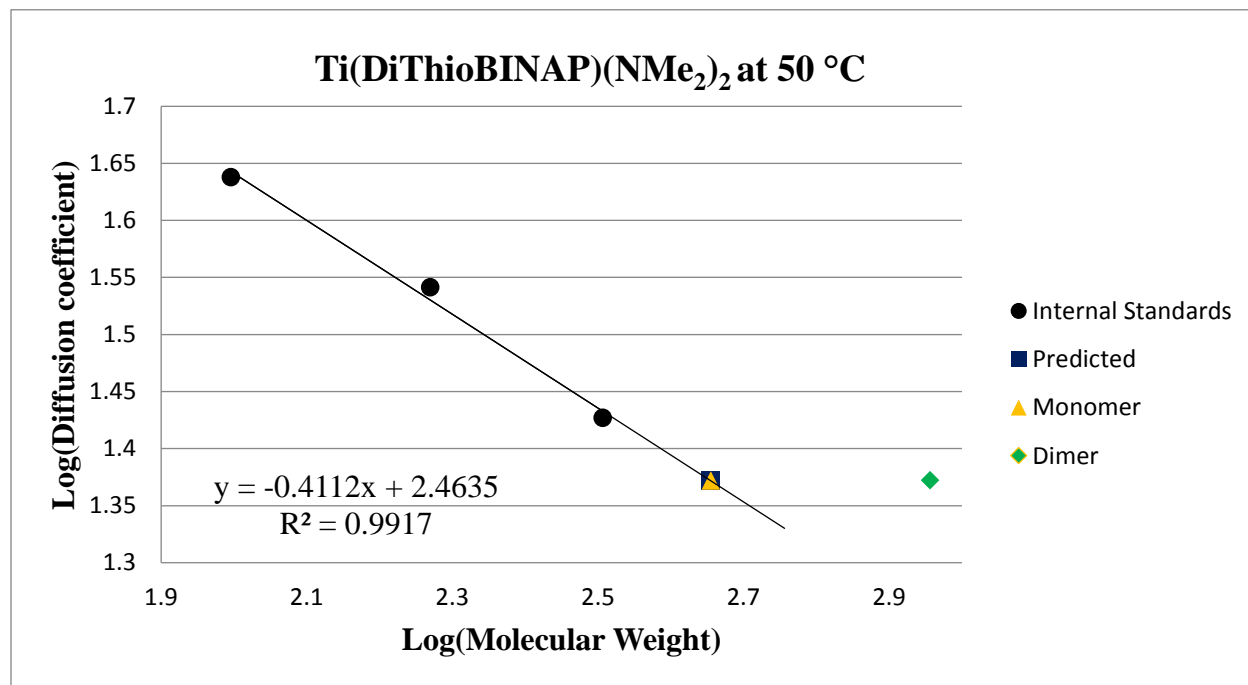
**Scheme 3.12.** Synthesis of  $\text{Ti(dithioBINAP)(NMe}_2)_2$  (**6**).



**Figure 3.21.** ORTEP structure of  $\text{Ti(dithioBINAP)(NMe}_2)_2$  (**6**).

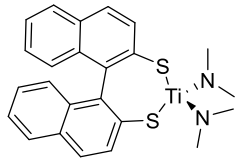
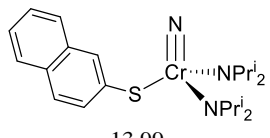
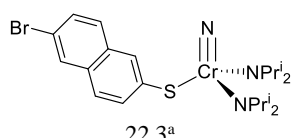
This precatalyst is a dimer in the solid state with bridging thiolates, as shown above in **Figure 3.21**. Initially we were dismissive of this precatalyst, but unlike many other dimeric precatalysts that we've made this one was soluble in toluene. Being soluble, we can study this

complex in solution to determine if it is indeed dimeric. What we found was at upon heating to 50 °C the complex is monomeric in solution. This was determined by molecular weight determination via NMR Diffusion-Ordered Spectroscopy (DOSY). (**Figure 3.22**)

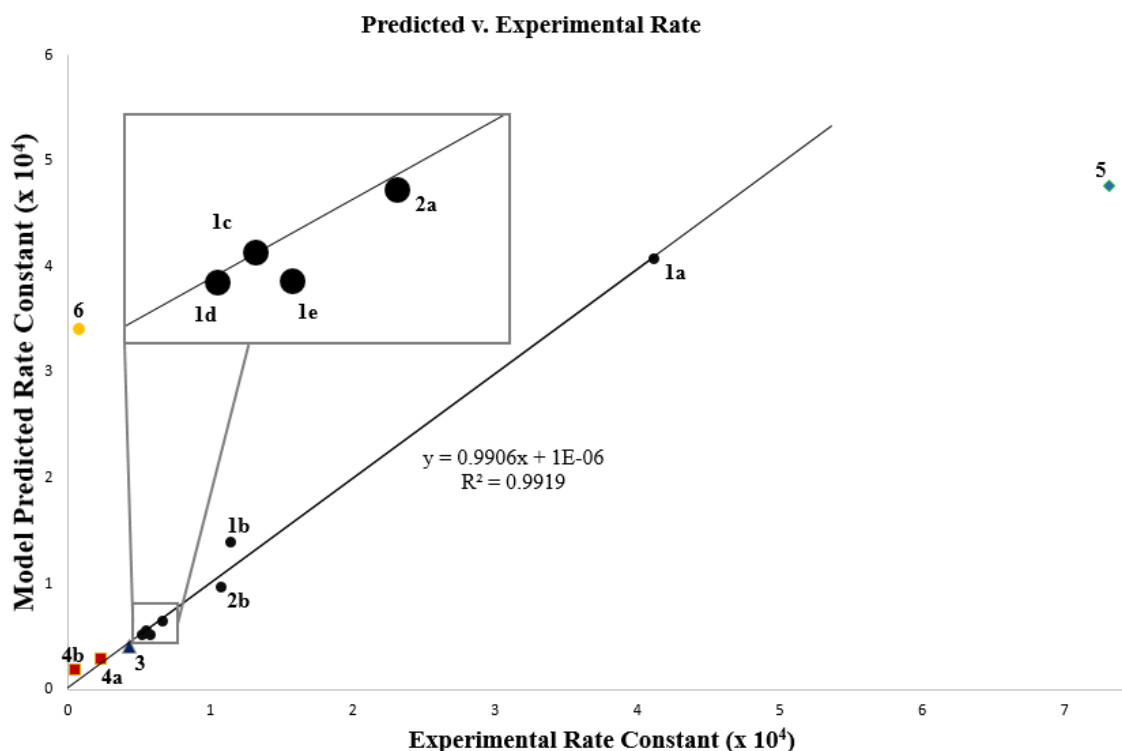


**Figure 3.22.** Molecular weight calibration of Ti(dithioBINAP)(NMe<sub>2</sub>)<sub>2</sub> (**6**) at 50 °C.

Excited by these findings, we started our kinetics studies of this precatalyst and we were surprised to find that the complex was an extremely slow hydroamination catalyst. Our model predicts the rate of this catalyst to be  $3.40 \times 10^{-4}$  and what we measured experimentally was  $7.9 \times 10^{-6}$ , over an order of magnitude slower! Shown in the figures below is the LDP, %  $V_{bur}$  and rate data, as well as, the updated rate plot with this new precatalyst included.

Ti Catalyst	Electronic Model LDP (kcal/mol)	Steric Model %V <sub>bur</sub> (if different)	k <sub>obs</sub> x 10 <sup>4</sup> (s <sup>-1</sup> )
 Ti(dithioBINAP)(NMe <sub>2</sub> ) <sub>2</sub> ( <b>6</b> )	 13.99	 22.3 <sup>a</sup>	0.079

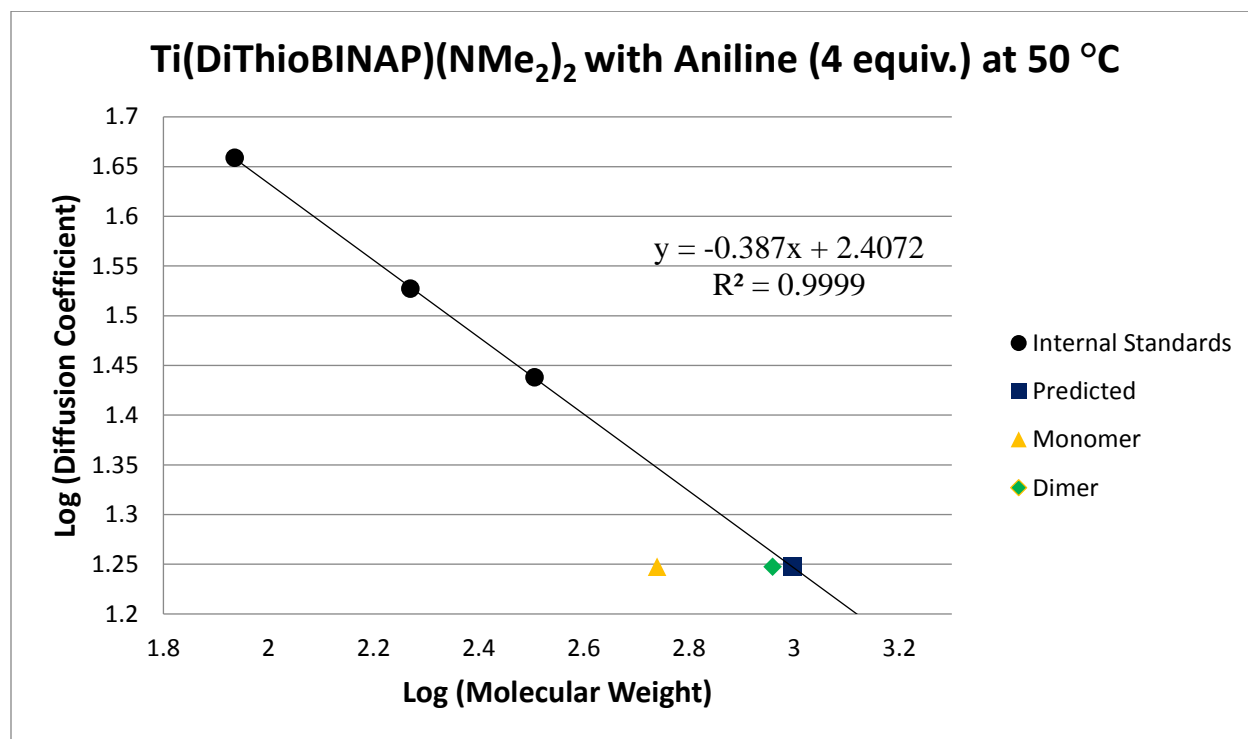
**Figure 3.23.** Rate, LDP, and %V<sub>bur</sub> used for modeling catalyst **6**. <sup>a</sup>See Section 3.7 for more details on this derivative.



**Figure 3.24.** Plot of experimental rate constant versus model predicted rate constant with catalyst **6**.

Once again, we had to determine why this catalyst doesn't fit with our model. Being already suspicious of this complex, we wondered if it could be dimerizing under the kinetic conditions. To test this, we conducted another DOSY experiment that mimicked the kinetic conditions to the best of our ability. The molecular weight determination for Ti(dithioBINAP)(NMe<sub>2</sub>)<sub>2</sub> (**6**), at 50 °C in the presence of excess aniline, indicates that the complex is dimeric in solution. (**Figure 3.25**) This

dimerization is likely to be what is slowing the catalysis, and is why we observe this deviation from our model. (For more details on all the DOSY experiments see **Section 3.8**)

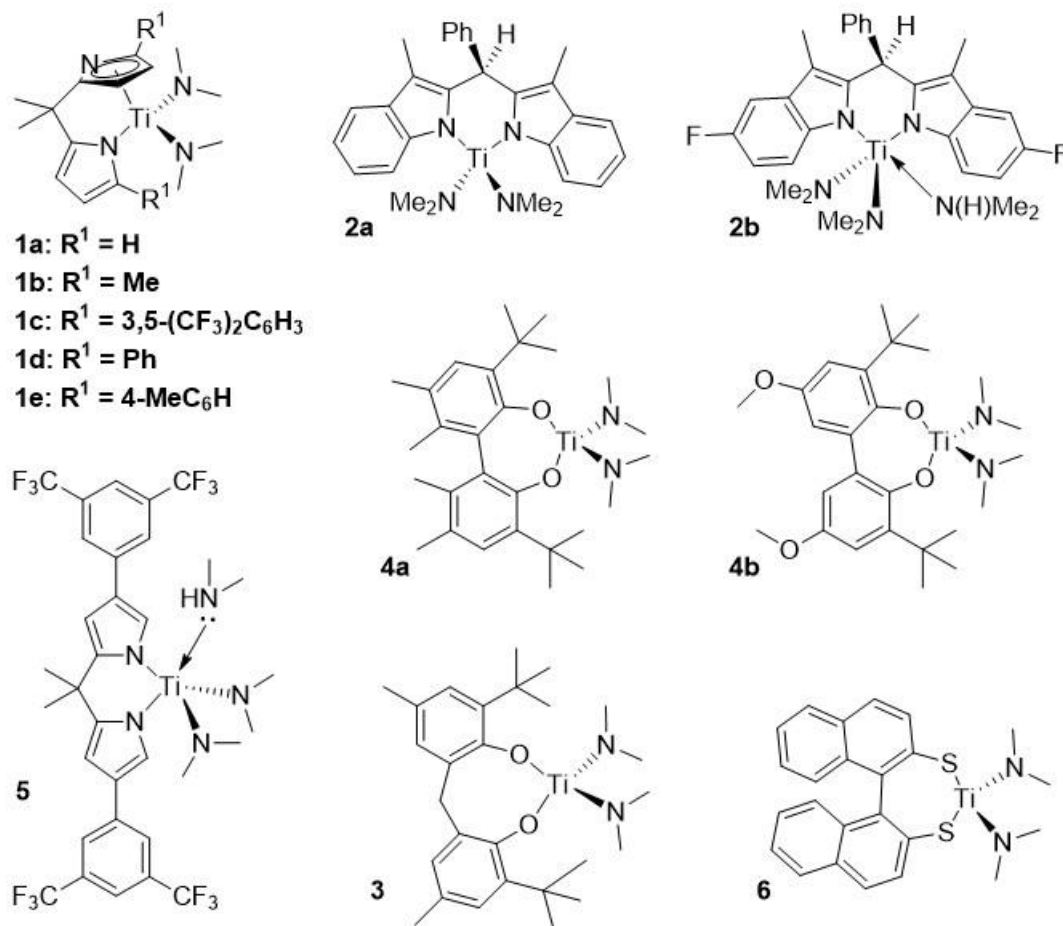


**Figure 3.25.** Molecular weight calibration of Ti(dithioBINAP)(NMe<sub>2</sub>)<sub>2</sub> (**6**) with excess aniline at 50 °C.

Even though our last two attempts to design a better catalyst didn't go as planned, in hindsight, we gained a tremendous amount of information, all of which will be discussed in detail in the following section.

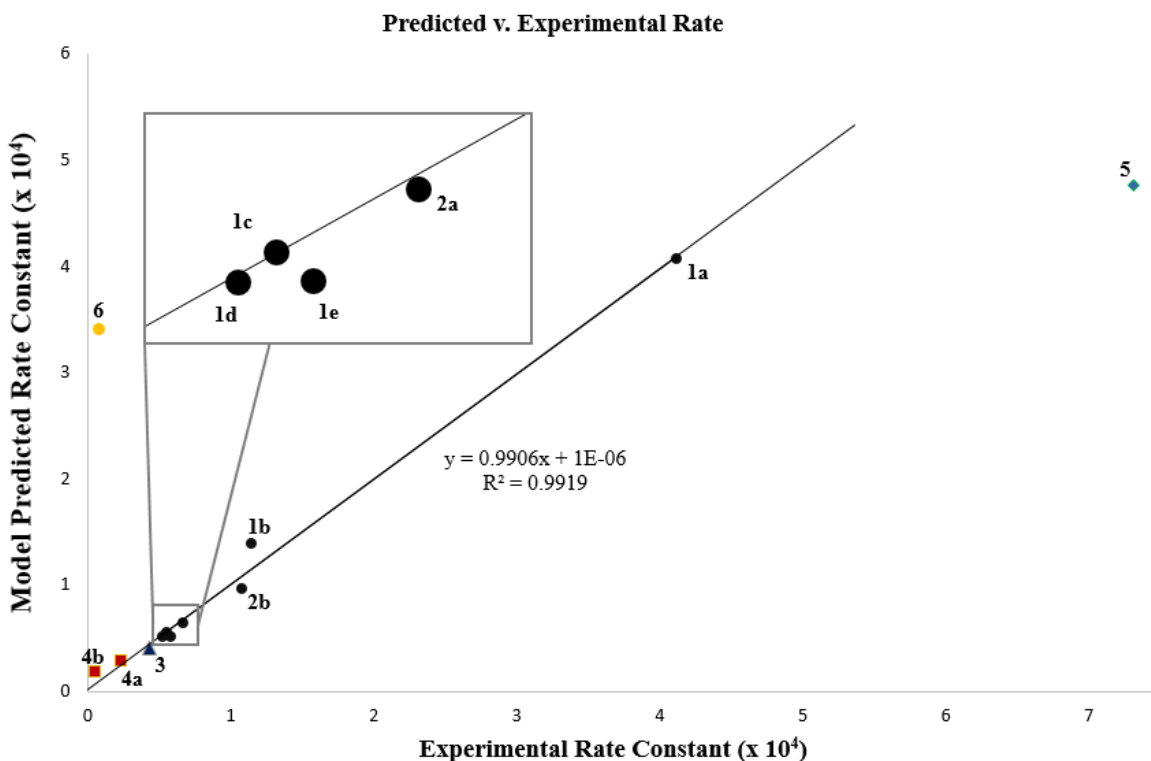
### 3.7 Results and Discussion

This section will reiterate key discoveries that we have made, as well as discuss our additional findings.



**Figure 3.26.** All titanium catalysts used in this study.





**Figure 3.27.** Completed plot for predicted versus experimental rate constant.

In **Figure 3.27**, is a plot of the predicted rate constant from the model versus the experimental rate constant. Depending on the ancillary ligand, the rates varied dramatically, giving half-lives from ~30 minutes (catalyst **1a**) to over 1.5 days (catalyst **4b**)!

The rates from the different catalysts covered a wide range, over two orders of magnitude. Again, the model points (Equation 2) are derived from the indole- and pyrrole-based catalysts shown in black, and the black model line shows excellent correlation ( $R^2 = 0.99$ ). The fit coefficients obtained by using the natural parameters are  $a = -6.88$ ,  $b = 1.75$ , and  $c = -0.635$ . If we scale the parameters (from  $-1$  to  $+1$ ) we obtain the coefficients  $a = 1.34$ ,  $b = 1.61$ , and  $c = -2.25$ . (**Figure 3.28**) The information we obtain by scaling the parameters, is now the parameter effects can be directly compared. From this we can see that by increasing the sterics of the ligand (higher % $V_{\text{bur}}$ ) results in lower rates. We also see that by increasing the LDP of the ligand, (i.e. weakly donating ligand, thus making a more Lewis acidic metal center) increases the rate. If we

compare these to coefficients side-by-side, we see that the absolute contribution of the sterics,  $-2.25(\%V_{bur})$ , effects the rate at almost 1.5 times more than the electronics,  $+1.61(LDP)$ . In short, to build a faster catalyst we want to use ligands that are sterically small (low  $\%V_{bur}$ ) and weakly donating (High LDP).

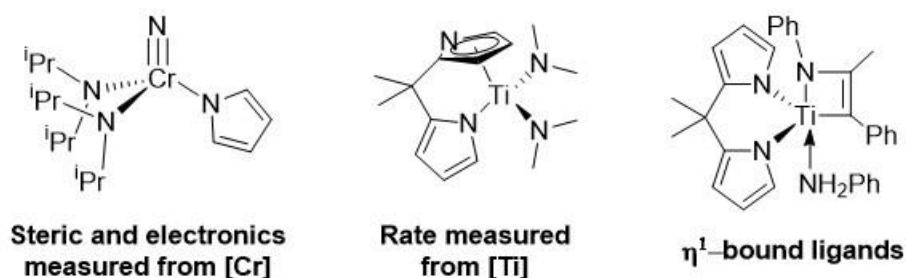
$k_{obs} \times 10^4 = a + b(LDP) + c(\%V_{bur})$	Equation 2
$k_{obs} \times 10^4 = -6.88 + 1.75(LDP) - 0.635(\%V_{bur})$	Natural Parameters
$k_{obs} \times 10^4 = 1.34 + 1.61(LDP) - 2.25(\%V_{bur})$	Scaled Parameters

**Figure 3.28.** Natural and Scale Parameters

Most of the ligands we examined in this study, fit well to the model line. Obviously, not all catalysts did fit to our model line, but it is very interesting why they do not fit. For instance, when we used catalyst **5**, we observed a rate that was much faster than predicted. After further experiments, we found that this catalyst produces by-products that incorporate more than one equivalent of alkyne; because we are monitoring the consumption of alkyne to determine the rate the catalyst is faster than expected. When measuring the rate for precatalyst **6**, we observe a rate that is much slower than predicted. Using molecular weight determination, *via* NMR DOSY, we could provide evidence that this catalyst dimerizes in solution; even at higher temperatures with excess aniline. This dimerization that is occurring is likely what is slowing the catalysis, giving the slower rate than expected. Without the model, after observing the slow catalysis rate, one could assume (erroneously) that thiolates are very donating to the metal center and that is why they are a poor catalyst. However, based on our model, thiolates could potentially be very active catalysts if the dimerization could be controlled. This fact could have been easily missed without the model.

Looking back at all the data collected, we can identify several unique features from this technique, that give insight into the catalytic reaction. First, it is known that indolyl- and pyrrolyl-

type ligands can undergo hapticity changes, we have even studied this previously in our group.<sup>51</sup> By using our model we can obtain additional information into this phenomenon. As shown in Figure 3.26, all the dipyrrolylmethane precatalysts (**1a–1e**) have one pyrrole bound  $\eta^1$  and one bound  $\eta^5$ , in their solid state. Again, all the ligands used to derive the electronic and steric parameter come from the chromium system, and, in the chromium system, all the ligands are exclusively  $\eta^1$ -coordinated, and yet they still fit well to the titanium system. Meaning, the model suggests that the active species has  $\eta^1$ -pyrrolide or  $\eta^1$ -indolide ligands in every case. (Figure 3.29) Therefore, this technique can suggest the mode of coordination for the ligands during key steps in the catalytic cycle.



**Figure 3.29.** Mode of coordination.

Second, this model can be expanded to other ligands sets and is not limited to heterocyclic ligands. It seems that any ligand, where a reasonable LDP and % $V_{bur}$  can be obtained, can be placed in the model. Thus, allowing diverse ligand sets to be investigated. As we have demonstrated, the kinetics derived from several phenol-based catalysts (shown in **Figure 3.27**) fit well to the same model we built based off pyrrole and indole ligands.

Third, the backbone and ring size of the ancillary ligands seem to have no impact on this system. Increasing the ring size on the chelating ligands from 6-, to 7-, to 8-membered rings or changing the linker entirely (even removing the linker!) have no effect on the rate. The rate seems to be solely determined by the steric and electronics of the attached ligands, with no ring effects observed.

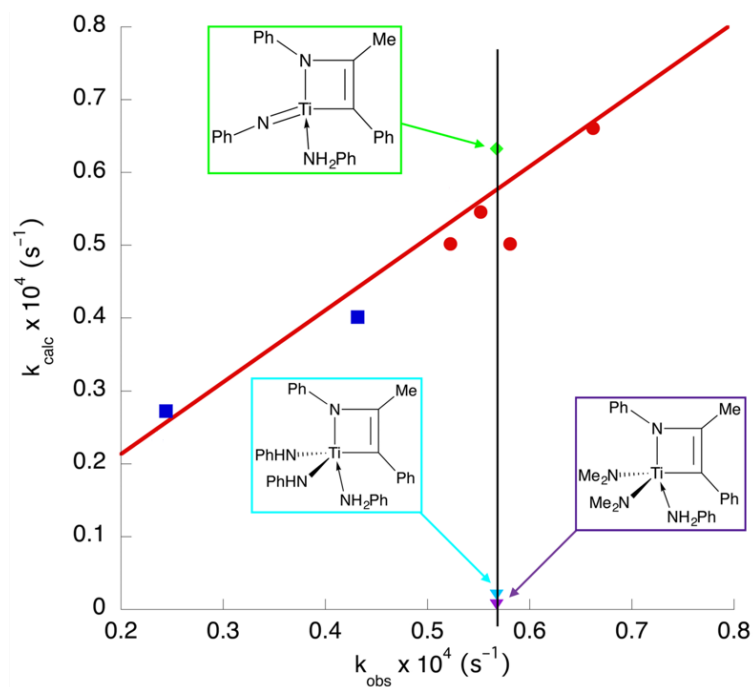
Fourth, catalyst **5** ( $\text{Ti}(\text{dpm}^{3-[\text{C}_6\text{H}_3(\text{CF}_3)_2]}) (\text{NMe}_2)_2$ ) an isomer of **1c**, does not fit with the model, even though all of the phenol-based catalyst did. Again, after further examination of this catalyst it was revealed to be producing by-products. Meaning this method can alert the researcher to additional chemistry occurring in the reaction, which could potentially lead to the discovery of new reaction pathways.

Fifth, catalysts that were slower (i.e. catalyst **6**) than the model predicted are likely undergoing dimerization, degradation or other deactivation processes. A reliable model that can tell the researcher what the rate could be, gives the researcher the incentive to investigate the nature of deactivation. This could potentially revive whole classes of catalysts which could be useful if designed properly, catalyst that might have been discarded based on flawed conclusions obtained only from activity data.

Lastly, the model can give insight into important active species where no other information is available. For example,  $\text{Ti}(\text{NMe}_2)_4$  is a quite fast alkyne hydroamination catalyst.<sup>52-53</sup> However, in this complex all ligands are protolytically labile. Meaning all of the dimethylamides ( $\text{NMe}_2$ ) may or may not be displaced by amine substrate (i.e. aniline). Assuming the protonolysis of the titanium-carbon bond is still the rate-determining step (see **Figure 3.5, C**), what could the two X ligands be in this intermediate? Could the X ligands be two dimethylamides, i.e.  $(\text{NMe}_2)_2$  or two anilides, i.e.  $(\text{NHPh})_2$ ? Looking at **Figure 3.30**, the red line is the model line derived from **Figure 3.27**, and the black line is the experimental rate constant from  $\text{Ti}(\text{NMe}_2)_4$ . Shown in **Figure 3.30** are the proposed intermediates (**C**) based off the mechanism in **Figure 3.5**. After measuring the LDP and %  $V_{\text{bur}}$  of  $-\text{NMe}_2$  and  $-\text{NHPh}$ , we can predict the rate for each of these possible active species. The rates for  $\text{X}_2 = (\text{NMe}_2)_2$  and  $(\text{NHPh})_2$  are shown as purple and cyan triangles.

According to the model both are too slow and neither of these possibilities fit with the model developed. What could the ancillary ligand be?

According to the model, sterics make a larger contribution to the rate than the electronics. With this in mind, we decided to test the hypothesis that maybe instead of having two bulky monoanionic ligands, maybe it is a single dianionic titanium imide instead. Even though an imide would be a very donating ligand, maybe the small size is what is giving it its speed. After determining the LDP and %V<sub>bur</sub> for the imide, and inserting that data into our model we observed that the calculated rate constant fits reasonably well with the experimental rate constant. This suggests that the imide could possibly be the active species. (*This study, to gain information about the active species, was conducted by my lab-mate Brennan Billow.*)



**Figure 3.30.** A close-up of the model plot in **Figure 3.27** with the points for the hypothetical active species in the Ti(NMe<sub>2</sub>)<sub>4</sub> catalysis added.<sup>1</sup>

As a result, this method may be able to give information about important species in reactions that are currently unobservable, thus aiding in catalyst design.<sup>19</sup>

### 3.8 Conclusion

As we have shown, using this method it is now possible to gain detailed information about high-valent catalyses, aiding in rational catalyst design and may even be able to give insight into important species in the catalytic cycle. We hope that this study will be a useful blueprint to other high-valent transition metal chemists, showing that LDP and %  $V_{\text{bur}}$  can help in catalyst design.

### 3.9 Experimental

This experimental data is taken from our publication on this research located at:

*Nat. Chem.* **2017**, 9, 837.

#### Additional Details on Modeling of Rate Constants

The fits were done using both the “natural” variables, the direct LDP and %V<sub>bur</sub> values, and scaled variables. The natural variables give a model that can be used to calculate the rate constant of a new catalyst if the LDP and %V<sub>bur</sub> values are known or can be accurately estimated. The scaled variables allow direct comparison between the different coefficients and comparison of electronic and steric factors. The scaling was done using the equation below, where  $x_i$  = scaled variable,  $u_i$  = natural variable,  $u_i^0$  = midpoint of the range of the natural variables, and  $\Delta u_i$  = the difference between the midpoint and the high value (half the full range).

$$x_i = \frac{u_i - u_i^0}{\Delta u_i}$$

The equations for the calculation of  $u_i^0$  and  $\Delta u_i$  are shown below.

$$\begin{aligned}\Delta u_i &= u_i^{high} - u_i^0 \\ u_i^0 &= \frac{u_i^{high} + u_i^{low}}{2}\end{aligned}$$

Using either the scaled or natural variables, a least squares fit to the data was done by solving the equation below. In the equation,  $y$  = single column matrix of the rate constants,  $b$  = single column matrix of the coefficients (listed as just a, b, and c in the manuscript),  $X$  = the model matrix which consists of the scaled or unscaled variables,  $X^t$  = transform of the model matrix. The equation below provides the least square values without being prone to local minima like iterative methods can be and required nothing more than an Excel spreadsheet to calculate the set of coefficients.

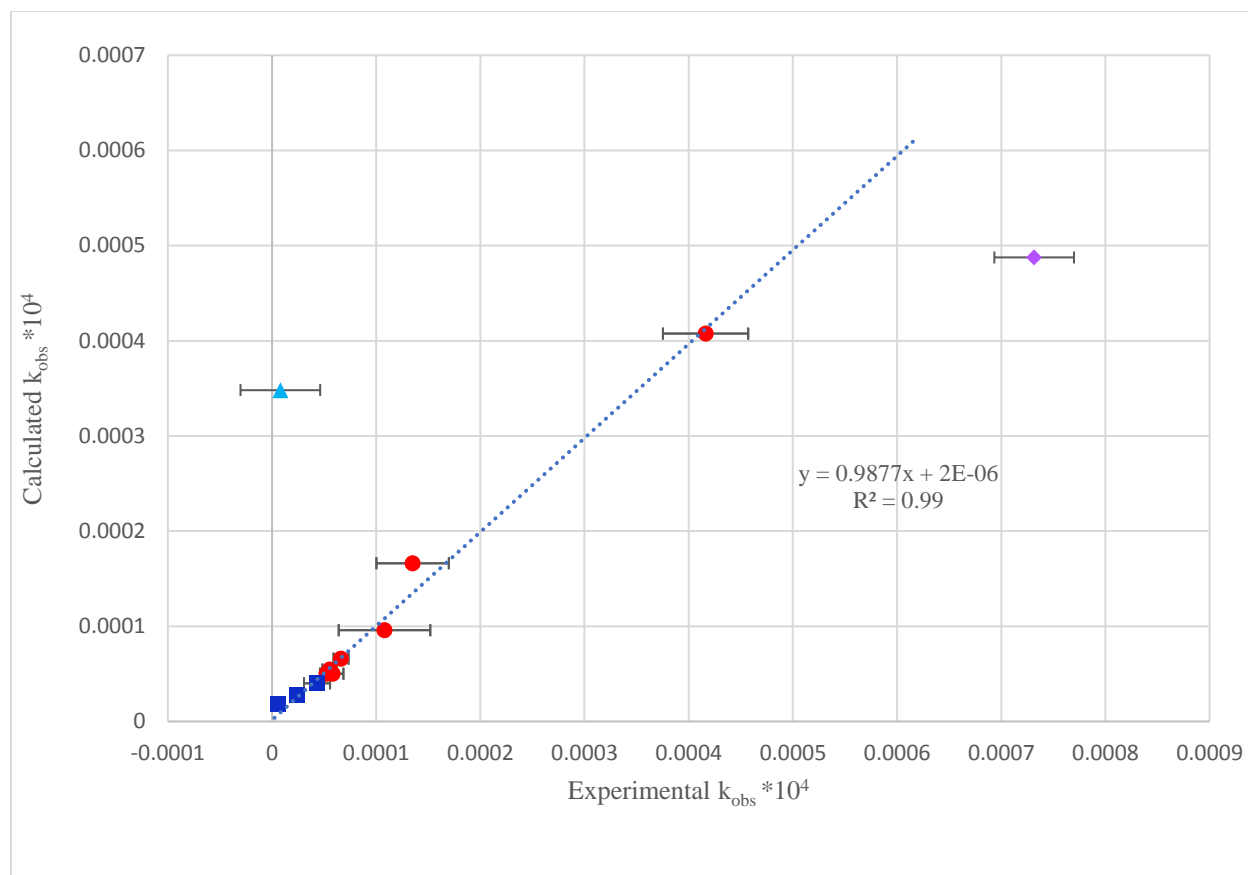
$$(X^t \bullet X)^{-1} \bullet X^t \bullet y = b$$

The equation with the natural variables in the matrices is shown below. In order to get the  $a$ -coefficient in the fit, a row of ones are added before the LDP and %V<sub>bur</sub> data. Only compounds **1a-1e** and **2a-b** were used to develop the model.

$$\left[ \begin{pmatrix} 1 & 1 & 1 & 1 & 1 & 1 & 1 \\ 12.49 & 13.64 & 12.66 & 13.91 & 14.03 & 13.46 & 14.32 \\ 22.6 & 20.4 & 22.6 & 26.7 & 27.1 & 23.7 & 27.9 \end{pmatrix} \begin{pmatrix} 1 & 12.49 & 22.6 \\ 1 & 13.64 & 20.4 \\ 1 & 12.66 & 22.6 \\ 1 & 13.91 & 26.7 \\ 1 & 14.03 & 27.1 \\ 1 & 13.46 & 23.7 \\ 1 & 14.32 & 27.9 \end{pmatrix} \right]^{-1} \begin{pmatrix} 1 & 1 & 1 & 1 & 1 & 1 & 1 \\ 12.49 & 13.64 & 12.66 & 13.91 & 14.03 & 13.46 & 14.32 \\ 22.6 & 20.4 & 22.6 & 26.7 & 27.1 & 23.7 & 27.9 \end{pmatrix} \begin{pmatrix} 0.66 \\ 4.16 \\ 1.08 \\ 0.55 \\ 0.52 \\ 1.35 \\ 0.58 \end{pmatrix} = \begin{pmatrix} a \\ b \\ c \end{pmatrix}$$

Solution of the above equation gives  $a = -6.88$ ,  $b = 1.75$ , and  $c = -0.635$ . The scaled variable coefficients were found similarly.<sup>54</sup>





**Figure 3.31.** Model plot with error bars.

Plot of the calculated rate constant versus the mean  $k_{obs}$  showing error bars at the 95% confidence level on the experimental measurement. In all cases, the rate constants were done in triplicate. The red points represent the seven heterocycle complexes that were used to generate the model, the dark blue squares are the aryloxide complexes, the purple diamond is the 3-Ar-pyrrole complex, which shows side reactions, and the cyan triangle is the dithioBINAP which shows catalyst dimerization.

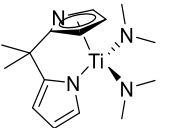
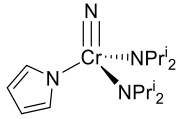
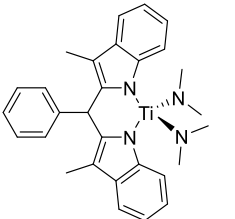
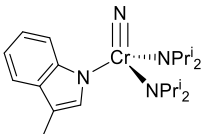
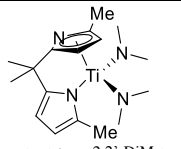
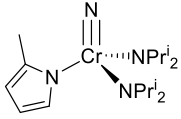
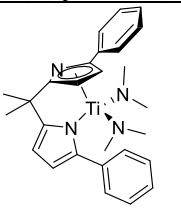
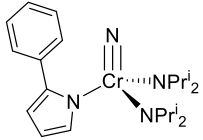
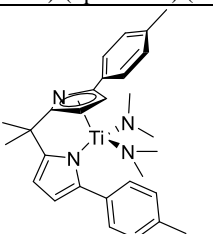
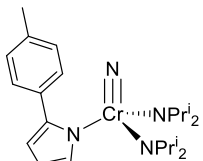
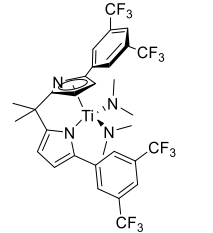
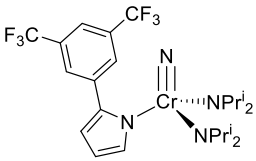
## General LDP Procedure

The rate constant for the exchange of the two methyne hydrogens of the isopropyl groups was measured using  $^1\text{H}$  NMR spin saturation transfer (SST). The temperature chosen for each experiment was based on that required to reach the slow exchange limit of the complex under investigation, in these cases between  $-30\text{ }^\circ\text{C}$  and  $25\text{ }^\circ\text{C}$ .  $T_1$  values were measured using the inversion recovery method. Samples were made between 0.02–0.03 M in  $\text{CDCl}_3$ .  $\Delta S^\ddagger$  for this rotation was shown to be  $-9\text{ cal}\cdot\text{mol}^{-1}\cdot\text{K}^{-1}$  for  $\text{NCr}(\text{N}^i\text{Pr}_2)_2\text{I}$  and assumed to be the same for the other compounds.<sup>55</sup>

## General Percent Buried Volume Considerations

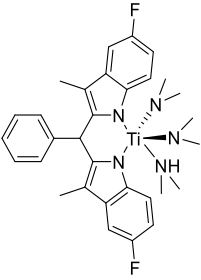
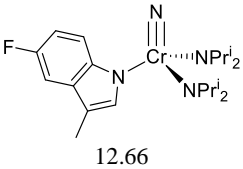
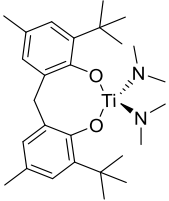
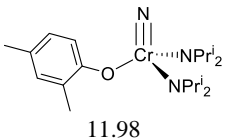
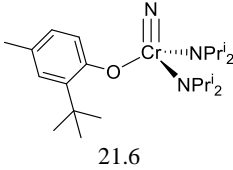
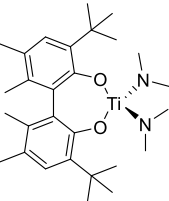
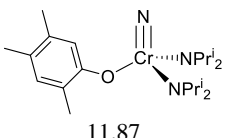
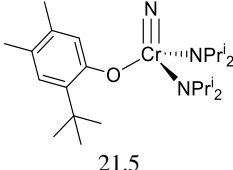
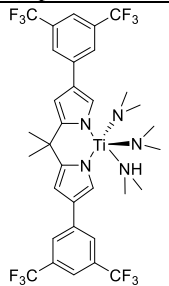
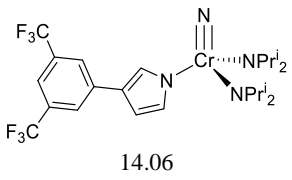
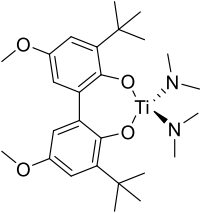
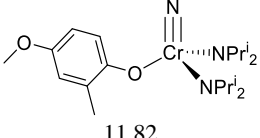
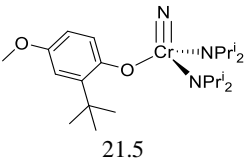
In calculating percent buried volume, the ligand structure was taken from the chromium complex crystal structure. The  $\text{NCr}(\text{N}^i\text{Pr}_2)_2$  fragment was deleted, leaving just the X ligand for analysis. This fragment, in conjunction with the bond length from the chromium crystal structure (Cr-X bond length) were used in the SambVca 2.0 program to calculate the  $\%V_{\text{bur}}$ .<sup>56</sup> This method was used for several reasons. First, the chromium molecules are easily crystallizable and provided an experimental basis for the measurement (as opposed to modeling computationally). Second, the chromium molecule is already the model for the electronic term, it was logical to use the same molecule to determine the steric factor. Finally, using just the ligand fragment eliminates as much bias for bonding angles, twisting, and torsions from sterics and crystal packing as possible. In other words, it is a better measure of the ligands sterics towards a more general set of high valent metals. The sphere radius was left at the default 3.5 Å. Other radii were tested, but the default gave the best correlation. Mesh spacing was left at the default value of 0.10, the atomic radii were used as

the default Bondi radii scale by 1.17, and for all ligands the H atoms were included in the calculations.

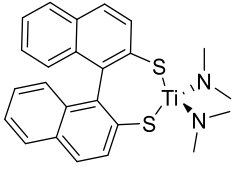
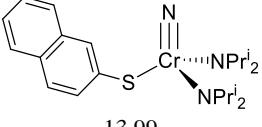
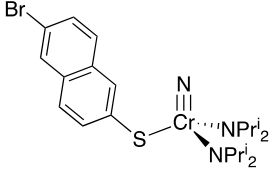
Ti Catalyst	Electronic Model LDP (kcal/mol)	Steric Model %V <sub>bur</sub> (if different)	k <sub>obs</sub> x 10 <sup>4</sup> (s <sup>-1</sup> )
 Ti(NMe <sub>2</sub> ) <sub>2</sub> (dpm) ( <b>1a</b> )	 13.64	20.4	4.16
 Ti(NMe <sub>2</sub> ) <sub>2</sub> (dim <sup>3</sup> Me) ( <b>2a</b> )	 12.49	22.6	0.662
 Ti(NMe <sub>2</sub> ) <sub>2</sub> (dpm <sup>2,2'</sup> -DiMe) ( <b>1b</b> )	 13.46	23.7	1.35
 Ti(NMe <sub>2</sub> ) <sub>2</sub> (dpm <sup>2</sup> -phenyl) ( <b>1d</b> )	 14.03	27.1	0.522
 Ti(NMe <sub>2</sub> ) <sub>2</sub> (dpm <sup>2</sup> -tolyl) ( <b>1e</b> )	 13.91	26.7	0.552
 Ti(NMe <sub>2</sub> ) <sub>2</sub> (dpm <sup>2</sup> -[C <sub>6</sub> H <sub>3</sub> (CF <sub>3</sub> ) <sub>2</sub> ]) ( <b>1c</b> )	 14.32	27.9	0.581

**Table 3.1.** Rates, LDP, and % V<sub>bur</sub> Used for Modeling.

**Table 3.1. (cont'd)**

 <p><b>Ti(NMe<sub>2</sub>)<sub>2</sub>(dim<sup>3</sup>Me<sup>5</sup>F) (2b)</b></p>	 <p>12.66</p>	<p>22.6</p>	<p>1.08</p>
 <p><b>Ti(NMe<sub>2</sub>)<sub>2</sub>(bis-phenoxide<sup>2</sup>-tBu-4-Me) (3)</b></p>	 <p>11.98</p>	 <p>21.6</p>	<p>0.432</p>
 <p><b>Ti(NMe<sub>2</sub>)<sub>2</sub>(biphenol<sup>2</sup>-tBu-4,5-diMe) (4a)</b></p>	 <p>11.87</p>	 <p>21.5</p>	<p>0.244</p>
 <p><b>Ti(NMe<sub>2</sub>)<sub>2</sub>(dpm<sup>3</sup>-[C<sub>6</sub>H<sub>3</sub>(CF<sub>3</sub>)<sub>2</sub>]) (5)</b></p>	 <p>14.06</p>	<p>20.3</p>	<p>7.32</p>
 <p><b>Ti(NMe<sub>2</sub>)<sub>2</sub>(biphenol<sup>2</sup>-tBu-4-OMe) (4b)</b></p>	 <p>11.82</p>	 <p>21.5</p>	<p>.0546</p>

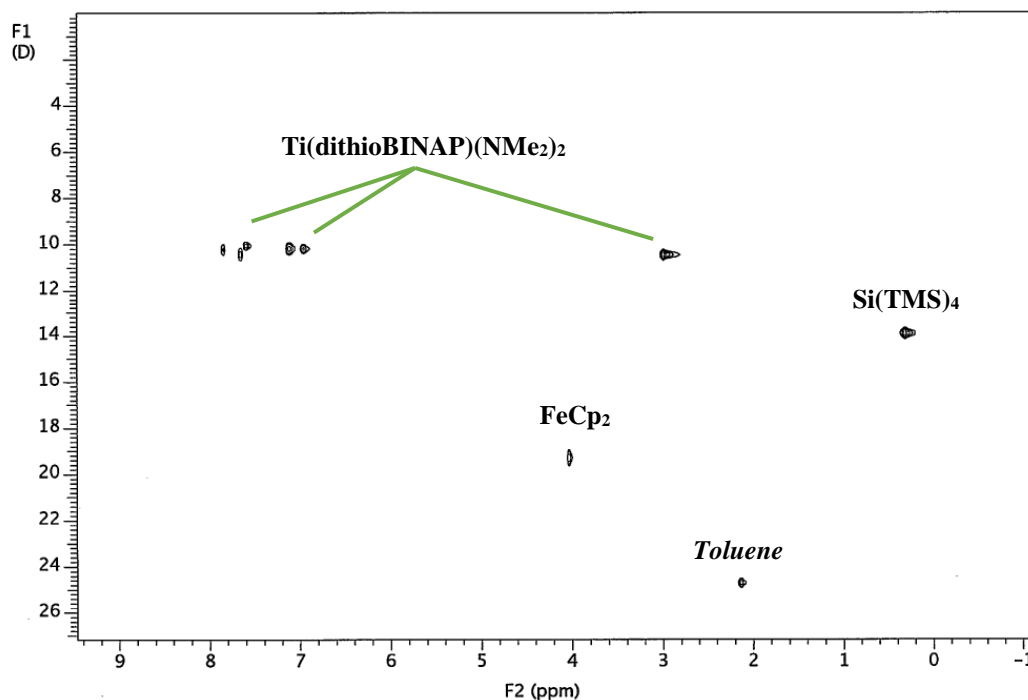
**Table 3.1. (cont'd)**

 <p>Ti(NMe<sub>2</sub>)<sub>2</sub>(dithioBINAP) (6)</p>	 <p>13.99</p>	 <p>22.3<sup>a</sup></p>	<p>0.0794</p>
---	--	---	---------------

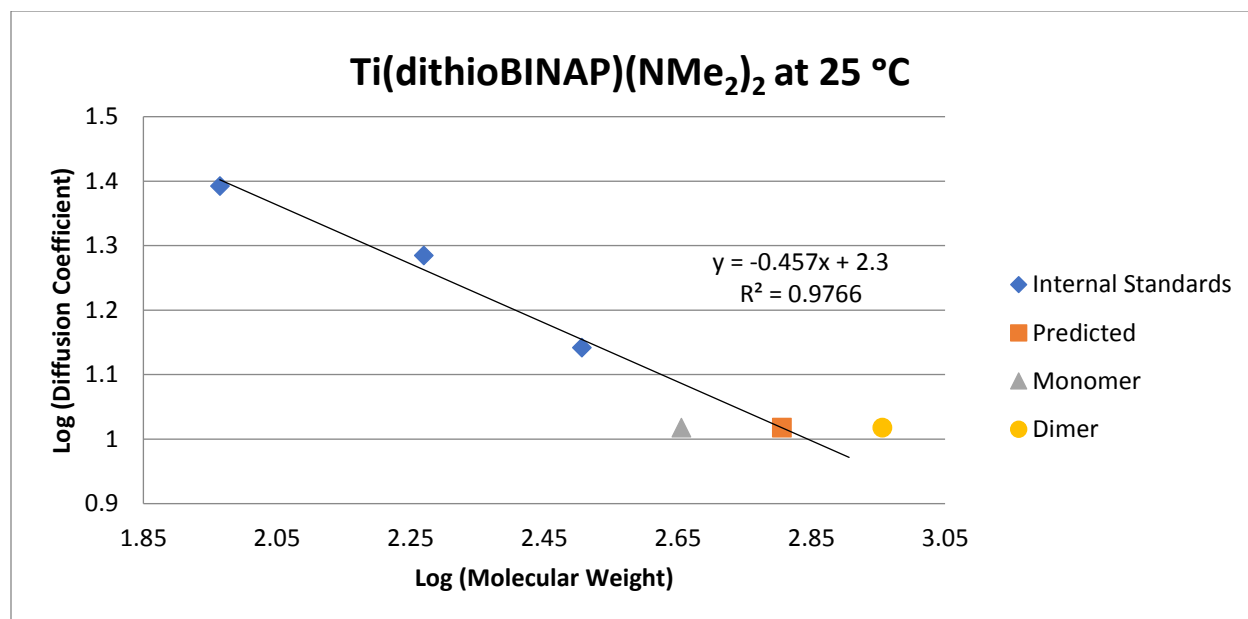
<sup>a</sup>In the case of the 2-thiolatonaphthalene chromium complex, the complex was isolated and used for the LDP value of 13.99 kcal/mol as shown; however, the compound always gave crystals that exhibited characteristics of being zwillling, a rare type of 3-fold merohedral twinning. The structure exhibited two separate types of full molecule disorder (disorder around the pseudo-3-fold of the Cr–N(nitrido) axis and inversion along the Cr–N(nitrido) vector). Consequently, even if the structure could be solved, it was unlikely that it would be of the quality desired to derive the steric parameter. Instead, we prepared the 6-bromo-2-thiolatonaphthalene derivative, and the structure from X-ray diffraction of this derivative was used to obtain the %V<sub>bur</sub> value. DFT optimizations of the 2-thiolatonaphthalene chromium complex without the bromide were also carried out using the full molecule, and two different minima for the thiolate ligand were found, one with the aromatic ring anti to the nitrido and another with the aromatic syn to the nitrido, which had %V<sub>bur</sub> values of 22.5% and 23.1% respectively. The experimental structure for the bromo derivative has the aromatic ring syn to the nitrido. In all cases and regardless of which steric parameter is used, the calculated rate for catalyst **6** is far faster than the experimental rate, which seems to be due to catalyst dimerization (vide infra).

## DOSY-NMR

The DOSY NMR experiments were recorded with a Varian Inova 600 spectrometer equipped with a 5 mm PFG switchable broadband probe operating at 599.89 MHz ( $^1\text{H}$ ). The Varian Dbppste\_cc (DOSY bipolar pulse pair simulated spin echo convection corrected) pulse sequence was utilized for all experiments. Following literature methods,<sup>57-59</sup> the molecular weight of  $\text{Ti}(\text{dithioBINAP})(\text{NMe}_2)_2$  (**6**) was analyzed using DOSY techniques. The internal molecular weight standards chosen for this experiment included ferrocene ( $\text{FeCp}_2$ ), tetrakis(trimethylsilyl)silane ( $\text{Si}(\text{TMS})_4$ ), *n*-hexane, and toluene. The experiment that was performed at room temperature was carried out in a threaded J. Young tube that was sealed with a Teflon stopper. The experiments that were performed at 50 °C were carried out utilizing a capillary tube (2 mm) to reduce and convection errors in the experiments and improve accuracy. An example of the DOSY spectrum obtained by this method is shown below in **Figure 3.32**.



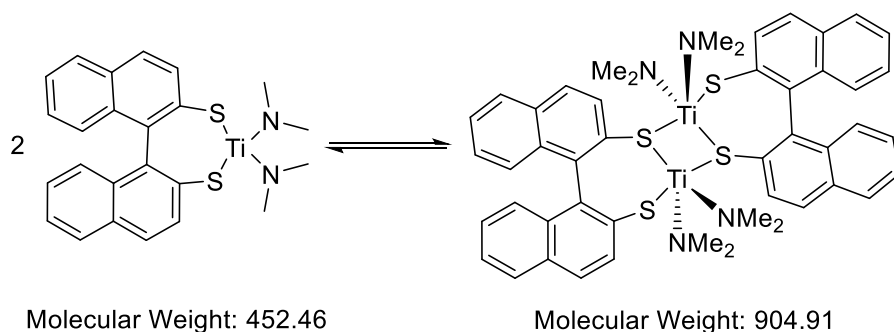
**Figure 3.32.** DOSY spectrum of  $\text{Ti}(\text{dithioBINAP})(\text{NMe}_2)_2$  (**6**) at 25 °C.



**Figure 3.33.** Molecular weight calibration of  $\text{Ti(dithioBINAP)(NMe}_2)_2$  (**6**) at 25 °C.

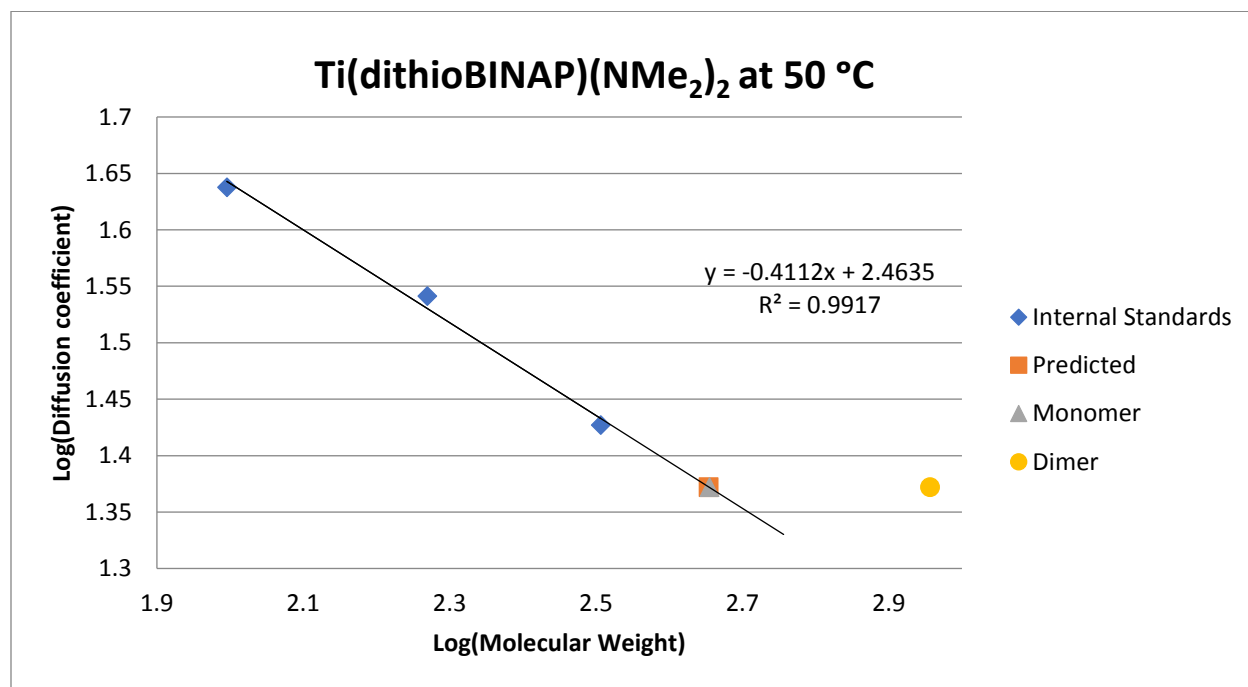
The log of diffusion coefficient vs log molecular weight plots for the internal standards  $\text{FeCp}_2$ , toluene, and  $\text{Si(TMS)}_4$  (shown as the blue diamonds) and  $\text{Ti(dithioBINAP)(NMe}_2)_2$  (shown as the red square) in toluene- $d_8$ . The predicted molecular weight of  $\text{Ti(dithioBINAP)(NMe}_2)_2$  at room temperature is  $639.06 \pm 51.52$  g/mol. The expected molecular weights for the monomer (shown as the green triangle) is 452.46 g/mol and the dimer (shown as the purple circle) is 904.91 g/mol.

Unfortunately, the results of this experiment were inconclusive as to which species is predominant in solution. However, in the solid state,  $\text{Ti(dithioBINAP)(NMe}_2)_2$  was found to be dimeric. Based on these observations,  $\text{Ti(dithioBINAP)(NMe}_2)_2$  could possibly be in equilibrium between the monomeric and dimeric complexes, as shown in the scheme below:



**Figure 3.34.** Molecular weight calibration of  $\text{Ti}(\text{dithioBINAP})(\text{NMe}_2)_2$  (**6**).

Heppert and co-workers have shown an analogous titanium binaphtholate complex to be dimeric at low temperatures, but upon heating undergoes rapid conversion to the monomeric complex.<sup>60</sup> Intrigued by these results an elevated temperature DOSY experiment was conducted.



**Figure 3.35.** Molecular weight calibration of  $\text{Ti}(\text{dithioBINAP})(\text{NMe}_2)_2$  (**6**) at 50 °C.

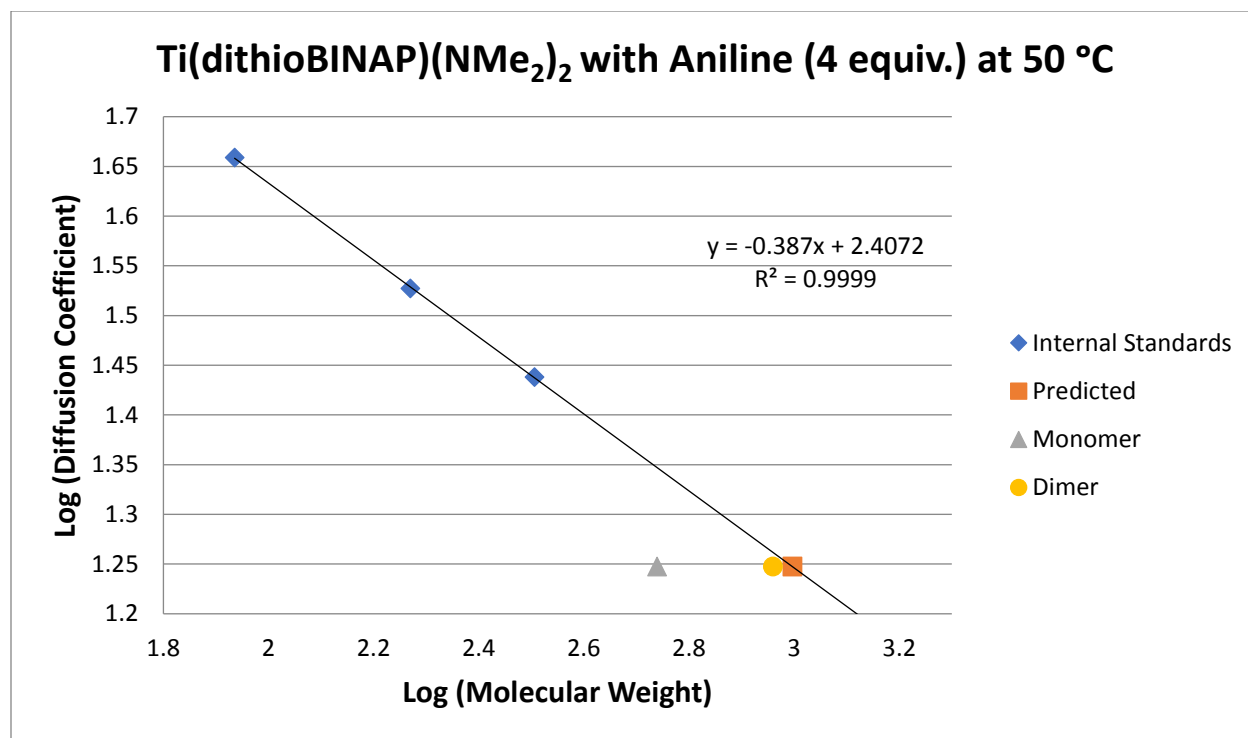
The log of diffusion coefficient vs log molecular weight plots for the internal standards  $\text{FeCp}_2$ , toluene, and  $\text{Si}(\text{TMS})_4$  (show as the blue diamonds) and  $\text{Ti}(\text{dithioBINAP})(\text{NMe}_2)_2$  (shown as the red square) in toluene- $\text{d}_8$ . The predicted molecular weight of  $\text{Ti}(\text{dithioBINAP})(\text{NMe}_2)_2$  at



50 °C is  $450.82 \pm 22.76$  g/mol. The expected molecular weights for the monomer (shown as the green triangle) is 452.46 g/mol and the dimer (shown as the purple circle) is 904.91 g/mol.

The results of this experiment suggest that, when  $\text{Ti}(\text{dithioBINAP})(\text{NMe}_2)_2$  is heated to 50 °C, the predominant species in solution is monomeric. In order to get a better understanding of what was occurring during the kinetic experiments another DOSY experiment was conducted to better mimic the kinetic conditions.

Due to error caused by thermal convection, this experiment could not be measured at the same temperature as the kinetic conditions. Instead, the DOSY experiment was conducted at 50 °C, like the previous experiment. Also, in the kinetic experiments 10 equivalents of aniline is used, however, using this much aniline, the  $^1\text{H}$  NMR signals for the titanium complex and the standards are too obscured to measure an accurate diffusion coefficient. Lessening the amount of excess aniline (to 4 equivalents), the  $^1\text{H}$  NMR signals are not obscured while still providing an environment similar to the kinetic conditions. The data collected from this DOSY experiment is shown in **Figure 3.36**.



**Figure 3.36.** Molecular weight calibration of Ti(dithioBINAP)(NMe<sub>2</sub>)<sub>2</sub> (**6**) with addition of aniline (4 equiv.) at 50 °C.

The log of diffusion coefficient vs log molecular weight plots for the internal standards FeCp<sub>2</sub>, *n*-hexane, and Si(TMS)<sub>4</sub> (show as the blue diamonds) and Ti(dithioBINAP)(NMe<sub>2</sub>)<sub>2</sub> (shown as the red square) in toluene-*d*<sub>8</sub>. The predicted molecular weight of Ti(dithioBINAP)(NMe<sub>2</sub>)<sub>2</sub> at 50 °C is 992.41 ± 48.35 g/mol. The expected molecular weight of the monomer Ti(dithioBINAP)(NHPh)<sub>2</sub> is 548.54 g/mol (shown as the green triangle). The expected molecular weight of the dimer [Ti(dithioBINAP)(=NPh)]<sub>2</sub> is 910.83 g/mol (shown as the purple circle).

The results of this experiment suggest that even at an elevated temperature (50 °C) in the presence of excess aniline the titanium species in solution is dimeric. If the titanium species is dimeric under the kinetic conditions then that species could be experiencing increased sterics around the metal center, as well as different electronic effects. These added effects would

drastically change the catalysis and are not accounted for in our model, which is likely why it doesn't correlate. While some dimerization occurs with the titanium imide active species with all the catalysts, the dimerization of the thiolate species in the presence of a large excess of amine is far more profound, which leads to the large inhibition.

## **<sup>1</sup>H DOSY Procedures**

*Ti(dithioBINAP)(NMe<sub>2</sub>)<sub>2</sub> (6) <sup>1</sup>H DOSY at 25 °C and 50 °C:*

Ti(dithioBINAP)(NMe<sub>2</sub>)<sub>2</sub> (11.0 mg, 0.025 mmol), FeCp<sub>2</sub> (4.65 mg, 0.025 mmol), Si(TMS)<sub>4</sub> (8.02 mg, 0.025 mmol), were added respectively to a volumetric flask. This was diluted to 2.00 mL with toluene-d<sup>8</sup>. The solution was mixed via pipette (i.e. the solution was drawn up into the pipette and dispensed back into the volumetric flask) five times to ensure the solution was well-mixed. Approximately 0.75 mL was transferred to a J. Young NMR tube and a <sup>1</sup>H DOSY experiment was run at 25 °C, with 15 points over the gradient range and 128 scans per point. The three internal standards for this experiment are FeCp<sub>2</sub> (4.04 ppm), Si(TMS)<sub>4</sub> (0.25 ppm), and the residual toluene (2.06 ppm).

The same solution prepared above was used for the DOSY experiment conducted at 50 °C. However, the solution was transferred into a capillary tube (2 mm) that was then placed into a NMR tube and sealed. This sample was allowed to equilibrate inside the NMR spectrometer at 50 °C for 3 hours prior to the <sup>1</sup>H DOSY experiment. The <sup>1</sup>H DOSY experiment was run at 50 °C, with 15 points over the gradient range and 1124 scans per point. The three internal standards for this experiment are FeCp<sub>2</sub> (4.04 ppm), Si(TMS)<sub>4</sub> (0.25 ppm), and the residual toluene (2.06 ppm).

*Ti(dithioBINAP)(NMe<sub>2</sub>)<sub>2</sub> <sup>1</sup>H DOSY at 50 °C with Aniline:*

Ti(dithioBINAP)(NMe<sub>2</sub>)<sub>2</sub> (11.0 mg, 0.025 mmol), FeCp<sub>2</sub> (4.65 mg, 0.025 mmol), Si(TMS)<sub>4</sub> (8.02 mg, 0.025 mmol), *n*-hexane (3.29  $\mu$ L, 0.025 mmol) and aniline (9.13  $\mu$ L, 0.10 mmol) were added respectively to a volumetric flask. This was diluted to 2.00 mL with toluene-*d*<sup>8</sup>. The solution was mixed via pipette (i.e. the solution was drawn up into the pipette and dispensed back into the volumetric flask) five times to ensure the solution was well-mixed. Approximately 0.75 mL of the solution was transferred into a capillary tube (2 mm) that was then placed into a NMR tube and sealed. This sample was allowed to equilibrate inside the NMR spectrometer at 50 °C for 3 hours prior to the <sup>1</sup>H DOSY experiment. The <sup>1</sup>H DOSY experiment was run at 50 °C, with 15 points over the gradient range and 1124 scans per point. The three internal standards for this experiment are FeCp<sub>2</sub> (4.04 ppm), Si(TMS)<sub>4</sub> (0.25 ppm), and *n*-hexane (0.88 ppm).

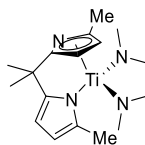
## General Considerations

All reactions and manipulations were carried out in an MBraun glovebox under a nitrogen atmosphere and/or using standard Schlenk techniques. Diethyl ether, pentane, acetonitrile, tetrahydrofuran, benzene, *n*-hexane and toluene were purchased from Aldrich Chemical Company. Diethyl ether, pentane, acetonitrile and toluene were purified by passing through alumina columns to remove water after being sparged with dry nitrogen to remove oxygen. Tetrahydrofuran, benzene, and hexane were sparged with dinitrogen to remove oxygen and distilled from sodium and benzophenone. 2,4-dimethyl phenol, 2-*tert*-butyl-4-methyl phenol, 2,2'-methylenebis(6-*tert*-butyl-4-methylphenol), 2-methyl-4-methoxyphenol and pyrrole-2-carboxyaldehyde were purchased from Aldrich Chemical Company and used as received. 3-methylindole and 2,4,5-trimethylphenol were purchased from Alfa Aesar and used as received. 3,3'-di-*tert*-butyl-5,5'-dimethoxy-[1,1'-biphenyl]-2,2'-diol was purchased from Strem Chemicals Inc. and used as received. 3-*tert*-butyl-4-hydroxyanisole was purchased from TCI America and was used as received. 2-phenylpyrrole, 2-tolylpyrrole, 2-(3,5-trifluoromethylphenyl)pyrrole,  $\text{H}_2\text{dpm}^{2-}[\text{C}_6\text{H}_3(\text{CF}_3)_2]$ ,  $\text{Ti}(\text{NMe}_2)_2(\text{dpm}^{2-}[\text{C}_6\text{H}_3(\text{CF}_3)_2])$  (**1c**),  $\text{H}_2\text{dpm}^{3-}[\text{C}_6\text{H}_3(\text{CF}_3)_2]$ ,  $\text{Ti}(\text{NMe}_2)_2(\text{dpm}^{3-}[\text{C}_6\text{H}_3(\text{CF}_3)_2])$  (**5**),  $\text{H}_2\text{dpm}$ ,  $\text{Ti}(\text{NMe}_2)_2(\text{dpm})$  (**1a**), 2-methylpyrrole,  $\text{H}_2\text{dpm}^{2\text{Me}}$ , 3-methyl-5-fluoroindole and di(3-methylindol-2-yl)phenylmethane, 2-*tert*-butyl-4,5-dimethyl phenol, 1,1'-binaphthalene-2,2'-dithiol, 3,3'-di-*tert*-butyl-5,5'-dimethoxy-[1,1'-biphenyl]-2,2'-diol and 6-bromo-2-naphthalenthio<sup>61</sup> were prepared following their literature procedures.<sup>27, 30, 62-70</sup> To remove all water and oxygen, all ligands were dissolved in benzene, sparged with nitrogen, and refluxed in a Dean-Stark trap overnight. The benzene was then removed *in vacuo*, and the solids were taken into the nitrogen glove box.  $\text{Ti}(\text{NMe}_2)_4$  was purchased from Gelest and used as received. In many cases, due to the

sensitivity of the reported complexes to air and moisture, elemental analysis could not be accurately performed. In these cases, bulk purity of the compound was determined by  $^1\text{H}$  NMR.

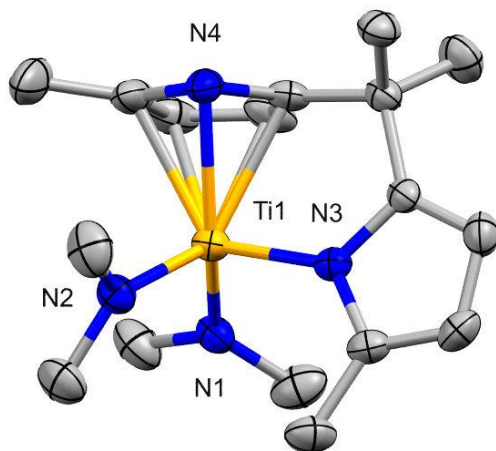
$\text{CDCl}_3$ ,  $\text{C}_6\text{D}_6$ , and toluene- $\text{d}_8$  were purchased from Cambridge Isotopes Laboratories, Inc. Toluene- $\text{d}_8$  and  $\text{C}_6\text{D}_6$  were sparged with dry dinitrogen and dried over 3 Å molecular sieves.  $\text{CDCl}_3$  was sparged with dinitrogen and distilled from  $\text{P}_2\text{O}_5$  prior to use. All NMR solvents were stored under an inert atmosphere. Spectra were taken on Varian instruments located in the Max T. Rogers Instrumentation Facility at Michigan State University. These include an Agilent DDR2 500 spectrometer equipped with a 5 mm pulsed-field-gradient (PFG) OneProbe and operating at 499.955 MHz ( $^1\text{H}$ ) and 125.77 MHz ( $^{13}\text{C}$ ), a Varian Inova 600 spectrometer equipped with a 5 mm PFG switchable broadband probe operating at 599.89 MHz ( $^1\text{H}$ ) and 564.30 MHz ( $^{19}\text{F}$ ), a UNITY plus 500 spectrometer equipped with a 5 mm Pulsed-Field-Gradient (PFG) switchable broadband probe and operating at 499.955 MHz ( $^1\text{H}$ ) and 125.77 ( $^{13}\text{C}$ ), as well as a Varian Unity Plus 500 spectrometer with a low gamma broadband probe operating at 36 MHz ( $^{14}\text{N}$ ). NMR chemical shifts are reported in ppm and referenced to the solvent peaks for  $^1\text{H}$  NMR ( $\text{CDCl}_3$ ,  $\delta$  7.26 ppm;  $\text{C}_6\text{D}_6$ ,  $\delta$  7.16 ppm; toluene- $\text{d}_8$ ,  $\delta$  2.08, 6.97, 7.01, 7.09 ppm) and  $^{13}\text{C}$  NMR ( $\text{CDCl}_3$ ,  $\delta$  77.16 ppm;  $\text{C}_6\text{D}_6$ ,  $\delta$  128.06 ppm; toluene- $\text{d}_8$ ,  $\delta$  20.43, 125.13, 127.96, 128.87, 137.48 ppm).  $^{14}\text{N}$  NMR chemical shifts are reported in ppm and referenced to the dinitrogen gas dissolved in solvents ( $\text{CDCl}_3$ ,  $\delta$  310.0 ppm), which in turn has been externally referenced against neat  $\text{CH}_3\text{NO}_2$  as 381.6 ppm; this procedure places  $\text{NH}_3$  as 0 ppm. Single crystal X-ray diffraction data was collected in the Center for Crystallographic Research at MSU.

## Synthesis of Titanium Complexes and Ligands



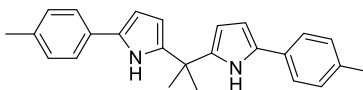
$Ti(dpm^{2,2'-DiMe})(NMe_2)_2$  (**1b**):

A 35 mL pressure tube, equipped with a micro stir bar, was loaded with  $Ti(NMe_2)_4$  (0.224 g, 1 mmol, 1 equiv.) and 3 mL of toluene. Then, a 20 mL scintillation vial was loaded with  $H_2dpm^{2Me}$  (0.202 g, 1 mmol, 1 equiv.) and 3 mL of toluene. Both solutions were then cooled in a liquid nitrogen cold well for 15 min. The solution of  $H_2dpm^{2,2'-DiMe}$  was added dropwise to the vigorously stirring solution of  $Ti(NMe_2)_4$ . The solution was stirred at room temperature for 1 h. The pressure tube was then sealed and heated at 65 °C. The reaction progress was monitored by  $^1H$  NMR and was completed after 36 h. Volatiles were removed *in vacuo* to yield a red viscous oil. This oil was dissolved in a minimum amount of pentane (~1.5 mL) and placed into a -30 °C freezer for 24-36 h to yield a red solid. This solid was recrystallized again in a minimum amount of pentane (~1.0 mL) to yield the product as clear red crystals (0.184 g, 55% yield).  $^1H$  NMR (toluene- $d_8$ , 500 MHz):  $\delta$  = 6.10 (d,  $J$  = 2.7 Hz, 2H, Pyrr-H), 5.90 (d,  $J$  = 3.1 Hz, 2H, Pyrr-H), 2.88 (s, 12H, - $NMe_2$ ), 2.25 (s, 6H, pyrr- $CH_3$ ), 1.78 (s, 6H,  $C(CH_3)_2$ ).  $^{13}C$  NMR (toluene- $d_8$ , 125 MHz):  $\delta$  = 166.37, 142.08, 114.59, 112.56, 51.46, 44.18, 34.79, 20.65. Elemental Analysis: Calcd. C, 60.71; H, 8.39; N, 16.66. Found: C, 60.56; H, 8.62; N, 16.32. M.p.: 68-69 °C.



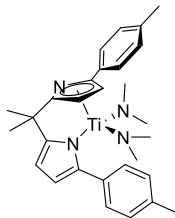
**Figure 3.37.** Crystal structure of  $\text{Ti}(\text{dpm}^{2,2'\text{-DiMe}})(\text{NMe}_2)_2$  (**1b**).





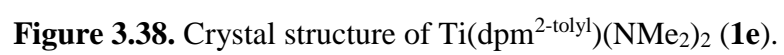
$H_2dpm^{2-tolyl}$ .

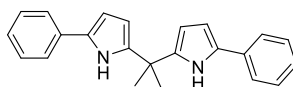
A 25 mL round bottom flask, equipped with a stir bar, was loaded with 2-tolylpyrrole (0.318 g, 2.02 mmol, 1 equiv.) and acetone (3.71 mL, 50.6 mmol, 25 equiv.). The flask was then sealed with a septum. The solution was stirred at room temperature while it was degassed under a flow of nitrogen. After 15 min, trifluoroacetic acid (0.047 mL, 0.61 mmol, 0.3 equiv.) was added via syringe. The reaction was monitored by TLC using hexanes:ethyl acetate (8:2, v/v) as the eluent. The reaction was complete after 2.5 h. The reaction was quenched with 0.1 M NaOH (30 mL), and the aqueous layer was extracted with Et<sub>2</sub>O (2 x 30 mL). The combined organic layers were dried over MgSO<sub>4</sub> and filtered. The solvent was removed *in vacuo* to give a viscous oil. The crude product was dry loaded onto silica gel. Purification was accomplished by flash column chromatography using hexanes:ethyl acetate:TEA (80:20:0.1) as the eluent to provide the product an off-white solid (0.483 g, 67% yield). Note: Depending on the purity of the TFA reaction times may vary, however, additional equiv. may be added. Increasing the equiv. of TFA up to 2.5 equiv. under the same conditions yields the respective product with no depreciation in yield. <sup>1</sup>H NMR (C<sub>6</sub>D<sub>6</sub>, 500 MHz): δ = 7.87 (s, 2H, N-H), 7.05 (d, *J* = 8.2 Hz, 4H, Ar-H), 6.85 (d, *J* = 8.0 Hz, 4H, Ar-H), 6.50-6.55 (m, 2H, Pyrr-H), 6.19 (dd, *J* = 2.7, 3.4 Hz, 2H, Pyrr-H), 2.06 (s, 6H, Ar-CH<sub>3</sub>), 1.52 (s, 6H, C(CH<sub>3</sub>)<sub>2</sub>). <sup>13</sup>C NMR (C<sub>6</sub>D<sub>6</sub>, 125 MHz): δ = 139.34, 135.02, 131.68, 130.29, 129.41, 123.51, 106.19, 105.64, 35.63, 29.39, 20.70. HRMS [M+H]<sup>+</sup>: Found: *m/z* 355.2174; Calcd for C<sub>25</sub>H<sub>27</sub>N<sub>2</sub> 355.2174. MS (EI): *m/z* 354 (M<sup>+</sup>). M.p.: 135-136 °C (dec.).



$Ti(dpm^{2-tolyl})(NMe_2)_2$  (**1e**):

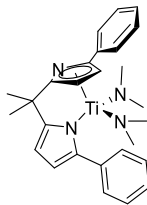
A 35 mL pressure tube, equipped with a stir bar, was loaded with  $Ti(NMe_2)_4$  (0.197 g, 0.88 mmol, 1 equiv.) in 3 mL of toluene. A 20 mL scintillation vial was loaded with  $H_2dpm^{2-tolyl}$  (0.312 g, 0.88 mmol, 1 equiv.) in 3 mL of toluene. Both solutions were then cooled in a liquid nitrogen cold well for 15 min. The solution of  $H_2dpm^{2-tolyl}$  was added dropwise to the vigorously stirring solution of  $Ti(NMe_2)_4$ . The reaction was stirred at room temperature for 1 h. The pressure tube was then sealed and heated at 75 °C. The reaction progress was monitored by  $^1H$  NMR and was completed after 48 h. Volatiles were removed *in vacuo* to yield a light orange solid. The solid was washed with cold pentane and the residual solvent was removed *in vacuo* to give the product as bright yellow powder (0.389 g, 91% yield). X-ray quality crystals can be grown by dissolving in the minimum amount of pentane and place into a -30 °C freezer for 24-36 h.  $^1H$  NMR (toluene- $d_8$ , 500 MHz):  $\delta$  = 7.52 (d,  $J$  = 8.1 Hz, 4H, Ar-H), 6.94 (d,  $J$  = 8.4 Hz, 4H, Ar-H), 6.38 (d,  $J$  = 2.9 Hz, 2H, Pyrr-H), 6.27 (d,  $J$  = 2.9 Hz, 2H, Pyrr-H), 2.55 (s, 12H,  $N(CH_3)_2$ ), 2.12 (s, 6H,  $Ar(CH_3)$ ), 1.91 (s, 6H,  $C(CH_3)_2$ ).  $^{13}C$  NMR (toluene- $d_8$ , 125 MHz):  $\delta$  = 161.99, 141.48, 136.23, 135.02, 128.99, 127.92, 110.40, 109.02, 47.08, 40.00, 30.35, 21.54. Elemental Analysis: Calcd. C, 71.30; H, 7.43; N, 11.47. Found: C, 70.85; H, 7.70; N, 11.44. M.p.: 122-123 °C.





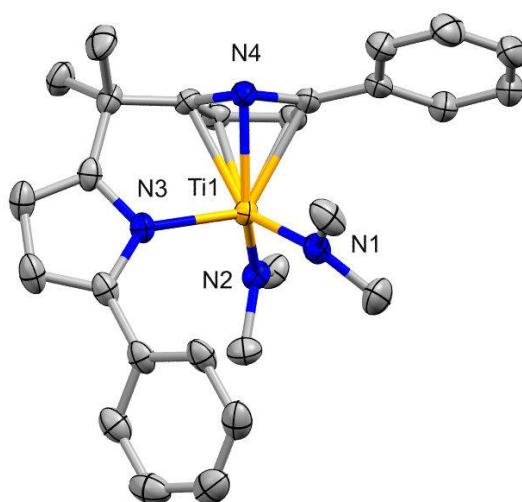
*H<sub>2</sub>dpm*<sup>2-phenyl</sup>:

A 25 mL round bottom flask, equipped with a stir bar, was loaded with 2-phenylpyrrole (0.466 g, 3.25 mmol, 1 equiv.) and acetone (5.97 mL, 81.0 mmol, 25 equiv.). The flask was then sealed with a septum. The solution was stirred at room temperature while being degassed under a flow of nitrogen. After 15 min, trifluoroacetic acid (0.111 mL, 0.97 mmol, 0.3 equiv.) was added via syringe. The reaction was monitored by TLC using hexanes:ethyl acetate (8:2, v/v) as the eluent. The reaction was complete after 4 h. The reaction was quenched with 0.1 M NaOH (30 mL) and the aqueous layer was extracted with ether (2 x 30 mL). The combined organic layers were dried over MgSO<sub>4</sub> and filtered. The solvent was removed in vacuo to yield a dark purple oil. The crude product was dry loaded onto silica gel. Purification was accomplished by flash column chromatography using hexanes:ethyl acetate:TEA (80:20:0.1) as the eluent to provide the product an off-white solid (0.392 g, 48% yield). Note: Depending on the purity of the TFA, reaction times may vary; however, additional equiv may be added. Increasing the equiv of TFA up to 2.5 equiv. under the same conditions yields the respective product with no depreciation in yield. <sup>1</sup>H NMR (C<sub>6</sub>D<sub>6</sub>, 500 MHz): δ = 7.85 (s, 2H, N-H), 7.07-7.04 (m, 4H, Ar-H), 7.00 (t, *J* = 7.7 Hz, 4H, Ar-H), 6.92 (t, *J* = 7.3 Hz, 2H, Ar-H), 6.55-6.51 (m, 2H, Pyrr-H), 6.21-6.17 (m, 2H, Pyrr-H), 1.51 (s, 6H, C(CH<sub>3</sub>)<sub>2</sub>). <sup>13</sup>C NMR (C<sub>6</sub>D<sub>6</sub>, 125 MHz): δ = 139.63, 132.81, 131.57, 128.74, 125.62, 123.44, 106.31, 106.16, 35.62, 29.31. HRMS [M-H]<sup>-</sup>: Found: *m/z* 325.1714.; Calcd for C<sub>23</sub>H<sub>21</sub>N<sub>2</sub> 325.1705. MS (EI): *m/z* 326 (M<sup>+</sup>). M.p.: 143-145 °C.

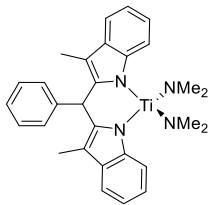


$Ti(NMe_2)_2(dpm^{2-phenyl})$  (**1d**):

A 35 mL pressure tube, equipped with a micro stir bar, was loaded with  $Ti(NMe_2)_4$  (0.202 g, 0.90 mmol, 1 equiv.) and 2 mL of toluene. A 20 mL scintillation vial was loaded with  $H_2dpm^{2-phenyl}$  (0.294 g, 0.90 mmol, 1 equiv.) and 2 mL of toluene. Both solutions were then cooled in a liquid nitrogen cold well for 15 min. The solution of  $H_2dpm^{2-phenyl}$  was added dropwise to the vigorously stirring solution of  $Ti(NMe_2)_4$ . The reaction was stirred at room temperature for 1 h. The pressure tube was then sealed and heated at 75 °C. The reaction progress was monitored by  $^1H$  NMR and was completed after 48 h. Volatiles were removed *in vacuo* to give a light orange solid. This solid was rinsed with cold pentane to yield the product as bright yellow powder. (0.361 g, 86% yield). X-ray quality crystals can be grown by dissolving in the minimum amount of pentane, with a few drops of toluene, and place into a -30 °C freezer for 24-36 h.  $^1H$  NMR ( $C_6D_6$ , 500 MHz):  $\delta$  = 7.60-7.57 (m, 4H, Ar-H), 7.09 (t,  $J$  = 7.6 Hz, 4H, Ar-H), 7.02-6.97 (m, 2H, Ar-H), 6.41 (d,  $J$  = 2.9 Hz, 2H, Pyrr-H), 6.28 (d,  $J$  = 2.9 Hz, 2H, Pyrr-H), 2.48 (s, 12H,  $N(CH_3)_2$ ), 1.93 (s, 6H,  $C(CH_3)_2$ ).  $^{13}C$  NMR ( $C_6D_6$ , 125 MHz):  $\delta$  = 161.54, 140.58, 136.89, 127.55, 127.16, 126.22, 110.18, 108.48, 46.31, 39.24, 29.63. Note: Despite multiple attempts, adequate elemental analysis couldn't be obtained. M.p.: 129-130 °C.

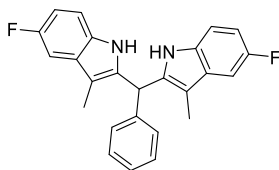


**Figure 3.39.** Crystal structure of  $\text{Ti}(\text{dpm}^{2\text{-phenyl}})(\text{NMe}_2)_2$  (**1d**).



*Ti(dim<sup>3Me</sup>)(NMe<sub>2</sub>)<sub>2</sub> (2a):*

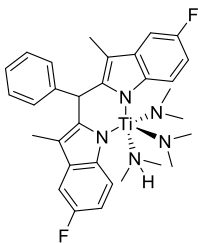
A 20 mL scintillation vial, equipped with a micro stir bar, was loaded with Ti(NMe<sub>2</sub>)<sub>4</sub> (0.224 g, 1.0 mmol, 1 equiv.) and 3 mL of ether. A separate 20 mL scintillation vial was loaded with H<sub>2</sub>dim<sup>3Me</sup> (0.350 g, 1.0 mmol, 1 equiv.) and 4 mL of ether. Both solutions were then cooled in a liquid nitrogen cold well for 15 min. The solution of H<sub>2</sub>dim<sup>3Me</sup> was added dropwise to the vigorously stirring solution of Ti(NMe<sub>2</sub>)<sub>4</sub>. The reaction mixture was stirred at room temperature for 14 h. Volatiles were removed *in vacuo* to give a red solid. The solid was washed with cold pentane and the residual solvent was removed *in vacuo* to yield the product as a dark red solid (0.444 g, 97% yield). <sup>1</sup>H NMR (C<sub>6</sub>D<sub>6</sub>, 500 MHz): δ = 7.64 (m, 2H, Ind-H), 7.31-7.27 (m, 2H, Ar-H), 7.27-7.23 (m, 2H, Ar-H), 7.23-7.19 (m, 2H, Ind/Ar-H), 6.92-6.89 (m, 4H, Ind-H), 6.89-6.85 (m, 1H, Ind-H), 6.09 (s, 1H, C-H), 2.92 (s, 6H, N(CH<sub>3</sub>)<sub>2</sub>), 2.53 (s, 6H, N(CH<sub>3</sub>)<sub>2</sub>), 2.33 (s, 6H, Ind-CH<sub>3</sub>). <sup>13</sup>C NMR (C<sub>6</sub>D<sub>6</sub>, 125 MHz): δ = 144.64, 143.64, 142.68, 129.83, 128.01, 127.99, 126.05, 121.97, 120.30, 118.17, 114.55, 109.32, 44.76, 41.50, 40.20, 8.56. Note: Despite multiple attempts, adequate elemental analysis couldn't be obtained. M.p.: 143-144 °C.



*H<sub>2</sub>dim*<sup>3Me5F</sup>:

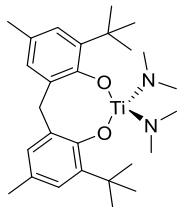
This compound was made by adapting/modifying a literature procedure.<sup>36</sup> Benzaldehyde (0.306 g, 2.88 mmol, 0.5 equiv.) was added to a stirred solution of 5-fluoro-3-methylindole (0.860g, 5.77 mmol, 1 equiv.) in 5 mL of ethanol. Concentrated sulfuric acid (0.031 mL, 0.577 mmol, 0.1 equiv) was added to the reaction solution and was then let stir for 24 h at room temperature. The mixture was concentrated *in vacuo* and washed with cold ethanol (2 x 1 mL). The product was then recrystallized by re-dissolving in minimum amount of warm ethanol (~3 mL) and placed into a –20 °C freezer, to give the product as dark purple crystals. This colored impurity can be removed by dissolving the product in benzene and passing it through a small Celite plug to give the product as a tan solid (1.29 g, 58% yield). <sup>1</sup>H NMR (C<sub>6</sub>D<sub>6</sub>, 500 MHz): δ = 7.22 (dd, *J* = 9.4, 2.5 Hz, 2H, Ind-H), 7.13 (s, 1H, Ar-H), 7.03 (m, 2H, Ar-H), 6.96 (s, 2H, N-H), 6.91-6.85 (m, 4H, Ar-H/Ind-H), 6.49 (dd, *J* = 8.8, 4.3 Hz, 2H, Ind-H), 5.64 (s, 1H, C-H), 1.86 (s, 6H, CH<sub>3</sub>). <sup>13</sup>C NMR (C<sub>6</sub>D<sub>6</sub>, 125 MHz): δ = 159.22, 157.35, 139.69, 134.71, 131.78, 130.13, 130.05, 128.91, 128.34, 128.20, 127.27, 111.55, 111.47, 110.06, 109.86, 109.03, 109.00, 103.71, 103.53, 41.01, 8.06. <sup>19</sup>F NMR (C<sub>6</sub>D<sub>6</sub>, 470 MHz): δ = –124.05 (td, *J* = 9.3, 4.3 Hz). MS (EI): *m/z* 386 (M<sup>+</sup>). HRMS [M+H]<sup>+</sup>: Found: *m/z* 385.1502.; Calcd for C<sub>25</sub>H<sub>19</sub>N<sub>2</sub>F<sub>2</sub> 385.1516. M.p.: 187-187 °C (dec.).





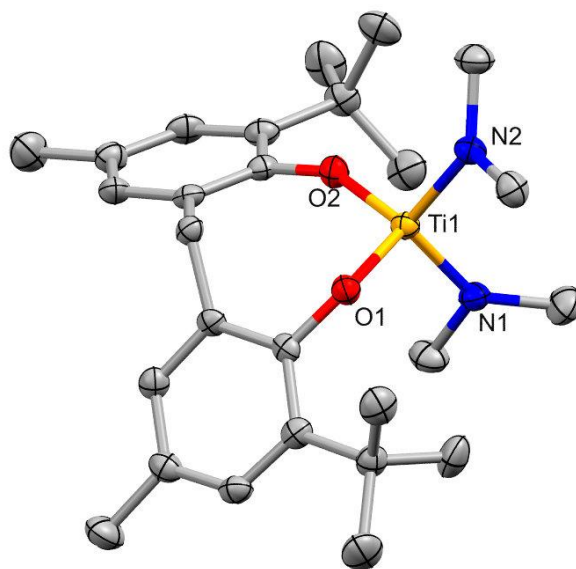
*Ti(dim<sup>3Me5F</sup>)(NMe<sub>2</sub>)<sub>2</sub>(HNMe<sub>2</sub>) (2b):*

A 20 mL scintillation vial, equipped with a micro stir bar, was loaded with Ti(NMe<sub>2</sub>)<sub>4</sub> (0.128 g, 1.0 mmol, 1 equiv.) and 3 mL of ether. A separate 20 mL scintillation vial was loaded with H<sub>2</sub>dim<sup>3Me5F</sup> (0.221 g, 1.0 mmol, 1 equiv.) and 4 mL of ether. Both solutions were then cooled in a liquid nitrogen cold well for 15 min. The solution of H<sub>2</sub>dim<sup>3Me5F</sup> was added dropwise to the vigorously stirring solution of Ti(NMe<sub>2</sub>)<sub>4</sub>. The reaction mixture was stirred at room temperature for 14 h. Volatiles were removed *in vacuo* to give a dark red solid. The crude product was washed with cold pentane and the residual solvent was removed *in vacuo* to yield the product as a brick red solid (0.381 g, 98% yield). <sup>1</sup>H NMR (toluene-*d*<sub>8</sub>, 500 MHz): δ = 7.53 (dd, *J* = 9.5, 2.4 Hz, 2H, Ind-H), 7.15-7.12 (m, 7H, Ar-H/Ind-H), 7.04 (d, *J* = 8.6, 4.4 Hz, 2H, Ind-H). 6.25 (s, 1H, C-H), 3.11 (s, 6H, NMe<sub>2</sub>), 2.79 (s, 6H, NMe<sub>2</sub>), 2.53 (s, 6H, CH<sub>3</sub>), 1.94 (d, *J* = 6.2 Hz, 6H, HNMe<sub>2</sub>), 1.71 (s, 1H, HNMe<sub>2</sub>). <sup>13</sup>C NMR (toluene-*d*<sub>8</sub>, 125 MHz): δ = 164.47, 162.61, 151.24, 147.66, 144.95, 135.71, 135.63, 132.98, 132.93, 131.15, 118.97, 118.90, 113.90, 113.70, 108.40, 108.22, 49.66, 47.80, 45.35, 43.49, 13.51. <sup>19</sup>F NMR (toluene-*d*<sub>8</sub>, 470 MHz): δ = -119.69 (s). Note: Despite multiple attempts, adequate elemental analysis couldn't be obtained. M.p.: 128-129 °C (dec.).

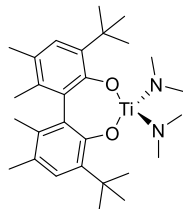


$Ti(NMe_2)_2(bis-phenoxide^{2tBu-4Me})$  (**3**):

A 35 mL pressure tube, equipped with a micro stir bar, was loaded with  $Ti(NMe_2)_4$  (0.336 g, 1.5 mmol, 1.5 equiv.) and 3 mL of toluene. A 20 mL scintillation vial was loaded with 2,2'-methylenebis(6-*tert*-butyl-4-methylphenol) (0.341 g, 1.0 mmol, 1 equiv.) and 2 mL of toluene. Both solutions were then cooled in a liquid nitrogen cold well for 15 min. Then the solution of 2,2'-methylenebis(6-*tert*-butyl-4-methylphenol) was added dropwise to the vigorously stirring solution of  $Ti(NMe_2)_4$ . The reaction mixture stirred at room temperature for 1 h. The pressure tube was then sealed and heated to 75 °C for 9 days. The volatiles were removed in vacuo to give a viscous dark orange oil. This oil was rinsed with cold pentane (3 x 1 mL), to remove the excess  $Ti(NMe_2)_4$ . The product was recrystallized by dissolving in the minimum amount of pentane and placed in a -30 °C freezer for 48 h, yielding the product as bright yellow crystals (0.286 g, 61% yield).  $^1H$  NMR ( $C_6D_6$ , 500 MHz):  $\delta$  = 7.16 (d,  $J$  = 2.1 Hz, 2H, Ar-H), 7.06 (d,  $J$  = 2.1 Hz, 2H, Ar-H), 4.18 (d,  $J$  = 13.7 Hz, 1H, C-H), 3.42 (d,  $J$  = 13.8 Hz, 1H, C-H), 3.35 (s, 6H,  $N(CH_3)_2$ ), 2.81 (s, 6H,  $N(CH_3)_2$ ), 2.22 (s, 6H, Ar- $CH_3$ ), 1.56 (s, 18H,  $C(CH_3)_3$ ).  $^{13}C$  NMR ( $C_6D_6$ , 125 MHz):  $\delta$  = 158.56, 136.64, 131.05, 129.35, 129.19, 125.50, 44.25, 44.12, 34.84, 32.71, 30.05, 20.85. Elemental Analysis: Calcd. C, 68.34; H, 8.92; N, 5.90. Found: C, 68.24; H, 9.40; N, 5.76. M.p.: 125-126 °C.

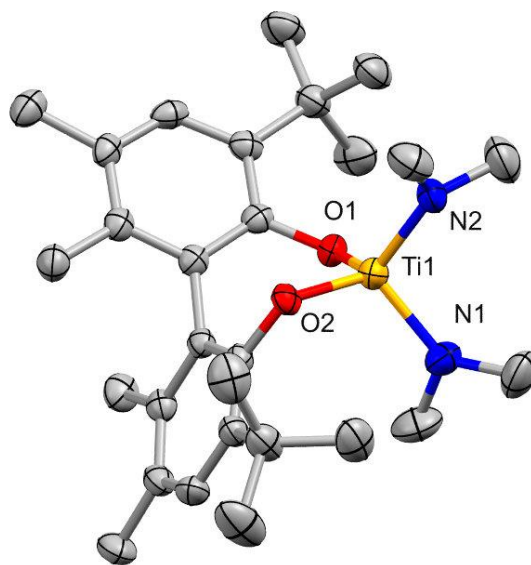


**Figure 3.40.** Crystal structure of  $\text{Ti}(\text{bis-phenoxide}^{2\text{tBu-4Me}})(\text{NMe}_2)_2$  (**3**).

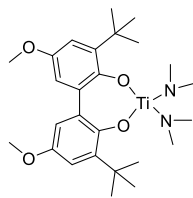


$Ti(NMe_2)_2(biphenol^{2tBu-4,5diMe})$  (**4a**):

A 20 mL scintillation vial, equipped with a micro stir bar, was loaded with  $Ti(NMe_2)_4$  (1.5 mmol, 0.336 g, 1.5 equiv.) and 5 mL of ether. A separate 20 mL scintillation vial was loaded with 3,3'-di-*tert*-butyl-5,5',6,6'-tetramethyl-[1,1'-biphenyl]-2,2'-diol (1.0 mmol, 0.355 g, 1 equiv.) and 5 mL of ether. Both solutions were then cooled in a liquid nitrogen cold well for 15 min. Then the solution of 3,3'-di-*tert*-butyl-5,5',6,6'-tetramethyl-[1,1'-biphenyl]-2,2'-diol was added dropwise to a vigorously stirring solution of  $Ti(NMe_2)_4$  over 15 min. The reaction mixture was stirred at room temperature for 14 h. The volatiles were removed *in vacuo* to give a viscous orange/yellow oil. This oil was rinsed with cold pentane (3 x 2 mL), to remove the excess  $Ti(NMe_2)_4$ , to give a bright yellow powder. This powder was then recrystallized from pentane to give bright yellow crystals of the product (0.327 g, 67% yield). Note: If addition is too fast or if using 1 equiv. of ligand to 1 equiv. of  $Ti(NMe_2)_4$  for this reaction, it produces the undesired  $Ti(Biphenol^{2tBu-4,5-diMe})_2$  predominately.  $^1H$  NMR ( $C_6D_6$ , 500 MHz):  $\delta$  = 7.25 (s, 2H, Ar-H), 2.85 (s, 12H,  $N(CH_3)_2$ ), 2.13 (s, 6H, Ar- $CH_3$ ), 1.77 (s, 6H, Ar- $CH_3$ ), 1.58 (s, 18H,  $C(CH_3)_3$ ).  $^{13}C$  NMR ( $C_6D_6$ , 125 MHz):  $\delta$  = 156.04, 134.83, 134.62, 128.33, 128.15, 127.39, 43.98, 34.82, 30.32, 20.15, 16.72. Note: Despite multiple attempts, adequate elemental analysis couldn't be obtained. M.p.: 186-187 °C.

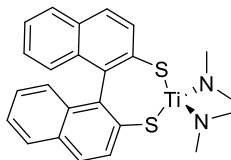


**Figure 3.41.** Crystal structure of  $\text{Ti}(\text{biphenol}^{2\text{-tBu-4,5-diMe}})(\text{NMe}_2)_2$  (**4a**).



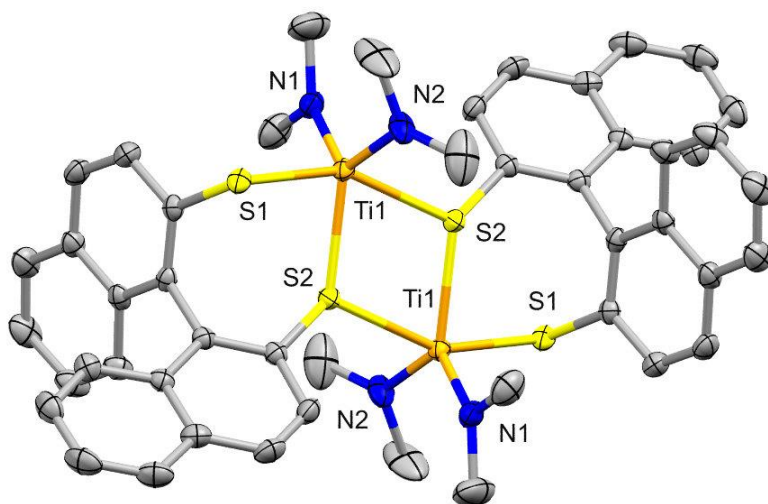
$Ti(NMe_2)_2(biphenol^{2tBu-4OMe})$  (**4b**):

A 20 mL scintillation vial, equipped with a micro stir bar, was loaded with  $Ti(NMe_2)_4$  (1.0 mmol, 0.224 g, 1.0 equiv.) and 5 mL of ether. A separate 20 mL scintillation vial was loaded with 3,3'-di-*tert*-butyl-5,5'-dimethoxy-[1,1'-biphenyl]-2,2'-diol (1.0 mmol, 0.358 g, 1 equiv.) and 5 mL of ether. Both solutions were then cooled in a liquid nitrogen cold well for 15 min. Then the solution of 3,3'-di-*tert*-butyl-5,5'-dimethoxy-[1,1'-biphenyl]-2,2'-diol was added dropwise to a vigorously stirring solution of  $Ti(NMe_2)_4$  over 15 min. The reaction mixture was stirred at room temperature for 16 h. The volatiles were removed *in vacuo* to give a viscous light red oil. This oil was dissolved in 5 mL of pentane and placed into a  $-30\text{ }^\circ\text{C}$  freezer. The pentane solution was passed through Celite and the filtrate was collected (solution was concentrated, cooled and filtered twice more to remove the unwanted by-product  $Ti(Biphenol^{2tBu-4OMe})_2$ ). The solvent was removed *in vacuo* to yield the product as a light orange/yellow powder (0.286 g, 58% yield).  $^1\text{H}$  NMR ( $\text{C}_6\text{D}_6$ , 500 MHz):  $\delta$  = 7.22 (d,  $J$  = 3.2 Hz, 2H, Ar-H), 7.12 (d,  $J$  = 3.2 Hz, 2H, Ar-H), 3.33 (s, 6H, -OMe), 2.90 (s, 12H,  $\text{N}(\text{CH}_3)_2$ ), 1.50 (s, 18H,  $\text{C}(\text{CH}_3)_3$ ).  $^{13}\text{C}$  NMR ( $\text{C}_6\text{D}_6$ , 125 MHz):  $\delta$  = 153.57, 152.66, 138.48, 130.12, 127.84, 127.65, 127.45, 114.41, 114.25, 54.80, 44.01, 35.30, 29.91. Note: Despite multiple attempts, adequate elemental analysis couldn't be obtained. M.p.: 78-79  $^\circ\text{C}$ .



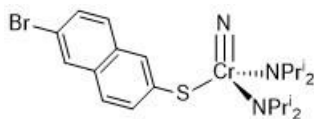
*Ti(DiThioBINAP)(NMe<sub>2</sub>)<sub>2</sub> (6):*

A 20 mL scintillation vials, equipped with a micro stir bar, was loaded with Ti(NMe<sub>2</sub>)<sub>4</sub> (0.327 g, 1.46 mmol, 1 equiv.) and 4 mL of toluene. A separate 20 mL scintillation vials was loaded with [1,1'-binaphthalene]-2,2'-dithiol (0.465 g, 1.46 mmol, 1 equiv.) and 6 mL of toluene. Both solutions were the cooled in a liquid nitrogen cold well for 15 min. The solution of [1,1'-binaphthalene]-2,2'-dithiol was added dropwise to the vigorously stirring solution of Ti(NMe<sub>2</sub>)<sub>4</sub>. The reaction mixture was stirred at room temperature for 14 h. Volatiles were removed in *vacuo* to give dark orange solid (0.654 g, 99% yield). X-ray quality crystals can be grown by vapor diffusion using toluene and ether at room temperature for 48 h. <sup>1</sup>H NMR (C<sub>6</sub>D<sub>6</sub>, 500 MHz): δ = 7.86 (d, *J* = 8.6 Hz, 2H, Ar-H), 7.60 (d, *J* = 8.7 Hz, 2H, Ar-H), 7.56 (d, *J* = 8.1 Hz, 2H, Ar-H), 7.17 (d, *J* = 8.4 Hz, 2H, Ar-H), 7.04 (ddd, *J* = 8.1, 7.0, 1.1 Hz, 2H, Ar-H), 6.90 (ddd, *J* = 8.3, 6.9, 1.3 Hz, 2H, Ar-H), 2.90 (s, 6H, N(CH<sub>3</sub>)<sub>2</sub>). <sup>13</sup>C NMR (C<sub>6</sub>D<sub>6</sub>, 125 MHz): δ = 140.56, 134.42, 133.24, 132.70, 132.48, 128.91, 128.17, 127.16, 127.08, 125.92, 44.91. Elemental Analysis: Calcd. C, 63.71; H, 5.35; N, 6.19. Found: C, 64.12; H, 5.56; N, 6.02. M.p.: 190-192 °C (dec).



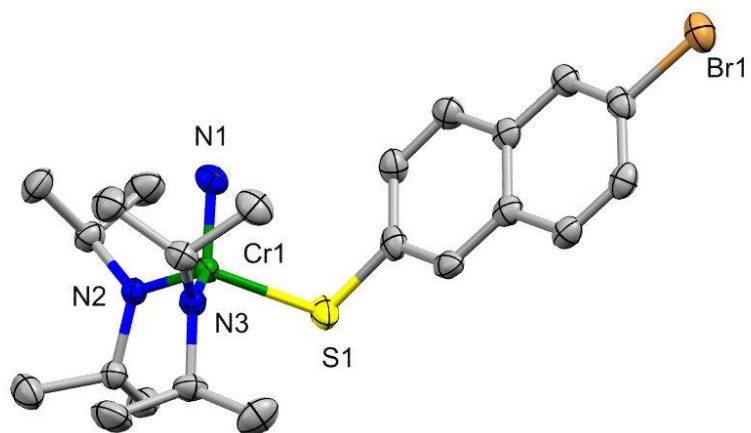
**Figure 3.42.** Crystal structure of  $\text{Ti}(\text{dithioBINAP})(\text{NMe}_2)_2$  (**6**).





$\text{NCr}(\text{N}^i\text{Pr}_2)_2(6\text{Br-HSNap})$ :

To a nearly frozen, stirring solution of  $\text{NCr}(\text{N}^i\text{Pr}_2)_3$  (125 mg, 0.340 mmol) in THF, a THF solution of the 6Br-HSNap (87 mg, 0.360 mmol) was added dropwise. The solution was allowed to stir for 18 h at 55 °C upon which time the color changed to a reddish-purple color. After that time, the volatiles were dried *in vacuo*, and the dark residue was extracted with ether. The solution was filtered over Celite and the filtrate concentrated. The ether solution was then left in the freezer for recrystallization at –30 °C overnight. The LDP value, which was measured but not used in this particular study, is 14.15 kcal/mol. (120 mg, 0.264 mmol, 78%).  $^1\text{H}$  NMR (500 MHz,  $\text{CDCl}_3$ )  $\delta$  = 8.09 (s, 1H, Ar-H), 7.88 (s, 1H, Ar-H), 7.80-7.78 (m, 1H, Ar-H), 7.53-7.51 (m, 2H, Ar-H), 7.46 – 7.44 (m, 1H, Ar-H), 5.34-5.26 (sept,  $J$  = 6.2 Hz, 2H,  $\text{CH}(\text{CH}_3)_2$ ), 3.79-3.71 (sept,  $J$  = 6.3 Hz, 2H,  $\text{CH}(\text{CH}_3)_2$ ), 1.81-1.80 (d,  $J$  = 6.3 Hz, 6H,  $\text{CH}(\text{CH}_3)_2$ ), 1.55-1.54 (d,  $J$  = 6.3 Hz, 6H,  $\text{CH}(\text{CH}_3)_2$ ), 1.18-1.15 (dd,  $J$  = 6.5, 4.5 Hz, 12H,  $\text{CH}(\text{CH}_3)_2$ ).  $^{13}\text{C}$  NMR (125 MHz,  $\text{CDCl}_3$ ):  $\delta$  = 141.06, 132.58, 132.11, 131.89, 130.09, 129.51, 129.11, 128.29, 125.92, 118.14, 59.21, 56.20, 30.43, 30.06, 21.99, 20.52.  $^{14}\text{N}$  NMR (36 MHz,  $\text{CDCl}_3$ ):  $\delta$  = 996.0, 404.2. M.p.: 149-151 °C.



**Figure 3.43.** Crystal structure of  $\text{NCr}(\text{N}^i\text{Pr}_2)_2(6\text{-BrSNap})$ .

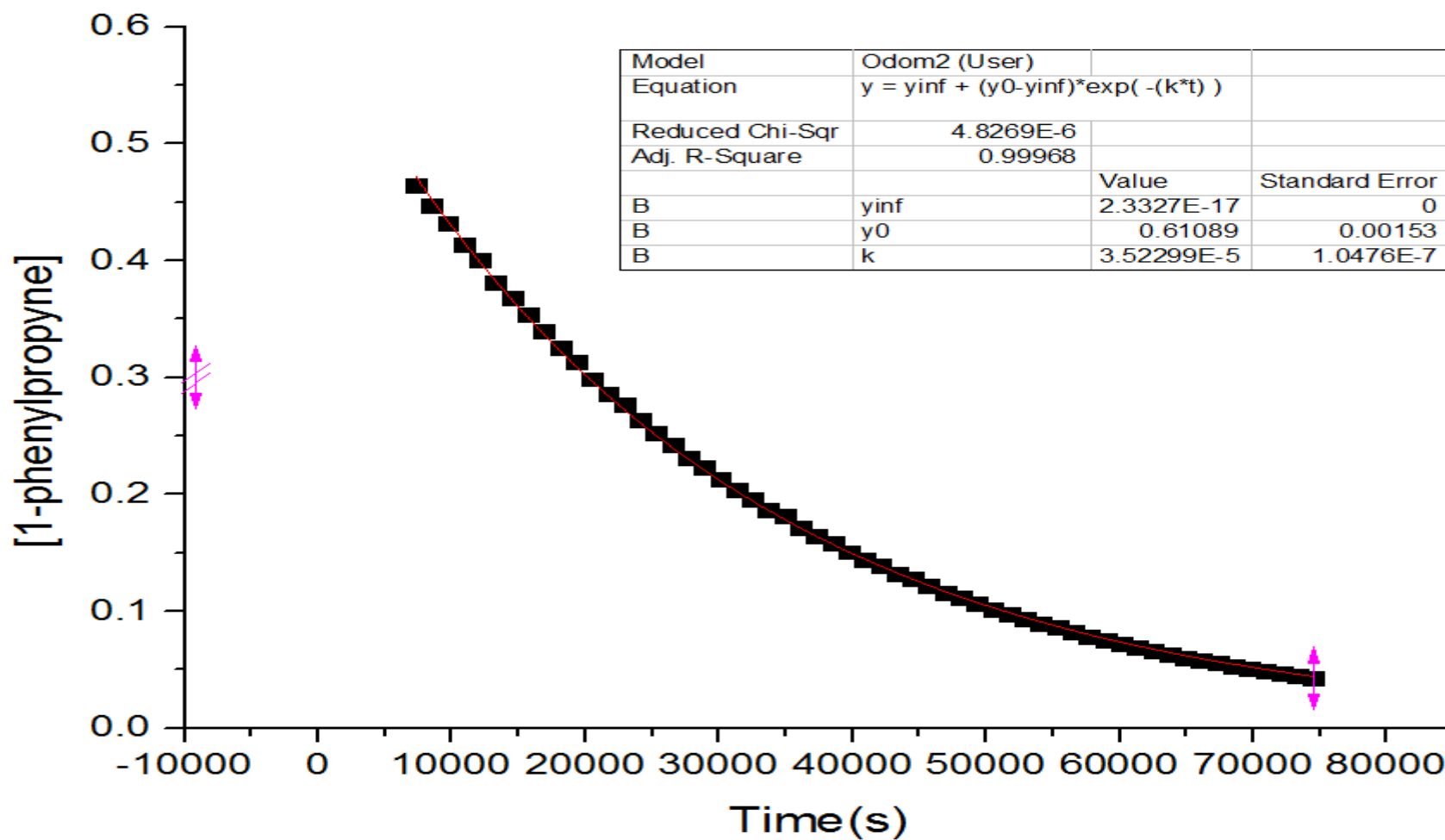
## General Procedure for Kinetics

All manipulations were done in an inert atmosphere drybox. A 2 mL volumetric flask was loaded the catalyst (10 mol%, 0.1 mmol) and ferrocene (0.0560 g, 0.3 mmol) as an internal standard. Next, 0.75 mL of toluene-d<sub>8</sub> was added to the volumetric flask and the solution was mixed by swirling the flask until all solids were dissolved. Once all solids were dissolved, aniline (911 μL, 10 mmol) and 1-phenylpropyne (125 μL, 1.0 mmol) were added respectively to the volumetric flask. Lastly, the solution was diluted to 2 mL with toluene-d<sub>8</sub>. The solution was mixed via pipette (i.e. the solution was drawn up into the pipette and dispensed back into the volumetric flask) five times to ensure the solution was well-mixed. An ample amount of solution (~0.75 mL) was loaded into a threaded J. Young tube that was sealed with a Teflon stopper. The tube was removed from the dry box and was heated at 75 °C in the NMR spectrometer (Varian Inova 600 spectrometer). The relative 1-phenylpropyne *versus* ferrocene concentration was monitored as a function of time. The fits are to the exponential decay of the starting material using the scientific graphing program Origin. The exact expression used to fit the data is shown below:<sup>71</sup>

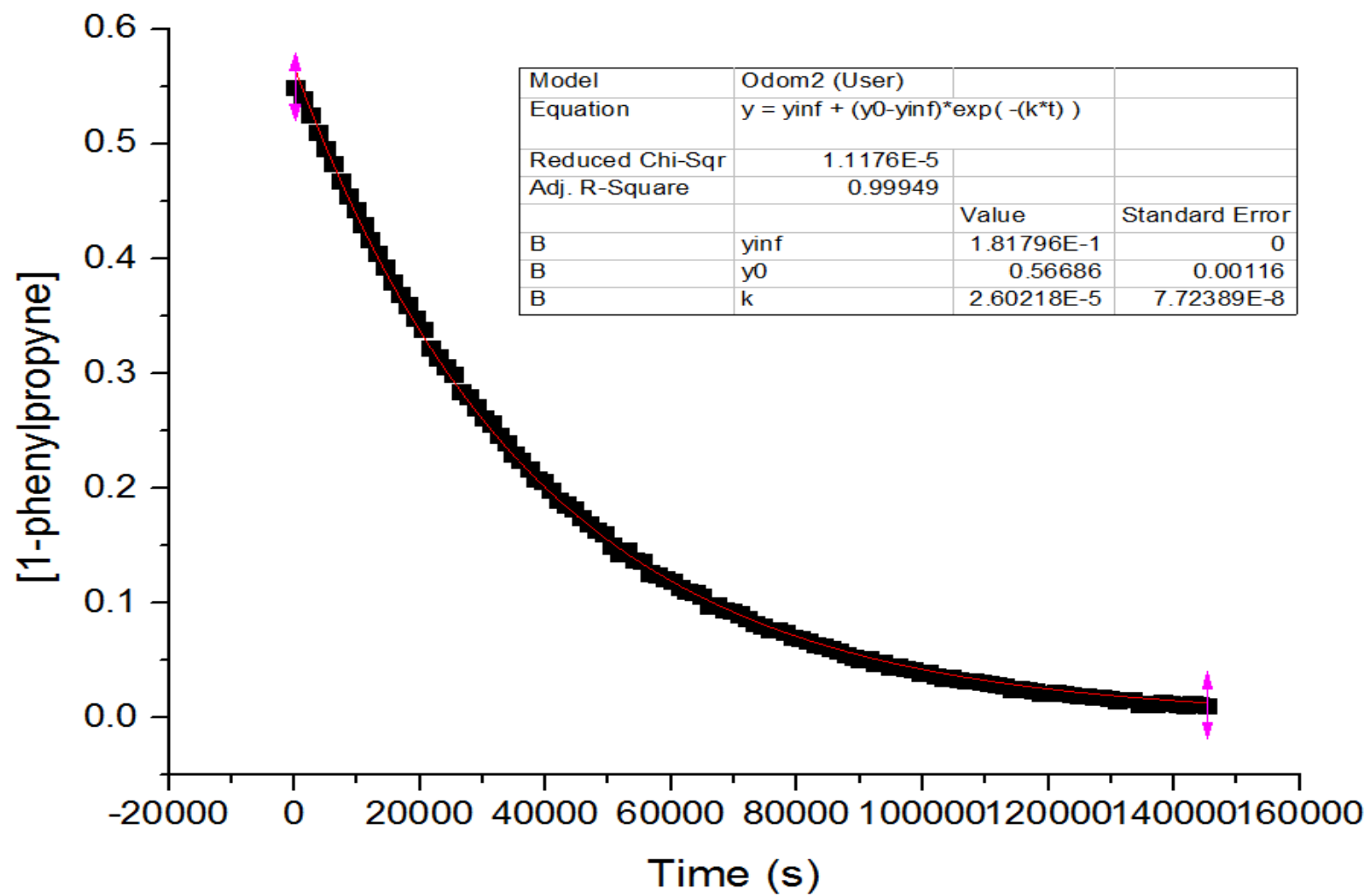
$$Y_t = Y_\infty + (Y_0 - Y_\infty)\exp^{-k_{obs}t}$$

Where Y = [1-phenylpropyne] at time t (Y<sub>t</sub>), infinity (Y<sub>∞</sub>), or at the start of the reaction (Y<sub>0</sub>). The variables Y<sub>∞</sub>, Y<sub>0</sub>, k<sub>obs</sub>, were optimized in the fits. Each kinetic experiment was completed in triplicate.

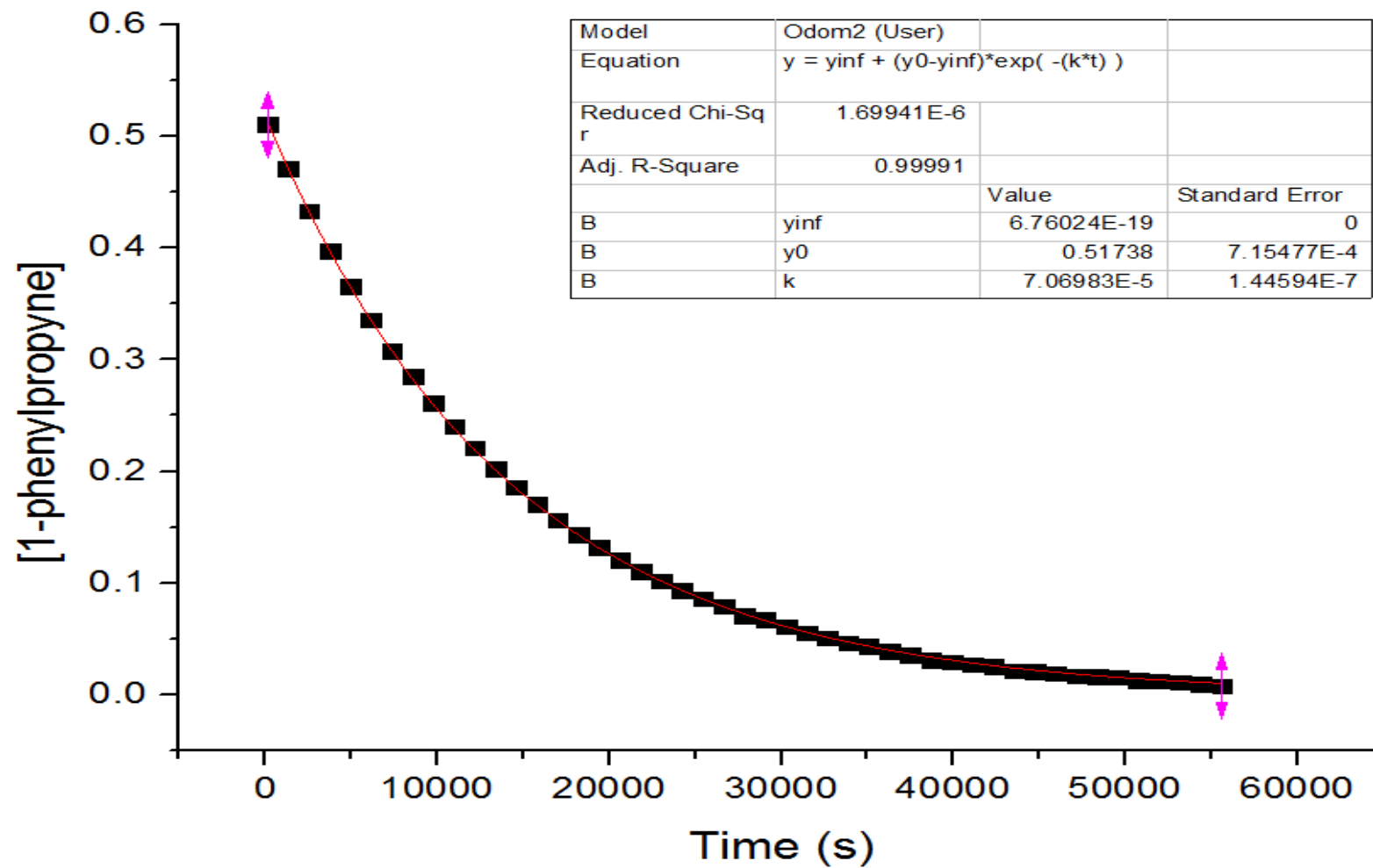
## Representative Plots for Kinetics



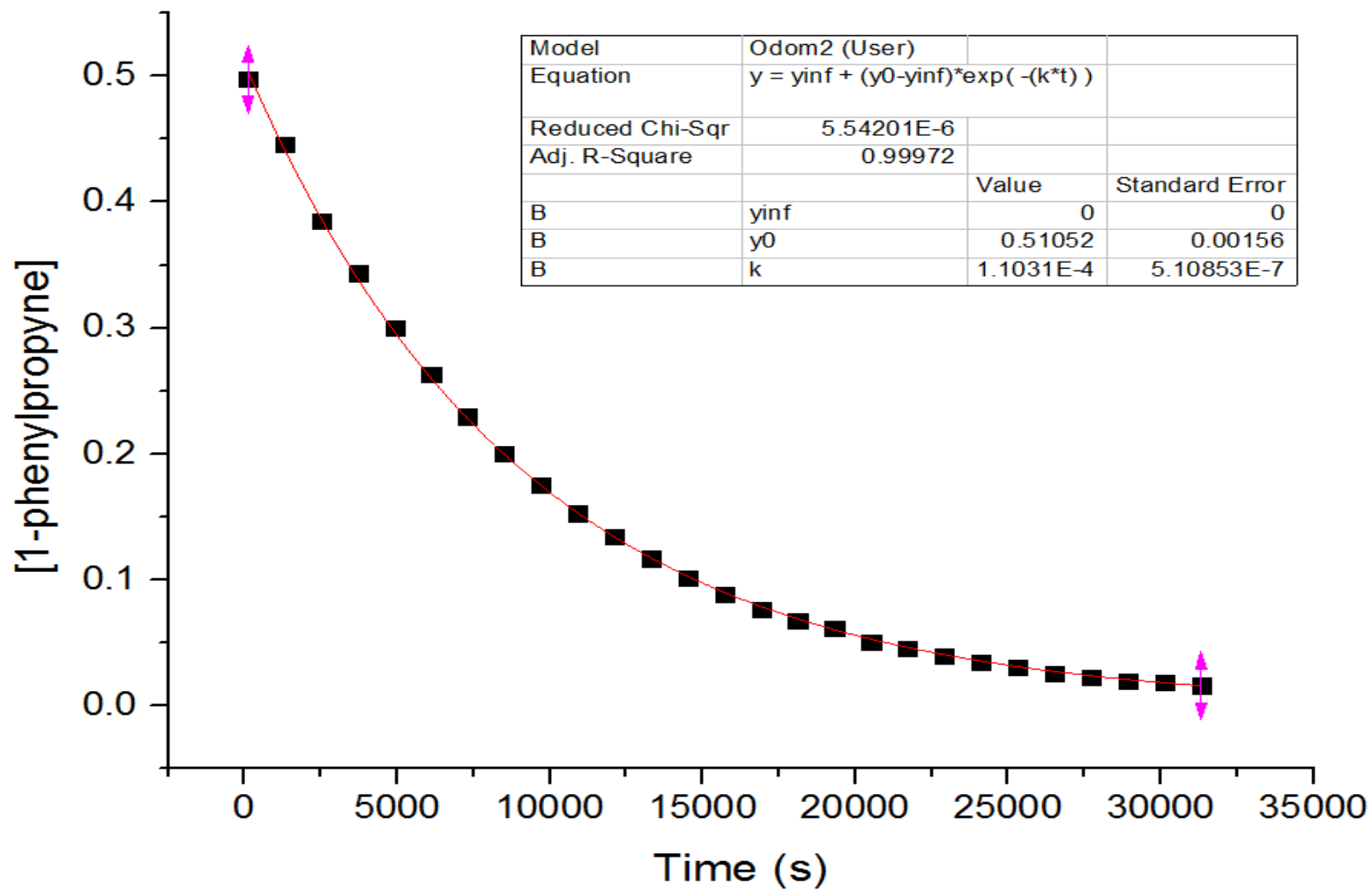
**Figure 3.44.** Plot of [1-phenylpropyne] vs time with  $\text{Ti}(\text{NMe}_2)_2(\text{bis-phenoxide}^{2\text{tBu-4Me}})$  (**3**).



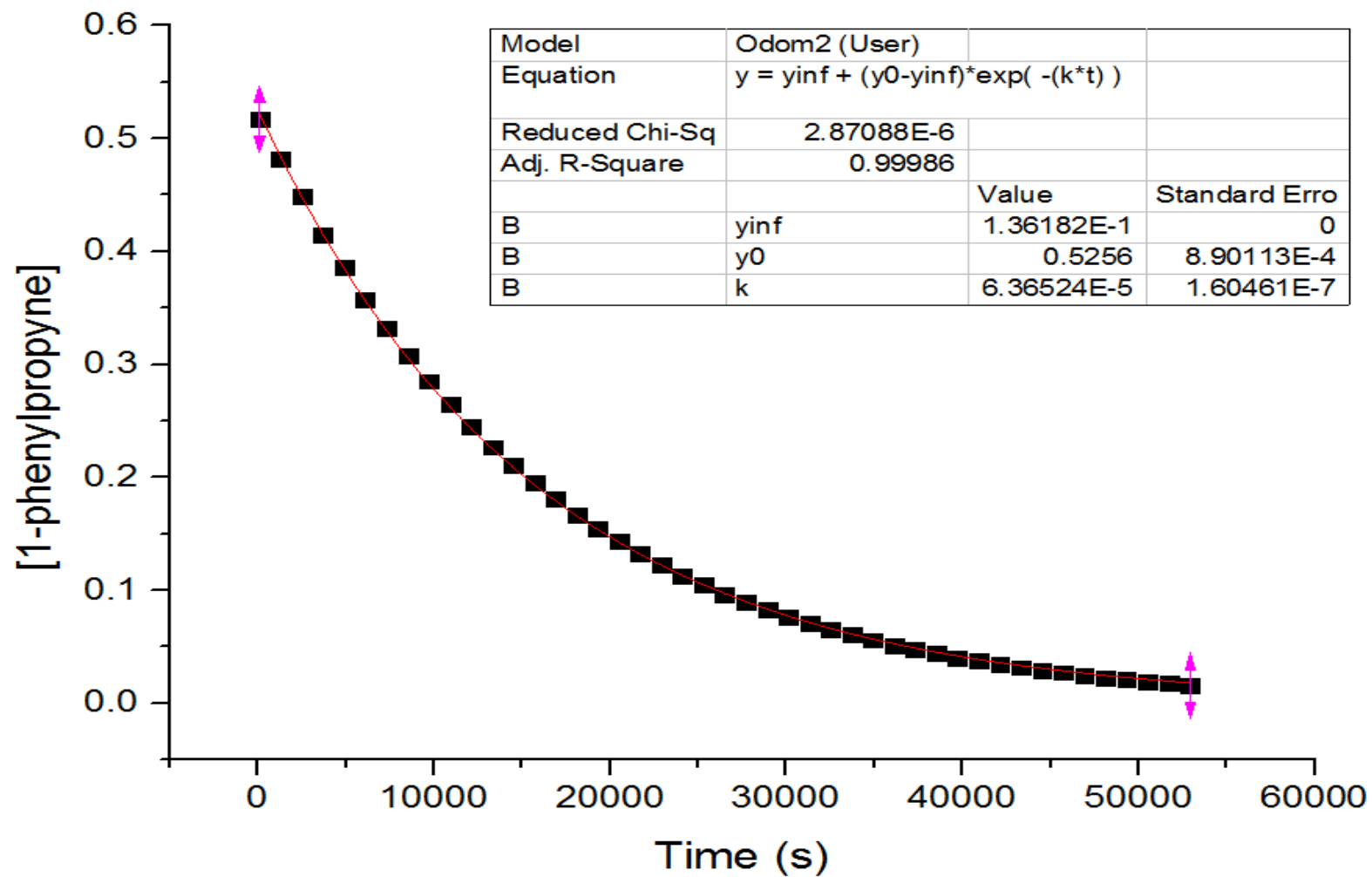
**Figure 3.45.** Plot of [1-phenylpropyne] vs time with  $\text{Ti}(\text{NMe}_2)_2(\text{biphenol}^{2\text{tBu-4,5-diMe}})$  (**4a**).



**Figure 3.46.** Plot of [1-phenylpropyne] vs time with  $\text{Ti}(\text{dim}^{\text{3Me}})(\text{NMe}_2)_2$  (**2a**).

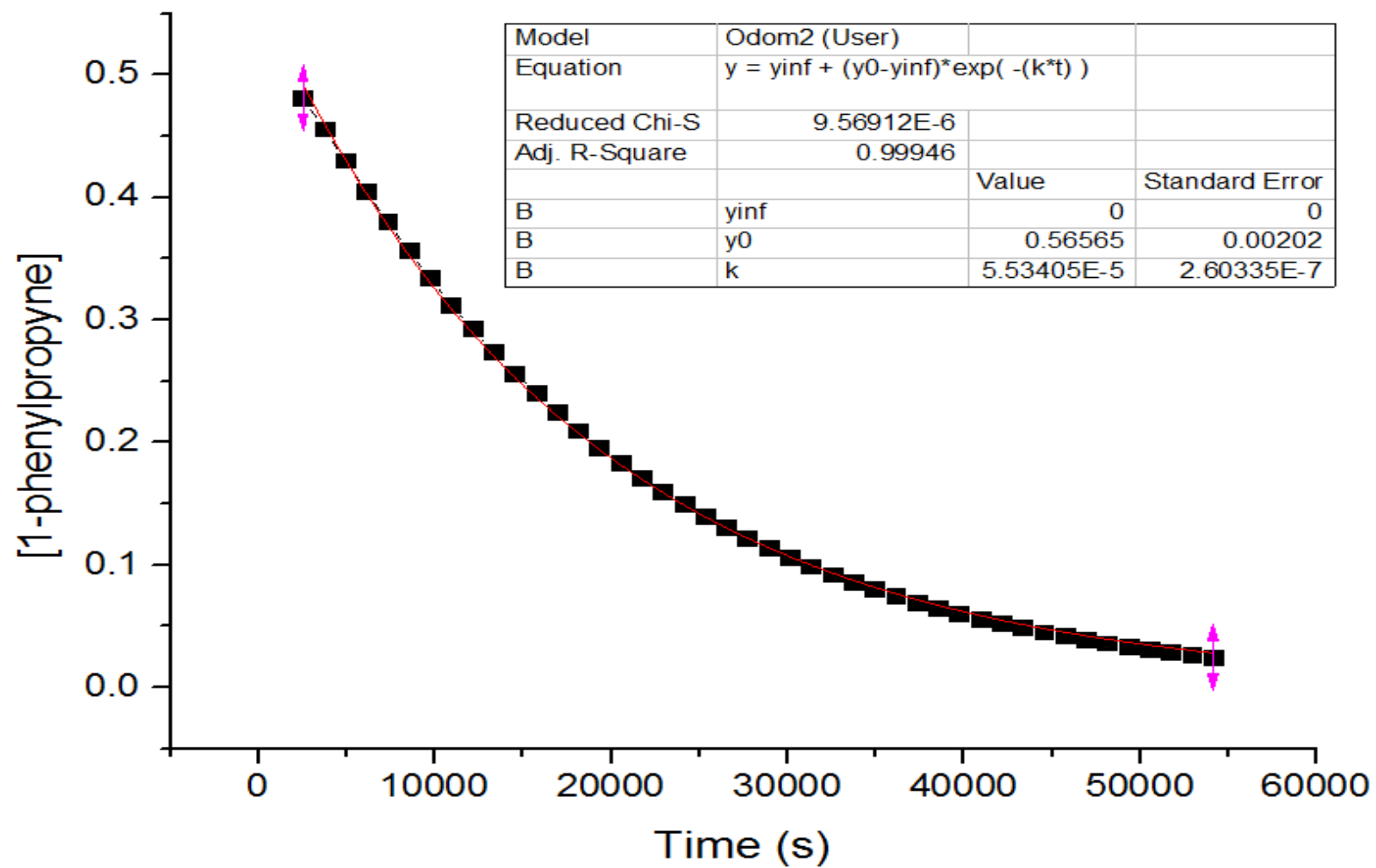


**Figure 3.47.** Plot of [1-phenylpropyne] vs time with  $\text{Ti}(\text{dim}^{3\text{Me-5F}})(\text{NMe}_2)_2(\text{HNMe}_2)$  (**2b**).

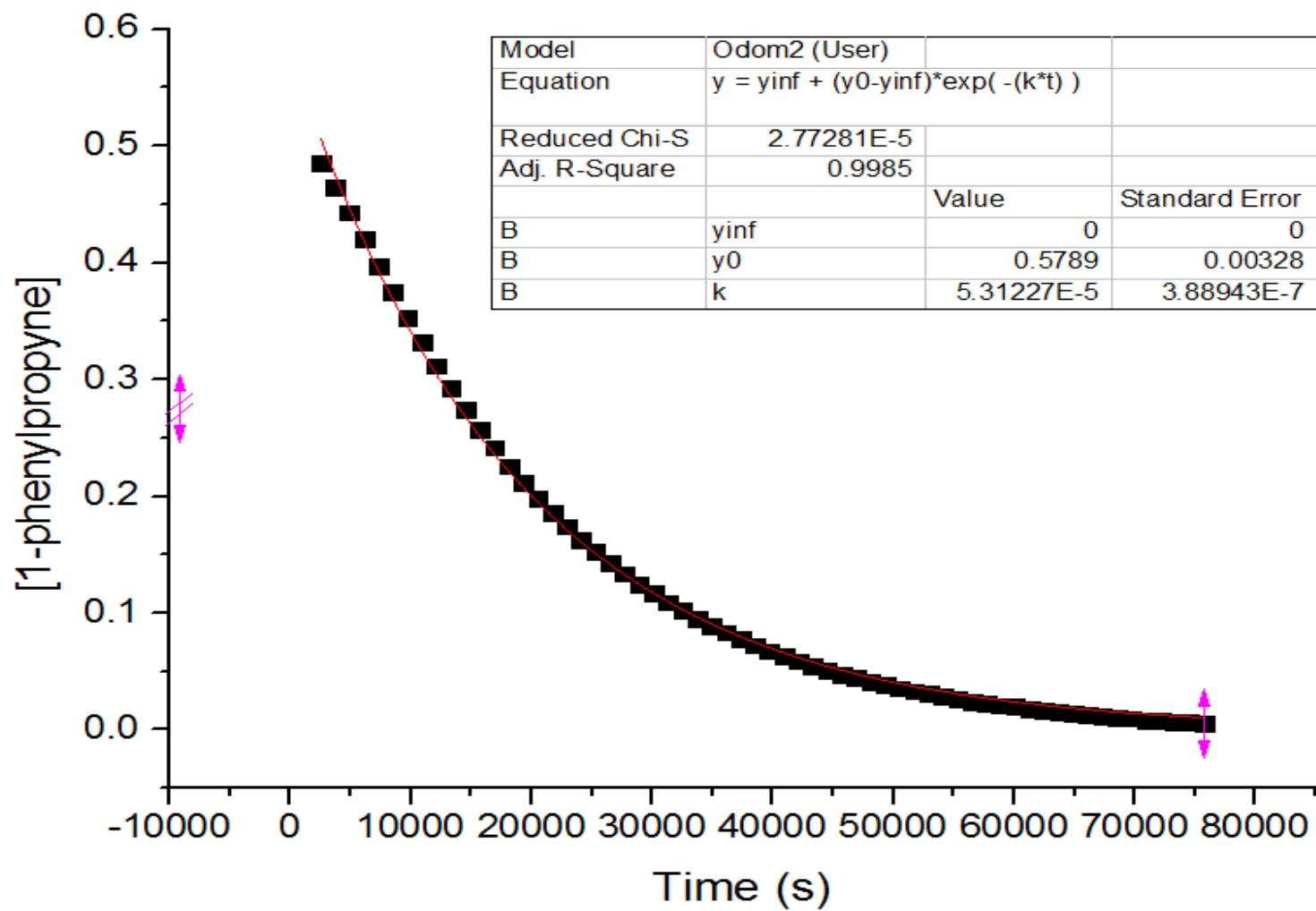


**Figure 3.48.** Plot of [1-phenylpropyne] vs time with  $\text{Ti}(\text{dpm}^{2-[\text{C}_6\text{H}_3(\text{CF}_3)_2]})(\text{NMe}_2)_2$  (**1c**).

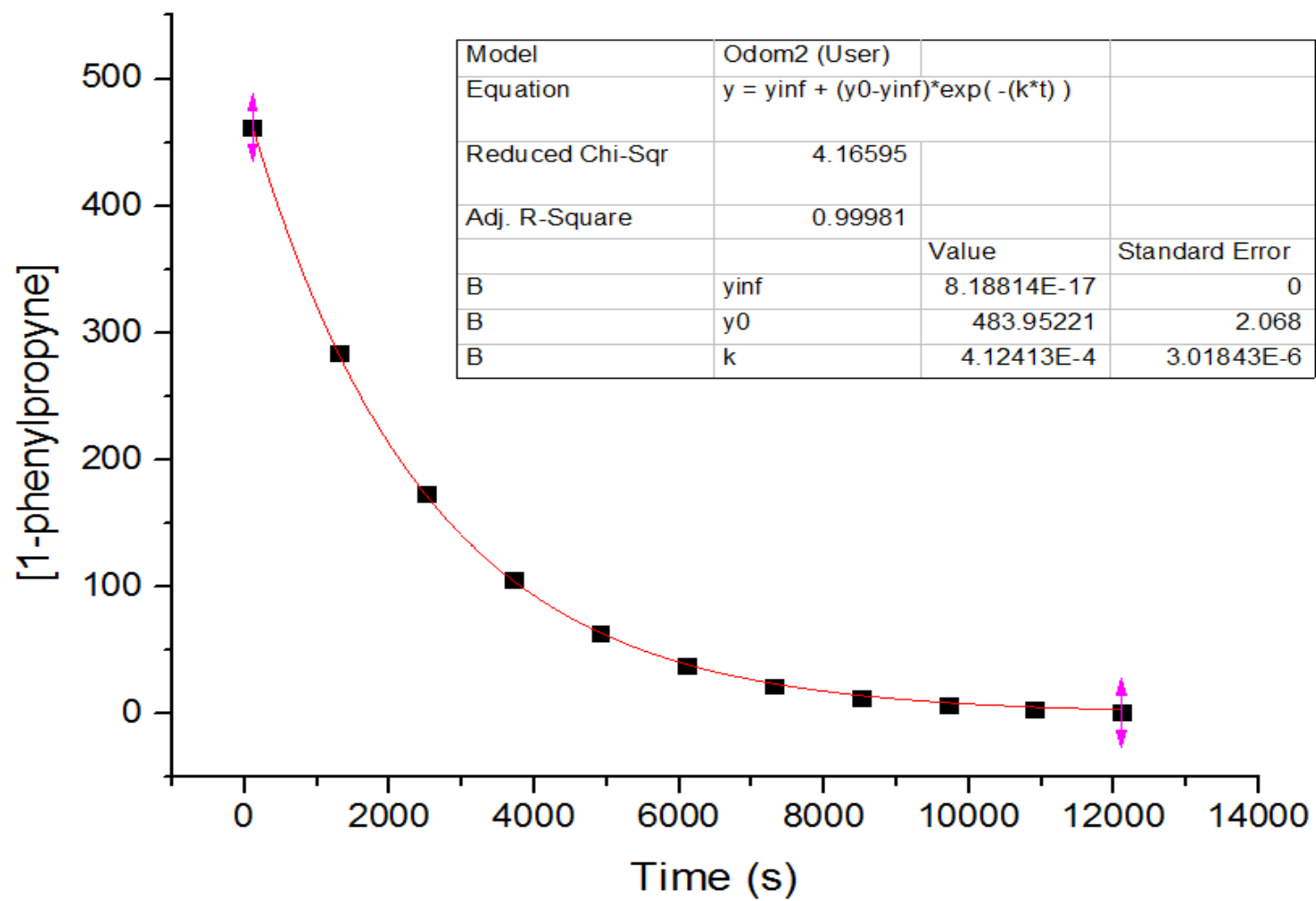




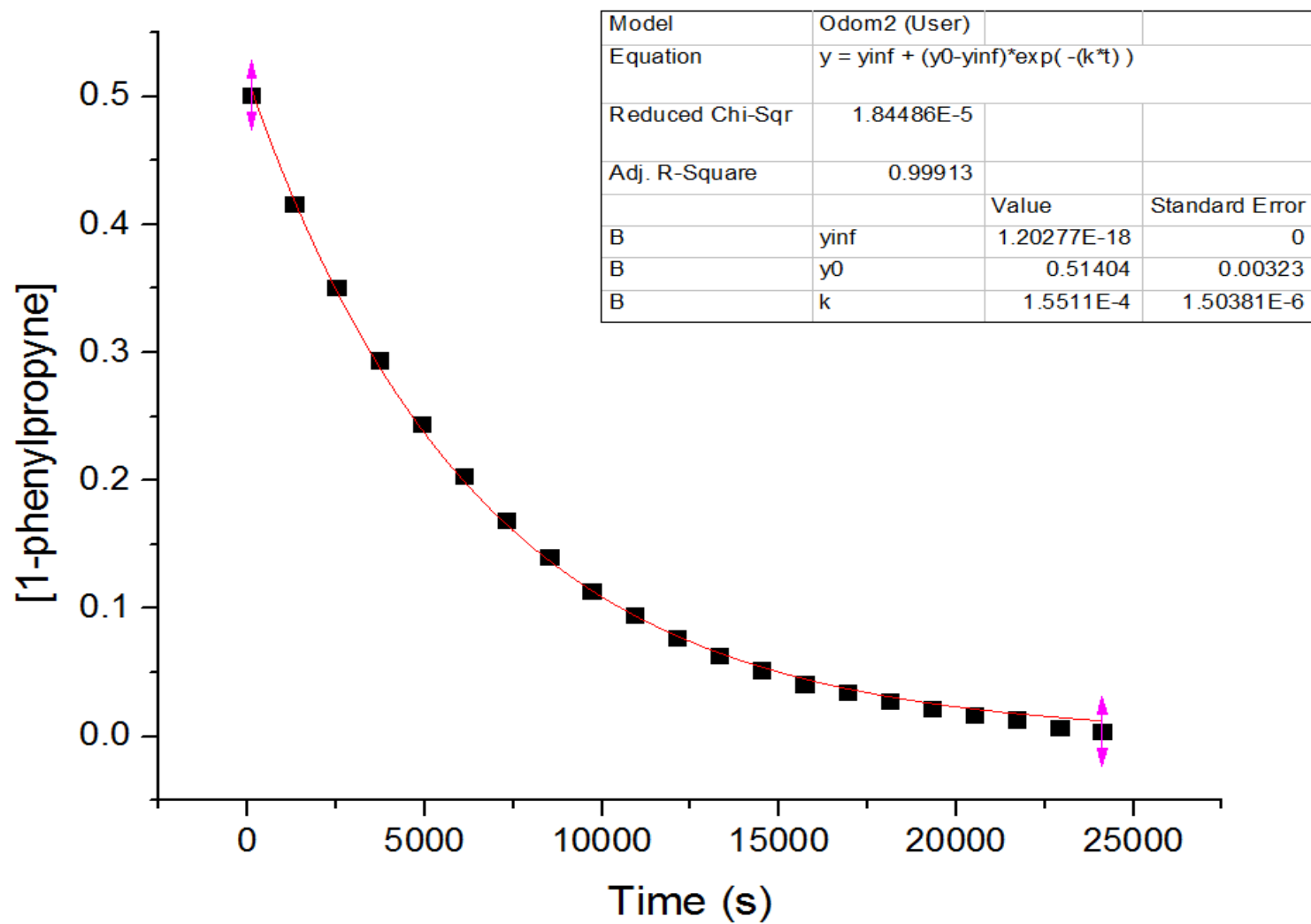
**Figure 3.49.** Plot of [1-phenylpropyne] vs time with  $\text{Ti}(\text{dpm}^{2-[\text{C}_6\text{H}_3(\text{CF}_3)_2]})(\text{NMe}_2)_2$  (**1d**).



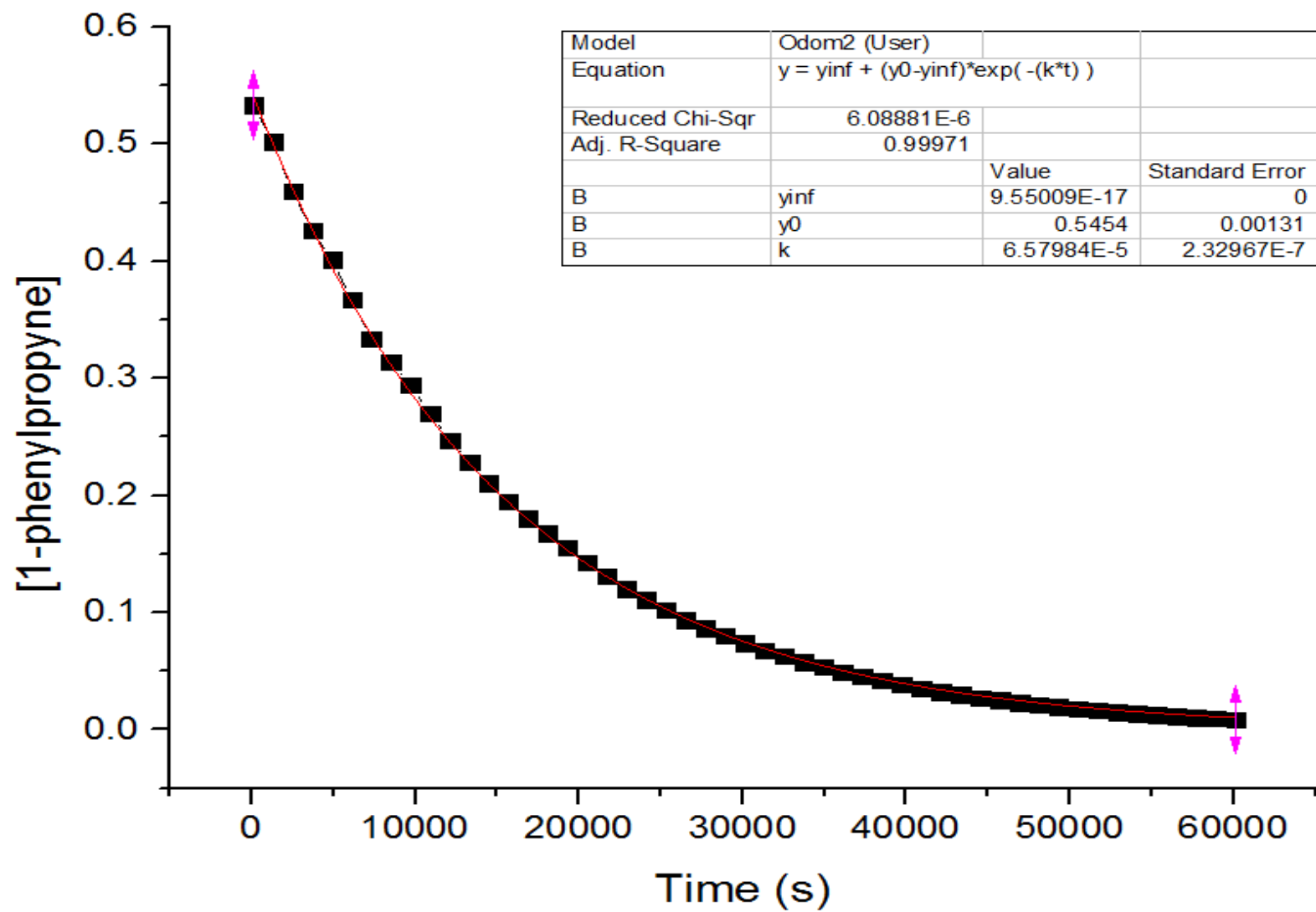
**Figure 3.50.** Plot of [1-phenylpropyne] vs time with  $\text{Ti}(\text{dpm}^{2\text{-tolyl}})(\text{NMe}_2)_2$  (**1e**).



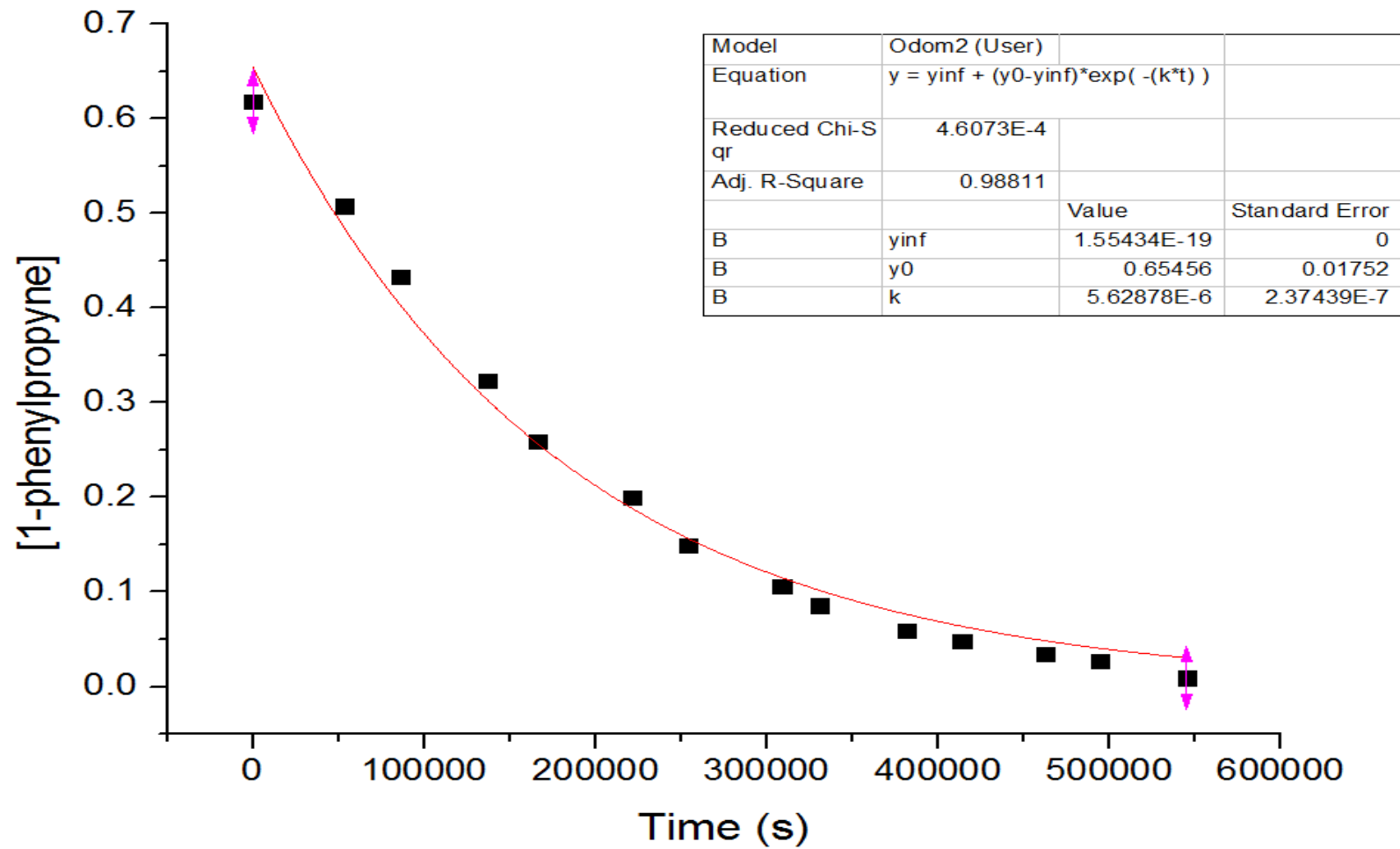
**Figure 3.51.** Plot of [1-phenyl]propyne] vs time with  $\text{Ti}(\text{dpm})(\text{NMe}_2)_2$  (**1a**).



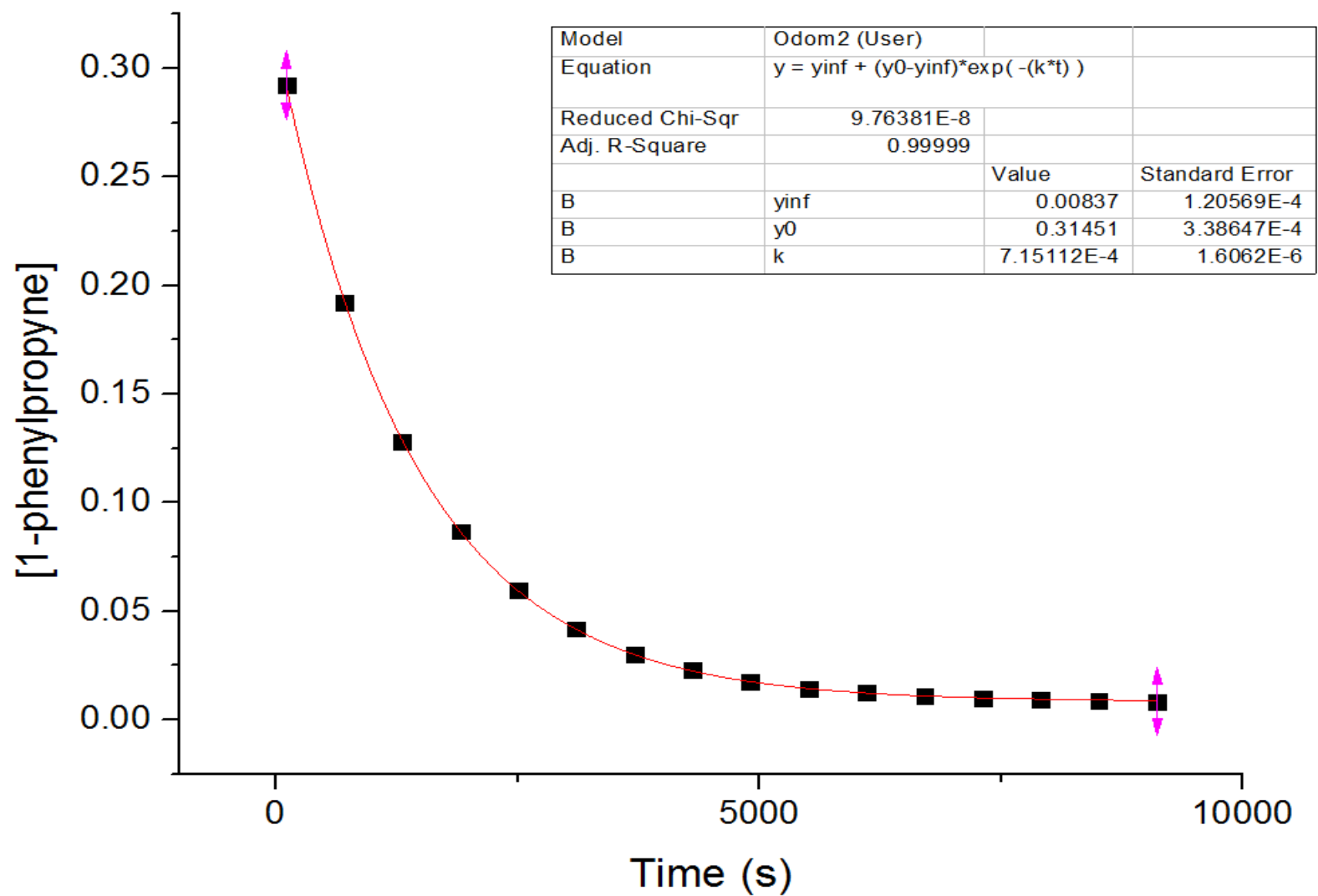
**Figure 3.52.** Plot of [1-phenylpropyne] vs time with  $\text{Ti}(\text{dpm}^{2,2'\text{-DiMe}})(\text{NMe}_2)_2$  (**1b**).



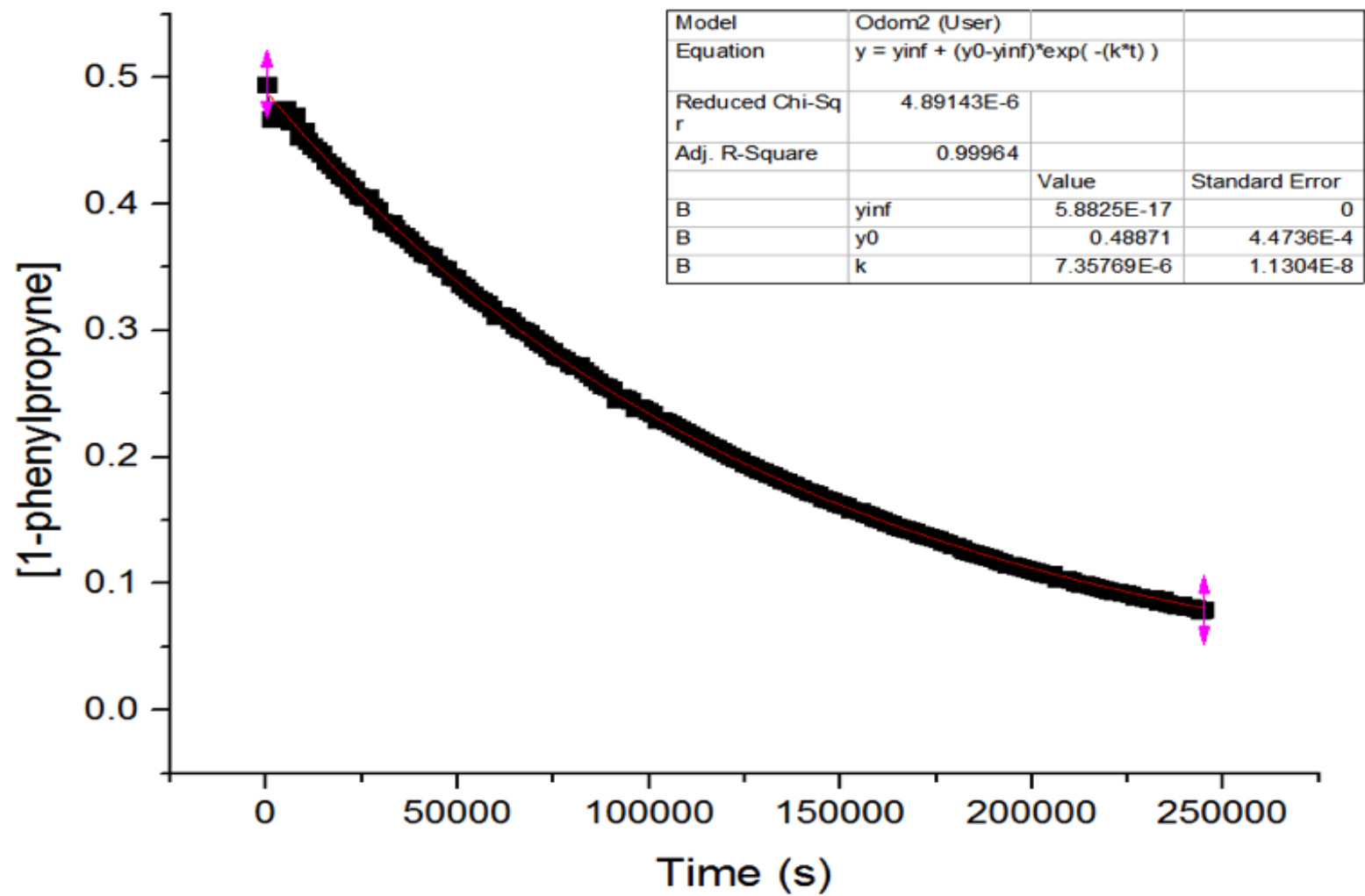
**Figure 3.53.** Plot of [1-phenylpropyne] vs time with  $\text{Ti}(\text{NMe}_2)_4$ .



**Figure 3.54.** Plot of [1-phenylpropyne] vs time with  $\text{Ti}(\text{NMe}_2)_2(\text{biphenol}^{2\text{tBu-4-OMe}})$  (**4b**).



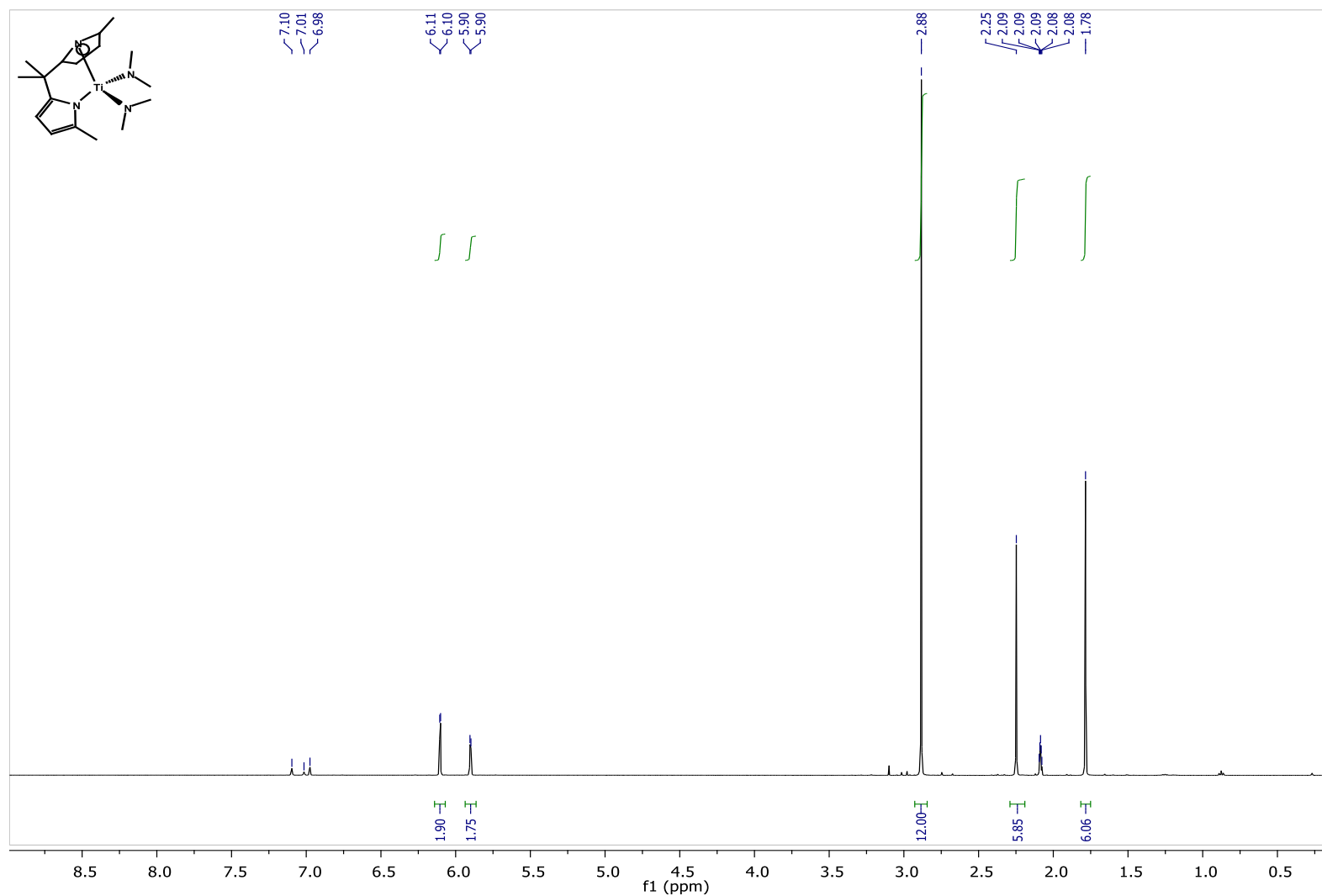
**Figure 3.55.** Plot of [1-phenylpropyne] vs time with  $\text{Ti}(\text{dpm}^{3\text{-}[\text{C}_6\text{H}_3(\text{CF}_3)_2]})(\text{NMe}_2)_2$  (**5**).



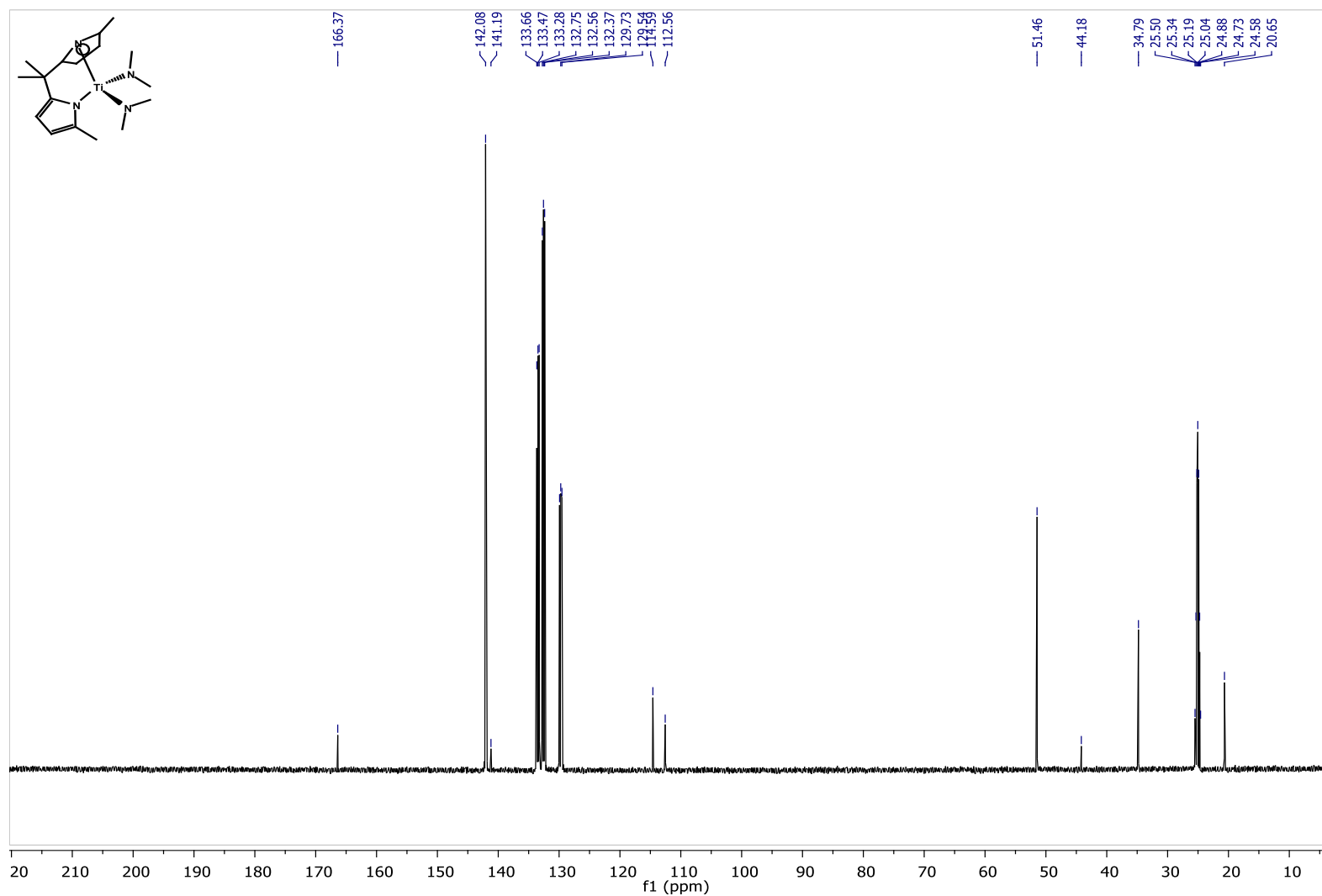
**Figure 3.56.** Plot of [1-phenylpropyne] vs time with Ti(dithioBINAP)(NMe<sub>2</sub>)<sub>2</sub> (**6**).



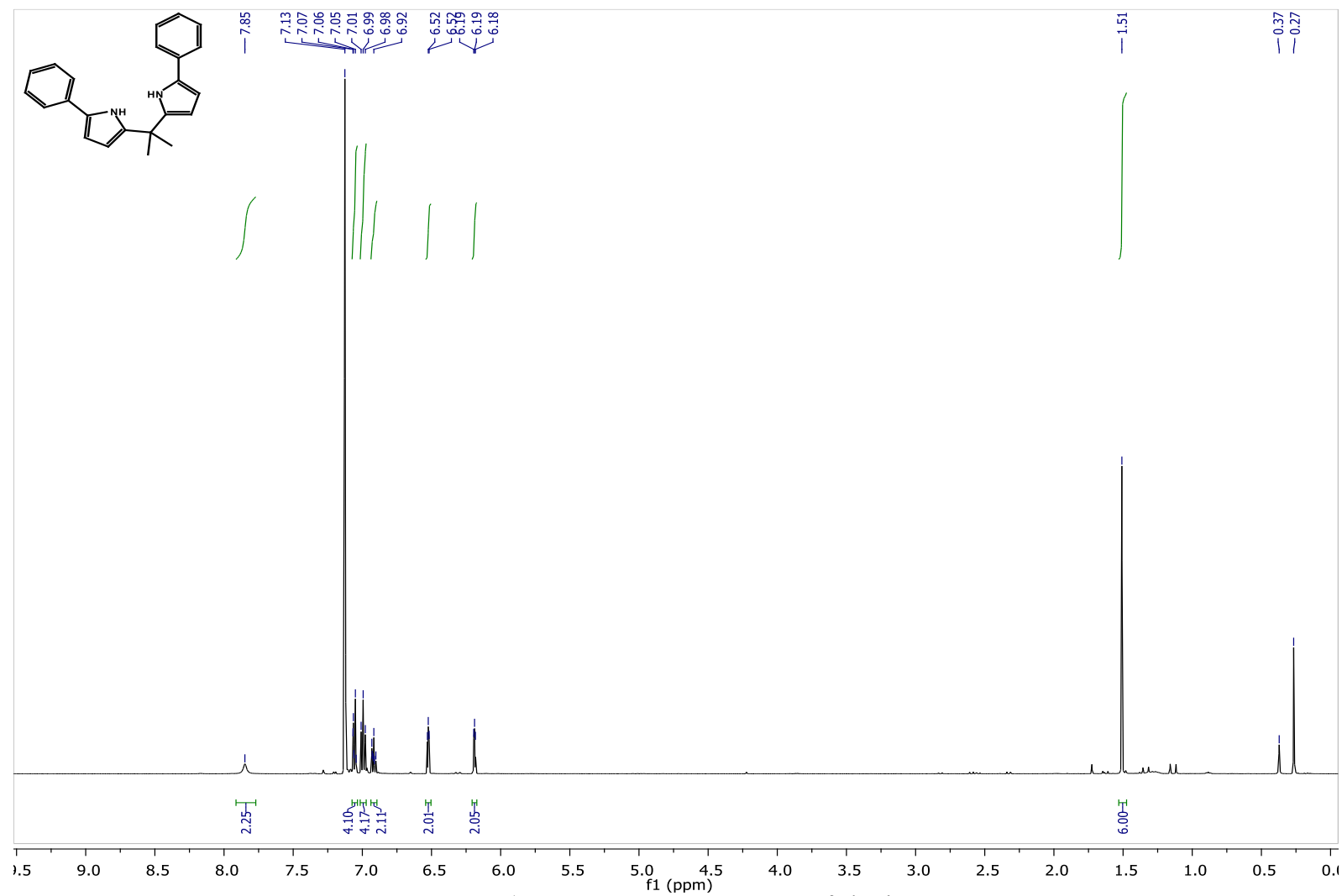
## NMR Spectra



**Figure 3.57.**  $^1\text{H}$  NMR Spectrum of  $\text{Ti}(\text{NMe}_2)_2(\text{dpm}^{2,2'\text{-DiMe}})$  (**1b**) in  $\text{toluene-d}_8$ .



**Figure 3.58.**  $^{13}\text{C}$  NMR Spectrum of  $\text{Ti}(\text{NMe}_2)_2(\text{dpm})_{2,2'\text{-DiMe}}$  (**1b**) in toluene- $\text{d}_8$ .



**Figure 3.59.**  $^1\text{H}$  NMR Spectrum of  $\text{H}_2\text{dpm}^{2\text{-phenyl}}$  in  $\text{C}_6\text{D}_6$ .

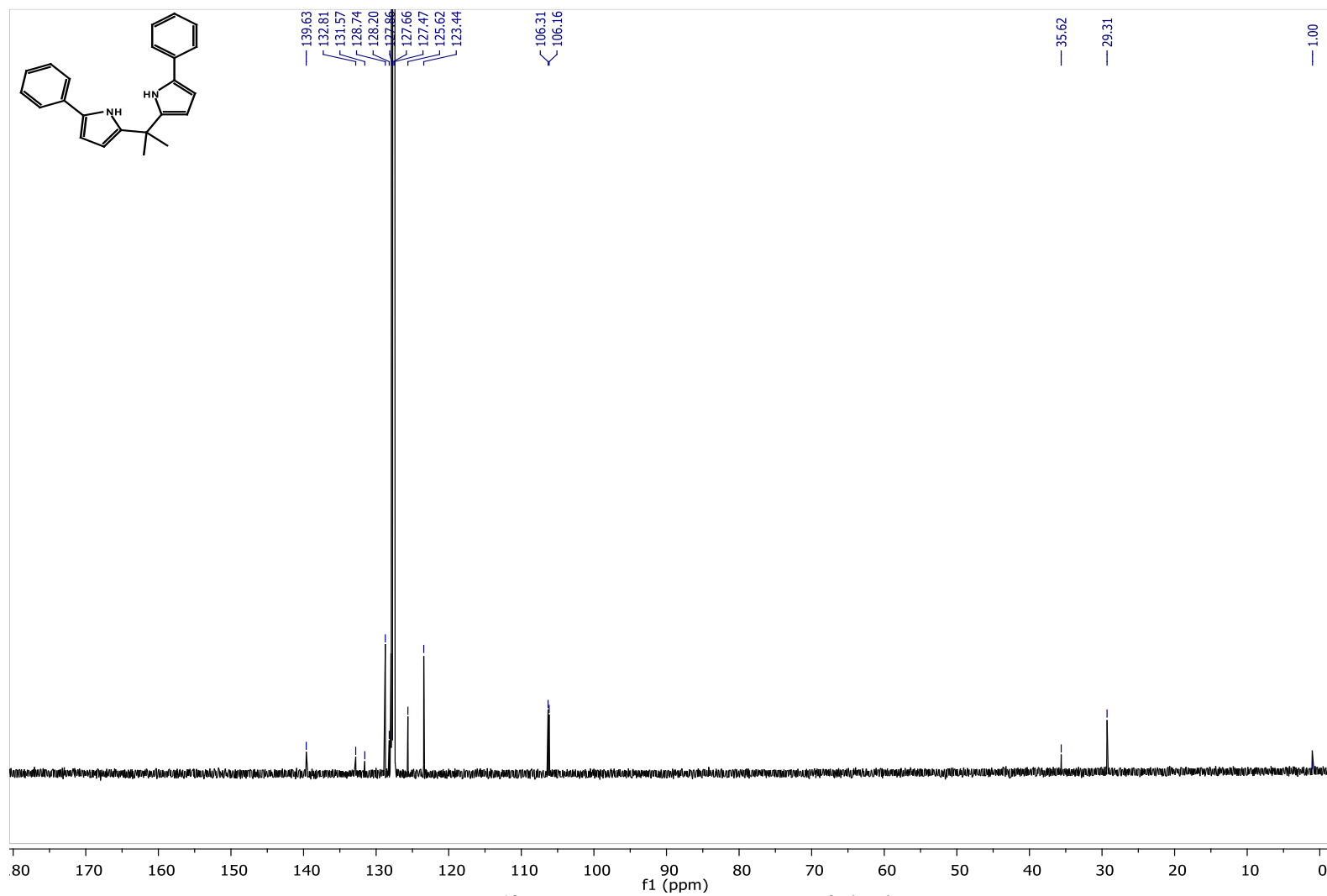
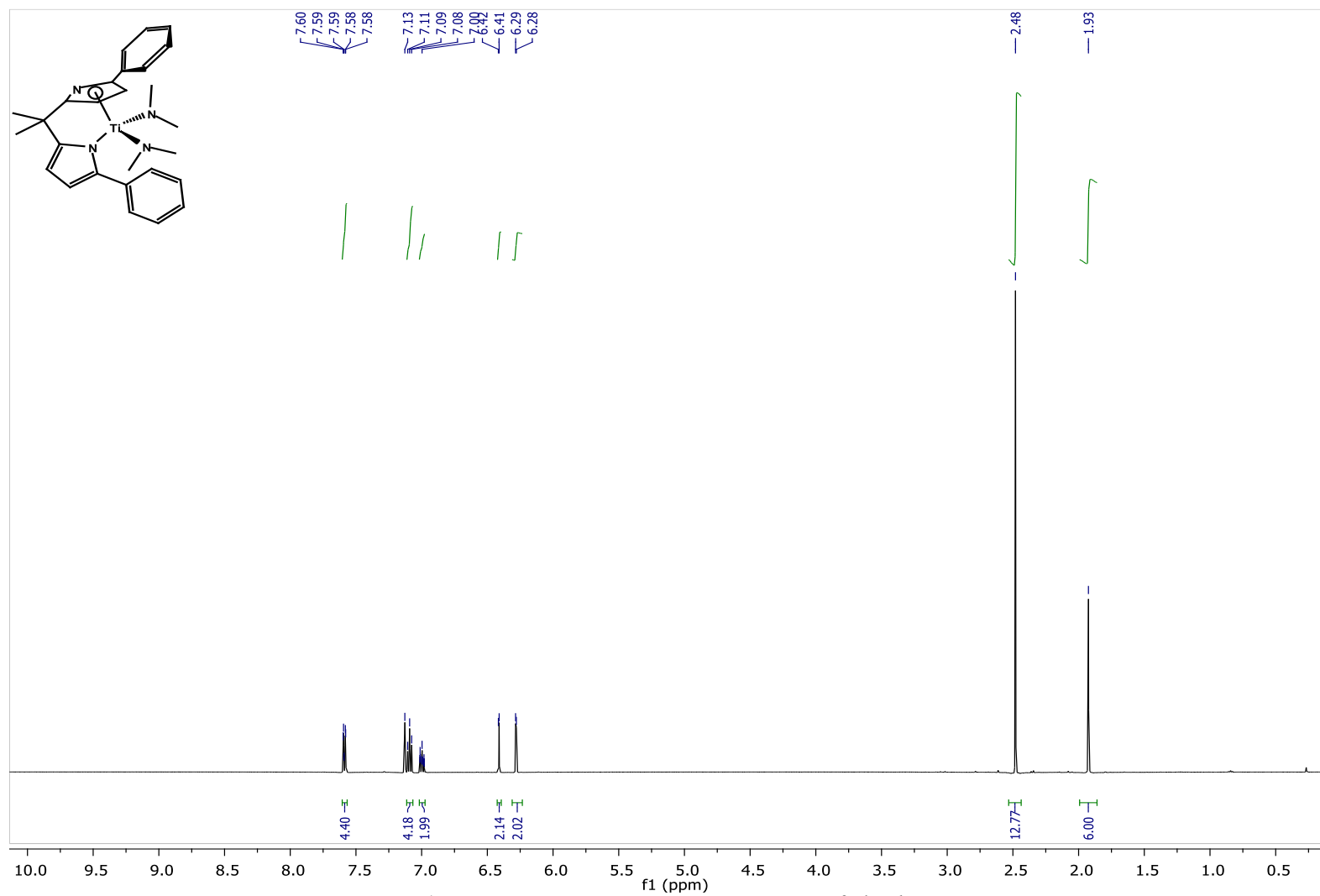
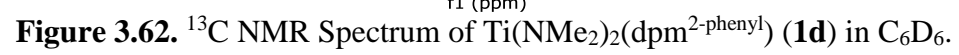
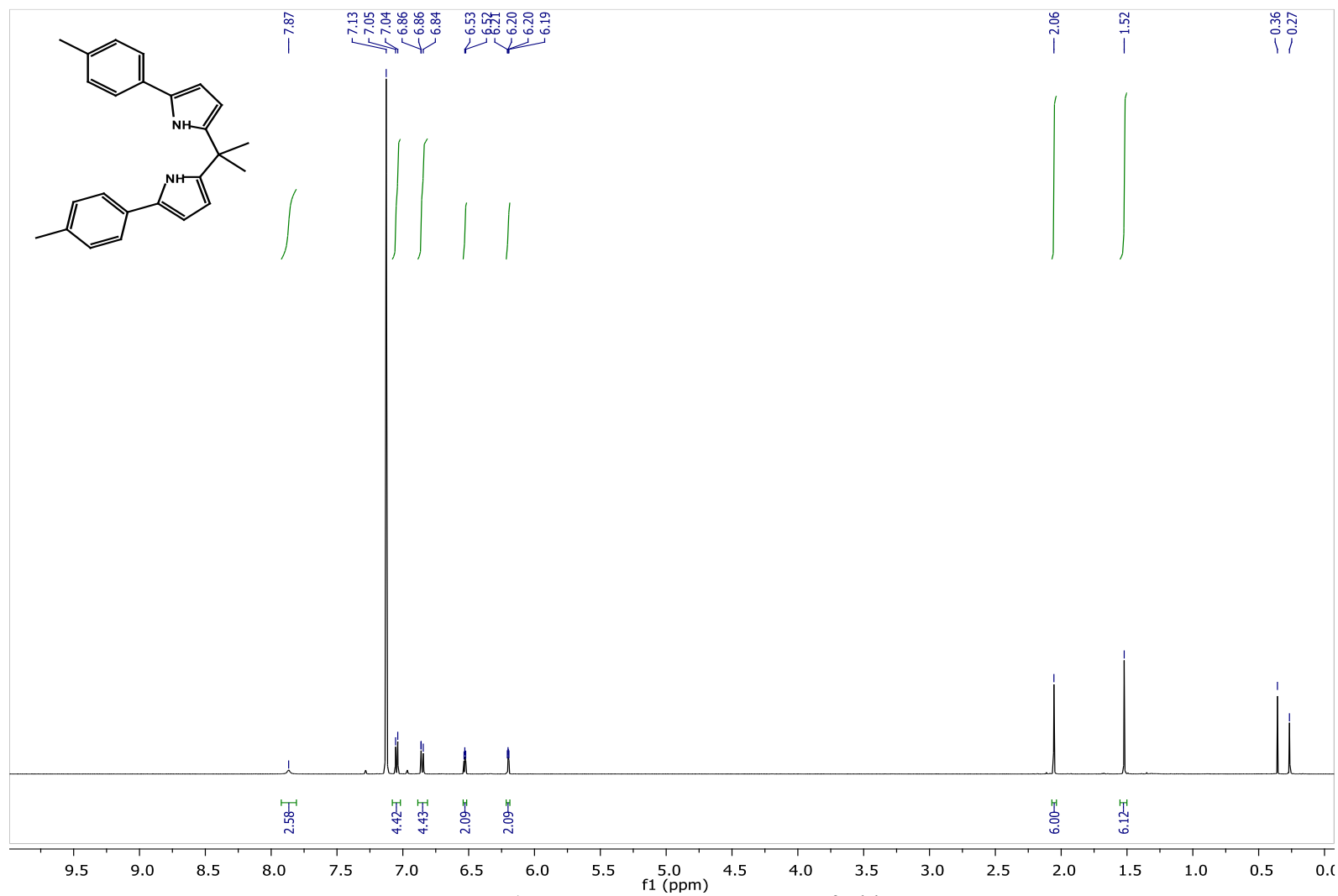


Figure 3.60.  $^{13}\text{C}$  NMR Spectrum of  $\text{H}_2\text{dpm}^{2\text{-phenyl}}$  in  $\text{C}_6\text{D}_6$ .

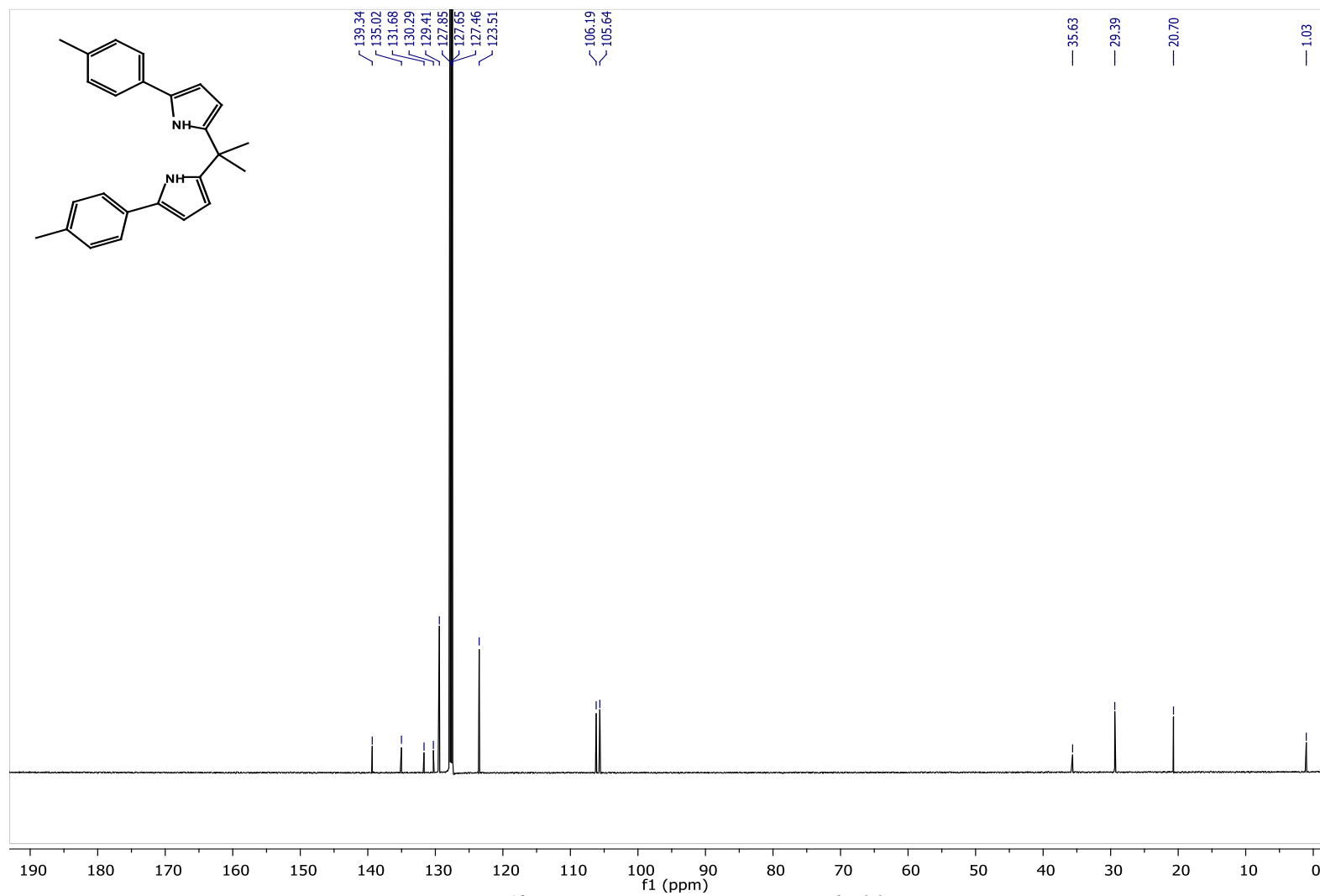


**Figure 3.61.**  $^1\text{H}$  NMR Spectrum of  $\text{Ti}(\text{NMe}_2)_2(\text{dpm}^{2\text{-phenyl}})$  (**1d**) in  $\text{C}_6\text{D}_6$ .



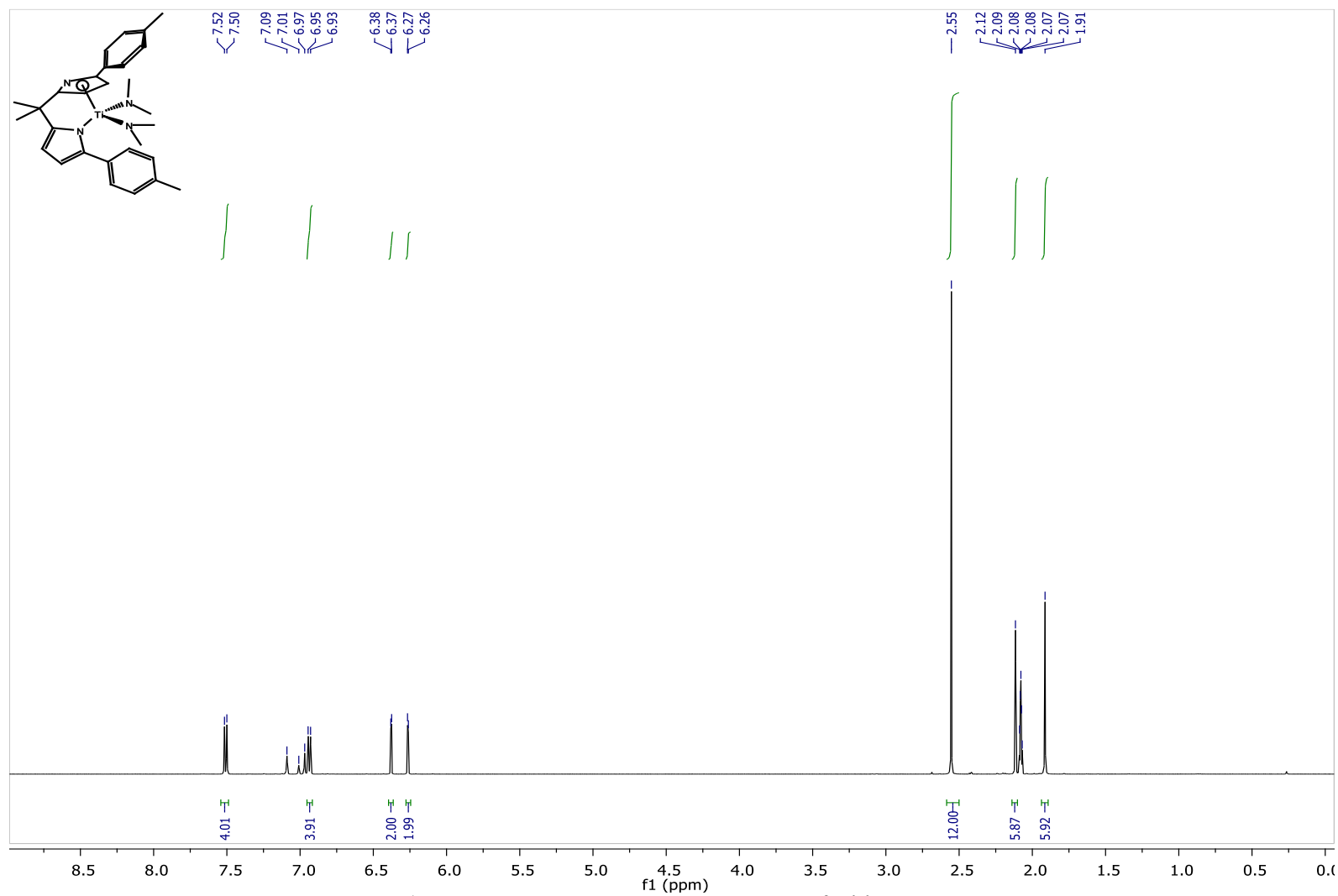


**Figure 3.63.**  $^1\text{H}$  NMR Spectrum of  $\text{H}_2\text{dpm}^{2\text{-tolyl}}$  in  $\text{C}_6\text{D}_6$ .

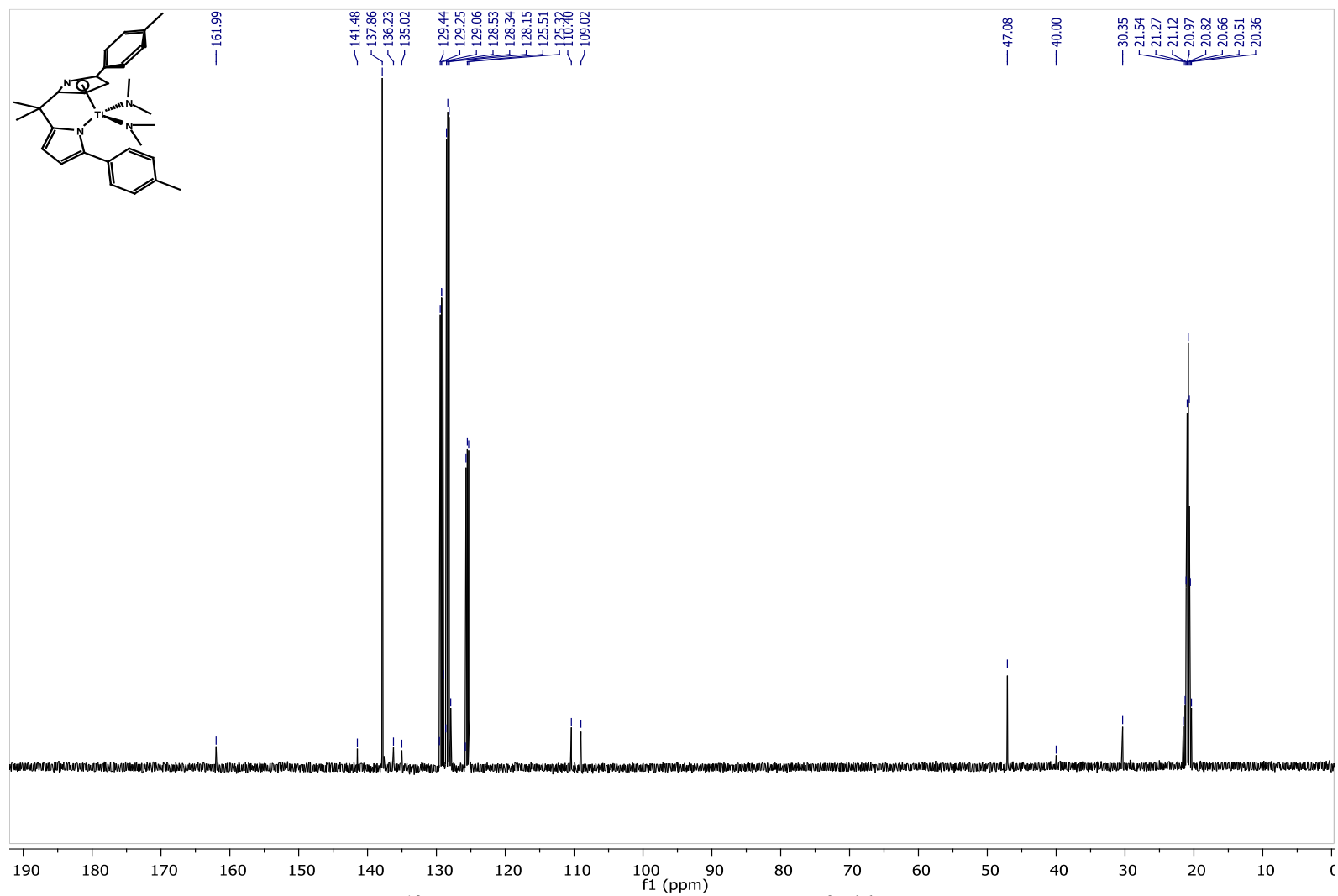


**Figure 3.64.**  $^{13}\text{C}$  NMR Spectrum of  $\text{H}_2\text{dpm}^{2\text{-tolyl}}$  in  $\text{C}_6\text{D}_6$ .

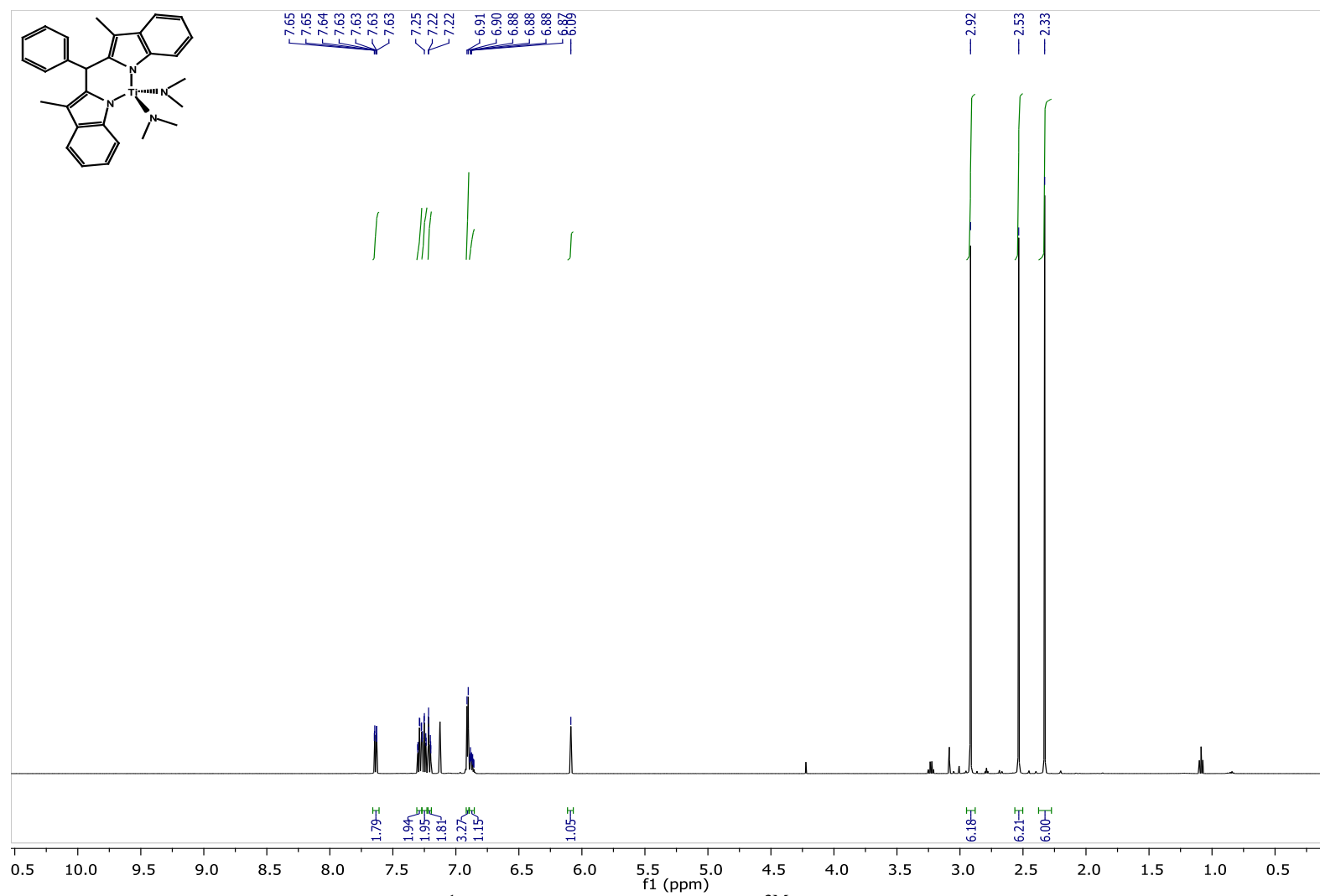




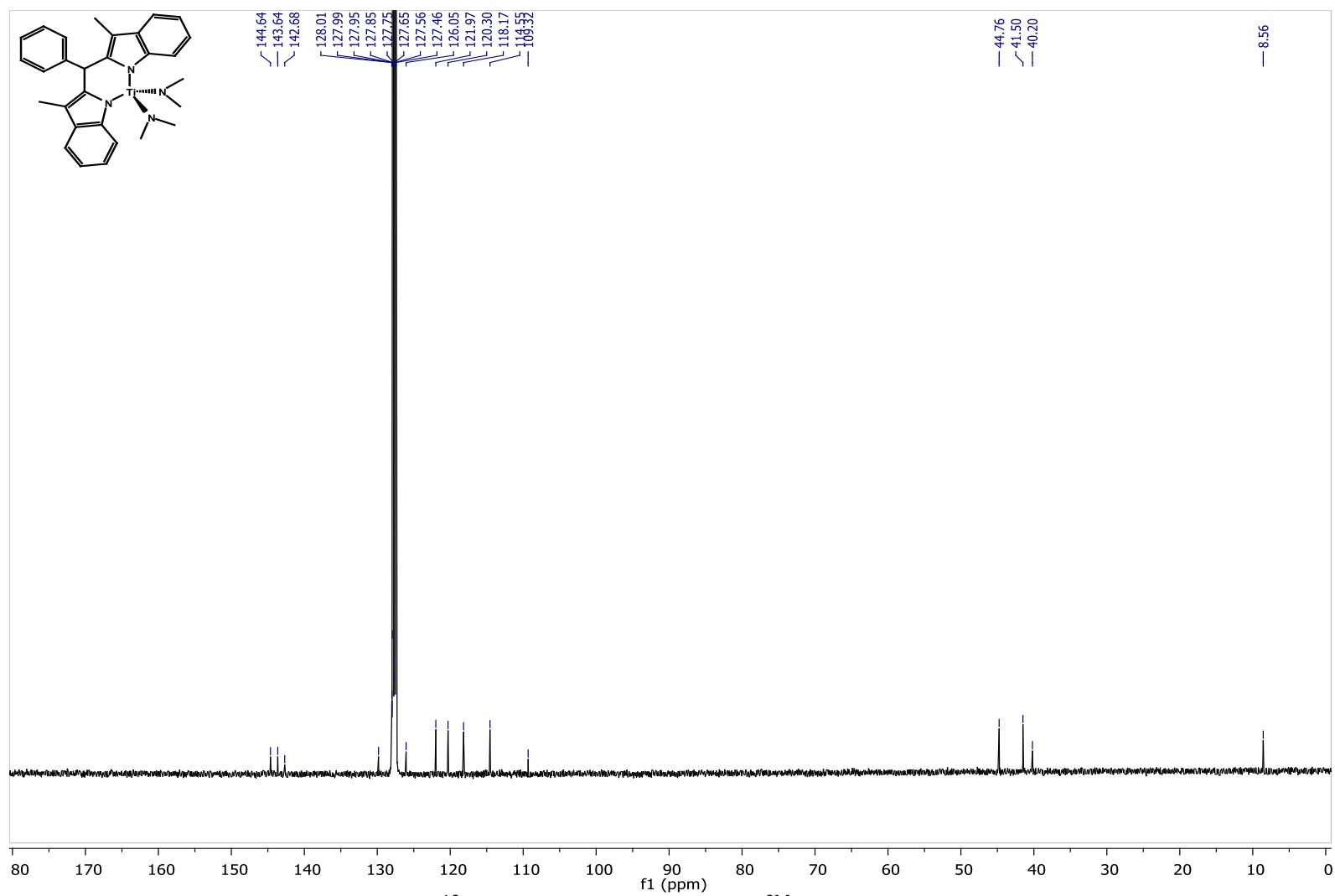
**Figure 3.65.**  $^1\text{H}$  NMR Spectrum of  $\text{Ti}(\text{NMe}_2)_2(\text{dpm}^{2\text{-tolyl}})$  (**1e**) in toluene- $\text{d}_8$ .



**Figure 3.66.**  $^{13}\text{C}$  NMR Spectrum of  $\text{Ti}(\text{NMe}_2)_2(\text{dpm}^{2\text{-tolyl}})$  (1e) in toluene- $\text{d}_8$ .



**Figure 3.67.**  $^1\text{H}$  NMR Spectrum of  $\text{Ti}(\text{dim}^3\text{Me})(\text{NMe}_2)_2$  (**2a**) in  $\text{C}_6\text{D}_6$ .



**Figure 3.68.**  $^{13}\text{C}$  NMR Spectrum of  $\text{Ti}(\text{dim}^3\text{Me})(\text{NMe}_2)_2$  (**2a**) in  $\text{C}_6\text{D}_6$ .

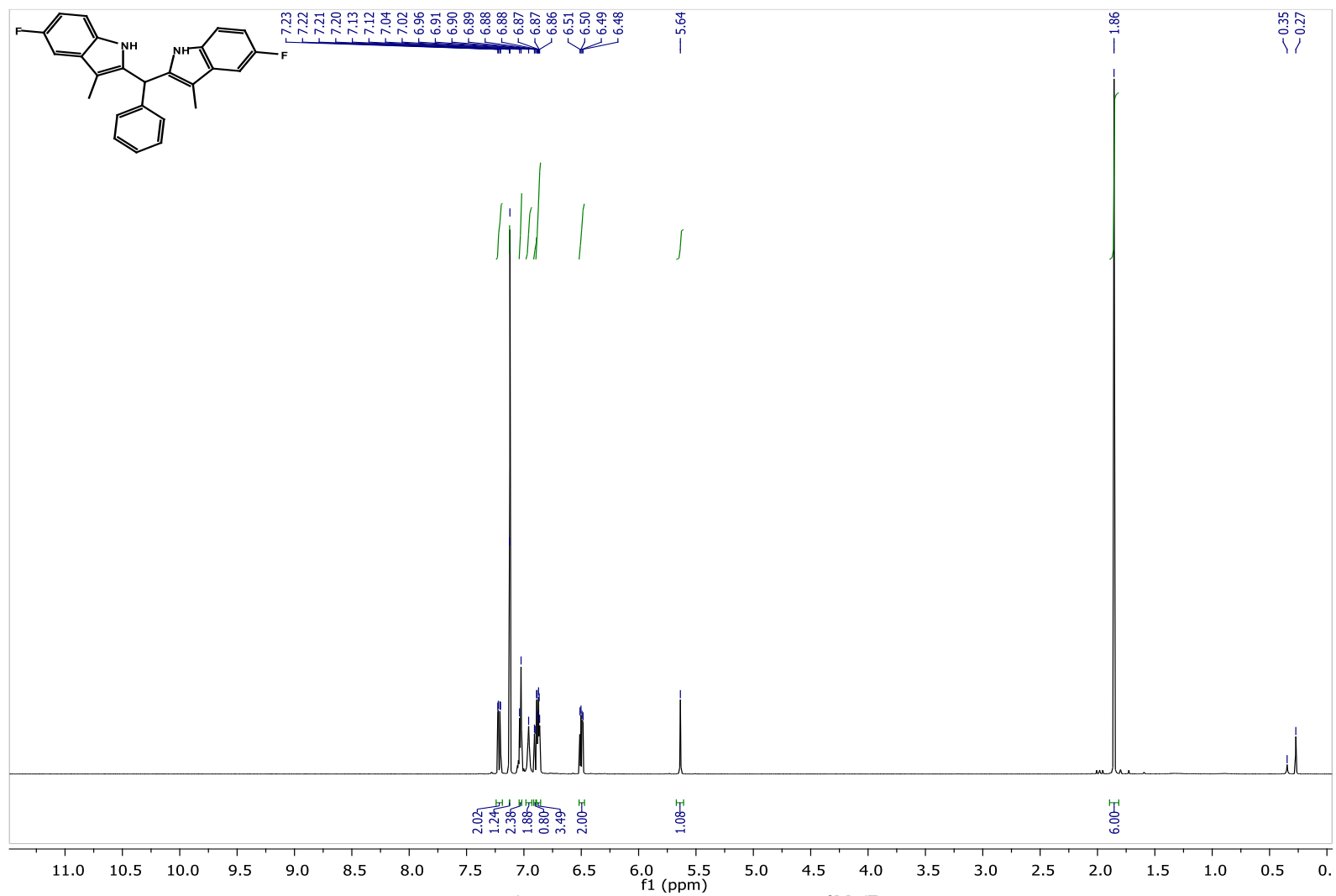
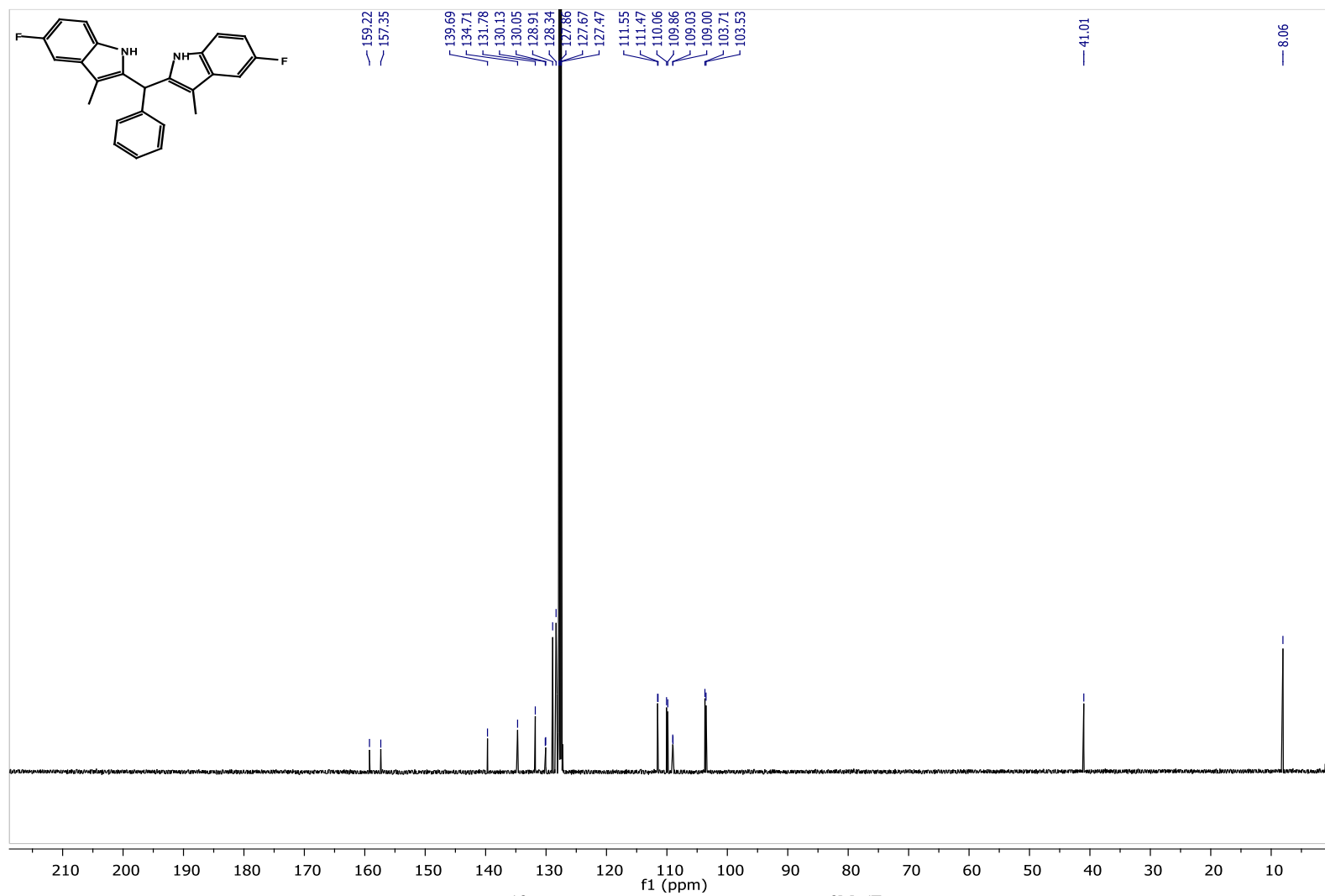
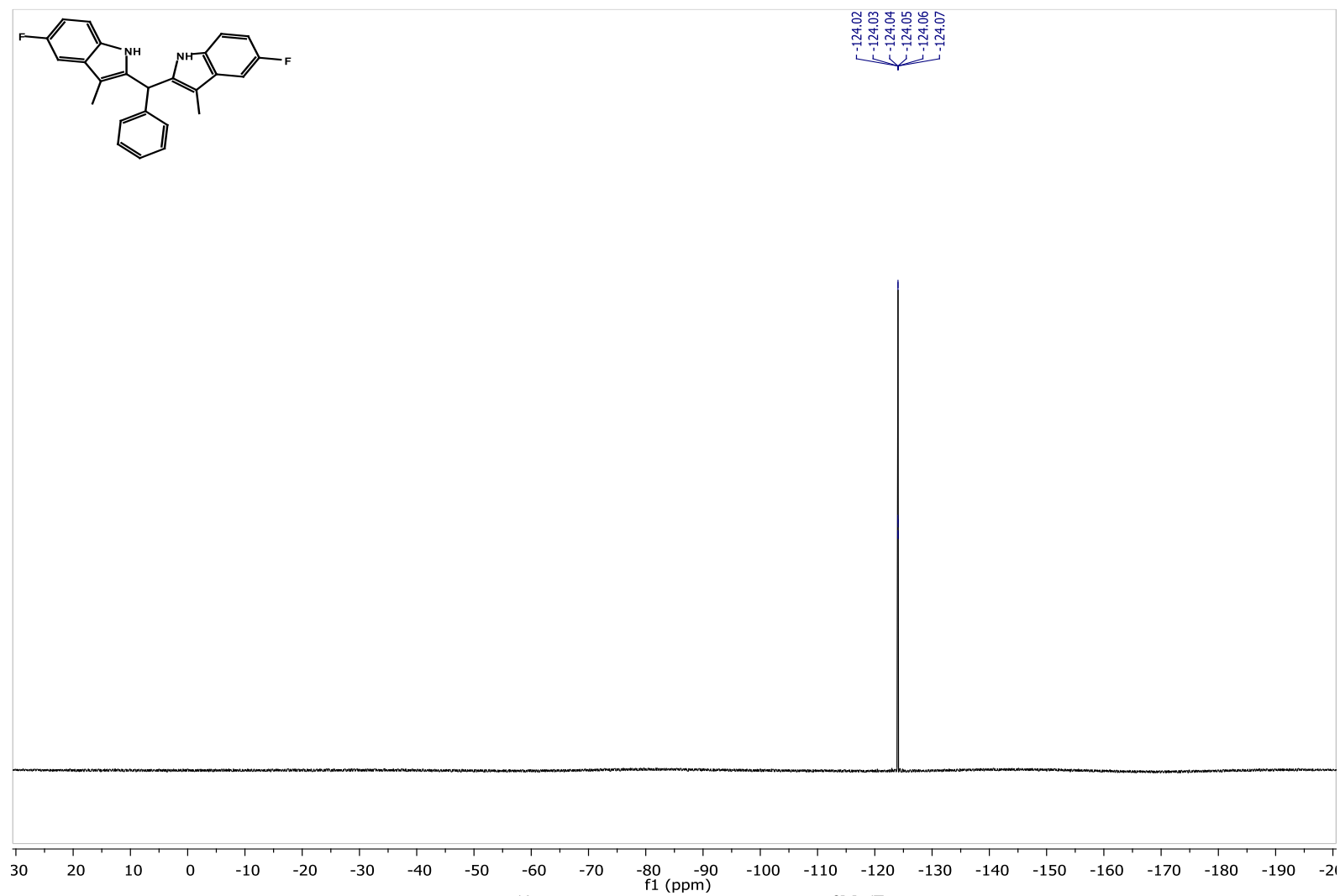


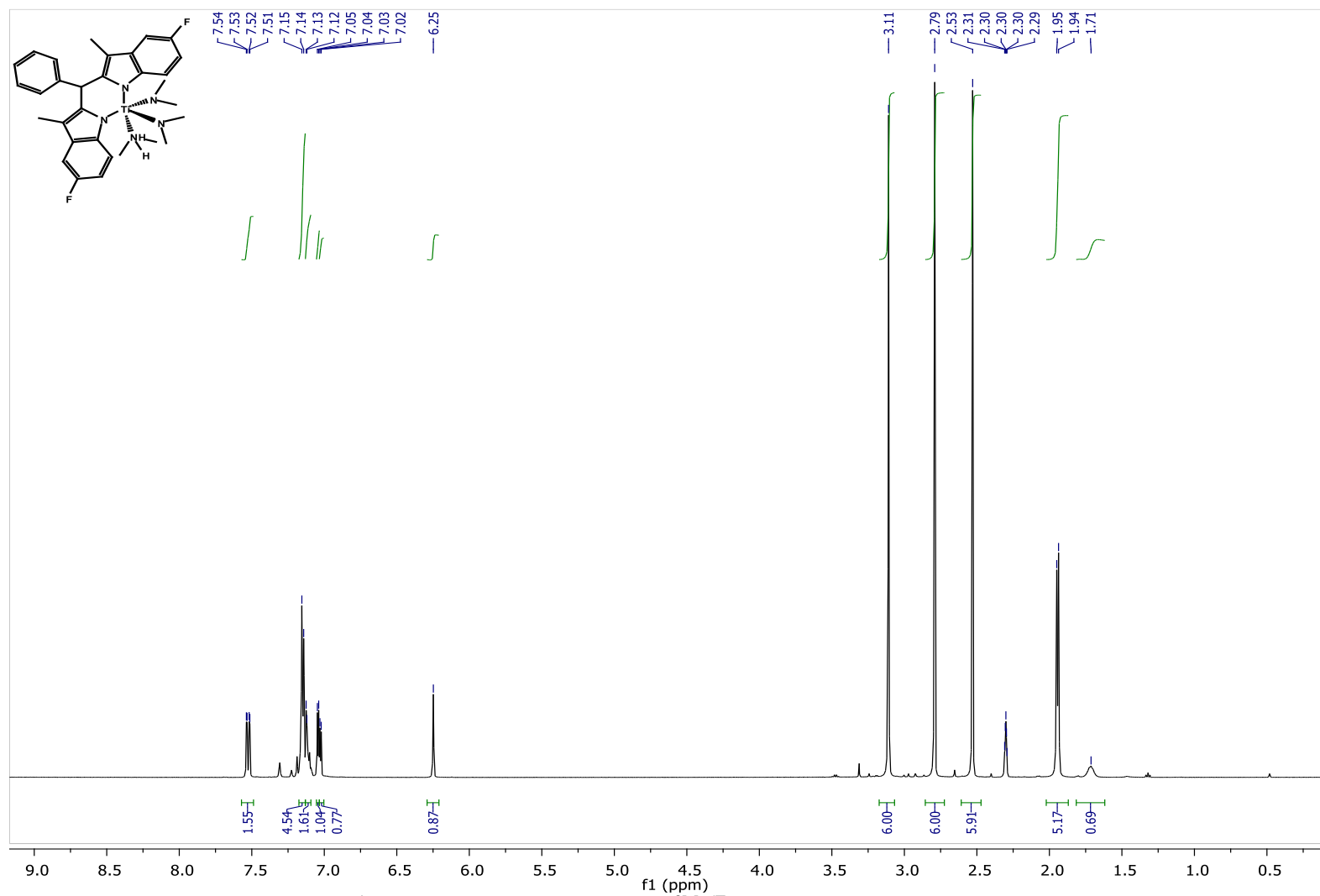
Figure 3.69.  $^1\text{H}$  NMR Spectrum of  $\text{H}_2\text{dim}^{\text{Me}_5\text{F}}$  in  $\text{C}_6\text{D}_6$ .



**Figure 3.70.**  $^{13}\text{C}$  NMR Spectrum of  $\text{H}_2\text{dim}^{\text{Me}_5\text{F}}$  in  $\text{C}_6\text{D}_6$ .

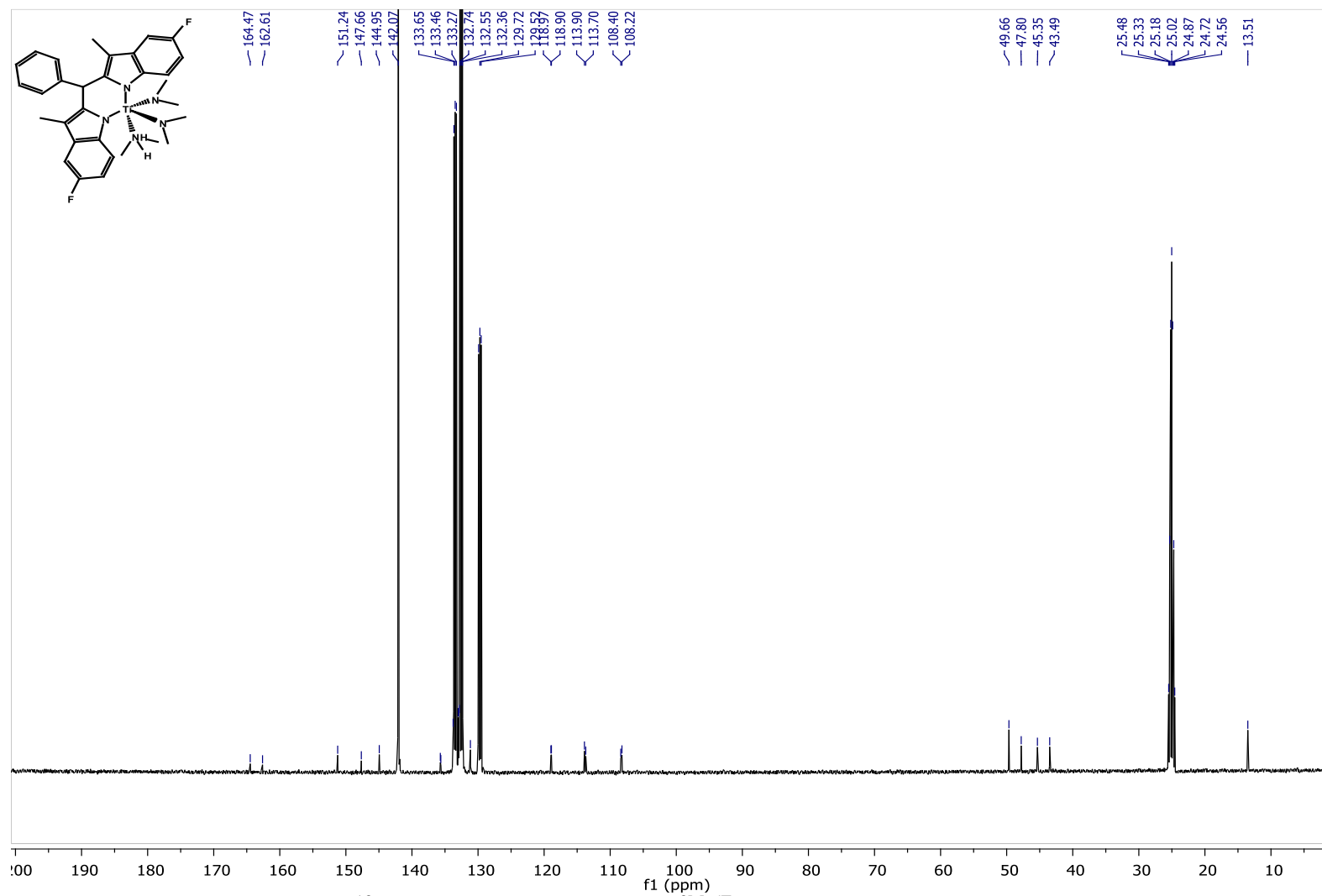


**Figure 3.71.**  $^{19}\text{F}$  NMR Spectrum of  $\text{H}_2\text{dim}^{3\text{Me}5\text{F}}$  in  $\text{C}_6\text{D}_6$ .

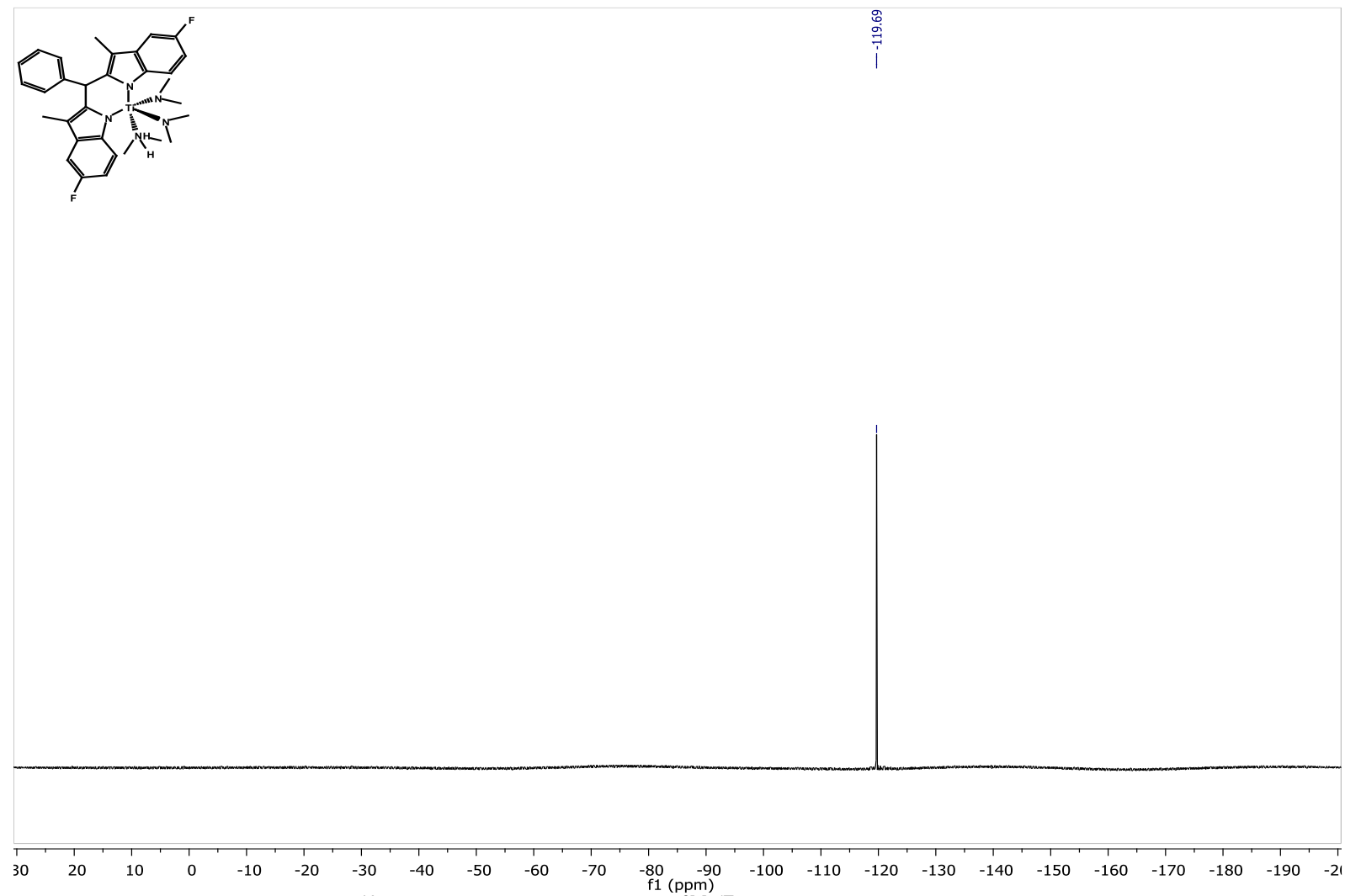


**Figure 3.72.**  $^1\text{H}$  NMR Spectrum of  $\text{Ti}(\text{dim}^3\text{Me}_5\text{F})(\text{NMe}_2)_2(\text{HNMe}_2)$  (**2b**) in toluene- $d_8$ .

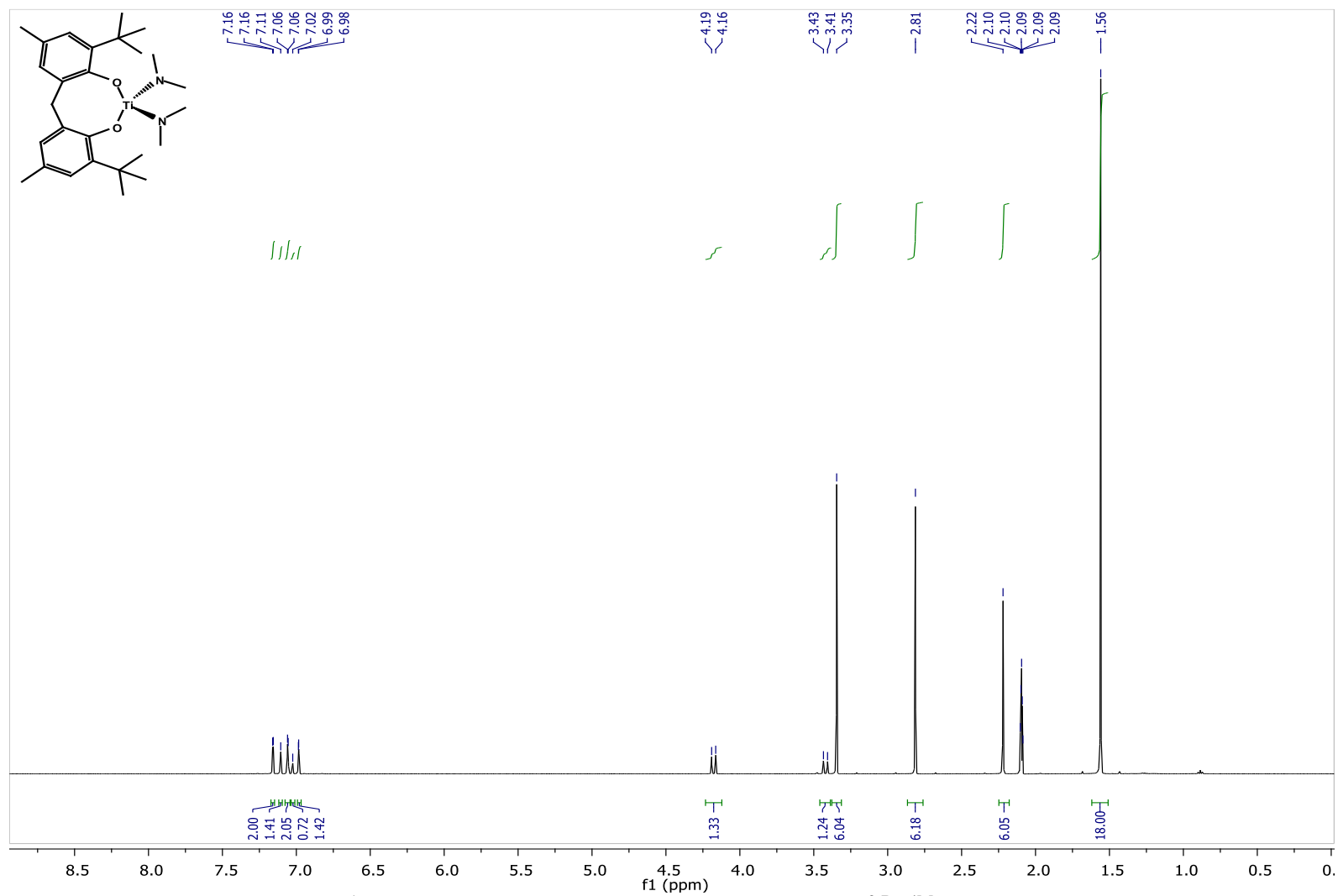




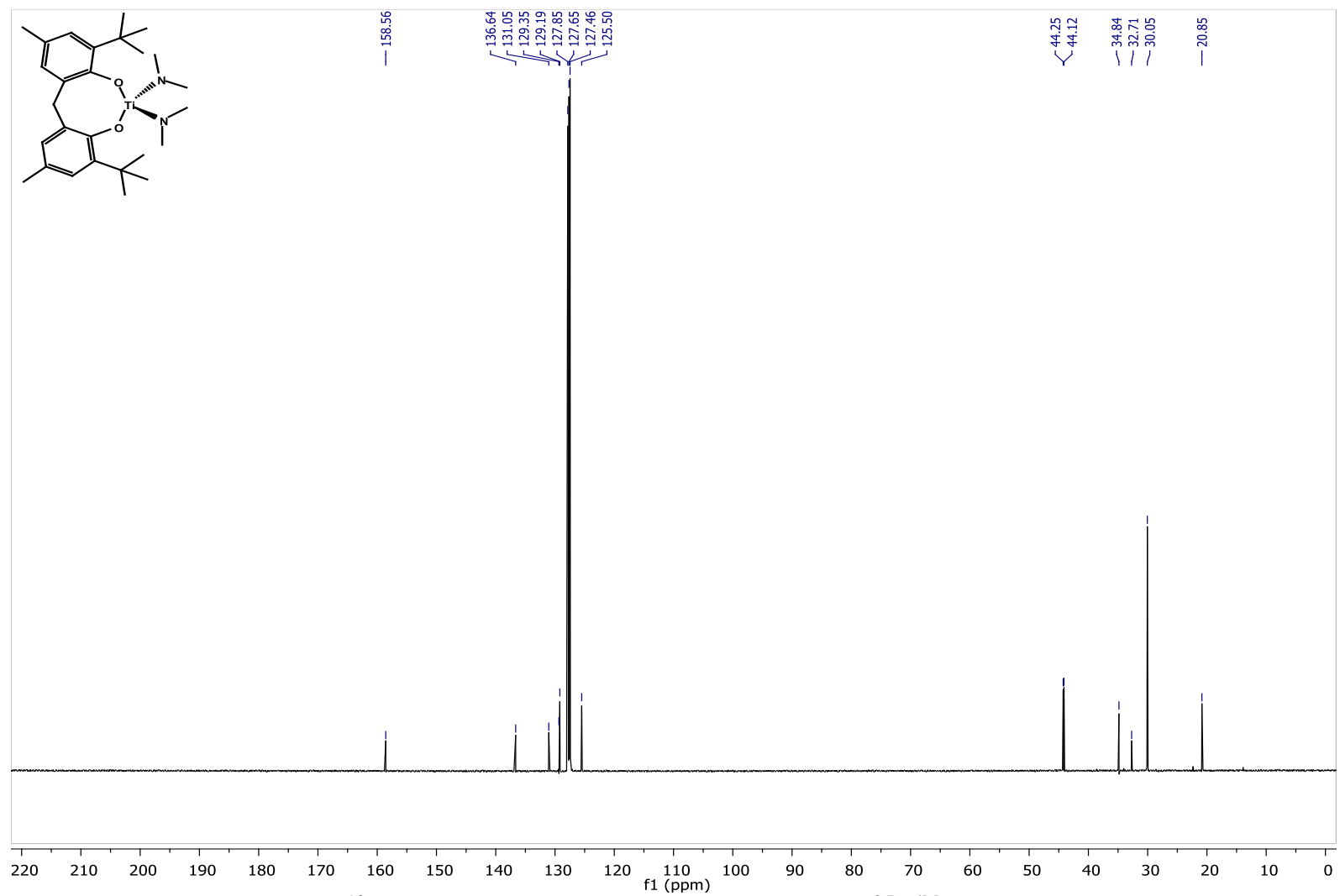
**Figure 3.73.**  $^{13}\text{C}$  NMR Spectrum of  $\text{Ti}(\text{dim}^3\text{Me}_5\text{F})(\text{NMe}_2)_2(\text{HNMe}_2)$  (**2b**) in toluene- $\text{d}_8$ .



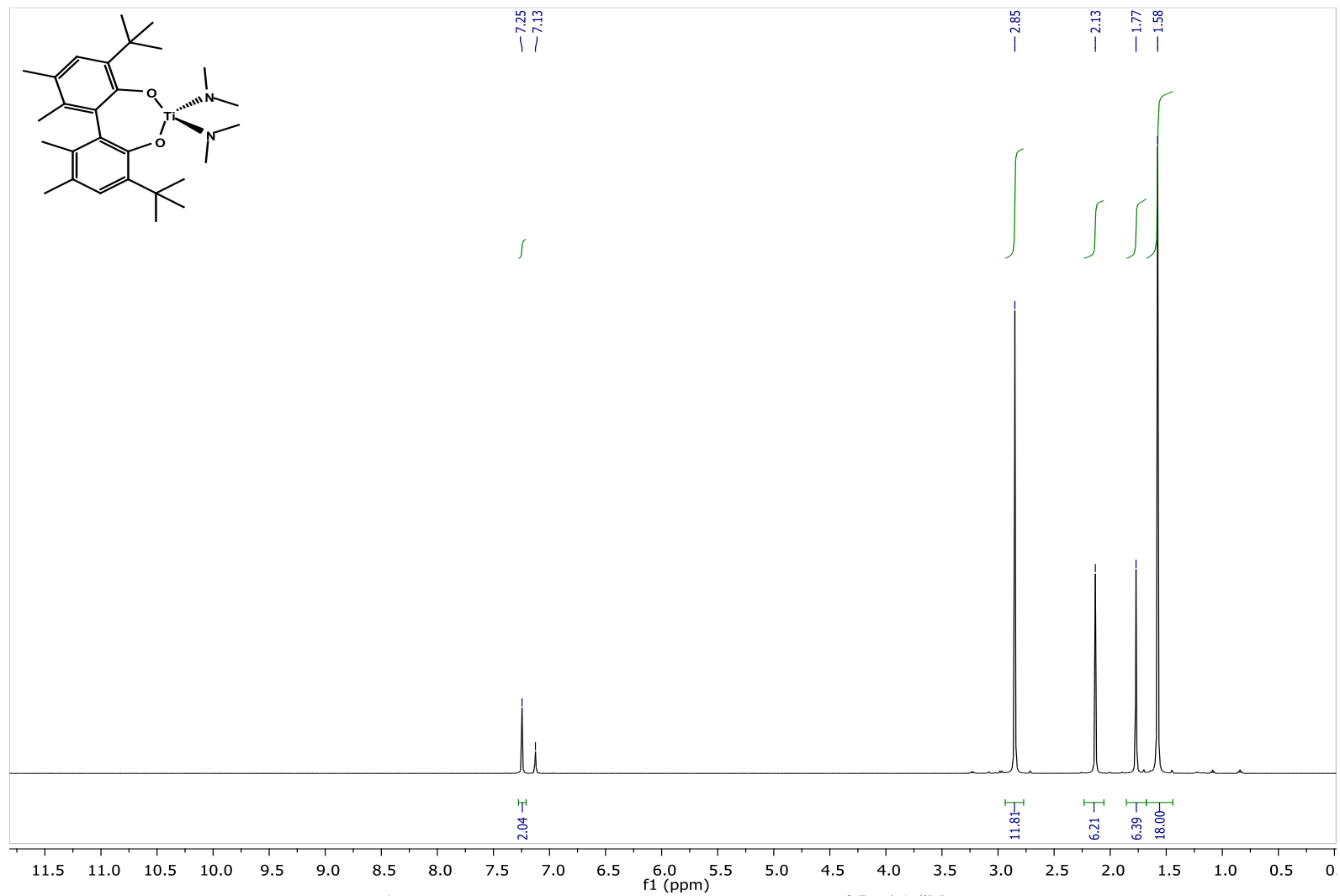
**Figure 3.74.**  $^{19}\text{F}$  NMR Spectrum of  $\text{Ti}(\text{dim}^{3\text{Me}5\text{F}})(\text{NMe}_2)_2(\text{HNMe}_2)$  (**2b**) in  $\text{toluene-d}_8$ .



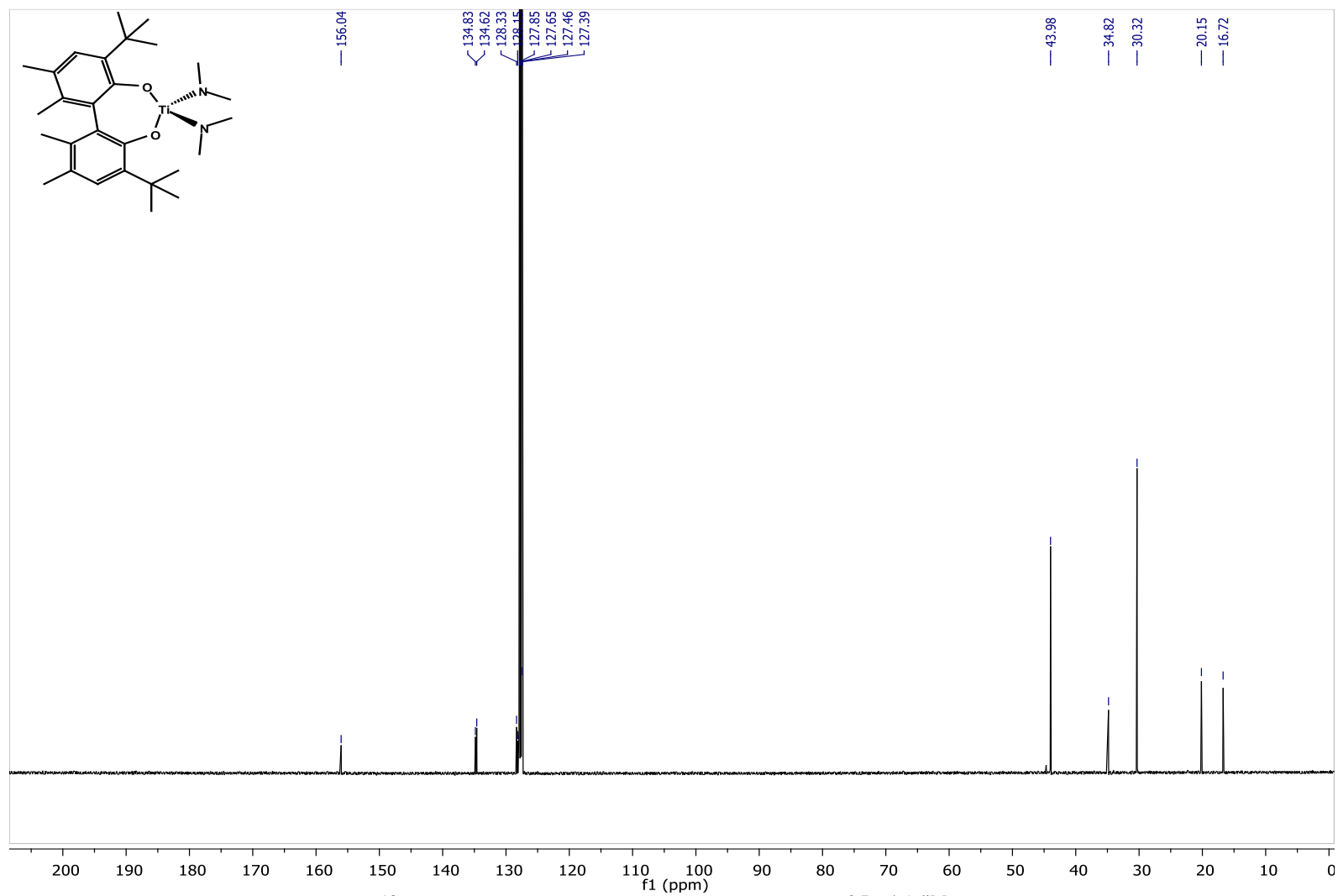
**Figure 3.75.**  $^1\text{H}$  NMR Spectrum of  $\text{Ti}(\text{NMe}_2)_2(\text{bis-phenoxide-}^{2t}\text{Bu-}^4\text{Me})$  (3) in  $\text{toluene-d}_8$ .



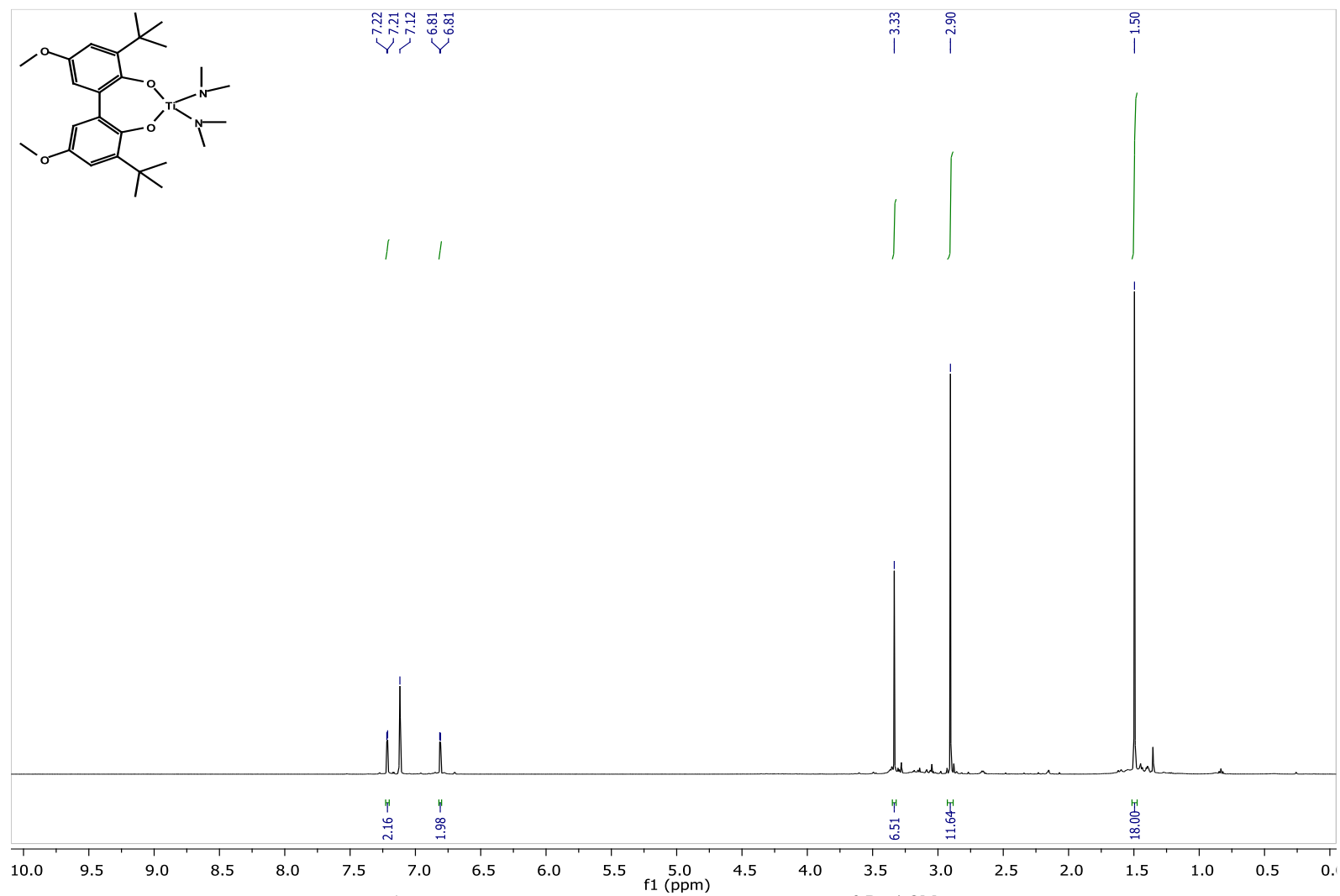
**Figure 3.76.**  $^{13}\text{C}$  NMR Spectrum of  $\text{Ti}(\text{NMe}_2)_2(\text{bis-phenoxide}^{2\text{tBu-4Me}})$  (3) in  $\text{toluene-d}_8$ .



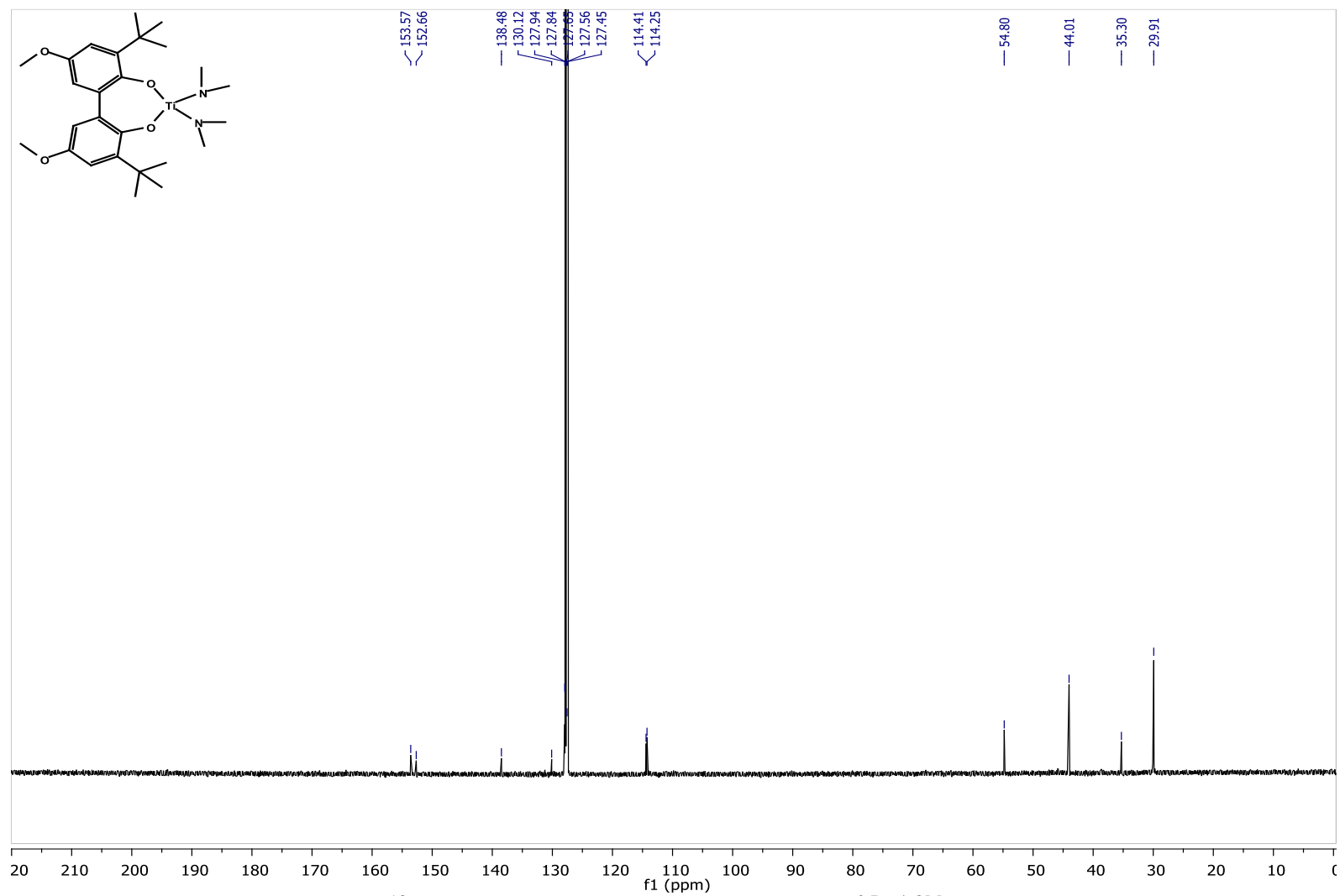
**Figure 3.77.**  $^1\text{H}$  NMR Spectrum of  $\text{Ti}(\text{NMe}_2)_2(\text{biphenol}^{2\text{tBu-4,5-diMe}})$  (**4a**) in  $\text{C}_6\text{D}_6$ .



**Figure 3.78.**  $^{13}\text{C}$  NMR Spectrum of  $\text{Ti}(\text{NMe}_2)_2(\text{biphenol}^{2\text{tBu-4,5-diMe}})$  (4a) in  $\text{C}_6\text{D}_6$ .

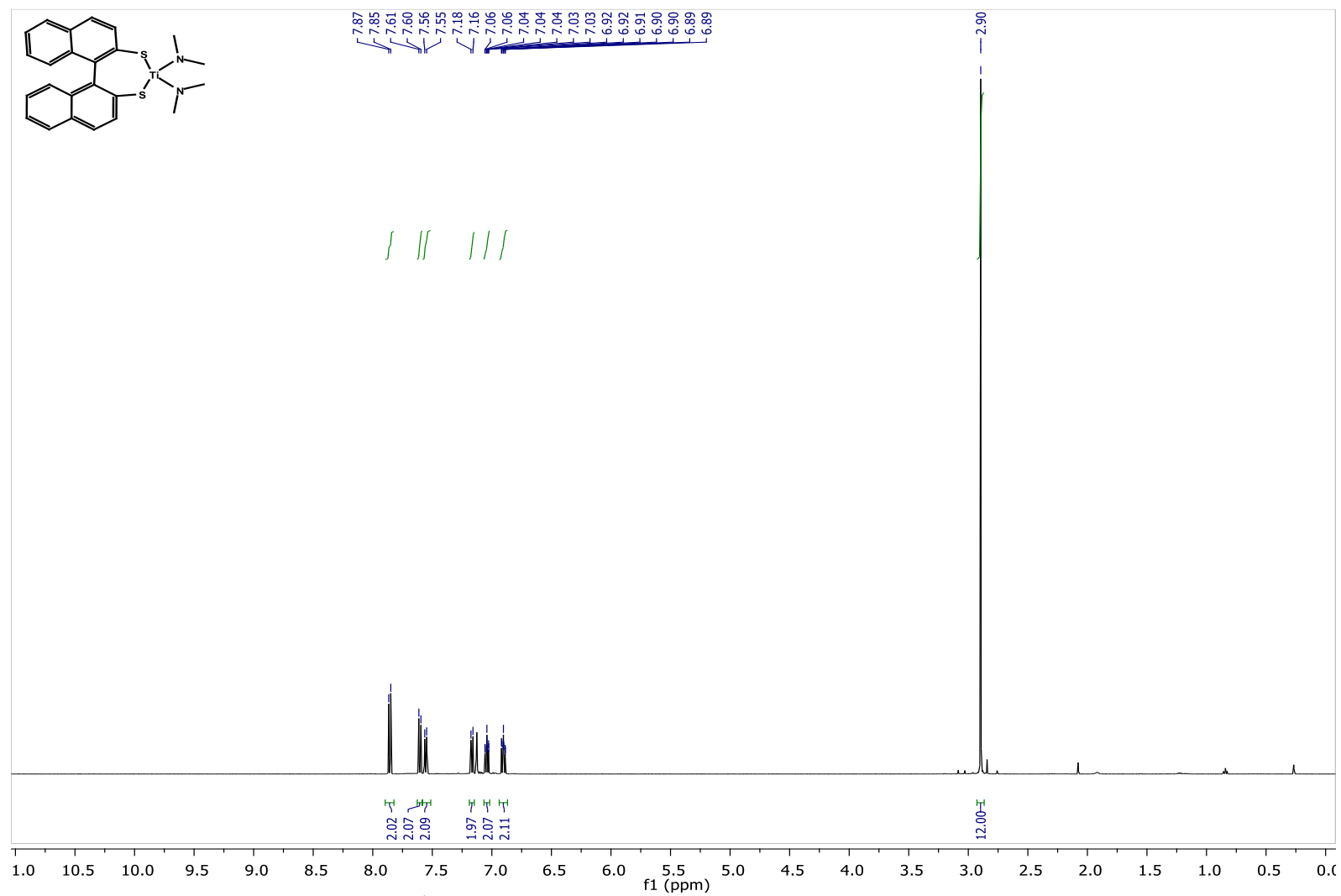


**Figure 3.79.**  $^1\text{H}$  NMR Spectrum of  $\text{Ti}(\text{NMe}_2)_2(\text{biphenol}^{2\text{tBu-4OMe}})$  (**4b**) in  $\text{C}_6\text{D}_6$ .

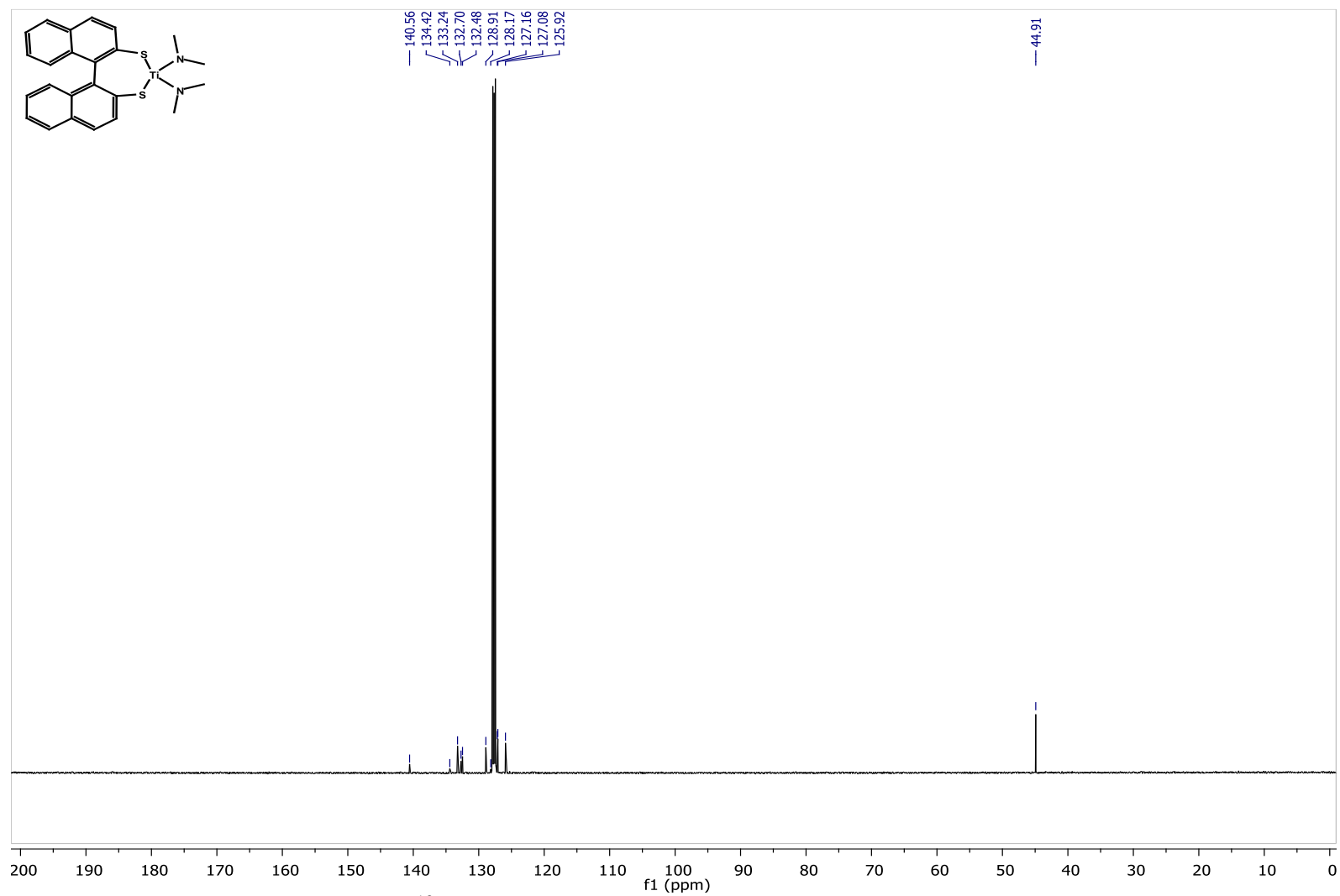


**Figure 3.80.**  $^{13}\text{C}$  NMR Spectrum of  $\text{Ti}(\text{NMe}_2)_2(\text{biphenol}^{2\text{tBu-4-OMe}})$  (**4b**) in  $\text{C}_6\text{D}_6$ .

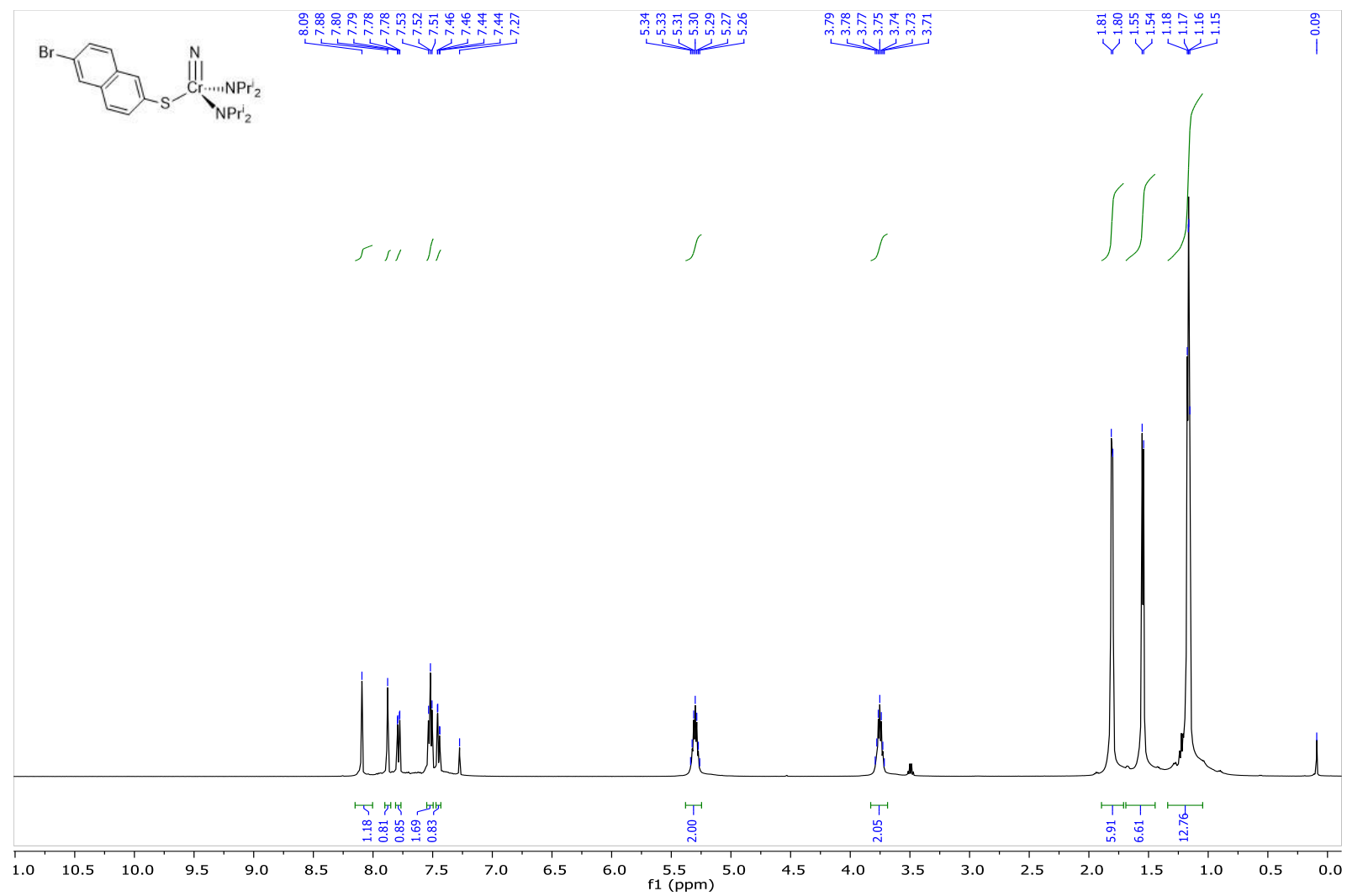




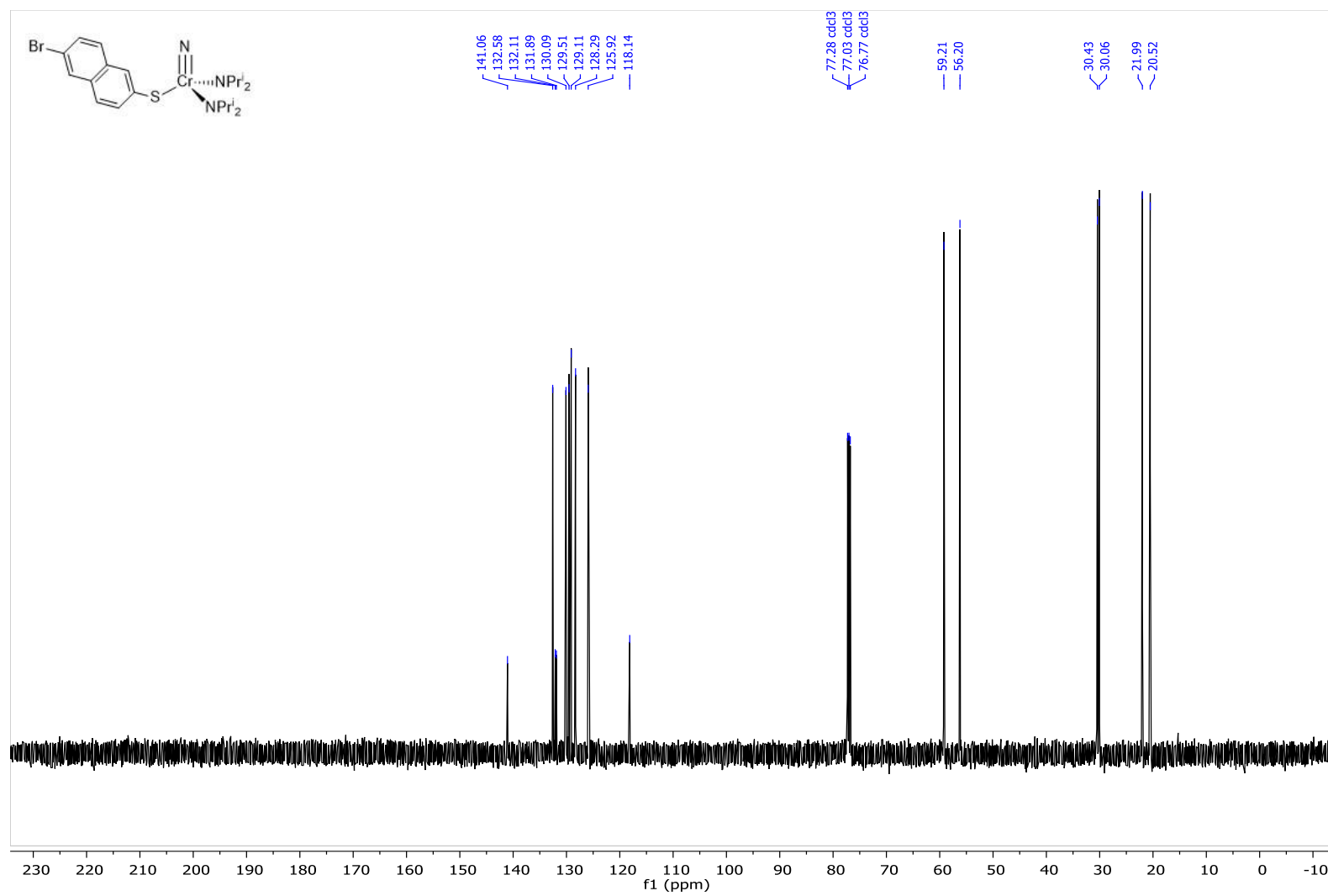
**Figure 3.81.**  $^1\text{H}$  NMR Spectrum of  $\text{Ti}(\text{dithioBINAP})(\text{NMe}_2)_2$  (6) in  $\text{C}_6\text{D}_6$ .



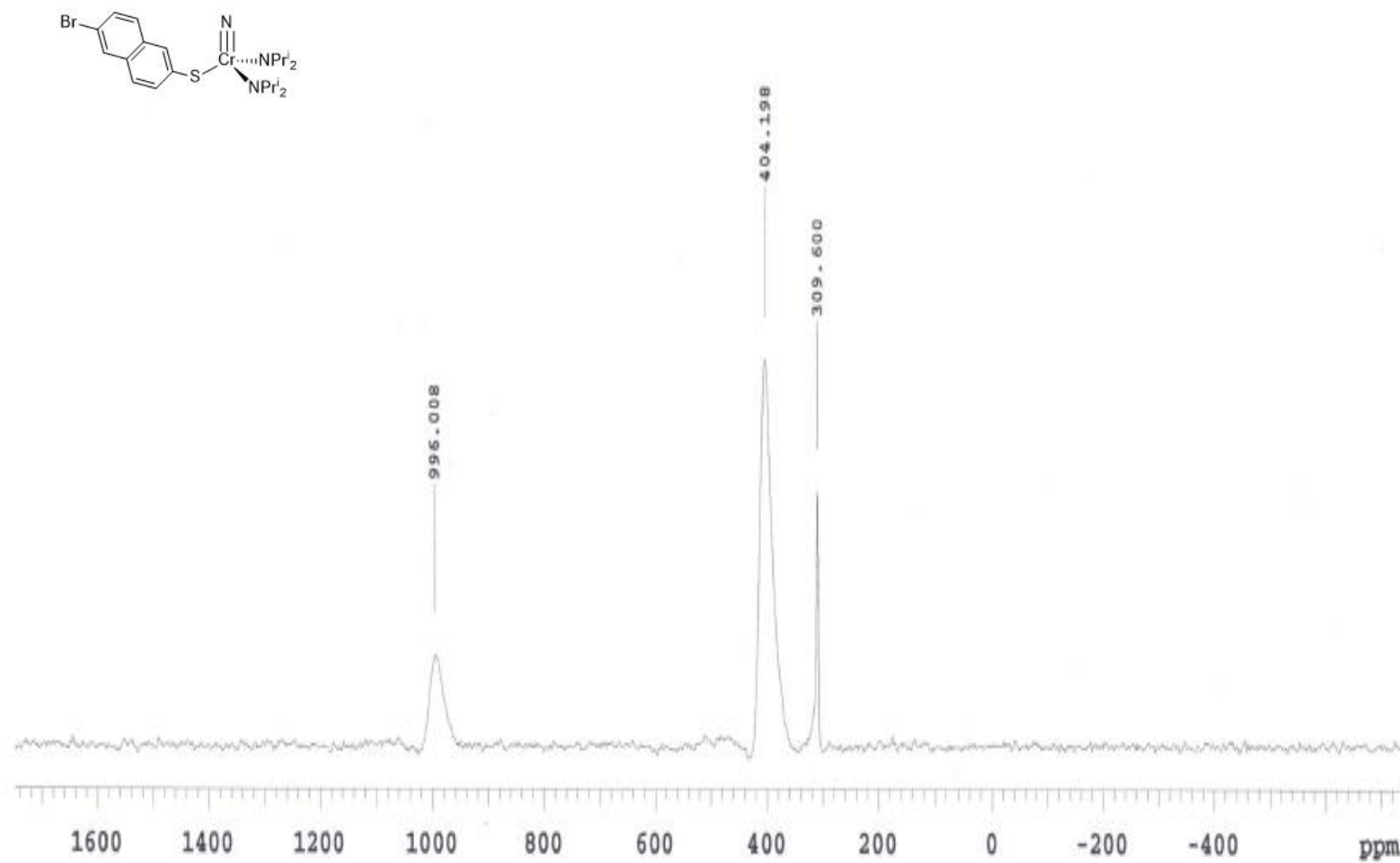
**Figure 3.82.**  $^{13}\text{C}$  NMR Spectrum of  $\text{Ti}(\text{dithioBINAP})(\text{NMe}_2)_2$  (**6**) in  $\text{C}_6\text{D}_6$ .



**Figure 3.83.**  $^1\text{H}$  NMR Spectrum of  $\text{NCr}(\text{N}^i\text{Pr}_2)_2(6\text{Br-SNap})$  in  $\text{CDCl}_3$ .



**Figure 3.84.**  $^{13}\text{C}$  NMR Spectrum of  $\text{NCr}(\text{N}^i\text{Pr}_2)_2(6\text{Br-SNap})$  in  $\text{CDCl}_3$ .



**Figure 3.85.**  $^{14}\text{N}$  NMR Spectrum of  $\text{NCr}(\text{N}^i\text{Pr}_2)_2(6\text{Br-SNap})$  in  $\text{CDCl}_3$ .

## REFERENCES

## REFERENCES

1. Billow, B. S.; McDaniel, T. J.; Odom, A. L., *Nat Chem* **2017**, 9, 837-842.
2. Adams, C., *Top. Catal.* **2009**, 52, 924-934.
3. Tolman, C. A., *Chem. Rev.* **1977**, 77, 313-348.
4. Alt, H. G.; Köppl, A., *Chem. Rev.* **2000**, 100, 1205-1222.
5. Klosin, J.; Fontaine, P. P.; Figueroa, R., *Acc. Chem. Res.* **2015**, 48, 2004-2016.
6. Sharpless, K. B., *Angew. Chem., Int. Ed* **2002**, 41, 2024.
7. Riera, A.; Moreno, M., *Molecules* **2010**, 15, 1041-73.
8. DiFranco, S. A.; Maciulis, N. A.; Staples, R. J.; Batrice, R. J.; Odom, A. L., *Inorg Chem* **2012**, 51, 1187-200.
9. Abel, E. W.; Bennett, M. A.; Wilkinson, G., *J. Chem. Soc.* **1959**, 2323-2327.
10. Strohmeier, W.; Müller, F.-J., *Chem. Ber.* **1967**, 100, 2812-2821.
11. Tolman, C. A., *J. Am. Chem. Soc.* **1970**, 92, 2953-2956.
12. Clavier, H.; Nolan, S. P., *Chem. Commun.* **2010**, 46, 841-861.
13. Tolman, C. A., *J. Am. Chem. Soc.* **1970**, 92, 2956-2965.
14. Manzer, L. E.; Tolman, C. A., *J. Am. Chem. Soc.* **1975**, 97, 1955-1956.
15. Bodner, G. M., *Inorg. Chem.* **1975**, 14, 1932-1935.
16. Mougél, V.; Santiago, C. B.; Zhizhko, P. A.; Bess, E. N.; Varga, J.; Frater, G.; Sigman, M. S.; Copéret, C., *J. Am. Chem. Soc.* **2015**, 137, 6699-6704.
17. Bemowski, R. D.; Singh, A. K.; Bajorek, B. J.; DePorre, Y.; Odom, A. L., *Dalton Trans* **2014**, 43, 12299-305.
18. Billow, B. S.; Bemowski, R. D.; DiFranco, S. A.; Staples, R. J.; Odom, A. L., *Organometallics* **2015**, 34, 4567-4573.
19. Beaumier, E. P.; Billow, B. S.; Singh, A. K.; Biros, S. M.; Odom, A. L., *Chem. Sci.* **2016**, 7, 2532-2536.

20. Aldrich, K. E.; Billow, B. S.; Holmes, D.; Bemowski, R. D.; Odom, A. L., *Organometallics* **2017**.
21. Müller, T. E.; Hultsch, K. C.; Yus, M.; Foubelo, F.; Tada, M., *Chem. Rev.* **2008**, *108*, 3795-3892.
22. Odom, A. L.; McDaniel, T. J., *Acc. Chem. Res.* **2015**, 150821102447001.
23. Gilbert, Z. W.; Hue, R. J.; Tonks, I. A., *Nat Chem* **2016**, *8*, 63-68.
24. Duncan, A. P., Bergman, R. G., *Chem. Rec.* **2002**, *2*, 431.
25. Pohlki, F.; Doye, S., *Angew. Chem. Int. Ed.* **2001**, *40*, 2305-2308.
26. Falivene, L.; Credendino, R.; Poater, A.; Petta, A.; Serra, L.; Oliva, R.; Scarano, V.; Cavallo, L., *Organometallics* **2016**, *35*, 2286-2293.
27. Swartz, D. L.; Odom, A. L., *Organometallics* **2006**, *25*, 6125-6133.
28. Swartz, D. L., 2nd; Staples, R. J.; Odom, A. L., *Dalton Trans* **2011**, *40*, 7762-8.
29. Littler, B. J.; Miller, M. A.; Hung, C.-H.; Wagner, R. W.; O'Shea, D. F.; Boyle, P. D.; Lindsey, J. S., *J. Org. Chem.* **1999**, *64*, 1391-1396.
30. Rieth, R. D.; Mankad, N. P.; Calimano, E.; Sadighi, J. P., *Org. Lett.* **2004**, *6*, 3981-3983.
31. Silverstein, R. M.; Ryskiewicz, E. E.; Willard, C.; Koehler, R. C., *J. Org. Chem.* **1955**, *20*, 668-672.
32. Chen, C.-Y.; Bocian, D. F.; Lindsey, J. S., *J. Org. Chem.* **2014**, *79*, 1001-1016.
33. Liddell, P. A.; Forsyth, T. P.; Senge, M. O.; Smith, K. M., *Tetrahedron* **1993**, *49*, 1343-1350.
34. Batrice, R. J.; Fridman, N.; Eisen, M. S., *Inorg Chem* **2016**.
35. Mason, M. R.; Fneich, B. N.; Kirschbaum, K., *Inorg. Chem.* **2003**, *42*, 6592-6594.
36. Mason, M. R., Barnard, T. S., Segla, M. F., Xie, B. & Kirschbaum, K. , *J. Chem. Crystallogr.* **2003**, *33*, 531.
37. Le Roux, E., *Coordination Chemistry Reviews* **2016**, *306*, 65-85.
38. Santora, B. P.; White, P. S.; Gagné, M. R., *Organometallics* **1999**, *18*, 2557-2560.



39. Azor, L.; Bailly, C.; Brelot, L.; Henry, M.; Mobian, P.; Dagorne, S., *Inorg Chem* **2012**, *51*, 10876-83.
40. Ackermann, L.; Bergman, R. G.; Loy, R. N., *J. Am. Chem. Soc.* **2003**, *125*, 11956-11963.
41. Tillack, A.; Khedkar, V.; Beller, M., *Tetrahedron Lett.* **2004**, *45*, 8875-8878.
42. Khedkar, V.; Tillack, A.; Beller, M., *Org. Lett.* **2003**, *5*, 4767-4770.
43. Tillack, A.; Khedkar, V.; Jiao, H.; Beller, M., *Eur. J. Org. Chem.* **2005**, *2005*, 5001-5012.
44. Li, C.; Xiong, K.; Yan, L.; Jiang, M.; Song, X.; Wang, T.; Chen, X.; Zhan, Z.; Ding, Y., *Catal. Sci. Technol.* **2016**, *6*, 2143-2149.
45. Kallepalli, V. A.; Shi, F.; Paul, S.; Onyeozili, E. N.; Maleczka, R. E.; Smith, M. R., *J. Org. Chem.* **2009**, *74*, 9199-9201.
46. He, H.; Chen, L.-Y.; Wong, W.-Y.; Chan, W.-H.; Lee, A. W. M., *Eur. J. Org. Chem.* **2010**, *2010*, 4181-4184.
47. Fabbri, D.; Delogu, G.; De Lucchi, O., *J. Org. Chem.* **1993**, *58*, 1748-1750.
48. Bandarage, U. K.; Simpson, J.; Smith, R. A. J.; Weavers, R. T., *Tetrahedron* **1994**, *50*, 3463-3472.
49. Burns, M.; Lloyd-Jones, G. C.; Moseley, J. D.; Renny, J. S., *J. Org. Chem.* **2010**, *75*, 6347-6353.
50. Hatano, M.; Maki, T.; Moriyama, K.; Arinobe, M.; Ishihara, K., *J. Am. Chem. Soc.* **2008**, *130*, 16858-16860.
51. Swartz, D. L., 2nd; Odom, A. L., *Dalton Trans* **2008**, 4254-8.
52. Shi, Y. H.; Ciszewski, J. T.; Odom, A. L., *Organometallics* **2001**, *20*, 3967-3969.
53. Bexrud, J. A.; Beard, J. D.; Leitch, D. C.; Schafer, L. L., *Org. Lett.* **2005**, *7*, 1959-1962.
54. Carlson, R., Carlson J. E., *Design and optimization in organic synthesis*. 2nd ed.; Elsevier: Amsterdam, 2005.
55. DiFranco, S. A.; Maciulis, N. A.; Staples, R. J.; Batrice, R. J.; Odom, A. L., *Inorg. Chem.* **2011**, *51*, 1187-1200.
56. Falivene, L.; Credendino, R.; Poater, A.; Petta, A.; Serra, L.; Oliva, R.; Scarano, V.; Cavallo, L., *Organometallics* **2016**.

57. Li, D. Y.; Kagan, G.; Hopson, R.; Williard, P. G., *Journal of the American Chemical Society* **2009**, *131*, 5627-5634.
58. Kiraly, P.; Swan, I.; Nilsson, M.; Morris, G. A., *Journal of Magnetic Resonance* **2016**, *270*, 24-30.
59. Lane, E. M.; Chapp, T. W.; Hughes, R. P.; Glueck, D. S.; Feland, B. C.; Bernard, G. M.; Wasylshen, R. E.; Rheingold, A. L., *Inorganic Chemistry* **2010**, *49*, 3950-3957.
60. Boyle, T. J.; Barnes, D. L.; Heppert, J. A.; Morales, L.; Takusagawa, F.; Connolly, J. W., *Organometallics* **1992**, *11*, 1112-1126.
61. Vilches-Herrera, M.; Miranda-Sepulveda, J.; Rebolledo-Fuentes, M.; Fierro, A.; Luhr, S.; Iturriaga-Vasquez, P.; Cassels, B. K.; Reyes-Parada, M., *Bioorganic & Medicinal Chemistry* **2009**, *17*, 2452-2460.
62. Odom, A. L.; McDaniel, T. J., *Accounts of Chemical Research* **2015**, *48*, 2822-2833.
63. Swartz II, D. L.; Staples, R. J.; Odom, A. L., *Dalton Trans.* **2011**, *40*, 7762-7768.
64. Batrice, R. J.; Fridman, N.; Eisen, M. S., *Inorganic Chemistry* **2016**.
65. Su, Y.-M.; Hou, Y.; Yin, F.; Xu, Y.-M.; Li, Y.; Zheng, X.; Wang, X.-S., *Organic Letters* **2014**, *16*, 2958-2961.
66. Mason, M.; Barnard, T.; Segla, M.; Xie, B.; Kirschbaum, K., *Journal of Chemical Crystallography* **2003**, *33*, 531-540.
67. van der Vlugt, J. I.; Hewat, A. C.; Neto, S.; Sablong, R.; Mills, A. M.; Lutz, M.; Spek, A. L.; Müller, C.; Vogt, D., *Advanced Synthesis & Catalysis* **2004**, *346*, 993-1003.
68. Murat-Onana, M. L.; Berini, C.; Minassian, F.; Pelloux-Leon, N.; Denis, J.-N., *Organic & Biomolecular Chemistry* **2010**, *8*, 2204-2211.
69. Alexander, J. B.; La, D. S.; Cefalo, D. R.; Hoveyda, A. H.; Schrock, R. R., *Journal of the American Chemical Society* **1998**, *120*, 4041-4042.
70. Hatano, M.; Maki, T.; Moriyama, K.; Arinobe, M.; Ishihara, K., *Journal of the American Chemical Society* **2008**, *130*, 16858-60.
71. Espenson, J., H., *Chemical Kinetics and Reaction Mechanisms*. 2nd Ed ed.; McGraw Hill: New York, 2002.

## Chapter 4. Quantifying Unsymmetrical Ancillary Ligand Effects in Titanium(IV)

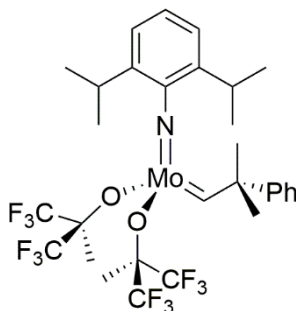
### Catalyzed Hydroamination

#### 4.1 Background and Motivation

As mentioned in **Chapter 3**, understanding the effects that the ancillary ligands have on the metal center is a crucial step in catalyst design. In Chapter 3, we demonstrated the use of the Ligand Donor Parameter (LDP) and Percent Buried Volume (%V<sub>bur</sub>) to model the rate of the reaction. All the ligands used in this study were symmetrical bidentate ligands. While conducting this study, we wondered how unsymmetrical ligands would affect the rate and how would we begin to model such ligands.

#### 4.2 Introduction into Unsymmetrical Ligand Environments

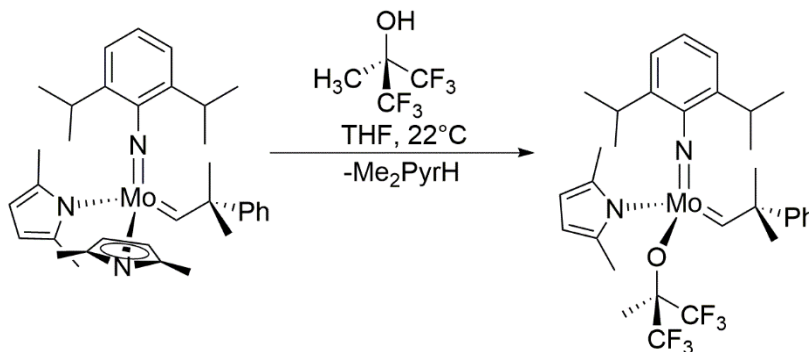
Schrock and coworkers' olefin metathesis is a reaction that has been extensively studied for ancillary ligand effects on a high-valent metal.<sup>1-2</sup> One of the discoveries found by Schrock's group was that as the Lewis acidity of their d<sup>0</sup> molybdenum catalysts increased, the reactivity also increases. However, during catalyst development they made another key discovery.



**Figure 4.1.** Schrock's olefin metathesis catalyst.<sup>2</sup>

In the early 2000's, Schrock's group started searching for a synthetic route that would allow them to prepare a large variety of Mo(=NAr)(=CHR')(OR'')<sub>2</sub> complexes. Easy access to these bisalkoxide complexes was needed to find suitable ligands for asymmetric reactions. Schrock's group envisioned that Mo(=NAr)(=CHR')(X)<sub>2</sub> derivatives would be the optimal starting material

to yield the desirable bisalkoxide complexes. However, upon reacting different  $\text{Mo}(=\text{NAr})(=\text{CHR}')(\text{X})_2$  derivatives with 2 equivalents of alcohol, they kept isolating monoalkoxide  $\text{Mo}(=\text{NAr})(=\text{CHR}')(\text{OR})(\text{X})$  complexes.<sup>2-4</sup> As shown in **Scheme 4.1.**, when  $\text{Mo}(=\text{NAr})(=\text{CHR}')(\text{Me}_2\text{Pyr})_2$  is reacted with an alcohol derivative it formed the monoalkoxide pyrrolide (MAP) species,  $\text{Mo}(=\text{NAr})(=\text{CHR}')(\text{OR})(\text{Me}_2\text{Pyr})$ .<sup>2, 5</sup>

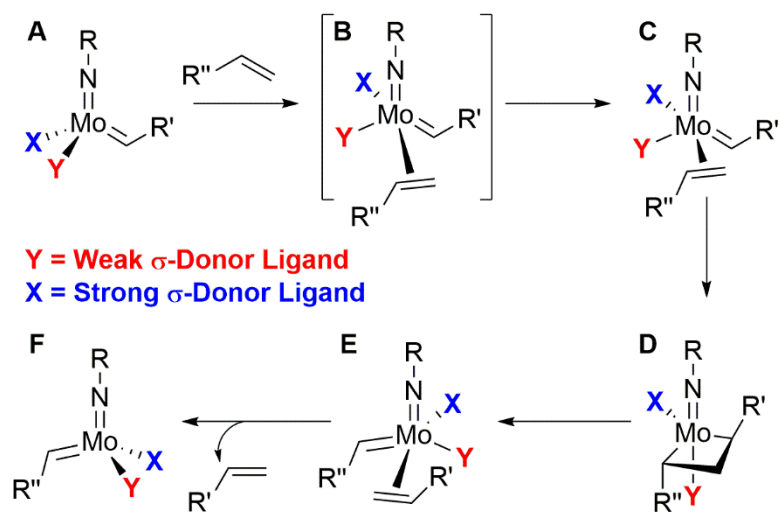


**Scheme 4.1.** Synthesis of a MonoAlkoxide Pyrrolide (MAP) complex.<sup>2</sup>

While this was not the intended product, Schrock's group recognized that these MAP complexes are chiral at the metal (i.e., have four different groups bound to the metal). Therefore, they became interested in using these complexes in asymmetric reactions. As Schrock's group started to study these MAP complexes an interesting discovery was made. While the bisalkoxide complexes (**Figure 4.1.**) are often highly reactive towards olefins, the bispyrrolide (**Scheme 4.1**) complexes are sluggish and do not readily react with olefins. Based off these findings, one would assume that the MAP derivative, like the one shown on the right in **Scheme 4.1**, would exhibit moderate reactivity towards olefins. However, this is *incorrect* and the MAP complexes often exhibit reactivity even greater than the bisalkoxides!<sup>2</sup>

Theoretical studies, conducted by Eisenstein and Copéret<sup>6-7</sup>, suggest that  $\text{Mo}(=\text{NR})(=\text{CHR}')(\text{X})(\text{Y})$  catalysts, where  $\text{X} \neq \text{Y}$ , should be more active than the bisalkoxide complexes. These studies predict that when X and Y are very different ligands, in particular a weak  $\sigma$ -donor (like an alkoxide or siloxide) and a strong  $\sigma$ -donor (like an alkyl), are more active than

the bisalkoxide species.<sup>2</sup> In Eisenstein and Copéret's calculations, they found that the barrier for distortion of the tetrahedral complex would be lower in energy with a strong  $\sigma$ -donor ligand (**X**) present. As shown in **Scheme 4.2** (moving from **A** to **B** to **C**), this distortion must occur before or during the alkene coordination. In order to minimize the unfavorable trans-influence, the site opposite of the donating group would be vacant. This allows the alkene substrate to approach *syn* to the weak  $\sigma$ -donor ligand (**Y**). Furthermore, the metallacyclobutane intermediate (**D**) also has minimal trans-influence because the imido is trans to the weak  $\sigma$ -donor instead of the strong  $\sigma$ -donor ligand.<sup>6, 8</sup> After the cycloreversion (**D** to **E**), the donor ligand is trans to the new olefin, and this leads to the disassociation of the new olefin. (**E** to **F**).

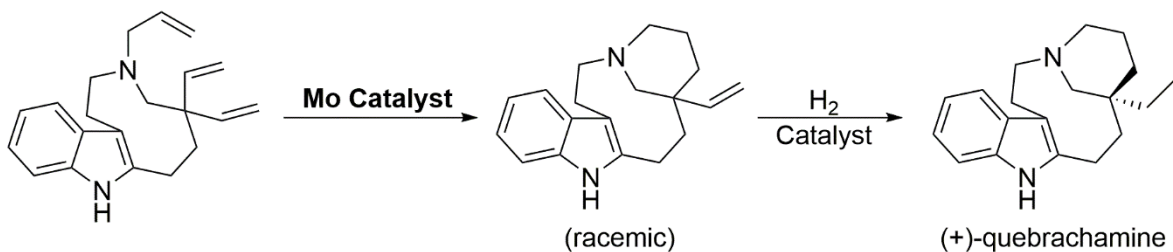


**Scheme 4.2.** A simplified version of Eisenstein and Copéret's mechanistic model.<sup>6, 8</sup>

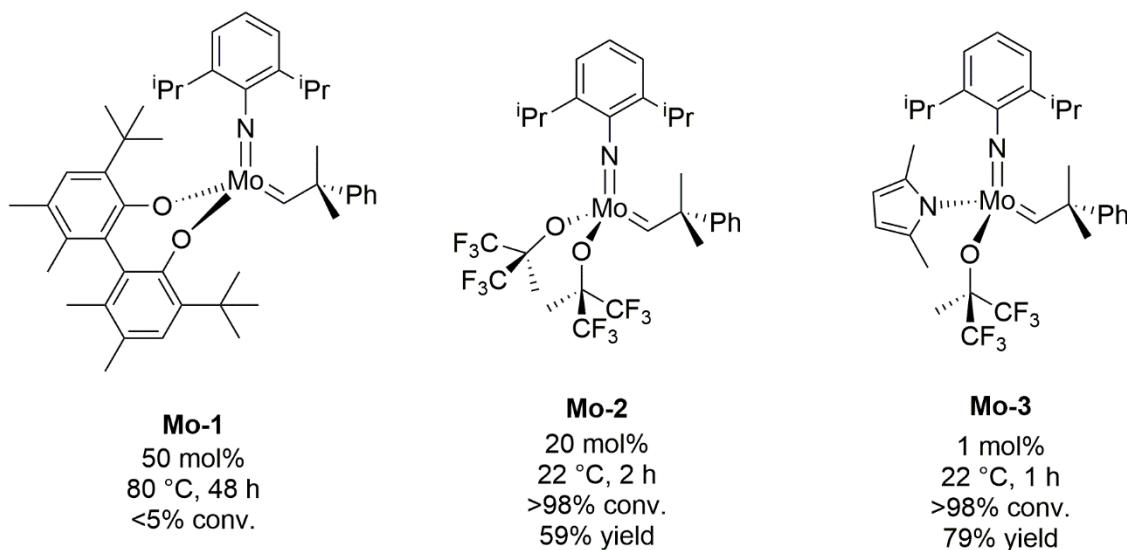
Having acquired this detailed understanding, of the relative arrangements for the imido, acceptor, and donor ligands, allowed the Schrock and Hoveyda groups design more efficient catalysts. Perhaps the best example that demonstrates the progression of their catalyst development, is found in the synthesis of the natural product quebrachamine. A challenging step in the synthesis of quebrachamine is the ring-closing metathesis (RCM) of the triene (shown in the top left of **Scheme 4.3**). Upon screening various molybdenum catalyst, they observed the expected

trends. Moving to a more Lewis acidic metal center (**Mo-1** to **Mo-2**) increases the catalysts activity and moving to a MAP derivative (**Mo-2** to **Mo-3**) further increases the activity.

**Proposed RCM route**

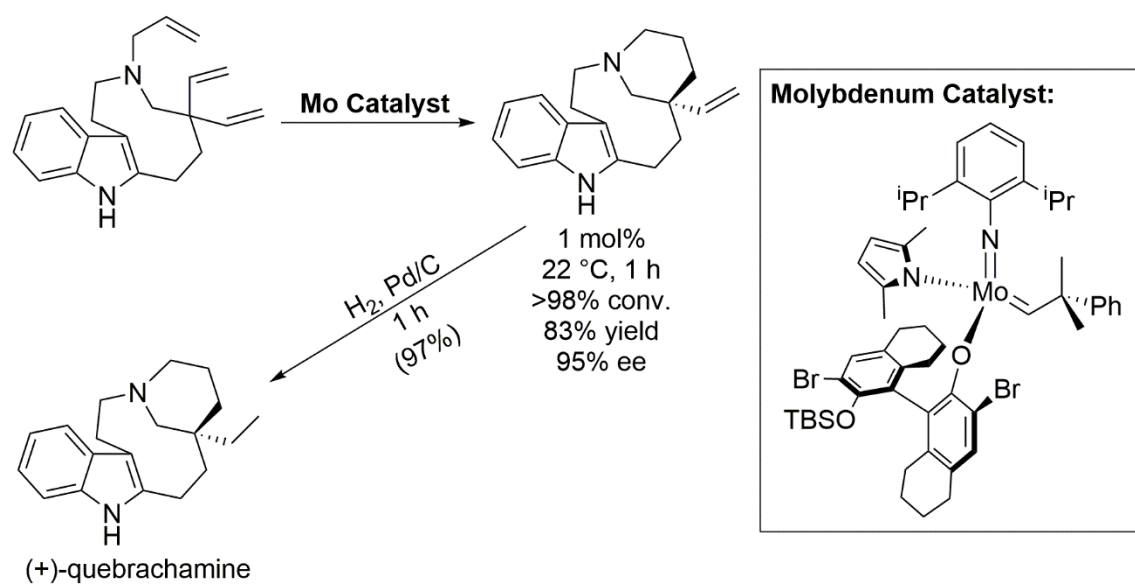


**Mo Catalyst Screening**



**Scheme 4.3.** A small representation of the molybdenum catalysts screened for the synthesis of quebrachamine.<sup>8-9</sup>

After further catalyst development, the Schrock and Hoveyda groups, were able to design a new class of chiral olefin metathesis catalysts. These catalysts proved to be effective at enantioselective ring-closing, as shown in **Scheme 4.4**.



**Scheme 4.4.** Application of chiral molybdenum catalyst for the synthesis of (+)-quebrachamine.<sup>8-9</sup>

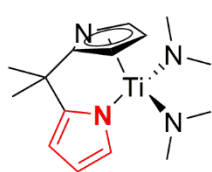
With this additional inspiration by the Schrock and Hoveyda group, we wondered if our system could also benefit by using two electronically and sterically different ligands and how we could we build a model with these unsymmetrical ligands.

### 4.3 Model Considerations and Ligand Development

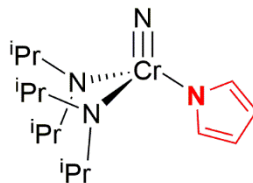
As we saw in **Chapter 3**, the sterics ( $\%V_{\text{bur}}$ ) and electronics (LDP) of each ligand was used to model the rate of the titanium catalyzed hydroaminations of alkynes<sup>10</sup>. Using a similar approach, we can think about how one might do this when unsymmetrical ligands are used. As shown the top of **Figure 4.2**, our original model used half each of the respected chelating ligand to determine the LDP and  $\%V_{\text{bur}}$  (i.e. the electronics and sterics of the dipyrrolylmethane ligand on titanium, was measured using the chromium-pyrrolyl complex). Our new model, shown at the bottom of **Figure 4.2**, will use both sides of the chelating ligand and each separate chelate will be used to determine the LDP and  $\%V_{\text{bur}}$ , on the chromium system. For example, for the **pyrrolyl-indolyl** complex (bottom left in **Figure 4.2**), the sterics and electronics will be measured from the chromium-pyrrolyl and chromium-indolyl complexes.



### Original Model



Rate measured  
from [Ti]

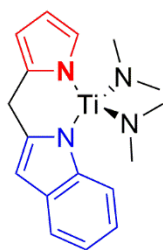


Steric and electronics  
measured from [Cr]

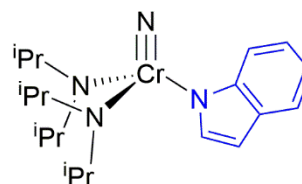
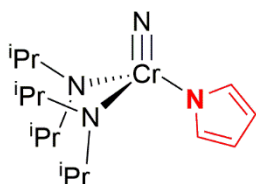
Equation used to model the reaction:

$$k_{\text{obs}} \times 10^4 = a + b(\text{LDP}) + c(\%V_{\text{bur}})$$

### New Model



Rate measured  
from [Ti]



Steric and electronics  
measured from both [Cr] complexes

Equation used to model the reaction:

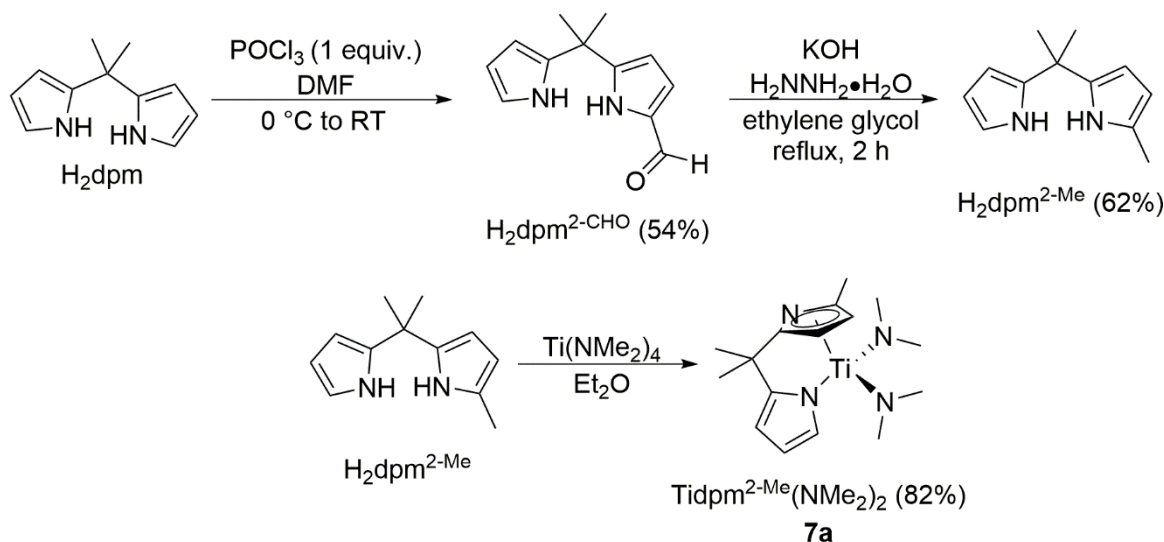
$$k_{\text{obs}} \times 10^4 = a + b(\text{LDP-1}) + c(\text{LDP-2}) + d(\%V_{\text{bur-1}}) + e(\%V_{\text{bur-2}})$$

**Figure 4.2.** Comparison of the original<sup>10</sup> and new model.

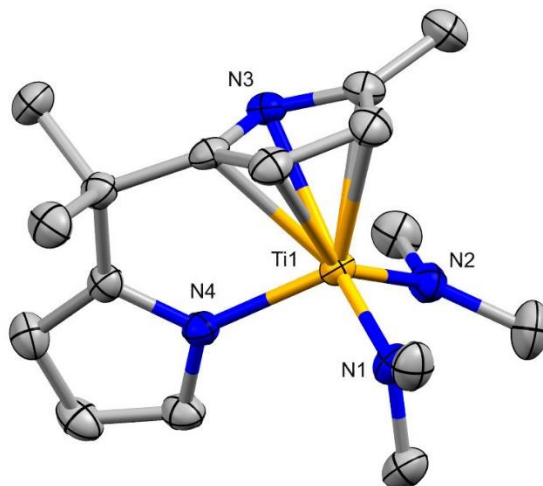
With this general idea in mind we sought to synthesize new unsymmetrical bidentate ligands to see what affects they had on the reaction rate. For these new ligands, we want high diversity, with a range of different sizes and donor abilities. Since we have already prepared a series of symmetrical ligands that could also be used in this new model, these symmetric ligands can act as a starting point for the new asymmetric ligands. By installing different groups onto one side of the symmetrical chelate, many unsymmetrical ligands can be synthesized from the previous ligand sets. Our dipyrrolylmethane ligands were the first ligands we sought to modify.

H<sub>2</sub>dpm can be mono formylated by the slow addition of Vilsmeier-Haack reagent to H<sub>2</sub>dpm. This produces the mono-aldehyde dipyrrolylmethane (H<sub>2</sub>dpm<sup>2-CHO</sup>) as the major product, in moderate yield.<sup>11</sup> H<sub>2</sub>dpm<sup>2-CHO</sup> can be reduced using Wolff-Kishner conditions to yield the mono-methyl dipyrrolylmethane (H<sub>2</sub>dpm<sup>2-Me</sup>). Addition of H<sub>2</sub>dpm<sup>2-Me</sup> to Ti(NMe<sub>2</sub>)<sub>4</sub> produces our first titanium pre-catalyst with an unsymmetrical ligand, Ti(dpm<sup>2-Me</sup>)(NMe<sub>2</sub>)<sub>2</sub> (**7a**) in good yield.

(Scheme 4.5)



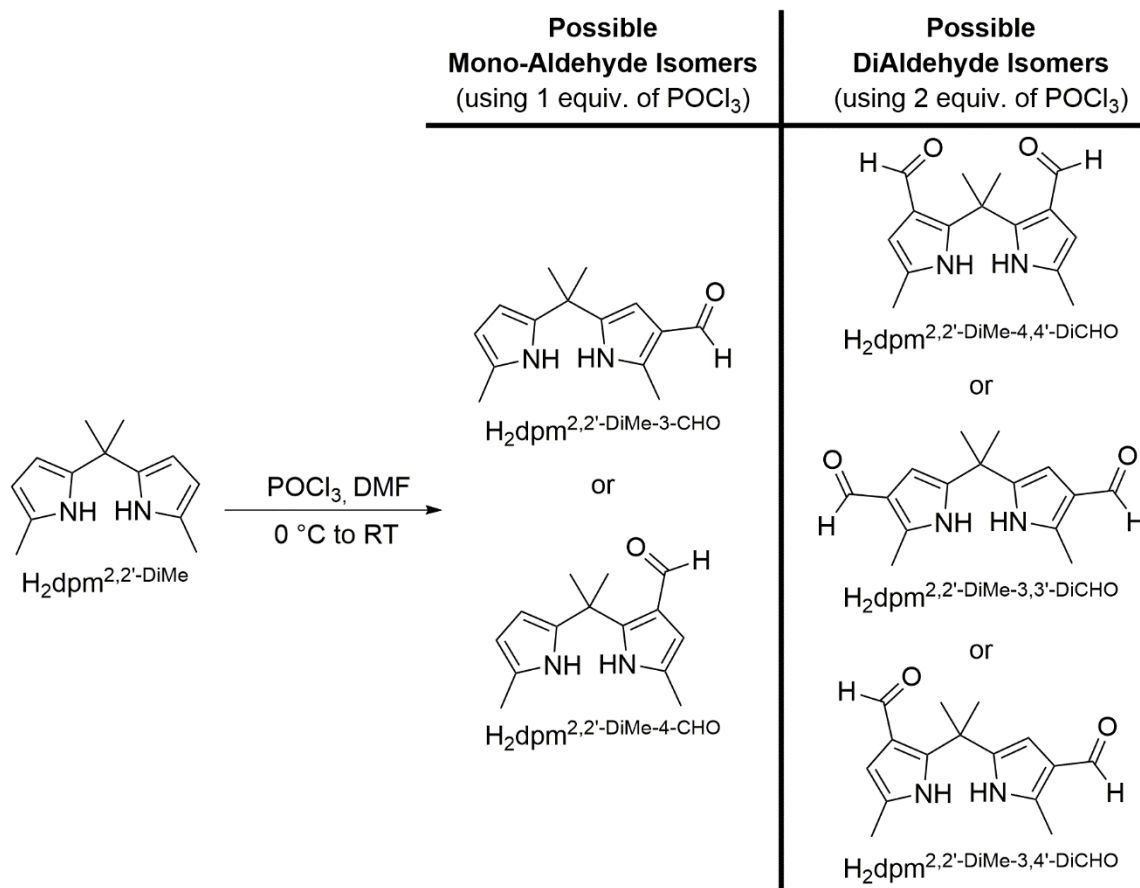
**Scheme 4.5.** Synthesis of H<sub>2</sub> dpm<sup>2-Me</sup> and Ti(dpm<sup>2-Me</sup>)(NMe<sub>2</sub>)<sub>2</sub> (**7a**).



**Figure 4.3.** Crystal Structure of  $\text{Ti}(\text{dpm}^{2\text{-Me}})(\text{NMe}_2)_2$  (**7a**).

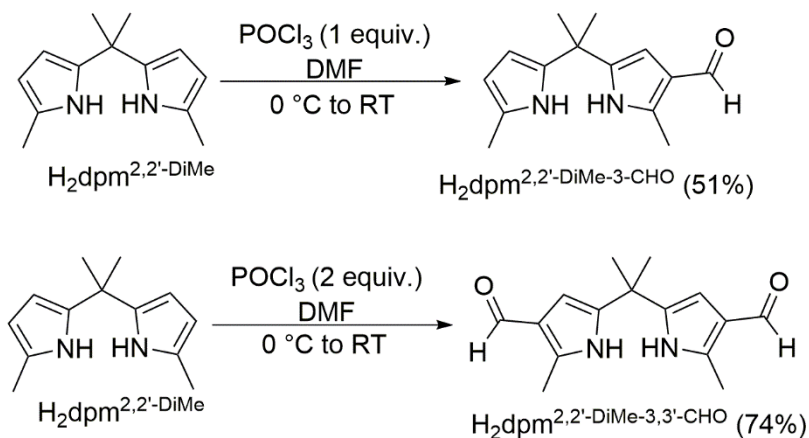
Having success with the installation of a single methyl group onto our dipyrrolylmethane moiety, we wondered if we could apply this single formylation procedure to other dipyrrolylmethane derivatives.

As mentioned in **Chapter 3**,  $\text{H}_2\text{dpm}$  can undergo a double formylation and successive reduction to make  $\text{H}_2\text{dpm}^{2,2'\text{-DiMe}}$  in high yield. Starting from  $\text{H}_2\text{dpm}^{2,2'\text{-DiMe}}$ , this ligand can also undergo a single formylation to make the  $\text{H}_2\text{dpm}^{2,2'\text{-DiMe-CHO}}$  as the major product, with a small amount of the di-aldehyde product being produced (with a ratio of 75:15:10 of mono, di, and leftover starting material). It should be mentioned that the di-aldehyde product ( $\text{H}_2\text{dpm}^{2,2'\text{-DiMe-CHO}}$ ) can be produced, selectively, by increasing the equivalents of Vilsmeier reagent used. While both of these reactions could produce different isomers, only one isomer is observed in each. Shown in **Scheme 4.6**, is the possible isomers of each.



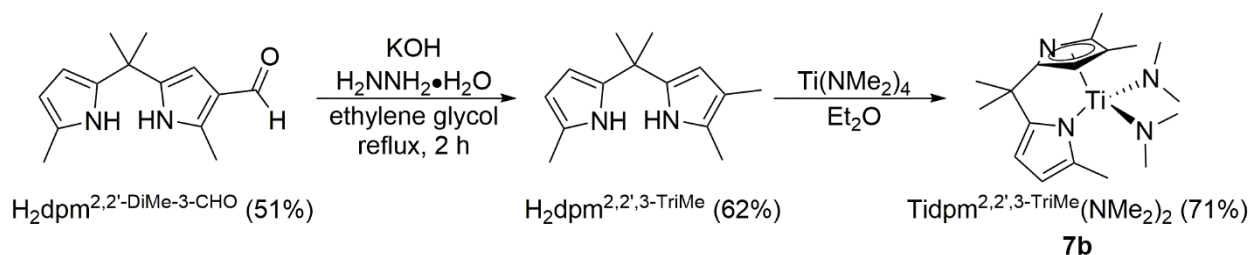
**Scheme 4.6.** Possible isomers for  $\text{H}_2\text{dpm}^{2,2'}\text{-DiMe-CHO}$  and  $\text{H}_2\text{dpm}^{2,2'}\text{-DiMe-DiCHO}$ .

To determine which isomer is being produced for each reaction, we turned to a series of NMR experiments. Ultimately, we were able to determine which isomers were being produced using 1D-NOESY (see **Section 4.7** for details). Shown in **Scheme 4.7**, is the synthesis of  $\text{H}_2\text{dpm}^{2,2'}\text{-DiMe-3-CHO}$  and  $\text{H}_2\text{dpm}^{2,2'}\text{-DiMe-3,3'-DiCHO}$  with their respected isomers.



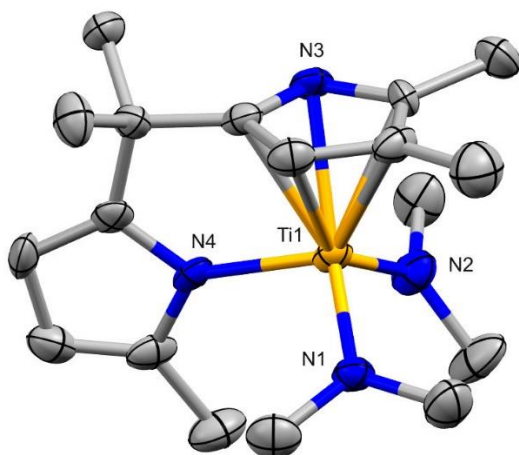
**Scheme 4.7.** Synthesis of  $\text{H}_2\text{dpm}^{2,2'\text{-DiMe-3-CHO}}$  and  $\text{H}_2\text{dpm}^{2,2'\text{-DiMe-3,3'-CHO}}$ .

After determining which isomer was being produced,  $\text{H}_2\text{dpm}^{2,2'\text{-DiMe-3-CHO}}$  underwent reduction, using Wolff-Kishner conditions, to make the 2,2',3-trimethyl-dipyrrolylmethane ( $\text{H}_2\text{dpm}^{2,2',3\text{-TriMe}}$ ). Addition of  $\text{H}_2\text{dpm}^{2,2',3\text{-TriMe}}$  to  $\text{Ti}(\text{NMe}_2)_4$  produces  $\text{Ti}(\text{dpm}^{2,2',3\text{-TriMe}})(\text{NMe}_2)_2$  in moderate yield.



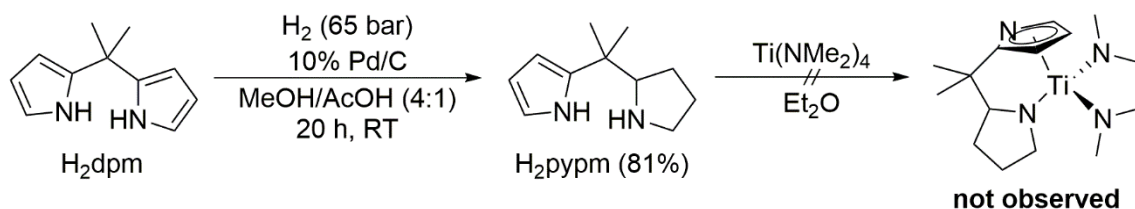
**Scheme 4.8.** Synthesis of  $\text{H}_2\text{dpm}^{2,2',3\text{-TriMe}}$  and  $\text{Ti}(\text{dpm}^{2,2',3\text{-TriMe}})(\text{NMe}_2)_2$  (**7b**).

After recrystallizing  $\text{Ti}(\text{dpm}^{2,2',3\text{-TriMe}})(\text{NMe}_2)_2$  (**7b**), the crystal structure also agrees with our assignment of  $\text{H}_2\text{dpm}^{2,2'\text{-DiMe-3-CHO}}$ . (**Figure 4.4**)



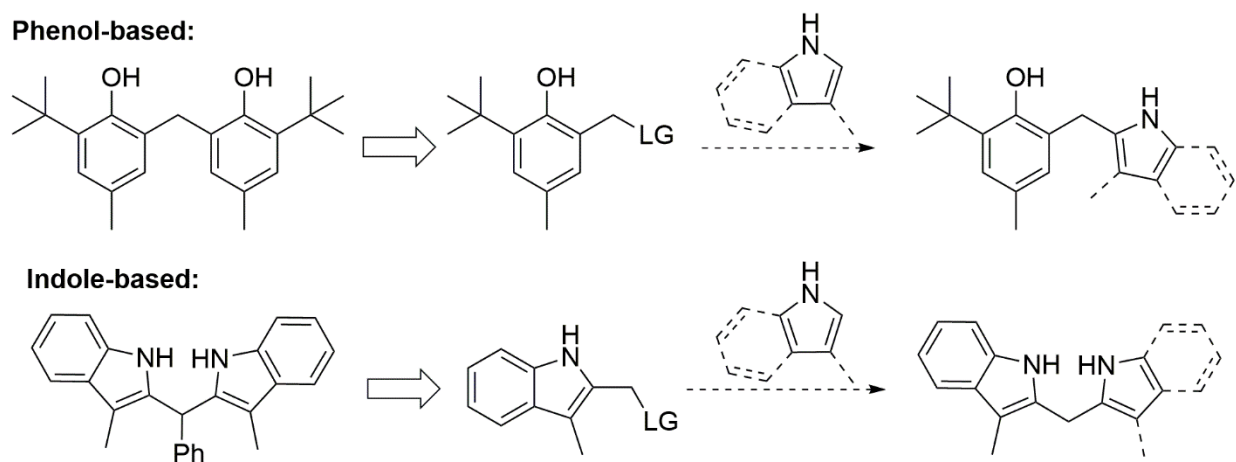
**Figure 4.4.** Crystal Structure of  $\text{Ti}(\text{dpm}^{\text{TriMe}})(\text{NMe}_2)_2$  (**7b**).

Seeking a more extreme electronic variant we wondered if we could synthesize the analogous pyrrole-pyrrolidinemethane (pypm) derivative. Pyrrole has an LDP of 13.64 kcal/mol, and, while we do not currently have an LDP for pyrrolidine, it should be similar to dimethylamine's LDP at 9.34 kcal/mol. This ligand would be a valuable addition to the model we want to build. It would be very interesting to observe how having such extreme differences in donating ability affects the rate of the reaction. Following a procedure by Neier and co-workers,<sup>12</sup>  $\text{H}_2\text{dpm}$  can be hydrogenated to give desired  $\text{H}_2\text{pypm}$  ligand in good yield. However, the addition of  $\text{H}_2\text{pypm}$  to  $\text{Ti}(\text{NMe}_2)_2$  resulted in decomposition (**Scheme 4.9**), possibly due to  $\beta$ -hydride elimination on the pyrrolidine ring.



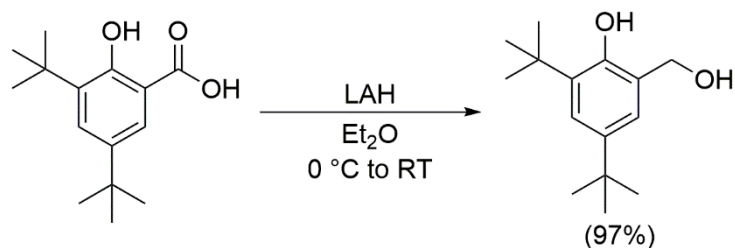
**Scheme 4.9.** The attempted synthesis of  $\text{Ti}(\text{pypm})(\text{NMe}_2)_2$ .

From here we decided to branch outward to further diversify our unsymmetrical ligands and started to develop ligands that were a combination of pyrrole-, indole- and phenol-based. To develop these different combinations of unsymmetrical ligands, if one side of the bidentate ligand remains the same while modifying the other side, we could observe what these changes had on the rate of the reaction. As shown in **Figure 4.5**, we can synthesize a common precursor to gain access to many different derivatives and monitor the steric and electronic changes one side at a time.



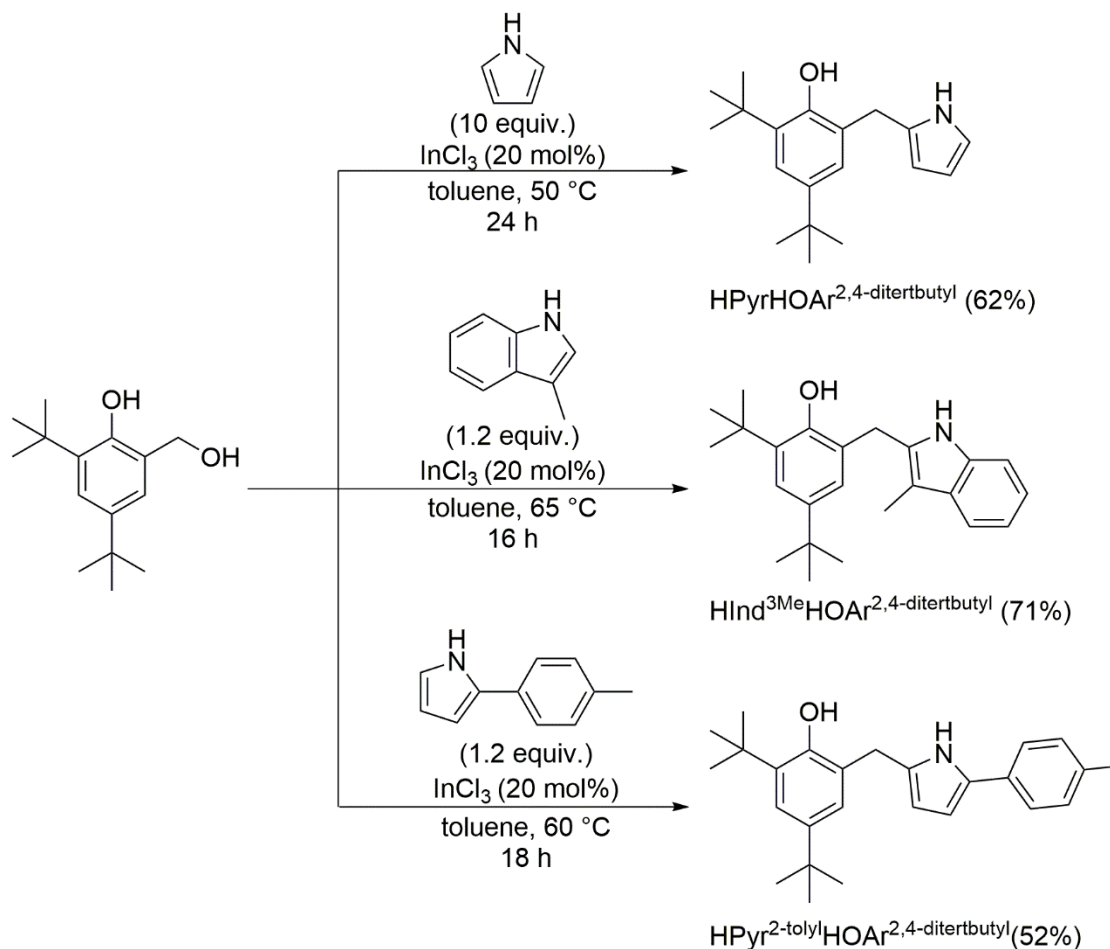
**Figure 4.5.** Strategy for unsymmetrical ligands.

For simplicity, it would be best to start with a phenol or indole derivative that was previously studied in our original model. A phenol precursor was synthesized by reduction of the benzoic acid derivative. (**Scheme 4.10**)



**Scheme 4.10.** Synthesis of the phenol precursor, 2,4-di-*tert*-butyl-6-(hydroxymethyl)phenol.

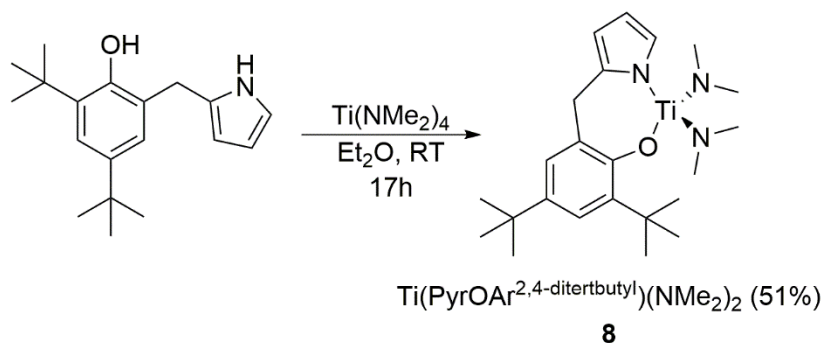
Starting from 2,4-di-*tert*-butyl-6-(hydroxymethyl)phenol, one can synthesize a variety of phenol-heterocyclic ligands. Treating the 2-hydroxylmethane precursor, in the presence of a Lewis acid, with different heterocycles gives access to phenol-heterocycle ligands. (**Scheme 4.11**)



**Scheme 4.11.** Synthesis of a variety of  $\text{HPyrHOAr}^{2,4\text{-diterbutyl}}$ ,  $\text{HInd}^{3\text{Me}}\text{HOAr}^{2,4\text{-diterbutyl}}$ ,  $\text{HPyr}^{2\text{-tolyl}}\text{HOAr}^{2,4\text{-diterbutyl}}$ .

Addition of  $\text{HPyrHOAr}^{2,4\text{-diterbutyl}}$  to  $\text{Ti}(\text{NMe}_2)_4$  produces  $\text{Ti}(\text{PyrOAr}^{2,4\text{-diterbutyl}})(\text{NMe}_2)_2$  in moderate yield. (**Scheme 4.12**)



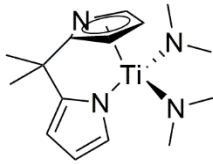
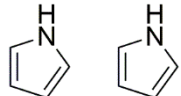
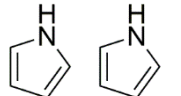
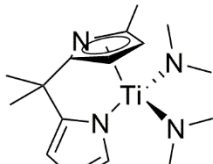
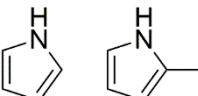
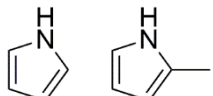
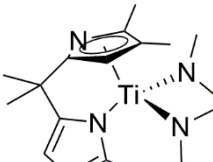
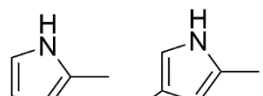
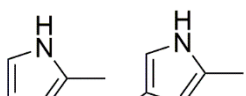
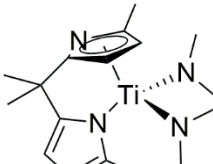
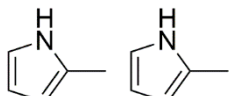
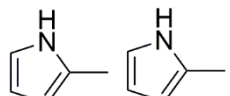
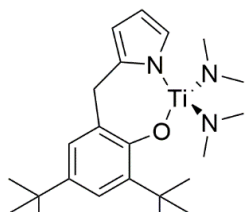
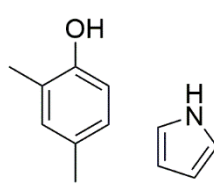
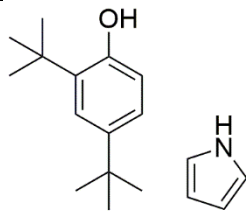
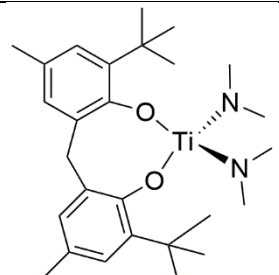
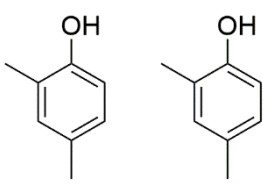
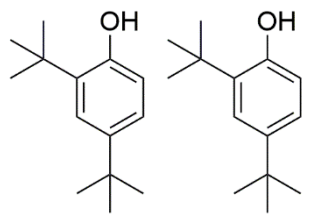


**Scheme 4.12.** Synthesis of  $\text{Ti}(\text{PyrOAr}^{2,4\text{-ditertbutyl}})(\text{NMe}_2)_2$  (**8**).

While this phenol-pyrrolyl derivative was successful, the phenol-indolyl was not. Attempting to bind  $\text{HInd}^{3\text{Me}}\text{HOAr}^{2,4\text{-ditertbutyl}}$  to titanium resulted in decomposition possibly due to abstraction of a benzylic hydrogen.

## 4.4 Results and Discussion

While more titanium catalysts with unsymmetrical ligands need to be developed before we can begin to model the rate of the reaction, we can still discuss the current trends and outlook of this project. Using the same kinetic conditions as in **Chapter 3**, we began to test our titanium pre-catalysts with unsymmetrical ligands. Shown in **Table 4.1**, is the current kinetic data from our titanium catalysts with unsymmetrical ligands compared to their symmetrical counterparts. With the installation of a single methyl group onto the dipyrrolylmethane moiety (moving from **1a** to **7a**) a significant decrease in the rate is observed. Based on our previous model, increasing the sterics and donor ability of the ligand should lead to a decrease in the rate. Addition of a methyl group should decrease the rate. From this perspective moving from the 2,2'-dimethyl- to the 2,2',3-trimethyl dipyrrolylmethane ligand (**1b** to **7b**), we would expect the trimethyl to have a lower rate. However,  $\text{Ti}(\text{dpm}^{2,2',3\text{-TriMe}})(\text{NMe}_2)_2$  (**7b**) was found to be faster than  $\text{Ti}(\text{dpm}^{2,2\text{-DiMe}})(\text{NMe}_2)_2$  (**1b**). This suggests that our system may benefit from an unsymmetrical bidentate. Furthermore, upon testing  $\text{Ti}(\text{PyrOAr}^{2,4\text{-ditertbutyl}})(\text{NMe}_2)_2$  (**8**), we again see a slight increase in the rate, when compared to its symmetrical counterpart,  $\text{Ti}(\text{bis-phenoxide}^{2\text{tBu-4-Me}})(\text{NMe}_2)_2$  (**3**).

Ti Catalyst	LDP (Average LDP)	%V <sub>bur</sub> (Average %V <sub>bur</sub> )	k <sub>obs</sub> x 10 <sup>4</sup> (s <sup>-1</sup> )
 Ti(dpm)(NMe <sub>2</sub> ) <sub>2</sub> ( <b>1a</b> )	 13.64    13.64 (13.64)	 20.4    20.4 (20.4)	4.16
 Ti(dpm <sup>2-Me</sup> )(NMe <sub>2</sub> ) <sub>2</sub> ( <b>7a</b> )	 13.64    13.46 (13.55)	 20.4    23.7 (22.05)	2.93
 Ti(dpm <sup>2,2',3-TriMe</sup> )(NMe <sub>2</sub> ) <sub>2</sub> ( <b>7b</b> )	 13.46    13.09 (13.28)	 23.7    23.1 (23.4)	1.79
 Ti(dpm <sup>2,2'-DiMe</sup> )(NMe <sub>2</sub> ) <sub>2</sub> ( <b>1b</b> )	 13.46    13.46 (13.46)	 23.7    23.7 (23.7)	1.35
 Ti(PyrOAr <sup>2,4-di-tertbutyl</sup> )(NMe <sub>2</sub> ) <sub>2</sub> ( <b>8</b> )	 11.98    13.64 (12.81)	 21.6    20.4 (21.0)	0.513
 Ti(bis-phenoxide <sup>2tBu-4-Me</sup> )(NMe <sub>2</sub> ) <sub>2</sub> ( <b>3</b> )	 11.98    11.98 (11.98)	 21.6    21.6 (21.6)	0.432

**Table 4.1.** Rates, LDP and %V<sub>bur</sub> for titanium catalysts with symmetrical<sup>10</sup> and unsymmetrical

ligands.<sup>13</sup>

With these preliminary results, there are a few trends that arise. In every case, for bulkier ligands we always observe a decrease in the rate. For example, when comparing the different dipyrrolylmethane catalysts (**1a**, **1b**, **7a**, and **7b**), as sterics increases the rate decreases. This trend is also observed when comparing **8** to **3**. This result is consistent with our previous model, in **Chapter 3**, which indicated that sterics have a negative effect on the rate (i.e. bulkier ligands decrease the rate). While it is easier to compare the ligands using their average LDP or %V<sub>bur</sub> values, the rate is *not* an average between the two. If we input the average LDP and %V<sub>bur</sub> values into our previous model, in **Chapter 3**, the predicted rates are not consistent with our experimental rates. (**Table 4.2**)

	<b>Predicted Rate Constant from Model x 10<sup>4</sup> (s<sup>-1</sup>)</b>	<b>Experimental Rate Constant x 10<sup>4</sup> (s<sup>-1</sup>)</b>
Ti(dpm <sup>2-Me</sup> )(NMe <sub>2</sub> ) <sub>2</sub> ( <b>7a</b> )	2.80	2.93
Ti(dpm <sup>2,2',3'-TriMe</sup> )(NMe <sub>2</sub> ) <sub>2</sub> ( <b>7b</b> )	1.49	1.79
Ti(PyrOAr <sup>2,4-ditertbutyl</sup> )(NMe <sub>2</sub> ) <sub>2</sub> ( <b>8</b> )	2.18	0.513

**Table 4.2.** Predicted rate, using previous model, versus experimental rate.

This observation is highlighted when looking at the predicted and experimental rate for Ti(PyrOAr<sup>2,4-ditertbutyl</sup>)(NMe<sub>2</sub>)<sub>2</sub> (**8**). If the rate was simply the average between the two ligands, the rate should be almost four times faster than was observed. Furthermore, in the case of our unsymmetrical dipyrrolylmethane catalysts, our experimental rate constant is always higher than what the predicted average is. Also, when comparing **7b** to **1b**, the overall smaller and more donating ligand is faster than the slightly larger but less donating ligand. Based off these preliminary results, *the system seems to favor one group of the unsymmetrical ligand being donating and small and the other being small and weakly donating*. This hypothesis leads into some very interesting questions such as: why are the unsymmetrical dipyrrolylmethane catalysts

faster, and why is  $\text{Ti}(\text{PyrOAr}^{2,4\text{-diterbutyl}})(\text{NMe}_2)_2$  (**8**) slower than predicted from the averages? To help analyze these questions we need to look at the rate determining step of the reaction. The rate determining step for the titanium catalyzed hydroamination of alkynes is the protonolysis of the  $\text{Ti-C}^{14}$  shown below in **Figure 4.6**.

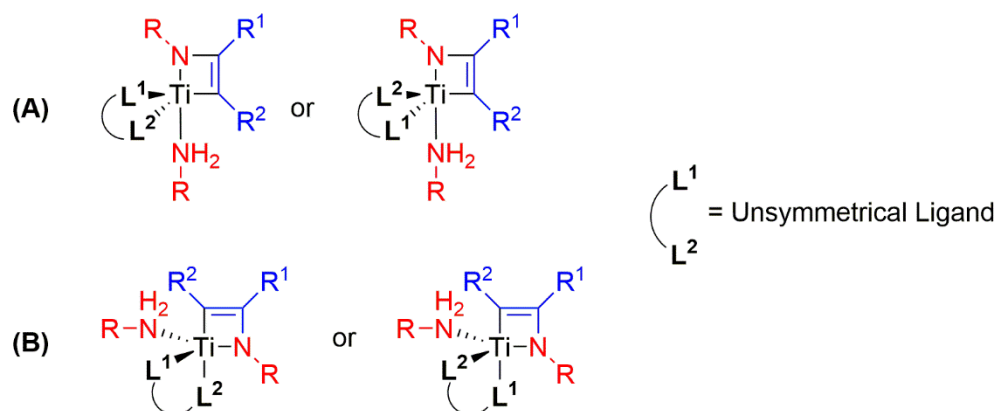


**Figure 4.6.** Proposed rate determining step of titanium-catalyzed hydroamination of alkynes.

While the titanium species is drawn as trigonal bipyramidal, there are other possible geometries this process could occur through. By analyzing the pros and cons of each of the possibilities, we may be able to suggest which geometry and ligand arrangement fits best with our observations based on the sterics and electronics of the ligands. For simplicity, we will only discuss two of the possible ligand arrangements in the geometry shown above.

Two possible ligand arrangements are shown in **Figure 4.7**. For the first possible arrangement, **A**, we wouldn't expect much of a difference for symmetrical or unsymmetrical ligands. In this arrangement, one might even expect this to be an average between the two groups on the unsymmetrical ligands. The ligands should have little influence on the metallacycle or the incoming amine. However, if the ligand rearranges to place a group trans to the carbon of the metallacycle, this could affect the rate of the reaction. For **B**, having a donating ligand trans to the carbon of the metallacycle should labilize the  $\text{Ti-C}$  bond speeding up the protonolysis and increasing the rate of the reaction. Using an unsymmetrical ligand with a stronger donating group and a weak donating group would have benefits over having a symmetrical ligand; one with either two strongly donating or weakly donating groups. Under this scenario, both unsymmetrical and

symmetrical ligands would benefit by being small and allowing more access to the metal by the incoming amine.



**Figure 4.7.** Possible geometries for titanium species.

As stated previously, there are several other possible geometries, each with their own different ligand arrangements. Once more unsymmetrical ligands have been developed this initial assessment can be revisited.

## 4.5 Future Ligand Development

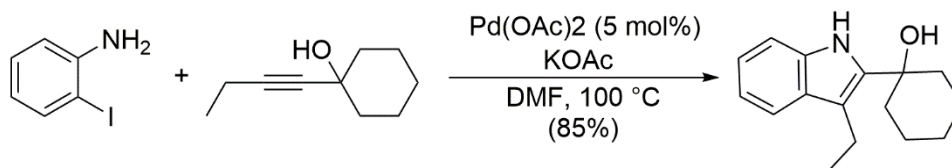
While the preliminary results in **Section 4.4** and **4.5** are very exciting, we must develop more unsymmetrical ligands to model this reaction. This section will address other synthetic routes into unsymmetrical ligands that avoid some of the potential downfalls discussed in **Section 4.3**. To build a robust model, many more unsymmetrical ligands need to be developed. Currently, only two kinds of unsymmetrical ligands have been assessed (i.e. pyrrolyl-pyrrolyl and phenol-pyrrolyl based ligands). Other unsymmetrical ligands, such as: pyrrolyl-indolyl, indolyl-indolyl and phenol-indolyl-based ligands, would be valuable entries into this model. The major drawback to several of the ligands investigated is the presence of benzylic hydrogens. The alternative syntheses discussed in this chapter are designed to avoid this problem.

As shown in **Section 4.3**, the Lewis acid-catalyzed condensation of 2-hydroxymethane derivatives with pyrrole (or indole) is an effective route into these unsymmetrical ligands. An elegant approach, that allows access to 2-(hydroxyalkyl)indole derivatives, is using Larock's indole synthesis.<sup>15</sup>



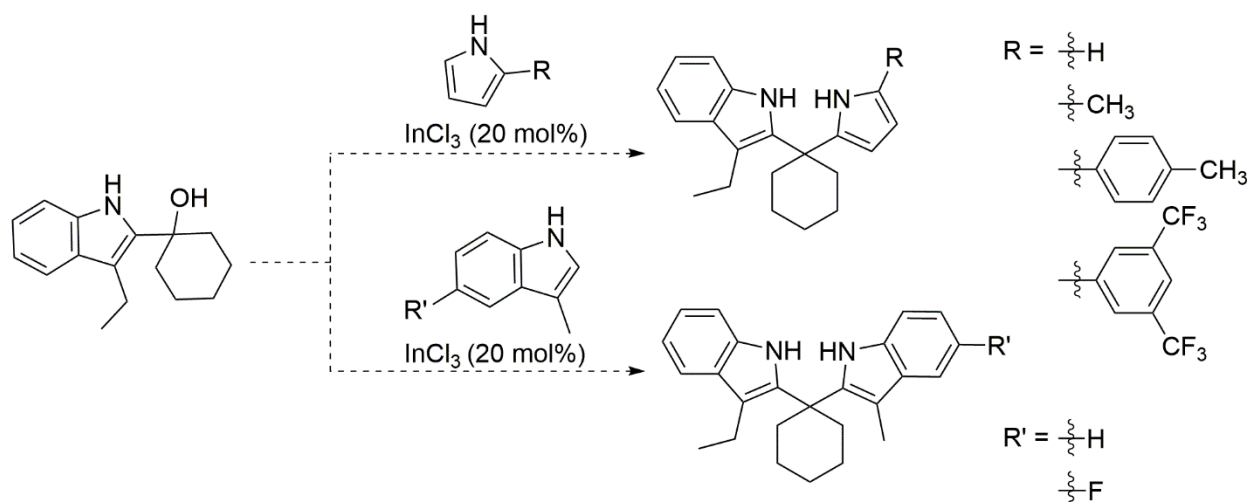
**Scheme 4.13.** Larock's indole synthesis.<sup>15</sup>

Larock's group was able to show that when a propargylic alcohol was used, they could selectively synthesize 2-(1-hydroxy-1-methyl)indole derivatives in high yield. (**Scheme 4.14**)



**Scheme 4.14.** Synthesis of 3-Ethyl-2-(1-hydroxycyclohexyl)indole.<sup>15</sup>

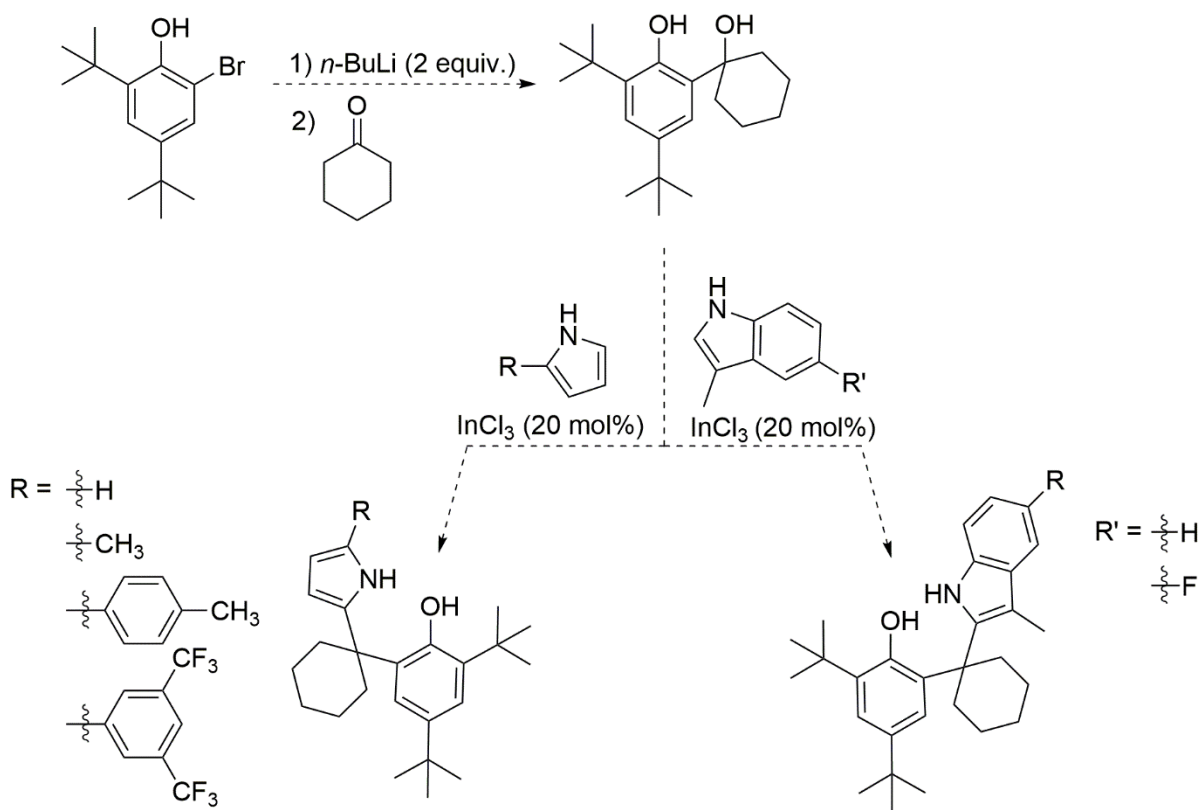
3-Ethyl-2-(1-hydroxycyclohexyl)indole, shown above, would be a valuable starting material for the synthesis of many different indolyl-based ligands. (**Scheme 4.15**)



**Scheme 4.15.** Proposed synthesis of unsymmetrical indolyl-based ligands.

To access 2-(hydroxyalkyl)phenol derivatives, we can envision starting from an *ortho*-halo phenol. Using an excess of an organolithium reagent, this phenol should undergo lithium-halogen exchange, which can then be quenched with a ketone derivative to provide the 2-(hydroxyalkyl)phenol derivative. Shown in **Scheme 4.16**, is the proposed synthesis of a new phenol precursor, 2,4-di-*tert*-butyl-6-(1-hydroxycyclohexyl)phenol, which could in-turn be used to synthesize several unsymmetrical phenol-based ligands.





**Scheme 4.16.** Proposed synthesis of a phenol precursor and unsymmetrical phenol-based ligands.

## **4.6 Conclusion**

As stated previously, the development of more diverse unsymmetrical ligands is needed before we can begin to model the reaction. However, the preliminary results suggest that our system may benefit from unsymmetrical ligands. As our group continues to explore these ligands it is exciting to think about all the new information that can potentially be gained through this methodology.

## 4.7 Experimental

### Synthetic Procedures

#### General Considerations

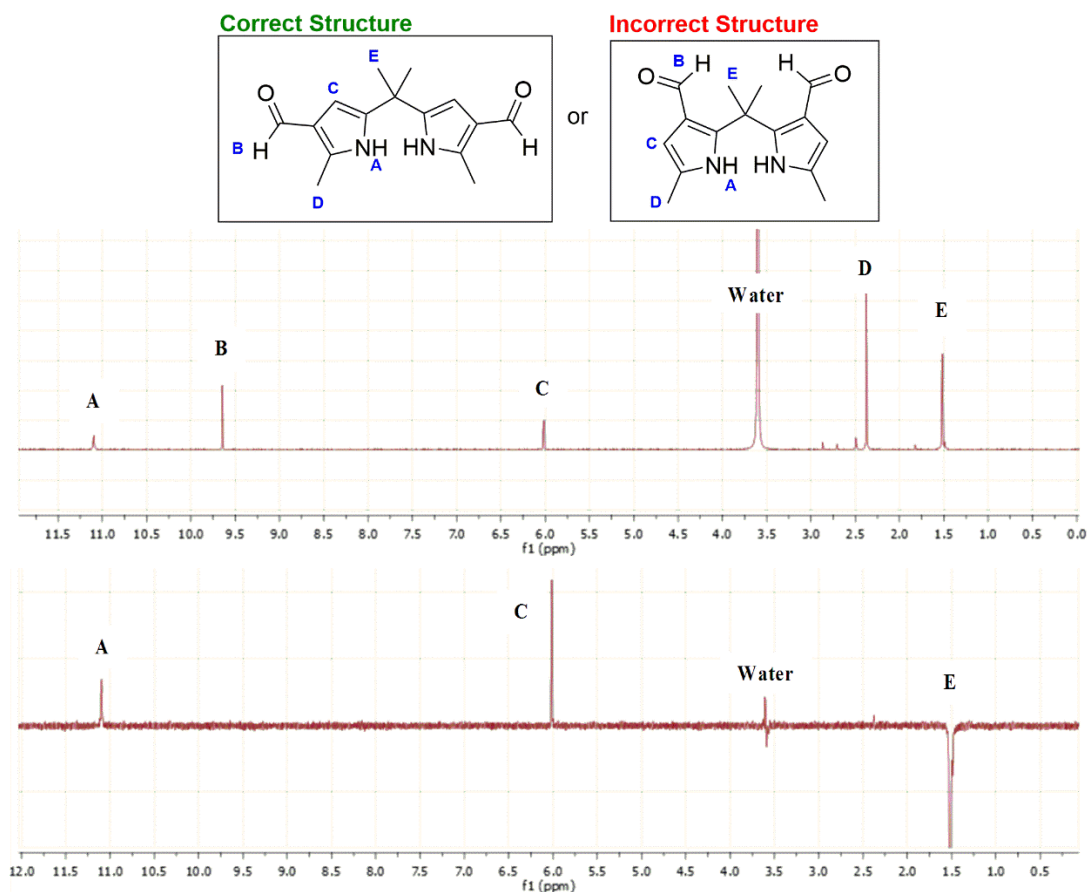
All reactions and manipulations were carried out in an MBraun glovebox under a nitrogen atmosphere and/or using standard Schlenk techniques. Diethyl ether, pentane, acetonitrile, tetrahydrofuran, benzene, *n*-hexane and toluene were purchased from Aldrich Chemical Company. Diethyl ether, pentane, acetonitrile and toluene were purified by passing through alumina columns to remove water after being sparged with dry nitrogen to remove oxygen. Tetrahydrofuran, benzene, and hexane were sparged with dinitrogen to remove oxygen and distilled from sodium and benzophenone. 5-formyl-2,2'-dimethylpyrromethane,  $\text{H}_2\text{dpm}^{2,2'\text{-DiMe}}$ ,  $\text{H}_2\text{pypm}$  were prepared with accordance to their literature procedures.<sup>11-12, 16</sup> To remove all water and oxygen, all ligands were dissolved in benzene, sparged with nitrogen, and refluxed in a Dean-Stark trap overnight. The benzene was then removed in vacuo, and the solids were taken into the nitrogen glove box.  $\text{Ti}(\text{NMe}_2)_4$  was purchased from Gelest and used as received. In many cases, due to the sensitivity of the reported complexes to air and moisture, elemental analysis could not be accurately performed. In these cases, bulk purity of the compound was determined by  $^1\text{H}$  NMR.

$\text{CDCl}_3$ ,  $\text{DMSO-d}_6$ ,  $\text{C}_6\text{D}_6$ , and toluene- $\text{d}_8$  were purchased from Cambridge Isotopes Laboratories, Inc. Toluene- $\text{d}_8$  and  $\text{C}_6\text{D}_6$  were sparged with dry dinitrogen and dried over 3 Å molecular sieves.  $\text{CDCl}_3$  was sparged with dinitrogen and distilled from  $\text{P}_2\text{O}_5$  prior to use. All NMR solvents were stored under an inert atmosphere. Spectra were taken on Varian instruments located in the Max T. Rogers Instrumentation Facility at Michigan State University. These include an Agilent DDR2 500 spectrometer equipped with a 5 mm pulsed-field-gradient (PFG) OneProbe and operating at 499.955 MHz ( $^1\text{H}$ ) and 125.77 MHz ( $^{13}\text{C}$ ), a Varian Inova 600 spectrometer

equipped with a 5 mm PFG switchable broadband probe operating at 599.89 MHz ( $^1\text{H}$ ) and 564.30 MHz ( $^{19}\text{F}$ ), a UNITY plus 500 spectrometer equipped with a 5 mm Pulsed-Field-Gradient (PFG) switchable broadband probe and operating at 499.955 MHz ( $^1\text{H}$ ) and 125.77 ( $^{13}\text{C}$ ). NMR chemical shifts are reported in ppm and referenced to the solvent peaks for  $^1\text{H}$  NMR ( $\text{CDCl}_3$ ,  $\delta$  7.26 ppm;  $\text{C}_6\text{D}_6$ ,  $\delta$  7.16 ppm; toluene- $\text{d}_8$ ,  $\delta$  2.08, 6.97, 7.01, 7.09 ppm, DMSO- $\text{d}_6$ ,  $\delta$  2.50 and 3.33 ppm) and  $^{13}\text{C}$  NMR ( $\text{CDCl}_3$ ,  $\delta$  77.16 ppm;  $\text{C}_6\text{D}_6$ ,  $\delta$  128.06 ppm; toluene- $\text{d}_8$ ,  $\delta$  20.43, 125.13, 127.96, 128.87, 137.48 ppm, DMSO- $\text{d}_6$ ,  $\delta$  39.5). When reporting the NMR data, the following abbreviations are used: singlet = s, doublet = d, triplet = t, quartet = q, doublet of doublets = dd, etc. For apparent peaks the abbreviations is app, followed by the multiplicity. For example, for an apparent triplet is abbreviation is app t, or an apparent quartet is app q. Single crystal X-ray diffraction data was collected in the Center for Crystallographic Research at MSU.

### Determination of H<sub>2</sub>dpm<sup>2,2'</sup>-DiMe-3,3'-DiCHO

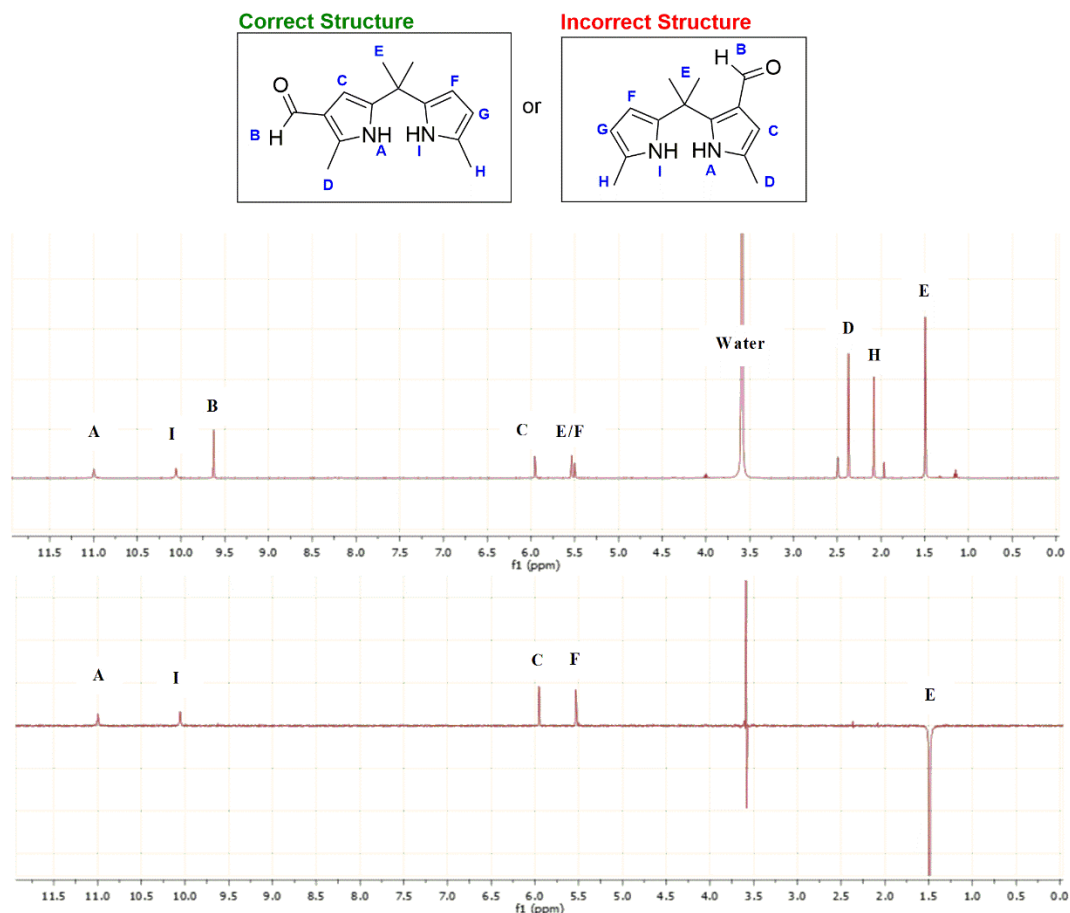
As mentioned in **Section 4.3**, there are three possible isomers, but only two of the three would be expected to exhibit five <sup>1</sup>H-NMR signals. These two isomers are shown below in **Figure 4.8**. One distinct difference between the two is the location of the aldehyde relative to the dimethylmethane linker. Therefore, if we saturated the signal for the methyl groups on the linker, labeled **E**, we can deduce which isomer is correct. For the structure on the right, if **E** is saturated, signals for the protons **A** (N–H) and **B** (–CHO) should be observed. For the structure on the left, if **E** is saturated, signals for the protons **C** (–CH) and **B** (–CHO) should be observed. As shown at the bottom of **Figure 4.8**, when **E** is saturated the signals for **C** (–CH) and **B** (–CHO) are observed. This suggests that the left structure is the correct isomer.



**Figure 4.8.** <sup>1</sup>H-NMR (top) and 1D-NOESY (bottom) spectra of H<sub>2</sub>dpm<sup>2,2'</sup>-DiMe-3,3'-DiCHO.

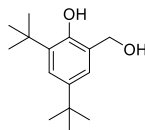
### Determination of H<sub>2</sub>dpm<sup>2,2'</sup>-DiMe-3-CHO

As mentioned in **Section 4.3**, there are two possible isomers. These two isomers are shown below in **Figure 4.9**. Similar two H<sub>2</sub>dpm<sup>2,2'</sup>-DiMe-3,3'-DiCHO, the difference between the two is the location of the aldehyde relative to the dimethylmethane linker. Therefore, if we saturated the signal for the methyl groups on the linker, labeled **E**, we can deduce which isomer is correct. For the structure on the right, if **E** is saturated, signals for the protons **A/I** (N–H), **F** (–CH), and **B** (–CHO) should be observed. For the structure on the left, if **E** is saturated, signals for the protons **C/F** (–CH) and **A/I** (N–H) should be observed. As shown at the bottom of **Figure 4.9**, when **E** is saturated the signals for **C/F** (–CH) and **A/I** (N–H) are observed, and **B** (–CHO) is absent. This suggests that the left structure is the correct isomer.



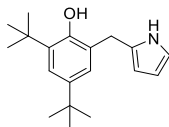
**Figure 4.9.** <sup>1</sup>H-NMR (top) and 1D-NOESY (bottom) spectra of H<sub>2</sub>dpm<sup>2,2'</sup>-DiMe-3-DiCHO.

## Synthesis of Titanium Complexes and Ligands



2,4-di-*tert*-butyl-6-(hydroxymethyl)phenol:

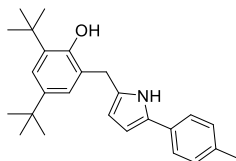
This procedure was adapted from a similar reduction by Stoltz and coworkers.<sup>17</sup> 3,5-di-*tert*-butyl-2-hydroxybenzoic acid (6.0 g, 23.97 mmol) was dissolved in diethyl ether (50 mL) and added dropwise to a solution of LiAlH<sub>4</sub> (2.00 g, 52.7 mmol) in diethyl ether (300 mL) at 0 °C. This mixture was allowed to warm up to room temperature and stirred for 6 h. The mixture was quenched with water (3.3 mL) and 15% NaOH (3.3 mL), followed by another addition of water (15 mL). This mixture was let stir for 30 min and an off-white precipitate formed. This precipitate was filtered and diluted in water. This mixture was then acidified with 1M HCl and extracted with ethyl acetate (3 x 50 mL). The extracted organic fractions and filtrate were dried with Na<sub>2</sub>SO<sub>4</sub>, filtered and concentrated in vacuo to give the product as a white-pinkish powder. (5.5 g, 97% yield). <sup>1</sup>H NMR (C<sub>6</sub>D<sub>6</sub>, 500 MHz): δ = 7.91 (s, 1H, PhO-H), 7.44 (d, *J* = 2.4 Hz, 1H, Ar-H), 6.66 (d, *J* = 2.4 Hz, 1H, Ar-H), 4.16-4.18 (d, *J* = 5.5 Hz, 2H, -CH<sub>2</sub>-), 1.62 (s, 9H, C(CH<sub>3</sub>)<sub>3</sub>), 1.29 (s, 9H, C(CH<sub>3</sub>)<sub>3</sub>). \*Note: No alkyl O-H resonance was observed. <sup>13</sup>C NMR (C<sub>6</sub>D<sub>6</sub>, 500 MHz): δ = 153.57, 141.05, 136.27, 124.07, 123.37, 122.41, 65.59, 34.94, 33.96, 31.50, 29.64. HRMS [M-H]<sup>-</sup>: Found: *m/z* 235.1702; Calcd for C<sub>15</sub>H<sub>23</sub>O<sub>2</sub> 235.1698. MS (EI): *m/z* 236 (M<sup>+</sup>). M.p.: 98-99 °C.



2-((1H-pyrrol-2-yl)methyl)-4,6-di-*tert*-butylphenol (HPyrHOAr<sup>2,4-ditertbutyl</sup>):

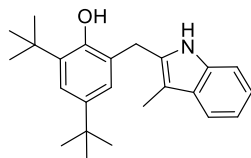
A 35 mL pressure tube, equipped with a stir bar, was loaded with pyrrole (1.34 g, 1.39 mL, 20 mmol), InCl<sub>3</sub> (0.088 g, 0.4 mmol), and lastly 2,4-di-*tert*-butyl-6-(hydroxymethyl)phenol (0.473 g, 2.0 mmol). The reaction was then heated at 50 °C for 24 h. After this time, the excess pyrrole was removed in vacuo. The crude product was purified by column chromatography using hexanes:ethyl acetate (85:15) as eluent to give the product as a tan solid (0.354 g, 62% yield). <sup>1</sup>H NMR (C<sub>6</sub>D<sub>6</sub>, 500 MHz): δ = 7.44 (d, *J* = 2.4 Hz, 1H, Ar-H), 6.94-6.95 (d, *J* = 2.3 Hz, 1H, Ar-H), 6.77 (s, 1H, N-H), 6.12-6.13 (dd, *J* = 3.9, 2.5 Hz, 1H, Pyrr-H), 6.07-6.09 (m, 1H, Pyrr-H), 5.98 (s, 1H, Pyrr-H), 5.38 (s, 1H, PhO-H), 3.55 (s, 2H, -CH<sub>2</sub>-), 1.51 (s, 9H, C(CH<sub>3</sub>)<sub>3</sub>), 1.32 (s, 9H, C(CH<sub>3</sub>)<sub>3</sub>). <sup>13</sup>C NMR (C<sub>6</sub>D<sub>6</sub>, 125 MHz): δ = 152.05, 141.95, 136.46, 125.05, 124.51, 122.78, 118.51, 108.39, 106.93, 34.87, 34.05, 31.56, 30.95, 29.70. \*Note: The resonance for the pyrrole quaternary carbon was not observed. HRMS [M+H]<sup>+</sup>: Found: *m/z* 286.2168; Calcd for C<sub>19</sub>H<sub>28</sub>N<sub>2</sub>O 286.2171. MS (EI): *m/z* 285 (M<sup>+</sup>). M.p.: 74-75 °C.





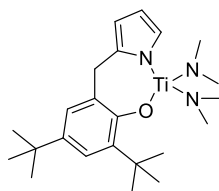
2-((1H-pyrrol-2-yl)methyl)-4,6-di-*tert*-butylphenol (HPyr<sup>2-tolyl</sup>HOAr<sup>2,4-ditertbutyl</sup>):

A 35 mL pressure tube equipped with a stir bar was loaded 2-tolylpyrrole (0.503 g, 3.20 mmol, 2.0 equiv.), InCl<sub>3</sub> (0.106 g, 0.480 mmol), 2,4-di-*tert*-butyl-6-(hydroxymethyl)phenol (0.378 g, 1.60 mmol) and toluene (6 mL). The reaction was heated at 60 °C for 18 h. The reaction was filtered, and the residue was rinsed with ethyl acetate. The solvent was removed in vacuo to yield the crude product as a dark purple solid. The crude product was purified by column chromatography using hexanes:ethyl acetate:TEA (95:5:3) as the eluent. The pure product is obtained as a light-pink/white solid (0.314 g, 52.3% yield). <sup>1</sup>H NMR (C<sub>6</sub>D<sub>6</sub>, 500 MHz): δ = 7.69 (s, 1H, N-H), 7.44-7.45 (d, *J* = 2.4 Hz, 1H, Ar-H), 7.07 (d, *J* = 2.4 Hz, 1H, Ar-H), 6.93-6.94 (d, *J* = 8.1 Hz, 2H, Ar-H), 6.85 (d, *J* = 7.9 Hz, 2H, Ar-H), 6.37 (app t, *J* = 3.0 Hz, 1H, Pyrr-H), 6.05 (dd, *J* = 2.7, 3.2 Hz, 1H, Pyrr-H), 5.38 (s, 1H, -OH), 3.66 (s, 2H, -CH<sub>2</sub>-), 2.07 (s, 3H, -CH<sub>3</sub>), 1.50 (s, 9H, C(CH<sub>3</sub>)<sub>3</sub>), 1.30 (s, 9H, C(CH<sub>3</sub>)<sub>3</sub>). <sup>13</sup>C NMR (C<sub>6</sub>D<sub>6</sub>, 125 MHz): δ = 151.74, 142.36, 136.52, 135.17, 133.04, 130.02, 129.29, 129.06, 125.11, 124.64, 123.59, 122.87, 108.83, 105.88, 34.85, 34.08, 31.52, 31.03, 29.72, 20.71. HRMS [M+H]<sup>+</sup>: Found: *m/z* 376.2634; Calcd for C<sub>26</sub>H<sub>34</sub>NO 376.2640. MS (EI): *m/z* 375 (M<sup>+</sup>). M.p.: 87-89 °C.



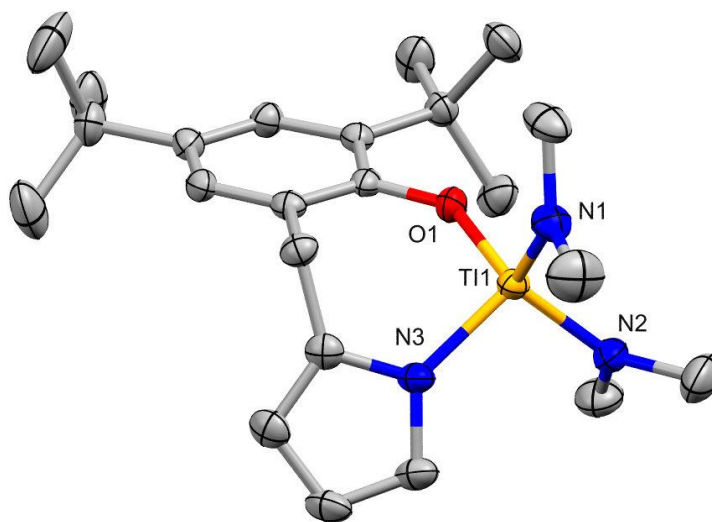
2,4-di-*tert*-butyl-6-((3-methyl-1H-indol-2-yl)methyl)phenol (HInd<sup>3Me</sup>HOAr<sup>2,4-ditertbutyl</sup>):

A 35 mL pressure tube equipped with a stir bar, was loaded with 3-methylindole (0.630 g, 4.80 mmol, 1.2 equiv.), InCl<sub>3</sub> (0.177 g, 0.800 mmol), 2,4-di-*tert*-butyl-6-(hydroxymethyl)phenol (0.945 g, 4.0 mmol) and toluene (8 mL). The reaction was heated at 65 °C for 16 h. The reaction was then filtered and the residue was rinsed with ethyl acetate. The solvent was removed in vacuo to yield the crude product as a dark purple solid. The crude product is purified by column chromatography using hexanes:ethyl acetate (9:1) as the eluent. The pure product is obtained as a light-yellow solid (0.991 g, 70.9% yield). <sup>1</sup>H NMR (C<sub>6</sub>D<sub>6</sub>, 500 MHz): δ = 7.47-7.49 (m, 1H, Ind-H), 7.44-7.45 (d, *J* = 2.4 Hz, 1H, Ar-H), 7.11-7.14 (m, 2H, Ind-H), 7.01 (d, *J* = 2.5 Hz, 1H, Ar-H), 6.88 (s, 1H, Ind-NH), 6.69-6.71 (m, 1H, Ind-H), 5.10 (s, 1H, PhOH), 3.65 (s, 2H, -CH<sub>2</sub>-), 2.13 (s, 3H, -CH<sub>3</sub>), 1.45 (s, 9H, C(CH<sub>3</sub>)<sub>3</sub>), 1.32 (s, 9H, C(CH<sub>3</sub>)<sub>3</sub>). <sup>13</sup>C NMR (C<sub>6</sub>D<sub>6</sub>, 125 MHz): δ = 151.65, 142.43, 136.39, 135.97, 130.39, 129.10, 125.21, 124.16, 122.95, 121.92, 119.44, 118.58, 110.60, 108.21, 34.79, 34.08, 31.53, 29.69, 28.68, 8.06. HRMS [M+H]<sup>+</sup>: Found: *m/z* 350.2479; Calcd for C<sub>24</sub>H<sub>32</sub>NO 350.2484. MS (EI): *m/z* 349 (M<sup>+</sup>). M.p.: 131-132 °C.

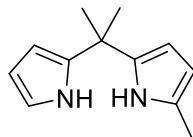


$Ti(PyrOAr^{2,4\text{-ditertbutyl}})(NMe_2)_2$  (**8**):

A 20 mL scintillation vial equipped with a micro stir bar was loaded  $Ti(NMe_2)_4$  (0.254 g, 1.33 mmol, 1 equiv.) and 4 mL of ether. A separate 20 mL scintillation vial was loaded with  $HPyrHOAr^{2,4\text{-ditertbutyl}}$  (0.323g, 1.33 mmol, 1 equiv.) and 4 mL of ether. Both solutions were then cooled in a liquid nitrogen cold well for 15 min. The solution of  $HPyrHOAr^{2,4\text{-ditertbutyl}}$  was added dropwise to the vigorously stirred solution of  $Ti(NMe_2)_4$ . The reaction mixture was stirred at room temperature for 7 h. Volatiles were removed in vacuo to give a yellow-orange solid. The solid was washed with cold pentane and the residual solvent was removed *in vacuo* to yield the product as a bright yellow solid (0.241 g, 51% yield).  $^1H$  NMR ( $C_6D_6$ , 500 MHz):  $\delta$  = 7.41 (d,  $J$  = 2.5 Hz, 1H, Ar-H), 7.30 (d,  $J$  = 2.5 Hz, 1H, Ar-H), 6.90 (dd,  $J$  = 2.5, 1.3 Hz, 1H, Pyrr-H), 6.40-6.41 (app t,  $J$  = 2.7 Hz, 1H, Pyrr-H), 6.24 (m, 1H, Pyrr-H), 3.90 (s, 2H,  $-CH_2-$ ), 2.93 (s, 12H, 2  $NMe_2$ ), 1.51 (s, 9H,  $C(CH_3)_3$ ), 1.30 (s, 9H,  $C(CH_3)_3$ ).  $^{13}C$  NMR ( $C_6D_6$ , 125 MHz):  $\delta$  = 159.97, 143.63, 135.07, 134.69, 131.09, 125.53, 124.99, 121.47, 109.06, 105.76, 44.28, 34.97, 34.45, 34.23, 31.51, 30.16. M.p.: 158-159 °C.

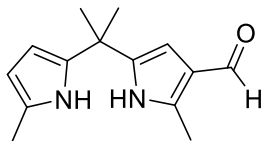


**Figure 4.10.** Crystal Structure of  $\text{Ti}(\text{PyrOAr}^{2,4\text{-di}i\text{tertbutyl}})(\text{NMe}_2)_2$  (**8**).



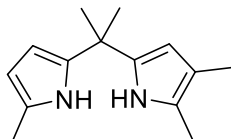
*H<sub>2</sub>dpm*<sup>2Me</sup>

To a dry 100 mL Schlenk flask was added 5-formyl-2,2'-dimethylpyrrolylmethane<sup>11</sup> (0.50 g, 2.47 mmol), KOH (0.99 g, 25.3 mmol), ethylene glycol (13 mL) and hydrazine hydrate (1.067 g, 21.31 mmol). The reaction mixture was degassed with nitrogen and let stir at 70 °C for 30 min. At this time, the reaction was heated at reflux (200 °C) for 2 h. The reaction mixture was then allowed to cool to room temperature and diluted with water (50 mL) and DCM (50 mL). The aqueous layer was extracted with DCM (3 x 50 mL). The organic layers were combined, dried with Na<sub>2</sub>SO<sub>4</sub>, and filtered. The crude product was purified using column chromatography on silica gel, using hexanes/ethyl acetate as the eluent (9:1) to yield the product as a light brown solid. (0.28 g, 60.2% yield). <sup>1</sup>H NMR (C<sub>6</sub>D<sub>6</sub>, 500 MHz): δ = 6.97 (s, 1H, Pyrr-NH), 6.83 (s, 1H, Pyrr-NH), 6.20-6.23 (m, 2H, Pyrr-H), 6.10-6.11 (m, 1H, Pyrr-H), 6.00-6.01 (app t, *J* = 2.8 Hz, 1H, Pyrr-H), 5.88-5.89 (m, 1H, Pyrr-H), 1.72 (s, 3H, -CH<sub>3</sub>), 1.44 (s, 6H, C(CH<sub>3</sub>)<sub>2</sub>). <sup>13</sup>C NMR (C<sub>6</sub>D<sub>6</sub>, 125 MHz): δ = 138.81, 137.10, 126.21, 116.66, 107.71, 105.52, 104.23, 103.65, 35.13, 29.37, 12.51. HRMS [M+H]<sup>+</sup>: Found: *m/z* 189.1401; Calcd for C<sub>12</sub>H<sub>17</sub>N<sub>2</sub> 189.1392. MS (EI): *m/z* 188 (M<sup>+</sup>). M.p.: 97-98 °C.



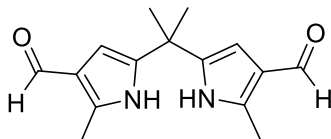
H<sub>2</sub>dpm<sup>2,2'-DiMe</sup>-3-CHO

In a dry 50 mL Schlenk flask, under nitrogen, the Vilsmeier reagent was prepared from DMF (9.0 mL, 117 mmol) and POCl<sub>3</sub> (0.97 mL, 10.4 mmol) added dropwise at 0 °C. The Vilsmeier reagent was allowed to warm up to room temperature and stir for 15 min. While under nitrogen, this reagent was then added dropwise to a solution of DMF (5 mL) and H<sub>2</sub>dpm<sup>2,2'-DiMe</sup> (2.31 g, 11.42 mmol) over 20 min, at 0 °C. The reaction mixture was allowed to stir for 3 h at 0 °C. To this reaction mixture was added aqueous KOH solution (2 M, 60 mL) and DCM (100 mL). This solution was allowed to stir for 20 min. The organic layer was then separated, washed with saturated aqueous NH<sub>4</sub>Cl, washed with water, and then dried over Na<sub>2</sub>SO<sub>4</sub>. The solvents (DCM and DMF) were removed in vacuo to give the crude product as a viscous orange oil. The crude product was purified by column chromatography on silica gel using hexanes/ethyl acetate (9:1) as the eluent to yield the product as a light orange-red solid (1.34 g, 51% yield). <sup>1</sup>H NMR (DMSO-d<sub>6</sub>, 500 MHz): δ = 11.00 (s, 1H, Pyrr-NH), 10.06 (s, 1H, Pyrr-NH), 9.63 (s, 1H, -CHO), 5.95-5.96 (d, *J* = 2.6 Hz, 1H, Pyrr-H), 5.53-5.54 (t, *J* = 2.9 Hz, 1H, Pyrr-H), 5.50 (m, 1 H, Pyrr-H) 2.37 (s, 3H, -CH<sub>3</sub>), 2.08 (s, 3H, -CH<sub>3</sub>), 1.49 (s, 6H, C(CH<sub>3</sub>)<sub>2</sub>). <sup>13</sup>C NMR (DMSO-d<sub>6</sub>, 125 MHz): δ = 184.60, 140.92, 138.76, 137.18, 126.37, 121.10, 104.63, 103.60, 102.58, 35.07, 28.70, 13.30, 11.33. HRMS [M+H]<sup>+</sup>: Found: *m/z* 231.1498; Calcd for C<sub>14</sub>H<sub>19</sub>N<sub>2</sub> 231.1497. MS (EI): *m/z* 230 (M<sup>+</sup>). M.p.: 174-175 °C.



H<sub>2</sub>dpm<sup>2,2',3-TriMe</sup>

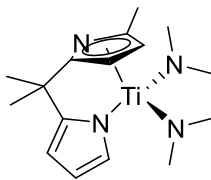
To a dry 100 mL Schlenk flask was added 5,5'-dimethyl-4-formyl-2,2'-dimethylpyrrolylmethane (1.49 g, 6.49 mmol), KOH (3.71 g, 66.3 mmol), ethylene glycol (13 mL) and hydrazine hydrate (2.75 mL, 55.9 mmol). The reaction mixture was degassed with nitrogen and let stir at 70 °C for 30 min. At this time, the reaction was heated at reflux (200 °C) for 2 h. The reaction mixture was then allowed to cool to room temperature and diluted with water (50 mL) and DCM (50 mL). The aqueous layer was extracted with DCM (3 x 50 mL). The organic layers were combined, dried with Na<sub>2</sub>SO<sub>4</sub>, and filtered. The crude product was purified using column chromatography on silica gel using hexanes/ethyl acetate as the eluent (9:1) to yield the product as a light brown solid. (0.87 g, 62% yield). <sup>1</sup>H NMR (C<sub>6</sub>D<sub>6</sub>, 500 MHz): δ = 7.02 (s, 1H, Pyr-NH), 6.82 (s, 1H, Pyr-NH), 6.06-6.07 (appt, *J* = 2.9 Hz, 1H, Pyrr-H), 5.90-5.92 (m, 2H, Pyrr-H), 2.06 (s, 3H, -CH<sub>3</sub>), 1.73 (s, 3H, -CH<sub>3</sub>) 1.67 (s, 3H, -CH<sub>3</sub>), 1.51 (s, 6H, C(CH<sub>3</sub>)<sub>2</sub>). <sup>13</sup>C NMR (C<sub>6</sub>D<sub>6</sub>, 125 MHz): δ = 137.63, 136.09, 126.03, 121.95, 113.01, 105.90, 105.64, 103.91, 35.08, 29.47, 12.50, 10.96, 10.33. HRMS [M+H]<sup>+</sup>: Found: *m/z* 215.1548; Calcd for C<sub>14</sub>H<sub>19</sub>N<sub>2</sub> 215.1548. MS (EI): *m/z* 214 (M<sup>+</sup>). M.p.: 76-77 °C.



$\text{H}_2\text{dpm}^{2,2'\text{-DiMe-3,3'-DiCHO}}$

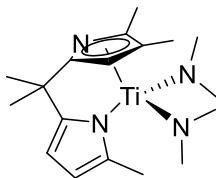
In a dry 50 mL Schlenk flask under nitrogen, the Vilsmeier reagent was prepared from DMF (22.0 mL, 281 mmol) and the dropwise addition of  $\text{POCl}_3$  (4.67 mL, 49.9 mmol) at 0 °C. The Vilsmeier reagent was allowed to warm up to room temperature and stir for 20 min. While under nitrogen, this reagent was then added dropwise to a solution of DMF (20 mL) and  $\text{H}_2\text{dpm}^{2,2'\text{-DiMe}}$  (5.05 g, 25 mmol) over 20 min at 0 °C. The reaction mixture was let stir for 2 h at 0 °C. Water (30 mL) was carefully added, followed by aqueous KOH solution (2 M, 125 mL), and the mixture was allowed to stir for 20 min. Once the reaction becomes strongly basic, the product precipitates out of solution. The precipitated product was collected by suction filtration and washed with water (3 x 30 mL). The product was let air dry on the frit to yield the product as a light brown powder (4.72 g, 74% yield).  $^1\text{H}$  NMR ( $\text{DMSO-d}_6$ , 500 MHz):  $\delta$  = 11.07 (s, 2H, Pyr-NH), 9.68 (s, 2H, -CHO), 6.02 (s, 2H, Pyr-H), 2.37 (s, 6H, 2 x -CH<sub>3</sub>) 1.53 (s, 6H, C(CH<sub>3</sub>)<sub>2</sub>).  $^{13}\text{C}$  NMR ( $\text{DMSO-d}_6$ , 125 MHz):  $\delta$  = 184.68, 139.56, 139.11, 121.22, 102.98, 34.95, 28.10, 11.33. HRMS  $[\text{M}+\text{H}]^+$ : Found:  $m/z$  259.1450; Calcd for  $\text{C}_{15}\text{H}_{19}\text{N}_2$  259.1447. MS (EI):  $m/z$  258 ( $\text{M}^+$ ). M.p.: 242 °C (dec.).





*Ti(dpm<sup>2Me</sup>)(NMe<sub>2</sub>)<sub>2</sub> (7a):*

A 35 mL pressure tube equipped with a micro stir bar was loaded with Ti(NMe<sub>2</sub>)<sub>4</sub> (0.575, 2.57 mmol, 1 equiv.) and 3 mL of toluene. A 20 mL scintillation vial was loaded with H<sub>2</sub>dpm<sup>2Me</sup> (0.483 g, 2.57mmol, 1 equiv.) and 3 mL of toluene. Both solutions were cooled in a liquid nitrogen cold well for 15 min. The cold solution of H<sub>2</sub>dpm<sup>2Me</sup> was added dropwise to the vigorously stirring solution of Ti(NMe<sub>2</sub>)<sub>4</sub>. The reaction was allowed to warm and then was stirred at room temperature for 1 h. The pressure tube was then sealed and heated at 65 °C. The reaction progress was monitored by <sup>1</sup>H NMR and was completed after 24 h. Volatiles were removed in vacuo to give a light red solid. This solid was rinsed with cold pentane to yield the product as an orange powder (0.67 g, 82% yield). X-ray quality crystals can be grown by dissolving the complex in the minimum amount of pentane and cooling to -30 °C. <sup>1</sup>H NMR (C<sub>6</sub>D<sub>6</sub>, 500 MHz): δ = 6.98-6.99 (dd, *J* = 2.5, 1.3 Hz, 1H, Pyrr-H) 6.49-6.50 (m, 1H, Pyrr-H), 6.31-6.30 (d, *J* = 2.5 Hz, 1H, Pyrr-H), 6.16-6.17 (dd, *J* = 3.0, 1.2 Hz, 1H, Pyrr-H), 5.97-5.98 (d, *J* = 2.5 Hz, 1H, Pyrr-H), 2.93 (s, 12H, 2 -N(CH<sub>3</sub>)<sub>2</sub>), 1.99 (s, 3H, -CH<sub>3</sub>) 1.78 (s, 6H, C(CH<sub>3</sub>)<sub>2</sub>). <sup>13</sup>C NMR (C<sub>6</sub>D<sub>6</sub>, 125 MHz): δ = 161.87, 161.65, 140.23, 123.57, 114.74, 113.64, 107.61, 101.52, 46.88, 39.51, 29.66, 14.99. Elemental Analysis: Calcd. C, 59.63; H, 8.13; N, 17.38. Found: C, 59.55; H, 8.48; N, 17.89. M.p.: 127-128 °C.



$Ti(dpm^{2,2',3-TriMe})(NMe_2)_2$  (**7b**):

A 35 mL pressure tube equipped with a micro stir bar was loaded with  $Ti(NMe_2)_4$  (0.228 g, 1.02 mmol, 1 equiv.) and 3 mL of toluene. A 20 mL scintillation vial was loaded with  $H_2dpm^{2,2',3-TriMe}$  (0.220 g, 1.02 mmol, 1 equiv.) and 3 mL of toluene. Both solutions were then cooled in a liquid nitrogen cold well for 15 min. The cold solution of  $H_2dpm^{2,2',3-TriMe}$  was added dropwise to the vigorously stirred solution of  $Ti(NMe_2)_4$ . The reaction was allowed to warm, and stirred at room temperature for 1 h. The pressure tube was then sealed and heated at 65 °C. The reaction progress was monitored by  $^1H$  NMR and was complete after 36 h. Volatiles were removed *in vacuo* to give a light red solid. This solid was rinsed with cold pentane to yield the product as a red-orange powder (0.252 g, 71% yield). X-ray quality crystals can be grown by dissolving the complex in the minimum amount of pentane and cooling to -30 °C.  $^1H$  NMR ( $C_6D_6$ , 500 MHz):  $\delta$  = 6.13 (d,  $J$  = 2.8 Hz, 1H, Pyrr-H) 5.99-6.00 (m, 2H, Pyrr-H), 2.85 (s, 12H, 2 x  $-N(CH_3)_2$ ), 2.29 (s, 3H,  $-CH_3$ ), 2.14 (s, 3H,  $-CH_3$ ), 1.83 (s, 6H,  $C(CH_3)_2$ ), 1.80 (s, 3H,  $-CH_3$ ).  $^{13}C$  NMR ( $C_6D_6$ , 125 MHz):  $\delta$  = 161.72, 160.44, 134.95, 112.06, 109.99, 109.67, 107.90, 105.36, 46.37, 39.21, 29.95, 15.85, 13.29, 11.25. Note: Despite multiple attempts, adequate elemental analysis was not obtained. M.p.: 108-109 °C.

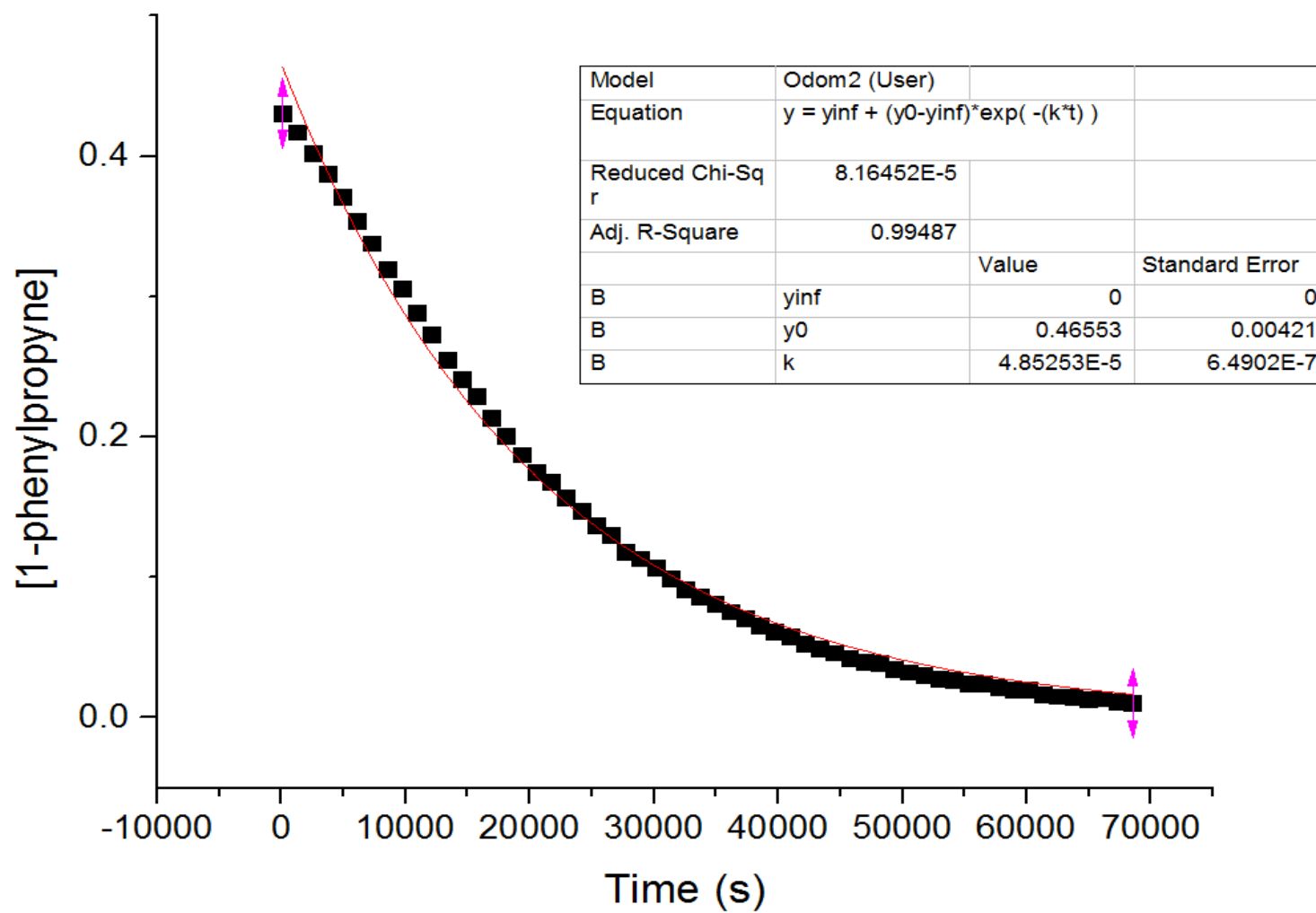
## General Procedure for Kinetics

All manipulations were done in an inert atmosphere drybox. A 2 mL volumetric flask was loaded the catalyst (10 mol%, 0.1 mmol) and ferrocene (0.0560 g, 0.3 mmol) as an internal standard. Next, 0.75 mL of toluene-d<sub>8</sub> was added to the volumetric flask, and the solution was mixed by swirling the flask until all solids were dissolved. Once all solids were dissolved, aniline (911 µL, 10 mmol) and 1-phenylpropyne (125 µL, 1.0 mmol) were added to the volumetric flask. Lastly, the solution was diluted to 2 mL with toluene-d<sub>8</sub>. The solution was mixed via pipette (i.e. the solution was drawn up into the pipette and dispensed back into the volumetric flask) five times to ensure the solution was well-mixed. An ample amount of solution (~0.75 mL) was loaded into a threaded J. Young tube that was sealed with a Teflon stopper. The tube was removed from the dry box and was heated at 75 °C in the NMR spectrometer (Varian Inova 600 spectrometer). The relative 1-phenylpropyne versus ferrocene concentration was monitored as a function of time. The fits are to the exponential decay of the starting material using the scientific graphing program Origin. The exact expression used to fit the data is shown below:<sup>18</sup>

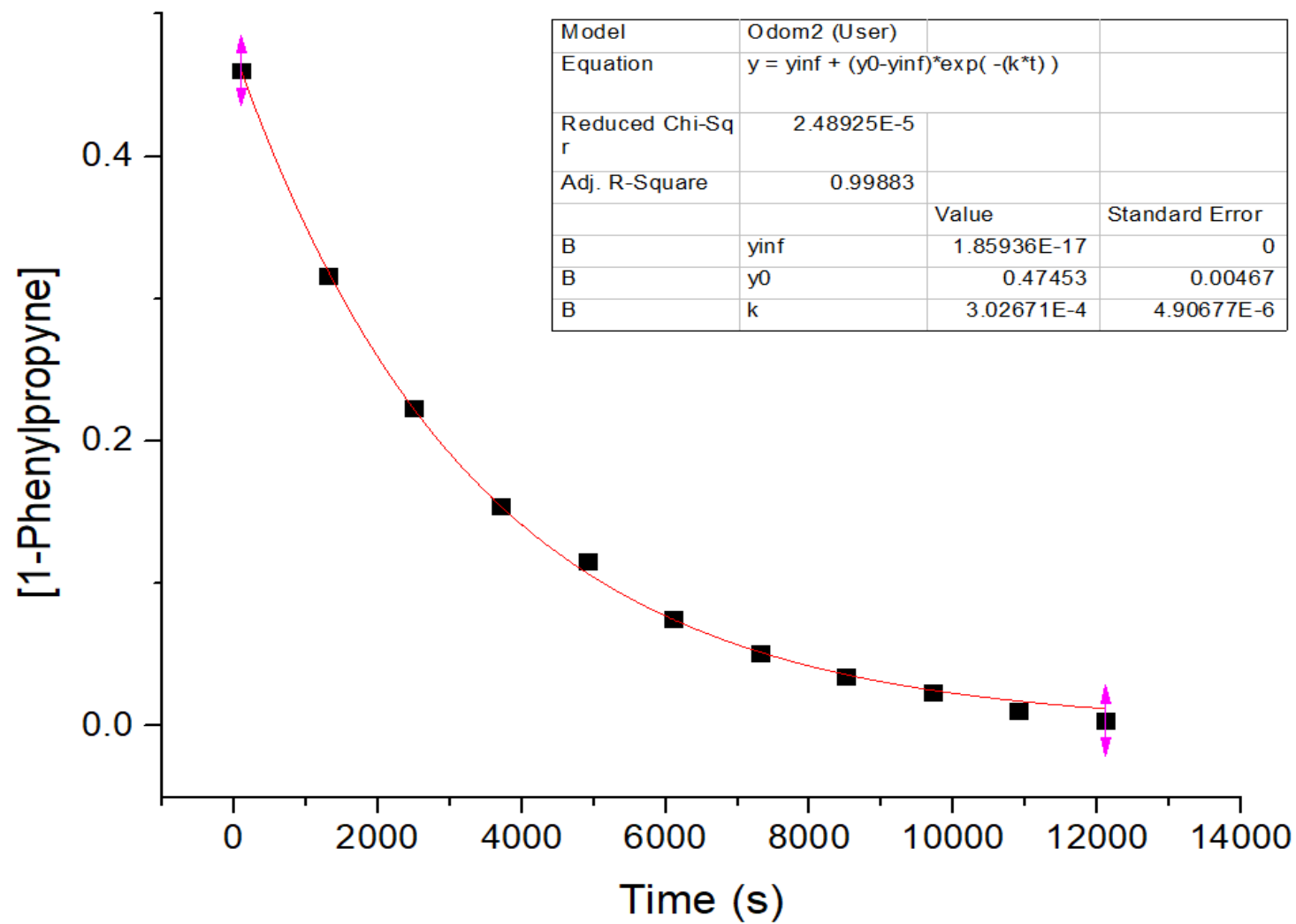
$$Y_t = Y_\infty + (Y_0 - Y_\infty)\exp^{-k_{obs}t}$$

Where Y = [1-phenylpropyne] at time t (Y<sub>t</sub>), infinity (Y<sub>∞</sub>), or at the start of the reaction (Y<sub>0</sub>). The variables Y<sub>∞</sub>, Y<sub>0</sub>, k<sub>obs</sub>, were optimized in the fits. Each kinetic experiment was completed in triplicate.

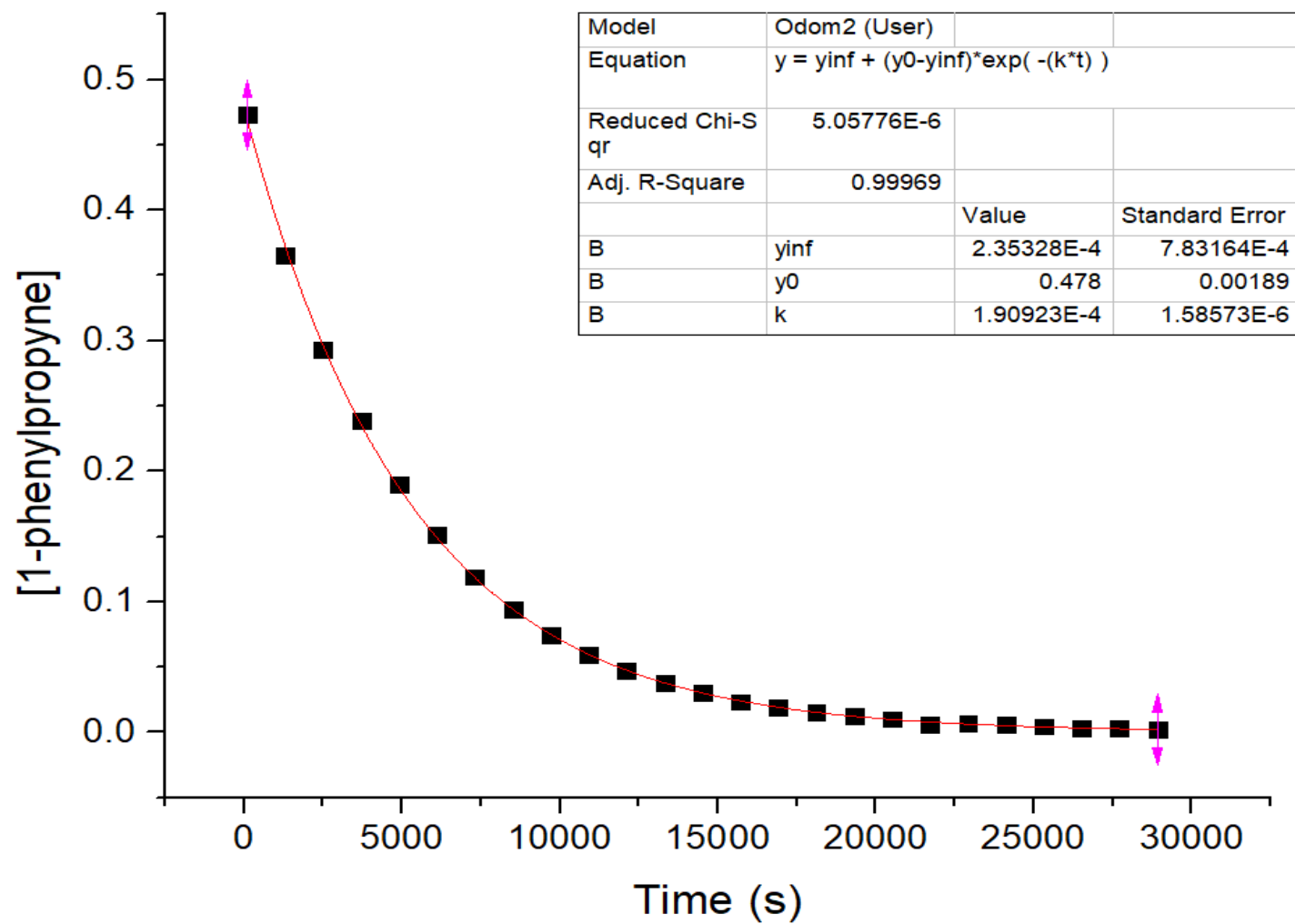
## Representative Plots for Kinetics



**Figure 4.11.** Plot of [1-phenylpropyne] vs time with  $\text{Ti}(\text{PyrOAr}^{2,4\text{-di}t\text{ertbutyl}})(\text{NMe}_2)_2$  (**8**).

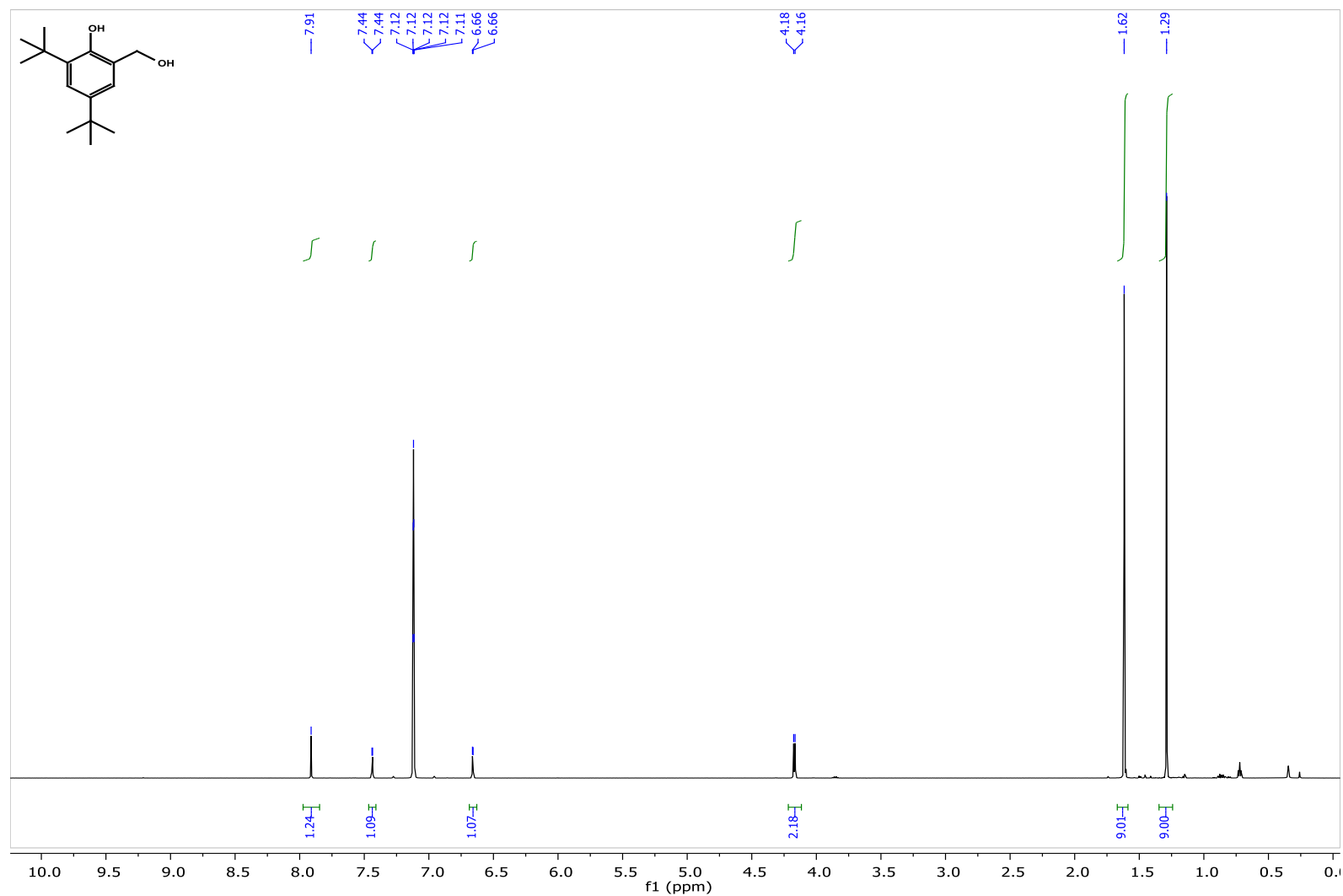


**Figure 4.12.** Plot of [1-phenylpropyne] vs time with  $\text{Ti}(\text{dpm}^{2\text{Me}})(\text{NMe}_2)_2$  (**7a**).

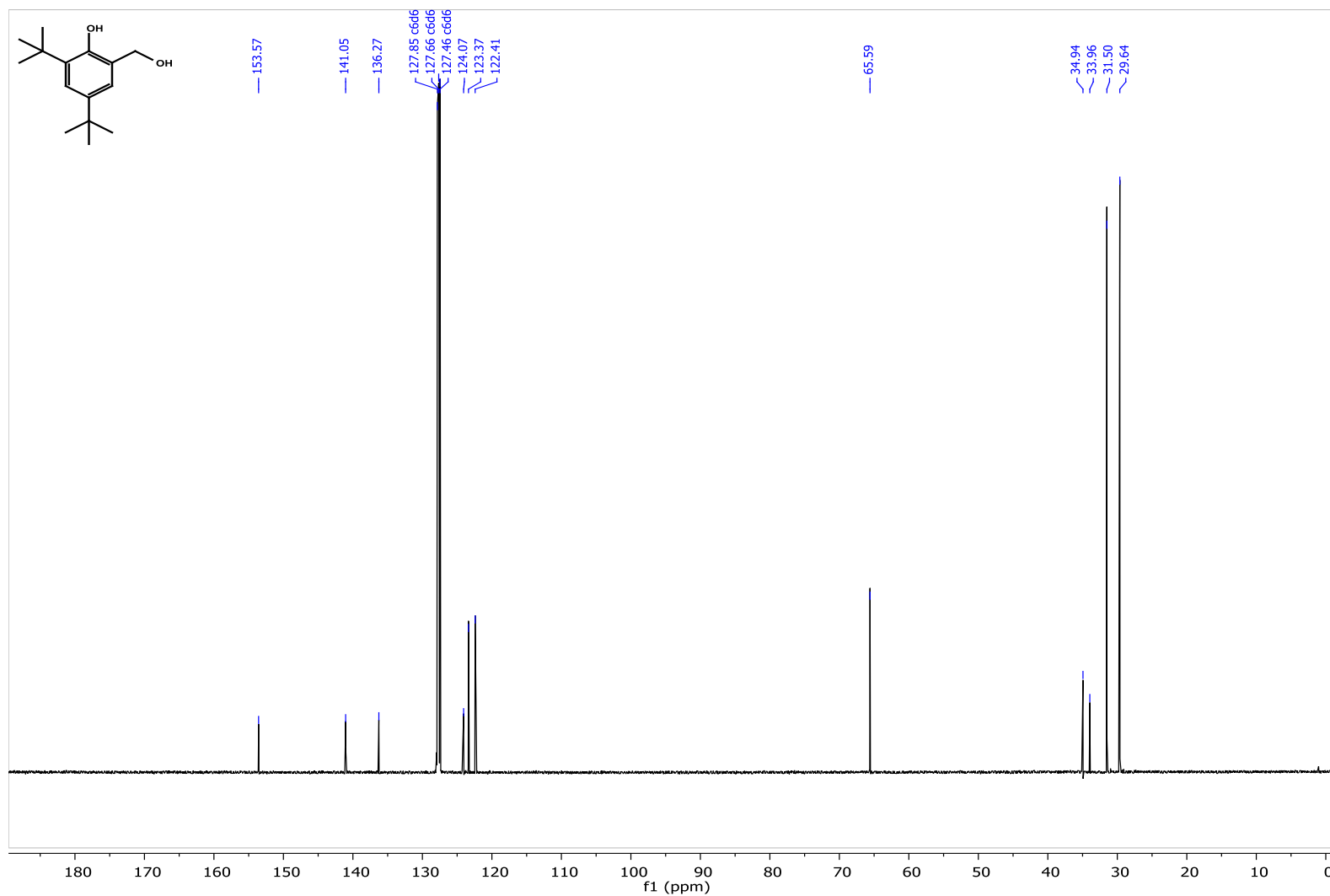


**Figure 4.13.** Plot of [1-phenylpropyne] vs time with  $\text{Ti}(\text{dpm}^{2,2',3\text{-TriMe}})(\text{NMe}_2)_2$  (**7b**).

## NMR Spectra

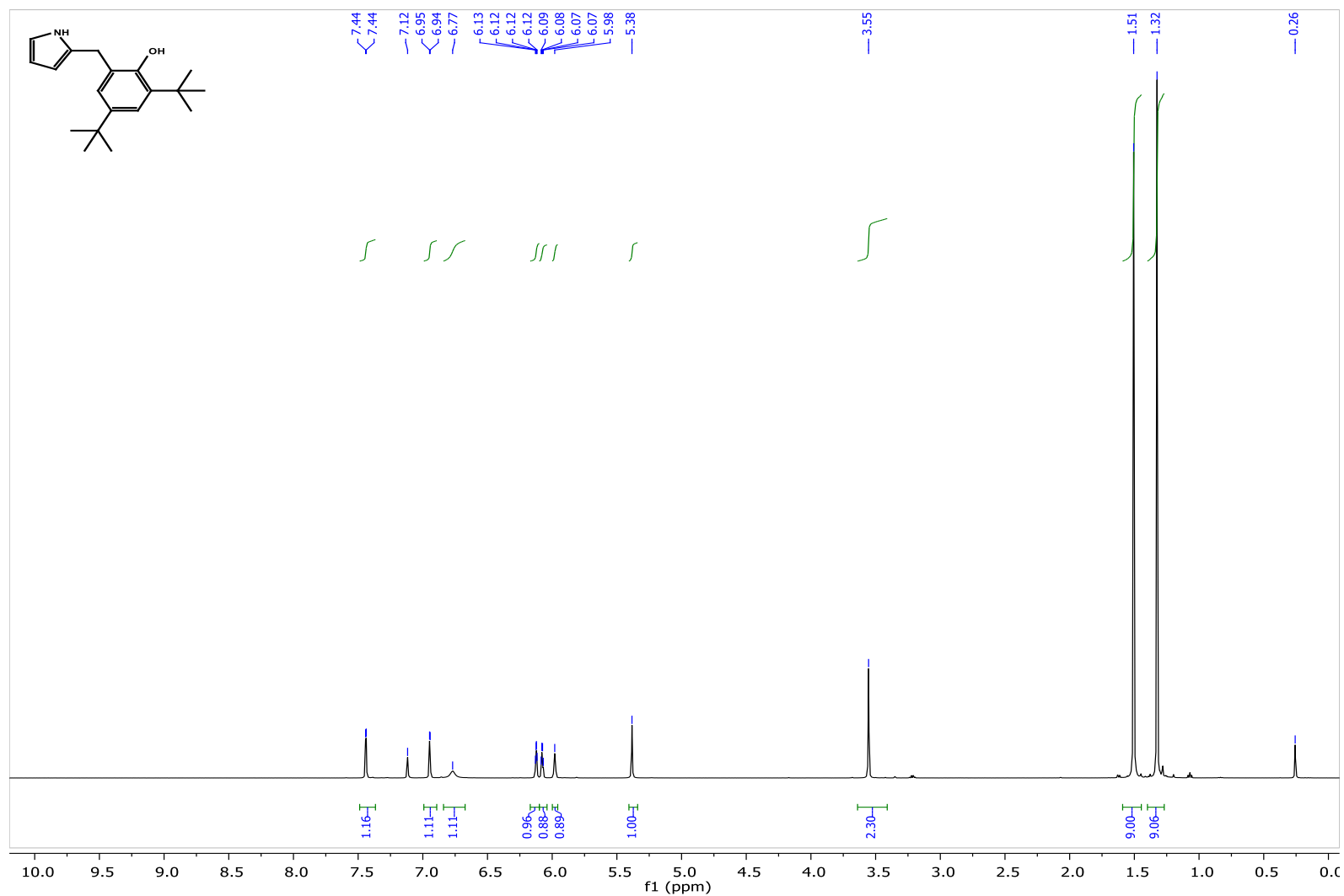


**Figure 4.14.**  $^1\text{H}$  NMR Spectrum of 2,4-di-*tert*-butyl-6-(hydroxymethyl)phenol in  $\text{C}_6\text{D}_6$ .

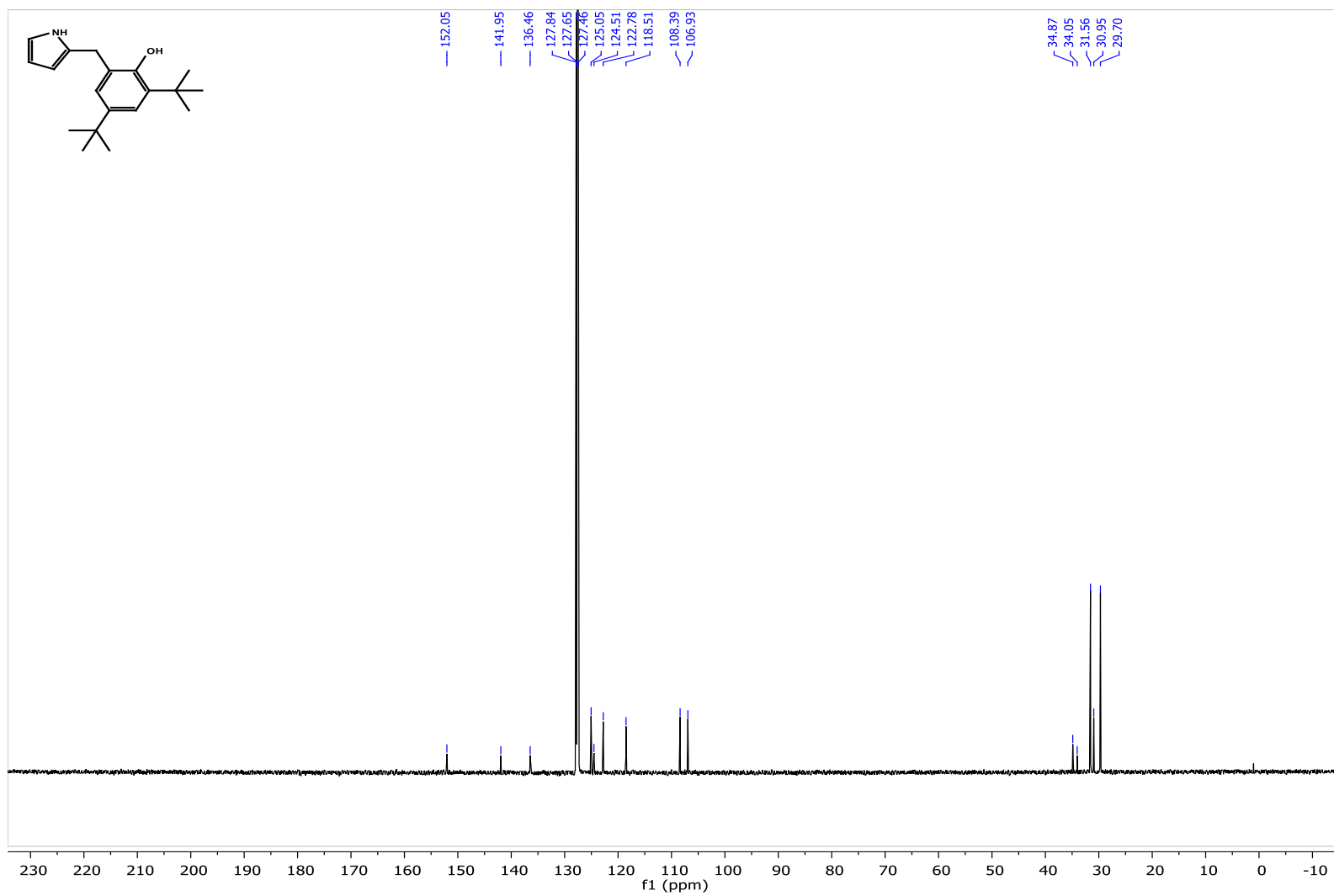


**Figure 4.15.**  $^{13}\text{C}$  NMR Spectrum of 2,4-di-*tert*-butyl-6-(hydroxymethyl)phenol in  $\text{C}_6\text{D}_6$ .

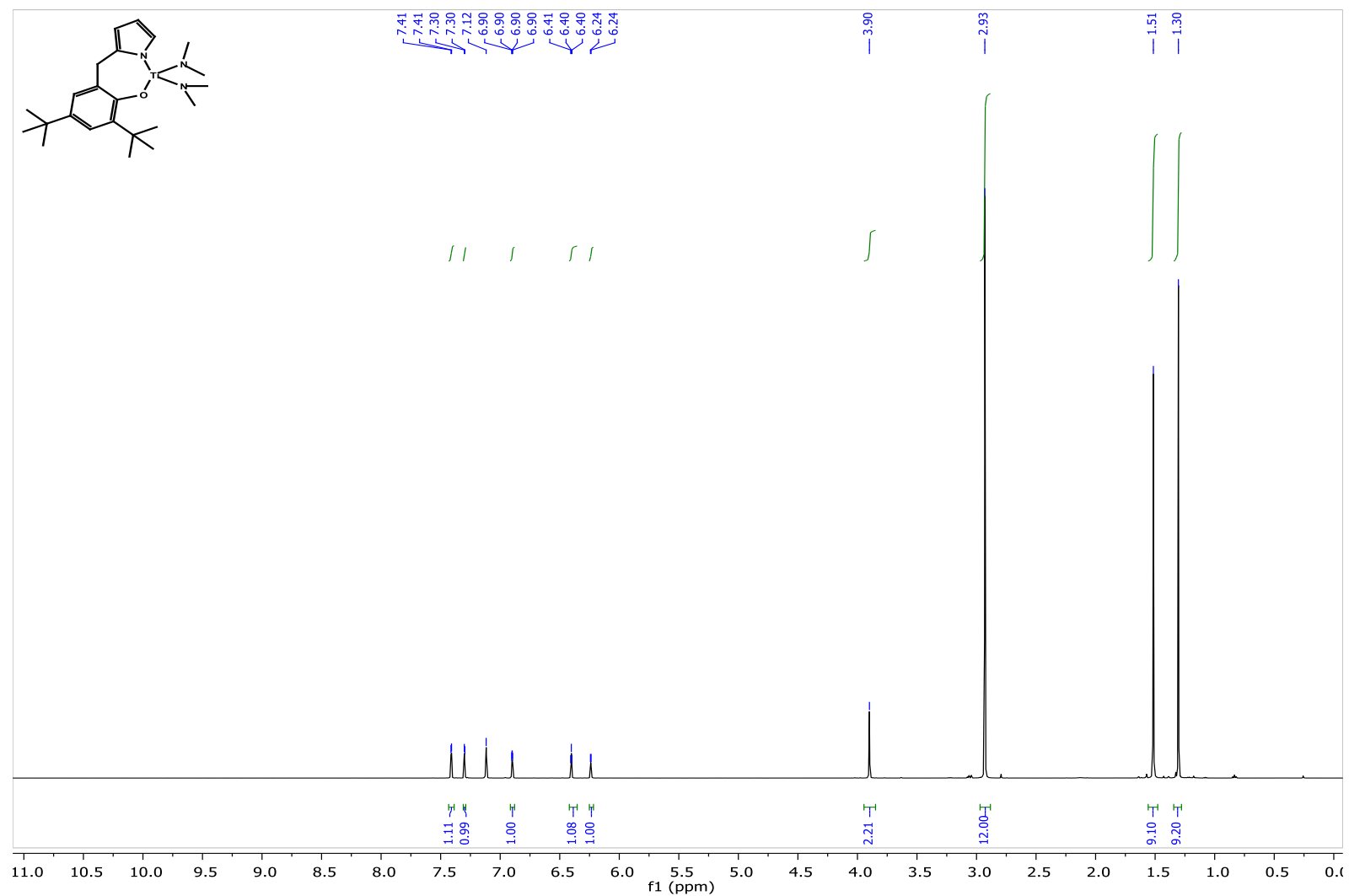




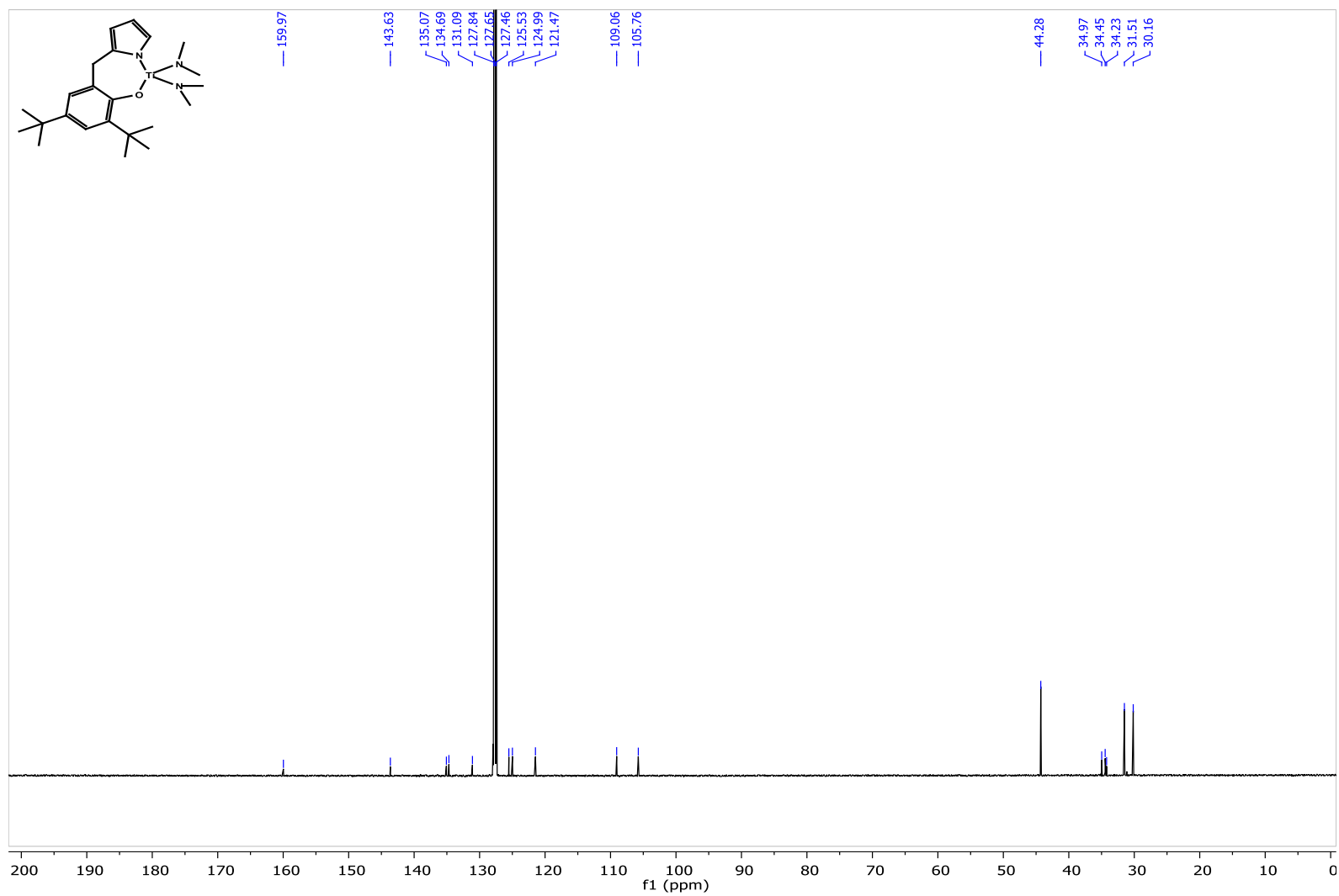
**Figure 4.16.** <sup>1</sup>H NMR Spectrum of HPyrHOAr<sup>2,4</sup>-ditertbutyl in C<sub>6</sub>D<sub>6</sub>.



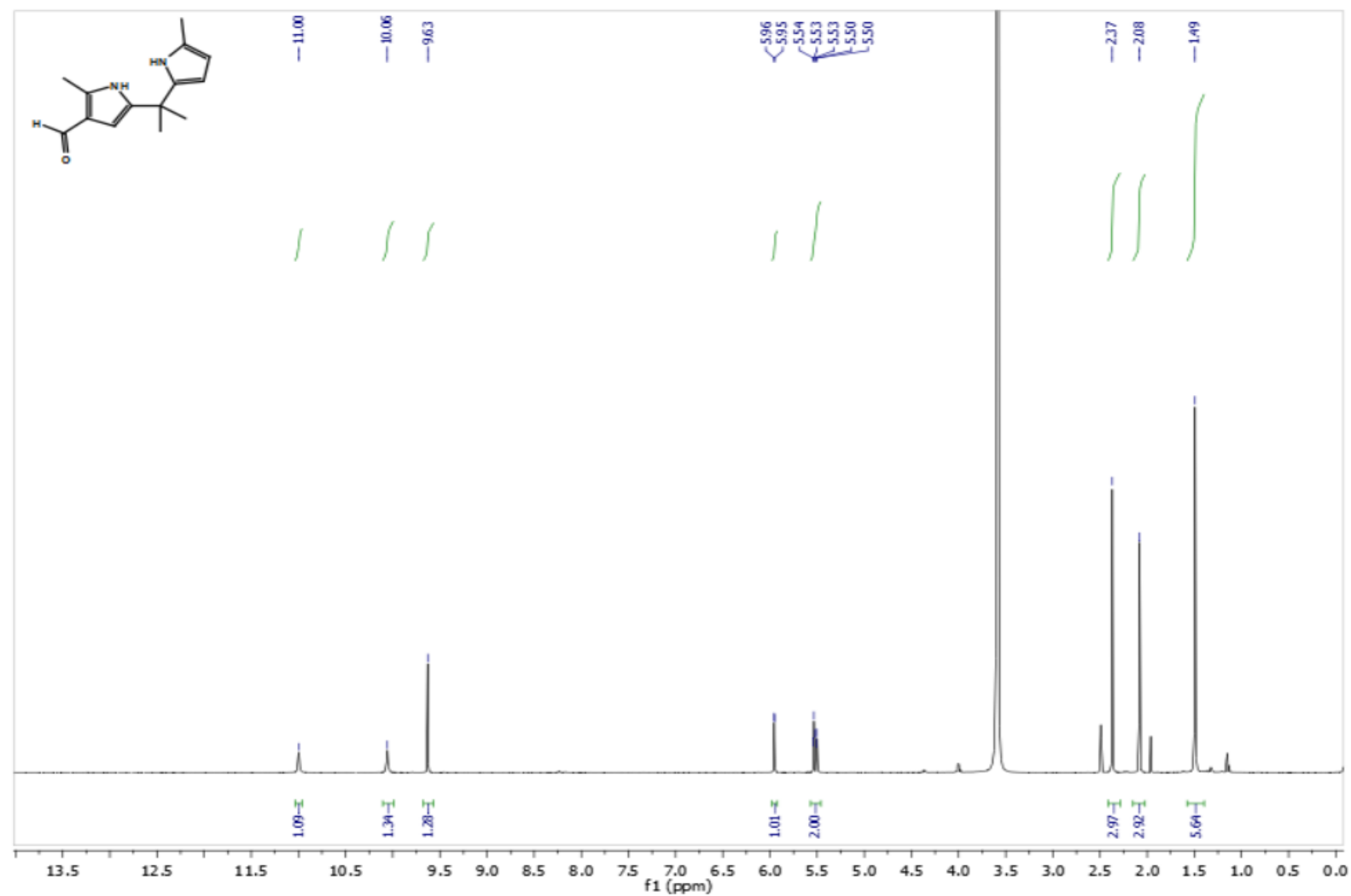
**Figure 4.17.**  $^{13}\text{C}$  NMR Spectrum of HPyrHOAr<sup>2,4</sup>-ditertbutyl in  $\text{C}_6\text{D}_6$ .



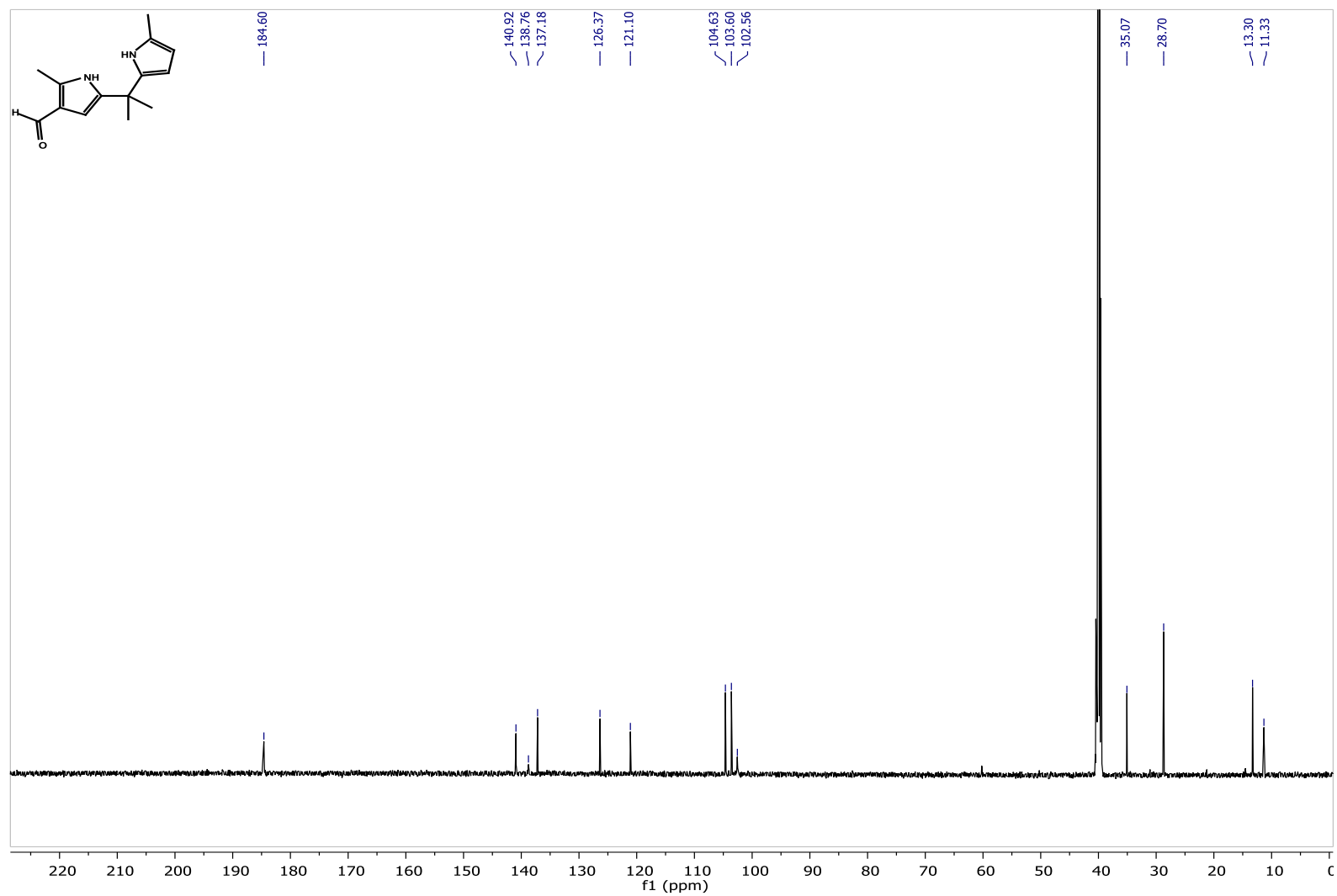
**Figure 4.18.**  $^1\text{H}$  NMR Spectrum of  $\text{Ti}(\text{PyraAr}^{2,4\text{-ditertbutyl}})(\text{NMe}_2)_2$  (**8**) in  $\text{C}_6\text{D}_6$ .



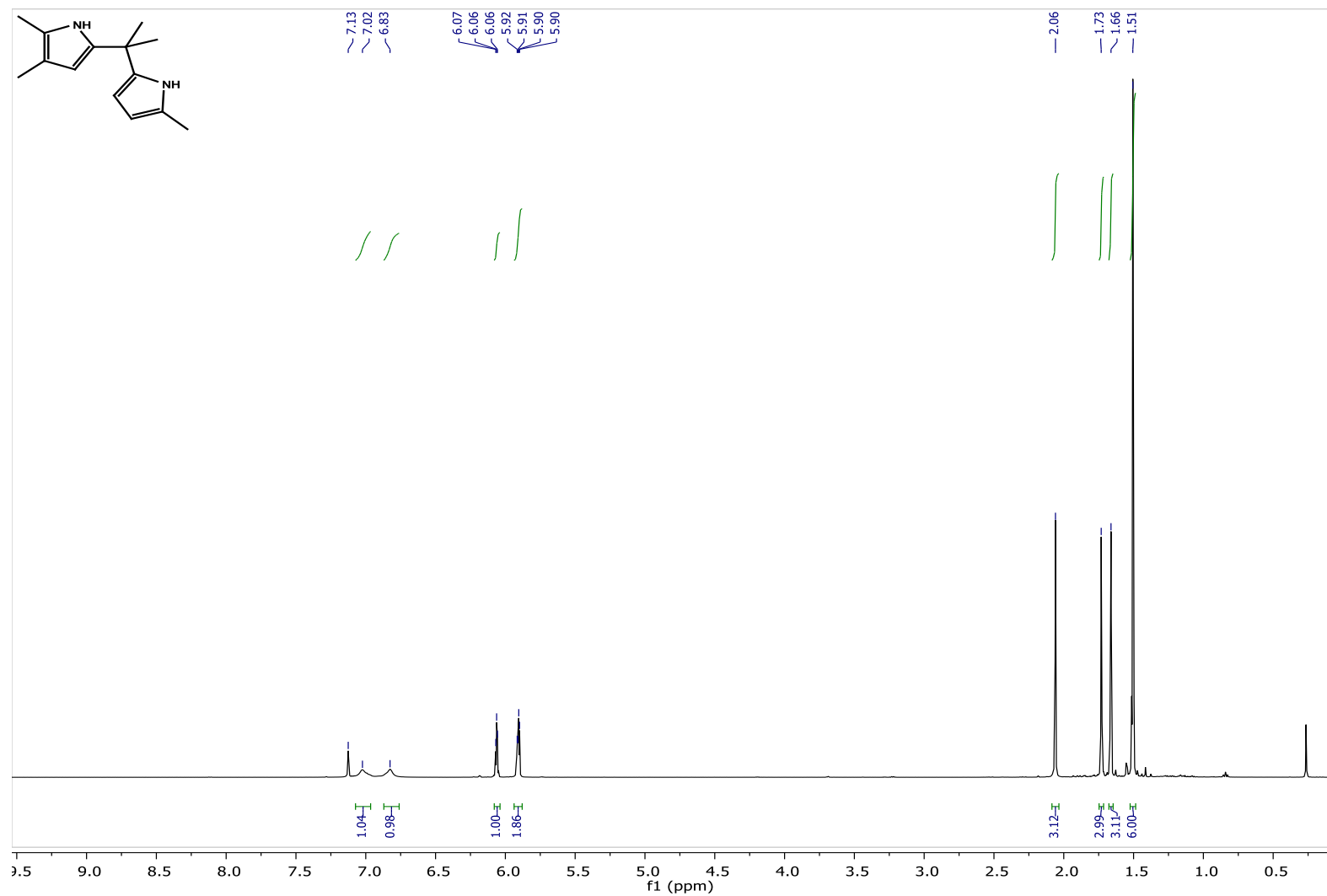
**Figure 4.19.**  $^{13}\text{C}$  NMR Spectrum of  $\text{Ti}(\text{PyrOAr}^{2,4\text{-di-tertbutyl}})(\text{NMe}_2)_2$  (8) in  $\text{C}_6\text{D}_6$ .



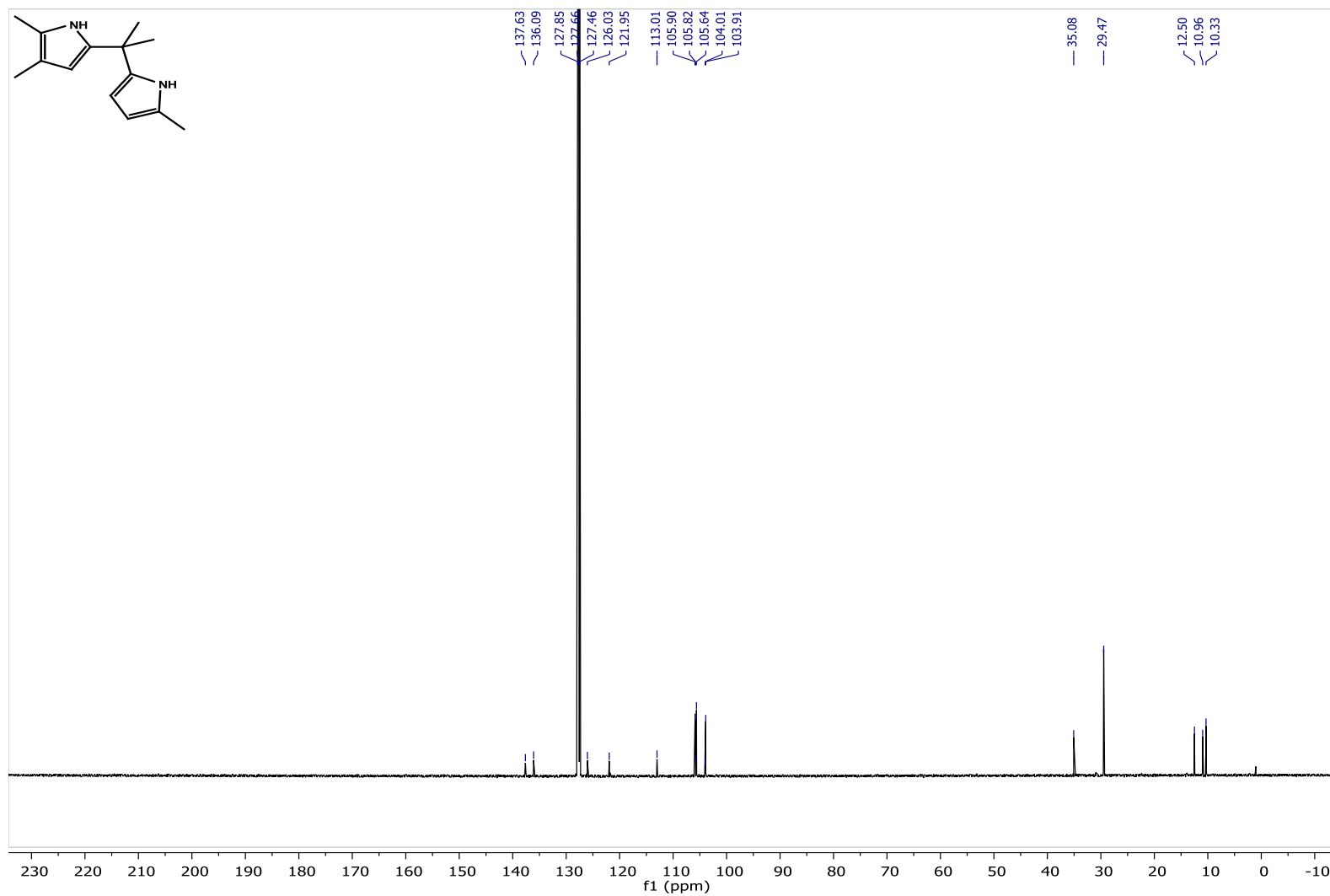
**Figure 4.20.**  $^1\text{H}$  NMR Spectrum of  $\text{H}_2\text{dpm}^{2,2'}\text{-DiMe-3-CHO}$  in  $\text{DMSO-d}_6$ .



**Figure 4.21.**  $^{13}\text{C}$  NMR Spectrum of  $\text{H}_2\text{dpm}^{2,2'}\text{-DiMe-3-CHO}$  in  $\text{DMSO-d}_6$ .

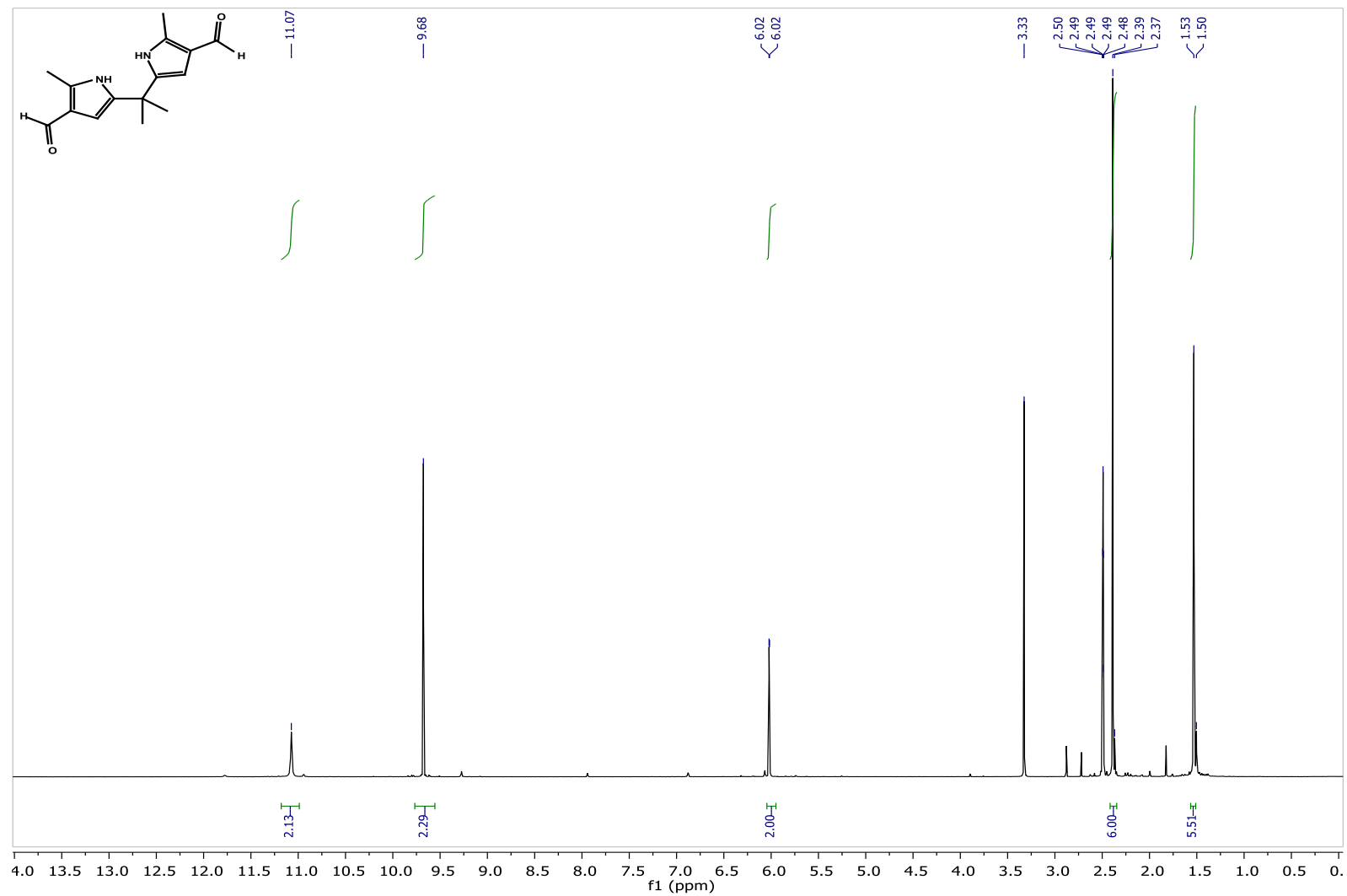


**Figure 4.22.**  $^1\text{H}$  NMR Spectrum of  $\text{H}_2\text{dpm}^{2,2',3}\text{-TriMe}$  in  $\text{C}_6\text{D}_6$ .

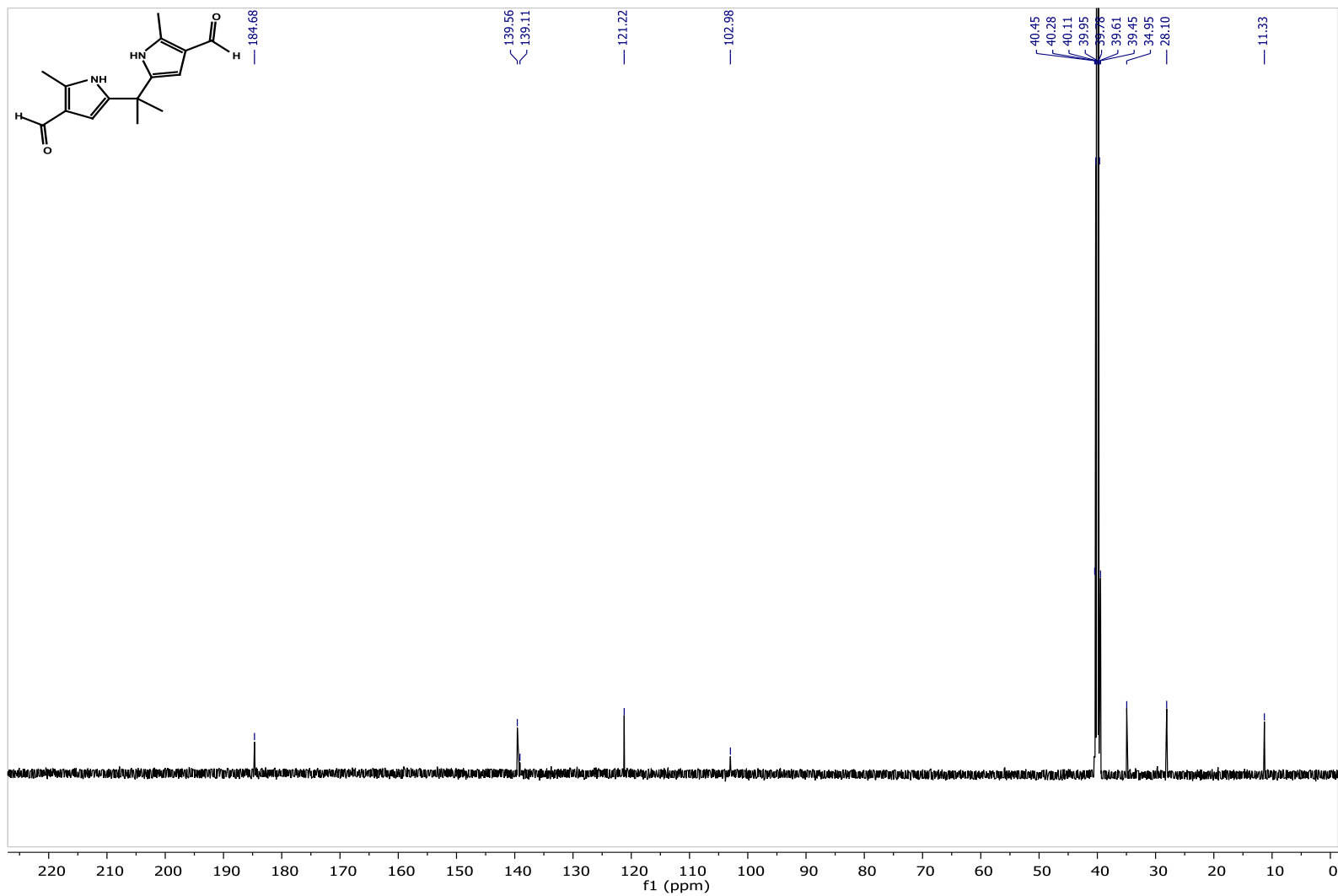


**Figure 4.23.**  $^{13}\text{C}$  NMR Spectrum of  $\text{H}_2\text{dpm}^{2,2',3}\text{-TriMe}$  in  $\text{C}_6\text{D}_6$ .

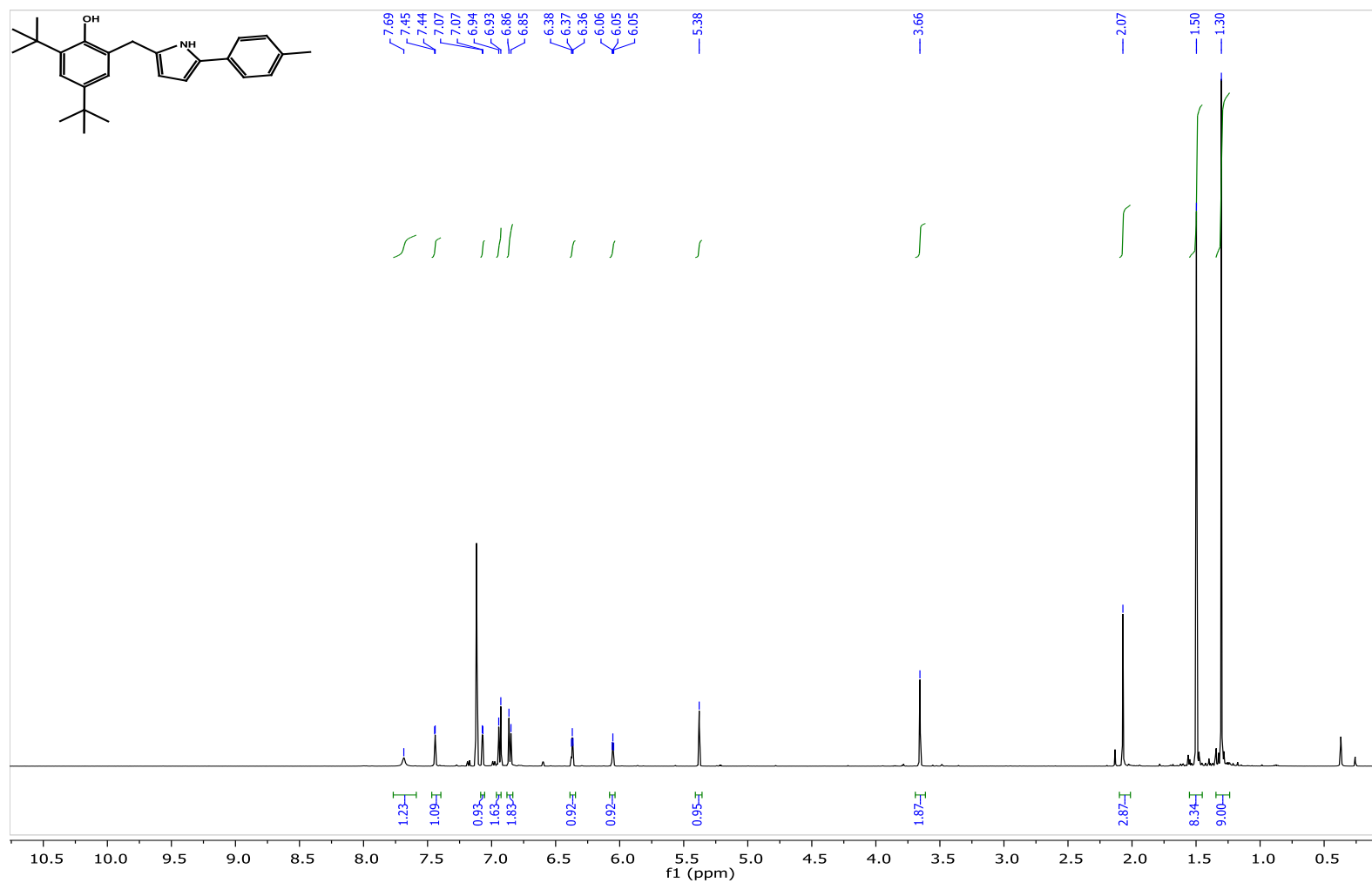




**Figure 4.24.**  $^1\text{H}$  NMR Spectrum of  $\text{H}_2\text{dpm}^{2,2'\text{-DiMe-3,3'-DiCHO}}$  in  $\text{DMSO-d}_6$ .



**Figure 4.25.**  $^{13}\text{C}$  NMR Spectrum of  $\text{H}_2\text{dpm}^{2,2'\text{-DiMe-3,3'-DiCHO}}$  in  $\text{DMSO-d}_6$ .



**Figure 4.26.** <sup>1</sup>H NMR Spectrum of HPyr<sup>2</sup>-tolylHOAr<sup>2,4</sup>-ditertbutyl in C<sub>6</sub>D<sub>6</sub>.

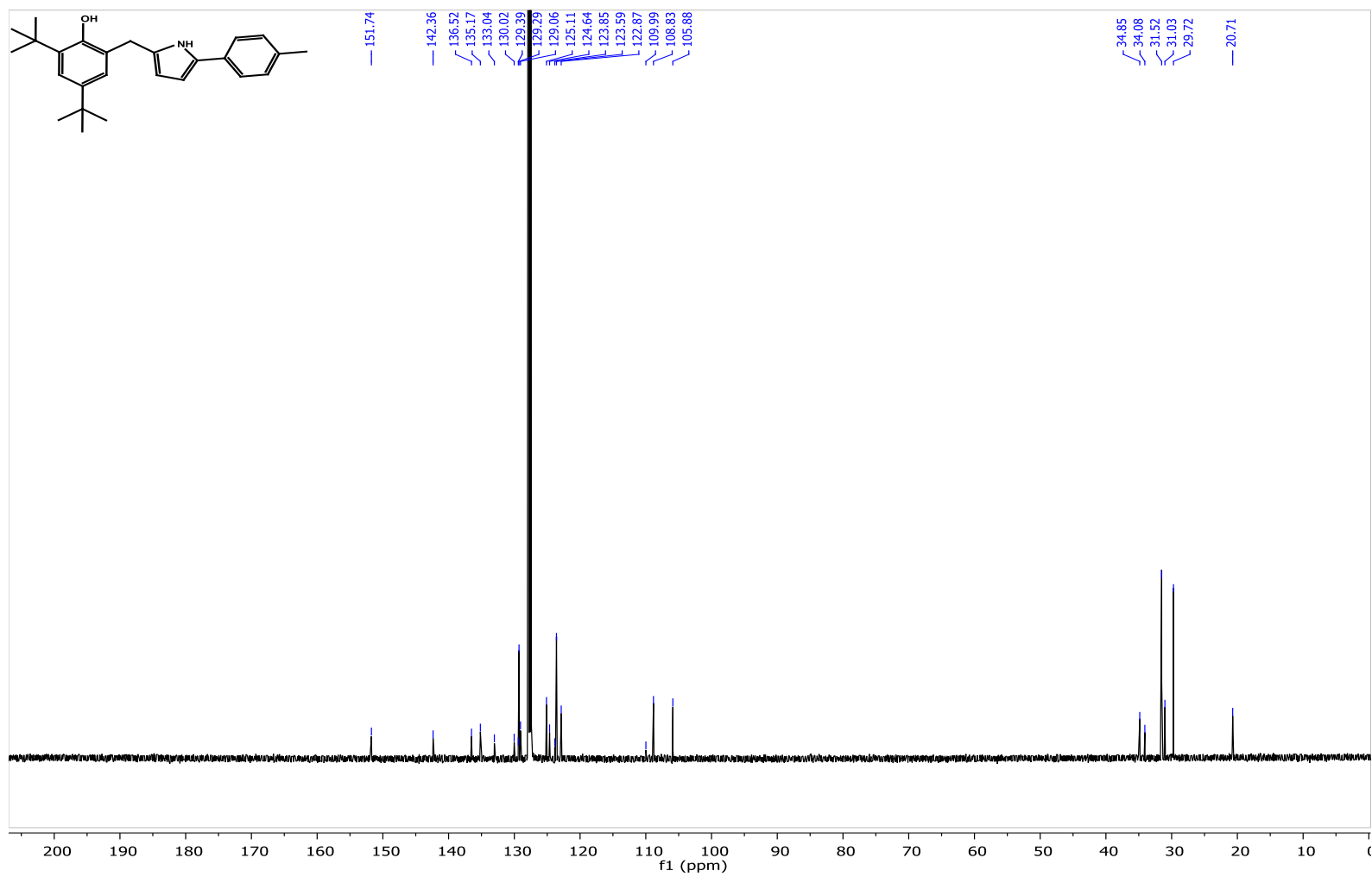
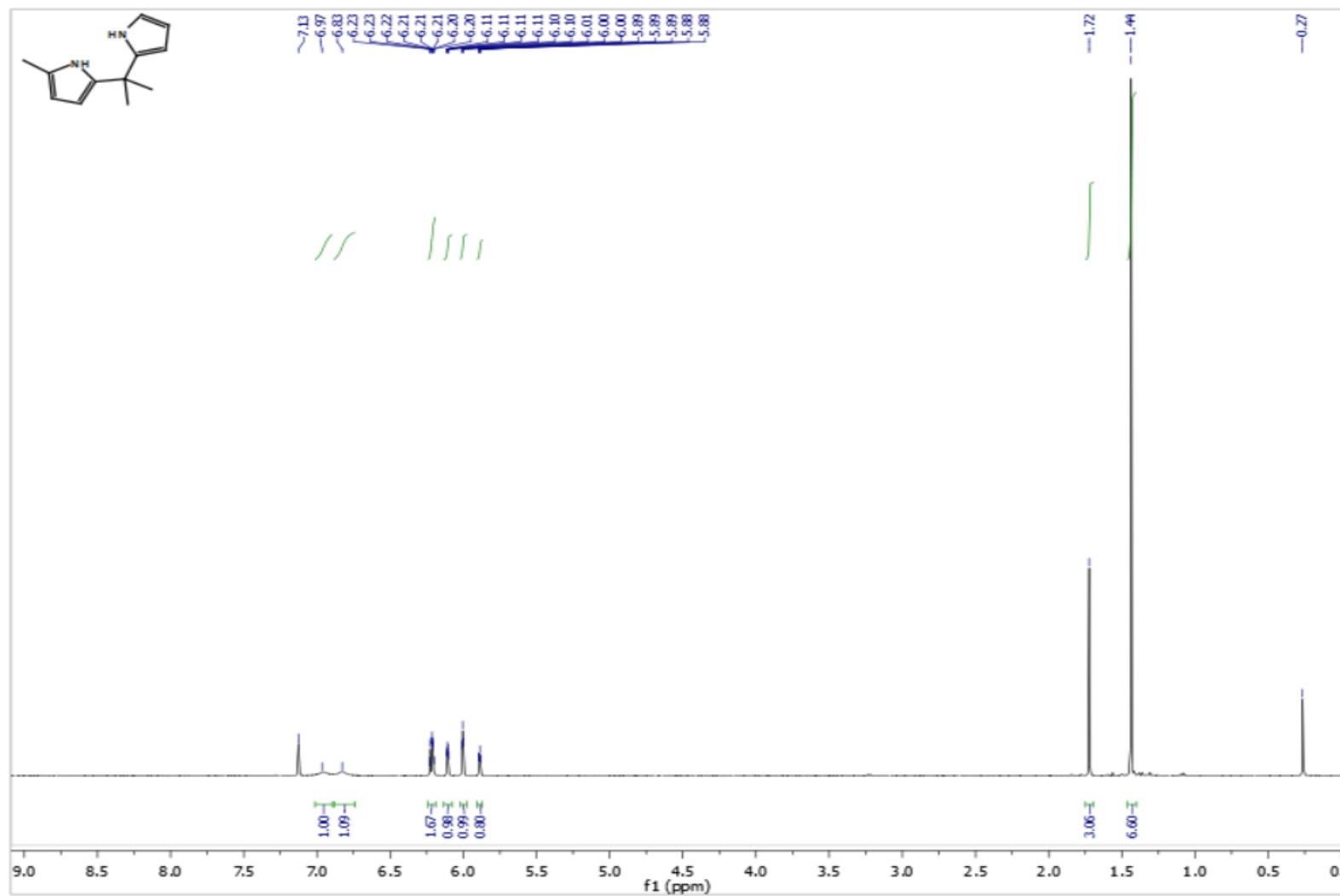
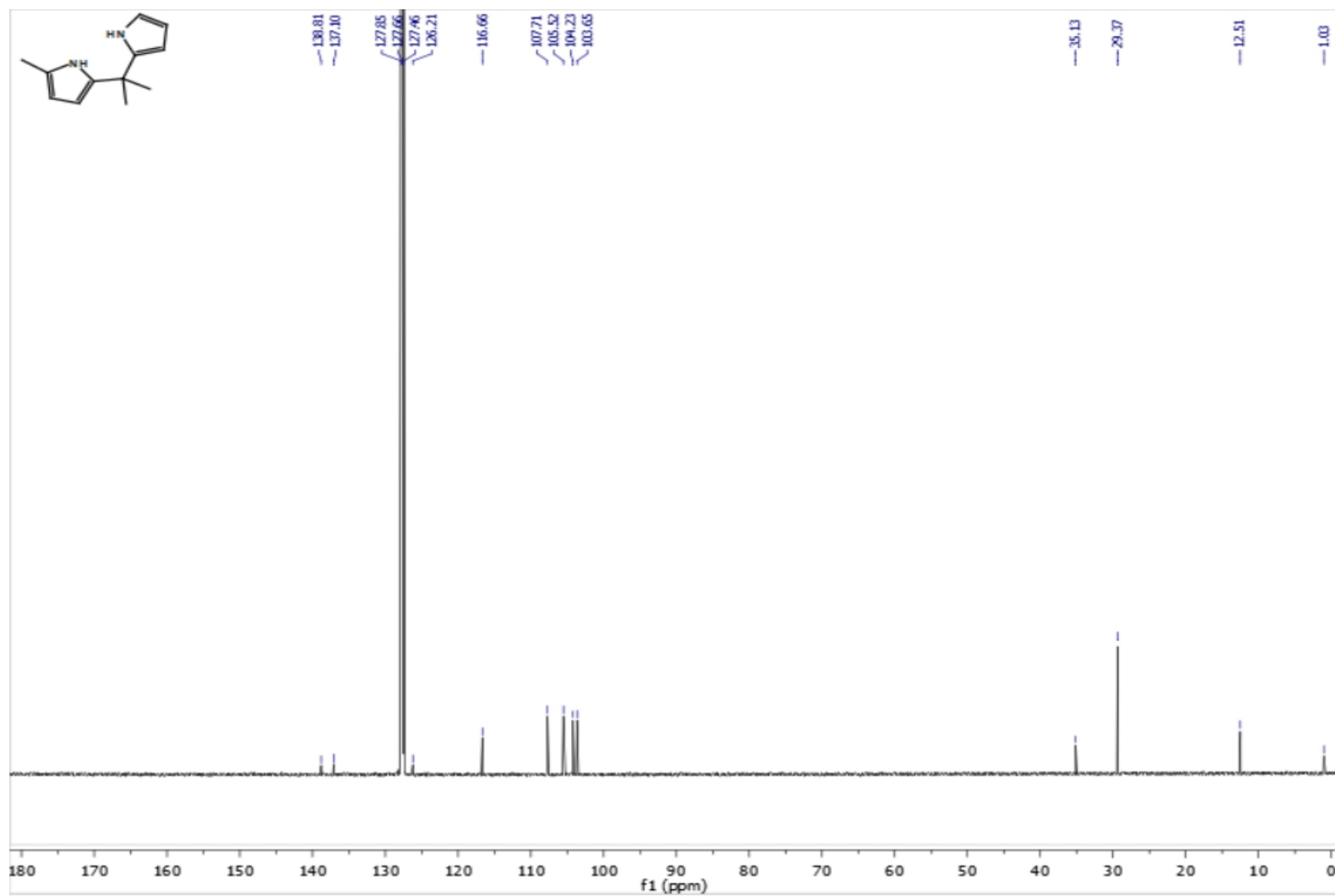


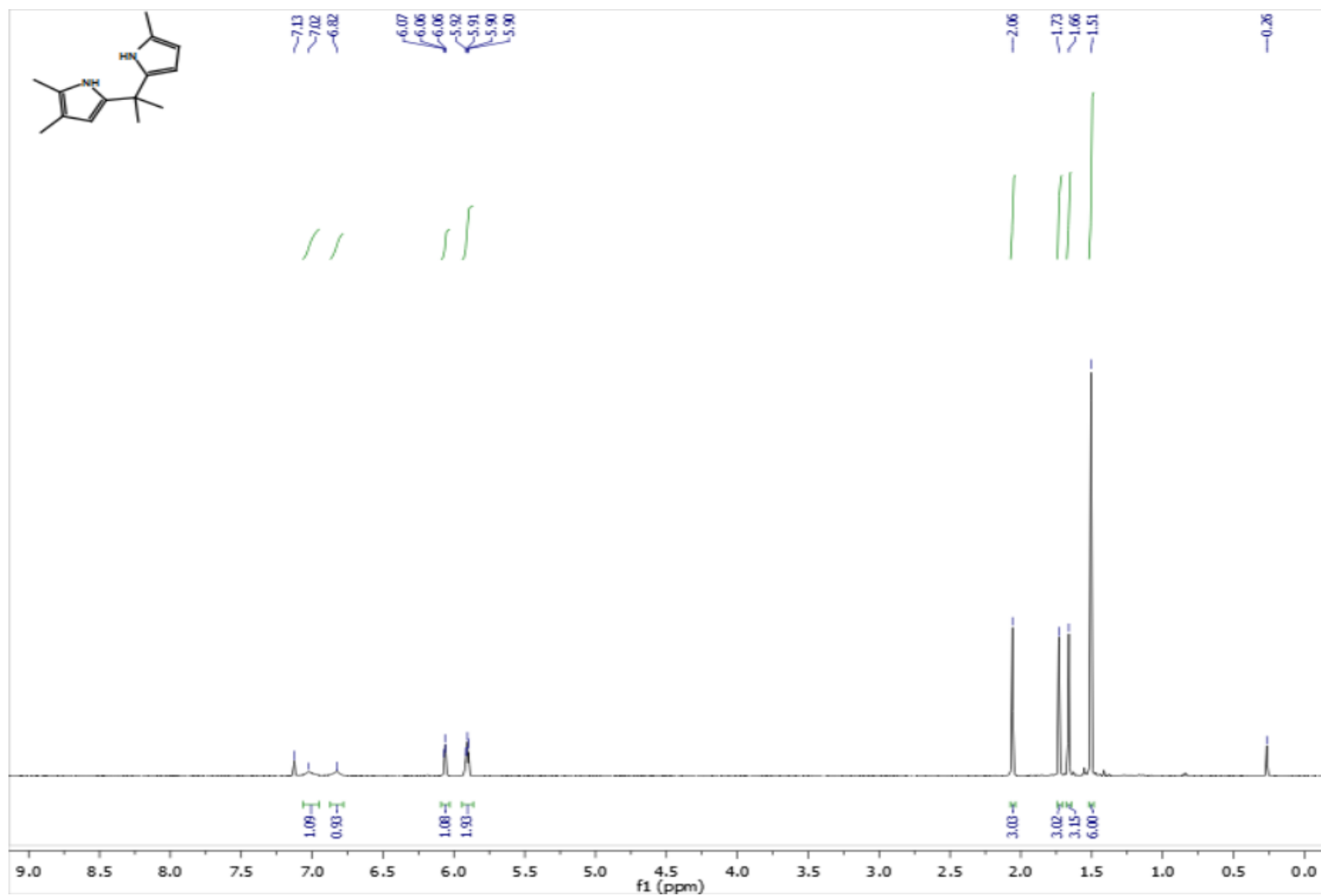
Figure 4.27. <sup>13</sup>C NMR Spectrum of HPyr<sup>2-tolyl</sup>HOAr<sup>2,4-ditertbutyl</sup> in C<sub>6</sub>D<sub>6</sub>.



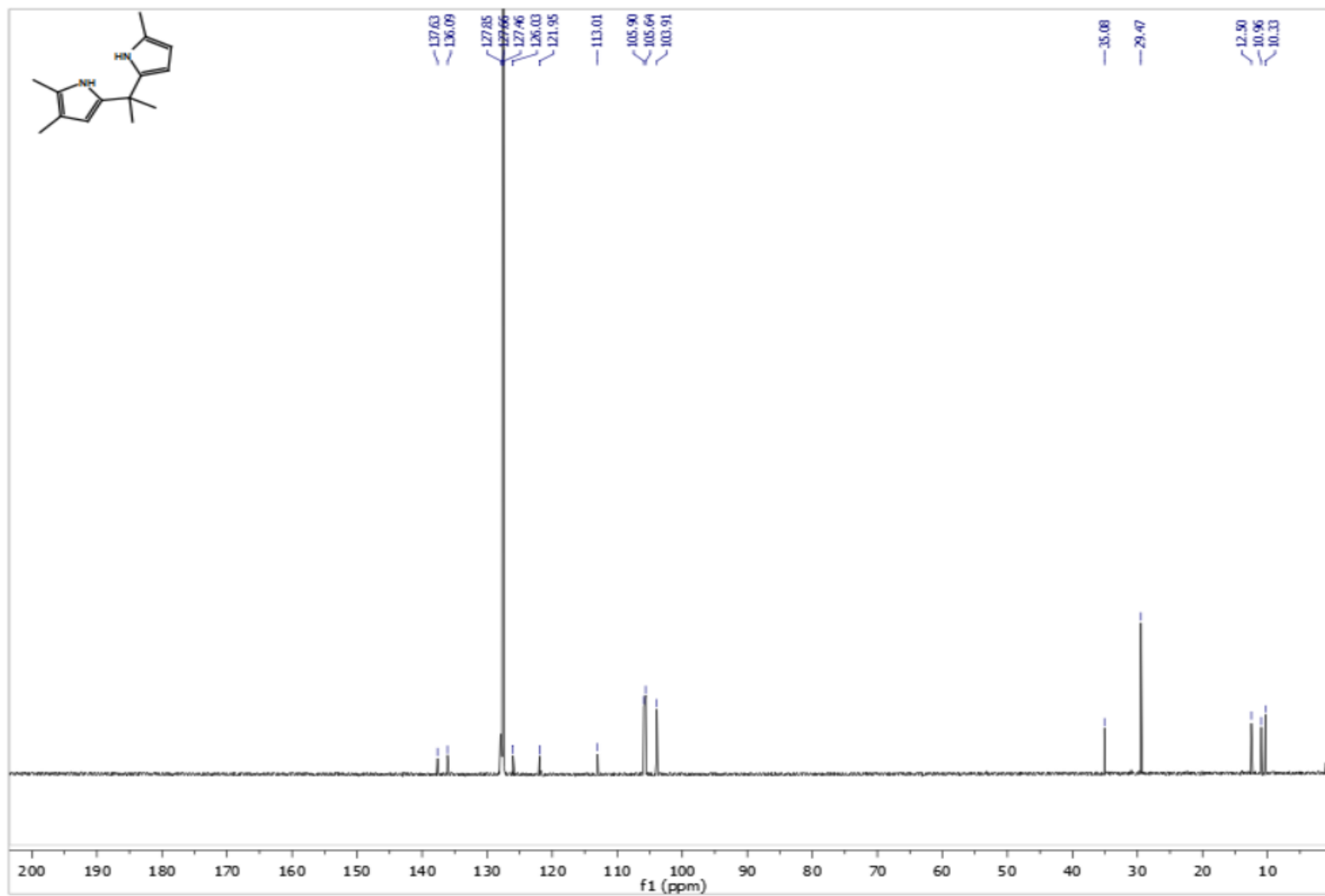
**Figure 4.28.**  $^1\text{H}$  NMR Spectrum of  $\text{H}_2\text{dpm}^{2\text{Me}}$  in  $\text{C}_6\text{D}_6$ .



**Figure 4.29.**  $^{13}\text{C}$  NMR Spectrum of  $\text{H}_2\text{dpm}^{2\text{Me}}$  in  $\text{C}_6\text{D}_6$ .

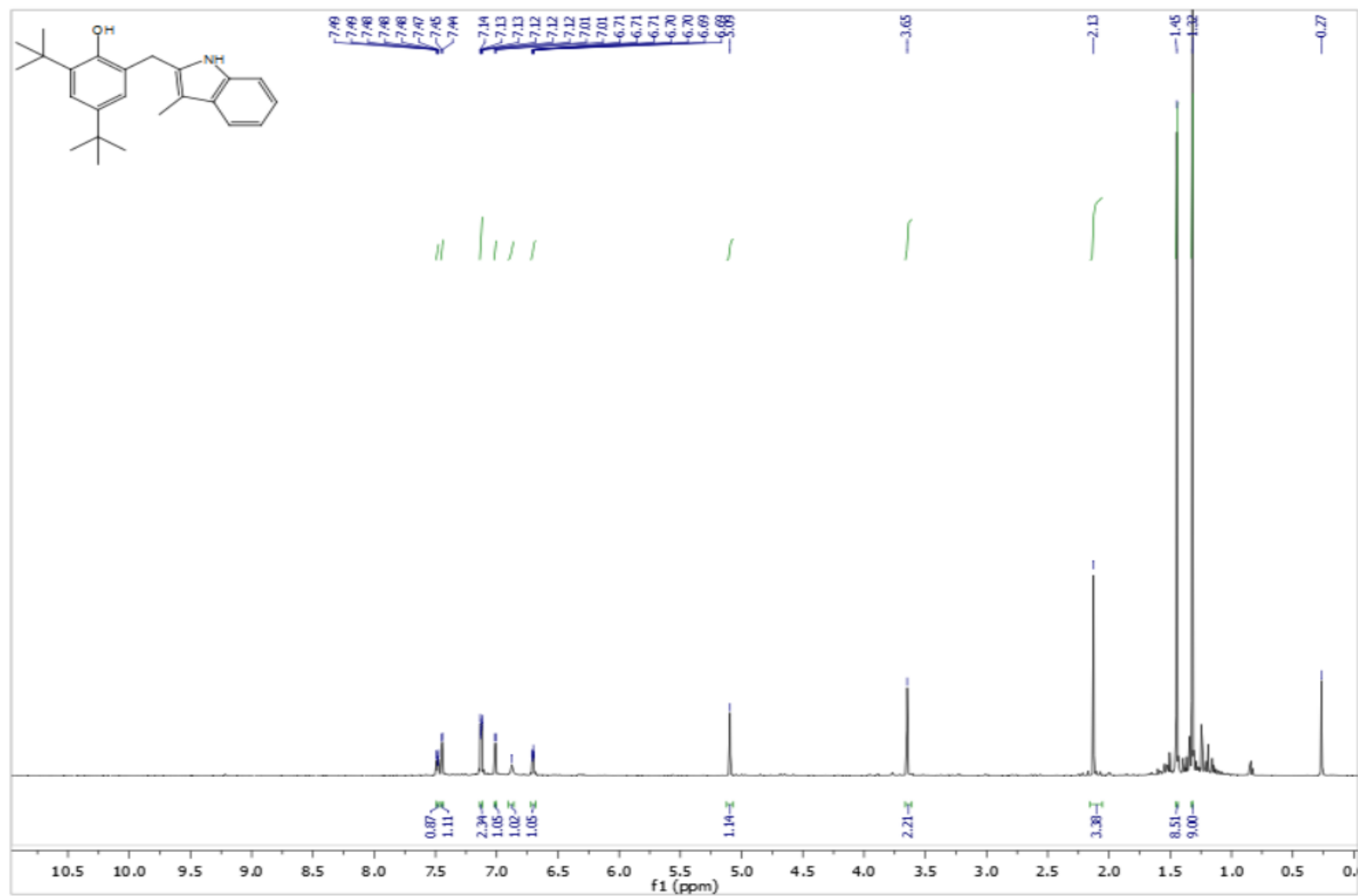


**Figure 4.30.**  $^1\text{H}$  NMR Spectrum of  $\text{H}_2\text{dpm}^{2,2',3}\text{-TriMe}$  in  $\text{C}_6\text{D}_6$ .

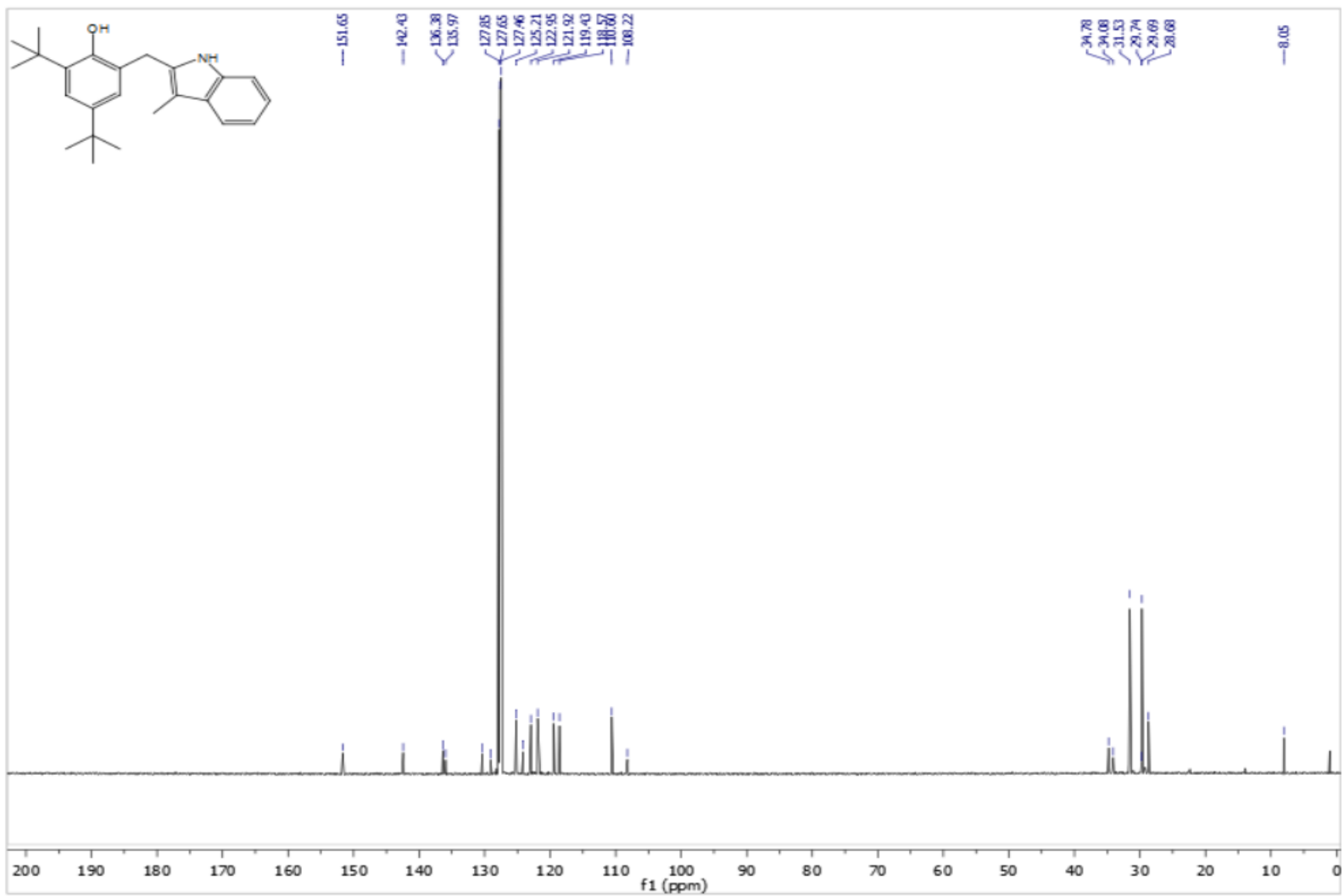


**Figure 4.31.**  $^{13}\text{C}$  NMR Spectrum of  $\text{H}_2\text{dpm}^{2,2',3}\text{-TriMe}$  in  $\text{C}_6\text{D}_6$ .

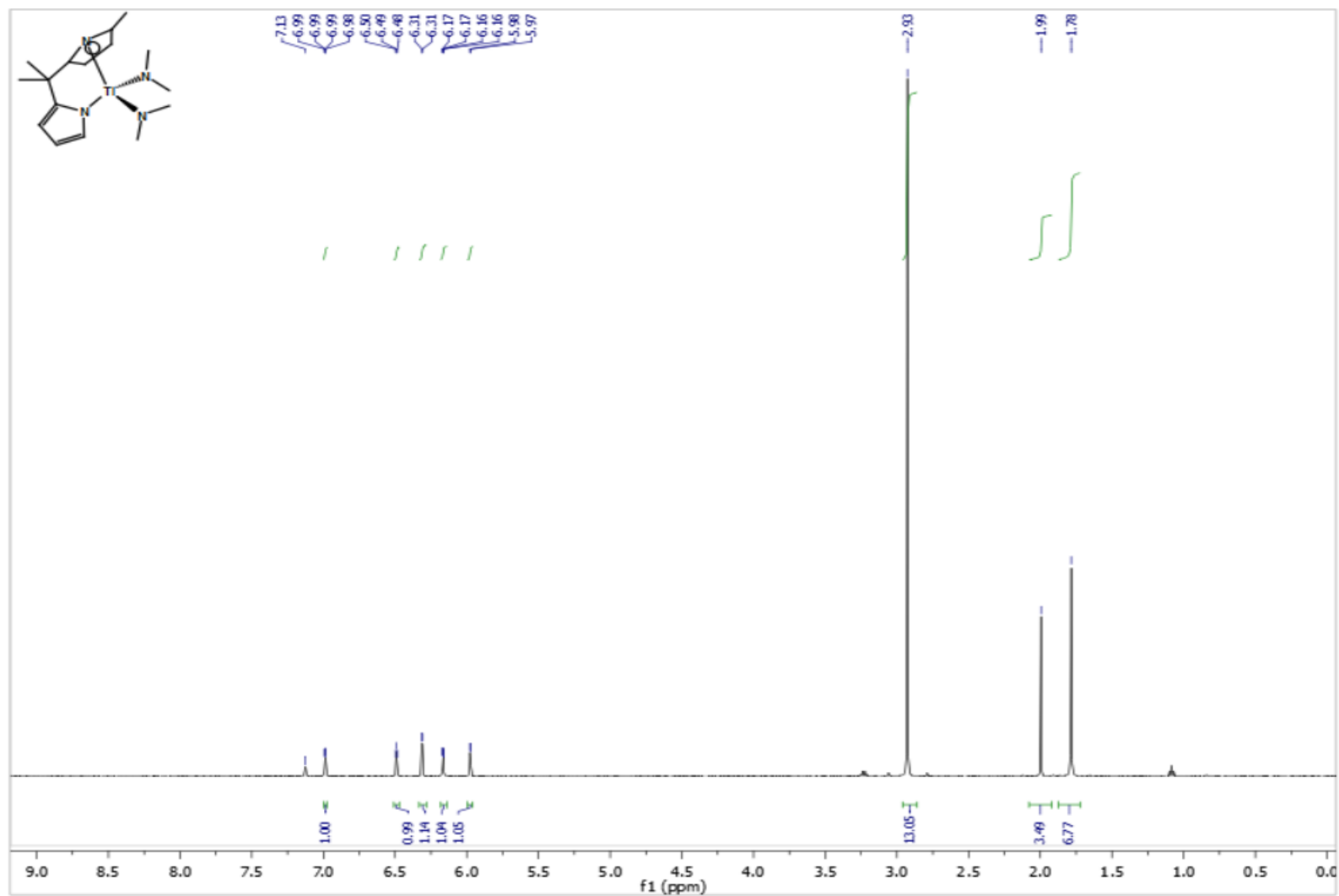




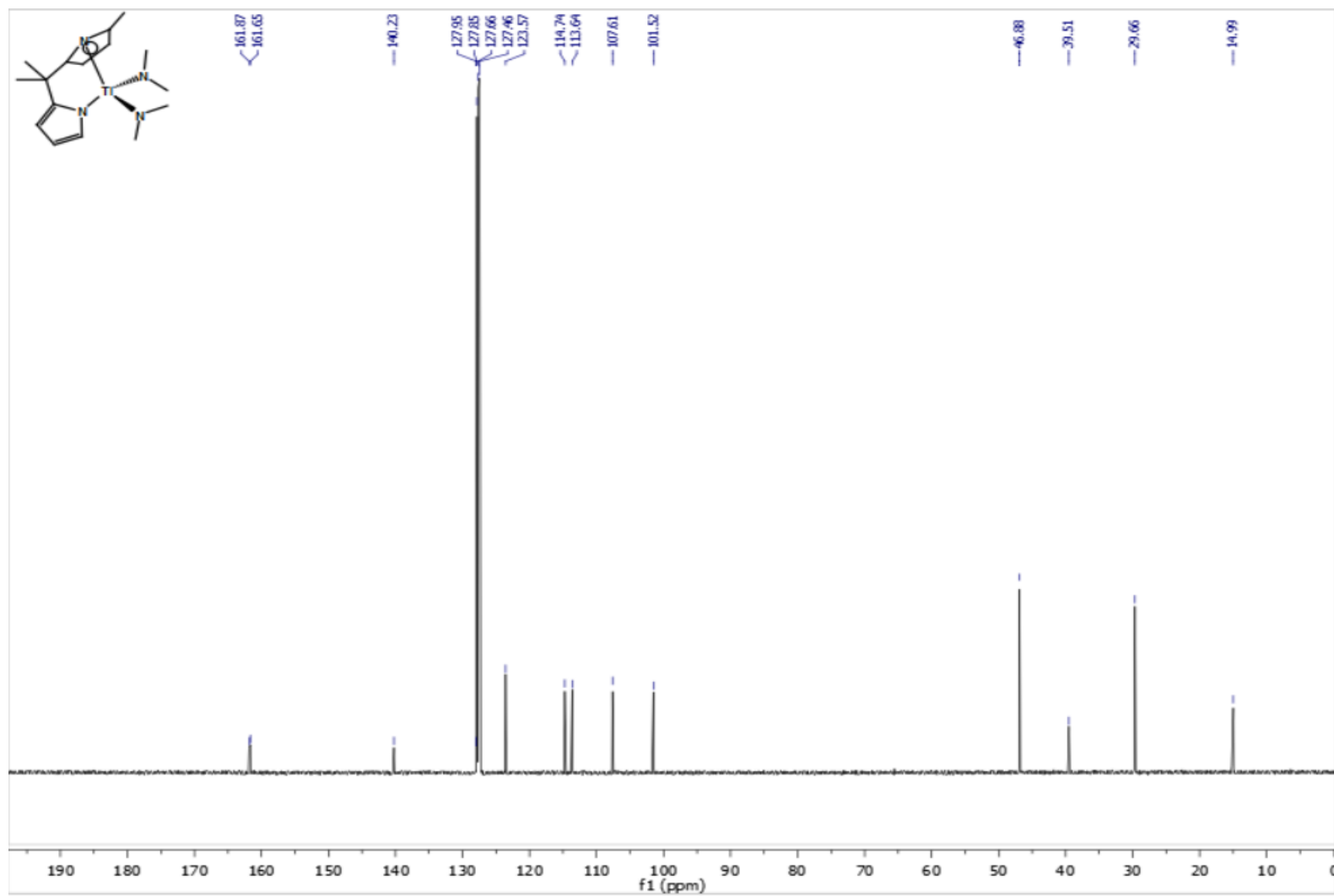
**Figure 4.32.** <sup>1</sup>H NMR Spectrum of Hind<sup>3</sup>MeHOAr<sup>2,4</sup>-ditertbutyl in C<sub>6</sub>D<sub>6</sub>.



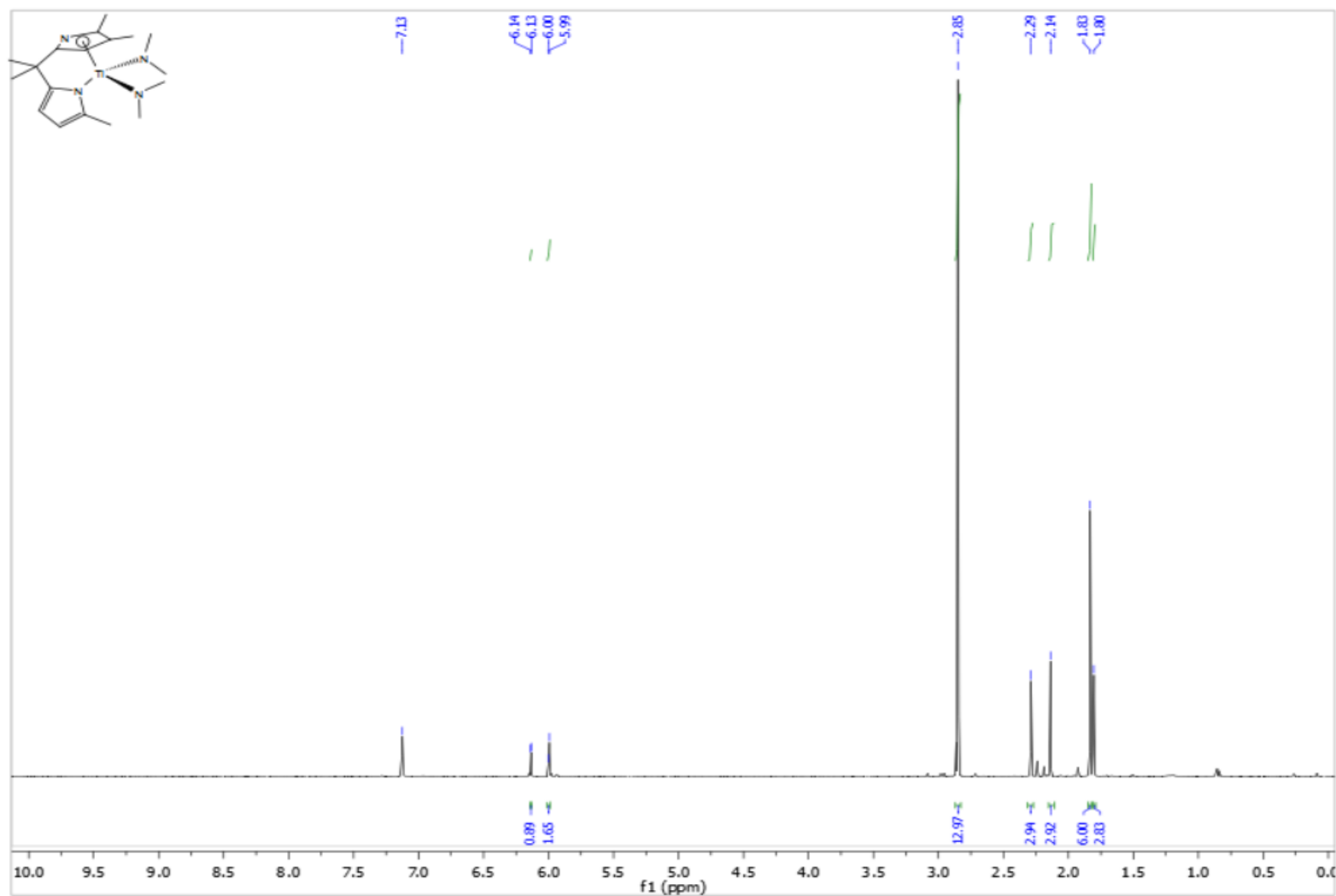
**Figure 4.33.** <sup>13</sup>C NMR Spectrum of Hind<sup>3</sup>MeHOAr<sup>2,4</sup>-ditertbutyl in C<sub>6</sub>D<sub>6</sub>.



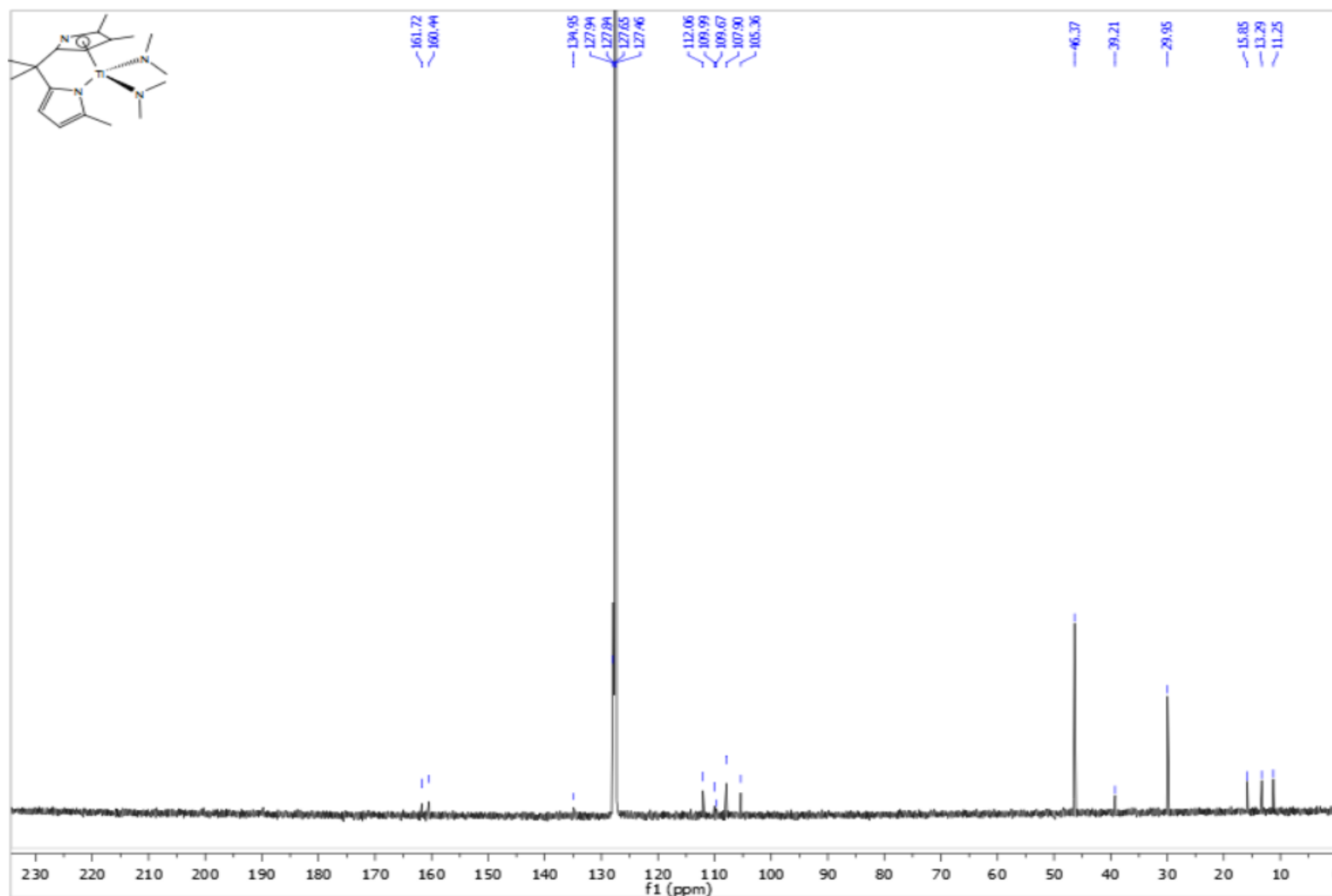
**Figure 4.34.** <sup>1</sup>H NMR Spectrum of Tidpm<sup>2Me</sup>(NMe<sub>2</sub>)<sub>2</sub> (**7a**) in C<sub>6</sub>D<sub>6</sub>.



**Figure 4.35.**  $^{13}\text{C}$  NMR Spectrum of  $\text{Tidpm}^{2\text{Me}}(\text{NMe}_2)_2$  (**7a**) in  $\text{C}_6\text{D}_6$ .



**Figure 4.36.**  $^1\text{H}$  NMR Spectrum of  $\text{Tidpm}^{2,2',3\text{-TriMe}}(\text{NMe}_2)_2$  (**7b**) in  $\text{C}_6\text{D}_6$ .



**Figure 4.37.**  $^{13}\text{C}$  NMR Spectrum of  $\text{Tidpm}^{2,2',3}\text{-TriMe}(\text{NMe}_2)_2$  (**7b**) in  $\text{C}_6\text{D}_6$ .

## REFERENCES

## REFERENCES

1. Schrock, R. R., *Chem. Rev.* **2002**, *102*, 145-180.
2. Schrock, R. R., *Chem. Rev.* **2009**, *109*, 3211-3226.
3. Sinha, A.; Schrock, R. R., *Organometallics* **2004**, *23*, 1643-1645.
4. Sinha, A.; Lopez, L. P. H.; Schrock, R. R.; Hock, A. S.; Müller, P., *Organometallics* **2006**, *25*, 1412-1423.
5. Singh, R.; Schrock, R. R.; Müller, P.; Hoveyda, A. H., *J. Am. Chem. Soc.* **2007**, *129*, 12654-12655.
6. Poater, A.; Solans-Monfort, X.; Clot, E.; Copéret, C.; Eisenstein, O., *J. Am. Chem. Soc.* **2007**, *129*, 8207-8216.
7. Solans-Monfort, X.; Clot, E.; Copéret, C.; Eisenstein, O., *J. Am. Chem. Soc.* **2005**, *127*, 14015-14025.
8. Hoveyda, A. H., *J. Org. Chem.* **2014**, *79*, 4763-4792.
9. Sattely, E. S.; Meek, S. J.; Malcolmson, S. J.; Schrock, R. R.; Hoveyda, A. H., *J. Am. Chem. Soc.* **2009**, *131*, 943-953.
10. Billow, B. S.; McDaniel, T. J.; Odom, A. L., *Nat Chem* **2017**, *9*, 837-842.
11. Eerdun, C.; Hisanaga, S.; Setsune, J.-i., *Angew. Chem. Int. Ed.* **2013**, *52*, 929-932.
12. Pordea, A.; Stoeckli-Evans, H.; Dalvit, C.; Neier, R., *Helv. Chim. Acta* **2012**, *95*, 2249-2264.
13. At this time the LDP or % Vbur was not determined for 2,3-dimethylpyrrole. However, the 2,4-dimethylpyrrole was known and should be a good approximation for the donor ability of the 2,3-dimethylpyrrole (LDP = 13.09). See how the 2,4-dimethylpyrrole and 2,3,4-trimethylpyrrole both have the same % Vbur (23.1), this value was used for the sterics.
14. Pohlki, F.; Doye, S., *Angew. Chem. Int. Ed.* **2001**, *40*, 2305-2308.
15. Larock, R. C.; Yum, E. K.; Refvik, M. D., *J. Org. Chem.* **1998**, *63*, 7652-7662.
16. Batrice, R. J.; Fridman, N.; Eisen, M. S., *Inorg Chem* **2016**.
17. Bergner, M.; Duquette, D. C.; Chio, L.; Stoltz, B. M., *Org. Lett.* **2015**, *17*, 3008-10.



18. Espenson, J., H., *Chemical Kinetics and Reaction Mechanisms*. 2nd Ed ed.; McGraw Hill: New York, 2002.